frontiers | Research Topics

Soil and sediment pollution, processes and remediation, volume II

Edited by
Jun Zhou, Hongbiao Cui, Zhu Li, Chunhao Gu and Buyun Du

Published in
Frontiers in Environmental Science

ISSN 1664-8714
ISBN 978-2-83251-112-1
DOI 10.3389/978-2-83251-112-1

About Frontiers

Frontiers is more than just an open access publisher of scholarly articles: it is a pioneering approach to the world of academia, radically improving the way scholarly research is managed. The grand vision of Frontiers is a world where all people have an equal opportunity to seek, share and generate knowledge. Frontiers provides immediate and permanent online open access to all its publications, but this alone is not enough to realize our grand goals.

Frontiers journal series

The Frontiers journal series is a multi-tier and interdisciplinary set of open-access, online journals, promising a paradigm shift from the current review, selection and dissemination processes in academic publishing. All Frontiers journals are driven by researchers for researchers; therefore, they constitute a service to the scholarly community. At the same time, the *Frontiers journal series* operates on a revolutionary invention, the tiered publishing system, initially addressing specific communities of scholars, and gradually climbing up to broader public understanding, thus serving the interests of the lay society, too.

Dedication to quality

Each Frontiers article is a landmark of the highest quality, thanks to genuinely collaborative interactions between authors and review editors, who include some of the world's best academicians. Research must be certified by peers before entering a stream of knowledge that may eventually reach the public - and shape society; therefore, Frontiers only applies the most rigorous and unbiased reviews. Frontiers revolutionizes research publishing by freely delivering the most outstanding research, evaluated with no bias from both the academic and social point of view. By applying the most advanced information technologies, Frontiers is catapulting scholarly publishing into a new generation.

What are Frontiers Research Topics?

Frontiers Research Topics are very popular trademarks of the *Frontiers journals series*: they are collections of at least ten articles, all centered on a particular subject. With their unique mix of varied contributions from Original Research to Review Articles, Frontiers Research Topics unify the most influential researchers, the latest key findings and historical advances in a hot research area.

Find out more on how to host your own Frontiers Research Topic or contribute to one as an author by contacting the Frontiers editorial office: frontiersin.org/about/contact

Soil and sediment pollution, processes and remediation, volume II

Topic editors

Jun Zhou — University of Massachusetts Lowell, United States
Hongbiao Cui — Anhui University of Science and Technology, China
Zhu Li — Institute of Soil Science, Chinese Academy of Sciences (CAS), China
Chunhao Gu — University of Delaware, United States
Buyun Du — Jiangsu Open University, China

Citation

Zhou, J., Cui, H., Li, Z., Gu, C., Du, B., eds. (2023). *Soil and sediment pollution, processes and remediation, volume II*. Lausanne: Frontiers Media SA.
doi: 10.3389/978-2-83251-112-1

Table of contents

frontiers | Frontiers in Environmental Science

TYPE Editorial
PUBLISHED 07 December 2022
DOI 10.3389/fenvs.2022.1105471

OPEN ACCESS

EDITED AND REVIEWED BY
Yuncong Li,
University of Florida, United States

*CORRESPONDENCE
Jun Zhou,
Jun_Zhou@uml.edu,
zhoujun@issas.ac.cn

SPECIALTY SECTION
This article was submitted to Soil Processes,
a section of the journal
Frontiers in Environmental Science

RECEIVED 22 November 2022
ACCEPTED 01 December 2022
PUBLISHED 07 December 2022

CITATION
Du B, Cui H, Gu C, Li Z and Zhou J (2022), Editorial: Soil and sediment pollution, processes and remediation, volume II.
Front. Environ. Sci. 10:1105471.
doi: 10.3389/fenvs.2022.1105471

Editorial: Soil and sediment pollution, processes and remediation, volume II

Buyun Du[1,2], Hongbiao Cui[3], Chunhao Gu[4], Zhu Li[5] and Jun Zhou[2,5]*

[1]College of Environmental Ecology, Jiangsu Open University, Nanjing, China, [2]Department of Environmental, Earth, and Atmospheric Sciences, University of Massachusetts, Lowell, MA, United States, [3]School of Earth and Environment, Anhui University of Science and Technology, Huainan, China, [4]Environmental Soil Chemistry Group, Department of Plant and Soil Sciences, Delaware Environmental Institute, University of Delaware, Newark, DE, United States, [5]Key Laboratory of Soil Environment and Pollution Remediation, Institute of Soil Science, Chinese Academy of Sciences, Nanjing, China

KEYWORDS

soil and sediment pollution, risk assessment, risk control, environmental process, remediation, pollutant, environmental modeling, biogeochemical process

Editorial on the Research Topic
Soil and sediment pollution, processes and remediation, volume II

Since industrialization, anthropogenic activities have generated a large amount of toxic organic and inorganic pollutants that have been emitted to the surface environment, posing several risks to ecological environment and public health (Song et al., 2017; Du et al., 2020). Industrial activities produce large numbers of pollutants (e.g., heavy metals, excess nutrient microelements, pesticides, antibiotics, environmental hormones, antibiotics resistance genes, pathogens, and microplastics) that reach soil and sediment *via* waste discharge, mining activities, abusive use of fertilizer and pesticides, and wastewater irrigation, atmospheric transport, and other disposal pathways (Liu et al., 2019; Zhou et al., 2020; Han et al., 2021; Liu et al., 2022). These pollutants can accumulate in soils and sediments, posing significant threats to food security. A lot of industrial sites are abandoned due to weak environmental management (insufficient management, legislation, and enforcement). The pollution process, migration, transformation, degradation, and accumulation of toxic pollutants in soils and sediments are not well understood and remediation are required if these soils are reused.

Most importantly, tracing the sources of pollutants is critical to understand their pollution levels and fates, which are effectively control soil and sediment pollution. There are many method has been used, such as concentration gradient, matrix models, relative enrichment factors, and isotopes. Recently, many remediation methods including physical, chemical, biological, and combined methods were proposed and adopted for the purpose of solving the problems of soil and sediment pollution (Song et al., 2017; Du et al., 2022; Khanam et al., 2022). The remediation method is usually dependent upon the pollutant characters and levels in soil and sediment. Through remediation, prime land in established locations can be reused (e.g., agricultural, residential, and commercial land), thereby lowering the pressure on green

land. Therefore, studies on the biogeochemical processes of soil and sediment pollution, control, and remediation are urgently needed. Since soil and sediment remediation followed by redevelopment prevent degradation of the environment, it is a topic of enormous public interest.

In this Research Topic, we wish to include studies on pollutants such as heavy metals, excess nutrient microelements, pesticides, antibiotics, environmental hormones, antibiotics resistance genes, pathogens, and microplastics. This Research Topic covers the following themes: 1) Sources, migration, and transformation of pollutants in soil and sediment; 2) Plant and microbe response and environmental effect in polluted soils; 3) Biogeochemistry and processes of pollutants between the atmosphere, organisms, water, and soil/sediment systems; 4) Safe use and risk assessment and control of contaminated soil and sediment; 5) Mitigation and remediation technologies; and 6) Environmental modeling of the fate and biogeochemical process of pollutants.

This collection of articles features critical interdisciplinary questions related to the environmental pollution, processes, and remediation of soil and sediment in understudied areas. It approaches a series of key questions surrounding the organic and inorganic pollutant detections, sources, accumulation characters, health risk assessments, dynamics with water, atmosphere, and microorganism, and remediation techniques. The authors of contributing papers are uniquely placed to debate the theme of soil and sediment pollution, processes and remediation. The contributors come from a range of disciplines, including Science, Technology Engineering and Mathematics (STEM) and these papers can solve real-world, urgent challenges that affect a range of societies. Of special interest is the discussion on the new method of electrostatic separation and differential scanning calorimetry for microplastic analysis in river sediments.

We hope this Special Issue can illuminate the opportunities and challenges involved in rethinking environmental pollution and processes of soil and sediment and the need for a multidisciplinary approach to fully remediate the contaminated soil and sediment. This has important implications for public health, policy guidelines, and practical solutions. To this end, we encourage more research to advance the topics of the papers contained herein, including but not limited to 1) Effectively identify the sources; 2) understand the mechanism of pollutant fate and biogeochemistry processes; 3) efficiently remove pollutants or stabilize pollutants; 4) develop more environmental friendly remediation measures and engineering technologies; 5) investigate the influences of global climate change on the fate, transformation, and transportation of the pollutants.

Author contributions

All authors listed have made a substantial, direct, and intellectual contribution to the work and approved it for publication.

Funding

This research was provided by the National Natural Science Foundation of China (42207277 and 42177234) and Key Scientific Research and Development Projects of Jiangxi Province (20194ABC28010).

Conflict of interest

The authors declare that the research was conducted in the absence of any commercial or financial relationships that could be construed as a potential conflict of interest.

Publisher's note

References

Du, B., Zhang, H., Ji, D., Huang, Z., Gan, F., and Jun, Z. (2022). Environmental contamination and health risk assessment to toxic elements in an active lead-zinc mining area. *Expo. Health*. doi:10.1007/s12403-022-00515-y

Du, B., Zhou, J., Lu, B., Zhang, C., Li, D., Zhou, J., et al. (2020). Environmental and human health risks from cadmium exposure near an active lead-zinc mine and a copper smelter, China. *Sci. Total Environ.* 720, 137585. doi:10.1016/j.scitotenv.2020.137585

Han, D., Wu, X., Li, R., Tang, X., Xiao, S., and Scholz, M. (2021). Critical review of electro-kinetic remediation of contaminated soils and sediments: Mechanisms, performances and technologies. *Water Air Soil Pollut.* 232 (8), 335–429. doi:10.1007/s11270-021-05182-4

Khanam, R., Kulsum, P. G. P. S., Debnath, S., Roychowdhury, T., and Mandal, B. (2022). Impact of soil amendment regimes on arsenic exposure to human through rice: Risk assessment and prediction for remediation. *Expo. Health*. doi:10.1007/s12403-022-00495-z

Liu, H.-L., Zhou, J., Li, M., Hu, Y.-m., Liu, X., and Zhou, J. (2019). Study of the bioavailability of heavy metals from atmospheric deposition on the soil-pakchoi (Brassica chinensis L.) system. *J. Hazard. Mater.* 362, 9–16. doi:10.1016/j.jhazmat.2018.09.032

Liu, H., Zhou, J., Li, M., Xia, R., Wang, X., and Zhou, J. (2022). Dynamic behaviors of newly deposited atmospheric heavy metals in the soil-pak choi system. *Environ. Sci. Technol.* 56 (17), 12734–12744. doi:10.1021/acs.est.2c04062

Song, B., Zeng, G., Gong, J., Liang, J., Xu, P., Liu, Z., et al. (2017). Evaluation methods for assessing effectiveness of *in situ* remediation of soil and sediment contaminated with organic pollutants and heavy metals. *Environ. Int.* 105, 43–55. doi:10.1016/j.envint.2017.05.001

Zhou, J., Du, B., Liu, H., Cui, H., Zhang, W., Fan, X., et al. (2020). The bioavailability and contribution of the newly deposited heavy metals (copper and lead) from atmosphere to rice (Oryza sativa L.). *J. Hazard. Mater.* 384, 121285. doi:10.1016/j.jhazmat.2019.121285

frontiers | Frontiers in Environmental Science

ORIGINAL RESEARCH
published: 04 July 2022
doi: 10.3389/fenvs.2022.937688

Response of Soil Fertility and Bacterial Community Composition to Vegetation Species in a Coal Mining Subsidence Area: A Survey After 20-Year Reclamation

Yuming Wang[1,2], *Yuchao Fan*[1,2]*, *Qiuya Wang*[1,2], *Shiwen Zhang*[1,2], *Yu Shi*[3] and *Xuebo Zheng*[4]*

[1]School of Earth and Environment, Anhui University of Science and Technology, Huainan, China, [2]Engineering Laboratory of Anhui Province for Comprehensive Utilization of Water and Soil Resources and Construction of Ecological Protection in Mining Area with High Groundwater Level, Anhui University of Science and Technology, Huainan, China, [3]State Key Laboratory of Crop Stress Adaptation and Improvement, School of Life Sciences, Henan University, Kaifeng, China, [4]Key Laboratory of Tobacco Biology and Processing, Ministry of Agriculture and Rural Affairs, Tobacco Research Institute, Chinese Academy of Agricultural Sciences, Qingdao, China

OPEN ACCESS

Edited by:
Zhu Li,
Institute of Soil Science (CAS), China

Reviewed by:
Yi Cheng,
Nanjing Normal University, China
Chao Ma,
Anhui Agricultural University, China

***Correspondence:**
Yuchao Fan
ahfanyuchao@126.com
Xuebo Zheng
zhengxuebo@caas.cn

Specialty section:
This article was submitted to Toxicology, Pollution and the Environment, a section of the journal Frontiers in Environmental Science

Received: 06 May 2022
Accepted: 16 May 2022
Published: 04 July 2022

Citation:
Wang Y, Fan Y, Wang Q, Zhang S, Shi Y and Zheng X (2022) Response of Soil Fertility and Bacterial Community Composition to Vegetation Species in a Coal Mining Subsidence Area: A Survey After 20-Year Reclamation. Front. Environ. Sci. 10:937688. doi: 10.3389/fenvs.2022.937688

Revegetation is an important restoration approach after reclamation in coal mining subsidence area. However, few studies have paid attention to the impacts of different vegetation species on soil fertility and bacterial community composition in the reclamation area filled with fly ash for a long time. In this study, soil fertility and bacterial community composition were investigated in a non-subsidence area (FCK) and a coal mining subsidence reclamation area restored vegetation with woody plants (pagoda trees, FS; peach trees, FP) and herbaceous plants (wheat-maize rotation, FW) for 20 years. Results showed that topsoil and subsoil nutrients including available K and alkali-hydrolyzable N, soil organic matter, and total carbon in the non-subsidence site were significantly higher than those in reclamation sites. Topsoil fertility indices (SFI) in reclamation sites were lower than that in non-subsidence site, and soil fertility index in FW was higher than that in FS and FP. Moreover, the SFI in topsoil (from −0.24 to 2.08) was significantly higher than that in subsoil (from −1.12 to −0.39). 16S rRNA gene sequencing analysis showed Proteobacteria, Acidobacteria and Actinobacteria were the dominant bacterial phyla in all sites, but the subsoil bacterial alpha indices (Shannon and Simpson) in the non-subsidence site were higher than those in reclamation sites. Principal coordinates analysis and non-metric multidimensional scaling analysis showed that the bacterial community composition in reclamation sites was significantly different from that in the non-subsidence site, and they were similar in the soil with wheat-maize rotation model between non-subsidence and reclamation sites. Co-occurrence network analysis noted that the network of dominant bacterial operational taxonomic units in the subsoil was more complex than that in the topsoil. Redundancy analysis suggested soil pH in topsoil and subsoil was an important driving factor for soil bacteria community composition. Overall, the reclamation site with the wheat-maize rotation model had higher soil fertility and bacterial community composition was similar to that of the non-subsidence site, indicating revegetation with the

wheat-maize rotation model is a good reclamation approach to improve soil fertility in coal mining subsidence area.

Keywords: soil bacterial community composition, reclamation, coal mining subsidence area, revegetation, bacterial alpha diversity

INTRODUCTION

With the development of industry, demands for coal resources are increasing in most countries over the world, especially in developing countries (Feng et al., 2019). For instance, coal consumption in China accounted for 56.8% of the total energy consumption in 2020 (Hu et al., 2022), and coal consumption will continue to grow by 3.4% in the next 20 years (Yu et al., 2022). The extensive exploitation of coal resources has caused serious environmental and social problems including land subsidence, land damage, and poor harvest (Wang et al., 2020; Ma et al., 2021). In high groundwater level areas, coal mining always resulted in land subsidence and changed terrestrial to aquatic ecosystems (Ma et al., 2021). Such dramatic environmental changes have destroyed agricultural lands and threatened the safe production of crops and the survival of local residents. Therefore, it is of great significance to repair the coal mining subsidence area.

Previous literature reviews have noted that fly ash, coal gangue, and other solid wastes can be used as filling materials in the coal mining subsidence areas and recover with surface soil above the filling materials (Ram and Masto, 2014; Hemalatha and Ramaswamy, 2017; Hu, 2019). Fly ash as a by-product of the coal-fired power station was widely used to fill the subsidence area (Hu, 2019). It can also provide lots of essential nutrients (K, Si, Fe, etc.) for plants (Ram and Masto, 2014), and its filling was beneficial for soil carbon sequestration and biodiversity conservation (Pandey, 2013). However, the filling substrates were significantly different from the subsoil and cannot effectively retain soil moisture and fertility, which may result in poor fertility and low soil productivity (Ma et al., 2019). For example, Duo and Hu (2018) reported that the soil quality significantly decreased after reclamation, and the crop yield was only 80.5% of that in the non-subsidence area after 5 years of reclamation (Duo and Hu, 2018). Consequently, the long-term changes in soil quality should be paid more attention in reclamation area filled with solid wastes/amendments.

Additionally, revegetation in reclamation area can effectively improve soil fertility and restore soil ecosystem functions (Zhou et al., 2020). It is essential to establish a self-sustaining revegetation ecosystem by selecting suitable plant species in the light of the condition of the subsidence areas (Kohler et al., 2016; Qu et al., 2017; Li and Liber, 2018). Numerous plants including woody plants (*Acacia catechu, Dalbergia sissoo, Pongamia pinnata* and *Terminalia bellirica*, etc.) (Srivastava et al., 2014) and herbaceous plants (grass, wheat, maize, *Ricinus communis, Vigna radiata, Saccharum munja*, etc.) (Pandey et al., 2012; Pandey, 2013; Yang et al., 2020) have been reported to revegetate in coal mining subsidence areas. However, little information is available on the impacts of vegetation species on soil microbial community composition in reclamation areas filled with fly ash. Soil microbial communities are critical to organic matter decomposition, nutrient cycling, long-term ecosystem stability and revegetation (Lehmann et al., 2011; Chen et al., 2017; Sun et al., 2019), and it is considered as an important indicator for the ecological restoration effect in coal mining subsidence area (Xu et al., 2019; Yuan et al., 2021). Natural succession of reclamation areas is a slow biogeochemical process and needs a long term before reaching a stable state (Ma et al., 2021). However, most studies about ecological restoration concentrated on a relatively short time (1–15 years) (Liu et al., 2018; Ma et al., 2019; Wang et al., 2020), and few studies were available on the evaluation of soil fertility and microbiome composition in reclamation areas.

In this study, a coal mining subsidence area filled with fly ash in eastern China was selected as the study area and soil samples were collected in four sites planted with woody plants (pagoda tree and peach tree) and herbaceous plants (wheat-maize rotation model) for 20 years. Here, we aim to 1) investigate soil physicochemical properties and fertility in reclamation areas; 2) evaluate the impacts of reclamation on soil bacterial community composition and biodiversity.

MATERIALS AND METHODS

Site Description

This study was conducted in a coal mining subsidence area (~100 ha, 116°85′-116°88′ E, 33°97′-33°98′ N) filled with fly ash in the eastern Huaibei city, Anhui Province, China (**Supplementary Figure S1**). The climate is characterized with a warm temperate semi-humid monsoon climate. The average annual precipitation and average annual temperature are 850 mm and 15.9°C in this area, respectively. Since high groundwater level existed above the coal bed, resulting in surface subsidence and land damage after long-term coal mining. In 2000, the surface soil (40 cm) was stripped and filled with fly ash in the subsidence area, and then covered the surface soil above the fly ash. During the next 20 years, most reclamation area was adopted a wheat-maize rotation model with two crops per year (FW), and part of the area was planted with pagoda trees (*Sophora japonica Linn*) (FS) and peach trees (*Prunus persica* L.) (FP), respectively. In addition, a non-subsidence site with a wheat-maize rotation model was also selected as the background area (FCK), which was 2.50 km to the reclamation area.

Sample Collection and Physicochemical Analysis

In November 2020, topsoil (0–20 cm) and subsoil (20–40 cm) samples were collected in each area. All soil samples were passed

through a 2 mm sieve. Half of the soil samples were dried at room temperature for chemical analysis, and the other samples were stored at −40°C for bioanalysis.

Soil pH was analyzed in a soil-to-water ratio of 1:2.50 (w/v) by pH electrode (PHS-3C, Shanghai, China). Soil organic matter (SOM), available phosphorus (AP), total phosphorus (TP), alkali-hydrolyzable nitrogen (AN), available potassium (AK) and total potassium (TK) were measured according to Lu (2000). Detailed information about the analysis methods is provided in **Supplementary Text S1**. An elemental analyzer (Vario Macro Cube, Elementar Company, Germany) was used to determine soil total nitrogen (TN) and total carbon (TC) concentrations (Wang et al., 2021).

Soil Biological Analysis

Soil whole DNA was extracted and purified according to the method of Cui H. et al. (2018). The concentration and purity of DNA were checked using NanoDrop One (Thermo Fisher Scientific, MA, United States). The standard bacterial primer set (515F and 806R) combined with barcode sequences (Caporaso et al., 2011) were used to amplify 16S rRNA genes (Cui H. et al., 2018). The Illumina Hiseq2500 platform was used for PE250 sequencing of the constructed amplicon library. Detailed information about the analysis methods is provided in **Supplementary Text S2**.

To clarify the associations among the soil key operational taxonomic units (OTUs), we selected the top 30 OTUs with the highest relative abundance in all sites (Hill et al., 2016). Spearman's correlation coefficient was chosen, and the threshold value of the correlation coefficient was 0.4. The network was analyzed by the tool of the Wekemo Bioincloud (https://www.bioincloud.tech). To evaluate the contributions of microbial populations to the overall community structure, the bipartite networks created in Cytoscape (3.8.2) were used to describe the associations between the OTUs and different sites (**Supplementary Text S3**) (Smoot et al., 2011; Jiao et al., 2017).

Statistical Analysis

The igraph and vegan in R (4.1.0) were used for statistical analysis The factor analysis was used to calculate the soil fertility index (SFI) (**Supplementary Text S4**) (Li et al., 2014; Guo et al., 2018). The relationships between soil physicochemical properties and microbial alpha diversity indexes were detected by Pearson correlation analysis. The phylum to genus-level abundance information was extracted by R to visualize using Origin 2021. Richness of OTUs, Chao1, ACE, Shannon, Simpson, and goods coverage indices were applied to characterize the bacterial alpha diversity. Principal coordinates analysis (PCoA) and non-metric multidimensional scaling (NMDS) were performed in the R software. The relationship between environmental parameters and bacteria was analyzed by redundancy analysis (RDA) which was performed by Lingbo MicroClass cloud application (http://www.cloud.biomicroclass.com/cloudplatform/softpage/CCA).
The linear discriminant analysis (LDA) effect size (LEfSe) method (http://www.cloud.biomicroclass.com/CloudPlatform/SoftPage/LF2) was performed to identify multiple taxonomical levels of potential biomarkers (LDA score threshold >3.0, factor

TABLE 1 | Impacts of vegetation species on the soil physicochemical properties.

Parameters		pH	WC (%)	TP (g kg^{-1})	AP (mg kg^{-1})	AK (mg kg^{-1})	TK (g kg^{-1})	TN (g kg^{-1})	AN (mg kg^{-1})	SOM (g kg^{-1})	TC (g kg^{-1})
0–20 cm	FCK	8.38 ± 0.04b	16.5 ± 0.86a	0.71 ± 0.06a	9.50 ± 0.78b	328 ± 10a	22.6 ± 0.58a	1.09 ± 0.13a	253 ± 9a	29.8 ± 1.08a	25.6 ± 2.04a
	FS	8.49 ± 0.07a	8.36 ± 2.18bc	0.67 ± 0.04a	9.07 ± 2.15b	292 ± 22b	24.3 ± 0.78a	0.66 ± 0.10b	116 ± 16b	18.1 ± 2.91bc	18.0 ± 0.87bc
	FP	8.57 ± 0.03a	7.30 ± 1.10c	0.71 ± 0.10a	9.15 ± 1.14b	254 ± 25c	17.3 ± 0.36b	0.47 ± 0.05c	68 ± 5c	15.0 ± 2.27c	15.7 ± 1.21c
	FW	8.14 ± 0.08c	10.2 ± 1.29b	0.76 ± 0.02a	14.6 ± 0.28a	290 ± 12b	18.0 ± 0.59b	0.82 ± 0.02b	125 ± 5b	21.1 ± 2.81b	19.7 ± 1.55b
20–40 cm	FCK	8.69 ± 0.02a	19.7 ± 0.6a	0.72 ± 0.1a	10.4 ± 3.04a	281 ± 13a	24.2 ± 0.32a	0.55 ± 0.06a	126 ± 27a	17.7 ± 0.21a	20.6 ± 0.20a
	FS	8.62 ± 0.06ab	9.74 ± 1.83b	0.76 ± 0.06a	10.3 ± 0.15a	226 ± 24b	18.2 ± 0.68b	0.48 ± 0.08ab	70 ± 1b	13.7 ± 2.62b	17.6 ± 1.68b
	FP	8.55 ± 0.06c	10.2 ± 1.69b	0.76 ± 0.08a	8.65 ± 0.29a	217 ± 21b	18.1 ± 0.27b	0.48 ± 0.04ab	56 ± 7b	10.9 ± 2.10b	17.7 ± 0.42b
	FW	8.63 ± 0.05ab	17.7 ± 2.41a	0.76 ± 0.05a	9.53 ± 2.02a	201 ± 7b	17.3 ± 0.68b	0.42 ± 0.04c	67 ± 4b	11.8 ± 2.30bc	16.4 ± 0.69b

Notes: Values are means ± standard deviation (n = 3) and different letters within the same column denote significant differences ($p < 0.05$) among different sites. WC, soil water content; TN, total nitrogen; TP, total phosphorus; TK, total potassium; AN, alkali-hydrolyzable nitrogen; AP, available phosphorus; AK, available potassium; SOM, soil organic matter; TC, total carbon. Site abbreviations are defined in ***Figure 1****.*

Kruskal–Wallis and Wilcoxon test with an alpha value of 0.05), the analysis strategy of multi-group classification analysis was used one against one (Chen et al., 2020).

RESULTS AND DISCUSSION

Soil Physicochemical Properties and Fertility

Soil physicochemical properties affected by different vegetation species were shown in **Table 1**. Topsoil was alkalinity in this area and its pH ranged from 8.14 to 8.69. Soil pH in FS and FP (wood land) were 0.11–0.53 units higher than those of FCK and FW (wheat field), suggesting that vegetation species influence soil pH, which was consistent with the findings of Deng et al. (2019) and Luo et al. (2022). Generally, the concentrations of WC, AK, TN, AN, SOM, and TC in FCK were the highest, and followed by FW (**Table 1**). For example, in the topsoil, WC in FCK was 0.98 1.26 and 0.62 times higher than that in FS, FP, and FW, respectively, and 0.64, 0.98 and 0.41 times higher for SOM. These results suggested filling reclamation caused soil water loss and fertility degradation, which also have been reported in previous study (Qu et al., 2018). However, concentrations of plant nutrients (including AP, SOM, and TC) of topsoil in FW were significantly higher than that in FS and FP ($p < 0.05$, **Table 1**), which suggested the wheat-maize rotation model was a good approach for the enhancement of soil fertility.

Similar to topsoil, most subsoil plant nutrients concentrations (including AK, TK, TN, AN, SOM, and TC) in FCK were higher than those in the other sites (**Table 1**). Moreover, subsoil pH (8.35–8.69) was higher than that of topsoil (8.05–8.57), and a similar trend was found for soil moisture content. In contrast to soil pH, contents of AK, TN, AN, and SOM in topsoil were higher than those in the subsoil. For example, topsoil SOM in FCK, FS, FP, and FW were 0.69, 0.32, 0.38, and 0.79 times higher than those of subsoil, respectively. In addition, the principal component analysis showed the eigenvalues of PC1 and PC2 were 3.61 and 1.47, respectively (**Supplementary Table S1**). The variance contribution rates were 51.6 and 21.0%, which can explain 72.6% of the total variance contribution. The score matrix of the PCA analysis showed that the loadings of TN, AK, and AN in PC1 exceeded 0.87 (**Supplementary Table S2**), indicating that these factors in PC1 play a significant role in soil fertility changes. SFI in the topsoil of FCK (2.08) was significantly greater than those of FS (−0.24) and FP (−0.56) ($p < 0.05$) (**Supplementary Table S3**), but there was no noticeable difference between FCK and FW (1.58) ($p > 0.05$, **Supplementary Table S3**). These results suggested that the soil fertility level in reclamation areas with woody plants was lower than that in the non-subsidence area with agricultural crops, and they also noted that the wheat-maize rotation model is an effective method to improve the soil fertility in the reclamation area.

Correlation analysis showed AK, AN, SOM, and TC were positively correlated with each other ($p < 0.05$, **Supplementary Figure S2**), especially for the positive correlation between TC and TN ($p < 0.01$). It may be due to the addition of nitrogen fertilizers that can promote plant growth and carbon accumulation (Qi et al., 2020). Moreover, we found the C/N ratios (**Supplementary Figure S3**) in the topsoil of wood land (33.33–33.78, FS and FT) were higher than those in the agricultural field (23.47–23.98, FCK and FW), which was also reported by Gao et al. (2014). This may be due to the intensive cultivation and agricultural management practices in agricultural fields resulting in the mineralization and loss of SOM to the atmosphere (Lal, 2002; Gao et al., 2014).

Soil Bacterial Community Composition

In all sites, 360,000 high-quality sequences and 7,141 different OTUs were obtained. The abundance of the dominant bacterial phyla/classes between reclamation and non-subsidence areas was shown in **Figure 1** and **Supplementary Figure S4**. Proteobacteria, Acidobacteria, and Actinobacteria were the most dominant bacterial phyla in the topsoil and subsoil, but their percentages were significantly different between topsoil and subsoil, suggesting the bacterial community composition was significantly different. For example, Proteobacteria in the topsoil of FCK accounted for 27.5%, which was 0.09 times lower than that in the subsoil of FW, and Acidobacteria in the subsoil of FS was higher compared to that in the topsoil of FS. Moreover, Proteobacteria in the topsoil of FW accounted for 40.1%, which was 0.46, 0.68 and 0.73 times higher than that in FCK, FS and FP, respectively. Similar to Wang et al. (2017), Gammaproteobacteria and Alphaproteobacteria were the dominant bacterial classes in the topsoil of the reclamation area, and accounted for 13.3 and 9.24% in all sites (**Figure 1**; **Supplementary Table S4**). Previous studies noted Gammaproteobacteria and Alphaproteobacteria participated in the process of nitrogen fixation (Madigan et al., 1984; Wolińska et al., 2020), thus their existence with large amounts in the reclamation area favored the enhancement of soil quality. In addition, the highest relative abundance of bacterial phylum and classes of FW was higher than that of FCK, FP and FS, indicating that the wheat-maize rotation model is a good selection to reconstruct the bacterial community in the reclamation area.

The bacterial richness in the reclamation sites (FS, FP and FW) for the topsoil were not significantly different from that in the non-subsidence site (FCK) (**Table 2**). There were no significant variations in the Chao1 (5,038–5,255) and ACE (4,934–5,195) indices of topsoil and subsoil among the four sites yet. These results indicated topsoil bacterial richness indices in the reclamation sites had reached a steady state within 20 years compared to the non-subsidence site. Previous studies have also reported soil bacterial communities reached a steady state within 15 and 20 years in reclamation areas (Li et al., 2018; Zhao et al., 2019). Moreover, Shannon and Simpson indices in the topsoil of non-subsidence site (FCK) were significantly higher than those in reclamation sites (**Table 2**), suggesting that different bacterial diversity existed between non-subsidence and reclamation sites. For example, Shannon indices in the topsoil of FK (non-subsidence site) were higher by 0.41, 0.14 and 0.29 than those in FS, FP and FW (reclamation sites) ($p < 0.05$). However, Shannon and Simpson indices for the subsoil had no significant differences between non-subsidence (FK) and reclamation sites (FS, FP and FW).

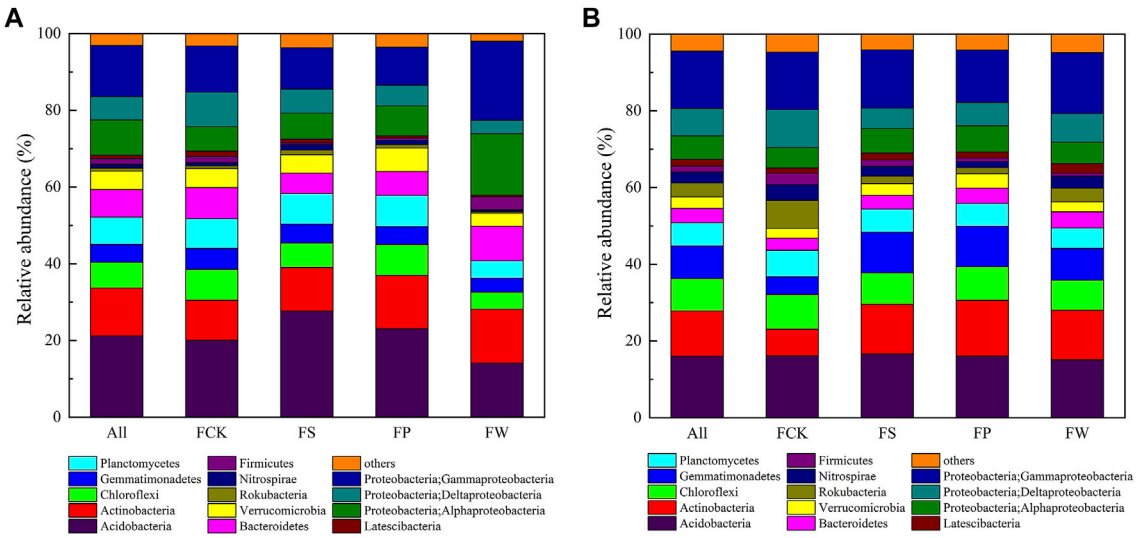

FIGURE 1 | Relative abundances of dominant bacterial phyla/classes in topsoil **(A)** and subsoil **(B)** among different sites. Relative abundances are based on the proportional frequencies of 16S rDNA sequences that could be classified at the phyla/classes level. Note: All, the whole soil samples; FCK, non-subsidence site (wheat-maize rotation); FS, reclamation site with pagoda trees; FP, reclamation site with peach trees; FW, reclamation site with wheat-maize rotation.

TABLE 2 | Impacts of vegetation species on the richness of OTU and alpha diversity indices.

Parameters		Richness of OTUs	Alpha diversity				
			Chao1	ACE	Shannon	Simpson	Goods coverage
0–20 cm	FCK	4,542 ± 41a	5,150 ± 164a	5,050 ± 72a	10.4 ± 0.08a	0.9982 ± 0.0001a	0.9938 ± 0.0004a
	FS	4,523 ± 145a	5,102 ± 166a	5,011 ± 154a	10.0 ± 0.11c	0.9963 ± 0.0013b	0.9937 ± 0.0002a
	FP	4,580 ± 81a	5,090 ± 57a	5,008 ± 81a	10.3 ± 0.08ab	0.9974 ± 0.0002ab	0.9942 ± 0.0003a
	FW	4,601 ± 91a	5,122 ± 137a	5,056 ± 117a	10.1 ± 0.14bc	0.9966 ± 0.0006b	0.9941 ± 0.0003a
20–40 cm	FCK	4,410 ± 298b	5,038 ± 285a	4,934 ± 271a	10.2 ± 0.21a	0.9974 ± 0.0006a	0.9934 ± 0.0001c
	FS	4,608 ± 183ab	5,100 ± 189a	5,036 ± 163a	10.1 ± 0.11a	0.9965 ± 0.0006ab	0.9941 ± 0.0000ab
	FP	4,580 ± 74ab	5,153 ± 6a	5,021 ± 44a	10.1 ± 0.03a	0.9961 ± 0.0003b	0.9940 ± 0.0002b
	FW	4,810 ± 102a	5,255 ± 106a	5,195 ± 104a	10.3 ± 0.11a	0.9972 ± 0.0002a	0.9944 ± 0.0001a

Notes: Values are means ± standard deviation (n = 3) and different letters within the same column denote significant differences ($p < 0.05$) among different sites. Site abbreviations are defined in ***Figure 1****.*

As shown in **Figure 2**, PCoA and NMDS analysis noted that microbial composition in woody plant revegetated sites (FS, FP) clustered together in the topsoil and subsoil, and a similar result was found by the cluster analysis at the phylum level (**Supplementary Figure S4**). Because woody plants had a robust root system and considerable amounts of exudates and mucilage which can strongly absorb soil nutrients (Yang et al., 2020), resulting in an substantial impact on the soil microbial community. These findings suggested that vegetation species significantly influenced soil bacterial community composition (Kohler et al., 2016). Moreover, the PCoA and NMDS (**Figure 2**) showed the soil bacterial community composition in the non-subsidence site was significantly differentiated from reclamation sites, indicating that reclamation changes the soil environment and influences the soil microbial community structure. It may be attributed to soil fertility in FCK being higher than that in the reclamation sites. In agreement with our study, Xu et al. (2020) also reported that soil organic carbon, inorganic nitrogen and other nutrients were the key factors affecting soil microbial diversity. Moreover, the PCoA and NMDS analysis indicated bacterial community composition in FW was the closest to the site of FCK (**Figure 2**) compared to other reclamation sites, thus the bacterial community composition in the two sites was similar and which may be due to the same wheat-maize rotation cultivation model. In addition, PCoA and NMDS analysis markedly separated topsoil and subsoil into two clusters (**Figure 2**), which indicated that the bacterial community composition in topsoil was different from that in the subsoil at each site, and it was in agreement with the result in **Figure 1**.

Identification of Biomarkers and Co-Occurrence Networks

LEfSe was used to identify the different biomarkers. As shown in **Supplementary Figure S5**, more bacterial taxa (93 clades, 15 phyla, 25 classes, 39 orders, and 27 families) in the topsoil were

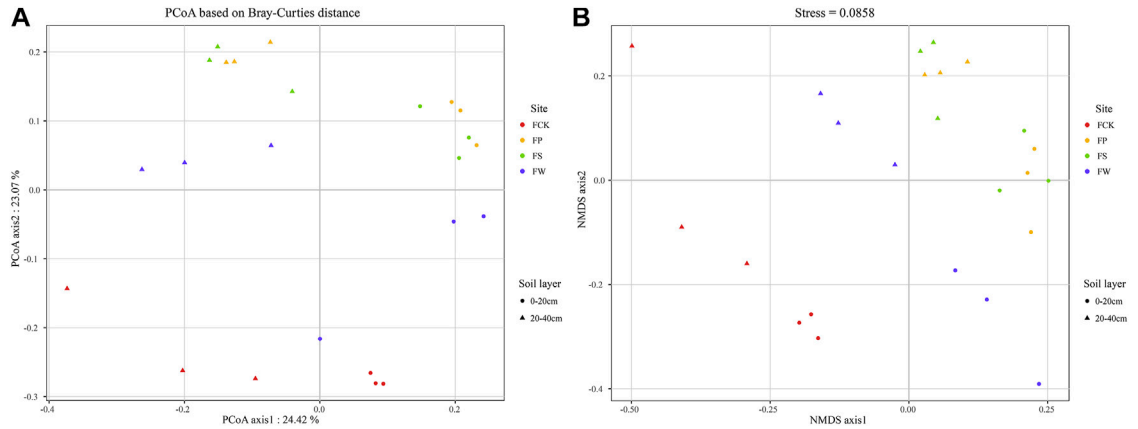

FIGURE 2 | Principal coordinates analysis (PCoA) ordination **(A)** and non-metric multidimensional scaling (NMDS) ordination **(B)** based on Bray-Curtis distance at OTU level showing the effects of different vegetation species on bacterial communities among different sites. The circles represent topsoil. The triangles represent subsoil. The colors of the nodes represent different sites. Note: Site abbreviations are defined in **Figure 1**.

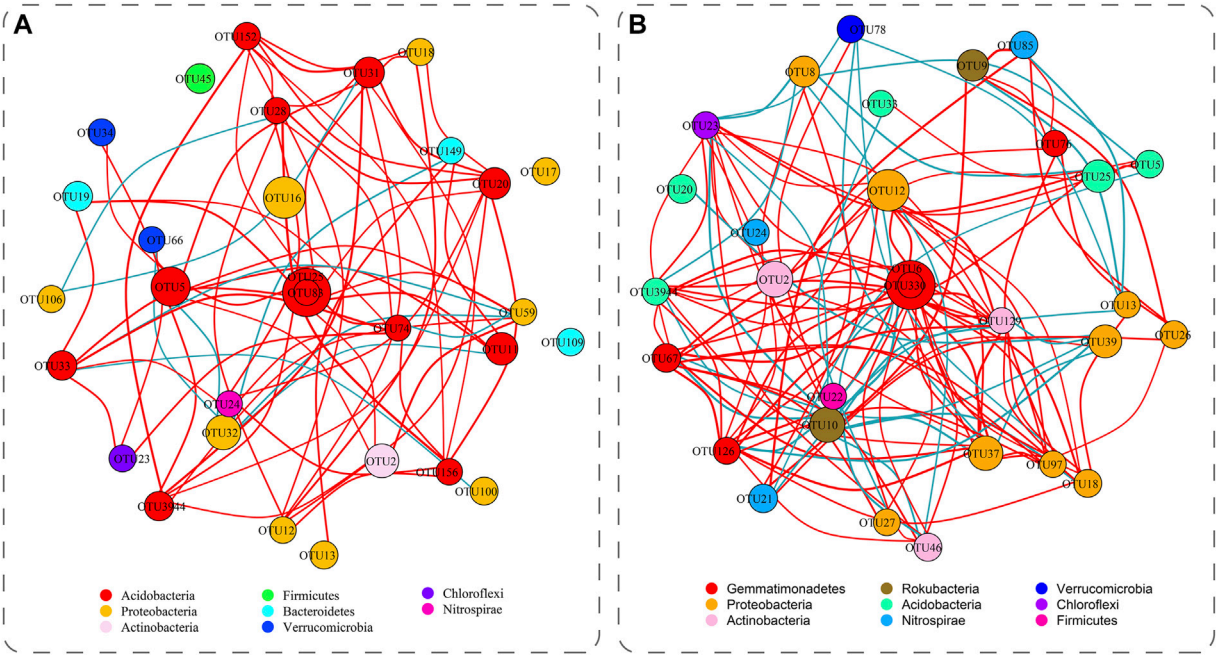

FIGURE 3 | The network of dominant bacterial OTUs of topsoil **(A)** and subsoil **(B)** in all sites. The nodes in the network represent the top 30 OTUs. The size of each node is proportional to the relative abundance. The red edge represents the positive correlation between OTUs, the blue edge represents the negative correlation. The colors of the nodes represent different soil bacteria phyla. Note: Site abbreviations are defined in **Figure 1**.

identified than that in the subsoil (78 clades, 12 phyla, 24 classes, 28 orders, and 25 families), which indicated that soil bacteria in the topsoil were more sensitive to the environmental disturbance than those in the subsoil. These biomarkers can be regarded as key microbial taxa shaping the metabolic threshold of the microbial community (Cui Y. et al., 2018). Chen et al. (2020) also noted biomarkers vary depending on the different environments and the relative abundance of core microorganisms. Moreover, the results of LDA revealed 37, 27, 13 and 16 bacterial phylotypes in the topsoil for FCK, FS, FP, and FW (**Supplementary Figure S6A**), and 27, 10, 30 and 11 bacterial phylotypes in the subsoil for FCK, FS, FP, and FW (**Supplementary Figure S6B**), respectively. The taxa and quantities of biomarkers were different between the non-subsidence and reclamation sites, which may be caused by the various soil quality and vegetation species.

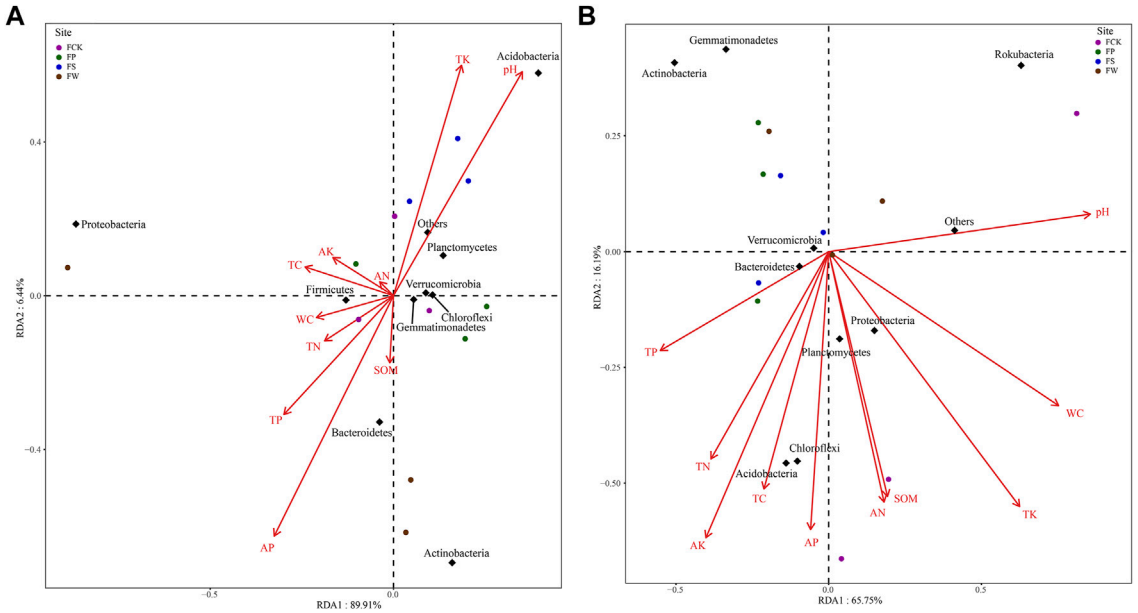

FIGURE 4 | Redundancy analysis (RDA) based on the bacterial community composition and soil characteristics in topsoil **(A)** and subsoil **(B)** among different sites. The red arrows represent soil physicochemical properties. Arrow length indicates the strength of correlation with a given ordination axis. The circles represent soil samples from different sites. The diamonds represent the major soil bacteria phylum. Note: Site abbreviations are defined in **Figure 1**. Soil physicochemical property abbreviations are defined in **Table 1**.

TABLE 3 | Pearson's correlation between alpha diversity indices of bacterial community and soil physicochemical properties.

Parameters		pH	WC	TP	AP	AK	TK	TN	AN	SOM	TC
0–20 cm	Richness of OTUs	0.27	−0.06	−0.20	−0.25	−0.09	0.10	−0.09	0.01	0.09	−0.16
	Chao1	0.23	0.05	−0.20	−0.29	0.07	0.19	0.05	0.17	0.13	0.00
	ACE	0.21	0.05	−0.21	−0.23	0.00	0.17	0.02	0.11	0.13	−0.04
	Shannon	0.09	**0.66***	0.21	−0.24	−0.09	−0.17	0.33	0.25	0.48	0.40
	Simpson	0.24	**0.66***	0.18	−0.45	−0.19	0.02	0.29	0.31	0.34	0.41
	Goods coverage	0.33	−0.20	−0.09	−0.21	−0.35	−0.10	−0.28	−0.23	0.04	−0.37
20–40 cm	Richness of OTUs	**−0.60***	−0.31	0.45	0.06	0.17	−0.56	0.10	−0.37	−0.18	0.06
	Chao1	−0.57	−0.24	0.47	0.07	0.24	−0.35	0.19	−0.34	−0.10	0.24
	ACE	−0.57	−0.25	0.46	0.13	0.24	−0.41	0.18	−0.28	−0.06	0.15
	Shannon	−0.17	0.18	0.21	−0.01	0.07	−0.13	−0.10	−0.24	−0.04	−0.08
	Simpson	0.30	**0.62***	−0.12	0.40	0.13	0.48	−0.13	0.22	0.37	−0.03
	Goods coverage	−0.53	−0.39	0.29	−0.20	−0.13	**−0.89*****	−0.19	−0.52	−0.49	−0.32

*Notes: Soil physicochemical property abbreviations are defined in **Table 1**. *, **, and *** indicate significant correlation at* $p < 0.05$, $p < 0.01$, *and* $p < 0.001$.

To describe the interactions among microbial communities, we performed a network analysis of the top 30 OTUs in abundance (**Figure 3**) and matched them in the NCBI database (**Supplementary Table S5, S6**). In the topsoil, OTU31 had 9 significant positive correlations and 1 significant negative correlation with other OTUs ($p < 0.05$), and OTU126 and OTU23 had 13 and 11 significant positive correlations, and 2 and 4 significant negative correlations with other OTUs ($p < 0.05$) in the subsoil (**Figure 3**). The above three OTUs all significantly correlated with the top 30 OTUs, thus they can be recognized as keystone taxa and play important roles in the soil reclamation process (Ma et al., 2020). Moreover, the network of dominant bacterial OTUs in the subsoil was more complex than that in the topsoil (**Figure 3**), suggesting the dominant OTU in the subsoil were more closely connected than those in the topsoil.

Nowadays, rare microorganisms have attracted more attention for their important ecological role in maintaining microbial diversity and mediating biogeochemical processes (Sauret et al., 2014; Jiao et al., 2017). To analyze the connection between rare microorganisms and different sites. The contribution of microbial taxa to the community structure and the associations between genus-level OTUs and sites were evaluated by the bipartite association network (**Supplementary Figure S7**). Similar to Cao et al. (2021), we found the number of OTUs classified as genera in bacterial communities was at a low level (less than 15%). We screened a total of 587 nodes and 4315 edges in all sites, and

they can be divided into 10 clusters and several keystone taxa according to the relationship between bacteria and sites. In co-occurrence network analysis, intermediate centrality represents the influence potential of an individual on the interaction between other nodes of the network (Greenblum et al., 2012). The core cluster was consisted by 451 nodes, and it accounted for 76.5% of the total nodes. The bipartite network analysis noted that most of OTUs were cross combinations, meaning similar taxa were presented among different sites, but their abundances were significantly different among all sites. In addition, several OTUs were connected to only a few sites, which may have specific environmental significance. For example, 27F-1492R_uncultured delta proteobacterium was a common genus of FCK and FW in the topsoil, which may be a keystone taxon in wheat-maize rotation mode.

Impacts of Soil Physicochemical Properties on Soil Microbial Community

Figure 4 showed the relationship between the top ten bacterial phyla and soil physicochemical properties. The first and second axes of RDA explained 89.9 and 6.44% of the variation in the bacterial community at the OTU level in the topsoil, while 65.8 and 16.2% were explained in the subsoil. (**Figure 4**). The total variation in bacterial community explained by the two axes exceeded 80% in both soil layers. Bacterial composition in all sites was significantly influenced by pH ($p = 0.044$) in the topsoil, and was significantly influenced by pH ($p = 0.003$), WC ($p = 0.001$), AK ($p = 0.010$) and TK ($p = 0.003$) in the subsoil (**Supplementary Table S7**). Moreover, Acidobacteria in the topsoil was positively correlated with pH, and Actinobacteria and Bacteroidetes were positively correlated with SOM, TN, TP, and AP (**Figure 4**). For the subsoil, Rokubacteria was positively correlated with pH, while Chloroflexi and Acidobacteria were positively correlated with AN, SOM, AP, TC, AK, and TN. These results suggested soil pH was a key driving factor for bacterial community structure (Ma et al., 2020; Ma et al., 2021), and further confirmed that soil nutrients can significantly influence soil bacterial communities in different reclamation areas (Wan and He, 2020).

In the topsoil, WC was positively correlated with the Shannon and Simpson indices ($p < 0.05$), but WC was negatively correlated with the Richness of OTUs ($p < 0.05$) in the subsoil (**Table 3**). For subsoil, soil pH was markedly negatively correlated with and Richness of OTUs ($p < 0.05$). Moreover, AN and SOM in the topsoil were positively correlated with alpha diversity indices, this may be because carbon and nitrogen sources are essential nutrients for microbial survival, and they are also important driving factors for the evolution of soil bacterial diversity (Liu et al., 2020). Interestingly, we found that the correlations between alpha-diversity indices and physicochemical properties (TP, AP, SOM, and pH) in the topsoil overall differed from those in the subsoil, which indicated that soil microorganisms in different soil layers were sensitive to the changes in soil physicochemical properties.

CONCLUSION

In this study, we found soil fertility in the non-subsidence site was significantly higher than that in reclamation sites, and topsoil SFI was higher than that in the subsoil. Furthermore, topsoil SFI in FW was higher than that in FS and FP. Proteobacteria, Acidobacteria and Actinobacteria were the dominant bacterial phyla in all sites, and topsoil bacterial Shannon and Simpson indices in FCK were significantly higher than those in reclamation sites. Soil bacterial community in reclamation sites was different from that in non-subsidence site based on the PCoA and NMDS analysis, and the bacterial community composition in FW was more similar to FCK compared with FS and FP. Moreover, co-occurrence network analysis showed topsoil had a more complex network of dominant OTUs compared with that of subsoil. Our study suggested that soil pH was an important driving factor for soil bacterial community composition. Results of this study suggested soil fertility in reclamation sites with a wheat-maize rotation model was higher and it had similar bacterial community composition to that in the non-subsidence site. Therefore, the wheat-maize rotation model is a good choice to improve soil fertility and soil bacterial community composition in coal mining subsidence area filled with fly ash.

DATA AVAILABILITY STATEMENT

The raw data supporting the conclusions of this article will be made available by the authors, without undue reservation.

AUTHOR CONTRIBUTIONS

Conceptualization: YW, YF, YS, and XZ. Methodology: YW, YF, YS, and XZ. Formal analysis: QW, SZ, and YS. Funding acquisition: YF, XZ, and YW. Project administration: YF, XZ, and YW. Resources: YW and YF. Supervision: XZ, YF, and YW. Validation: XZ, YW, and YF. Investigation: YW, YF, QW, SZ, and XZ. Visualization: YF, QW, SZ, YS, and YW. Writing—original draft: YW, YF, SZ, YS, and XZ Writing—review and editing: YW, YF, YS, and XZ.

FUNDING

This research was supported by the Natural Science Foundation of Universities of Anhui Province (KJ2020ZD35), the Graduate Innovation Fund Project of Anhui University of Science and Technology (2021CX2011), the Technology R&D Project of Huaibei Mining Group (2020-113 and 2022-103), the National Natural Science Foundation of China (31901195), and the Shandong Provincial Natural Science Foundation (ZR2019BD062).

SUPPLEMENTARY MATERIAL

The Supplementary Material for this article can be found online at: https://www.frontiersin.org/articles/10.3389/fenvs.2022.937688/full#supplementary-material

REFERENCES

Cao, M., Cui, L., Sun, H., Zhang, X., Zheng, X., and Jiang, J. (2021). Effects of Spartina Alterniflora Invasion on Soil Microbial Community Structure and Ecological Functions. *Microorganisms* 9 (1), 138. doi:10.3390/microorganisms9010138

Caporaso, J. G., Lauber, C. L., Walters, W. A., Berg-Lyons, D., Lozupone, C. A., Turnbaugh, P. J., et al. (2011). Global Patterns of 16S rRNA Diversity at a Depth of Millions of Sequences per Sample. *Proc. Natl. Acad. Sci. U.S.A.* 108, 4516–4522. doi:10.1073/pnas.1000080107

Chen, J., Nan, J., Xu, D., Mo, L., Zheng, Y., Chao, L., et al. (2020). Response Differences between Soil Fungal and Bacterial Communities under Opencast Coal Mining Disturbance Conditions. *Catena* 194, 104779. doi:10.1016/j.catena.2020.104779

Chen, Y.-L., Deng, Y., Ding, J.-Z., Hu, H.-W., Xu, T.-L., Li, F., et al. (2017). Distinct Microbial Communities in the Active and Permafrost Layers on the Tibetan Plateau. *Mol. Ecol.* 26 (23), 6608–6620. doi:10.1111/mec.14396

Cui, H., Shi, Y., Zhou, J., Chu, H., Cang, L., and Zhou, D. (2018a). Effect of Different Grain Sizes of Hydroxyapatite on Soil Heavy Metal Bioavailability and Microbial Community Composition. *Agric. Ecosyst. Environ.* 267, 165–173. doi:10.1016/j.agee.2018.08.017

Cui, Y., Fang, L., Guo, X., Wang, X., Wang, Y., Li, P., et al. (2018b). Responses of Soil Microbial Communities to Nutrient Limitation in the Desert-Grassland Ecological Transition Zone. *Sci. Total Environ.* 642, 45–55. doi:10.1016/j.scitotenv.2018.06.033

Deng, J., Yin, Y., Luo, J., Zhu, W., and Zhou, Y. (2019). Different Revegetation Types Alter Soil Physical-Chemical Characteristics and Fungal Community in the Baishilazi Nature Reserve. *PeerJ* 6, e6251. doi:10.7717/peerj.6251

Duo, L., and Hu, Z. (2018). Soil Quality Change after Reclaiming Subsidence Land with Yellow River Sediments. *Sustainability* 10 (11), 4310. doi:10.3390/su10114310

Feng, Y., Wang, J., Bai, Z., and Reading, L. (2019). Effects of Surface Coal Mining and Land Reclamation on Soil Properties: A Review. *Earth Sci. Rev.* 191, 12–25. doi:10.1016/j.earscirev.2019.02.015

Gao, Y., He, N., Yu, G., Chen, W., and Wang, Q. (2014). Long-Term Effects of Different Land Use Types on C, N, and P Stoichiometry and Storage in Subtropical Ecosystems: A Case Study in China. *Ecol. Eng.* 67, 171–181. doi:10.1016/j.ecoleng.2014.03.013

Greenblum, S., Turnbaugh, P. J., and Borenstein, E. (2012). Metagenomic Systems Biology of the Human Gut Microbiome Reveals Topological Shifts Associated with Obesity and Inflammatory Bowel Disease. *Proc. Natl. Acad. Sci. U.S.A.* 109 (2), 594–599. doi:10.1073/pnas.1116053109

Guo, X.-M., Zhao, T.-Q., Chang, W.-K., Xiao, C.-Y., and He, Y.-X. (2018). Evaluating the Effect of Coal Mining Subsidence on the Agricultural Soil Quality Using Principal Component Analysis. *Chil. J. Agric. Res.* 78 (2), 173–182. doi:10.4067/S0718-58392018000200173

Hemalatha, T., and Ramaswamy, A. (2017). A Review on Fly Ash Characteristics - Towards Promoting High Volume Utilization in Developing Sustainable Concrete. *J. Clean. Prod.* 147, 546–559. doi:10.1016/j.jclepro.2017.01.114

Hill, R., Saetnan, E. R., Scullion, J., Gwynn-Jones, D., Ostle, N., and Edwards, A. (2016). Temporal and Spatial Influences Incur Reconfiguration of Arctic Heathland Soil Bacterial Community Structure. *Environ. Microbiol.* 18 (6), 1942–1953. doi:10.1111/1462-2920.13017

Hu, Y., Zhang, R., Qie, X., and Liu, H. (2022). Evaluation of China's Coal Resource Energy Carbon Emission Efficiency in the Whole Life Cycle. *China Environ. Sci.* (in Chinese). doi:10.19674/j.cnki.issn1000-6923.20220218.002

Hu, Z. (2019). The 30 years' Land Reclamation and Ecological Restoration in China: Review, Rethinking and Prospect. *Coal Sci. Technol.* 47 (1), 25–35. (in Chinese). doi:10.13199/j.cnki.cst.2019.01.004

Jiao, S., Zhang, Z., Yang, F., Lin, Y., Chen, W., and Wei, G. (2017). Temporal Dynamics of Microbial Communities in Microcosms in Response to Pollutants. *Mol. Ecol.* 26 (3), 923–936. doi:10.1111/mec.13978

Kohler, J., Caravaca, F., Azcón, R., Díaz, G., and Roldán, A. (2016). Suitability of the Microbial Community Composition and Function in a Semiarid Mine Soil for Assessing Phytomanagement Practices Based on Mycorrhizal Inoculation and Amendment Addition. *J. Environ. Manage.* 169, 236–246. doi:10.1016/j.jenvman.2015.12.037

Lal, R. (2002). Soil Carbon Dynamics in Cropland and Rangeland. *Environ. Pollut.* 116, 353–362. doi:10.1016/s0269-7491(01)00211-1

Lehmann, J., Rillig, M. C., Thies, J., Masiello, C. A., Hockaday, W. C., and Crowley, D. (2011). Biochar Effects on Soil Biota - A Review. *Soil Biol. Biochem.* 43 (9), 1812–1836. doi:10.1016/j.soilbio.2011.04.022

Li, J. P., Xu, M. F., Su, Z. Y., Sun, Y. D., and Hu, Y. Q. (2014). Soil Fertility Quality Assessment under Different Vegetation Restoration Patterns. *Acta Eco. Sin.* 34 (9), 2297–2307. (in Chinese). doi:10.5846/stxb201306111672

Li, J., Xin, Z., Yan, J., Li, H., Chen, J., and Ding, G. (2018). Physicochemical and Microbiological Assessment of Soil Quality on a Chronosequence of a Mine Reclamation Site. *Eur. J. Soil Sci.* 69 (6), 1056–1067. doi:10.1111/ejss.12714

Li, S., and Liber, K. (2018). Influence of Different Revegetation Choices on Plant Community and Soil Development Nine Years after Initial Planting on a Reclaimed Coal Gob Pile in the Shanxi Mining Area, China. *Sci. Total Environ.* 618, 1314–1323. doi:10.1016/j.scitotenv.2017.09.252

Liu, T., Wu, X., Li, H., Alharbi, H., Wang, J., Dang, P., et al. (2020). Soil Organic Matter, Nitrogen and pH Driven Change in Bacterial Community Following Forest Conversion. *For. Ecol. Manag.* 477, 118473. doi:10.1016/j.foreco.2020.118473

Liu, Z., Chen, M., Li, Y., Huang, Y., Fan, B., Lv, W., et al. (2018). Different Effects of Reclamation Methods on Macrobenthos Community Structure in the Yangtze Estuary, China. *Mar. Pollut. Bull.* 127, 429–436. doi:10.1016/j.marpolbul.2017.12.038

Lu, R. K. (2000). *Agricultural Chemical Analysis of Soil*. Beijing: China Agriculture Press. (in Chinese).

Luo, Y., Zheng, Z., Wu, P., and Wu, Y. (2022). Effect of Different Direct Revegetation Strategies on the Mobility of Heavy Metals in Artificial Zinc Smelting Waste Slag: Implications for Phytoremediation. *Chemosphere* 286, 131678. doi:10.1016/j.chemosphere.2021.131678

Ma, J., Gonzalez-Ollauri, A., Zhang, Q., Xiao, D., and Chen, F. (2021). Ecological Network Analysis to Assess the Restoration Success of Disturbed Mine Soil in Zoucheng, China. *Land Degrad. Dev.* 32 (18), 5393–5411. doi:10.1002/ldr.4116

Ma, J., Lu, Y., Chen, F., Li, X., Xiao, D., and Wang, H. (2020). Molecular Ecological Network Complexity Drives Stand Resilience of Soil Bacteria to Mining Disturbances Among Typical Damaged Ecosystems in China. *Microorganisms* 8 (3), 433. doi:10.3390/microorganisms8030433

Ma, K., Zhang, Y., Ruan, M., Guo, J., and Chai, T. (2019). Land Subsidence in a Coal Mining Area Reduced Soil Fertility and Led to Soil Degradation in Arid and Semi-Arid Regions. *Int. J. Environ. Res. Public Health* 16 (20), 3929. doi:10.3390/ijerph16203929

Madigan, M., Cox, S. S., and Stegeman, R. A. (1984). Nitrogen Fixation and Nitrogenase Activities in Members of the Family Rhodospirillaceae. *J. Bacteriol.* 157 (1), 73–78. doi:10.1128/jb.157.1.73-78.1984

Pandey, V. C., Singh, K., Singh, R. P., and Singh, B. (2012). Naturally Growing *Saccharum Munja* L. on the Fly Ash Lagoons: A Potential Ecological Engineer for the Revegetation and Stabilization. *Ecol. Eng.* 40, 95–99. doi:10.1016/j.ecoleng.2011.12.019

Pandey, V. C. (2013). Suitability of Ricinus Communis L. Cultivation for Phytoremediation of Fly Ash Disposal Sites. *Ecol. Eng.* 57, 336–341. doi:10.1016/j.ecoleng.2013.04.054

Qi, L., Zhou, P., Yang, L., and Gao, M. (2020). Effects of Land Reclamation on the Physical, Chemical, and Microbial Quantity and Enzyme Activity Properties of Degraded Agricultural Soils. *J. Soils Sediments* 20 (2), 973–981. doi:10.1007/s11368-019-02432-1

Qu, J.-F., Hou, Y.-L., Ge, M.-Y., Wang, K., Liu, S., Zhang, S.-L., et al. (2017). Carbon Dynamics of Reclaimed Coal Mine Soil under Agricultural Use: A Chronosequence Study in the Dongtan Mining Area, Shandong Province, China. *Sustainability* 9 (4), 629. doi:10.3390/su9040629

Qu, J. F., Tan, M., Hou, Y. L., Ge, M. Y., Wang, A. N., Wang, K., et al. (2018). Effects of the Stability of Reclaimed Soil Aggregates on Organic Carbon in Coal Mining Subsidence Areas. *Appl. Eng. Agric.* 34 (5), 843–854. doi:10.13031/aea.12829

Ram, L. C., and Masto, R. E. (2014). Fly Ash for Soil Amelioration: A Review on the Influence of Ash Blending with Inorganic and Organic Amendments. *Earth Sci. Rev.* 128, 52–74. doi:10.1016/j.earscirev.2013.10.003

Sauret, C., Séverin, T., Vétion, G., Guigue, C., Goutx, M., Pujo-Pay, M., et al. (2014). 'Rare Biosphere' Bacteria as Key Phenanthrene Degraders in Coastal Seawaters. *Environ. Pollut.* 194, 246–253. doi:10.1016/j.envpol.2014.07.024

Smoot, M. E., Ono, K., Ruscheinski, J., Wang, P.-L., and Ideker, T. (2011). Cytoscape 2.8: New Features for Data Integration and Network Visualization. *Bioinformatics* 27 (3), 431–432. doi:10.1093/bioinformatics/btq675

Srivastava, N. K., Ram, L. C., and Masto, R. E. (2014). Reclamation of Overburden and Lowland in Coal Mining Area with Fly Ash and Selective Plantation: A Sustainable Ecological Approach. *Ecol. Eng.* 71, 479–489. doi:10.1016/j.ecoleng.2014.07.062

Sun, S., Sun, H., Zhang, D., Zhang, J., Cai, Z., Qin, G., et al. (2019). Response of Soil Microbes to Vegetation Restoration in Coal Mining Subsidence Areas at Huaibei Coal Mine, China. *Int. J. Environ. Res. Public Health* 16 (10), 1757. doi:10.3390/ijerph16101757

Wan, P., and He, R. (2020). Soil Microbial Community Characteristics under Different Vegetation Types at the National Nature Reserve of Xiaolongshan Mountains, Northwest China. *Ecol. Inf.* 55, 101020. doi:10.1016/j.ecoinf.2019.101020

Wang, K., Zhang, J., Yi, Q., Wang, X., and Yi, Y. (2021). Metals in Sediments and Their Accumulation in Zostera Japonica in Different Sediment Habitats of the Yellow River Estuary. *J. Soils Sediments* 21 (3), 1539–1549. doi:10.1007/s11368-021-02875-5

Wang, L., Li, J., Yang, F., E, Y., Raza, W., Huang, Q., et al. (2017). Application of Bioorganic Fertilizer Significantly Increased Apple Yields and Shaped Bacterial Community Structure in Orchard Soil. *Microb. Ecol.* 73 (2), 404–416. doi:10.1007/s00248-016-0849-y

Wang, X., Li, Y., Wei, Y., Meng, H., Cao, Y., Lead, J. R., et al. (2020). Effects of Fertilization and Reclamation Time on Soil Bacterial Communities in Coal Mining Subsidence Areas. *Sci. Total Environ.* 739, 139882. doi:10.1016/j.scitotenv.2020.139882

Wolińska, A., Włodarczyk, K., Kuźniar, A., Marzec-Grządziel, A., Grządziel, J., Gałązka, A., et al. (2020). Soil Microbial Community Profiling and Bacterial Metabolic Activity of Technosols as an Effect of Soil Properties Following Land Reclamation: A Case Study from the Abandoned Iron Sulphide and Uranium Mine in Rudki (South-Central Poland). *Agronomy* 10 (11), 1795. doi:10.3390/agronomy10111795

Xu, M., Gao, D., Fu, S., Lu, X., Wu, S., Han, X., et al. (2020). Long-Term Effects of Vegetation and Soil on the Microbial Communities Following Afforestation of Farmland with Robinia Pseudoacacia Plantations. *Geoderma* 367, 114263. doi:10.1016/j.geoderma.2020.114263

Xu, Z., Zhang, Y., Yang, J., Liu, F., Bi, R., Zhu, H., et al. (2019). Effect of Underground Coal Mining on the Regional Soil Organic Carbon Pool in Farmland in a Mining Subsidence Area. *Sustainability* 11 (18), 4961. doi:10.3390/su11184961

Yang, Y., Cheng, H., Liu, L., Dou, Y., and An, S. (2020). Comparison of Soil Microbial Community between Planted Woodland and Natural Grass Vegetation on the Loess Plateau. *For. Ecol. Manag.* 460, 117817. doi:10.1016/j.foreco.2019.117817

Yu, X., Cui, Y., Chen, Y., Chang, I.-S., and Wu, J. (2022). The Drivers of Collaborative Innovation of the Comprehensive Utilization Technologies of Coal Fly Ash in China: A Network Analysis. *Environ. Sci. Pollut. Res.*. doi:10.1007/s11356-022-19816-5

Yuan, C., Li, F., Yuan, Z., Li, G., and Liang, X. (2021). Response of Bacterial Communities to Mining Activity in the Alpine Area of the Tianshan Mountain Region, China. *Environ. Sci. Pollut. Res.* 28 (13), 15806–15818. doi:10.1007/s11356-020-11744-6

Zhao, Y., Zhang, F., Yang, L., Wang, D., and Wang, W. (2019). Response of Soil Bacterial Community Structure to Different Reclamation Years of Abandoned Salinized Farmland in Arid China. *Arch. Microbiol.* 201 (9), 1219–1232. doi:10.1007/s00203-019-01689-x

Zhou, W.-H., Wang, Y.-T., Lian, Z.-H., Yang, T.-T., Zeng, Q.-W., Feng, S.-W., et al. (2020). Revegetation Approach and Plant Identity Unequally Affect Structure, Ecological Network and Function of Soil Microbial Community in a Highly Acidified Mine Tailings Pond. *Sci. Total Environ.* 744, 140793. doi:10.1016/j.scitotenv.2020.140793

Conflict of Interest: The authors declare that this study received funding from Huibei Mining (Group) Co., Ltd. The funder was not involved in the study design, collection, analysis, interpretation of data, the writing of this article or the decision to submit it for publication.

Publisher's Note: All claims expressed in this article are solely those of the authors and do not necessarily represent those of their affiliated organizations, or those of the publisher, the editors and the reviewers. Any product that may be evaluated in this article, or claim that may be made by its manufacturer, is not guaranteed or endorsed by the publisher.

frontiers | Frontiers in Environmental Science

TYPE Original Research
PUBLISHED 09 August 2022
DOI 10.3389/fenvs.2022.979286

OPEN ACCESS

EDITED BY
Hongbiao Cui,
Anhui University of Science and Technology, China

REVIEWED BY
Liugen Zheng,
Anhui University, China
Yizhang Liu,
Institute of Geochemistry (CAS), China

*CORRESPONDENCE
Qingguang Li,
leeqg12@163.com

SPECIALTY SECTION
This article was submitted to Toxicology, Pollution and the Environment, a section of the journal Frontiers in Environmental Science

RECEIVED 27 June 2022
ACCEPTED 13 July 2022
PUBLISHED 09 August 2022

CITATION
Du S, An L, Huang J, Li Q, Wu P and Guo X (2022), Sources and migration characteristics of fluorine in the river water of a small karst watershed influenced by coal mining. *Front. Environ. Sci.* 10:979286. doi: 10.3389/fenvs.2022.979286

Sources and migration characteristics of fluorine in the river water of a small karst watershed influenced by coal mining

Shuangxue Du, Li An, Jiangxun Huang, Qingguang Li*, Pan Wu and Xingqiang Guo

College of Resources and Environmental Engineering, Key Laboratory of Karst Georesources and Environment, Ministry of Education, Guizhou University, Guiyang, China

In high-fluorine geological background areas, the supergene geochemical process of fluorine has an impact on regional environmental health and safety, which has long been the focus of attention. However, in karst areas characterized by a high incidence of endemic fluorosis, the migration and transformation of fluorine in surface water have not received sufficient attention. This study investigated the joint influence of the weathering and erosion of carbonate rocks and coal-bearing strata on a typical small watershed. Accordingly, 239 samples representing 13 periods of hydrochemical samples were systematically collected to clarify the source, migration, and transformation characteristics of fluorine in surface water. The results revealed that the pH of the Huatan River was low in the rainy season and high in the dry season. The annual variation range of fluorine concentration was 0.11–0.40 mg/L. Although mining development produced acid mine drainage with high fluorine concentration, its impact at the watershed scale appeared to be limited. In terms of spatial scale, the concentration of fluorine in the Huatan River increased gradually from upstream to downstream. The dissolution of fluorite and other fluorine-bearing minerals had not reached the saturation state. The fluorine in the watershed primarily came from the dissolution of fluorine-bearing minerals, followed by the contribution of atmospheric precipitation. The release of fluorine adsorbed on the surface of clay minerals was not the main source of this element. The leaching of the watershed was shown to represent a critical transport process concerning fluorine in the Huatan River, and evaporation had a notable impact on the enrichment of fluorine in water.

KEYWORDS

fluorine-bearing minerals, leaching, evaporation, D-excess, acid mine drainage

1 Introduction

Fluoride, an essential trace element in the human body, is also an identified cause endemic environmental health events, such as dental fluorosis and bone fluorosis (Guo et al., 2021; Li et al., 2020; Wang et al., 2021; Balcerzak, 2022). The World Health Organization lists fluoride among the top ten chemicals of public health concern and indicates that the guideline limit for fluoride in drinking water should not exceed 1.5 mg/L (Aghapour et al., 2018; Wang et al., 2020). According to the Groundwater Quality Standard (GB14848-2017), Surface Water Environmental Quality Standard (GB3838-2002), and Living Drinking Water Sanitation Standard (GB 5749–2022), the content of fluoride in drinking water shall not exceed 1.0 mg/L (He et al., 2020; Cao et al., 2022; Hao et al., 2022). Globally, more than 200 million people are affected by drinking water containing fluoride levels exceeding these standards (Strunecka and Strunecky, 2020; Vithanage and Bhattacharya, 2015; Wang et al., 2020). In an aqueous environment, the primary forms of fluorine are F^-, HF, FeF^+, FeF_2^+, MnF^+, AlF_2^+, AlF^{2+}, AlF_3(aq), AlF_4^-, MgF^+, CaF^+, NaF, and many other forms (Deng et al., 2011). Li X. et al. (2016) indicated that fluoride easily forms stable complex compounds with Al in acidic water. With increasing pH, the contents of NaF, MgF^+, and CaF^+ increase gradually, and weakly alkaline water bodies are dominated by ionic F^- (Li X. et al., 2016; Hao et al., 2022).

According to Fuge (2019) and Savenko and Savenko, (2020), the average fluorine concentration in unpolluted surface freshwaters worldwide is relatively low, ranging from < 0.05 to 1.6 mg/L, with a median of 0.1 mg/L. Fluoride in water has long been a matter of concern mainly because of the local health risks posed by excessive intake of fluoride. Scholarly attention to this issue has also mainly focused on the source and enrichment mechanism of fluoride in groundwater, along with health risk assessment (Ozsvath, 2009; Ghosh et al., 2013; Feng et al., 2020; Liu et al., 2021; Masood et al., 2022; Wu et al., 2022). Recent research has found high fluoride levels in groundwater widely distributed in the north, northeast, and northwest regions of China, mainly in shallow groundwater (He et al., 2020). In practical terms, the concentration of fluorine in water is affected by many factors, such as pH, dissolution and precipitation of fluorine-bearing minerals, the ion exchange process, evaporation, and so on. In alkaline water, HCO_3^- and OH^- are more likely to replace the adsorbed or isomorphic fluorine ions in clay, mica, and other fluorine-bearing minerals, resulting in increasing fluorine concentrations in surface water (Wenzel and Blum, 1992; Deng et al., 2011; Emenike et al., 2018).

Unfortunately, at the surface watershed scale, especially in terms of the high geological background area of fluorine in Southwest China, the migration and transformation process of fluorine in the surface water system has received inadequate scholarly attention. The endemic fluorosis area, represented by the Bijie region in Southwest China, has a high soil fluoride content of 5,979 mg/kg (Wang et al., 2021). Furthermore, in the medium-to high-sulfur coal mining area of southwest China, the weathering of sulfide-rich coal-bearing strata can produce serious acid pollution in surface water (Zhang et al., 2021; Huang et al., 2022). The fluorine content in acid mine drainage (AMD) from the Zhijin mining area in Guizhou has been reported to be as high as 4.94 mg/L (Li X. et al., 2016). However, many factors are known to affect the geochemical process of fluorine in acidic water, and systematic research examining this topic remains scarce (Deng et al., 2011; Miguel et al., 2017). Therefore, the release of fluorine in the process of surface soil leaching may have a notable impact on the enrichment of fluorine in surface watershed water (Wenzel and Blum, 1992).

Thus, a typical small watershed in Jinsha County, Guizhou Province, which is controlled by the superposition of weathering and erosion of carbonate rocks and coal-bearing strata, was selected as the research object for this study. In the study area, we conducted a systematic collection and analysis of hydrochemical samples in different seasons in the watershed in order to reveal the temporal and spatial distribution characteristics of fluorine in the river water, as well as to clarify the sources, migration, and transformation characteristics in the process of surface water migration.

2 Materials and methods

2.1 Overview of the study area

The Huatan River is located at east longitude 106°29′10″–106°42′24″and north latitude 27°20′43″–27°26′4″, at an altitude of 760–1,095 m. This narrow and long watershed is a secondary water system in the middle and lower reaches of the Wujiang River.

The terrain is high in the southwest and low in the northeast. The river under consideration empties into the Pianyan River in the east. The drainage area is 321 km^2, the total length of the river is 59 km, the natural drop is 220m, the average gradient is 5.7‰, and the annual average runoff is 130 million m^3. On the left bank of the river are three tributaries with catchment areas greater than 20 km^2. The Huatanhe Reservoir is located upstream of the study area and is an important local drinking water source. The Huatan River Watershed is characterized as the subtropical monsoon humid climate zone, featuring a mild climate, annual average rainfall of 1,057 mm, annual average temperature of 15.1°C, and annual average sunshine of 1,120.2 h. Due to the development of karst landforms, funnels, peaks, depressions, sinkholes, ambushes, and natural bridges are omnipresent.

The geotectonic position of the study area is located in the northeast structural deformation area of Bijie, Zunyi fault arch of

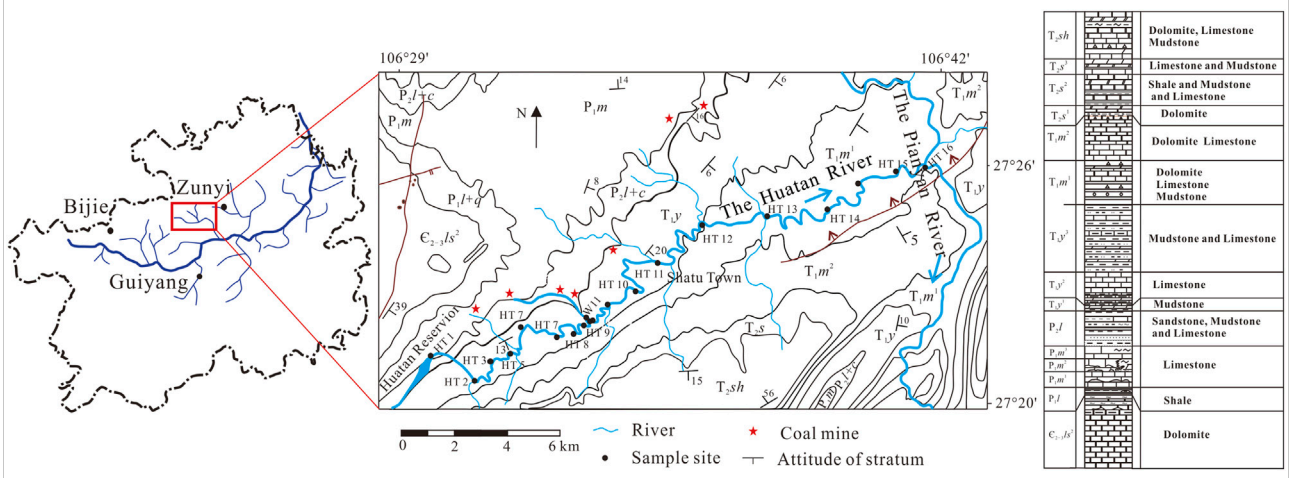

FIGURE 1
The regional geology and sampling point distribution of the Huatan River ($Є_{2-3}ls$: Cambrian Loushanguan group; P_1l: Permian Liangshan Formation; P_1m: Permian Maokou Formation; P_2l: Permian Longtan Formation; P_2c: Permian Changxing Formation; T_1y: Triassic Yelang formation; T_1yn: Triassic Yongningzhen formation).

the Yangtze paraplatform, and Qianbei platform uplift. The structural features are mainly NE trending folds and fault zones, forming a barrier fold combination of wide and gentle anticlines and tight and narrow synclines. The area includes two groups of fault structures: NE trending and nearly EW trending.

The exposed strata in the study area include the lower Permian Maokou Formation (P_1m), the upper Longtan Formation (P_2l), the Changxing Formation (P_2c), and the lower Triassic Yelang Formation (T_1y). Lithologically, the strata mainly comprise carbonate rocks and clastic rocks. Carbonate rocks mainly include the Permian Qixia Formation (P_1q), Maokou Formation (P_1m), Changxing Formation (P_2c), Triassic Yelang Formation (T_1y), and Yongningzhen Formation (T_1yn). Specifically, the Longtan Formation is a coal-bearing rock series, with a thickness of about 95–110 m, containing 4–8 coal layers, and the coal is medium-sulfur anthracite. The Andi anticline is the primary coal controlling structure in the study area. The strata are monoclinal, and the occurrence is relatively stable. In the southeast wing of the anticline structure are many coal mines, such as the Huixin Coal Mine, the Yutiancheng Coal Mine, the Hongxing Coal Mine, the Hebian Coal Mine, and the Changsheng Coal Mine.

2.2 Sample collection and analysis

For the purposes of this study, we chose 18 sampling points in the Huatan River. One sampling point in the stream was affected by AMD (Figure 1). From August 2020 to November 2021, 13 time points of water samples were collected month by month. In addition, two groups of atmospheric precipitation samples were collected in June and August 2021. During sampling, pH, water temperature (T/°C), conductivity (EC), and other variable parameters were recorded on site. The instrument used was the YSI Pro Plus multiparameter water-quality analyzer. Before sampling, the instrument electrodes were calibrated in advance. All samples collected were filtered through a 0.45 μm nylon membrane. Nitric acid was added to each subsample for cation analysis to adjust the pH < 2.0. Each subsample for anion analysis was filtered without reagent and stored in a 50 ml centrifuge tube. All samples were kept in the refrigerator at 4°C until analysis.

Anions, including F^-, Cl^-, NO_3^-, and SO_4^{2-}, were measured using the Dionex ICS-90 Ion Chromatography system (Dionex Corporation, Sunnyvale, CA, United States), while Ca^{2+}, Mg^{2+}, Na^+, K^+, and soluble SiO_2 were determined via the Vista MPX inductively coupled plasma optical emission spectrometer (ICP-OES; Varian, Inc., Palo Alto, CA, United States). Blank samples, parallel samples, and standard samples were added for quality control, and the charge conservation was controlled within ± 5%.

3 Results

The collected data revealed that the pH of the Huatan River was low in summer and autumn (rainy season) and high in winter and spring (dry season). The pH range was 7.47–8.96 (Table 1), and the average value was 8.19, which is generally weak alkaline. The pH in the stream (W11) affected by AMD was always acidic throughout the year, with a range of variation of 4.95–6.91 and an average of 6.43.

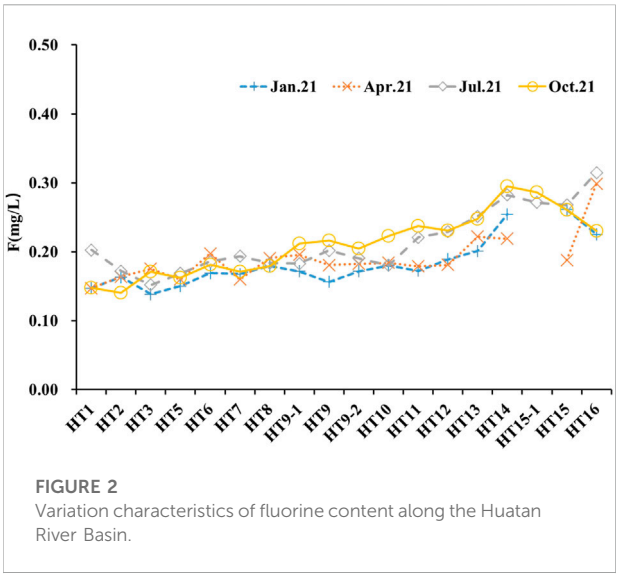

FIGURE 2
Variation characteristics of fluorine content along the Huatan River Basin.

In terms of fluoride concentration, the annual variation range was 0.11–0.40 mg/L (Table 2), with an average of only 0.20 mg/L: Far lower than the limit of 1.0 mg/L for fluoride concentration in drinking water but higher than the average level of unpolluted rivers in the world. In the stream affected by AMD (W11), the concentration of fluorine varied from 0.45 to 1.54 mg/L, with an average of 1.05 mg/L, which was significantly higher than the concentration of fluorine in the Huatan River (Figure 2). In terms of spatial scale, the concentration of fluorine in the Huatan River Watershed demonstrated a gradually increasing trend from upstream to downstream. This finding may be explained by the location of mining activities in the basin, which are mainly in the middle and lower reaches. In terms of time scale, differences in fluorine concentration levels were not very obvious. According to the average level in the watershed, the rainy season was more than 0.20 mg/L, while the dry season was less than 0.20 mg/L.

4 Discussion

4.1 Relationship between fluorine content and hydrochemical parameters

Previous studies have shown that pH drives the form transformation of fluorine in water and is also an important factor affecting the adsorption and desorption of fluorine on the surface of clay minerals. According to Wenzel and Blum (1992), the solubility of fluorite is the smallest when the pH value is 6.0–6.5. Under acidic conditions, the hydroxyl groups on the surface of metal oxides and hydroxides (Al_2O_3, $Fe(OH)_2$) are easily replaced by ionic F^- (Li et al., 2015; Li et al., 2018). Meanwhile, under alkaline conditions, the adsorbed F^- on the surface of silicate minerals will be replaced by HCO_3^- and OH^-, increasing the content of F^- in water (Parfitt and Russell, 1977; Bhatnagar et al., 2011; Mukherjee and Singh, 2020).

The current study findings revealed that the fluorine content in the AMD water samples significantly increased as pH decreased; in contrast, the fluorine content in the Huatan River water samples remained stable and did not increase as pH increased (Figure 3A). This observation indicates that the influence of pH on the resolution of adsorbed fluorine on the surface of silicate minerals in the watershed was limited. Theoretically, summer and autumn are rainy seasons with higher temperatures. Dilution from rainwater should result in a lower concentration of fluorine in river water than in dry seasons. However, as Figure 3 (b) shows, the concentration of fluorine in the Huatan River was higher in the rainy season than in the dry season. This observation may reflect the enhanced leaching and dissolution of fluorine-containing minerals in the rainy season. In addition, as can be seen in Figure 3, EC, SO_4^{2-}, HCO_3^-, Ca^{2+}, and soluble SiO_2 had no noteworthy correlation with fluorine. Obviously, the impact of these parameters in terms of fluoride levels in the river water was limited.

4.2 Hydrochemical composition of the huatan river

Hydrochemical composition of bodies of water often inherits the chemical composition characteristics of the bedrock in the source area (Gaillardet et al., 1999; Li Q. et al., 2016). Based on the ion ratio analysis of Na Standardization (Figure 4A), the hydrochemical composition of the river water in the Huatan River Watershed was primarily controlled by the dissolution of carbonate rocks and silicate rocks, and the influence of evaporates was weak. This finding is consistent with the geological background that carbonate rocks and coal-bearing rock series are widely distributed in the study area. According to the molar ratio of Mg/Ca and Na/Ca, the chemical composition of the river water in the Huatan River Watershed also demonstrated the common influence of dolomite and limestone (Figure 4B). Therefore, fluoride in carbonate rock and silicate rock may have been the dominant source of fluoride in the river water. Previous studies have also shown that carbonate-bound fluorine may be a predominant form of fluorine (Xu and Luo, 2008; Peng et al., 2021).

We sought to further reveal the impact of bedrock weathering and erosion on the chemical composition of river water in the watershed by mapping ion-equivalent concentrations of Ca^{2+}+Mg^{2+} and HCO_3^- + SO_4^{2-} and stoichiometric analysis. From the results presented in Figure 5A, it can be seen that most of the data points are located above the 1:1 evolution line, indicating that the dissolution of carbonate rocks and gypsum had a crucial impact on the chemical composition of the river water. Most of the data points are distributed above the evolution line, indicating the influence of additional HCO_3^- and SO_4^{2-} supplements. Meanwhile, in Figure 5B, after deducting the influence of the carbonate dissolution process

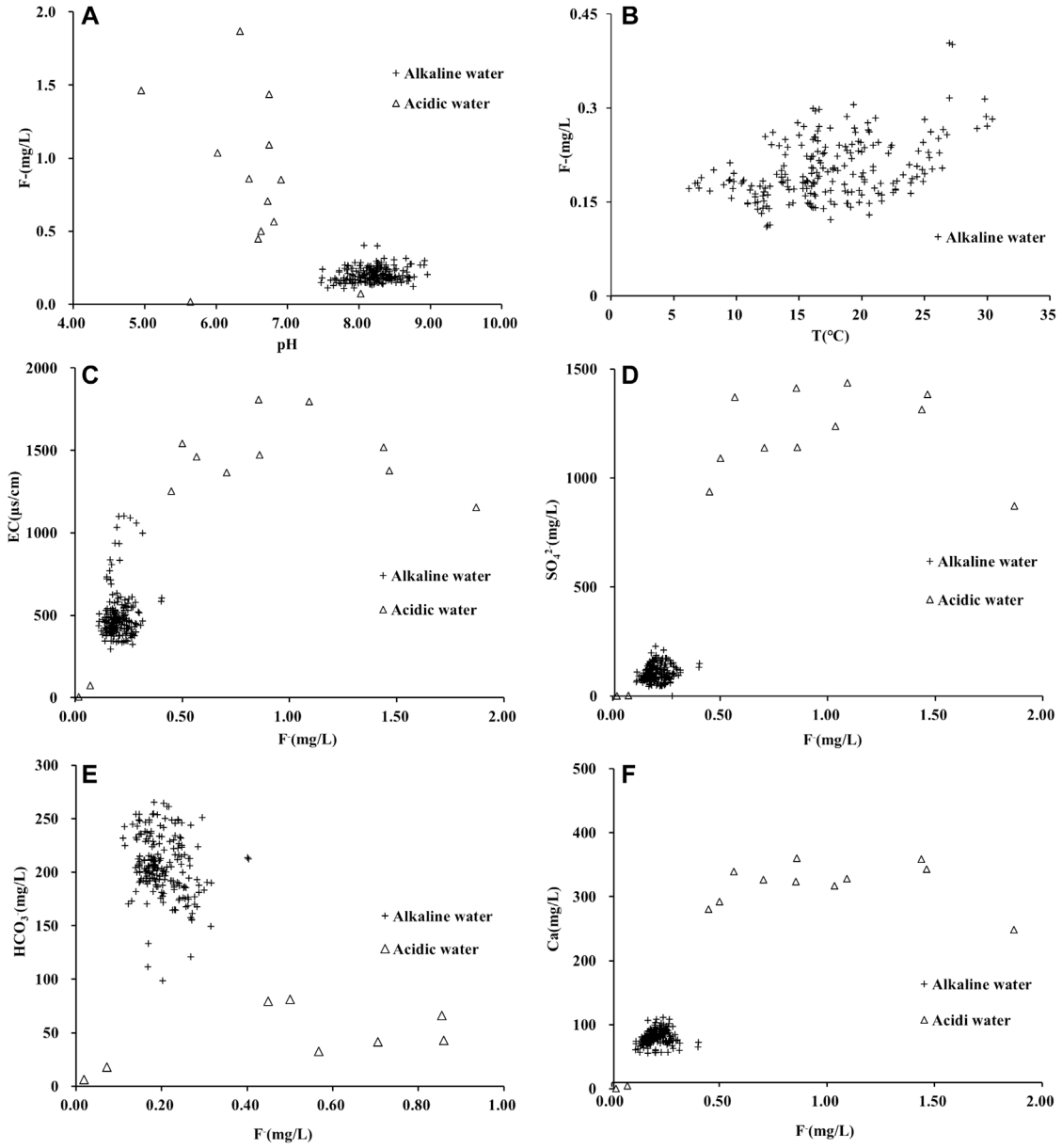

FIGURE 3
Correlation between fluorine content and different hydrochemical parameters in Huatan River Basin. (In all subgraphs, the cross symbol represents alkaline water, and the hollow triangle represents acidic water).

(Ca^{2+}+Mg^{2+}-0.5* HCO_3^-), most data points fall near the 1: 1 evolution line, which further confirms that gypsum dissolution contributed a large quantity of SO_4^{2-} at the experimental site.

It is generally believed that Cl^- mainly comes from atmospheric precipitation and the dissolution of evaporates (Gaillardet et al., 1999; Zhong et al., 2017). Since the molar concentration ratio of Cl^- to Na^+ in atmospheric precipitation is close to 1:1, it can be derived from Figure 5C that the content of Na^+ in the Huatan River was much higher than that of Cl^-. Therefore, it is unlikely that Na^+ was mainly introduced by from atmospheric precipitation. Considering that the contribution of evaporation was also minimal, Na^+ more likely resulted from the ion exchange process and the dissolution of silicate minerals such as clay. The problem is that the dissolved SiO_2 component in Figure 5D seems to have exerted a limited impact on fluorine in the Huatan River. Therefore, even if an extensive dissolution process of silicate minerals was occurring in the watershed, the release of adsorbed fluorine from clay minerals was not the principal source of fluorine in the Huatan River.

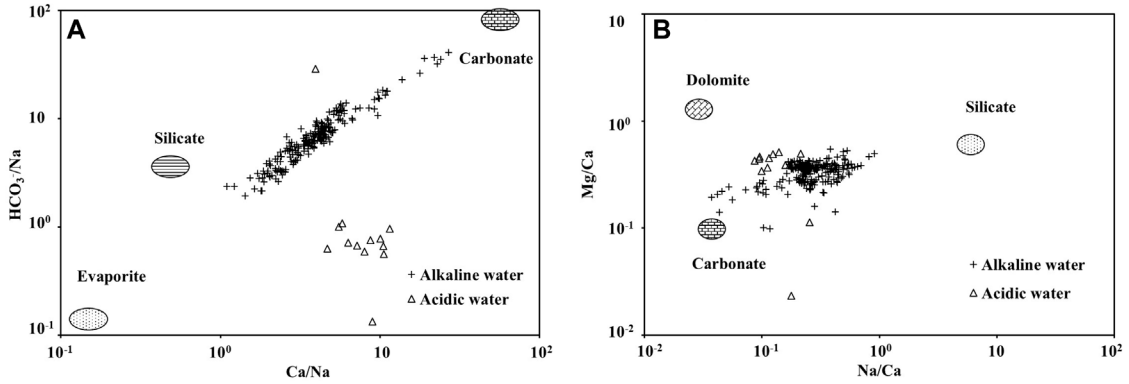

FIGURE 4
Identification of chemical sources in the Chetian River based on **(A)** HCO_3^-/Na^+ versus Ca^{2+}/Na^+ and **(B)** Mg^{2+}/Ca^{2+} versus Na^+/Ca^{2+}.

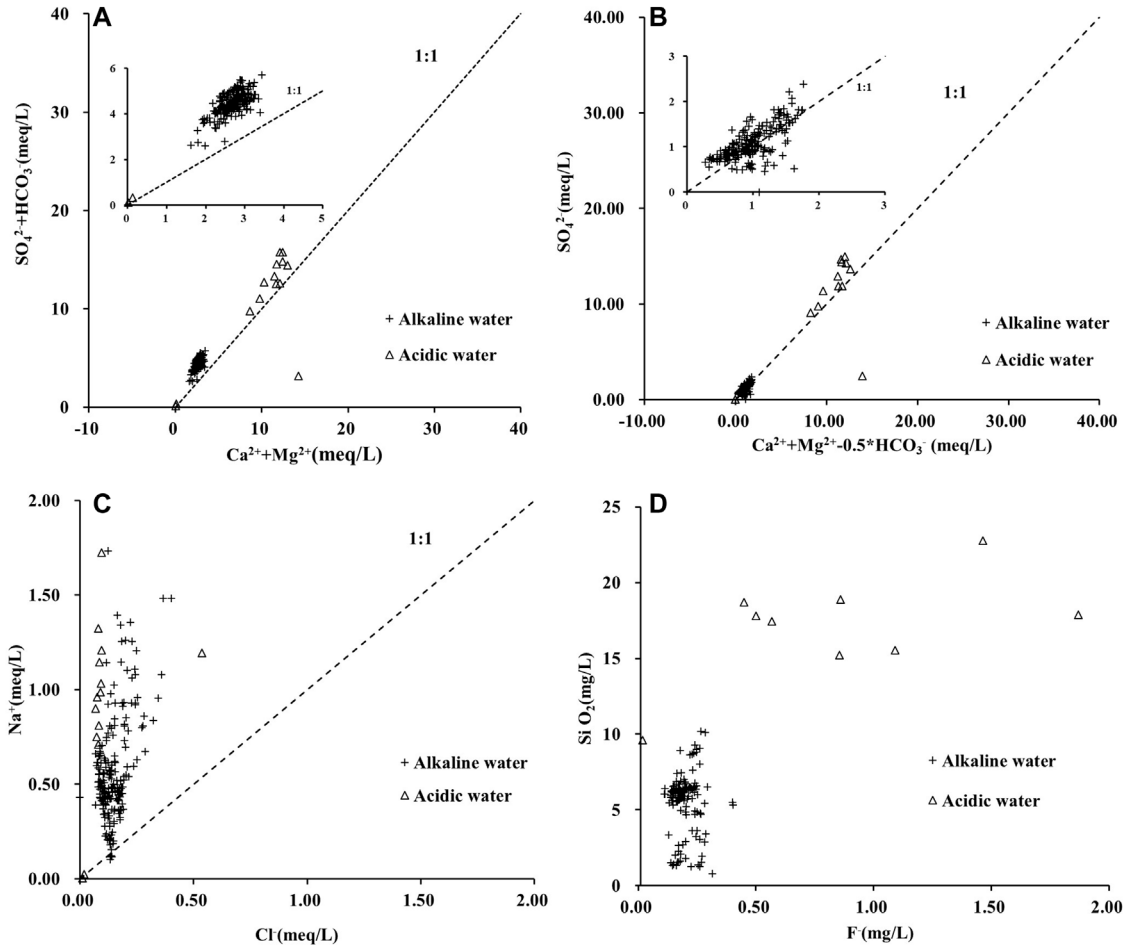

FIGURE 5
Recognition of the contribution of minerals' dissolution to water chemical composition based on scatterplots of **(A)** $Ca^{2+}+Mg^{2+}$ versus $HCO_3^- + SO_4^{2-}$; **(B)** $(Ca^{2+}+Mg^{2+})–0.5*HCO_3^-$ versus SO_4^{2-}; **(C)** Na^+ versus Cl^-; **(D)** F^- versus SiO_2.

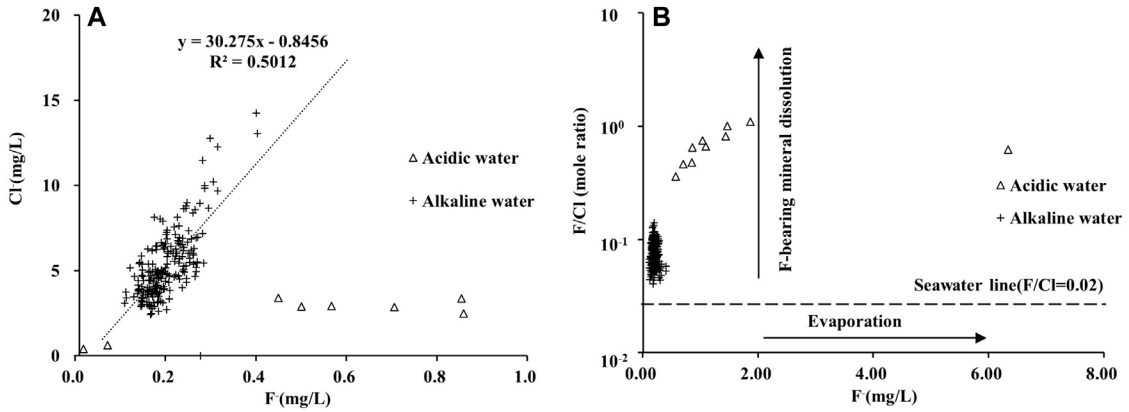

FIGURE 6
(A) Relationship between Cl^- and F^-; **(B)** F^-/Cl^- versus F^- in the Huatan River.

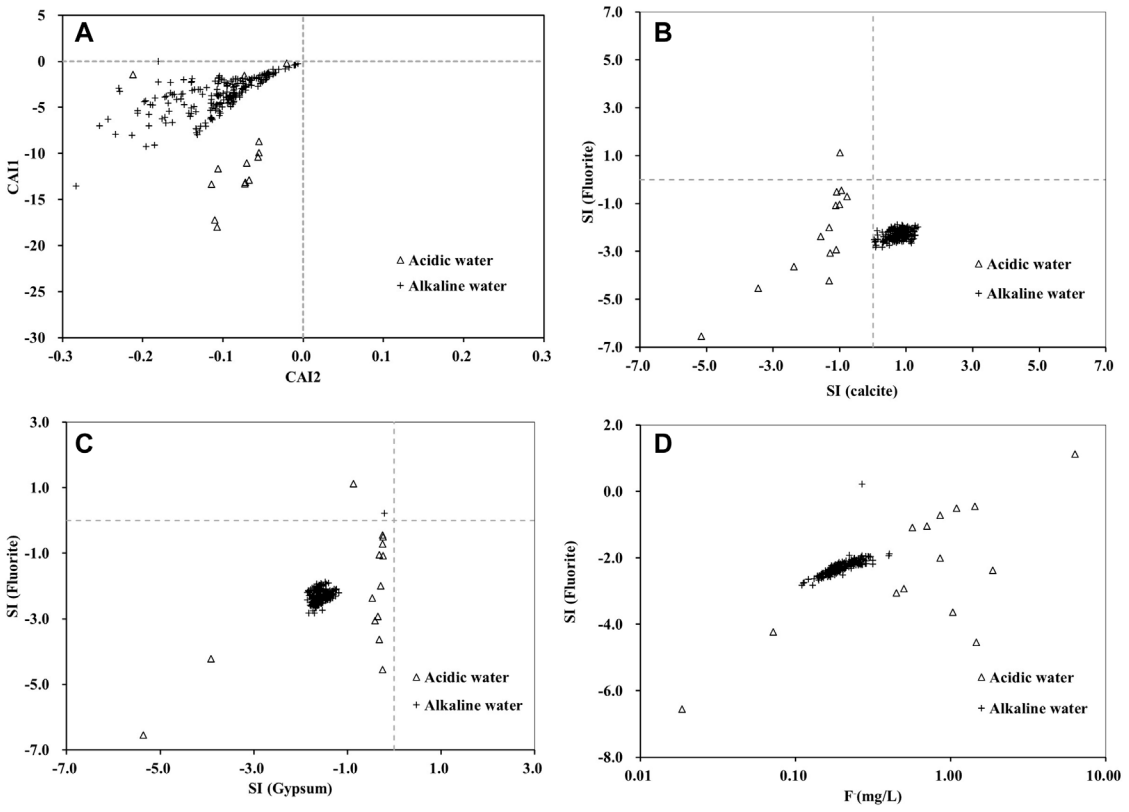

FIGURE 7
Plots of **(A)** CAI-1 versus CAI-2 used to describe cation exchange; **(B)** calcite saturation index versus fluorite saturation index; **(C)** fluorite saturation index versus gypsum saturation index; **(D)** fluorite concentration versus fluorite saturation index.

4.3 Sources of fluorine in the huatan river

Cl^- and F^- are halogens with very similar chemical properties. As illustrated in Figure 6A, a certain correlation existed between Cl^- and F^- in the river water of the Huatan River Watershed. The two rainwater samples collected in June and August 2021 revealed concentrations of fluorine of 0.02 mg/L and 0.07 mg/L, respectively; meanwhile, the concentration of fluorine in the

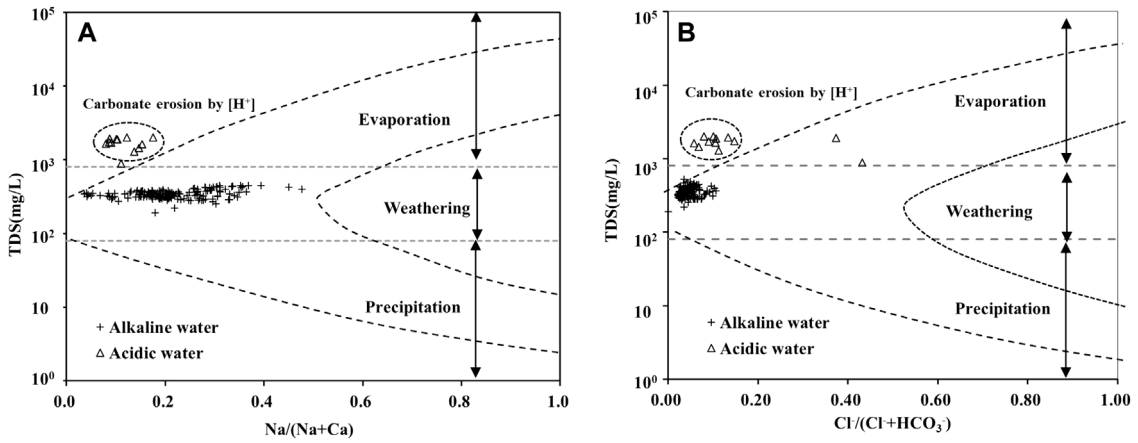

FIGURE 8
Gibbs diagram of the Huatan River based on the relationship of **(A)** TDS versus $Na^+/(Na^+ + Ca^{2+})$; **(B)** TDS versus $Cl^-/(Cl^- + HCO_3^-)$.

TABLE 1 pH data of river water in different months in the Huatan River Basin.

Date position	20.08	20.11	20.12	21.01	21.03	21.04	21.05	21.06	21.07	21.08	21.09	21.10	21.11
HT1	8.13	7.83	8.14	8.28	8.76	8.59	8.58	7.68	8.96	7.48	7.64	7.47	7.79
HT2	7.55	7.94	8.03	7.99	8.11	8.38	8.15	7.60	7.83	7.79	7.81	7.74	7.56
HT3	7.86	8.09	8.27	8.33	8.34	8.46	8.15	7.72	8.03	7.88	7.95	7.87	7.93
HT5	7.98	8.32	8.46	8.59	8.49	8.67	7.80	7.68	7.90	7.66	8.08	8.09	8.21
HT6	7.92	8.24	8.26	8.53	8.45	8.61	8.16	7.74	8.01	7.72	7.99	8.09	7.90
HT7	7.93	8.30	8.40	8.44	8.39	8.69	8.34	7.90	8.22	7.96	8.18	8.16	8.16
HT8	7.88	8.35	8.41	8.41	8.32	8.68	8.37	7.78	8.21	7.49	8.20	8.19	8.16
HT9-1		8.41	8.43	8.54	8.38	8.56	8.52	7.84	8.26	8.10	8.25	8.14	8.18
HT9	7.53	8.05	8.16	8.26	8.20	8.61	8.41	7.66	8.08	7.92	8.02	8.00	7.91
HT9-2		8.22	8.27	8.32	8.31	8.71	8.43	7.99	8.21	7.89	8.22	8.20	8.16
HT10	8.13	8.33	8.34	8.41	8.38	8.70	8.41	8.08	8.27	7.91	8.25	8.20	8.22
HT11	7.92	8.37	8.40	8.46	8.34	8.37	8.49	8.07	8.17	7.83	8.25	8.21	8.30
HT12	7.95	8.39	8.41	8.51	8.32	8.50	8.52	8.06	8.23	7.84	8.26	8.23	8.25
HT13	8.04	8.27	8.34	8.42	8.19	8.43	8.17	8.06	8.24	7.85	8.16	8.02	8.09
HT14	8.22	8.29	8.39	8.36	8.62	8.67	8.20	8.14	8.27	7.94	8.30	8.24	8.30
HT15-1									8.29	7.80	8.01	8.02	8.11
HT15	8.24		8.15	8.24	8.68	8.77	8.72	8.31	8.38	8.16	8.07	7.85	7.90
HT16	8.32	8.12	8.11	8.24	8.73	8.92	8.49	8.35	8.66	8.26	8.26	7.72	7.90
W11	6.17	6.81	6.74	6.91	6.58	6.74	6.72	6.02	6.46	4.95	6.33	6.59	6.63
AVE.	7.97	8.22	8.29	8.37	8.41	8.61	8.35	7.92	8.23	7.86	8.11	8.02	8.06

Huatan River varied from 0.11 to 0.40 mg/L, with an average of 0.20 mg/L. Therefore, although atmospheric deposition should have contributed a certain amount of exogenous fluorine to the Huatan River, it was not the river's main source of fluorine. Prior research has shown that during the process of evaporation, the molar concentrations of Cl^- and F^- increase in the same proportion; in contrast, the process of dissolution of fluorine-bearing minerals results in an increased concentration of F^-, while the concentration

TABLE 2 Data of fluorine concentration in different months in Huatan River Basin (mg/L).

Date position	20.08	20.11	20.12	21.01	21.03	21.04	21.05	21.06	21.07	21.08	21.09	21.10	21.11
HT1	0.19	0.17	0.18	0.15	0.12	0.15	0.17	0.17	0.20	0.18	0.13	0.15	0.11
HT2	0.11	0.17	0.16	0.16	0.15	0.16	0.14	0.17	0.17	0.18	0.14	0.14	0.11
HT3	0.20	0.15	0.18	0.14	0.14	0.18	0.17	0.15	0.15	0.16	0.15	0.17	0.11
HT5	0.12	0.15	0.16	0.15	0.14	0.16	0.27	0.15	0.17	0.18	0.15	0.16	0.14
HT6	0.17	0.17	0.15	0.17	0.19	0.20	0.18	0.16	0.19	0.22	0.15	0.18	0.14
HT7	0.15	0.18	0.18	0.17	0.24	0.16	0.20	0.17	0.19	0.23	0.19	0.17	0.15
HT8	0.08	0.19	0.18	0.18	0.25	0.19	0.22	0.16	0.18	0.24	0.20	0.18	0.14
HT9-1		0.18	0.18	0.17	0.24	0.20	0.15	0.21	0.18	0.23	0.16	0.21	0.13
HT9	0.16	0.19	0.18	0.16	0.20	0.18	0.16	0.16	0.20	0.19	0.18	0.22	0.15
HT9-2		0.19	0.19	0.17	0.25	0.18	0.21	0.19	0.19	0.25	0.21	0.20	0.17
HT10	0.23	0.21	0.20	0.18	0.20	0.18	0.24	0.21	0.18	0.25	0.20	0.22	0.17
HT11	0.10	0.20	0.18	0.17	0.22	0.18	0.27	0.20	0.22	0.24	0.23	0.24	0.17
HT12	0.18	0.18	0.18	0.19	0.30	0.18	0.24	0.19	0.23	0.27	0.24	0.23	0.16
HT13	0.15	0.24	0.21	0.20	0.23	0.22	0.23	0.23	0.25	0.26	0.24	0.25	0.18
HT14	0.23	0.25	0.24	0.25	0.23	0.22	0.25	0.26	0.28	0.28	0.25	0.30	0.19
HT15-1									0.27	0.25	0.27	0.29	0.20
HT15	0.15		0.24	0.26	0.26	0.19	0.28	0.29	0.27	0.26	0.40	0.26	0.20
HT16	0.22	0.26	0.25	0.23	0.28	0.30	0.31	0.32	0.31	0.28	0.40	0.23	0.20
W11	1.26	0.57	1.09	0.86	1.54	1.44	0.71	1.03	0.86	1.46	1.87	0.45	0.50
AVE.	0.16	0.19	0.19	0.18	0.21	0.19	0.22	0.20	0.21	0.23	0.22	0.21	0.16

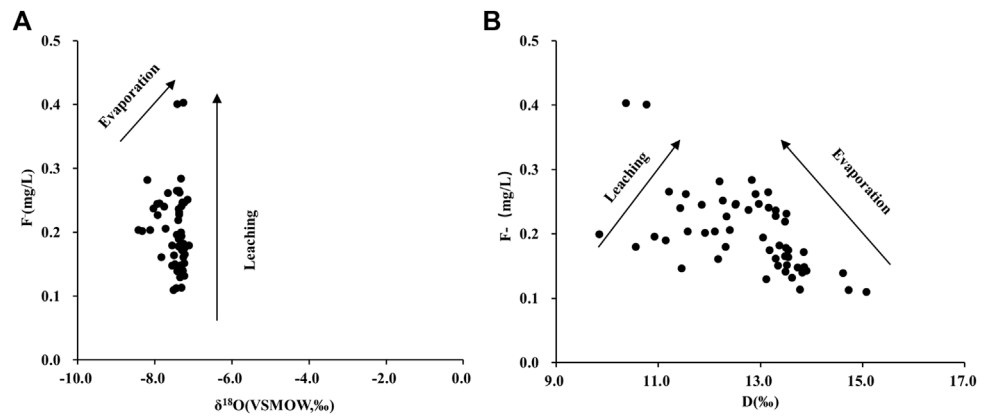

FIGURE 9
(A) Plot of F^- concentration versus $\delta^{18}O$; **(B)** Plot of F^- concentration versus D-excess.

of Cl^- remains stable (Olaka et al., 2016). In light of those previous findings, evaporation was not the main process that induced an increase in fluorine concentration in the surface water in the watershed under consideration. Therefore, the fluorine in the Huatan River may be mainly attributed to the dissolution of fluorine minerals in the watershed (Figure 6B.

4.4 Dissolution and ion exchange of fluorine-bearing minerals

To date, the known fluorine-bearing minerals include fluorite (CaF_2), fluorapatite ($Ca_5(PO_4)_3F$), magnesium fluoride (MgF_2), aluminophosphate ($AlPO_4(F, OH)$), and

others, totaling more than 80 kinds (Deng et al., 2011; Barathi et al., 2019). Under alkaline conditions, the supersaturated state of calcite, dolomite, and other carbonate minerals will promote the reduction of Ca^{2+} and Mg^{2+} concentration and accelerate the dissolution of fluorite, fluorapatite, and other fluorine-bearing minerals, leading to increasing F^- concentration [Eqs. 1–3] (Chen et al., 2020; Zhang et al., 2021; Hao et al., 2022).

$$CaF_2 + 2HCO_3^- \rightarrow CaCO_3 + 2F^- + H_2O + CO_2 \quad (1)$$

$$CaF_2 + H_2O + CO_2(g) \rightarrow CaCO_3 + 2F^- + 2H^+ \quad (2)$$

$$Ca_5(PO_4)_3F + OH^- \rightarrow Ca_5(PO_4)_3OH + F^- \quad (3)$$

$$CaF_2 + SO_4^{2-} + 2H_2O \rightarrow CaSO_4 \bullet 2H_2O + 2F^- \quad (4)$$

The results of the saturation index show that the dissolution of fluorite in the Huatan River Watershed had not reached a saturation state (Figure 7). Calcite revealed supersaturation, which obviously accelerated the dissolution of fluorite, fluorapatite, and other fluorine-bearing minerals. Furthermore, as F^- concentration increased, the saturation index of fluorite demonstrated the law of synchronous increase. Consequently, the dissolution of fluorite can be deemed a vital source of fluorine in the watershed.

In addition, according to Eq. 4, high concentrations of SO_4^{2-} can promote the dissolution of fluorite (Shao et al., 2021; Hao et al., 2022). In the Huatan River Watershed, gypsum also demonstrated an unsaturated state. Mining development in the study area caused the oxidation of a large number of sulfides and transported a large amount of SO_4^{2-} into the Huatan River, which obviously further promoted the dissolution of fluorite.

The chloro-alkaline index (CAI-1 and CAI-2) can be used to estimate the exchange process between main cations in water (Magesh et al., 2020; Hao et al., 2022). When CAI-1 and CAI-2 are less than 0, Ca^{2+} and Mg^{2+} in water tend to exchange with Na^+ and K^+ in silicate minerals. When both CAI-1 and CAI-2 are > 0, Na^+ and K^+ in water tend to exchange with Ca^{2+} and Mg^{2+} in carbonate minerals. Thus, Figure 7A reveals an obvious trend in terms of Ca^{2+} and Mg^{2+} in water replacing Na^+ and K^+ in silicate minerals in the Huatan River Watershed. This conclusion is observably consistent with the view in Figure 5C. Hence, this process can be considered conducive to the release of adsorbed F^- from silicate minerals.

4.5 Evaporation and leaching in the huatan river watershed

A Gibbs diagram is useful for describing the three processes that control changes in water chemical composition: Evaporation, atmospheric rainfall, and water–rock interactions (Li et al., 2015; Li Q. et al., 2016). A perusal of Figure 8A reveals that the impact of atmospheric precipitation and evaporation on the hydrochemical composition of the Huatan River Watershed is minimal. Under the condition where TDS remains basically unchanged, the Na/(Na + Ca) ratio maintains a wide variation range, simply reflecting the process of Ca^{2+} and Mg^{2+} replacing Na^+ and K^+ in silicate minerals, as shown in Figure 7A, in which $Cl^-/(Cl^-+HCO_3^-)$ remains stable.

Evaporation is a notable means of oxygen isotope fractionation in surface water. When strong evaporation is taking place, the oxygen isotope composition becomes heavier, and the F^- concentration in the water body also increases synchronously. At the same time, in the process of evaporation, because the enrichment of ^{18}O is higher than that of D, the D excess will be less than 10‰ (Chen et al., 2021; Mandal et al., 2021; Pant et al., 2021). In addition, during the leaching process, the concentration of F^- increased; however, the variation of $\delta^{18}O$ was limited.

In order to further reveal the influence of evaporation and leaching on F^- enrichment in the watershed, we analyzed the hydrogen and oxygen isotopic composition of water samples in August, September, and November 2021. Figure 9 illustrates the evaporation and leaching processes. As can be observed from the figure, both evaporation and the leaching process had a certain impact on the enrichment of F^- in the watershed; moreover, the impact of the leaching process was more obvious. This conclusion is consistent with the F^-–Cl^- molar ratio (Figure 6B) and Gibbs diagram (Figure 7).

5 Conclusion

The annual variation range of fluorine concentration in the Huatan River Watershed is 0.11–0.40 mg/L, with an average of 0.20 mg/L. In terms of seasonal variation characteristics, the fluorine concentration was higher in the rainy season than in the dry season. The fluorine concentration in the Huatan River also showed spatial variation, increasing gradually along the flow direction; that said, the impact of AMD input on fluorine concentration in the watershed was limited. The water chemical composition of the Huatan River Watershed was generally controlled by the dissolution of carbonate and silicate rocks, and the influence of evaporation was weak. Lastly, the Huatan River Watershed revealed an obvious process where Ca^{2+} and Mg^{2+} was replacing Na^+ and K^+ in silicate minerals.

The dissolution of fluorite and other fluorine-bearing minerals was determined to be a major source of fluorine in the watershed water. Meanwhile, atmospheric precipitation contributed an observable share of fluorine to the Huatan River Watershed. According to the results of the saturation index calculation, the dissolution of fluorite in the Huatan River Watershed was not saturated, and calcite was in a supersaturated state, which was conducive to the dissolution of fluorite, fluorapatite, and other fluorine-bearing minerals. Thus, albeit both evaporation and the leaching process had an evident impact on the enrichment of F^- in the watershed, the influence of the watershed scale leaching process was more obvious.

Data availability statement

The raw data supporting the conclusions of this article will be made available by the authors, without undue reservation.

Author contributions

DS Writing-original draft Data curation Formal analysis Investigation LQ Conceptualization Funding acquisition Writing-review and; editing Data curation Formal analysis Investigation AL Conceptualization Writing-review and; editing Formal analysis Resources HJ Conceptualization Formal analysis WP Supervision Conceptualization Formal analysis GX Investigation Formal analysis.

Funding

This study was sponsored by the National Key Research and Development Plan of China (No.2019YFC1805300), the National Natural Science Foundation of China (Nos. 41867050, U1612442), the Guizhou Provincial Science and Technology Foundation (No. [2019]1,096), the Guizhou Province Talent Base Project (No.RCJD 2018–21), and the First-class Discipline Construction Project of Guizhou Province (No.GNYL [2017] 007).

Conflict of interest

The authors declare that the research was conducted in the absence of any commercial or financial relationships that could be construed as a potential conflict of interest.

Publisher's note

All claims expressed in this article are solely those of the authors and do not necessarily represent those of their affiliated organizations, or those of the publisher, the editors and the reviewers. Any product that may be evaluated in this article, or claim that may be made by its manufacturer, is not guaranteed or endorsed by the publisher.

References

Aghapour, S., Bina, B., Tarrahi, M. J., Amiri, F., and Ebrahimi, A. (2018). Distribution and health risk assessment of natural fluoride of drinking groundwater resources of Isfahan, Iran, using GIS. *Environ. Monit. Assess.* 190 (3), 137. doi:10.1007/s10661-018-6467-z

Balcerzak, M. (2022). "Biomonitoring of human exposure to fluorine," in *Handbook of bioanalytics* (Cham: Springer International Publishing), 1–18.

Barathi, M., Kumar, A. S. K., and Rajesh, N. (2019). Impact of fluoride in potable water–An outlook on the existing defluoridation strategies and the road ahead. *Coord. Chem. Rev.*, 387, 121–128. doi.org/doi:10.1016/j.ccr.2019.02.006

Bhatnagar, A., Kumar, E., and Sillanpää, M. (2011). Fluoride removal from water by adsorption—A review. *Chem. Eng. J.*, 171(3), 811–840. doi.org/doi:10.1016/j.cej.2011.05.028

Cao, H., Xie, X., Wang, Y., and Liu, H. (2022). Predicting geogenic groundwater fluoride contamination throughout China. *J. Environ. Sci.*, 115, 140–148. doi.org/doi:10.1016/j.jes.2021.07.005

Chen, Q., Dong, F., Jia, Z., Wei, J., Jia, C., An, M., et al. (2020). The experimental study of fluorine-leaching ability of granite with different solutions: A new insight into the dynamic of groundwater fluorine levels along coastal zones. *J. Contam. Hydrology*, 235, 103703. doi.org/doi:10.1016/j.jconhyd.2020.103703

Chen, X., Jiang, C., Zheng, L., Zhang, L., Fu, X., Chen, S., et al. (2021). Evaluating the Genesis and dominant processes of groundwater salinization by using hydrochemistry and multiple isotopes in a mining city. *Environ. Pollut.* 283, 117381. doi:10.1016/j.envpol.2021.117381

Deng, Y., Nordstrom, D. K., and McCleskey, R. B. (2011). Fluoride geochemistry of thermal waters in yellowstone national park: I. Aqueous fluoride speciation. *Geochimica Cosmochimica Acta*, 75(16), 4476–4489. doi.org/doi:10.1016/j.gca.2011.05.028

Emenike, C. P., Tenebe, I. T., and Jarvis, P. (2018). Fluoride contamination in groundwater sources in Southwestern Nigeria: Assessment using multivariate statistical approach and human health risk. *Ecotoxicol. Environ. Saf.*, 156, 391–402. doi.org/doi:10.1016/j.ecoenv.2018.03.022

Feng, F., Jia, Y., Yang, Y., Huan, H., Lian, X., Xu, X., et al. (2020). Hydrogeochemical and statistical analysis of high fluoride groundwater in northern China. *Environ. Sci. Pollut. Res.* 27 (28), 34840–34861. doi:10.1007/s11356-020-09784-z

Fuge, R. (2019). Fluorine in the environment, a review of its sources and geochemistry. *Appl. Geochem.* 100, 393–406. doi:10.1016/j.apgeochem.2018.12.016

Gaillardet, J., Dupré, B., Louvat, P., and Allegre, C. J. (1999). Global silicate weathering and CO2 consumption rates deduced from the chemistry of large rivers. *Chem. Geol.*, 159(1-4), 3–30. doi.org/doi:10.1016/S0009-2541(99)00031-5

Ghosh, A., Mukherjee, K., Ghosh, S. K., and Saha, B. (2013). Sources and toxicity of fluoride in the environment. *Res. Chem. Intermed.* 39 (7), 2881–2915. doi:10.1007/s11164-012-0841-1

Guo, J., Wu, H., Zhao, Z., Wang, J., and Liao, H. (2021). Review on health impacts from domestic coal burning: Emphasis on endemic fluorosis in Guizhou Province, southwest China. *Rev. Environ. Contam. Toxicol.* 258, 1–25. doi:10.1007/398_2021_71

Hao, C., Sun, X., Xie, B., and Hou, S. (2022). Increase in fluoride concentration in mine water in Shendong mining area, Northwest China: Insights from isotopic and geochemical signatures. *Ecotoxicol. Environ. Saf.* 236, 113496. doi:10.1016/j.ecoenv.2022.113496

He, X., Li, P., Ji, Y., Wang, Y., Su, Z., Elumalai, V., et al. (2020). Groundwater arsenic and fluoride and associated arsenicosis and fluorosis in China: Occurrence, distribution and management. *Expo. Health* 12 (3), 355–368. doi:10.1007/s12403-020-00347-8

Huang, J., Li, Q., Wu, Pan., Wang, S., Guo, M., and Liu, K. (2022). The effects of weathering of coal-bearing stratum on the transport and transformation of DIC in karst watershed. *Sci. Total Environ.* 838, 156436. doi:10.1016/j.scitotenv.2022.156436

Li, C., Gao, X., and Wang, Y. (2015). Hydrogeochemistry of high-fluoride groundwater at Yuncheng Basin, northern China. *Sci. Total Environ.*, 508, 155–165. doi.org/doi:10.1016/j.scitotenv.2014.11.045

Li, D., Gao, X., Wang, Y., and Luo, W. (2018). Diverse mechanisms drive fluoride enrichment in groundwater in two neighboring sites in northern China. *Environ. Pollut.*, 237, 430–441. doi.org/doi:10.1016/j.envpol.2018.02.072

Li, M., Qu, X., Miao, H., Wen, S., Hua, Z., Ma, Z., et al. (2020). Spatial distribution of endemic fluorosis caused by drinking water in a high-fluorine area in Ningxia, China. *Environ. Sci. Pollut. Res.* 27 (16), 20281–20291. doi:10.1007/s11356-020-08451-7

Li, Q., Ju, Y., Lu, W., Wang, G., Neupane, B., Sun, Y., et al. (2016b). Water-rock interaction and methanogenesis in formation water in the southeast Huaibei coalfield, China. *Mar. Petroleum Geol.*, 77, 435–447. doi.org/doi:10.1016/j.marpetgeo.2016.06.021

Li, X., Wu, P., Han, Z., and Shi, J. (2016a). Sources, distributions of fluoride in waters and its influencing factors from an endemic fluorosis region in central Guizhou, China. *Environ. Earth Sci.* 75 (11), 981. doi:10.1007/s12665-016-5779-y

Liu, J., Peng, Y., Li, C., Gao, Z., and Chen, S. (2021). A characterization of groundwater fluoride, influencing factors and risk to human health in the southwest plain of Shandong Province, North China. *Ecotoxicol. Environ. Saf.*, 207, 111512. doi.org/doi:10.1016/j.ecoenv.2020.111512

Magesh, N. S., Botsa, S. M., Dessai, S., Mestry, M., Leitao, T. D. L., Tiwari, A., et al. (2020). Hydrogeochemistry of the deglaciated lacustrine systems in Antarctica: Potential impact of marine aerosols and rock-water interactions. *Sci. Total Environ.*, 706, 135822. doi.org/doi:10.1016/j.scitotenv.2019.135822

Mandal, R., Das, A., Sudheer, A. K., Kumar, S., Verma, S., Gaddam, M., et al. (2021). Sources, controls, and probabilistic health risk assessment of fluoride contamination in groundwater from a semi-arid region in Gujarat, Western India: An isotope–hydrogeochemical perspective. *Environ. Geochem. Health* 43 (10), 4043–4059. doi:10.1007/s10653-021-00894-2

Masood, N., Hudson-Edwards, K. A., and Farooqi, A. (2022). Groundwater nitrate and fluoride profiles, sources and health risk assessment in the coal mining areas of Salt Range, Punjab Pakistan. *Environ. Geochem. Health* 44 (3), 715–728. doi:10.1007/s10653-021-00987-y

Miguel, M. G., Barreto, R. P., and Pereira, S. Y. (2017). Study of a tropical soil in order to use it to retain aluminum, iron, manganese and fluoride from acid mine drainage. *J. Environ. Manag.* 204, 563–570. doi:10.1016/j.jenvman.2017.09.024

Mukherjee, I., and Singh, U. K. (2020). Fluoride abundance and their release mechanisms in groundwater along with associated human health risks in a geologically heterogeneous semi-arid region of east India. *Microchem. J.*, 152, 104304. doi.org/doi:10.1016/j.microc.2019.104304

Olaka, L. A., Wilke, F. D., Olago, D. O., Odada, E. O., Mulch, A., Musolff, A., et al. (2016). Groundwater fluoride enrichment in an active rift setting: Central Kenya rift case study. *Sci. Total Environ.* 545, 641–653. doi:10.1016/j.scitotenv.2015.11.161

Ozsvath, D. L. (2009). Fluoride and environmental health: A review. *Rev. Environ. Sci. Biotechnol.* 8 (1), 59–79. doi:10.1007/s11157-008-9136-9

Pant, N., Rai, S. P., Singh, R., Kumar, S., Saini, R. K., Purushothaman, P., et al. (2021). Impact of geology and anthropogenic activities over the water quality with emphasis on fluoride in water scarce Lalitpur district of Bundelkhand region, India. *Chemosphere*, 279, 130496. doi.org/doi:10.1016/j.chemosphere.2021.130496

Parfitt, R. L., and Russell, J. D. (1977). Adsorption on hydrous oxides. IV. Mechanisms of adsorption of various ions on goethite. *J. Soil Sci.*, 28(2), 297–305. doi.org/doi:10.1111/j.1365-2389.1977.tb02238.x

Peng, B., Li, X., Ma, Z., and Qi, Y. (2021). Release of fluorine and chlorine during increase of phosphate rock grade by calcination and digestion. *Environ. Pollut.*, 270, 116321. doi.org/doi:10.1016/j.envpol.2020.116321

Savenko, V. S., and Savenko, A. V. (2020). Fluorine in the surface water of bering island. *Water Resour.*, 47(4), 624–628. doi.org/doi:10.1134/S009780782004017X

Shao, S., Ma, B., Chen, Y., Zhang, W., and Wang, C. (2021). Behavior and mechanism of fluoride removal from aqueous solutions by using synthesized $CaSO_4{\cdot}2H_2O$ nanorods. *Chem. Eng. J.*, 426, 131364. doi.org/doi:10.1016/j.cej.2021.131364

Strunecka, A., and Strunecky, O. (2020). Mechanisms of fluoride toxicity: From enzymes to underlying integrative networks. *Appl. Sci.*, 10(20), 7100. doi.org/doi:10.3390/app10207100

Vithanage, M., and Bhattacharya, P. (2015). Fluoride in the environment: Sources, distribution and defluoridation. *Environ. Chem. Lett.* 13 (2), 131–147. doi:10.1007/s10311-015-0496-4

Wang, M., Zhang, L., Liu, Y., Chen, D., Liu, L., Li, C., et al. (2021). Spatial variation and fractionation of fluoride in tobacco-planted soils and leaf fluoride concentration in tobacco in Bijie City, Southwest China. *Environ. Sci. Pollut. Res.* 28 (20), 26112–26123. doi:10.1007/s11356-020-11973-9

Wang, T., Shao, Z., Yu, H., and Bah, H. (2020). Distribution of fluoride in surface water and a health risk assessment in the upper reaches of the Yongding River. *J. Geogr. Sci.* 30 (6), 908–920. doi:10.1007/s11442-020-1761-4

Wenzel, W. W., and Blum, W. E. (1992). Fluorine speciation and mobility in F-contaminated soils. *Soil Sci.* 153 (5), 357–364. doi:10.1097/00010694-199205000-00003

Wu, S., Wang, Y., Iqbal, M., Mehmood, K., Li, Y., Tang, Z., et al. (2022).Challenges of fluoride pollution in environment: Mechanisms and pathological significance of toxicity–A review. *Environ. Pollut.*, 304 119241. doi:10.1016/j.envpol.2022.119241

Xu, L. R., and Luo, K. L. (2008). Studies on mode of occurrence of fluorine in rocks. *Environ. Chem.* 27 (1), 91–95. doi:10.3321/j.issn:0254-6108.2008.01.021

Zhang, M., Hao, H., Tian, L., Wang, J., Li, Y., Sun, Y., et al. (2021). Enrichment mechanisms of gallium and indium in No. 9 coals in anjialing mine, ningwu coalfield, north China, with a preliminary discussion on their potential health risks. *Minerals*, 11(1), 64. doi:10.3390/min11010064

Zhang, Z., Li, G., Su, X., Zhuang, X., Wang, L., Fu, H., et al. (2021). Geochemical controls on the enrichment of fluoride in the mine water of the Shendong mining area, China. *Chemosphere*, 284, 131388. doi.org/doi:10.1016/j.chemosphere.2021.131388

Zhong, J., Li, S. L., Tao, F., Yue, F., and Liu, C. Q. (2017). Sensitivity of chemical weathering and dissolved carbon dynamics to hydrological conditions in a typical karst river. *Sci. Rep.* 7 (1), 42944. doi:10.1038/SREP42944

frontiers | Frontiers in Environmental Science

TYPE Original Research
PUBLISHED 19 August 2022
DOI 10.3389/fenvs.2022.946298

OPEN ACCESS

EDITED BY
Chunhao Gu,
University of Delaware, United States

REVIEWED BY
Juris Burlakovs,
University of Latvia, Latvia
Łukasz Jurczyk,
University of Rzeszow, Poland

*CORRESPONDENCE
Zhangdong Wei,
10380012@vip.henu.edu.cn
Ming Xu,
mingxu@henu.edu.cn

SPECIALTY SECTION
This article was submitted to Toxicology, Pollution and the Environment, a section of the journal Frontiers in Environmental Science

RECEIVED 17 May 2022
ACCEPTED 29 July 2022
PUBLISHED 19 August 2022

CITATION
Wang L, Zeraatpisheh M, Wei Z and Xu M (2022), Heavy metal pollution and risk assessment of farmland soil around abandoned domestic waste dump in Kaifeng City.
Front. Environ. Sci. 10:946298.
doi: 10.3389/fenvs.2022.946298

Heavy metal pollution and risk assessment of farmland soil around abandoned domestic waste dump in Kaifeng City

Lin Wang[1,2,3], Mojtaba Zeraatpisheh[1,3], Zhangdong Wei[2]* and Ming Xu[1,3,4]*

[1]College of Geography and Environmental Science, Henan University, Kaifeng, China, [2]Miami College, Henan University, Kaifeng, China, [3]Henan Key Laboratory of Earth System Observation and Modeling, Henan University, Kaifeng, China, [4]BNU-HKUST Laboratory for Green Innovation, Beijing Normal University, Zhuhai, China

In order to understand the heavy metal pollution and potential ecological risk of farmland soil around the waste dump in the eastern suburb of Kaifeng clearly and provide a scientific basis for the remediation of heavy metals in farmland soil, the single factor pollution index method, Nemero comprehensive pollution index method and Hakanson potential ecological risk method were used to evaluate the heavy metal pollution status and potential ecological risk degree of farmland in this area at the same time. The ArcGIS software was employed to map the spatial distribution of heavy metal pollution and potential ecological risks. The results show that the average values of heavy metals in this area are higher than the soil Background Value of Kaifeng City, and the problem of excessive heavy metals in the soil is significant. Of the 41 surface soil samples, Cd's heavy and moderate pollution rates were up to 15% and 38%, respectively, and the potential ecological risk caused by Cd element was quite serious, and more than 35% of the soil samples were at higher potential ecological risk. The comprehensive review results showed that 38% of the samples were heavy pollution, and 23% of the sample soils were at higher potential ecological risk. The spatial distribution characterized by the levels of most heavy metals and the extent of potential ecological risk showed high levels in the center of the dump, with a gradual decrease towards the outward radiation zone. This means dust and leachate from waste dump are major causes of heavy metal contamination and potential ecological risks. In addition, the retrieval of the waste mound soil from landfills by villagers as soil fertilizer for rapeseed also caused, to some extent, the transfer of the waste mound contaminants.

KEYWORDS

waste dump, agricultural soils, heavy metals, pollution investigation, ecological risk

Introduction

As China's reform and opening-up progress continue to accelerate, the economy is rapidly developing, and its increasingly large city size, urban population, and area are increasing year by year. The consequent urban domestic waste is increasing, which has become a serious problem in urban development in China (Hogland et al., 2002; Huang et al., 2019). Kaifeng City is an important tourism city in Central China, where population growth and urbanization are also very rapid. Since 1990, the annual rise in waste production has been fast, among which municipal solid waste (MSW) is increasing rapidly. Meanwhile, limited by the technical conditions for domestic waste disposal in Kaifeng City, a large volume of domestic waste is mainly disposed of in simple landfills or indirect stacks. Therefore, a large number of hazardous materials, such as heavy metals (HMs), organic pollutants, microorganisms, etc., will be generated during the decomposition of domestic, municipal waste (Yahya et al., 2019), and the hazardous materials can seriously contaminate the local soil and the surrounding environment through fluctuations and downwelling fluids (Alam et al., 2020). Heavy metals in soils are toxic to plants, animals, and humans, and longer exposure leads to bioconcentration (Gao et al., 2019). MSW is usually composed of different forms of toxic and carcinogenic heavy metal elements that may penetrate soil and water bodies. Arsenic (As), cadmium (Cd), chromium (Cr), and nickel (Ni) are classified as class 1 carcinogens by the IARC and are also toxic in nature (IARC, 2018).

Moreover, heavy metal enrichment would be absorbed by different crops and thus enter into a complex food chain, thus causing serious ecological risk (Wakeel et al., 2020). In humans, long-term exposure to contaminated soil tends to negatively affect the central nervous, gastric, and respiratory systems (Khanam R. et al., 2019; Tseng et al., 2019). In addition, previous studies have reported that long-term exposure to heavy metals such as chromium, cadmium, and nickel can cause allergies, asthma, dermatitis, diarrhea, and even lung cancer (Bhattacharya et al., 2015; Moreira et al., 2018).

Current studies on MSW are mainly focused on the physicochemical properties of soil and soil heavy metal contamination after waste stacks (Wan et al., 2012; Li et al., 2014). Zhang et al. (2020) Studies have found that long-term dumps of waste cause a decrease in soil pH, while soil organic matter, total N, available P, and available K increase. Evaluation of the environmental quality of soils from landfill sites in Bangou County, Tibet, revealed that the levels of heavy metals were significantly elevated in the soil surrounding the landfill (Zeng et al. 2021). Li et al. (2015) measured Cu, Zn, Pb, and Cd levels in soil and vegetables from Kaifeng Eastern suburban agricultural soils and showed that Cd contamination was very severe and Zn and Pb genera were slightly contaminated, which was confirmed by Jiang Y. L. et al. (2020). Chen et al. (2020) determined that sewage irrigation and industrial and mining pollution of farmland soil in the eastern suburb of Kaifeng are the actual sources of soil heavy metal pollution in Kaifeng and proposed a multiple linear regression model with an attenuation function to quantify the accumulation of heavy metals in soil by previously determined pollution sources.

This research was focused on the open-air waste dump in the eastern suburb of Kaifeng. High-density samples were carried out on the surrounding farmland by concentric circle sampling, and the content characteristics and spatial distribution of heavy metals in soil were investigated and analyzed, the degree of soil heavy metal pollution and potential ecological risk were evaluated so as to provide a theoretical basis for a reasonable treatment of domestic waste and soil remediation. The study aims to provide data support and model determination for heavy metal pollution assessment of farmland around open-air waste dump.

Materials and methods

Study area

Kaifeng is located in the Middle East of Henan Province. The overall terrain of the whole city is relatively flat. The altitude range is 69–78m. The average annual precipitation is about 630mm, and the average annual temperature is 14°C. It is dominated by the southerly wind in summer and northerly wind in winter, belonging to the continental monsoon climate of the warm temperate zone. The soil quality of the Kaifeng area is formed by the alluvial of the Yellow River. The basic type belongs to yellow tide soil, with a deep soil layer and sandy texture. This study takes the waste dump (34°45′47.46″ N, 114°24′14.93″ E, 72m) as the center, and there are many villages nearby. Almost every village has several farmlands and grows a variety of agricultural products. The waste dump (This place is called Yangzhengmen Waste Mountain) covers an area of 0.066 km^2. Due to the limited capacity of urban garbage treatment, it has been storing urban domestic garbage since 1960, forming a high garbage mountain. A total of 300000 m^3 of garbage are accumulated in the waste dump. The Songlou, Hengchuanwan, Yangzhengmen villages, and other villages are located within 1 km of radiation. Within one kilometer around the waste dump, the color steel insulation board processing plant is located in the East, the vegetable planting area and atmospheric particulate matter settlement monitoring point are built in the southwest. Within 1–2 km around the waste dump, liulizhuang village is in the west, Baita village is in the northwest, and yuxiuqi ecological wetland park is also built in the southeast. Within 2–3 km around the waste dump, chenyanli village, Xiazhang village, Taohua village and other villages are located within the radiation range, and the East is the junction of urban and rural areas, with commercial, residential communities, primary and secondary schools and cash crop planting areas. The open stacking of waste dumps in the eastern suburb of Kaifeng has

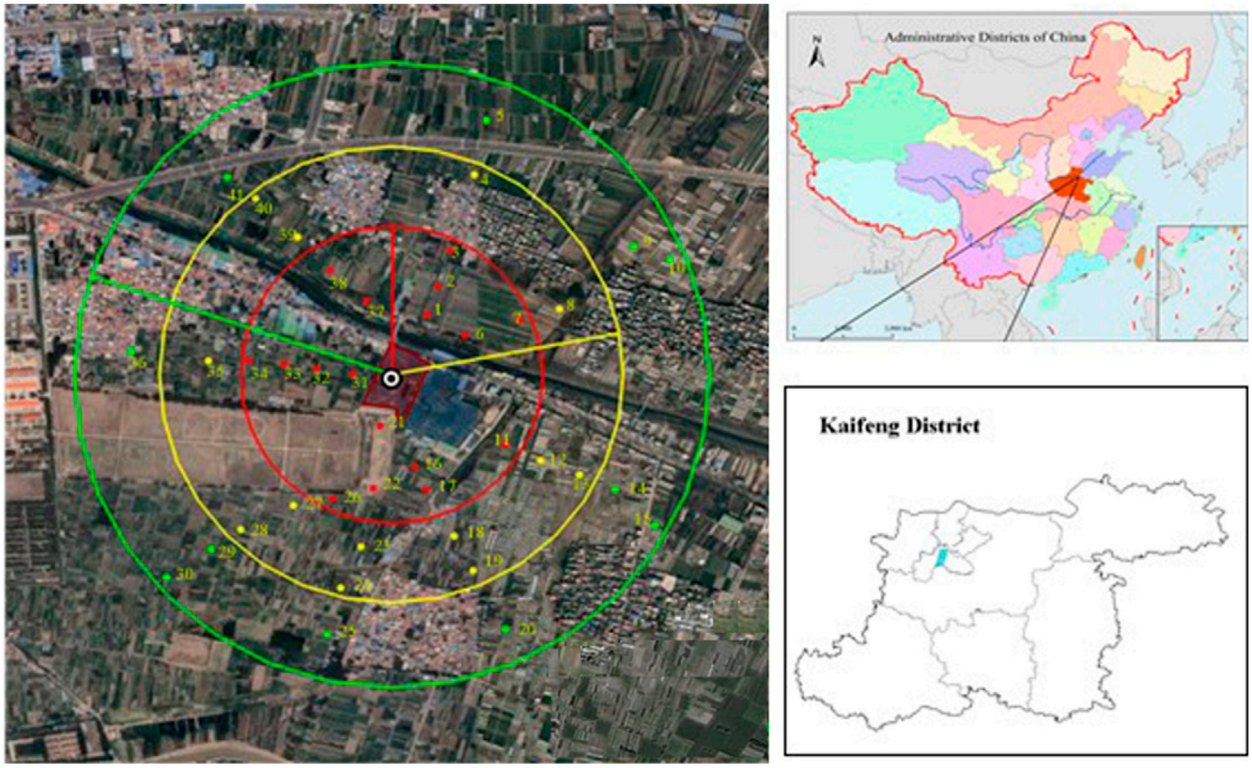

FIGURE 1
Map of the study area and distribution of sampling points. *The center of the concentric circle is the waste dump.

already affected the region's ecological environment. The content of heavy metals in the surrounding farmland soil may reach the pollution level. Due to the enrichment of heavy metals in crops it has a potential threat to the health of local residents.

Sample collection

This study has taken the waste dump in the eastern suburb of Kaifeng as the center and investigates the pollution of farmland soil within 2 km around in a concentric circle (the sampling time was November 2020). The land is subordinate to Nanjiao Township, with a population of 23120. As shown in Figure 1, taking the waste dump as the center of the study area, the study is divided into an inner circle (500 m range, No. 1–17 samples), a middle circle (0.5–1 km range, No. 18–30 samples) and an outer circle (1–2.5 km, No. 31–41 samples). Soil samples are taken from waste dump and farms in the study area and shown in Figure 1 and Table 1. Soil samples were randomly collected by the plum blossom distribution method from 0 to 20 cm in the surface layer and 20–40 cm in the middle layer of croplands, and as shown in Figure 1, a total of 80 point soil samples were taken. Sample 5 kg soil at each point by quartering method, record the longitude, latitude, altitude, and other information of the sampling point, and mark it. The soil samples were air-dried (at room temperature 25°C), crushed, and stones were removed, and then screened with 20 mesh.

Methods of sample analysis

The pH was determined in deionized water with a ratio of 1:2.5 (w/v), using a pH meter (pHS-3C, Leici, China) (Biswas and Mukherjee, 2008). Available phosphorous (AP) and total nitrogen (TN) were extracted with sodium bicarbonate and determined by molybdenum antimony anti Colorimetry. Organic matter (OM) was titrated with potassium dichromate according to the trial implementation of standards for pollution risk control of agricultural land for soil environmental quality (Biswas and Mukherjee, 2008). The farmland pollution risk screening value items were mandatory items, including Cd, As, Pb, Cr, Cu, Ni, and Zn. The total amount of Cd, As, Pb, Cr, Cu, Ni, and Zn were determined by digestion of HNO_3, $HClO_4$ and HF (volume ratio 8:5:2). All samples were replicated 3 times, and the average value was taken.

TABLE 1 Coordinates of the sampling point.

NO. of sampling point	Latitude	NO. of sampling point	Latitude
1	34.7593 N, 114.3928 E	21	34.7546 N, 114.3894 E
2	34.7604 N, 114.3933 E	22	34.7538 N, 114.3887 E
3	34.7628 N, 114.3949 E	23	34.7524 N, 114.3888 E
4	34.7643 N, 114.3958 E	24	34.7505 N, 114.3869 E
5	34.7659 N, 114.3966 E	25	34.7475 N, 114.3888 E
6	34.7586 N, 114.3967 E	26	34.7539 N, 114.3864 E
7	34.7599 N, 114.4000 E	27	34.7541 N, 114.3827 E
8	34.7606 N, 114.4018 E	28	34.7519 N, 114.3786 E
9	34.7617 N, 114.4030 E	29	34.7500 N, 114.3800 E
10	34.7625 N, 114.4039 E	30	34.7451 N, 114.3712 E
11	34.7556 N, 114.3937 E	31	34.7578 N, 114.3883 E
12	34.7547 N, 114.3930 E	32	34.7581 N, 114.3870 E
13	34.7536 N, 114.3944 E	33	34.7585 N, 114.3852 E
14	34.7536 N, 114.3969 E	34	34.7586 N, 114.3836 E
15	34.7500 N, 114.4000 E	35	34.7588 N, 114.3824 E
16	34.7522 N, 114.3916 E	36	34.7588 N, 114.3804 E
17	34.7511 N, 114.3922 E	37	34.7603 N, 114.3880 E
18	34.7500 N, 114.3912 E	38	34.7616 N, 114.3875 E
19	34.7491 N, 114.3925 E	39	34.7633 N, 114.3863 E
20	34.7421 N, 114.3937 E	40	34.7644 N, 114.3852 E
41	34.7661 N, 114.3841 E		

TABLE 2 Soil pollution risk screening value of agricultural land.

NO.	Elements	Risk screening values			
		pH ≤ 5.5	5.5 < pH ≤ 6.5	6.5 < pH ≤ 7.5	pH > 7.5
1	Cd	0.3	0.3	0.3	0.6
2	As	40	40	30	25
3	Pb	70	90	120	170
4	Cr	150	150	200	250
5	Cu	50	50	100	100
6	Ni	60	70	100	190
7	Zn	200	200	250	300

Evaluation method of soil heavy metal pollution

In this study, the single factor pollution index method and Nemero comprehensive pollution index method were used to jointly evaluate the heavy metal pollution of farmland in this area (Khademi et al., 2019). The screening value of farmland pollution risk is shown in Table 2 (Egbueri et al., 2020; Jiang H. et al., 2020; Monged et al., 2020).

Single-factor pollution load index (P_i) and integrated pollution load index (IP_i) were employed to assess the overall level of HMs pollution in the soil samples of the studied area. The pollution load index was determined using the Eq. 1:

$$P_i = \frac{c_i}{s_i} \quad (1)$$

where P_i is the pollution load index for the examined HMs, C_i is the concentration of HMs in a soil sample (mg kg^{-1}), and Si is the

TABLE 3 Graded evaluation standards of heavy metal pollution index.

Levels	P_i	Pollution evaluation	P_N	Pollution evaluation
I	$P_i<1$	Non-pollution	$P_N \leq 0.7$	Cleaning (safety)
II	$1 \leq P_i<2$	Lightly polluted	$0.7 < P_N \leq 1.0$	Still Clean (Alert)
III	$2 \leq P_i<3$	Medium polluted	$1.0 < P_N \leq 2.0$	Lightly polluted
IV	$P_i \geq 3$	Heavy polluted	$2.0 < P_N \leq 3.0$	Medium polluted
V			$P_N>3$	Heavy polluted

TABLE 4 Hierarchical evaluation standards of potential ecological risks of heavy metals.

Levels	E_r^i	RI	Pollution evaluation
I	E_r^i <40	$RI < 150$	Low risk
II	$40 \leq P_i<80$	$150 \leq RI < 300$	Moderate risk
III	$80 \leq E_r^i$ <160	$300 \leq RI < 600$	High risk
IV	$160 \leq E_r^i$ <320	$600 \leq RI < 1200$	Very high risk
V	$E_r^i \geq 320$	$RI \geq 1200$	Extremely high risk

permitted standard of the same metal (mg kg^{-1}) (Men et al., 2018). For calculation of integrated pollution load index (P_N), Eq. 2 was used as follows:

$$P_N = \sqrt{\frac{\left(\frac{1}{n}\sum_{i=1}^{n} Pi\right)^2 + P_{\text{imax}}2}{2}} \quad (2)$$

P_{imax} is the maximum value of P_i, and Piave is the average value of the sum of all P_i, i.e., the three HMs from the 20 sampling sites. If the P_i value is greater than unity, it suggests the existence of pollution or the presence of pollutants, while no pollution loads are inferred. Suppose the value is lower than or equal to unity. Among them, the grading criteria of PN are shown in Table 3 (Yari et al., 2021).

Combined with the principle of the single factor pollution index method, it is considered that as long as one pollutant exceeds the standard, the soil sample exceeds the standard, so the main heavy metals and their harm degree can be determined. The Nemero-comprehensive pollution index method considers a single factor with the most serious pollution and avoids the influence of subjective factors in the weight coefficient in the weighting process. It can more comprehensively reflect the soil environmental quality of the farmland (Yari et al., 2021). The classification and evaluation criteria of the heavy metal pollution index are shown in Table 3.

Potential ecological risk assessment method of soil heavy metals

The potential ecological risk index (PERI) is based on the necessary test item - farmland pollution risk screening value in the trial implementation of standards for pollution risk control of agricultural land for soil environmental quality. Hakanson's potential ecological risk index method evaluated the ecological risk of heavy metal pollution in farmland soil in this area. The classification evaluation standard of the potential risk of heavy metals was established (Hakanson, 1980), as shown in Table 4.

In Table 4, the calculation formula of single factor potential ecological risk index E_r^i is

$$E_r^i = P_i \cdot T_r^i \quad (3)$$

where is the corresponding Toxicity Coefficient of heavy metal element *i* (Cd is 30, As is 10, Pb is 5, Cr is 2, Cu is 5, Ni is 5, and Zn is 1). The calculation formula of comprehensive potential ecological risk index RI is

$$\text{RI} = \sum_{n=1}^{i} E_r^i \quad (4)$$

The single factor potential ecological risk index can reflect the risk degree of each heavy metal, respectively, and the comprehensive potential ecological risk index can reflect the comprehensive risk of a variety of heavy metals.

Data analysis

Through Excel 2019 software, the contents of 7 kinds of necessary heavy metal elements, soil pollution index, and potential ecological risk index of farmland soil around 40 sampling points of an open-air waste dump in the eastern suburb of Kaifeng are statistically analyzed and calculated, and the sampling points are located and mapped by GISMAP software. The classification and classification standard of colors are divided by different degrees corresponding to the single factor pollution index method, Nemero comprehensive pollution index method, and Hakanson potential ecological risk index method (explained by figure legend). According to the observed values of the known sample points in the area, the inverse distance weight method is used to predict the values other than the sample points in the area (Tong et al., 2012). Due to the low complexity of the data, in order to quickly interpolate from the sparse data on irregularly spaced samples, this study selects the inverse distance weight method (IDW) for spatial

TABLE 5 Physico-chemical properties of the soil samples from the study area.

	Mean ± SD	Rang	CV (%)
pH	7.68 ± 0.36	6.55–8.60	4.70(%)
OM(%)	2.03% ± 0.95%	0.11%–4.37%	46.96(%)
TN (%)	16% ± 4%	4%–25%	23.10(%)
AP (g·kg^{-1})	0.24 ± 0.05	0.15–0.36	21.23(%)

interpolation analysis and mapping through Arc Map software (Xiao et al., 2019).

Results and discussion

General characteristics of soils contaminated with municipal solid wastes

Through the potentiometric method for determining soil pH, the pH values of 40 farmland soil in the study area were measured. The results showed that the soil pH values of 80 samples (topsoil and middle soil) ranged from 7.21 to 8.52, the median was 7.73, and the standard deviation was 0.36, indicating that the soil in this area was slightly alkaline or alkaline. The average organic matter content of 80 soil samples in the study area was 2.03%, and the coefficient of variation was 46.96%; the average value of total nitrogen content was 16.00%, and the coefficient of variation was 23.10%; The average value of available phosphorus content was 0.24 g kg^{-1} and the coefficient of variation was 21.23%. Table 5 shows the specific physical and chemical properties and contents of the soil.

Spatial distribution of heavy metals

As shown in the data results in Table 6, the samples in the waste dump are seriously polluted, among which Cd, Pb, As and Zn exceed the standard seriously. The contents of 7 necessary heavy metals of farmland soil in the study area are shown in Table 6, in which the Cd concentration in surface soil ranges from 0.37 mg kg^{-1}–3.00 mg kg^{-1}. The range of Cd of 20–40 cm soil is 0.37–3.00 mg kg^{-1} and the median is 1.27 mg kg^{-1}, which is similar to the median value of soil Cd (0.83 mg kg^{-1}) of soil around Kaifeng reported by Li et al. (2015). The range of Ni in topsoil is 148.63–254.28 mg kg^{-1}, with a median of 198.75 mg kg^{-1}. The range of Ni in the middle soil is 168.33–245.37 mg kg^{-1}, with a median of 1.27 mg kg^{-1}, which is similar to the median value of soil Ni (0.83 mg kg^{-1}) reported by Li et al. (2015). Based on the variation coefficients of these seven different heavy metals, it is found that the variation coefficient pattern is Cu (55.77%) > Cd (42.36%) > As (41.07%) > Zn (38.70%) > Cr (28.39%) > Pb (27.43%) > Ni (11.40%). Cu and Cd have strong variation coefficients, indicating that Cu and Cd are most affected by external pollution factors and human activities in this area. The variation coefficient of Ni is the smallest, indicating that it is

TABLE 6 Statistical results of heavy metals content in farmland soil and the waste dump samples in the study area.

Soil layer	Element	Concentration/(mg·kg^{-1})			SD	CV(%)	Background value
		Mean	Rang	Median			
Surface	Cr	51.32	23.19–90.8	52.00	14.57	28.39	63.80
	Ni	200.41	148.63–254.28	198.75	22.82	11.40	30.06
	Cu	52.30	20.86–155.67	39.70	29.16	55.77	19.70
	Zn	258.07	104.91–554.56	229.92	99.86	38.70	60.10
	As	16.98	8.83–52.53	15.68	6.97	41.07	11.40
	Cd	1.27	0.37–3.00	1.27	0.54	42.36	0.074
	Pb	33.72	16.37–63.72	33.69	9.25	27.43	19.60
Mesocosms	Cr	48.26	29.10–103.06	45.57	14.61	30.34	63.80
	Ni	196.83	168.33–245.37	194.87	15.71	7.98	30.06
	Cu	48.02	16.96–224.21	36.68	38.20	79.54	19.70
	Zn	227.72	56.52–466.61	213.96	83.41	36.62	60.10
	As	16.45	9.96–54.51	15.19	7.31	44.40	11.40
	Cd	1.20	0.27–2.99	1.11	0.56	46.60	0.074
	Pb	32.20	16.55–55.30	30.48	8.50	26.41	19.60
Samples of the waste dump	Cr	90.96	80.77–109.26	89.97	11.01	12.11	—
	Ni	252.31	223.59–274.38	262.10	24.08	9.54	—
	Cu	128.58	96.00–163.88	130.02	25.36	19.72	—
	Zn	486.57	344.82–618.22	517.99	105.31	21.64	—
	As	15.82	14.75–17.05	15.80	0.83	5.29	—
	Cd	1.82	1.70–2.09	1.77	0.16	8.71	—
	Pb	80.57	72.85–90.45	77.97	7.94	9.85	—

less affected by human activities and the content changes little in space. In addition, the range of soil heavy metal content at each sampling point varies greatly. The average values of heavy metals measured are higher than the soil background value of Kaifeng City except for Cr. Among them, the more serious Cd, Cu, Pb, Ni, and Zn are 17.16, 2.65, 1.72, 6.67, and 4.29 times the background value, respectively, indicating that the long-term open-air waste stacking and atmospheric deposition in this area have caused heavy metal pollution in farmland soil, which may increase the potential ecological risk of farmland. The experimental results show that the average values of Cd and Ni in the measured heavy metals are higher than the risk screening values of farmland soil pollution, indicating that Cd and Ni elements may be risky to the quality and safety of agricultural products, crop growth or soil ecology, and soil environmental testing and agricultural products should be strengthened in collaboration Monitoring (Egbueri et al., 2020; Monged et al., 2020).

Soil heavy metal pollution evaluation

In this study, the single factor pollution index method and the Nemero comprehensive pollution index method are used to evaluate the heavy metal pollution of farmland in this area. It can be seen from Table 6 that the average values of the single factor pollution index of the measured heavy metal elements are 0.21, 1.05, 0.52, 0.86, 0.68, 2.12, and 0.20, respectively. The value of Ni is greater than 1, indicating that there is slight pollution of Ni in the area, and the value of Cd is greater than 2, indicating that there is moderate pollution of Cd in the area. The floating dust formed by waste transportation and open stacking may be the main cause of soil heavy metal pollution. According to the Nemero comprehensive pollution index method principle, $1.0 < P_N \leq 2.0$ can be judged as mild pollution, while the survey results show that the average value is 1.61 and the maximum value is as high as 3.66. In terms of the total amount of heavy metal elements, the heavy metal pollution of farmland in this area is serious, and the main contributors to exceeding heavy metals are Cd and Cu. Li et al. (2015) conducted crop and soil investigation on the farmland in the eastern suburb of Kaifeng and found that the Cd content in the local farmland soil was very high, which was basically consistent with the conclusion of this paper. Heavy metals are potential long-term pollutants in soil, which are not easy to leach with water and cannot be decomposed by soil microorganisms but can be enriched by organisms, which often makes heavy metals accumulate gradually in the soil environment and difficult to remove transfer. Therefore, soil heavy metal pollution is more difficult and harmful than water environment heavy metal pollution. This study analyzes the content of heavy metals and Nemero comprehensive pollution index at 40 sampling points by spatial interpolation through the inverse distance weight method in ArcGIS. The results are shown in Figure 2. It can be seen that the content of Cd and Ni in farmland soil in this area is the highest, the pollution degree is the most serious, and the pollution distribution is the most extensive. This is due to the non-standard management of open-air waste dump for many years and the leakage of dust and leachate from the dump (Khademi et al., 2019). It can be seen that in addition to Cu and As, the spatial distribution characteristics of the content of most other heavy metals are high in the central area of the waste dump, and the content in the outward radiation area gradually decreases, indicating that the content distribution is indeed affected by the dust and leachate of the waste dump in the open air (Mutafela et al., 2020). The leachate from the waste dump will also cause heavy metal pollution to the surrounding farmland through surface runoff and underground runoff (Cossu et al., 2018). By comparison, it is found that the content, pollution degree, and pollution distribution of heavy metals in middle soil and surface soil are similar. Therefore, it shows light pollution above the middle soil under the dual action of continuous farmland tillage and open-air discharge of waste dump in this area. This phenomenon also explains the fact that there is long-term pollution in the waste dump. In addition, during the sampling survey, this study found that part of the farmland soil in the village came from the crushed waste residue retrieved by the villagers from the waste dump for crop fertilizer, which also caused the transfer of farmland soil near the center of the waste dump to a certain extent.

The pollution degree of the single factor pollution index and Nemero comprehensive pollution index of different elements in the total sample is shown in Figure 3. It can be seen that according to the evaluation of the single factor pollution index method, there are serious pollution phenomena in the total amount of Cd and Cu, including 62% mild pollution of Ni and 15% severe pollution of Cd. However, there is no pollution of Cr and Pb in the sampled farmland soil. As and Cu in farmland in most areas are pollution-free, and only 5% of farmland is slightly polluted. The distribution of Cd pollution is relatively complex. 8% of farmland is free of pollution, 38% of farmland is slightly polluted, 38% of farmland is moderately polluted, and 15% of farmland is heavily polluted. In addition, according to the Nemero comprehensive pollution index evaluation, 3% of the farmland soils sampled in this area are in a safe state, 8% are in a warning state, 56% are slightly polluted, and 21% are moderately polluted, and 3% are heavily polluted. Chen et al. (2020) analyzed the distribution characteristics of heavy metals in the soil around the fertilizer plant in the eastern suburb of Kaifeng and found that the contents of Cu, Pb, Zn, Cd, and other heavy metals in the soil around the fertilizer plant are significantly high, which has been seriously polluted by heavy metals. Ma et al. (2014) have concluded that there is no pollution of Ni, Zn, Cu, and Pb in the farmland soil far away from the industrial park in different functional areas of Kaifeng County. The overall environmental quality of the core area is excellent, and only Cd is good and average in some areas. Most areas in the core area of the comprehensive evaluation are pollution-free, and the soil's environmental quality is excellent. This is because the farmland in the western suburb is far away from the industrial

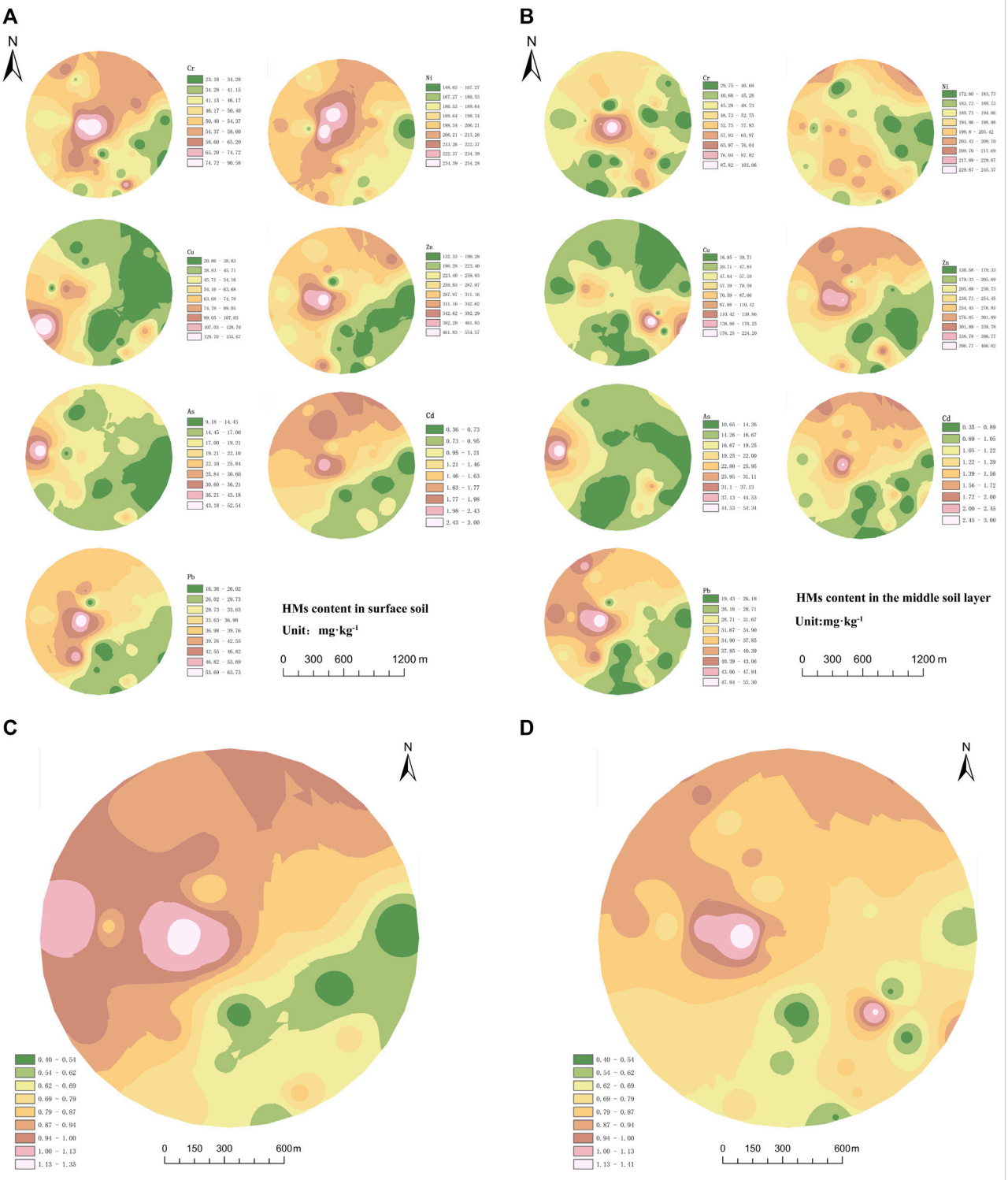

FIGURE 2
Spatial distribution of Single-factor pollution index and Nemero comprehensive pollution index. **(A)** Single-factor pollution index in surface soil; **(B)** Single-factor pollution index in the middle soil layer; **(C)** Nemero comprehensive pollution index in surface soil; **(D)** Nemero comprehensive pollution index in the middle soil layer. *Stars represent the waste dumps.

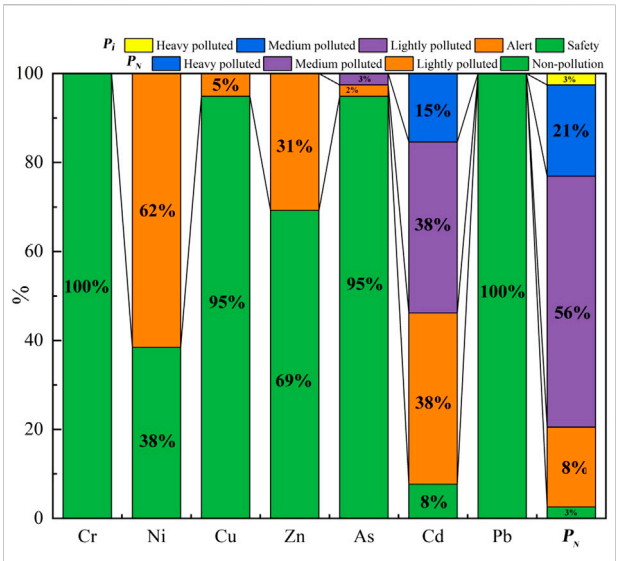

FIGURE 3
Distribution of soil heavy metal pollution.

TABLE 7 The potential ecological risk index E_r^i and RI of different heavy metals.

Sample	E_r^i							*RI*
	Cr	Ni	Cu	Zn	As	Cd	Pb	
Max	0.72	6.69	7.78	1.85	21.01	155.07	1.87	168.85
Median	0.19	3.91	1.04	0.35	3.53	18.47	0.48	29.31
Min	0.42	5.23	1.98	0.77	6.27	63.34	0.99	80.47
Mean	0.41	5.27	2.61	0.86	6.79	63.49	0.99	80.43
SD	0.12	0.60	1.45	0.33	2.78	26.89	0.27	29.13
CV(%)	28.29	11.41	55.77	38.70	41.06	42.37	27.43	36.21

park and open-air landfill, which reduces the heavy metal pollution and potential ecological risk, which is consistent with the conclusion of this paper.

Potential ecological risk assessment of soil heavy metals

Considering the toxicity differences of different heavy metals, this study adopts Hakanson's potential ecological risk index method to evaluate the ecological risk of heavy metal pollution in farmland soil in this area. The potential ecological risk index of different heavy metals is shown in Table 7. The average values of the single factor potential ecological risk indexes of the measured heavy metal elements are 0.42, 5.27, 2.61, 0.86, 6.79, 63.49, and 0.99, respectively. Among them, the potential ecological risk indexes of as, Pb, Cr, Cu, Ni, and Zn are all less than 40, and the values of Pb, Cr, Ni, and Zn are far less than 40, so the ecological risk is very low. However, the average value of Cd is greater than 80 but less than 160, and the maximum value is as high as 155, indicating that there is a high potential ecological risk of Cd in this area. In addition, the average value of the comprehensive potential ecological risk index is 80.43, less than 150. However, there are more than 150 sample points in the central area of the landfill, indicating that there is a medium potential ecological risk under the comprehensive consideration of the pollution of these seven heavy metals in this area.

The potential ecological risk index is analyzed by spatial interpolation through the inverse distance weight method in ArcGIS. The results are shown in Figures 4A,B. It can be clearly shown the potential ecological risk degree of different areas in the study area. The content of Cd in farmland soil in this area is high, and the Toxicity Coefficient of Cd is as high as 30. Therefore, the potential ecological risk caused by Cd is very serious, and other elements have a lower toxicity coefficient than Cd. Therefore, although heavy metal pollution exceeds the standard to varying degrees, the potential ecological risk is relatively low. Generally speaking, the relatively high potential ecological risks caused by different elements are mainly concentrated around the Tonglushan site, and the farther the distance is, the lower the potential ecological risk is. This also proves that the transportation of dust, leachate, and residue produced by open-air stacking waste is the main reason for the potential ecological risk to the surrounding soil. It can be seen from the comparison of Figures 4C,D that the potential health risk index of Mesocosms soil is lower than that of surface soil.

For the potential ecological risk caused by Cd, 30% of the sample soil is at low potential ecological risk, 35% of the sample soil is at medium potential ecological risk, 23% of the sample soil is at high potential ecological risk, 5% of the sample soil is at high potential ecological risk, and 7% of the sample soil is at ultra-high potential ecological risk, which is similar to the conclusion of "potential ecological risk of Cd in farmland soil around Daye Lake" studied by (Jiang et al., 2020). Cadmium is a non-essential element of the human body. It can be enriched in the body to form cadmium, this protein, which accumulates in the liver and kidney, resulting in cadmium poisoning. Cadmium is widely used in industrial production, which is easier to be absorbed by crops than other heavy metals and is easy to be discharged into the environment through waste gas, wastewater, and waste residue, resulting in pollution (Essien et al., 2019). Pollution sources are mainly mining and transportation of mineral resources, smelting and electroplating non-ferrous metals, and factories using cadmium compounds as raw materials or catalysts (Shao and Yang, 2020). Many industrial products in municipal solid waste need cadmium-containing raw materials or catalysts. Therefore, the dust and leachate of these wastes cause cadmium pollution in local soil in different ways. Another main reason may be closely related to the application of phosphorus fertilizer and pesticide, which have a long history, wide range, and large amount. Therefore, cadmium from phosphorus fertilizer and some pesticides in crops may exceed cadmium from other pollution sources (Shi et al., 2019). The potential ecological risk

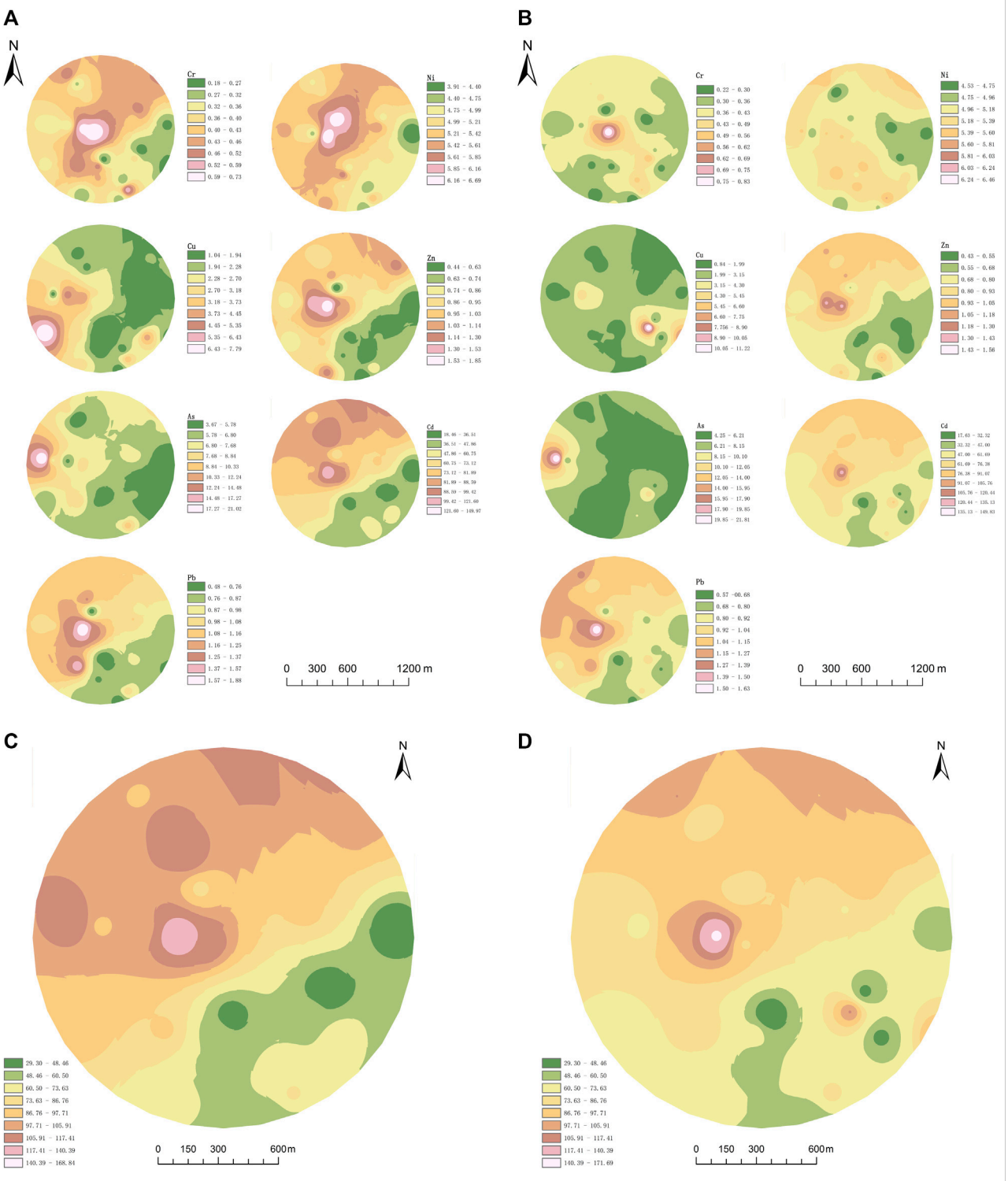

FIGURE 4
Spatial distribution of potential ecological risks of soil heavy metals. *Stars represent the waste dumps.

of other elements is low, and only Ni has a low proportion of high-risk sample soil. Considering the potential ecological risks, among the 80 sample varieties, 92% of the sample soil is at low risk, 8% of the sample soil is at medium risk, and there is no high-risk sample soil. Soledad et al. analyzed the content and distribution of Hg, Pb, Cd, Cr, as, Cu, and Zn in the surface sediment of Texcoco saline lake and

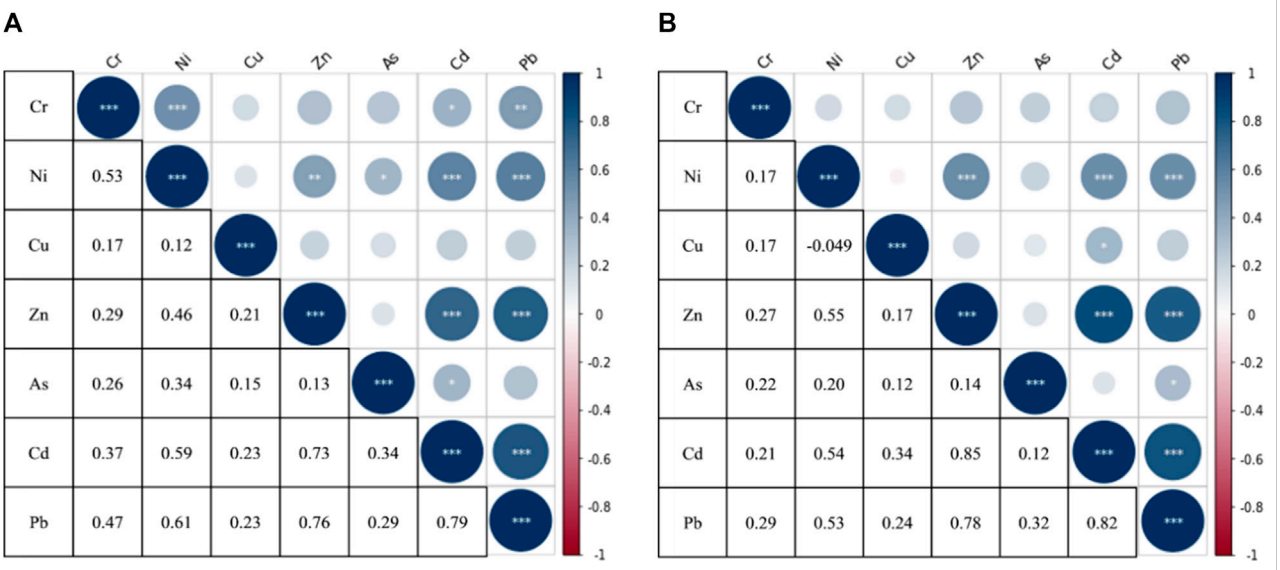

FIGURE 5
Pearson correlation matrix between total heavy metals. **(A)** Suface; **(B)** Mesocosms; *$p \leq 0.05$, **$p \leq 0.01$, and the size of the circle represents the absolute value of the correlation coefficient.

found that the comprehensive potential ecological risk index in this area is 65.70–128.72, with an average value of 227.63, most of which belong to low risk, which is basically consistent with the conclusion of this study (Soledad et al., 2020).

Analysis on correlation and source of heavy metals in soil

Because the source, migration, and transformation of heavy metal elements in soil usually have a certain relationship, the correlation analysis can intuitively reflect the degree of correlation between various elements. It can be seen from Figure 5A that the total amount of heavy metals in the topsoil of Cr, Ni, Zn, Cd, and Pb in the study area has a significant positive correlation with each other at the level of 0.05, and the correlation coefficient is greater than 0.5; The total amount of heavy metals in Cd has a significant positive correlation with Zn at the level of 0.05. The total amount of heavy metals in Ni has a significant positive correlation with Cr at the level of 0.05. The total amount of heavy metals in Cu has a weak or no correlation with other elements. It can be seen from Figure 5B that the total amount of heavy metals in the middle soil of Cr, Ni, Zn, Cd and Pb in the study area has a significant positive correlation with each other at the level of 0.05, and the correlation coefficient is greater than 0.5; The total amount of heavy metals in Cd has a significant positive correlation with Zn at the level of 0.05, and the correlation coefficients are greater than 0.8; The total amount of heavy metals in Cu has weak or no correlation with other elements. According to the correlation analysis of the total amount of heavy metals in surface and middle soil, the correlation between Ni, Zn, and Cd is significant. There is a significant positive correlation between Zn and Cd elements, and their spatial distribution characteristics of potential ecological risk index are basically the same, but their correlation with other elements is weak or no correlation. Combined with the characteristics of high Cd and Pb elements in individual points in the central and western regions, the two sources are more in line with the law of local leakage of dust activities in the open-air stacking of waste.

According to the above analysis, the correlation between Cr, Ni, Cu, Zn, As, Cd, and Pb elements is good, which is suitable for principal component analysis. KMO and Bartlett methods were used to test the total data of heavy metals Cr, Ni, Cu, Zn, As, CD, and Pb in soil. The results showed that KMO was 0.762 and 0.747, respectively, and the companion probability of the Bartlett sphericity test was 0.000, which met the data requirements of principal component analysis. The results of principal component analysis show that: Two factors with large eigenvalues are extracted from the upper soil, accounting for 66.67% of the total variance of the explanatory variable. Three factors with large eigenvalues are extracted from the middle soil, accounting for 77.68% of the total variance of the explanatory variable. Factor 1 and factor 2 can reflect most of the information from the original data. The elements with a high first-factor load of total heavy metals are Cr, Cu, Zn, as, Cd, and Pb, and the variance contribution rate can reach 81.8%, indicating that Cr, Cu, Zn, as, Cd, and Pb have homology (Ma et al., 2018). The pollution of heavy metals in the soil near a municipal waste dump in northern China was studied. The results showed that the high

contents of heavy metals were mainly as, Cd, Pb, Zn and Cu, and their sources were mainly floating dust and leachate caused by the open stacking of municipal waste in the region. Combined with the statistical analysis and spatial distribution law of heavy metals, it can be seen that the main sources of Cr, Cu, Zn, as, Cd and Pb are waste dust and leachate input caused by the non-standard management of waste dumps in the eastern suburbs. The elements with the higher load of the second factor are Ni and Cr, and the contribution rate of variance is 14.8%. Combined with the previous research on ecological risk and spatial distribution, the ecological risk of Ni and Cr is low, the coefficient of variation is small, and Cr is usually in the residual form (Wang et al., 2019; Jiang T. et al., 2020). Therefore, the main source of the second factor is more in line with the law of natural input. This result is consistent with the research conclusion of Sun et al. (2018) and María et al. (2011). that is, Ni and Cr are more derived from the parent material and background of soil formation and belong to natural source metals.

Conclusions

1) The single factor pollution index of each element is between 0.01 and 5.58, the single factor indexes of Cd and as are 1.50 and 2.13, respectively, and the evaluation results are light pollution and light pollution, respectively. The single factor index of Pb exceeds 5, which belongs to heavy pollution. The enrichment factors of As, Hg, and Zn are 3.73, 10.4, and 22.4, which belong to moderate pollution, heavy pollution, and serious pollution, respectively. The enrichment factor of Cd and Pb exceeds 40, which belongs to extremely heavy pollution and is obviously polluted by artificial pollution.
2) The content of heavy metals in the soil measured in the study area is higher than the background value of the soil in Kaifeng City, and the variation range is large. The heavy metal pollution problem is significant. Cd has the strongest coefficient of variation, which is strongly affected by human activities. Among the detected heavy metal elements, Cd and Ni have serious pollution phenomena, but due to the high toxicity of Cd, the heavy metal pollution and potential ecological risks caused by Cd are the most serious. The spatial distribution characteristics of the content of most heavy metals and the degree of potential ecological risk in the area are as follows: the central area of the mining area is high, and the outward radiation area gradually decreases, indicating that the floating dust and leachate caused by the open-air stacking of urban waste in the area are the main causes of heavy metal pollution and potential ecological risk. In addition, the villagers took the soil from the waste dump as farmland soil, which also caused the transfer of heavy metal pollution to a certain extent.
3) The results of correlation and principal component analysis of total and available heavy metals in soil showed that the correlation between Cu, Zn, as, Cd, and Pb was significant, and the main source was the input of industrial production activities; There is a significant positive correlation between Cd and Zn, but there is no correlation with other elements; The main source of Ni is more in line with the law of natural input.
4) In the next study, different spatial interpolation methods of soil heavy metals [such as ordinary Kriging (OK), inverse distance weight method (IDW), and radial basis function method (RBF)] can be used to improve the reliability of the analysis results. In addition, increasing the scope of the study area and sampling density will also help to improve the analysis accuracy further.

Data availability statement

The original contributions presented in the study are included in the article/Supplementary Material, further inquiries can be directed to the corresponding authors.

Author contributions

Conceptualization, ZW and MX. Investigation and methodology, ZW. Formal analysis, ZW. Resources, MX and WL. Supervision, MX and WL. Writing—original draft, LW. Writing—review and editing, MZ. All authors have read and agreed to the published version of the manuscript.

Conflict of interest

The authors declare that the research was conducted in the absence of any commercial or financial relationships that could be construed as a potential conflict of interest.

Publisher's note

Supplementary material

The Supplementary Material for this article can be found online at: https://www.frontiersin.org/articles/10.3389/fenvs.2022.946298/full#supplementary-material

References

Alam, P., Sharholy, M., and Ahmad, K. (2020). "A study on the landfill leachate and its impact on groundwater quality of Ghazipur area, New Delhi, India," in *Recent developments in waste management*. Editor A. Kalamdhad (Singapore: Springer), 345–358. doi:10.1007/978-981-15-0990-2_27

Bhattacharya, B. D., Nayak, D. C., Sarkar, S. K., Biswas, S. N., Rakshit, D., and Ahmed, M. K. (2015). Distribution of dissolved trace metals in coastal regions of Indian sundarban mangrove wetland: a multivariate approach. *J. Clean. Prod.* 96, 233–243. doi:10.1016/j.jclepro.2014.04.030

Biswas, T. D., and Mukherjee, S. K. (2008). *Textbook of soil science*. Second ed. New Delhi, India: Tata McGraw-Hill publishing company.

Chen, Z. F., Hua, Y. X., Wei, Z. D., and Pei, J. C. (2020). Analysis of heavy metal pollution sources in peri-urban farmland based on positive definite matrix factor Analysis model. *Acta Sci. Circumstantiae)* 40 (01), 276–283. doi:10.13671/j.hjkxxb.2019.0380

Cossu, R., Zuffianò, L. E., Limoni, P. P., Giorgio, G. D., Pizzardini, P., Miano, T., et al. (2018). How can the role of leachate on nitrate concentration and groundwater quality be clarified? An approach for landfills in operation (Southern Italy). *Waste Manag.* 77, 156–165. doi:10.1016/j.wasman.2018.05.014

Egbueri, J. C., Ukah, B. U., Ubido, O. E., and Unigwe, C. O. (2020). A chemometric approach to source apportionment, ecological and health risk assessment of heavy metals in industrial soils from southwestern Nigeria. *Int. J. Environ. Anal. Chem.* 98, 1–19. doi:10.1080/03067319.2020.1769615

Essien, J. P., Inam, E. D., Ikpe, D. I., Udofia, G. E., and Benson, N. U. (2019). Ecotoxicological status and risk assessment of heavy metals in municipal solid wastes dumpsite impacted soil in Nigeria. *Environ. Nanotechnol. Monit. Manag.* 11 (100), 100215. doi:10.1016/j.enmm.2019.100215

Gao, M., Lin, Y., Shi, G. Z., Li, H. H., Yang, Z. B., Xu, X. X., et al. (2019). Bioaccumulation and health risk assessments of trace elements inhousefly (*Musca domestica* L.) larvae fed with food wastes. *Sci. Total Environ.* 682, 485–493. doi:10.1016/j.scitotenv.2019.05.182

Hakanson, L. (1980). An ecological risk index for aquatic pollution control.a sedimentological approach. *Water Res.* 14, 975–1001. doi:10.1016/00431354(80)90143-8

Hogland, W. (2002). Remediation of an old landsfill site: soil analysis, leachate quality and gas production. *Environ. Sci. Pollut. Res. Int.* 1, 49–54. doi:10.1007/bf02987426

Huang, Y., Wang, Y., Sun, Y., Kai, Y., and Chen, L. (2019). Microbial community structure and population distribution characteristics in short-term landfill-age garbage dumps. *J. Environ. Sci. (Beijing, China)* 39 (12), 4122–4131. doi:10.13671/j.hjkxxb.2019.0318

IARC (2018). Chromium (IV) compounds. IARC Monograph 100C. Available at: https://monographs.iarc.fr/wp-content/uploads/2018/06/mono100C-9.pdf (Accessed January 24, 2022).

Jiang, H., Cai, L., Wen, H., Hu, G., Chen, L., and Luo, J. (2020). An integrated approach to quantifying ecological and human health risks from different sources of soil heavy metals. *Sci. Total Environ.* 701, 134466. doi:10.1016/j.scitotenv.2019.134466

Jiang, T., Lin, W. W., Cao, Y. J., Li, K., Xuan, Y. X., Li, R., et al. (2020). Pollution and ecological risk assessment and source apportionment of heavy metals in sediments of Qingliangshan Reservoir in the Meijiang Basin. *Chin. J. Environ. Sci.* 41 (12), 5410–5418. doi:10.13227/j.hjkx.202003018

Jiang, Y. L., Ruan, X. L., and Ma, J. H. (2020). Characteristics and classification management of heavy metal pollution in polluted farmland near a battery factory in Xinxiang City. *Acta Sci. Circumstantiae.* 40 (02), 645–654. doi:10.13671/j.hjkxxb.2019.0343

Khademi, H., Gabarrón, M., Abbaspour, A., Martínez-Martínez, S., Faz, A., and Acosta, J. A. (2019). Environmental impact assessment of industrial activities on heavy metals distribution in street dust and soil. *Chemosphere* 217, 695–705. doi:10.1016/j.chemosphere.2018.11.045

Khanam, R., Kumar, A., Nayak, A., Shahid, M., Tripathi, R., Vijayakumar, S., et al. (2019). Metal(loid)s (As, Hg, Se, Pb and Cd) in paddy soil: bioavailability and potential risk to human health. *Sci. Total Environ.* 699, 134330. doi:10.1016/j.scitotenv.2019.134330

Li, Y. M., Ma, J. H., Liu, D. X., Sun, Y. L., and Chen, Y. F. (2015). Assessment of heavy metal pollution and potential ecological risks in soil in Kaifeng City. *Chin. J. Environ. Sci.* 36 (03), 1037–1044. doi:10.13227/j.hjkx.2015.03.037

Li, Y. X., Huang, Y., Wang, N., Yang, J., Xu, M. M., Sun, B., et al. (2014). Characteristics of heavy metal pollution and health risk assessment of domestic waste dump near the outskirts of a city in Shandong Province. *Environ. Chem. (Beijing, China)* 33 (09), 1476–1483. doi:10.7524/j.issn.0254-6108.014.09.009

Ma, J. H., Ma, S. Y., and Chen, Y. Z. (2014). Migration and accumulation of heavy metals in soil-crop-human hair system in a polluted irrigation area of Henan Province. *Acta Sci. Circumstantiae.* 34 (06), 1517–1526. doi:10.13671/j.hjkxxb.2014.0216

Ma, W., Tai, L., Qiao, Z., Zhong, L., Wang, Z., Fu, K., et al. (2018). Contamination source apportionment and health risk assessment of heavy metals in soil around municipal solid waste incinerator: a case study in North China. *Sci. Total Environ.* 631, 348–357. doi:10.1016/j.scitotenv.2018.03.011

María, T. R., Ofelia, M., Elizabeth, H., Lozano, R., and Tapia-Cruz, V. (2011). The study of metal contamination in urban topsoils of Mexico City using GIS. *Environ. Earth Sci.* 62 (5), 899–905. doi:10.1007/s12665-010-0584-5

Men, C., Liu, R., Xu, F., Wang, Q., Guo, L., and Shen, Z. (2018). Pollution characteristics, risk assessment, and source apportionment of heavy metals in road dust in Beijing, China. *Sci. Total Environ.* 612, 138–147. doi:10.1016/j.scitotenv.2017.08.123

Monged, M. H. E., Hassan, H. B., and El-Sayed, S. A. (2020). Spatial distribution and ecological risk assessment of natural radionuclides and trace elements in agricultural soil of northeastern nile valley, Egypt. *Water Air Soil Pollut.* 231, 338. doi:10.1007/s11270-020-04678-9

Moreira, L. J., da Silva, E. B., Fontes, M. P., Liu, X., and Ma, L. (2018). Speciation, bio-accessibility and potential risk of chromium in Amazon forest soils. *Environ. Pollut.* 239, 384–391. doi:10.1016/j.envpol.2018.04.025

Mutafela, R. N., Mantero, J., Jani, Y., Thomas, R., Holm, E., and Hogland, W. (2020). Radiometrical and physico-chemical characterisation of contaminated glass waste from a glass dump in Sweden. *Chemosphere* 241, 124964. doi:10.1016/j.chemosphere.2019.124964

Shao, L., and Yang, X. (2020). Analysis of water pollution sources in copper smelting industry. *Chin. J. Min. Mag.* 29 (S1), 551–553. doi:10.12075/j.issn.1004-4051.2020.S1.04

Shi, T., Zhang, Y., Gong, Y., Ma, J., Wei, H., Wu, X., et al. (2019). Status of cadmium accumulation in agricultural soils across China (1975–2016): from temporal and spatial variations to risk assessment. *Chemosphere* 230, 136–143. doi:10.1016/j.chemosphere.2019.04.208

Soledad, M. S., Meza-Olvera, E., Shruti, V. C., and Sedeno-Diaz, J. E. (2020). Assessment of metal contamination and their ecological risks in wetland sediments of the former Texcoco saline lake, Mexico. *J. Soils Sediments* 20, 2912–2930. doi:10.1007/s11368-020-02613-3

Sun, H., Bi, R. T., Guo, Y., Cai, M., and Guo, Z. X. (2018). Source apportionment analysis of trace metal contamination in soils of Guangdong province, China. *Acta Sci. Circumstantiae.* 38 (2), 704–714. doi:10.13671/j.hjkxxb.2017.0351

Tong, Z. Q., Gu, L., Duan, H. J., and Ma, J. H. (2012). Spatial distribution of heavy metals in roadside soils based on kriging interpolation: a case study of zhengzhou-kaifeng section along the 310th national highway. *Acta Sci. Circumstantiae.* 32 (12), 3030–3038. doi:10.13671/j.hjkxxb.2012.12.020

Tseng, C. H., Lee, I. H., and Chen, Y. (2019). Evaluation of hexavalent chromium concentration in water and its health risk with a system dynamics model. *Sci. Total Environ.* 669, 103–111. doi:10.1016/j.scitotenv.2019.03.103

Wakeel, A., Xu, M., and Gan, Y. (2020). Chromium-induced reactive oxygen species accumulation by altering the enzymatic antioxidant system and associated cytotoxic, genotoxic, ultrastructural, and photosynthetic changes in plants. *Int. J. Mol. Sci.* 21, 728. doi:10.3390/ijms21030728

Wan, S. M., Xi, B. D., Li, M. X., and Xia, X. F. (2012). Effects of long-term accumulation of rural domestic waste on soil nitrification rate and respiration rate. *J. Northeast Agric. Univ. Chin. Ed.* . 43 (11), 67–71. doi:10.19720/j.cnki.issn.1005-9369.2012.11.014

Wang, Y. Y., Li, F. F., Wang, X. Y., Yang, Z. H., Han, K., and Ruan, X. L. (2019). Spatial distribution and risk assessment of heavy metal contamination in surface farmland soil around a lead and zinc smelter. *J. Environ. Sci. (Beijing, China)* 40 (1), 437–444. doi:10.13227/j.hjkx.201803031

Xiao, Y. T., Zhang, R. X., and Wu, P. (2019). Review on common spatial interpolation methods for soil heavy metal analysis. *Environ. Sci. Technol. (Wuhan, China)* 42 (3), 198–205. doi:10.19672/j.cnki.1003-6504.2019.03.028

Yahya, J., Burlakovs, J., Augustsson, A., Marcia, M., and Hogland, W. (2019). Physicochemical and toxicological characterization of hazardous wastes from an old glasswork dump at southeastern part of Sweden. *Chemosphere* 237, 124568. doi:10.1016/j.chemosphere.2019.124568

Yari, A. A., Varvani, J., and Zare, R. (2021). Assessment and zoning of environmental hazard of heavy metals using the Nemerow integrated pollution index in the vineyards of Malayer city. *Acta Geophys.* 69 (1), 149–159. doi:10.1007/s11600-020-00514-0

Zeng, D., Meng, D., and Zhou, W. (2021). Comprehensive analysis and evaluation of environmental impact of landfill in Bangor County, Tibet. *J. Environ. Eng. Technol. (Beijing, China)* 11 (1), 202–208. doi:10.12153/j.issn.1674-991X.20200062

Zhang, Q. Q., Xu, B., and Li, Y. Z. (2020). Effect of application method of compost products of food waste on soil physicochemical properties. *Landsc. Archit.* 7, 74–79. doi:10.12193/j.laing.2020.07.0074.013

frontiers | Frontiers in Environmental Science

TYPE Original Research
PUBLISHED 24 August 2022
DOI 10.3389/fenvs.2022.976618

OPEN ACCESS

EDITED BY
Hongbiao Cui,
Anhui University of Science and Technology, China

REVIEWED BY
Kailou Liu,
Jiangxi Institute of Red Soil, China
Yuji Jiang,
Institute of Soil Science (CAS), China
Yanfang Feng,
Jiangsu Academy of Agricultural Sciences (JAAS), China

*CORRESPONDENCE
Ping Cong,
congping@caas.cn
Xuebo Zheng,
zhengxuebo@caas.cn

†These authors have contributed equally to this work

SPECIALTY SECTION
This article was submitted to Toxicology, Pollution and the Environment, a section of the journal Frontiers in Environmental Science

RECEIVED 23 June 2022
ACCEPTED 27 July 2022
PUBLISHED 24 August 2022

CITATION
Du J, Meng L, Qiu M, Chen S, Zhang B, Song W, Cong P and Zheng X (2022), Ammonia-oxidizing archaea and ammonia-oxidizing bacteria communities respond differently in oxy-gen-limited habitats.
Front. Environ. Sci. 10:976618.
doi: 10.3389/fenvs.2022.976618

Ammonia-oxidizing archaea and ammonia-oxidizing bacteria communities respond differently in oxy-gen-limited habitats

Jialin Du[1,2†], Lin Meng[1†], Mingsheng Qiu[3], Shuaiwei Chen[4], Binghui Zhang[5], Wenjing Song[1], Ping Cong[1*] and Xuebo Zheng[1*]

[1]Tobacco Research Institute of Chinese Academy of Agricultural Sciences, Qingdao, China, [2]College of Agronomy, Qingdao Agricultural University, Qingdao, China, [3]Longyan City Company of Fujian Tobacco Company, Longyan, China, [4]China Tobacco Shandong Industrial Co., Ltd., Longyan, China, [5]Fujian Branch of China Tobacco Company, Fuzhou, China

Ammonia-oxidizing archaea (AOA) and bacteria (AOB) are the most important ammonia oxidation functional community, while the coastal environment just provides a different oxygen environment for the ammonia oxidation process. However, few surveys concentrated on the influence of oxygen concentration on the niche specialization of AOA and AOB in the ocean intertidal zones. Here, high-throughput sequencing by Illumina MiSeq and qPCR were applied to detect the change of abundance, diversity as well as community structure of both AOA and AOB with 0–60 cm sediments depth in the intertidal zone in Qingdao, China. Results showed that the AOA/AOB *amoA* gene copy numbers and AOA/AOB OTU numbers rate increased as sediment depth went more profound, which indicated that AOA was more adaptive to oxygen-limited niches compared to AOB. Oxygen indeed led to the niche specialization of AOA and AOB in intertidal sediments. The dominant AOA and AOB were the clusters of *Nitrosopumilus* and *Nitrosospira*, respectively, which indicated ecological success in the intertidal zone. A significant and positive correlation ($p < 0.01$) between AOB abundance/AOB OTU numbers and Oxidation-reduction potential (ORP) was observed. In addition, both total nitrogen (TN) ($p < 0.01$) and pH ($p < 0.05$) were significantly negatively correlated to AOB abundance. TN was also significantly negatively correlated to AOB OTU numbers ($p < 0.05$). Hence, oxygen led to niche specialization of AOA and AOB, especially under anoxic conditions, AOA played a dominant role in the process of ammonia oxidation. The *Nitrosopumilus* and *Nitrosospira* clusters were the dominant AOA and AOB, respectively, representing an ecological success in the intertidal zone.

KEYWORDS

AOA, AOB, niche specialization, intertidal zone, high-throughput sequencing

Introduction

Nitrification, a vital role in the ecosystem nitrogen cycle, converts ammonia to nitrate through nitrite (Beeckman et al., 2018). Three kinds of microorganisms of ammonia oxidizers, nitrite oxidizers, and complete ammonia oxidizers were involved in the nitrification process (Stein and Klotz, 2016). Ammonia-oxidizing bacteria (AOB) were long thought to be the only microorganism that performed ammonia oxidation, the first rate-limiting step in nitrification. However, the ammonia oxidation theory was changed after discovering ammonia-oxidizing archaea (AOA) (Konneke et al., 2005). To date, several strains of AOA, such as Candidatus *Nitrososphaera gargensis* (Hatzenpichler et al., 2008), Candidatus *Nitrosocaldus yellowstonii* (de la Torre et al., 2008), Candidatus *Nitrosoarchaeum limnia SFB1* (Blainey et al., 2011), and Candidatus *Nitrosotalea devanaterra* (Lehtovirta-Morley et al., 2011), were enriched or isolated from various ecosystems. Until now, both AOA and AOB have been shown to perform ammonia-oxidizing (de la Torre et al., 2008; Hatzenpichler et al., 2008; Jia and Conrad, 2009). Various AOA and AOB functional gene abundance, community structures, and activity patterns were reported in different biotopes (Wang et al., 2020). Environmental factors play a crucial role in the niche differentiation between AOA and AOB. Moreover, the AOA and AOB relative contribution to ammonia oxidation in various ecosystems gradually become the hot spots in the field of ammonia oxidation.

As reported previously, a series of environmental factors may cause the niche specialization between AOA and AOB, such as pH, temperature, salinity, ammonia concentrations, and oxygen concentrations. AOA seems to be more adaptive in niches with lower pH and more likely to dominate the process of ammonia oxidation in acidic niches (Gubry-Rangin et al., 2011; Prosser and Nicol, 2012). AOB was more adaptable than AOA with increasing abundance but no composition alteration at elevated temperature (Zhang et al., 2019). Microcosm test also verified that pH and temperature were vital factors that led to the niche specialization of AOA and AOB (Aigle et al., 2020). Ammonia, as one of the substrates for ammonia oxidation, could cause niche specialization of AOA and AOB. The concentration of ammonia half-saturation constant of some AOB strains (Martens-Habbena et al., 2009; Jung et al., 2011; Kim et al., 2012) was much higher than AOA strains, indicated that AOA had a higher affinity for ammonia than AOB. The half-saturation constants of Candidatus *Nitrosoarchaeum koreensis MY1*, Candidatus *Nitrososphaera* sp. *JG1* and *Nitrosopumilus maritimus SCM1* were 0.69 , 2.15 μM, and 133 nM, respectively, which were much lower than that of *Nitrosomonas europaea* (K_m = 553 μM) (Martens-Habbena et al., 2009). Therefore, AOA is more competitive than AOB in the oligotrophic environment (Beman et al., 2008; Verhamme et al., 2011). In other substrates for ammonia oxidation, oxygen could also lead to niche specialization of AOA and AOB. The half-saturation constants for oxygen of AOA, such as Candidatus *Nitrosoarchaeu mkoreensis MY1*, Candidatus *Nitrososphaera* sp. *JG1* and *N. maritimus SCM1* were 10.38, 4.67, and 3.90 μM, separately (Martens-Habbena et al., 2009; Jung et al., 2011; Kim et al., 2012), which were much lower than that of *Nitrosomonas oligotropha NL7* (76.3 μM) and *N. europaea C-31* (183.3 μM) (Park et al., 2010; Park and Noguera, 2007). The affinities of AOA for oxygen were much higher than that of AOB, which means that AOA had competitive advantages over AOB in oxygen-limited environments. The AOA lived better in many oxygen-limited environments. AOA dominated the transcriptome and probably dominated the ammonia oxidation process in the oxygen minimum zone (Stewart et al., 2012). The increasing AOA OTU number and abundance ratio (AOA: AOB) in flooded soil proved that AOA could better adapt to low oxygen conditions (Liu et al., 2015).

The intertidal zone is an ecological crisscross zone with significant environmental and ecological functions affected by marine and terrestrial ecosystems (Community structure and organization of tidepools). The daily tidal rhythm made the sediment is submerged or exposed to air. As one of the biggest wharves in Qingdao, the Shazikou wharf is significantly affected by human activities and the decayed fish, which provided enough ammonia nitrogen for the ammonia-oxidizing microbes in nearby intertidal zones. The ecological distribution, including the community structure and AOA/AOB abundance in intertidal zones, have been discussed previously (Bernhard et al., 2005; Zhang et al., 2015; Hu et al., 2019). However, the relationships between oxygen concentration and niche specialization of AOA and AOB have not been investigated, especially, the ecological distribution of AOA and AOB under oxy-gen-limited habitats under different layers/depth of the sediments. So, the main objectives of this research are: 1) to study the difference of abundances and community structure of AOA and AOB in different layers/depth of the sediments in the intertidal zones, 2) to explore which, AOA or AOB, was the main driver performing ammonia oxidation in different layers/depth of the sediments in intertidal zones, 3) to evaluate how the oxygen concentration influences the niche specialization of AOA and AOB in intertidal zones.

Materials and methods

Description of sampling sites

The sampling sites were distributed in Shazikou wharf coast (36°6′N, 120°33′E). The Shazikou wharf was built in 1976 and was one of the biggest wharves in Qingdao, China. The region is located in the north temperate monsoon region, with a temperate monsoon climate. Regulated by the marine environment, it also

has significant marine climate characteristics. The mean annual temperature is 12.6°C, and the mean annual rainfall is 734.3 mm. The sunshine duration is 2281.4 h, with a frost-free period of 179 days. Coastal lowlands or coastal beaches are typical saline soils.

Collection and physicochemical properties analysis of sediment

The sediment samples were collected using a cylindrical soil sample from the ocean intertidal zone near the Shazikou wharf in Qingdao, Shandong Province. Three sampling sites (biological triplicates) along the sandy beach were selected. For each site, different depths (0–10, 10–20, 20–30, 30–40, 40–50, and 50–60 cm, namely S_{0-10}, S_{10-20}, S_{20-30}, S_{30-40}, S_{40-50}, S_{50-60}, respectively) were sampled, and the sediments in the same depth were mixed. Totally six sediment samples were obtained. Each sample was divided into two subsamples: one, stored at 4°C, was used to analyze physicochemical properties; another, frozen at −80°C, was applied to molecular analysis. The soil pH was determined at a soil: water ratio of 1:5 with a conductivity meter (FE38-FiveEasyPlus™, Mettler-Toledo, Zurich, Switzerland). The oxidation-reduction potential (ORP) was measured by an ORP meter (ORP-2096, Boqu, China). The content of moisture content (MC) was measured at the same time with soil samples collecting, and the method of oven-drying at 105°C for 10 h. Total nitrogen (TN) was measured by Kjeldahl method. The ammonium (NH_4^+-N) and nitrate (NO_3^--N) were leached with KCl solution (1 mol L^{-1}), and the filtrate was taken and measured by a continuous flow analyzer (Seal-AA3, Germany). The nitrite (NO_2^--N) was determined by ultraviolet spectrophotometry (Liu et al., 2013).

DNA extraction and quantitative PCR of *amoA* genes

Total genomic DNA was extracted from the fresh soil samples by employing the E.Z.N.A.® soil DNA Kit (Omega Bio-tek, Norcross, GA, United States) as the protocols of manufacturer. The final DNA concentration of extracts was determined using a NanoDrop 2000 UV-vis spectrophotometer (Thermo Scientific, Wilmington, United States). The extracted DNA quality was assessed on 1% agarose gel using a nanometer droplet spectrophotometer (ND-1000; Isogen Life Science, Netherlands) to measure the concentration of DNA.

For the quantification of genes (AOB/AOA *amoA*) copy numbers, the Abi7300 fluorescent quantitative PCR instrument (Applied Biosystems, United States) was applied to perform real-time PCR. Specific primers were used to amplify target genes. The forward primer sequence of AOA-*amoA* is STAATGGTCTGGCTTAGACG (5′–3′), and the reverse primer is GCGGCCATCCATCTGTATGT (5′–3′). The forward primer sequence of AOB-*amoA* is GGGGTTTCTACTGGTGGT (5′–3′), and the reverse primer is CCCCTCKGS AAAGCCTTCTTC (5′–3′) (Park et al., 2008). The reaction system (Supplementary Table S1) and reaction conditions (Supplementary Table S2) are shown in the supporting materials. The constructed plasmid was identified by sequencing. Then the plasmid value was measured at 260 nm by UV spectrophotometer (NanoDrop2000, Thermo Fisher Scientific, United States), and converted into gene copies (copies g^{-1} dry soil) by formula. The standard curve was prepared by 10-fold gradient dilution of the constructed plasmids (10^{-1}–10^{-7} for AOB *amoA*, 10^{-2}–10^{-8} for AOA *amoA*) (Hu et al., 2019).

High-throughput sequencing and bioinformatic analysis for the *amoA* genes

The AOB and AOA *amoA* genes were amplified using the two primer sets mentioned above, and the protocols used to amplify have been previously reported (Shen et al., 2008; Pester et al., 2012). Illumina MiSeq sequencing, carried out by Personal (Shanghai, China), was applied to ensure the excellent coverage of each clone library. Bar code oligonucleotides were connected to the ends of two pairs of primers to distinguish *amoA* amplicons of different samples. For each sample, triplicate PCR products were obtained and then mixed. PCR products length was subsequently determined by electrophoresis in a 1.5% agarose gel. Bioinformatic analysis was conducted with the Mothur software package (Schloss et al., 2009). After the screening, trimming, and chimeras checking procedures, the high-quality reads were left for further analysis. Both AOA and AOB *amoA* genes were grouped into OTUs using an 85% similarity as a previously recommended cut-off value (Pester et al., 2012). The obtained sequences were submitted to the RDP pipeline using the FrameBot tool to remove non-amoA sequences (Wang et al., 2013). The OTUs were taxonomically categorized using neighbor-joining phylogenetic trees constructed from representative sequences with the longest length of the amoA genes. AOA amoA representatives were matched with an existing high-quality amoA database (Pester et al., 2012), while AOB amoA representatives were matched with GeneBank reference sequences. The taxonomy-derived reference sequences were combined with the Kimura 2-parameter distance (MEGA 6.0), and the bootstrap values were calculated using 1,000 repetitions (Kumar et al., 2016). In addition, the diversity indices of ACE, Chao1, Shannon, and Simpson for each OTU were also calculated.

TABLE 1 The physiochemical properties of the sediment samples (mean ± *SE*, *n* = 3).

Sample names	pH	ORP (mV)	MC (%)	NH_4^+-N (mg/kg)	NO_2^--N (mg/kg)	NO_3^--N (mg/kg)	TIN (mg/kg)	TN (g/kg)
S_{0-10}	5.45 ± 0.09d	149.07 ± 3.13a	25.12 ± 0.41d	1.32 ± 0.09d	0.18 ± 0.01c	10.75 ± 0.17d	12.25 ± 0.49e	0.86 ± 0.01c
S_{10-20}	5.91 ± 0.13c	105.88 ± 2.76b	35.23 ± 1.00c	1.30 ± 0.07d	0.18 ± 0.01c	4.99 ± 0.08e	6.47 ± 0.30f	1.24 ± 0.01b
S_{20-30}	6.01 ± 0.07c	76.86 ± 1.71d	41.44 ± 1.01ab	1.55 ± 0.10d	0.48 ± 0.03b	12.73 ± 0.15b	14.76 ± 0.77d	1.28 ± 0.02b
S_{30-40}	6.56 ± 0.12a	75.10 ± 1.89d	44.02 ± 1.12a	6.21 ± 0.22a	0.79 ± 0.05a	16.89 ± 0.41a	23.90 ± 1.02a	1.52 ± 0.02a
S_{40-50}	6.23 ± 0.10bc	83.17 ± 2.31c	39.50 ± 0.89b	3.77 ± 0.11c	0.67 ± 0.03a	16.21 ± 0.22a	20.65 ± 0.84b	1.27 ± 0.02b
S_{50-60}	6.29 ± 0.09ab	89.39 ± 2.18c	39.56 ± 0.65b	4.98 ± 0.14b	0.51 ± 0.02b	11.61 ± 0.11c	17.11 ± 0.75c	1.60 ± 0.03a

Note: Different letters in a single column indicate a significant difference between the treatments at $p < 0.05$. S_{0-10}, sediment sampled from 0 to 10 cm layer; S_{10-20}, sediment sampled from 10 to 20 cm layer; S_{20-30}, sediment sampled from 20 to 30 cm layer; S_{30-40}, sediment sampled from 30 to 40 cm layer; S_{40-50}, sediment sampled from 40 to 50 cm layer; S_{50-60}, sediment sampled from 50 to 60 cm layer. ORP, oxidation-reduction potential; MC, moisture content; NH_4^+-N, ammonium nitrogen; NO_2^--N, nitrous nitrogen; NO_3^--N, nitrate nitrogen; TIN, total inorganic nitrogen; TN, total nitrogen.

Statistical analysis

Pearson correlation analysis with a 0.05 significance level was used to determine the correlation between the AOA/AOB diversities or abundances and environmental factors. In addition, the representative sequences with the longest length were selected for the following phylogenetic analyses, which were conducted with MEGA 6 through a neighbor-joining tree using Kimura 2-parameter distance with 1,000 bootstrap replicates (Tamura et al., 2013). Redundancy analysis (RDA) was performed to investigate the relationship between AOA/AOB microbial community structure and the environmental factors with CANOCO 5.0 (CANOCO, Microcomputer Power Inc., Ithaca, NY, United States).

Results

Physicochemical properties of sediment samples

Determination of physicochemical properties of sediment samples are showed in Table 1. All the sediments had acidic pH (i.e., 5.45–6.56). The pH value of the upper layer sediment samples (S_{0-10}) was relatively lower than the other five layers. Middle and deep layers (S_{30-40}, S_{40-50}, and S_{50-60}) had higher pH values, and S_{30-40} showed the highest pH of 6.56, which probably resulted from the higher nitrification rates in the upper layer sediments. However, the ORP of the upper layer sediments was much higher than the rest of the samples by 40.79%–98.50%. The moisture varied from 25.12% to 44.02%, and the middle layer (S_{20-30}, S_{30-40}) was the highest of other layer sediments. The NH_4^+-N content of the six sediment samples ranged from 1.32 to 6.21 mg kg^{-1}, and the peak was found in the sample of S_{30-40}, which was significantly higher than the other five sediment samples by 24.70%–377.70%. All the sediment samples had low NO_2^--N content, and the upper layer sediment samples (S_{0-10}, S_{20-30}) were the lowest. The NO_3^--N content ranged from 4.99 to 16.89 mg/kg, and the NO_3^--N content in S_{30-40} and S_{40-50} layers was higher than that of the other layers. The TIN of middle and deep layers was higher than the upper layers, and S_{30-40} was higher than the rest samples by 15.74%–269.40%. As for the TN, the content ranged from 857.77 to 1604.05 mg kg^{-1}, and the TN content increased as the depth went deeper.

Abundance of ammonia-oxidizing archaea and ammonia-oxidizing bacteria

The AOA *amoA* gene copy numbers in the upper layers (S_{0-10}, S_{10-20}) were much lower than that in the middle (S_{20-30}, S_{30-40}) and deep (S_{40-50}, S_{50-60}) layer (Figure 1). On the contrary to AOA *amoA* genes, the number of AOB *amoA* genes in the upper layers (S_{0-10}, S_{10-20}) was much higher than that in the middle (S_{20-30}, S_{30-40}) and deep (S_{40-50}, S_{50-60}) layer (Figure 1). The ratio of AOA/AOB *amoA* gene copy numbers ranged from 0.04 to 150.75 in the six sediment samples, and the ratio increased dramatically from upper layers to deep layers. The ratios of AOA/AOB *amoA* genes in the six sediment samples were 0.04 (S_{0-10}), 0.11 (S_{10-20}), 8.20 (S_{20-30}), 7.07(S_{30-40}), 86.77 (S_{40-50}) and 150.75 (S_{50-60}), respectively. In the upper layers (S_{0-10}, S_{10-20}), where the oxygen was sufficient, AOB won the competition with AOA and maybe the main driver of ammonia oxidation. However, in the middle (S_{20-30}, S_{30-40}) and deep layer (S_{40-50}, S_{50-60}), where the environment became anoxic, the higher affinities of AOA for oxygen could help them to win the competition with AOB. In the middle tidal zone, where the oxygen was relatively sufficient, the number of AOB *amoA* genes was higher than AOA. In the subtidal zones where oxygen was limited, AOA outnumbered AOB (Hu et al., 2019). From the point of abundance, oxygen concentration indeed led to the niche specialization of AOA and AOB.

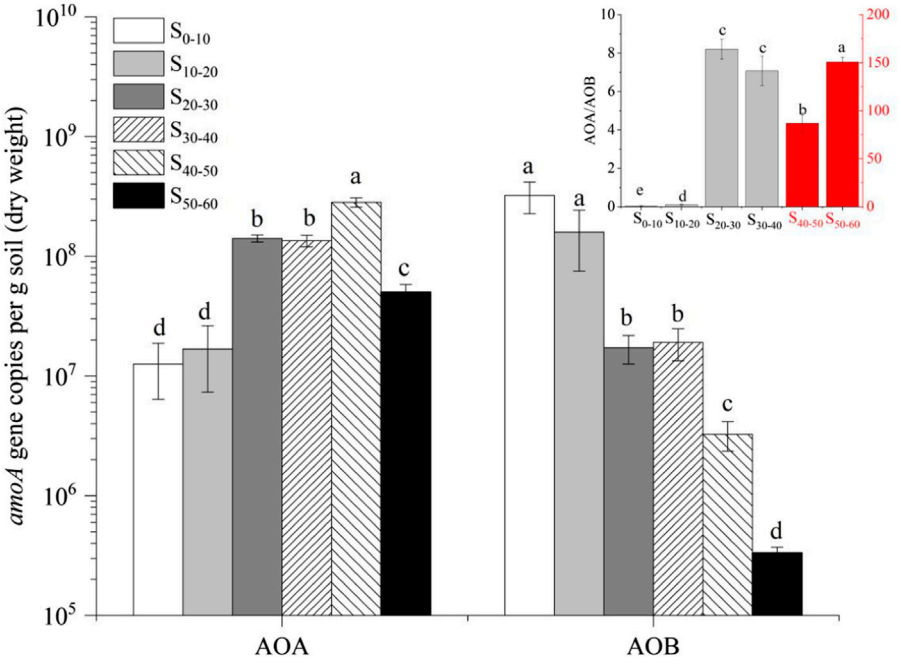

FIGURE 1
Quantitative analysis of AOA and AOB in the six sediment samples (means, *SE*s displayed with errors bars, n = 3). S_{0-10}, sediment sampled from 0 to 10 cm layer; S_{10-20}, sediment sampled from 10 to 20 cm layer; S_{20-30}, sediment sampled from 20 to 30 cm layer; S_{30-40}, sediment sampled from 30 to 40 cm layer; S_{40-50}, sediment sampled from 40 to 50 cm layer; S_{50-60}, sediment sampled from 50 to 60 cm layer. AOA, ammonia-oxidizing archaea; AOB, ammonia-oxidizing bacteria. In the figure in the upper right corner, four gray columns corresponded to the principal coordinate axis, and two red columns corresponding to the sub coordinate axis.

TABLE 2 The OTU numbers and the diversity index of AOA in the soil samples (mean ± *SE*, n = 3).

Sample names	Coverage (%)	Shannon	Simpson	Chao	Ace
S_{0-10}	99.91	1.03 ± 0.01d	0.49 ± 0.01a	17.88 ± 0.80c	19.28 ± 0.75c
S_{10-20}	99.94	1.39 ± 0.01b	0.32 ± 0.01b	18.36 ± 0.77c	19.68 ± 0.88c
S_{20-30}	99.90	1.38 ± 0.01b	0.33 ± 0.01b	22.87 ± 0.91b	24.41 ± 1.01b
S_{30-40}	99.96	1.28 ± 0.02c	0.34 ± 0.01b	15.08 ± 0.75c	15.78 ± 0.80d
S_{40-50}	99.85	1.46 ± 0.02a	0.32 ± 0.01b	25.20 ± 0.95b	23.93 ± 0.94b
S_{50-60}	99.80	1.38 ± 0.02b	0.36 ± 0.01b	30.74 ± 1.05a	29.28 ± 1.19a

Note: Different letters in a single column indicate a significant difference between the treatments at $p < 0.05$. S_{0-10}, sediment sampled from 0 to 10 cm layer; S_{10-20}, sediment sampled from 10 to 20 cm layer; S_{20-30}, sediment sampled from 20 to 30 cm layer; S_{30-40}, sediment sampled from 30 to 40 cm layer; S_{40-50}, sediment sampled from 40 to 50 cm layer; S_{50-60}, sediment sampled from 50 to 60 cm layer.

Diversity of ammonia-oxidizing archaea and ammonia-oxidizing bacteria

High-quality sequences of AOA and AOB, after quality control procedures, were applied to the analysis of diversity. In AOA, 17144 high-quality sequences were obtained for the six samples of sediment. The coverages of the six AOA *amoA* gene clone libraries were all higher than 99.0%, ranging from 99.80% to 99.96% among the 18 OTUs obtained from the AOA *amoA* gene (Table 2). The AOA OTU numbers of the six sediment samples ranged from 10 to 15, with S_{30-40} (10 OTUs) and S_{50-60} (15 OTUs) displayed the lowest and highest diversity, respectively (Table 2). The OTU numbers in deep layers were higher than those in the upper and middle layers (Figure 2). The coverage of the six AOB *amoA* gene clone libraries was ranged from 99.96 to 100.00% (Table 3). The sample S_{0-10} showed the highest diversity, holding 11 OTUs in total, which was higher than the rest five

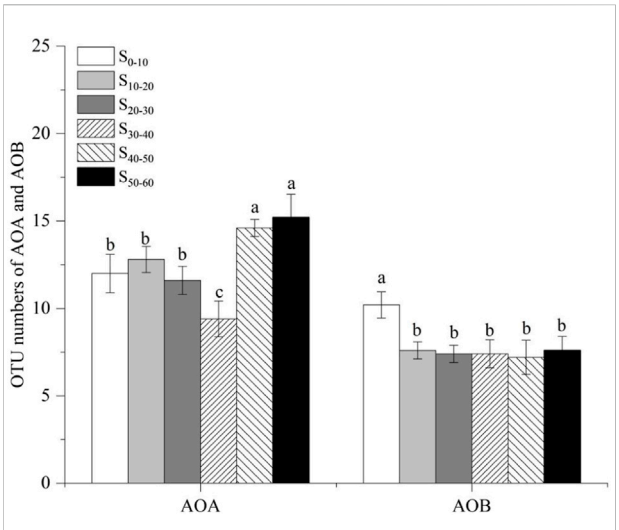

FIGURE 2
The OTU numbers of AOA and AOB in the six sediment samples (means, *SE* displayed with errors bars, n = 3). S_{0-10}, sediment sampled from 0 to 10 cm layer; S_{10-20}, sediment sampled from 10 to 20 cm layer; S_{20-30}, sediment sampled from 20 to 30 cm layer; S_{30-40}, sediment sampled from 30 to 40 cm layer; S_{40-50}, sediment sampled from 40 to 50 cm layer; S_{50-60}, sediment sampled from 50 to 60 cm layer. AOA, ammonia-oxidizing archaea; AOB, ammonia-oxidizing bacteria.

sediment samples. The OTU numbers in the rest of the five samples were all the same, holding 8 OTUs. Similar to the change rules of abundance, the AOB OTU numbers decreased as sediment depth went deeper, which indicated that AOB was not tolerant or adaptable to hypoxic environment. The AOB OTU numbers were higher in the non-flooded zones where the oxygen concentration was sufficient than in the flooded zones where the environment was anoxic. The diversity of AOA was always higher than AOB in all the sediment samples (Table 3), and the ratio of AOA/AOB OTU numbers increased from 1.09 to 1.88 as the sediment depth went deeper, which was similar to the changing pattern of the abundance.

Phylogenetic analysis and community structure of ammonia-oxidizing archaea/ammonia-oxidizing bacteria

For AOA, 17144 high-quality sequences after quality control procedures were obtained for the six sediment samples. As showed in Figure 3, the representative sequences of the 18 OTUs, according to the *amoA* genes classification of AOA (Pester et al., 2012), have been grouped into four different clusters. Neither *Nitrosotalea* nor Thermal-related AOA was found in all the sediment samples. *Nitrosophaera* cluster contained 3 OTUs (OTU 12, OUT 15, OTU 18), a total of 9 sequences. OTU 12 (containing 3 seqs) belonging to *Nitrosophaera* cluster was retrieved from samples S_{20-30} and S_{40-50}, OTU 15 (containing 2 seqs) was detected in sample S_{0-10} and S_{50-60}, and OTU 18 (containing 4 seqs) was only retrieved from deep layer samples (S_{40-50}, S_{50-60}). The rest of the 15 OTUs all belonged to the *Nitrosopumilus* cluster. Among the 17144 sequences, 17135 accounted for 99.94% of all obtained sequences belonged to the *Nitrosopumilus* cluster. AOB obtained 18865 sequences from 6 sediment samples by the same quality control procedure as AOA, and then these sequences were assigned to 11 OTUs using the 15% cut-off recommended previously (Purkhold et al., 2000). The representative sequences of the 11 OTUs were subsequently grouped into two clusters, as showed in Figure 4. OTU 9 and OTU 10 were clustered into the *Nitrosomonas*, and the remaining 9 OTUs belonged to the *Nitrosospira* cluster. Only 35 sequences belonged to the cluster of *Nitrosomonas*. All six AOB communities were primarily composed of *Nitrosospira*-related sequences.

Environmental factors that influence the diversity and communities of ammonia-oxidizing archaea and ammonia-oxidizing bacteria

As shown in Table 4, the linear relationship between various environmental factors and OTU number, *amoA* gene abundance as

TABLE 3 The OTU numbers and the diversity index of AOB in the soil samples (mean ± *SE*, n = 3).

Sample names	Coverage (%)	Shannon	Simpson	Chao	Ace
S_{0-10}	99.98	1.16 ± 0.02ab	0.53 ± 0.01b	20.20 ± 1.00a	22.37 ± 0.52b
S_{10-20}	99.96	1.13 ± 0.01bc	0.55 ± 0.01b	15.30 ± 0.61c	16.57 ± 0.50c
S_{20-30}	99.97	0.94 ± 0.01c	0.63 ± 0.01a	16.79 ± 0.68bc	17.85 ± 0.45c
S_{30-40}	100.00	0.95 ± 0.01c	0.63 ± 0.01a	18.51 ± 0.89ab	24.93 ± 0.73a
S_{40-50}	100.00	1.16 ± 0.02ab	0.54 ± 0.01b	17.85 ± 0.57b	25.28 ± 0.91a
S_{50-60}	100.00	1.30 ± 0.02a	0.52 ± 0.01b	16.96 ± 0.43bc	17.94 ± 0.60c

Note: Different letters in a single column indicate a significant difference between the treatments at $p < 0.05$. S_{0-10}, sediment sampled from 0 to 10 cm layer; S_{10-20}, sediment sampled from 10 to 20 cm layer; S_{20-30}, sediment sampled from 20 to 30 cm layer; S_{30-40}, sediment sampled from 30 to 40 cm layer; S_{40-50}, sediment sampled from 40 to 50 cm layer; S_{50-60}, sediment sampled from 50 to 60 cm layer.

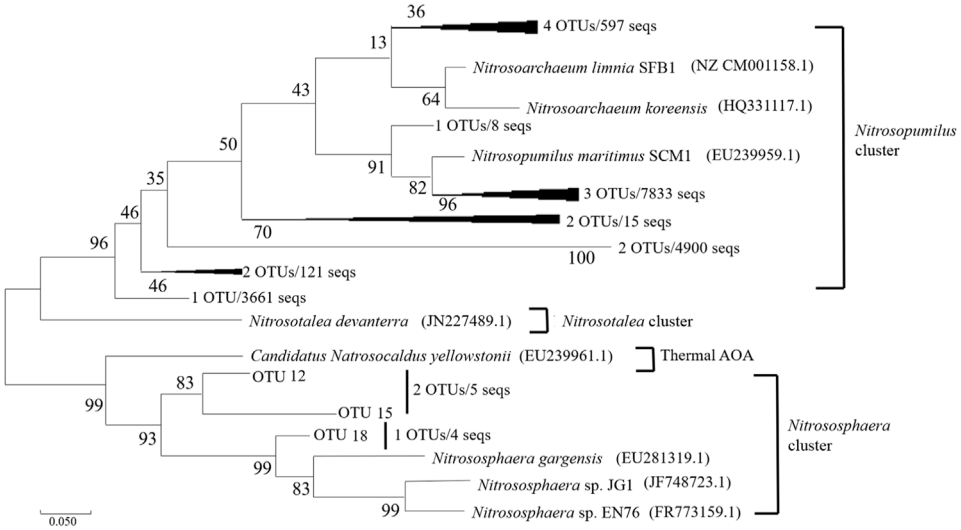

FIGURE 3
Maximum-Likelihood phylogenetic tree showing the phylogenetic affiliations of the AOA sequences recovered from the sediment samples. The numbers at the nodes are percentages that indicate the levels of bootstrap support from 2,000 replicates. The scale bar represents 0.05 nucleic acid substitutions per nucleotide position.

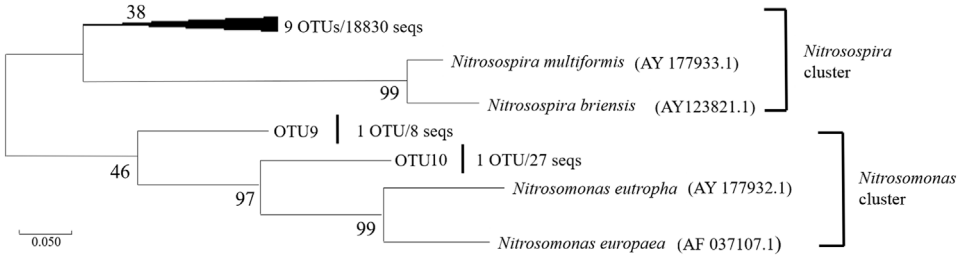

FIGURE 4
Maximum-Likelihood phylogenetic tree showing the phylogenetic affiliations of the AOB sequences recovered from the sediment samples. The numbers at the nodes are percentages that indicate the levels of bootstrap support from 2,000 replicates. The scale bar represents 0.05 nucleic acid substitutions per nucleotide position.

well as AOA/AOB diversity index was determined by the Pearson correlation coefficient. ORP was positively correlated with AOB's abundance and OTU numbers ($p < 0.01$), indicating that AOB preferred the niches with higher oxygen concentrations. On the contrary, a negative correlation between ORP and AOA abundance was observed in Table 4, implying that AOA preferred the niches with lower oxygen concentrations. Moreover, these results could be due to the higher oxygen affinity of AOA than that of AOB. Significantly negative correlation between MC and AOB abundance ($p < 0.01$)/AOB OTU numbers ($p < 0.05$) was also observed. The AOB abundance was significantly negatively correlated to the TN ($p < 0.01$) and pH ($p < 0.05$). In addition, TN was also significantly negatively with AOB OTU numbers ($p < 0.05$).

In order to further study the dominant role of the environmental factors of different sediment site in AOA and AOB community structure, the redundancy analysis (RDA) was used to rank the influencing factors (Figure 5). Figure 5A performed the relationship between AOA community structure and environmental factors. The explanation degree of each factor for AOA community structure distribution on the horizontal axis was 54.06%, and on the vertical axis was 22.25%. Therefore, it mainly

10.3389/fenvs.2022.976618

TABLE 4 Correlation analysis of environmental factors and AOA, AOB abundance, OTU numbers, and diversity index.

Environmental factors	Pearson correlation coefficient				
	Relative abundance		Ratio of abundance	Number of OTUs	
	AOA	AOB	AOA:AOB	AOA	AOB
pH	0.300	−0.020*[1]	0.423	−0.919	−0.055
ORP	−0.184	0.002**	−0.576	0.976	0.001**
MC	0.250	−0.004**	0.605	−0.871	−0.014*
NH_4^+-N	0.503	−0.178	0.320	−0.887	−0.392
NO_2^--N	0.090	−0.051	0.519	−0.727	−0.242
NO_3^--N	0.083	−0.273	0.676	−0.600	−0.755
TIN	0.142	−0.187	0.516	−0.670	−0.583
TN	0.674	−0.029*	0.252	0.760	−0.045*

Note: Significance levels are indicated as follows: **, 0.01; *, 0.05. ORP, oxidation-reduction potential; MC, moisture content; NH_4^+-N, ammonium nitrogen; NO_2^--N, nitrous nitrogen; NO_3^--N, nitrate nitrogen; TIN, total inorganic nitrogen; TN, total nitrogen. AOA, ammonia-oxidizing archaea; AOB, ammonia-oxidizing bacteria.

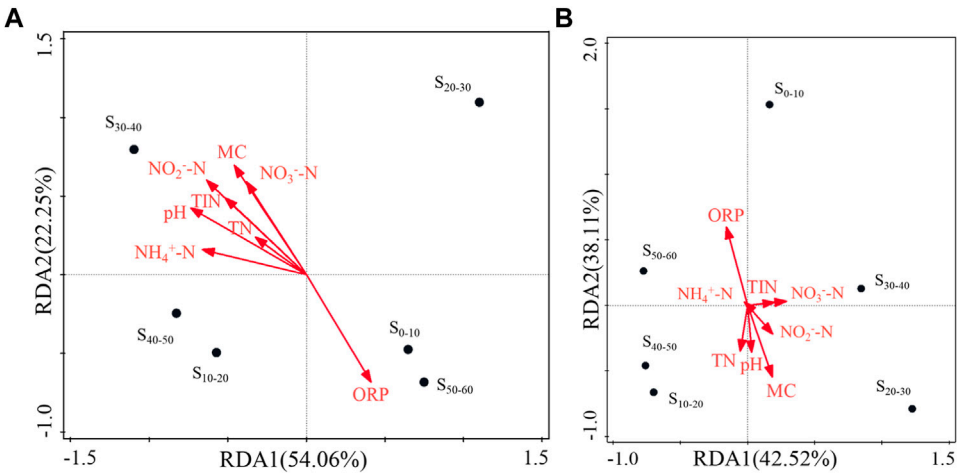

FIGURE 5
Redundancy analysis between AOA **(A)** and AOB **(B)** flora structure and environmental factors. S_{0-10}, sediment sampled from 0 to 10 cm layer; S_{10-20}, sediment sampled from 10 to 20 cm layer; S_{20-30}, sediment sampled from 20 to 30 cm layer; S_{30-40}, sediment sampled from 30 to 40 cm layer; S_{40-50}, sediment sampled from 40 to 50 cm layer; S_{50-60}, sediment sampled from 50 to 60 cm layer. ORP, oxidation-reduction potential; MC, moisture content; NH_4^+-N, ammonium nitrogen; NO_2^--N, nitrous nitrogen; NO_3^--N, nitrate nitrogen; TIN, total inorganic nitrogen; TN, total nitrogen.

referred to the vector projection length of each factor vector on the horizontal axis. NH_4^+-N, pH, and NO_2^--N were the main factors affected the AOA community structure distribution because of their long projection (>0.05) on the horizontal axis. ORP had the opposite performance with other environmental factors, which was also consistent with the results in Table 4. Figure 5B performed the relationship between AOB community structure and environmental factors. The explanation degree of each factor for AOB community structure distribution on the horizontal axis was 42.52%, and on the vertical axis was 38.43%. ORP and MC were the important environmental factors that affected the AOB community structure distribution because of their long projection on the horizontal and vertical axis. The results of RDA were consistent with those of correlation analysis

(Table 4) to a certain extent, which confirmed the significant effects of OPR and MC on the distribution of AOB community.

Discussion

The difference of abundances and community structure of ammonia-oxidizing archaea and ammonia-oxidizing bacteria

The number of AOA and AOB *amoA* genes observed in this work was similar toa previous study in the intertidal zones in Zhoushan, Zhejiang province (Hu et al., 2019). Hu found that the AOA and AOB *amoA* gene copy numbers in the intertidal zone ranged from 10^7 to 10^8. The AOB *amoA* gene copy numbers in this study were relatively lower since samples S_{40-50} and S_{50-60} were collected in the deep layers of the sediments. The ratios of AOA/AOB *amoA* genes increased as the depth of the sediments went deeper, indicating that AOA may dominate the ammonia oxidation in the deep layer. This founding was in accordance with the previous work focusing on the ammonia-oxidizing microbes in soils (Leininger et al., 2006). Leininger reported that the ratios of AOA/AOB *amoA* genes increased from 55 to 842 with soil depth went deeper. This phenomenon could be explained by the higher affinities of AOA for oxygen compared to AOB (Martens-Habbena et al., 2009; Jung et al., 2011; Kim et al., 2012). In the subtidal zones where oxygen was limited, AOA outnumbered AOB (Hu et al., 2019). From the point of abundance, oxygen concentration indeed led to the niche specialization of AOA and AOB.

Overall, the change rule of the AOA OTU numbers was similar to the AOA abundance. Both of them increased with sediment depth. AOA showed higher diversity as oxygen concentration became lower, according to previous work in water-level-fluctuating zones in Three Gorges Reservoir (Liu et al., 2015). At higher oxygen concentrations of non-flooded areas, AOA OTU values were lower. However, AOA OTU values were higher in the relatively low oxygen concentration in flooded areas. This phenomenon represented that AOA was more adaptive to the oxygen-limited environments. A total of 18865 high-quality AOA sequences were obtained from 6 sediment samples, and these sequences were assigned to 11 OTUs using 15% as cut-off value (Purkhold et al., 2000). All the six sediment samples were predominantly composed of sequences that belonged to the *Nitrosopumilus* cluster. The observation of the *Nitrosopumilus* cluster dominance over the *Nitrosophaera* cluster in this research was consistent with the previous reportsin the intertidal zones in Zhoushan Island (Hu et al., 2019) and Chongming eastern intertidal sediments (Zheng et al., 2013). The most AOA belongs to the cluster of *Nitrosopumilus* (73%) confirmed by the phylogeny and meta-data analyses of AOA amoA sequences, which was nearly twice as much as the *Nitrososphaera* cluster (37%) (Alves et al., 2018). These results of the dominance of the *Nitrosospira* cluster over the *Nitrosomonas* cluster were consistent with the previous report in the coastal Pearl River estuary (Cao et al., 2011). The lower concentration of ammonia nitrogen (0.03–0.11 mm NH_4^+) in the intertidal zone of Qingdao may help to explain the absolute dominance of *Nitrosoma*. The cluster of *Nitrosomonas* has a lower substrate affinity which leads to higher substrate concentration adaption. Conversely, the *Nitrosospira* cluster has relatively higher substrate affinity and is more likely to survive in environments with a low concentration of substrate (Zheng et al., 2014; Yu et al., 2016).

Environmental factors

Ammonia oxidizing microorganisms (AOA and AOB) were the most critical microorganisms involved in nitrification and were the first rate-limiting step in the nitrification process. Studies showed that the abundance of AOA and AOB were significantly related to nitrogen forms and soil pH (Segal et al., 2017). Our results (Figure 5) also showed that NH_4^+-N, pH, and NO_2^--N were the main factors affected the AOA community structure distribution. AOB was the main driver of nitrification in alkaline soils, while AOA was the main driver of nitrification in acidic soils (Hu et al., 2013; Zhang et al., 2012; Lu et al., 2012). Thus, a significantly negative correlation was shown between AOB and pH in our study (Table 4). These results consistently confirmed the characteristics of niche differentiation of AOA and AOB. AOB tended to play a leading role in neutral or alkaline environments with high nitrogen and pH value, while AOA was more suitable to dominate in acidic and low nitrogen soil (Ke et al., 2013; Qin et al., 2013). However, our consequence showed that AOB was significantly negatively correlated with TN and ORP, which was the opposite of some other studies. For example, studies of Di et al. (2010) and Pratscher et al. (2011) showed that a high nutrient environment was more conducive to the growth of AOB, while AOA was more suitable to grow in a low nitrogen environment. Most of these studies were aimed at the upper soil. However, our research range varied from 0 to 60 cm soil layer. The differential changes of ammonia oxidation bacteria in different soil layers might be an important reason for the correlation with environmental factors. Some studies showed that the reduction of ORP was conducive to improve the abundance of AOB (Ke and Lu, 2012), and AOA was easier to fix in a low CO_2 environment (Martens-Habbena et al., 2009). This was contrary to the result that AOB likes niches with high oxygen concentration in our study. On the one hand, it was related to the different pH and salinity of different tested soils

(Min et al., 2016). On the other hand, it was also related to the different flooding conditions between different soil layers (Ke and Lu, 2012). Therefore, it was necessary to study further the effects of multiple environmental factors on ammonia-oxidizing bacteria in the future.

Conclusion

In summary, our results showed the changing pattern of AOA and AOB abundance and diversity with sediment depth. In upper layers, the AOB abundance was higher compared to that of AOA. In contrast, AOA abundance outnumbered AOB in deep layers. Both the AOA/AOB *amoA* gene copy numbers rate and AOA/AOB OTU numbers rate increased as sediment depth went deeper, which indicated that oxygen indeed led to the niche specialization of AOA and AOB. AOA won the competition with AOB in the oxygen-limited niches. AOA may be dominant in the ammonia oxidation process in the deep layers. The *Nitrosopumilus* cluster and *Nitrosospira* cluster were the dominant AOA and AOB, respectively, representing ecological success in the intertidal zone.

Data availability statement

The raw data supporting the conclusion of this article will be made available by the authors, without undue reservation.

Author contributions

Conceptualization, JD; methodology, LM; formal analysis, PC; data curation, MQ; writing—original draft preparation, SC and BZ; writing—review and editing, WS; supervision, XZ. All authors have read and agreed to the published version of the manuscript.

Funding

This work was funded by the the Agricultural Science and Technology Innovation Program (ASTIP No. CAAS-ZDRW202201) and the Provincial Natural Science Foundation of Shandong (ZR2021QD036).

Conflicts of interest

Author MQ was employed by Longyan City Company of Fujian Tobacco Company. Author SC was employed by China Tobacco Shandong Industrial Co., Ltd. Author BZ was employed by Fujian Branch of China Tobacco Company.

The remaining authors declare that the research was conducted in the absence of any commercial or financial relationships that could be construed as a potential conflict of interest.

Publisher's note

All claims expressed in this article are solely those of the authors and do not necessarily represent those of their affiliated organizations, or those of the publisher, the editors and the reviewers. Any product that may be evaluated in this article, or claim that may be made by its manufacturer, is not guaranteed or endorsed by the publisher.

Supplementary material

The Supplementary Material for this article can be found online at: https://www.frontiersin.org/articles/10.3389/fenvs.2022.976618/full#supplementary-material

References

Aigle, A., Gubry-Rangin, C., Thion, C., Estera-Molina, K. Y., Richmond, H., Pett-Ridge, J., et al. (2020). Experimental testing of hypotheses for temperature- andpH-based niche specialization of ammonia oxidizing archaea and bacteria. *Environ. Microbiol.* 22, 4032–4045. doi:10.1111/1462-2920.15192

Alves, R. J. E., Minh, B. Q., Urich, T., von Haeseler, A., and Schleper, C. (2018). Unifying the global phylogeny and environmental distribution of ammonia-oxidising archaea based on amoA genes. *Nat. Commun.* 9, 1517. doi:10.1038/s41467-018-03861-1

Beeckman, F., Motte, H., and Beeckman, T. (2018). Nitrification in agricultural soils: Impact, actors and mitigation. *Curr. Opin. Biotechnol.* 50, 166–173. doi:10.1016/j.copbio.2018.01.014

Beman, J. M., Popp, B. N., and Francis, C. A. (2008). Molecular and biogeochemical evidence for ammonia oxidation by marine crenarchaeota in the gulf of California. *ISME J.* 2, 429–441. doi:10.1038/ismej.2007.118

Bernhard, A. E., Donn, T., Giblin, A. E., and Stahl, D. A. (2005). Loss of diversity of ammonia-oxidizing bacteria correlates with increasing salinity in an estuary system. *Environ. Microbiol.* 7, 1289–1297. doi:10.1111/j.1462-2920.2005.00808.x

Blainey, P. C., Mosier, A. C., Potanina, A., Francis, C. A., and Quake, S. R. (2011). Genome of a low-salinity ammonia-oxidizing archaeon determined by single-cell and metagenomic analysis. *PLOS ONE* 6, e16626. doi:10.1371/journal.pone.0016626

Cao, H., Hong, Y., Li, M., and Gu, J. (2011). Diversity and abundance of ammonia-oxidizing prokaryotes in sediments from the coastal pearl river estuary to the south China sea. *Antonie Leeuwenhoek* 100, 545–556. doi:10.1007/s10482-011-9610-1

de la Torre, J. R., Walker, C. B., Ingalls, A. E., Koenneke, M., and Stahl, D. A. (2008). Cultivation of a thermophilic ammonia oxidizing archaeon synthesizing crenarchaeol. *Environ. Microbiol.* 10, 810–818. doi:10.1111/j.1462-2920.2007.01506.x

Di, H., Cameron, K. C., Shen, J., Winefield, C. S., O'Callaghan, M., Bowatte, S., et al. (2010). Ammonia-oxidizing bacteria and archaea grow under contrasting soil nitrogen conditions. *FEMS Microbiol. Ecol.* 72, 386–394. doi:10.1111/j.1574-6941.2010.00861.x

Gubry-Rangin, C., Hai, B., Quince, C., Engel, M., Thomson, B. C., James, P., et al. (2011). Niche specialization of terrestrial archaeal ammonia oxidizers. *Proc. Natl. Acad. Sci. U. S. A.* 108, 21206–21211. doi:10.1073/pnas.1109000108

Hatzenpichler, R., Lebedeva, E. V., Spieck, E., Stoecker, K., Richter, A., Daims, H., et al. (2008). A moderately thermophilic ammonia-oxidizing crenarchaeote from a

hot spring. *Proc. Natl. Acad. Sci. U. S. A.* 105, 2134–2139. doi:10.1073/pnas.0708857105

Hu, H., Zhang, L., Dai, Y., Di, H., and He, J. (2013). pH-dependent distribution of soil ammonia oxidizers across a large geographical scale as revealed by high-throughput pyrosequencing. *J. Soils Sediments* 13, 1439–1449. doi:10.1007/s11368-013-0726-y

Hu, J., Liu, S., Yang, W., He, Z., Wang, J., Liu, H., et al. (2019). Ecological success of the nitrosopumilus and nitrosospira clusters in the intertidal zone. *Microb. Ecol.* 78, 555–564. doi:10.1007/s00248-019-01359-x

Jia, Z., and Conrad, R. (2009). Bacteria rather than Archaea dominate microbial ammonia oxidation in an agricultural soil. *Environ. Microbiol.* 11, 1658–1671. doi:10.1111/j.1462-2920.2009.01891.x

Jung, M., Park, S., Min, D., Kim, J., Rijpstra, W. C., Damste, J. S. S., et al. (2011). Enrichment and characterization of an autotrophic ammonia-oxidizing archaeon of mesophilic crenarchaeal group I.1a from an agricultural soil. *Appl. Environ. Microbiol.* 77, 8635–8647. doi:10.1128/aem.05787-11

Ke, X., Angel, R., Lu, Y., and Conrad, R. (2013). Niche differentiation of ammonia oxidizers and nitrite oxidizers in rice paddy soil. *Environ. Microbiol.* 15, 2275–2292. doi:10.1111/1462-2920.12098

Ke, X., and Lu, Y. (2012). Adaptation of ammonia-oxidizing microorganisms to environment shift of paddy field soil. *FEMS Microbiol. Ecol.* 80, 87–97. doi:10.1111/j.1574-6941.2011.01271.x

Kim, J. G., Jung, M. Y., Park, S. J., Rijpstra, W. I. C., Damste, J. S. S., Madsen, E. L., et al. (2012). Cultivation of a highly enriched ammonia-oxidizing archaeon of thaumarchaeotal group I.1b from an agricultural soil. *Environ. Microbiol.* 14, 1528–1543. doi:10.1111/j.1462-2920.2012.02740.x

Konneke, M., Bernhard, A. E., de la Torre, J. R., Walker, C. B., Waterbury, J. B., and Stahl, D. A. (2005). Isolation of an autotrophic ammonia-oxidizing marine archaeon. *Nature* 437, 543–546. doi:10.1038/nature03911

Kumar, S., Stecher, G., and Tamura, K. (2016). MEGA7: Molecular evolutionary genetics analysis version 7.0 for bigger datasets. *Mol. Biol. Evol.* 33, 1870–1874. doi:10.1093/molbev/msw054

Lehtovirta-Morley, L. E., Stoecker, K., Vilcinskas, A., Prosser, J. I., and Nicol, G. W. (2011). Cultivation of an obligate acidophilic ammonia oxidizer from a nitrifying acid soil. *Proc. Natl. Acad. Sci. U. S. A.* 108, 15892–15897. doi:10.1073/pnas.1107196108

Leininger, S., Urich, T., Schloter, M., Schwark, L., Qi, J., Nicol, G. W., et al. (2006). Archaea predominate among ammonia-oxidizing prokaryotes in soils. *Nature* 442, 806–809. doi:10.1038/nature04983

Liu, S., Shen, L., Lou, L., Tian, G., Zheng, P., and Hu, B. (2013). Spatial distribution and factors shaping the niche segregation of ammonia-oxidizing microorganisms in the qiantang river, China. *Appl. Environ. Microbiol.* 79, 4065–4071. doi:10.1128/aem.00543-13

Liu, S., Hu, B., He, Z., Zhang, B., Tian, G., Zheng, P., et al. (2015). Ammonia-oxidizing archaea have better adaptability in oxygenated/hypoxic alternant conditions compared to ammonia-oxidizing bacteria. *Appl. Microbiol. Biotechnol.* 99, 8587–8596. doi:10.1007/s00253-015-6750-7

Lu, L., Han, W., Zhang, J., Wu, Y., Wang, B., Lin, X., et al. (2012). Nitrification of archaeal ammonia oxidizers in acid soils is supported by hydrolysis of urea. *ISME J.* 6, 1978–1984. doi:10.1038/ismej.2012.45

Martens-Habbena, W., Berube, P. M., Urakawa, H., de la Torre, J. R., and Stahl, D. A. (2009). Ammonia oxidation kinetics determine niche separation of nitrifying Archaea and Bacteria. *Nature* 461, 976–979. doi:10.1038/nature08465

Min, W., Guo, H., Zhang, W., Zhou, G., Ma, L., Ye, J., et al. (2016). Irrigation water salinity and N fertilization: Effects on ammonia oxidizer abundance, enzyme activity and cotton growth in a drip irrigated cotton field. *J. Integr. Agric.* 15, 1121–1131. doi:10.1016/s2095-3119(15)61158-3

Park, H. D., and Noguera, D. R. (2007). Characterization of two ammonia-oxidizing bacteria isolated from reactors operated with low dissolved oxygen concentrations. *J. Appl. Microbiol.* 102, 1401–1417. doi:10.1111/j.1365-2672.2006.03176.x

Park, S. J., Park, B. J., and Rhee, S. K. (2008). Comparative analysis of archaeal 16S rRNA and amoA genes to estimate the abundance and diversity of ammonia-oxidizing archaea in marine sediments. *Extremophiles* 12, 605–615. doi:10.1007/s00792-008-0165-7

Park, B. J., Park, S. J., Yoon, D. N., Schouten, S., Damste, J. S. S., and Rhee, S. K. (2010). Cultivation of autotrophic ammonia-oxidizing archaea from marine sediments in coculture with sulfur-oxidizing Bacteria. *Appl. Environ. Microbiol.* 76, 7575–7587. doi:10.1128/aem.01478-10

Pester, M., Rattei, T., Flechl, S., Groengroeft, A., Richter, A., Overmann, J., et al. (2012). amoA-based consensus phylogeny of ammonia-oxidizing archaea and deep sequencing of amoA genes from soils of four different geographic regions. *Environ. Microbiol.* 14, 525–539. doi:10.1111/j.1462-2920.2011.02666.x

Pratscher, J., Dumont, M. G., and Conrad, R. (2011). Ammonia oxidation coupled to CO_2 fixation by archaea and bacteria in an agricultural soil. *Proc. Natl. Acad. Sci. U. S. A.* 108, 4170–4175. doi:10.1073/pnas.1010981108

Prosser, J. I., and Nicol, G. W. (2012). Archaeal and bacterial ammonia-oxidisers in soil: The quest for niche specialisation and differentiation. *Trends Microbiol.* 20, 523–531. doi:10.1016/j.tim.2012.08.001

Purkhold, U., Pommerening-Roser, A., Juretschko, S., Schmid, M. C., Koops, H. P., and Wagner, M. (2000). Phylogeny of all recognized species of ammonia oxidizers based on comparative 16S rRNA and amoA sequence analysis: Implications for molecular diversity surveys. *Appl. Environ. Microbiol.* 66, 5368–5382. doi:10.1128/aem.66.12.5368-5382.2000

Qin, H., Yuan, H., Zhang, H., Zhu, Y., Yin, C., Tan, Z., et al. (2013). Ammonia-oxidizing archaea are more important than ammonia-oxidizing bacteria in nitrification and NO_3 (-)-N loss in acidic soil of sloped land. *Biol. Fertil. Soils* 49, 767–776. doi:10.1007/s00374-012-0767-1

Schloss, P. D., Westcott, S. L., Ryabin, T., Hall, J. R., Hartmann, M., Hollister, E. B., et al. (2009). Introducing mothur: Open-source, platform-independent, community-supported software for describing and comparing microbial communities. *Appl. Environ. Microbiol.* 75, 7537–7541. doi:10.1128/aem.01541-09

Segal, L. M., Miller, D. N., McGhee, R. P., Loecke, T. D., Cook, K. L., Shapiro, C. A., et al. (2017). Bacterial and archaeal ammonia oxidizers respond differently to long-term tillage and fertilizer management at a continuous maize site. *Soil Tillage Res.* 168, 110–117. doi:10.1016/j.still.2016.12.014

Shen, J., Zhang, L., Zhu, Y., Zhang, J., and He, J. (2008). Abundance and composition of ammonia-oxidizing bacteria and ammonia-oxidizing archaea communities of an alkaline sandy loam. *Environ. Microbiol.* 10, 1601–1611. doi:10.1111/j.1462-2920.2008.01578.x

Stein, L. Y., and Klotz, M. G. (2016). The nitrogen cycle. *Curr. Biol.* 26, 94–98. doi:10.1016/j.cub.2015.12.021

Stewart, F. J., Ulloa, O., and DeLong, E. F. (2012). Microbial meta transcriptomics in a permanent marine oxygen minimum zone. *Environ. Microbiol.* 14, 23–40. doi:10.1111/j.1462-2920.2010.02400.x

Tamura, K., Stecher, G., Peterson, D., Filipski, A., and Kumar, S. (2013). MEGA6: Molecular evolutionary genetics analysis version 6.0. *Mol. Biol. Evol.* 30, 2725–2729. doi:10.1093/molbev/mst197

Verhamme, D. T., Prosser, J. I., and Nicol, G. W. (2011). Ammonia concentration determines differential growth of ammonia-oxidising archaea and bacteria in soil microcosms. *ISME J.* 5, 1067–1071. doi:10.1038/ismej.2010.191

Wang, Q., Quensen, J. F., 3rd, Fish, J. A., Lee, T. K., Sun, Y., Tiedje, J. M., et al. (2013). Ecological patterns of nifH genes in four terrestrial climatic zones explored with targeted metagenomics using FrameBot, a new informatics tool. *MBio* 4, e00513. doi:10.1128/mbio.00592-13

Wang, C., Tang, S., He, X., and Ji, G. (2020). The abundance and community structure of active ammonia-oxidizing archaea and ammonia-oxidizing bacteria shape their activities and contributions in coastal wetlands. *Water Res.* 171, 115464. doi:10.1016/j.watres.2019.115464

Yu, S., Yao, P., Liu, J., Zhao, B., Zhang, G., Zhao, M., et al. (2016). Diversity, abundance, and niche differentiation of ammonia-oxidizing prokaryotes in mud deposits of the eastern China marginal seas. *Front. Microbiol.* 7, 137. doi:10.3389/fmicb.2016.00137

Zhang, L., Hu, H., Shen, J., and He, J. (2012). Ammonia-oxidizing archaea have more important role than ammonia-oxidizing bacteria in ammonia oxidation of strongly acidic soils. *ISME J.* 6, 1032–1045. doi:10.1038/ismej.2011.168

Zhang, Y., Chen, L. J., Dai, T. J., Sun, R. H., and Wen, D. H. (2015). Ammonia manipulates the ammonia-oxidizing archaea and bacteria in the coastal sediment-water microcosms. *Appl. Microbiol. Biotechnol.* 99, 6481–6491. doi:10.1007/s00253-015-6524-2

Zhang, Q., Li, Y., He, Y., Brookes, P. C., and Xu, J. (2019). Elevated temperature increased nitrification activity by stimulating AOB growth and activity in an acidic paddy soil. *Plant Soil* 445, 71–83. doi:10.1007/s11104-019-04052-7

Zheng, Y., Hou, L., Liu, M., Lu, M., Zhao, H., Yin, G., et al. (2013). Diversity, abundance, and activity of ammonia-oxidizing bacteria and archaea in Chongming eastern intertidal sediments. *Appl. Microbiol. Biotechnol.* 97, 8351–8363. doi:10.1007/s00253-012-4512-3

Zheng, Y., Hou, L., Newell, S., Liu, M., Zhou, J., Zhao, H., et al. (2014). Community dynamics and activity of ammonia-oxidizing prokaryotes in intertidal sediments of the Yangtze Estuary. *Appl. Environ. Microbiol.* 80, 408–419. doi:10.1128/aem.03035-13

frontiers | Frontiers in Environmental Science

TYPE Original Research
PUBLISHED 26 August 2022
DOI 10.3389/fenvs.2022.980893

OPEN ACCESS

EDITED BY
Jun Zhou,
University of Massachusetts Lowell,
United States

REVIEWED BY
Hailong Liu,
Yangzhou University, China
Buyun Du,
University of Massachusetts Lowell,
United States

*CORRESPONDENCE
Chao Wu,
ekinpaul1004@163.com

SPECIALTY SECTION
This article was submitted to Soil Processes,
a section of the journal
Frontiers in Environmental Science

RECEIVED 29 June 2022
ACCEPTED 13 July 2022
PUBLISHED 26 August 2022

CITATION
Dun Y, Wu C, Zhou M, Tian X and Wu G (2022), Wheat straw- and maize straw-derived biochar effects on the soil cadmium fractions and bioaccumulation in the wheat–maize rotation system.
Front. Environ. Sci. 10:980893.
doi: 10.3389/fenvs.2022.980893

Wheat straw- and maize straw-derived biochar effects on the soil cadmium fractions and bioaccumulation in the wheat–maize rotation system

Yu Dun[1,2], Chao Wu[1,2]*, Ming Zhou[3], Xia Tian[1,2] and Guoqing Wu[1,2]

[1]Institute of Hydrogeology and Environmental Geology, Chinese Academy of Geological Sciences, Shijiazhuang, Hebei, China, [2]Key Laboratory of Groundwater Contamination and Remediation of Hebei Province and China Geological Survey, Shijiazhuang, Hebei, China, [3]New Energy Geological Team of Hebei Coalfield Geological Bureau, Xingtai, Hebei, China

Wheat–maize rotation is one of the most popular systems and successful intensification cropping systems in Northern China, while soils in some of this area are contaminated by cadmium (Cd). However, few studies have performed experiments on the reduction of Cd accumulation in the wheat–maize rotation system. In this study, wheat- and maize-derived biochars are applied to the Cd-contaminated soil to reduce the Cd accumulation in the wheat and maize plants. The results showed that soil biochar applications can significantly decrease DTPA-extracted Cd concentrations by 12.7–26.0% and 13.1–20.5% by wheat- and maize-derived biochars, respectively. Sequential extractions showed that biochar applications significantly reduced the Cd mobility and bioavailability in soils and changed the exchangeable and carbonate-bound fractions of Cd to organic material-bound and residual fractions. The biochar applications increased the plant growth, yield, and quality of both wheat and maize, especially a significant increase in high dosages. The biochar applications also improved the antioxidant enzyme activities and reduced the reduction of MDA in both wheat and maize roots. The Cd concentrations in wheat grains were reduced by 38.1–91.5% and 65.9–80%, and maize grain Cd concentrations were reduced by 20.9–54.2% and 30.8–44% by wheat- and maize-derived biochar applications, respectively, and the Cd concentrations in the root, stem, and leaf were also significantly reduced. The wheat-derived biochar was more effective on the Cd reduction in soil bioavailable fractions and Cd accumulation in crop plants.

KEYWORDS

DTPA-extracted Cd, sequential extractions, antioxidant enzyme, yield, translocation factor

Introduction

Anthropogenic activities (e.g., non-ferrous/ferrous mining and smelting, biosolids, and manures, pesticides, and fertilizers) have released large amounts of heavy metals to the earth's surface environment (e.g., pedosphere) over the past decades (Proshad et al., 2018; Jafarabadi et al., 2020). One of the widely concerned metals cadmium (Cd) is known to be widespread in the environment and toxic to humans and ecosystems (Bashir et al., 2020; Cui et al., 2020; Huang et al., 2021). Compared to most of the heavy metals, Cd shows relatively high mobility and toxicity, and crops can readily take up Cd from soils and transfer it into food chains, threatening human health (Du et al., 2020; Zhang et al., 2021). More than 50% of the world's population subsists on wheat and maize as staple food (Nuss and Tanumihardjo, 2010; Pang et al., 2020). However, agricultural soils and crops contaminated with Cd are becoming a global concern, especially in eastern Asia. In China, Cd ranked first among all the pollutants with the sample points of 7% exceeding the tolerance limit (GB 15618-1995) (Wang et al., 2015). The serious soil pollution resulted in wheat samples collected from fields with Cd contamination exceeding the national food threshold (0.1 mg kg^{-1}, GB 2762-2017) (Qu et al., 2020; Zhuang et al., 2021).

Exposure to Cd can lead to many chronic diseases, such as respiratory cancer, early atherosclerosis, and kidney damage (Fatima et al., 2019; Du et al., 2020). Reduction of staple Cd accumulation is the most effective way to reduce Cd exposure risk, as staple food is the dominant pathway of the daily Cd intake and becomes the major source of Cd exposure (Li et al., 2021; Zhuang et al., 2023). Many strategies have been applied to reduce wheat and corn Cd accumulation in Cd-contaminated soils, but most of them have a high technical barrier or environmental hazard (Wang L. et al., 2021; Cao et al., 2021). Biochar is pyrolyzed by thermal decomposition of raw biomass at a wide range of temperatures under the condition of hypoxia (Thengane and Bandyopadhyay, 2020; Siddique et al., 2021). Biochar is widely studied and applied to heavy-metal-contaminated soils as it has a large amount of microporous structure, high specific surface area, and organic functional groups, which can potentially regulate the soil pH and structure and decrease the mobilization of soil heavy metals via adsorption and precipitation (Cui et al., 2021). Additionally, the raw biomass and temperature during pyrolysis can also influence the performance of heavy metal immobilization, and their immobilization mechanisms also varied from each other (Inyang et al., 2016).

Recent studies showed that applications of biochar to soils could effectively immobilize Cd in soils and reduce Cd accumulation in crops, such as rice, rice–rape–corn rotation, wheat, and lettuce (Abbas et al., 2017; Zheng et al., 2017; Qu et al., 2020; Zong et al., 2021). Generally, a large number of studies are available for lab incubation experiments and rice Cd accumulation experiments where biochar can effectively immobilize and reduce Cd accumulation in rice from contaminated acid soils (Zheng et al., 2017; Bashir et al., 2020; Cui et al., 2021). Wheat–maize rotation is one of the most popular systems and successful intensification cropping systems in Northern China, which has produced about 45 and 30% of the national wheat and maize, respectively (Kamaruzzaman et al., 2021). Additionally, soil, maize, and wheat Cd contaminations have been reported in these areas (Zhuang et al., 2021; Zhuang et al., 2023); however, few studies have performed experiments on the reduction of Cd concentrations in the wheat–maize rotation system. In the current study, the goals of the pot experiment in the greenhouse were: 1) to evaluate the ability of wheat/maize-straw biochar on the reduction of the Cd bioaccumulation from soils under the wheat–maize rotation system; and 2) to explore the biochar impact on the soil Cd chemical fractions and the translocation of soil bioavailable Cd to the wheat and maize plants.

Materials and methods

Soil and biochar preparation

Pot soil samples were collected from the plow layer of a wheat–maize rotation field in the sewage irrigated area of Xiaohe, Shijiazhuang City, China, which is alkaline sandy loam. The polluted soils were collected using a stainless steel shovel at various locations and then pooled, ground thoroughly, and removed plant residue and scree. The collected soils were dried in the greenhouse and then grounded to less than 2 mm. Other basic properties of the soil like pH, soil organic matter (SOC), and cation exchange capacity (CEC) were measured as 7.9, 1.47%, and 23.2 cmol kg^{-1}, respectively; total N and alkali-hydrolyzed N concentrations were 880 and 84.8 mg kg^{-1}, respectively; total P and available P concentrations were 22.4 and 1.47 mg kg^{-1}, respectively. Because the experiment soils were located downstream of the industrial zone, the mean concentration was 1.45 ± 0.13 mg kg^{-1}. The soil was polluted by Cd based on the soil environment quality risk control standard (GB 15618–2018, pH > 7.5, 0.6 mg kg^{-1}).

Wheat and maize straws were washed with tap water to remove impurities, air-dried to constant weight, and then cut into particle sizes (<1 cm). The straw pieces were pyrolyzed in a ceramic crucible at 500°C in a muffle furnace for 3 h blowing with N_2 (0.5 dm^3 min^{-1}). Then, the biochar was cooled down, sifted through a 50-mesh sieve, and stored in a clean bag for the pot experiment.

Experimental design

The experiment was conducted in the greenhouse including three treatments at two levels (low dosage (L) and high dosage (H)): 1) control treatment (CK), 2) wheat stalk biochar (WB-L

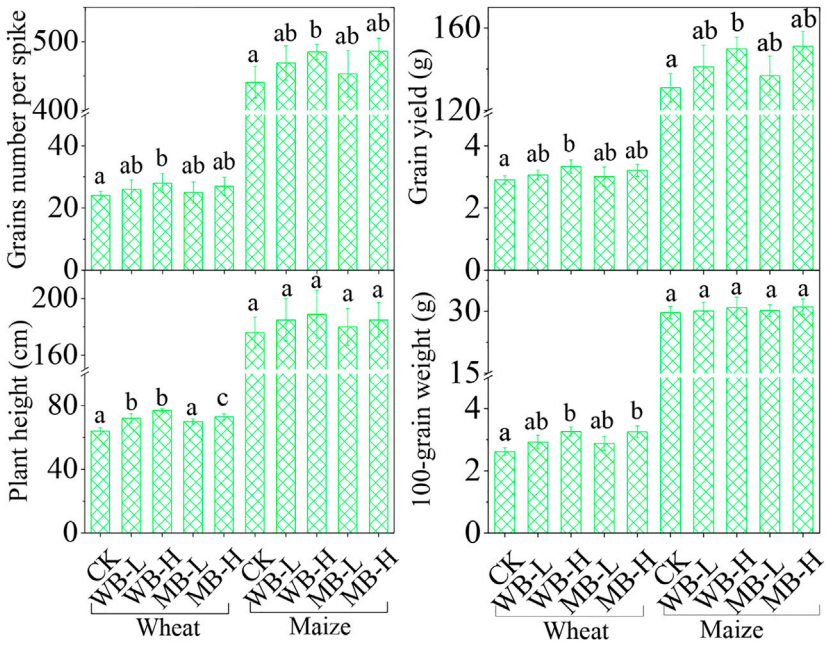

FIGURE 1
Effect of biochar on grain number per spike, grain yield, plant height, and 100-grain weight of wheat and maize.

and WB-H), and 3) maize straw biochar (MB-L and MB-H). Totally, five treatments were performed with environmental triplicate. Initially, 10 kg of the contaminated soil was placed in each ceramic pot, and the prepared biochar was added at 1 and 2% levels as low dosage (L) and high dosage (H), respectively. After 2 weeks, the biochar thoroughly mixed and balanced with the soil, and fifteen wheat seeds were sown in. During the seedling stage, wheat seedlings were thinned to five per pot. Then, the wheat plants were harvested at the mature stage. Sequentially, two maize seedlings per pot were planted in the same soils. The nutrition solution containing N, P, and K was also applied at the seeding stage of the two crops.

Soil and plant sample collection and analysis

During the filling stage, the wheat and maize roots were collected to measure the activities of the antioxidant enzymes and malondialdehyde (MDA). The activities of superoxide dismutase (SOD), axial tomography (CAT), peroxidase (POD), and MDA were determined spectrophotometrically, which were detailed in the previous study (Wu et al., 2020). Briefly, MDA activities were determined using 0.1% thiobarbituric acid. Antioxidant enzyme (SOD, POD, CAT, and APX) activities were determined spectrophotometrically. Fresh wheat root was ground into small pieces in liquid nitrogen for the determination of antioxidant enzyme activities. Phosphate buffer (0.05 M) with a pH of 7.8 was used to standardize the samples and centrifuged at 4 °C for 10 min (12,000 r). The supernatants were transferred for further analysis.

In the mature stages, whole wheat and maize plants were collected and separated into root, stem, leaf, and grains in the laboratory. All the tissues were cleaned with tap water, rinsed with Milli-Q water, and dried in the oven at 90°C for 0.5 h and then at 60°C to constant weight. Each pot soil was mixed thoroughly and about 500 g was collected after wheat and maize harvest. All the samples were milled through 100-mesh using a coffee grinder. For Cd measurement, the plant samples were digested by an acid mixture of HNO_3: $HClO_4$ (v: v = 5: 1) in a conical flask and kept overnight. On the following day, the conical flasks were placed on an electric hot plate at 80°C for 2 h, gradually increased to 120°C for 2 h, and then kept at 160°C. The soil samples were digested with an acid mixture of HNO_3, $HClO_4$, and HF. Bioavailable Cd was extracted with 0.005 M DTPA at pH 7.3 and shaken for 2 h. The sequential extraction was conducted based on the approach performed by Tessier's method (Tessier et al., 1980). Five fractions of Cd were chemically extracted, i.e., an exchangeable fraction (EX), a carbonate-bound fraction (CB), Fe-Mn oxide-bound (OX), organic material-bound (OM), and a residual fraction (RE). The digested and extracted solutions were filtered through a 0.45-μM membrane into centrifuge tubes. The Cd concentrations were measured using ICP-MS (NexION 2000, Perkin Elmer, United States).

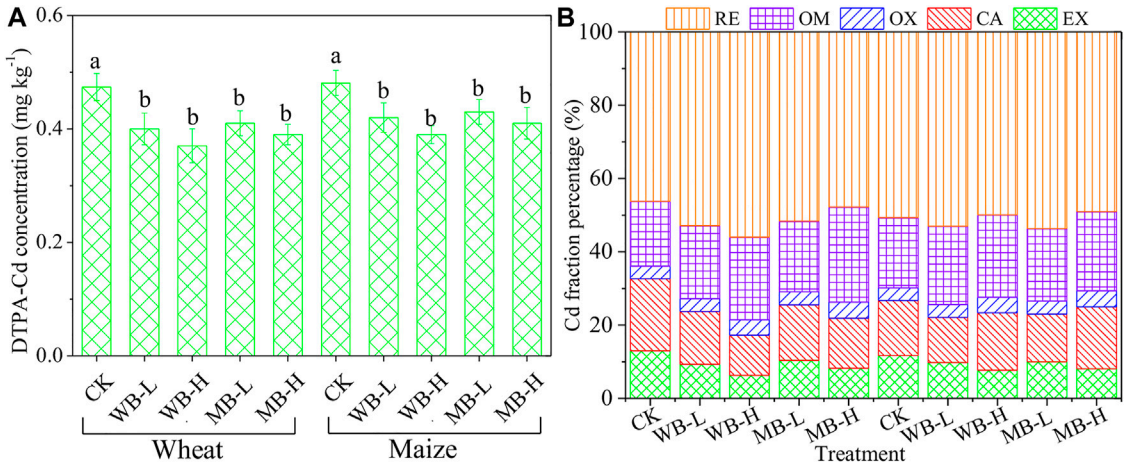

FIGURE 2
Effect of biochar on DTPA-extractable Cd **(A)** and Cd fractions in soils **(B)**.

Quality assurance and quality control during the measurement were conducted with triplicate, blanks, matrix spikes, and standard materials (GBW10020 (GSB–11) and GBW07427 (GSS-13)). The recoveries of Cd in soil and plant standard materials were in the range of 89–103% and 96–108%, respectively. The soil and biochar properties were measured according to the previous study by Zong et al. (2021).

Data analysis

The translocation factor (TF) and bioconcentration factors (BCFs) of wheat and maize are calculated using the following equations (Zhou et al., 2020):

$$TF_{m-n} = C_m/C_n, \quad (1)$$

$$BCF = C_m/C_{soil}, \quad (2)$$

where m and n are the plant upper and lower parts and C_{soil} is the Cd concentrations in the soil.

Statistical significance was determined by one-way ANOVA using SPSS 22.0, and all variations in means were significant at the $p = 0.05$ level (two-tailed). All figures were plotted by Origin 2021 software.

Results

Wheat and maize yield

The biochar application significantly increased soil pH after the harvest of wheat. The variations in soil pH were relatively proportionable to the dosage of biochar. Soil pH significantly increased by 3.65–4.6% for wheat-biochar treatments and by 3.9–5.3% for maize-biochar treatments after wheat harvest compared to CK, respectively. After maize harvest, we observed similar results. Soil organic carbon was also notably enhanced by the biochar applications during the wheat–maize rotation system, especially at high biochar applications, indicating that biochar applications have potential effects on the soil improvement of its low fertility.

Compared to the control treatment, the biochar applications increased plant growth, yield, and quality of both wheat and maize (Figure 1). For example, WB-H and MB-H significantly increased the grain yield and grain number per spike for both wheat and maize ($p < 0.05$). The plant height and 100-grain weight of wheat was also significantly increased by the high dosage of biochar implications ($p < 0.05$), but not for maize ($p > 0.05$).

Soil cadmium mobility

The results of DTPA-extracted Cd concentrations in the soils of wheat and maize are shown in Figure 2A. In the CK treatment, DTPA-extracted Cd concentrations were 0.47 and 0.48 mg kg^{-1} in the soils after wheat and maize harvest, respectively. Biochar addition significantly reduced the DTPA-extracted Cd fraction at both low and high dosage treatments ($p < 0.05$). The DTPA-extracted Cd concentrations significantly decreased to 0.37–0.42 and 0.39–0.41 mg kg^{-1} in the treatments of WB-H and MB-H in wheat–maize rotation soils, respectively.

The results showed that the DTPA-extracted Cd concentrations were reduced by 15.6, 26.0, 17.3, and 20.5% with WB-L, WB-H, MB-L, and MB-H treatments, respectively, in wheat-harvested soils. The DTPA-extracted Cd

concentrations were reduced by 12.7, 21.7, 13.1, and 16.5% in treatments of WB-L, WB-H, MB-L, and MB-H of maize-harvested soils. It followed that soil DTPA-extracted Cd was more reduced but not significantly in the high dosage treatment than that in the low dosage treatment ($p > 0.05$). Additionally, more DTPA-extracted Cd was reduced compared to that in MB-treated soils during the wheat–maize rotation. These results suggest that biochar applications can significantly decrease the DTP-extracted Cd concentrations in soils compared to the CK treatment.

Soil cadmium chemical fractions

Sequential extractions were conducted to explore the biochar application impact on Cd fractions in wheat–maize rotation soils (Figure 2B). In CK, Cd was mainly in RE, CB, OM, and EX and the lowest in the OX. The results display that high dosage of biochar applications was more effective than the lower dosage in the reduction of the fractions of EX and CB and increasing OM and RE fractions of Cd. In the wheat growing season, the EX fractions decreased considerably to 9.3 and 10.3% at the low dosage and 6.3 and 8.2% at the high dosage of biochar applications compared to that of 13.0% in the control treatment. CB fractions of Cd were also reduced with biochar applications, while the OX fractions had no significant reduction. In the maize growing season, the EX Cd decreased considerably to 9.7 and 9.9% at the low dosage and 7.6 and 8.0% at the high dosage of biochar applications compared to that of 11.6% in the control treatment. CB fractions of Cd were also reduced with biochar applications, while the OX fractions had no significant reduction. The OM and RE fractions significantly increased to 19.2–25.9% and 49.9–56.0% compared to those of 17.7 and 46.3% in the control treatment. Therefore, biochar applications changed EX and CB fractions of Cd to OM and RE fractions. These results indicate that the soil Cd bioavailability was reduced by biochar applications, which would reduce the Cd uptake risks by plants. Sequential extractions suggested that biochar applications significantly influence the distributions of soil Cd fractions.

Plant activities of the antioxidant enzymes and malondialdehyde

To explore the effects of wheat and maize biochar on the antioxidant system in Cd-stressed wheat and maize, MDA, CAT, SOD, and POD activities in the wheat and maize roots after biochar applications were measured and shown in Figure 3. For wheat, the MDA activities were significantly reduced with high dosage of both WB and MB applications by 28.0 and 20.1% ($p < 0.05$), respectively, and for maize, high dosages also significantly decreased the MDA activities by 31.3 and 27.6% ($p < 0.05$); however, there were no significant differences between the low dosage of biochar applications compared to control treatments of both wheat and maize ($p > 0.05$). The high dosages of both wheat- and maize biochar (WB-H and MB-H) significantly increased the CAT and POD activities in wheat compared to the control treatment by 15.6–18.2% and 12.5–15.7% ($p < 0.05$) and also significantly increased these activities in maize by 18.5–19.0% and 23.4–24.6% ($p < 0.05$), respectively. However, the low dosage had no effects on the CAT and POD activities in both wheat and maize ($p > 0.05$). Additionally, both wheat and maize biochar at low and high dosages can also significantly increase the SOD activities compared to control treatments for both wheat and maize, particularly at the high dosages that can increase the averaged 168 and 36.8% of SOD activities in wheat and maize, respectively. Our results indicate that biochar applications can improve the antioxidant enzyme activities and reduce MDA in both wheat and maize roots.

Cadmium concentrations in wheat and maize

The effects of biochar on the Cd accumulations in wheat and maize are shown in Figure 4. In CK, wheat grain Cd concentration was 0.21 mg kg^{-1}, which was about 1.1 times higher than the safe limit value of the National Food Safety Standard (0.1 mg kg^{-1}) (GB 2762, 2017), but the Cd concentration in the maize grain (0.091 mg kg^{-1}) was under the limit. Both wheat and maize roots depicted the highest Cd concentration (1.12 and 0.98 mg kg^{-1}) among other plant parts, displaying the following order: root > stem > leaf > grain. The biochar applications can significantly decrease all the Cd concentrations in wheat and maize tissues at both levels of biochar dosages ($p < 0.05$). For example, the Cd concentrations in wheat grains were reduced by 38.1–91.5% and 65.9–80.0% by WB and MB applications, and maize grain Cd concentrations were reduced by 20.9–54.2% and 30.8–44% by WB and MB applications. For roots, both biochars significantly decreased the Cd concentrations by 24.1–62.4% in wheat and 23.5–42.9% in maize. Leaf Cd concentrations were also significantly reduced by 32.3–71.4% and 17.4–36.8% for wheat and maize, respectively, and stem Cd concentrations were reduced by 32.1–80.6% and 15.6–34.2%, respectively.

Discussion

Mechanisms of soil cadmium immobilization by biochar

Biochar applications can effectively decrease the bioavailability and immobilize the Cd in contaminated soil in the wheat–maize rotation system. The important phenomenon reducing bioavailability and mobility of soil Cd after biochar

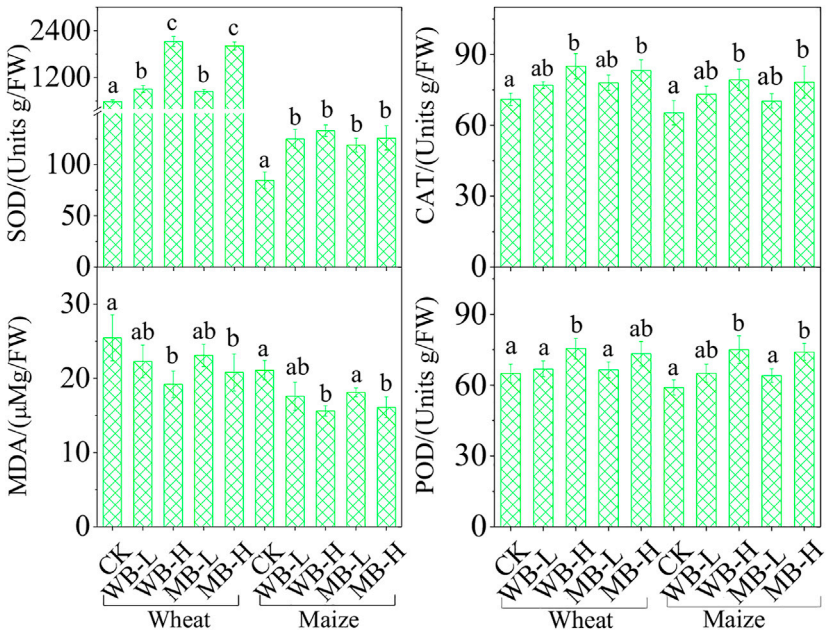

FIGURE 3
Effects of biochar on SOD, CAT, MDA, and POD activities in wheat and maize.

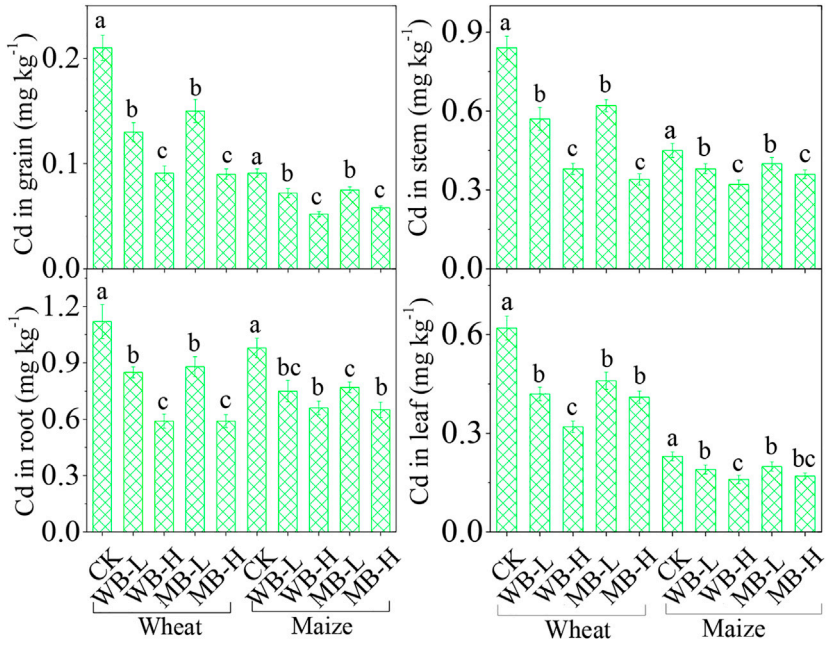

FIGURE 4
Effect of biochar on Cd concentrations in grain, stem, leaf, and root in wheat and maize.

TABLE 1 Basic properties of soil and biochar.

Parameter	WB	MB	CK-soil	WB-L-soil	WB-H-soil	MB-L-soil	MB-H-soil
Cd (mg kg^{-1})	0.55	0.28	1.45	1.43	1.42	1.44	1.42
pH	10.63	9.71	7.9	7.96	8.03	7.975	8.06
CEC (cmol kg^{-1})	35.8	32.5	23.3	23.9	29.8	24.1	28.3
SOC (g/kg)	756	691	14.7	18.8	20.1	17.6	18.9
Alkali	110	79	ND	ND	ND	ND	ND
Surface area (m^2 g^{-1})	2.2	3.6	ND	ND	ND	ND	ND
Total pore volume (cm^3 g^{-1})	0.21	0.39	ND	ND	ND	ND	ND
Average pore radius (nm)	12.1	9.3	ND	ND	ND	ND	ND
Average pore diameter (4V/A, nm)	3,698	2,134	ND	ND	ND	ND	ND
Porosity (%)	78	77	ND	ND	ND	ND	ND

applications is the availability of cations (Ca^{2+}, Mg^{2+}, K^{+}, and Zn^{2+}) and nutrients (nitrogen, silicon, and phosphorus). Some studies showed that the biochar applications bring large amounts of nutrients into contaminated soils (Kim et al., 2015; Xia et al., 2021; Gong et al., 2022). Additionally, high specific surface area and presence of negative charges decrease the bioavailability by the electrostatic interaction, increase the presence of organic functional groups, and form the sulfhydryl and phosphate precipitation (Cui et al., 2021; Yang et al., 2021; Gong et al., 2022).

In general, soil pH plays a role in heavy-metal speciation, mobility, and bioavailability in polluted soils because most of the metals are available in soils with acidic pH values. Biochar is normally alkaline, and our results confirmed that biochar applications can significantly increase soil pH with increasing application rates (Table 1). This enhancement of pH neutralized the free-state H^{+} and thus in turn increased the hydrolysis of Cd, increased its immobilization by soil and the biochar in soils, and accelerated the transformation of exchangeable fractions to the organic-bound and residual Cd fractions (Gong et al., 2022). This phenomenon was also observed in this study that showed biochar applications had significant effects on the transformation of EX and CB Cd fractions to OM and RE Cd fractions (Figure 2). The enhancement of pH can also strengthen Cd complexation, reducing the desorption of Cd^{2+} from soils (Xiang et al., 2021). Furthermore, decreased hydrogen ions can reduce the production of Cd solubility products and thus reduce the Cd bioavailability.

Large specific surface area, high micro-porous structure, and abundant large porosity distribution of biochar promote soil to contain the biochar in soil pores. The large specific surface area and high micro-porous structure also contained high electronegativity that can promote the electrostatic adsorption of positively charged ions (Inyang et al., 2016; Guo et al., 2020). The adsorption strength is dependent on the negatively charged groups on the biochar surface, that is, increasingly negative with the increase of pH values (He et al., 2019). Soil pH increased by biochar applications would also facilitate the electrostatic adsorption of Cd in this study. Additionally, in general, biochar contains high CEC and can release large amounts of cations, such as Ca^{2+}, Mg^{2+}, K^{+}, and Zn^{2+}, which can promote the cationic exchange with soil solution heavy metals on the biochar surface (Xu et al., 2016). Thus, the biochars can increase their adsorption capability for heavy metals, for e.g., Cd, Pb, and Cu (Li et al., 2017; Wu et al., 2021). A previous study by Lei et al. (2019) found that the animal-derived biochars contained about 27% higher Ca than plant-derived biochar, so ion exchanges were regarded as the dominant pathway of animal-derived biochars during the adsorption of heavy-metal ions.

The surface functional groups of biochars can also immobilize metal ions through ion exchange processes and surface complexation, particularly for biochars with relatively low mineral concentrations (Uchimiya et al., 2010; He et al., 2019). Previous studies suggested that crop straw-made biochars mainly immobilize heavy metals through the surface-complexation formation (Jiang and Xu, 2013; Lahori et al., 2017). The functional groups, for e.g., phenolic –OH, –COOH, –C=O–, and –C=N, largely exist in biochars, providing binding sites to form complexes, which increase the adsorption and immobilization for Cd (Uchimiya, 2014; Zong et al., 2021). Soil heavy metals adsorbed by biochar functional groups are regarded as the key mechanism in heavy-metal immobilization (Sun et al., 2021). Additionally, iron and manganese oxides and inorganic ions such as Si, Se, S, and Cl contained in biochar can complex with heavy metals, (e.g., Cd^{2+}), reducing the mobility and bioavailability in soils (Lahori et al., 2017). A previous study suggested that the main reason of soil DTPA-extractable Cu reduction was from the complexation of functional groups with Cu in the soils (Wang Y. et al., 2021). Furthermore, precipitation between the mineral elements in biochar and soil heavy metals was considered another mechanism of Cd immobilization of heavy metals, especially with biochar contained with mineral elements (e.g., P, S, and Se). For instance, the biochar produced by impregnation of P with the

TABLE 2 Cd bioaccumulation factor (BAF) and translocation factor (TF) of wheat and maize tissues.

Crop	BAF					TF			
	Treatment	Root	Stem	Leaf	Grain	G/S	L/S	S/R	G/R
Wheat	CK	0.77 ± 0.06	0.58 ± 0.03	0.43 ± 0.02	0.14 ± 0.01	0.25 ± 0.02	0.74 ± 0.05	0.75 ± 0.03	0.19 ± 0.01
	WB-L	0.59 ± 0.02	0.39 ± 0.03	0.29 ± 0.01	0.09 ± 0.01	0.23 ± 0.01	0.74 ± 0.03	0.67 ± 0.10	0.15 ± 0.02
	WB-H	0.41 ± 0.03	0.26 ± 0.01	0.22 ± 0.01	0.06 ± 0.00	0.24 ± 0.02	0.84 ± 0.06	0.64 ± 0.04	0.15 ± 0.01
	MB-L	0.61 ± 0.04	0.43 ± 0.02	0.32 ± 0.02	0.1 ± 0.01	0.24 ± 0.03	0.74 ± 0.08	0.70 ± 0.03	0.17 ± 0.01
	MB-H	0.41 ± 0.02	0.23 ± 0.01	0.28 ± 0.01	0.06 ± 0.00	0.26 ± 0.02	1.21 ± 0.06	0.58 ± 0.04	0.15 ± 0.01
Maize	CK	0.68 ± 0.04	0.31 ± 0.02	0.16 ± 0.01	0.06 ± 0.00	0.20 ± 0.01	0.51 ± 0.03	0.46 ± 0.03	0.09 ± 0.01
	WB-L	0.52 ± 0.04	0.26 ± 0.01	0.13 ± 0.01	0.05 ± 0.00	0.19 ± 0.02	0.50 ± 0.05	0.51 ± 0.02	0.1 ± 0.010
	WB-H	0.46 ± 0.03	0.22 ± 0.01	0.11 ± 0.01	0.04 ± 0.00	0.16 ± 0.01	0.50 ± 0.05	0.48 ± 0.03	0.08 ± 0.00
	MB-L	0.53 ± 0.02	0.28 ± 0.02	0.14 ± 0.01	0.05 ± 0.00	0.19 ± 0.01	0.50 ± 0.04	0.52 ± 0.05	0.10 ± 0.01
	MB-H	0.45 ± 0.03	0.25 ± 0.01	0.12 ± 0.01	0.04 ± 0.00	0.16 ± 0.01	0.47 ± 0.04	0.55 ± 0.03	0.09 ± 0.00

TABLE 3 Regression relationship between DTPA-extracted and exchangeable Cd in soils and Cd concentrations in wheat and maize tissues.

Cd in Tissues	Wheat root	Wheat grain	Wheat leaf	Wheat stem	Maize root	Maize grain	Maize leaf	Maize stem
DTPA-Cd	0.86*	0.93*	0.98*	0.85*	0.94*	0.93*	0.96*	0.96*
Exchangeable Cd	0.9*	0.92*	0.96	0.88*	0.92*	0.99*	0.99*	0.94*

* means significant correlation.

pyrolysis of bamboo can enhance the Cd absorption capacity by 10 times, and the solution Cd removal efficiency increased by 85% (Zhang et al., 2018).

Effects of biochars on the cadmium reduction in plants

Our results suggested that the soil applications of wheat- and maize-derived biochars can improve both wheat and maize growth and yield (Figure 1). Reduced grain yield, grain number per spike, plant height, and 100-grain weight of wheat and corn would result from the toxic effects induced by Cd, as previous studies found that Cd is toxic to plants, causing nutrient loss, reduction of antioxidant enzyme activities, and damage to photosynthesis in plants (Anwar et al., 2019; Wu et al., 2020; Zhou et al., 2020; Liu et al., 2021; Zhou et al., 2021; Li et al., 2022). It is also reported that Cd can also produce oxidative stress via high binding capacity for oxygen, nitrogen, and sulfur atoms, which resulted in reactive oxygen species (ROS) accumulation (Anwar et al., 2019). In this study, wheat and maize roots had the highest Cd concentrations in the control treatments, whereas wheat- and maize-derived biochar applications decreased their levels, as shown in Figure 3. The increased ROS is from higher Cd concentration and toxicity in wheat and maize roots in the control treatment as oxidative stress induced by Cd was well elucidated in wheat (Kaya et al., 2020), maize (Alharby et al., 2021), and other plants (Dabral et al., 2019; Gao et al., 2020). MDA contents reduced by biochar applications would be due to the reduction of Cd concentrations in wheat and maize tissues (Figures 3, 4). Previous studies also found that biochar applications can not only decrease oxidative stress in other plant species cultivated in Cd-contaminated soils but also reduce the oxidative stress by other heavy metals (Hafeez et al., 2019; Yue et al., 2019; Qu et al., 2020). Furthermore, biochar applications can also decrease the oxidative stress of wheat and maize in this study (Figure 3) and some other plants under the stresses of heavy metals in previous studies (Abbas et al., 2017; Hafeez et al., 2019; Alharby et al., 2021). For example, rice-straw biochar application elevated SOD, CAT, and POD by 18, 958, and 27%, respectively, in *Brassica napus* L. planted in the Cd-contaminated soils (Lei et al., 2022). Our results suggested that the enhancement of the enzyme activities resulted from decreased Cd concentrations in wheat and maize tissues and increased the plant tolerance to soil Cd stresses, thus improving the plant growth (Figures 1, 4).

The effects of biochar applications on TFs and BAFs in wheat and maize are shown in Table 2. Biochar applications significantly reduced BAFs, particularly in both wheat- and maize-derived biochar at high application rates. Additionally, the biochar applications also significantly decrease TFs from root

to stems and grains ($TF_{S/R}$ and $TF_{G/R}$) and also increase Cd in stem translocation to leaves in the high dosage treatments of wheat. More Cd transported to the leaf from the stem would be due to the wheat node allocation of Cd in the stem as previous studies suggest that node can allocate heavy metals and nutrient ions to grains and leaves (Feng et al., 2021). Additionally, the biochar applications would enhance the photosynthetic physiology (Shahbaz et al., 2019), which can also promote Cd in the stem transporting to the leaf. Our results agree with other findings that high dosages of biochars can decrease the Cd transport from roots to shoots (Zong et al., 2021). The Cd translocation from underground tissues to aboveground tissues is regarded as one of the most important factors in determining the accumulations of heavy metals in plants (Wang et al., 2020). In this study, regression analysis showed that the Cd concentrations in wheat and maize tissues (root, stem, leaf, and grain) were significantly correlated with bioavailable Cd (DTPA-extracted and exchangeable Cd) (Table 3), which indicates that the soil Cd bioavailability is directly contributed to the Cd accumulation in these crops. Therefore, reduction of bioavailable Cd concentrations in the soils is the most effective approach to reduce the soil Cd migration to crops and control food safety. Zong et al. (2021) also found that crop straw-derived biochar induced the Cd reduction in the rice–rape–corn rotation system that was notably correlated with the decreased DTPA extracted in soils. Additionally, high cation (e.g., Ca^{2+}, Mg^{2+}, K^{+}, and Zn^{2+}) concentration in biochar would be another reason for the reduction of Cd accumulation in wheat and maize tissues. These cautions can complete with Cd during the root Cd uptake and thus reduce the Cd uptake by crop roots (Xu et al., 2016).

Conclusion

Wheat straw- and maize straw-derived biochar applications to the Cd-contaminated soils can significantly decrease DTPA-extracted Cd concentrations by 12.7–26.0% and 13.1–20.5%, respectively, and WB applications can reduce more DTPA-extracted Cd in soils than MB applications during the wheat–maize rotation. Sequential extractions suggested that biochar applications can decrease the Cd bioavailability in biochar-amended soils and changed the EX and CB fractions of Cd to OM and RE fractions. For wheat and maize, the biochar applications increased the plant growth, yield, and quality of both wheat and maize, especially a significant increase in high dosages can also improve the antioxidant enzyme activities and reduce the reduction of MDA in both wheat and maize roots. The Cd concentrations in the wheat grains were reduced by 38.1–91.5% and 65.9–80% under WB and MB applications, and maize grain Cd concentrations were reduced by 20.9–54.2% and 30.8–44.0% under WB and MB applications, respectively. Cd concentrations in the root, stem, and leaf are also significantly reduced under WB and MB applications.

Although biochar applications can significantly reduce the Cd accumulation in wheat and maize grains, more effective approaches are necessary to qualify relevant transporters and provide useful information for breeding in the future. Additionally, mitigation strategies are in development, and short-term and long-term solutions with cost-effectiveness are needed to cope with the current Cd-contaminated paddy fields and Cd accumulation in rice grains. Moreover, long-term field trials are highly desirable to examine the residual effects of biochar amendments on different soil types and environmental conditions.

Data availability statement

The original contributions presented in the study are included in the article/Supplementary Material; further inquiries can be directed to the corresponding author.

Author contributions

YD: collected and analyzed samples, organized data, and wrote the manuscript; CW: designed experiments and wrote and revised the manuscript; MZ: collected and analyzed samples; XT: designed experiments; GW: collected samples.

Funding

This research was supported by the National Key R and D Program of China (2019YFC1805300).

Conflict of interest

Author MZ was employed by the company New Energy Geological Team of Hebei Coalfield Geological Bureau.

The remaining authors declare that the research was conducted in the absence of any commercial or financial relationships that could be construed as a potential conflict of interest.

Publisher's note

References

Abbas, T., Rizwan, M., Ali, S., Zia-ur-Rehman, M., Qayyum, M. F., Abbas, F., et al. (2017). Effect of biochar on cadmium bioavailability and uptake in wheat (*Triticum aestivum* L.) grown in a soil with aged contamination. *Ecotoxicol. Environ. Saf.* 140, 37–47. doi:10.1016/j.ecoenv.2017.02.028

Alharby, H. F., Al-Zahrani, H. S., Hakeem, K. R., Alsamadany, H., Desoky, E.-S. M., Rady, M. M., et al. (2021). Silymarin-enriched biostimulant foliar application minimizes the toxicity of cadmium in maize by suppressing oxidative stress and elevating antioxidant gene expression. *Biomolecules* 11 (3), 465. doi:10.3390/biom11030465

Anwar, S., Khan, S., Hussain, I., Bashir, R., and Fahad, S. (2019). Chelators induced uptake of cadmium and modulation of water relation, antioxidants, and photosynthetic traits of maize. *Environ. Sci. Pollut. Res.* 26 (17), 17577–17590. doi:10.1007/s11356-019-05170-6

Bashir, S., Hussain, Q., Jun, Z., Qingling, F., Houben, D., and Hongqing, H. (2020). Efficiency of KOH-modified rice straw-derived biochar for reducing cadmium mobility, bioaccessibility and bioavailability risk index in red soil. *Pedosphere* 30 (6), 874–882. doi:10.1016/s1002-0160(20)60043-1

Cao, X., Gao, X., Zeng, X., Ma, Y., Gao, Y., Baeyens, W., et al. (2021). Seeking for an optimal strategy to avoid arsenic and cadmium over-accumulation in crops: Soil management vs cultivar selection in a case study with maize. *Chemosphere* 272, 129891. doi:10.1016/j.chemosphere.2021.129891

Cui, H., Li, H., Zhang, S., Yi, Q., Zhou, J., Fang, G., et al. (2020). Bioavailability and mobility of copper and cadmium in polluted soil after phytostabilization using different plants aided by limestone. *Chemosphere* 242, 125252. doi:10.1016/j.chemosphere.2019.125252

Cui, H., Wang, Q., Zhang, X., Zhang, S., Zhou, J., Zhou, D., et al. (2021). Aging reduces the bioavailability of copper and cadmium in soil immobilized by biochars with various concentrations of endogenous metals. *Sci. Total Environ.* 797, 149136. doi:10.1016/j.scitotenv.2021.149136

Dabral, S., Yashaswee, Varma, A., Choudhary, D. K., Bahuguna, R. N., and Nath, M. (2019). Biopriming with Piriformospora indica ameliorates cadmium stress in rice by lowering oxidative stress and cell death in root cells. *Ecotoxicol. Environ. Saf.* 186, 109741. doi:10.1016/j.ecoenv.2019.109741

Du, B., Zhou, J., Lu, B., Zhang, C., Li, D., Zhou, J., et al. (2020). Environmental and human health risks from cadmium exposure near an active lead-zinc mine and a copper smelter, China. *Sci. Total Environ.* 720, 137585. doi:10.1016/j.scitotenv.2020.137585

Fatima, G., Raza, A. M., Hadi, N., Nigam, N., and Mahdi, A. A. (2019). Cadmium in human diseases: it's more than just a mere metal. *Indian J. Clin. biochem.* 34 (4), 371–378. doi:10.1007/s12291-019-00839-8

Feng, J., Shen, R. F., and Shao, J. F. (2021). Transport of cadmium from soil to grain in cereal crops: A review. *Pedosphere* 31 (1), 3–10. doi:10.1016/s1002-0160(20)60015-7

Gao, M., Chang, X., Yang, Y., and Song, Z. (2020). Foliar graphene oxide treatment increases photosynthetic capacity and reduces oxidative stress in cadmium-stressed lettuce. *Plant Physiology Biochem.* 154, 287–294. doi:10.1016/j.plaphy.2020.06.021

Gong, H., Zhao, L., Rui, X., Hu, J., and Zhu, N. (2022). A review of pristine and modified biochar immobilizing typical heavy metals in soil: Applications and challenges. *J. Hazard. Mater.* 432, 128668. doi:10.1016/j.jhazmat.2022.128668

Guo, M., Song, W., and Tian, J. (2020). Biochar-facilitated soil remediation: Mechanisms and efficacy variations. *Front. Environ. Sci.* 183, 521512. doi:10.3389/fenvs.2020.521512

Hafeez, F., Rizwan, M., Saqib, M., Yasmeen, T., Ali, S., Abbas, T., et al. (2019). Residual effect of biochar on growth, antioxidant defence and cadmium (cd) accumulation in rice in a cd contaminated saline soil. *Pak. J. Agric. Sci.* 56 (1), 197–204. doi:10.21162/pakjas/19.7546

He, L., Zhong, H., Liu, G., Dai, Z., Brookes, P. C., Xu, J., et al. (2019). Remediation of heavy metal contaminated soils by biochar: Mechanisms, potential risks and applications in China. *Environ. Pollut.* 252, 846–855. doi:10.1016/j.envpol.2019.05.151

Huang, X., Yu, H., Zhao, X., Guo, X., Ye, Y., and Xu, Z. (2021). Spatial variation in cadmium and mercury and factors influencing their potential ecological risks in farmland soil in poyang lake plain, China. *Front. Environ. Sci.* 9, 641497. doi:10.3389/fenvs.2021.641497

Inyang, M. I., Gao, B., Yao, Y., Xue, Y., Zimmerman, A., Mosa, A., et al. (2016). A review of biochar as a low-cost adsorbent for aqueous heavy metal removal. *Crit. Rev. Environ. Sci. Technol.* 46 (4), 406–433. doi:10.1080/10643389.2015.1096880

Jafarabadi, A. R., Mitra, S., Raudonytė-Svirbutavičienė, E., and Bakhtiari, A. R. (2020). Large-scale evaluation of deposition, bioavailability and ecological risks of the potentially toxic metals in the sediment cores of the hotspot coral reef ecosystems (Persian Gulf, Iran). *J. Hazard. Mater.* 400, 122988. doi:10.1016/j.jhazmat.2020.122988

Jiang, J., and Xu, R.-k. (2013). Application of crop straw derived biochars to Cu (II) contaminated ultisol: Evaluating role of alkali and organic functional groups in Cu (II) immobilization. *Bioresour. Technol.* 133, 537–545. doi:10.1016/j.biortech.2013.01.161

Kamaruzzaman, M., Wang, Z., Wu, M., Yang, L., Han, Y., Li, G., et al. (2021). Promotion of tomato growth by the volatiles produced by the hypovirulent strain QT5-19 of the plant gray mold fungus Botrytis cinerea. *Microbiol. Res.* 247, 126731. doi:10.1016/j.micres.2021.126731

Kaya, C., Ashraf, M., Alyemeni, M. N., and Ahmad, P. (2020). Responses of nitric oxide and hydrogen sulfide in regulating oxidative defence system in wheat plants grown under cadmium stress. *Physiol. Plant.* 168 (2), 345–360. doi:10.1111/ppl.13012

Kim, H.-S., Kim, K.-R., Kim, H.-J., Yoon, J.-H., Yang, J. E., Ok, Y. S., et al. (2015). Effect of biochar on heavy metal immobilization and uptake by lettuce (Lactuca sativa L.) in agricultural soil. *Environ. Earth Sci.* 74 (2), 1249–1259. doi:10.1007/s12665-015-4116-1

Lahori, A. H., Zhang, Z., Guo, Z., Li, R., Mahar, A., Awasthi, M. K., et al. (2017). Beneficial effects of tobacco biochar combined with mineral additives on (im) mobilization and (bio) availability of Pb, Cd, Cu and Zn from Pb/Zn smelter contaminated soils. *Ecotoxicol. Environ. Saf.* 145, 528–538. doi:10.1016/j.ecoenv.2017.07.071

Lei, M., Li, Z., Zhang, B., Wang, X., Tie, B., Ayaz, T., et al. (2022). Mechanisms of stress alleviation after lime and biochar applications for Brassica napus L. In cadmium-contaminated soil. *Adsorpt. Sci. Technol.* 2022, 4195119. doi:10.1155/2022/4195119

Lei, S., Shi, Y., Qiu, Y., Che, L., and Xue, C. (2019). Performance and mechanisms of emerging animal-derived biochars for immobilization of heavy metals. *Sci. Total Environ.* 646, 1281–1289. doi:10.1016/j.scitotenv.2018.07.374

Li, H., Dong, X., da Silva, E. B., de Oliveira, L. M., Chen, Y., and Ma, L. Q. (2017). Mechanisms of metal sorption by biochars: Biochar characteristics and modifications. *Chemosphere* 178, 466–478. doi:10.1016/j.chemosphere.2017.03.072

Li, W., He, X., Zhang, J., and Liu, K. (2022). Determination of soil cadmium threshold for potato. *Front. Environ. Sci.* 10, 808362. doi:10.3389/fenvs.2022.808362

Li, Y., Chen, W., Yang, Y., Wang, T., and Dai, Y. (2021). Quantifying source-specific intake risks of wheat cadmium by associating source contributions of soil cadmium with human health risk. *Ecotoxicol. Environ. Saf.* 228, 112982. doi:10.1016/j.ecoenv.2021.112982

Liu, K., Liu, H., Zhou, X., Chen, Z., and Wang, X. (2021). Prediction of cadmium transfer from soil to potato in karst soils, China. *Front. Environ. Sci.* 9, 684887. doi:10.3389/fenvs.2021.684887

Nuss, E. T., and Tanumihardjo, S. A. (2010). Maize: A paramount staple crop in the context of global nutrition. *Compr. Rev. food Sci. food Saf.* 9 (4), 417–436. doi:10.1111/j.1541-4337.2010.00117.x

Pang, Y., Liu, C., Wang, D., Amand, P. S., Bernardo, A., Li, W., et al. (2020). High-resolution genome-wide association study identifies genomic regions and candidate genes for important agronomic traits in wheat. *Mol. Plant* 13 (9), 1311–1327. doi:10.1016/j.molp.2020.07.008

Proshad, R., Kormoker, T., Mursheed, N., Islam, M. M., Bhuyan, M. I., Islam, M. S., et al. (2018). Heavy metal toxicity in agricultural soil due to rapid industrialization in Bangladesh: A review. *Int. J. Adv. Geosciences* 6 (1), 83. doi:10.14419/ijag.v6i1.9174

Qu, M., Chen, J., Huang, B., and Zhao, Y. (2020). Exploring the spatially varying relationships between cadmium accumulations and the main influential factors in the rice-wheat rotation system in a large-scale area. *Sci. Total Environ.* 736, 139565. doi:10.1016/j.scitotenv.2020.139565

Shahbaz, A. K., Ramzani, P. M. A., Saeed, R., Turan, V., Iqbal, M., Lewińska, K., et al. (2019). Effects of biochar and zeolite soil amendments with foliar proline spray on nickel immobilization, nutritional quality and nickel concentrations in wheat. *Ecotoxicol. Environ. Saf.* 173, 182–191. doi:10.1016/j.ecoenv.2019.02.025

Siddique, A. B., Rahman, M. M., Islam, M. R., Mondal, D., and Naidu, R. (2021). Response of iron and cadmium on yield and yield components of rice and translocation in grain: Health risk estimation. *Front. Environ. Sci.* 9, 716770. doi:10.3389/fenvs.2021.716770

Sun, T., Xu, Y., Sun, Y., Wang, L., Liang, X., Jia, H., et al. (2021). Crayfish shell biochar for the mitigation of Pb contaminated water and soil: Characteristics, mechanisms, and applications. *Environ. Pollut.* 271, 116308. doi:10.1016/j.envpol.2020.116308

Tessier, A., Campbell, P., and Bisson, M. (1980). Trace metal speciation in the yamaska and st. Francois rivers (quebec). *Can. J. Earth Sci.* 17 (1), 90–105. doi:10.1139/e80-008

Thengane, S. K., and Bandyopadhyay, S. (2020). Biochar mines: Panacea to climate change and energy crisis? *Clean. Technol. Environ. Policy* 22 (1), 5–10. doi:10.1007/s10098-019-01790-1

Uchimiya, M. (2014). Influence of pH, ionic strength, and multidentate ligand on the interaction of CdII with biochars. *ACS Sustain. Chem. Eng.* 2 (8), 2019–2027. doi:10.1021/sc5002269

Uchimiya, M., Lima, I. M., Thomas Klasson, K., Chang, S., Wartelle, L. H., and Rodgers, J. E. (2010). Immobilization of heavy metal ions (CuII, CdII, NiII, and PbII) by broiler litter-derived biochars in water and soil. *J. Agric. Food Chem.* 58 (9), 5538–5544. doi:10.1021/jf9044217

Wang, L., Cui, X., Cheng, H., Chen, F., Wang, J., Zhao, X., et al. (2015). A review of soil cadmium contamination in China including a health risk assessment. *Environ. Sci. Pollut. Res.* 22 (21), 16441–16452. doi:10.1007/s11356-015-5273-1

Wang, L., Zhang, Q., Liao, X., Li, X., Zheng, S., Zhao, F., et al. (2021a). Phytoexclusion of heavy metals using low heavy metal accumulating cultivars: A green technology. *J. Hazard. Mater.* 413, 125427. doi:10.1016/j.jhazmat.2021.125427

Wang, Y., Zhang, K., Lu, L., Xiao, X., and Chen, B. (2020). Novel insights into effects of silicon-rich biochar (Sichar) amendment on cadmium uptake, translocation and accumulation in rice plants. *Environ. Pollut.* 265, 114772. doi:10.1016/j.envpol.2020.114772

Wang, Y., Zheng, K., Zhan, W., Huang, L., Liu, Y., Li, T., et al. (2021b). Highly effective stabilization of Cd and Cu in two different soils and improvement of soil properties by multiple-modified biochar. *Ecotoxicol. Environ. Saf.* 207, 111294. doi:10.1016/j.ecoenv.2020.111294

Wu, C., Dun, Y., Zhang, Z., Li, M., and Wu, G. (2020). Foliar application of selenium and zinc to alleviate wheat (*Triticum aestivum* L.) cadmium toxicity and uptake from cadmium-contaminated soil. *Ecotoxicol. Environ. Saf.* 190, 110091. doi:10.1016/j.ecoenv.2019.110091

Wu, J., Wang, T., Wang, J., Zhang, Y., and Pan, W.-P. (2021). A novel modified method for the efficient removal of Pb and Cd from wastewater by biochar: Enhanced the ion exchange and precipitation capacity. *Sci. Total Environ.* 754, 142150. doi:10.1016/j.scitotenv.2020.142150

Xia, Y., Li, Y., Sun, Y., Miao, W., and Liu, Z. (2021). Co-pyrolysis of corn stover with industrial coal ash for *in situ* efficient remediation of heavy metals in multi-polluted soil. *Environ. Pollut.* 289, 117840. doi:10.1016/j.envpol.2021.117840

Xiang, J., Lin, Q., Yao, X., and Yin, G. (2021). Removal of Cd from aqueous solution by chitosan coated MgO-biochar and its *in-situ* remediation of Cd-contaminated soil. *Environ. Res.* 195, 110650. doi:10.1016/j.envres.2020.110650

Xu, P., Sun, C.-X., Ye, X.-Z., Xiao, W.-D., Zhang, Q., Wang, Q., et al. (2016). The effect of biochar and crop straws on heavy metal bioavailability and plant accumulation in a Cd and Pb polluted soil. *Ecotoxicol. Environ. Saf.* 132, 94–100. doi:10.1016/j.ecoenv.2016.05.031

Yang, T., Xu, Y., Huang, Q., Sun, Y., Liang, X., Wang, L., et al. (2021). An efficient biochar synthesized by iron-zinc modified corn straw for simultaneously immobilization Cd in acidic and alkaline soils. *Environ. Pollut.* 291, 118129. doi:10.1016/j.envpol.2021.118129

Yue, L., Lian, F., Han, Y., Bao, Q., Wang, Z., Xing, B., et al. (2019). The effect of biochar nanoparticles on rice plant growth and the uptake of heavy metals: Implications for agronomic benefits and potential risk. *Sci. Total Environ.* 656, 9–18. doi:10.1016/j.scitotenv.2018.11.364

Zhang, S., Xu, Y., Wu, M., Mao, X., Yao, Y., Shen, Q., et al. (2021). Geogenic enrichment of potentially toxic metals in agricultural soils derived from black shale in northwest Zhejiang, China: Pathways to and risks from associated crops. *Ecotoxicol. Environ. Saf.* 215, 112102. doi:10.1016/j.ecoenv.2021.112102

Zhang, S., Zhang, H., Cai, J., Zhang, X., Zhang, J., Shao, J., et al. (2018). Evaluation and prediction of cadmium removal from aqueous solution by phosphate-modified activated bamboo biochar. *Energy fuels.* 32 (4), 4469–4477. doi:10.1021/acs.energyfuels.7b03159

Zheng, R., Sun, G., Li, C., Reid, B. J., Xie, Z., Zhang, B., et al. (2017). Mitigating cadmium accumulation in greenhouse lettuce production using biochar. *Environ. Sci. Pollut. Res.* 24 (7), 6532–6542. doi:10.1007/s11356-016-8282-9

Zhou, J., Zhang, C., Du, B., Cui, H., Fan, X., Zhou, D., et al. (2020). Effects of zinc application on cadmium (Cd) accumulation and plant growth through modulation of the antioxidant system and translocation of Cd in low- and high-Cd wheat cultivars. *Environ. Pollut.* 265, 115045. doi:10.1016/j.envpol.2020.115045

Zhou, J., Zhang, C., Du, B., Cui, H., Fan, X., Zhou, D., et al. (2021). Soil and foliar applications of silicon and selenium effects on cadmium accumulation and plant growth by modulation of antioxidant system and Cd translocation: Comparison of soft vs. durum wheat varieties. *J. Hazard. Mater.* 402, 123546. doi:10.1016/j.jhazmat.2020.123546

Zhuang, Z., Niño-Savala, A. G., Mi, Z.-d., Wan, Y.-n., Su, D.-c., Li, H.-f., et al. (2021). Cadmium accumulation in wheat and maize grains from China: Interaction of soil properties, novel enrichment models and soil thresholds. *Environ. Pollut.* 275, 116623. doi:10.1016/j.envpol.2021.116623

Zhuang, Z., Wang, Q., Huang, S., NiñoSavala, A. G., Wan, Y., Li, H., et al. (2023). Source-specific risk assessment for cadmium in wheat and maize: Towards an enrichment model for China. *J. Environ. Sci.* 125, 723–734. doi:10.1016/j.jes.2022.02.024

Zong, Y., Xiao, Q., Malik, Z., Su, Y., Wang, Y., Lu, S., et al. (2021). Crop straw-derived biochar alleviated cadmium and copper phytotoxicity by reducing bioavailability and accumulation in a field experiment of rice-rape-corn rotation system. *Chemosphere* 280, 130830. doi:10.1016/j.chemosphere.2021.130830

frontiers | Frontiers in Environmental Science

TYPE Original Research
PUBLISHED 05 September 2022
DOI 10.3389/fenvs.2022.990471

OPEN ACCESS

EDITED BY
Buyun Du,
Jiangsu Open University, China

REVIEWED BY
Yongbing Cai,
Anhui Science and Technology University, China
Wei Liu,
China University of Geosciences Wuhan, China
Yuchuan Sun,
Southwest University, China

*CORRESPONDENCE
Wei Li,
liwei210@126.com

SPECIALTY SECTION
This article was submitted to Toxicology, Pollution and the Environment, a section of the journal Frontiers in Environmental Science

RECEIVED 10 July 2022
ACCEPTED 21 July 2022
PUBLISHED 05 September 2022

CITATION
An X, Li W, Lan J, Di X and Adnan M (2022), Seasonal co-pollution characteristics of parent-PAHs and alkylated-PAHs in karst mining area soil of Guizhou, Southwest China. *Front. Environ. Sci.* 10:990471. doi: 10.3389/fenvs.2022.990471

Seasonal co-pollution characteristics of parent-PAHs and alkylated-PAHs in karst mining area soil of Guizhou, Southwest China

Xianjin An [1,2†], Wei Li [3*], Jiacheng Lan [1,2], Xinyue Di [4] and Muhammad Adnan [5,6]

[1]School of Karst Science, Guizhou Normal University, Guiyang, China, [2]State Engineering Technology Institute for Karst Desertification Control, Guiyang, China, [3]College of Biology and Environmental Engineering, Guiyang University, Guiyang, China, [4]School of Geography and Environmental Engineering, Gannan Normal University, Ganzhou, China, [5]State Key Laboratory of Environmental Geochemistry, Institute of Geochemistry, Chinese Academy of Sciences, Guiyang, China, [6]University of Chinese Academy of Sciences, Beijing, China

The research on polycyclic aromatic hydrocarbons (PAHs) in karst soil mainly focuses on 16 kinds of parent-PAHs (p- PAHs), and little attention is given to alkylated-PAHs (a-PAHs) with higher concentration and greater toxicity. Five surface soils of coal mining area and their surrounding areas in karst area were sampled as subject investigated, and the spatiotemporal pollution characteristics of p-PAHs and a-PAHs were analyzed to discuss the impact of karst soil properties and environmental conditions on the migration of a-PAHs. The research results showed that the pollution concentration of a-PAHs in the soil of the southwestern karst area, especially the coal mining area, was significantly higher compared to the 16 kinds of p-PAHs, and the average concentration of the p-PAHs was 177.29 ± 37.36 ng/g; the concentration of a-PAHs was 346.87 ± 104.91 ng/g; the concentration of PAHs presented a seasonal pattern of that in winter > spring > autumn > summer. At the same time, seasonal rainfall could affect and change the occurrence state of PAHs in karst soils, but the effect on p-PAHs was weaker than on a-PAHs. The concentration of PAHs in the coal mining area and forest soil were 651.68 ng/g and 755.38 ng/g, respectively, so they belonged to contaminated soil, while the concentrations of two cultivated soil and abandoned soil were 475.51 ng/g, 367.58 ng/g and 370.63 ng/g, respectively, belonging to weakly contaminated. Toxicity assessment showed that p-BaP with a maximum toxic equivalent of 62.35 ng/g, C_1-BaP (42.09 ng/g), DaA (37.82 ng/g) and C_{1-3} BaA (25.91 ng/g) were toxic PAHs with higher risk. The results of the correlation study showed that soil organic carbon, soil clay and soil calcium content were the dominant factors affecting the spatiotemporal distribution of PAHs of soils in karst coal mining areas and their surrounding areas. The research can provide data guidance for the management, control and restoration of soil pollution in karst areas, and offer a reference for Guizhou province to implement the big-ecological strategy.

KEYWORDS
karst, soil, parent-PAHs, alkylated-PAHs, seasonal variations, pollution characteristics

Introduction

Global karst landforms were widely distributed, accounting for about 15% of the terrestrial area (Larson and Mylroie, 2018). Guizhou province was China's distribution center of karst landforms (Yan et al., 2019). Karst areas are vulnerable to various exogenous pollutants due to their extremely fragile ecosystems and thin soil layers. The coal-dominated energy consumption structure, rapid urbanization, and the increasing number of motor vehicles have made Guizhou province karst soil a major "sink" of PAHs. Research pointed out that the total emission of PAHs was 1730 tons in Guizhou province, ranking fourth in the country in 2003 (Xu et al., 2006), and Guizhou province's overall emission intensity was also at a high level in China (Zhang et al., 2007). Han et al. (2019) pointed out that China emitted 32,700 tons of PAHs because of incomplete fuel combustion in 2016, and the emission intensity of Guizhou province was high. Zhang et al. (2022) pointed out that the pollutant concentration of soil PAHs near the coal-fired power plant in the karst area of Guizhou province reached 12.2 mg/kg.

The occurrence, migration and fate of 16 kinds of p-PAHs in the environmental priority control pollutants in soil have been widely studied, but the total polycyclic aromatic compounds (PACs) in the environment not only contain 16 kinds of p-PAHs, but also include a-PAHs, nitro-polycyclic aromatic hydrocarbons (n-PAHs), dibenzothiophenes (DBTs), etc. In recent years, researchers have found that aerosols (Wei et al., 2015), bituminous coal (Zhang et al., 2021), coking plants and coal gangue (Lin et al., 2017; Liang et al., 2018), oil-contaminated sites (Golzadeh et al., 2021), untreated sludge and municipal wastewater (Hellou et al., 1999) include not only 16 kinds of p-PAHs, but also a large number of a-PAHs whose proportion was often greater than p-PAHs. The main sources of a-PAHs included the accompanying products of petroleum, namely diagenetic sources; a-PAHs also existed in raw coal; the processing and combustion of petroleum and coal products also released a part of a-PAHs. The substitution reaction of p-PAHs in the environment also increased the concentration of a-PAHs in the environment. Studies have found that a-PAHs may be significantly more toxic than p-PAHs (Andersson and Achten 2015; Golzadeh et al., 2021). The study believed that PAHs with a "Bay region" structure was the key molecular feature that affected whether PAHs would lead to mutagenesis, carcinogenesis and teratogenesis. The study also found that 38 kinds of a-PAHs had the above three effects (Baird et al., 2007).

The climate, precipitation and various Earth surface processes in southwest China's karsts were extremely complicated, which may affect PAH's environmental migration and final fate. Lan et al. (2016, 2018) showed that rainfall events changed the distribution of PAHs in karst groundwater, the mass concentration of PAHs in water increased with the increase of rainfall or flow, and the ecological risk of underground water changed during rainfall. Zhu et al. (2022) showed that high ring PAHs were more enriched in the soil of typical karst trough valleys in Chongqing, and soil PAHs generally caused a low risk of carcinogenicity. Qian et al. (2020) showed that low cyclic PAH was mainly found in the karst cave sediment, and PAHs distribution had no significant relationship with the sediment particle size. Ye et al. (2015) believed that the migration of PAHs in karst areas was mainly controlled by two mechanisms: organic matter and water dissolution. They believed that energy combustion and traffic pollution, and atmospheric deposition were the main pollution pathway for PAHs in the study area. An et al. (2021) believed that the migration of PAHs in karst soil was closely related to natural ecological processes such as freezing and thawing. Freeze-thaw cycles may affect the form of calcium ions in the karst environment, thereby changing the microscopic morphology and structure of soil organic matter, resulting in chvvvanges in PAHs occurrence state and desorption process. The research on PAHs in the karst environment mainly focused on groundwater and 16 kinds of p-PAHs, while the more toxic a-PAHs and 16 kinds of p-PAHs in soil had not been reported.

Meanwhile, the physicochemical properties of a-PAHs and p-PAHs were quite different, which may affect the occurrence, migration and toxicity in the environment (Kang et al., 2016). The pollution of a-PAHs in southwestern karst areas, especially in coal-rich areas, would inevitably affect soil health and groundwater safety, and ultimately affected the safety of the entire regional ecosystem and human health. In addition, the unique climatic conditions in the karst area of Guizhou province may change the occurrence and migration of p-PAHs and a-PAHs. Hence, studying the pollution characteristics of a-PAHs in karst areas was necessary. The main purpose of this study was to find out the temporal and spatial distribution tendency of PAHs in the soil of karst coal-rich areas in different seasons, analyze the possible influencing factors, calculate the ecological risk value. The research can provide data guidance for the management, control and restoration of soil pollution in karst areas, and provide a reference for implementing the big ecology strategy in Guizhou province.

Material and methods

Sample collection

The study selected five surface soils (0–10 cm) in a coal mining area in Hezhang County, Guizhou province (Figure 1). The coal mining area was 2.29 km^2, and the production scale was

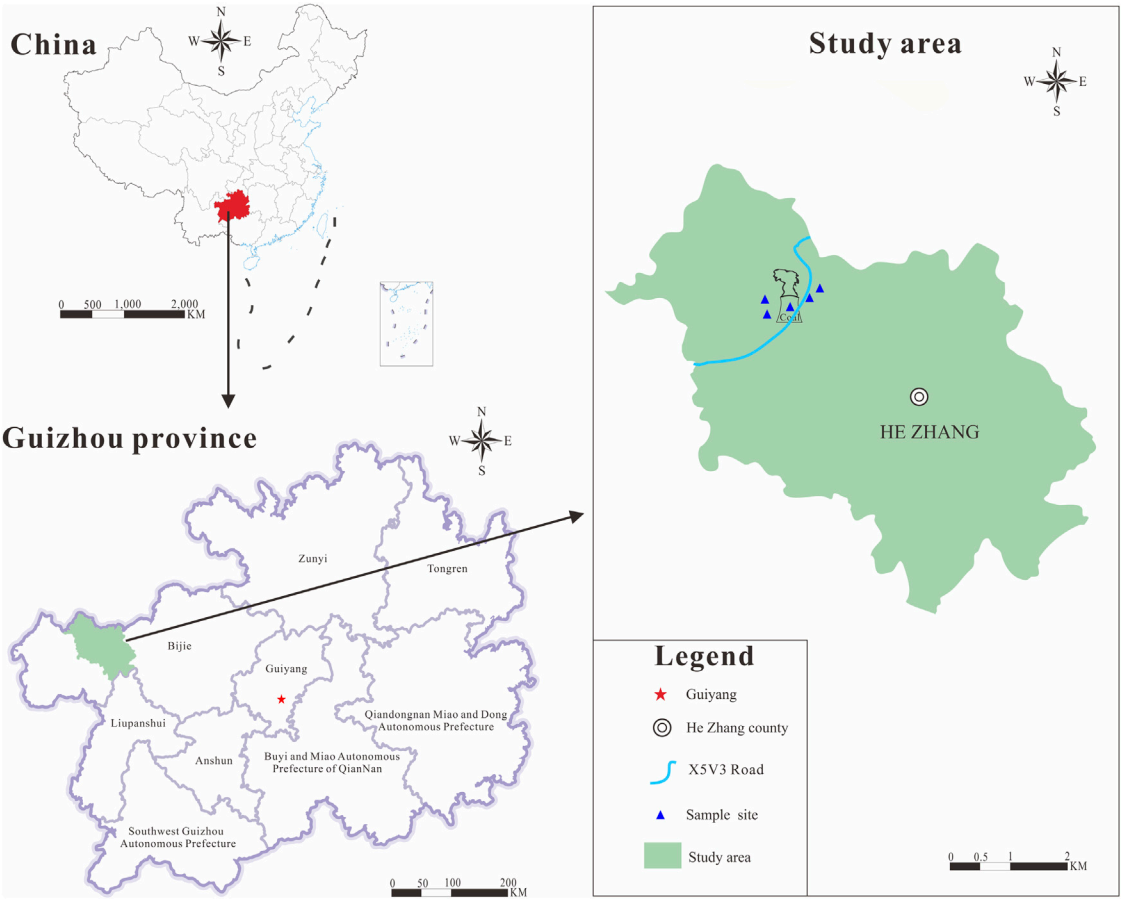

FIGURE 1
Location of samples site of karst soil in Guizhou province.

0.45 Mt/a. The coal-bearing formation of the coal mine was Xuanwei Group (P3x), which mainly was lignite with medium high sulfur and low volatile anthracite. The study was conducted in March, 2021 (spring, with continuous light rain for a week before sampling), June, 2021 (summer, with a heavy rain for a week before sampling), September, 2021 (autumn, without rainfall for a week before sampling), and December, 2021 (winter, without rainfall for a week before sampling). 10 m × 10 m surface soil mixed sample was collected by the W-type sampling method, which was air-dried at room temperature in the laboratory in the dark to remove plant roots and debris, ground and screened through a 100-mesh stainless steel sieve, and put in a sealed bag for later use. The basic characteristics of the soil are shown in Table 1. The total organic carbon (TOC) was measured by an organic element analyzer (vario Macro cube), and the cation exchange capacity (CEC) was measured by the NH_4Cl-NH_4OAc method. The total calcium amount of the soil (TCA) was digested using aqua regia-perchloric acid and determined by the ICP-OES method. Soil texture was determined using a laser particle size analyzer (BT-9300ST).

Instruments and reagents

The main experimental apparatus included Agilent 6890/5973B gas chromatography-mass spectrometer (equipped with EI ionization source and automatic sampler); rotary evaporator (VORTEX-5), ultrasonic cleaner (KG-250DE type), centrifuge (TGL -16C).

N-hexane and dichloromethane were products of Thermal Fisher, the United States; methanol and anhydrous sodium sulfate were bought from Sinopharm Group Corporation. The standard mixed samples of 16 kinds of p-PAHs were purchased from AccuStandard, the United States, and the standard

TABLE 1 Physical and chemical properties of the soil at the sampling sites.

Sample	pH	TOC (%)	CEC (cmol/kg)	TCA (10^{-3} cmol/kg)	Soil texture(%)			Descriptions
					Silt	Clay	Sand	
S1	6.39	3.55	11.28	5.21	33.26	20.23	46.51	The soil in the mining area, without the vegetation
S2	7.62	3.84	23.57	3.22	19.24	43.92	36.84	Abandoned soil, with horsetail pine
S3	7.48	5.61	12.28	4.38	11.36	67.06	21.58	Slope soil, perennial planting pepper
S4	7.24	4.47	14.57	3.47	40.29	24.54	35.17	Cultivated soil, mainly planting corn
S5	7.37	9.46	26.45	6.35	26.48	39.03	34.49	Forest soil

solutions of 12 a-PAHs were purchased from Ehrenstorfer, Germany. Preprocessing standard internal D_8-naphthalene, quantitative internal standard D_{10}-acenaphthene, D_{10}-phenanthrene, D_{12}-perylene, D_{12}-chrysen, and injection internal standard D_{14}-tribiphenyl were purchased from Cambridge Isotope Laboratories.

Extraction and analysis

Ultrasonic extraction was used to extract the p-PAHs and a-PAHs in the soil. Briefly, 5 g sample was put into a 10 ml screw-top glass test tube, then 2 g high-temperature treated anhydrous sodium sulfate was added, then 100 μL with 20 μg/ml recovery internal standard D_8-naphthalene was added, and meanwhile 10 ml of dichloromethane was added. At a constant water temperature of 20°C, the sample was sonicated for 5 h, and stirred once per hour during ultrasonication. The supernatant was transferred to a centrifuge tube, centrifuged at 14,000 r/min for 5 min, and then transferred to a rotary evaporator, which was concentrated to 0.5 ml, transferred to a 1.5 ml brown injection bottle. 100 μL with 400 ng/g quantitative internal standard (D_{10}-acenaphthene, D_{10}-phenanthrene, and D_{12}-perylene) was added. The sample capacity was fixed to 1 ml using methanol, and evenly was mixed in a vortexer for 5 min to tested on the machine.

The sample was measured by GC-MS, and the specific chromatographic parameters were as follows: temperature programming of the chromatographic column (DB-5MS, 30 m × 0.25 mm × 0.25 μm, United States) started from 70°C, and held for 1 min; the chromatographic column was heated to 180°C at 15°C/min, held for 2 min; heated to 220°C at 10°C/min, held for 0.5 min, and finally heated to 300°C at 8°C/min, held for 5 min. The carrier gas was helium, the flow rate was constant flow with 1.0 ml/min; the injection port temperature was 280°C, and the injection volume was 1 μL without split sampling. Mass spectrometry parameters: electron bombardment ion source, ionization voltage 70 eV, ion source temperature 230°C, interface temperature 280°C, mass scanning range m/z 50–550, in full scan mode, solvent delay for 4 min.

Data processing and quality control

The p-PAHs were determined by gas chromatography-mass spectrometry, specifically referred to by Lan et al. (2016). The a-PAHs were qualitatively and quantitatively analyzed using MassLynx V4.2 software by referring to the mass spectrum of the standard sample and the mass spectrum in the standard mass spectrum database (NIST Mass Spectral Database), and qualitative analysis was made based on retention time. The relative response factor (RF) internal standard method was used for quantitative analysis; the components of a-PAHs not included in the standard sample were quantified according to the response factors of PAHs or a-PAHs with the closest retention time in the homologues or the chromatogram (Qian et al., 2022). The *RF* calculation formula was as follows:

$$RF = \frac{K_{S-PAH}}{K_{IS}} \quad (1)$$

In Eq. 1, $K_{S\text{-}PAH}$ was the regression curve slope of a single PAH standard substance; K_{IS} was the regression curve slope of the added standard internal substance corresponding to a single PAH standard substance.

All samples were subject to a strict quality assurance and quality control system: 3 parallel samples were set for each sample, and the recovery standard sample was added; the actual recovery ranges were D_8-naphthalene (83.2% ± 6.3%), D_{10}-Acenaphthene (79.2% ± 8.4%), D_{10}-phenanthrene (95.1% ± 2.8%), D_{12}-chrysen (98.2% ± 3.4%), D_{12}-perylene (102.6% ± 6.5%); one blank was added for every 10 samples, and the concentration range of naphthalene was 0.03–0.95 ng/g in the blank sample; the final data were revised from the blank and corrected for recovery.

Results

Concentration characteristics of ∑PACs

35 kinds of PACs (14 kinds of p-PAHs and 21 kinds of a-PAHs) were detected in the samples, and the concentrations of 14 kinds of p-PAHs ranged from 224.66 ± 55.78 ng/g to

TABLE 2 Concentration of $\sum_{16}$ p-PAHs in samples of soil (ng/g).

p-PAH	S1[a]	S2	S3	S4	S5	Average
Nap	11.46 ± 1.17	5.26 ± 1.3	14.38 ± 1.42	4.95 ± 2.1	13.93 ± 3.97	9.99 ± 1.99
Acy	ND	ND	ND	ND	ND	ND
Ace	ND	ND	ND	ND	ND	ND
Flu	15.55 ± 2.13	11.25 ± 2.55	12.49 ± 3.83	10.74 ± 1.43	16.14 ± 2.48	13.23 ± 2.48
Phe	16.37 ± 2.42	8.72 ± 1.72	16.82 ± 3.11	9.6 ± 2.84	23.18 ± 3.46	14.93 ± 2.71
Ant	17.12 ± 1.77	10.39 ± 2.01	13.03 ± 2.27	10.36 ± 3.14	17.03 ± 2.98	13.59 ± 2.43
Fla	17.83 ± 2.62	12.51 ± 1.39	13.44 ± 2.71	11.46 ± 2.37	24.82 ± 5.19	16.01 ± 2.86
Pyr	23.47 ± 3.04	12.47 ± 2.48	17.27 ± 4.42	9.64 ± 1.64	16.73 ± 3.77	15.92 ± 3.07
BaA	12.33 ± 2.29	10.16 ± 1.57	11.7 ± 3.08	9.03 ± 1.09	16.99 ± 5.23	12.04 ± 2.65
Chr	11.06 ± 2.06	9.88 ± 1.84	12.89 ± 3.76	7.84 ± 1.69	18.6 ± 6.69	12.05 ± 3.21
BbF	19.39 ± 2.2	14.52 ± 2.31	20.42 ± 8.26	14.2 ± 1.29	27.92 ± 7.36	19.29 ± 4.28
BkF	6.47 ± 2.12	6.38 ± 3.06	11.41 ± 2.99	8.01 ± 1.98	10.31 ± 3.21	8.52 ± 2.67
BaP	14.15 ± 2.46	9.89 ± 2.06	15.2 ± 1.93	7.82 ± 2.13	15.3 ± 5.10	12.47 ± 2.73
DaA	13.2 ± 1.51	5.88 ± 1.35	13.18 ± 4.05	5.56 ± 2.43	ND	7.56 ± 1.87
InP	12.54 ± 1.06	7.13 ± 1.27	9.35 ± 2.95	5.28 ± 1.46	11.32 ± 3.26	9.12 ± 2.00
BgP	16.72 ± 1.62	12.25 ± 2.51	14.47 ± 3.5	6.97 ± 1.32	12.41 ± 3.09	12.56 ± 2.41
2–3 ring∑PAHs	60.49 ± 7.48	35.61 ± 7.58	56.72 ± 10.62	35.63 ± 9.50	70.28 ± 12.89	51.75 ± 9.62
4 ring∑PAHs	64.68 ± 10.01	45.02 ± 7.28	55.29 ± 13.97	37.96 ± 6.78	77.14 ± 20.88	56.02 ± 11.78
5–6 ring∑PAHs	82.47 ± 10.95	56.05 ± 12.56	84.03 ± 23.68	47.84 ± 10.61	77.25 ± 22.02	69.52 ± 15.96
∑PAHs	207.64 ± 28.45	136.67 ± 27.42	196.04 ± 48.27	121.43 ± 26.89	224.66 ± 55.78	177.29 ± 37.36

Note: ND was not detected (the same below).

[a]Indicates the average concentration of samples at the same location in the four-sampling season. [Abbreviations: Nap, Naphthalene; Acy, Acenaphthylene; Ace, Acenaphthene; Flu, Fluorene; Phe, Phenanthrene; Ant, Anthracene; Fla, Fluoranthene; Pyr, Pyrene; BaA, Benzo(a)anthracene; Chr, Chrysene; BbF, Benzo(b)fluoranthene; BkF, Benzo(k)fluoranthene; BaP, Benzo(a)pyrene; DaA, Dibenzo(a,h)anthracene; InP, Indeno(1,2,3-cd)pyrene; BgP, Benzo(g,hi)perylene].

121.43 ± 26.89 ng/g, with an average value of 177.29 ± 37.36 ng/g; 21 kinds of a-PAHs concentrations ranged from 530.72 ± 172.17 ng/g to 444.04 ± 94.19 ng/g, with an average value of 346.87 ± 104.91 ng/g (Tables 2, 3). The two p-PAHs (acenaphthylene and acenaphthene) were not detected in the karst soil, but their alkyl-substituted hydrocarbons had high concentrations. According to analysis from the polluted site, the forest soil sampling site (S5) had the maximum concentration of p-PAHs (224.66 ± 66.82 ng/g), and the soil sampling site of traditional corn crop cultivated soil (S4) had the minimum value of p-PAHs (121.43 ± 31.94 ng/g). The specific concentration tendency was S5 > S1 > S3 > S2 > S4. Forest soil sampling site (S5) had the maximum concentration of the a-PAH (530.72 ± 172.17 ng/g), and cultivated corn crop soil (S4) still was the minimum value (249.21 ± 94.69 ng/g). The specific concentration tendency was S5 > S1 > S3 > S4 > S2. According to analysis from the sampling season: the average concentration of total PAHs in the five sampling sites was winter (588.01 ng/g) > spring (573.26 ng/g) > autumn (499.41 ng/g) > summer (435.95 ng/g). The average concentration of p-PAHs in the five sampling sites was winter (203.09 ± 41.65 ng/g) > autumn (177.56 ± 36.21 ng/g) > spring (169.31 ± 40.25 ng/g) > summer (159.18 ± 60.17 ng/g). Except for the winter in which the concentration of the S1 was higher than that of the other four sampling sites, the concentration of the sampling site was exhibited with S5 > S1 > S3 > S2 > S4 in other seasons. However, there were differences in the seasonal distribution characteristics of a-PAHs. The seasonal distribution order of the five soil samples was spring (403.95 ± 41.65 ng/g) > winter (384.92 ± 113.38 ng/g) > autumn (321.85 ± 104.19 ng/g) > summer (276.77 ± 91.31 ng/g). Except for the spring sampling in which the content of a-PAHs in cultivated soil (S4) was lower than that in the abandoned soil (S2), the general trend of a-PAHs concentrations was S5 > S1 > S3 > S4 > S2 in the four seasons. A comparison of the concentration distribution of PAHs in different sites and in different sampling seasons with the soil properties of the sampling sites revealed that the spatial distribution of p-PAHs and a-PAHs were closely related to soil organic carbon content.

The ∑PACs in the mining area (S5) were significantly higher than in the other 4 sampling sites (Table 4); the p-PAHs concentration at all sampling sites was lower than the a-PAHs concentration. The a-PAHs accounted for 63%–70% of PACs, with an average value of 64%, which indicated that a-PAHs might be the main type of PAHs of the sampling sites surface soil in the karst area. In different seasons, the concentrations of PAHs in the soil were significantly different, with the total concentration of PAHs in the soil in winter and spring higher than that in autumn and summer.

TABLE 3 Concentration of $\sum_{21}$ a-PAHs in samples of soil (ng/g).

a-PAH	CAS	S1	S2	S3	S4	S5	Average
1-Methylnaphthalene	90-12-0	25.64 ± 2.79	17.81 ± 2.09	22 ± 3.57	20.78 ± 2.35	24.33 ± 7.96	22.11 ± 3.75
2-Methylnaphthalene	91-57-6	21.92 ± 2.03	21.38 ± 1.52	22.1 ± 4.01	16.81 ± 1.72	31.59 ± 4.92	22.76 ± 2.84
2 -Ethylnaphthalene	2949-26-0	7.83 ± 1.35	4.54 ± 4.43	5.74 ± 4.22	6.15 ± 4.23	11.58 ± 3.23	7.17 ± 3.49
2,7-Dimethylnaphthalene	582-16-1	24.22 ± 2.58	14.62 ± 1.92	13.74 ± 2.52	13.83 ± 2.17	25.33 ± 6.21	18.34 ± 3.08
2,3,5- Trimethylnaphthalene	2245-38-7	20.04 ± 4.33	10.8 ± 3.41	15.46 ± 4.46	13.56 ± 3.85	28.47 ± 10.99	17.66 ± 5.41
1-Methylfluorene	1730-37-6	25.93 ± 6.97	14.84 ± 3.15	16.17 ± 4.10	13.99 ± 3.56	27.74 ± 10.14	19.73 ± 5.59
9-Methylfluorene	2523-37-7	27.83 ± 7.95	11.07 ± 1.55	14.47 ± 3.36	13.87 ± 9.22	28.7 ± 4.99	19.19 ± 5.41
1,9-Dimethylfluorene	17057-98-6	22.96 ± 6.01	12.82 ± 4.47	16.75 ± 5.84	15.97 ± 5.05	34.82 ± 12.66	20.66 ± 6.81
1-Methylanthracene	610-48-0	29.97 ± 5.46	14.28 ± 4.07	14.15 ± 5.31	15.41 ± 4.60	53.5 ± 8.37	25.46 ± 5.56
2-Methylanthracene	613-12-7	27.52 ± 6.87	8.06 ± 1.01	10.44 ± 7.12	10.01 ± 6.53	21.07 ± 7.61	15.42 ± 5.83
9,10-Dimethylanthracene	781-43-1	23.93 ± 2.25	10.94 ± 2.82	14.3 ± 2.21	13.2 ± 3.18	28.85 ± 12.96	18.24 ± 4.68
2,9,10-Trimethylanthracene	63018-94-0	26.28 ± 5.05	10.4 ± 3.78	10.74 ± 4.92	7.89 ± 4.26	19.15 ± 9.66	14.89 ± 5.53
7-Methylbenz[a]anthracene	2541-69-7	20.78 ± 5.84	10.24 ± 4.36	13.36 ± 5.70	12.8 ± 4.92	26.97 ± 11.56	16.83 ± 6.47
12-Methylbenz[a]anthracene	2422-79-9	15.72 ± 1.74	12.44 ± 1.31	15.99 ± 12.56	14.52 ± 9.74	31.78 ± 13.22	18.09 ± 7.71
7,12-Dimethylbenz[a]anthracene	57-97-6	25.92 ± 3.57	9.57 ± 2.67	11.97 ± 3.52	11.94 ± 3.02	25.15 ± 8.61	16.91 ± 4.27
2-Methylphenanthrene	2531-84-2	22.12 ± 1.08	7.54 ± 3.66	10.79 ± 4.93	7.94 ± 7.87	25.97 ± 4.61	14.87 ± 4.43
9-Methylphenanthrene	883-20-5	14.16 ± 3.84	7.7 ± 2.86	9.25 ± 3.75	8.86 ± 3.24	18.65 ± 8.24	11.72 ± 4.39
4,5-Methylenephenanthrene	203-64-5	18.03 ± 8.99	3.79 ± 1.88	4.74 ± 3.8	5.19 ± 2.13	9.55 ± 4.99	8.26 ± 4.36
2,3,5-Trimethylphenanthrene	3674-73-5	12.7 ± 4.97	6.08 ± 3.71	7.79 ± 4.91	7.46 ± 4.19	15.72 ± 7.46	9.95 ± 5.05
1-Methylpyrene	3442-78-2	23.35 ± 3.90	16.3 ± 2.91	22.24 ± 3.81	12.04 ± 3.29	27.06 ± 5.88	20.2 ± 3.96
6-Methylbenzo[a]pyrene	2381-39-7	7.23 ± 6.64	5.73 ± 4.96	7.33 ± 6.45	7.02 ± 5.59	14.78 ± 7.95	8.42 ± 6.32
2 ring $\Sigma A_{1\text{-}3}$ Nap[a]		99.64 ± 13.07	69.14 ± 13.37	79.03 ± 18.76	71.11 ± 14.31	121.29 ± 33.29	88.04 ± 18.56
3 ring $\Sigma A_{1\text{-}3}$ Flu/Ant/Phe[b]		313.82 ± 70.59	139.75 ± 41.28	170.88 ± 71.97	159.04 ± 71.51	367.59 ± 125.05	230.22 ± 76.08
4–5 ring $\Sigma A_{1\text{-}2}$ Pyr/BaA/BaP[c]		30.58 ± 10.54	22.03 ± 7.87	29.57 ± 10.26	19.06 ± 8.88	41.84 ± 13.84	28.62 ± 10.28
Σa-PAHs		444.04 ± 94.19	230.92 ± 62.52	279.48 ± 100.99	249.21 ± 94.69	530.72 ± 172.17	346.87 ± 104.91

[a]Means alkylated homologues of the 1-3 substituted of 2 ring naphthalene.
[b]Means alkylated homologues of the 1-3 substituted of 3 ring fluorene, fluorene and phenanthrene.
[c]Means alkylated homologues of the 1-2 substituted of 4–5 ring pyrene, benz[a]anthracene and benzo[a]pyrene.

TABLE 4 Distribution and ration of different kinds of PAHs content in sampling sites.

Sample	ΣPACs (ng/g)	Σp-PAHs (ng/g)	Σa-PAHs (ng/g)	Ratio (a/p)	Ratio (p/Σ)	Ratio (a/Σ)
S1	651.68	207.64	444.04	2.14	0.32	0.68
S2	367.58	136.67	230.92	1.69	0.37	0.63
S3	475.51	196.04	279.48	1.43	0.41	0.59
S4	370.63	121.43	249.21	2.05	0.33	0.67
S5	755.38	224.66	530.72	2.36	0.30	0.70
Total	2620.78	886.43	1734.35	1.96	0.34	0.66

∑PACs pollution pattern

In all sampling sites, the a-PAHs were a significantly higher proportion than p-PAHs, and the proportion of a-PAHs accounted for 59%–70% of the total aromatic hydrocarbons. In terms of 16 kinds of p-PAHs, the concentration of 2–3-ring PAHs ranged from 35.61 ± 7.58 ng/g to 70.28 ± 12.89 ng/g, with an average value of 51.75 ± 9.62 ng/g, accounting for 29.19%; the concentration of 4-ring p-PAHs ranged from 37.96 ± 6.78 ng/g to 77.14 ± 20.88 ng/g, with an average value of 56.02 ± 11.78 ng/g, accounting for 31.60%; the concentration of 5–6-ring p-PAHs ranged from 56.05 ± 12.56 ng/g to 84.03 ± 23.68 ng/g, with an average value of 69.52 ± 15.96 ng/g, accounting for 39.21%. The 2-ring a-PAHs had the highest value of 121.29 ± 33.29 ng/g in the

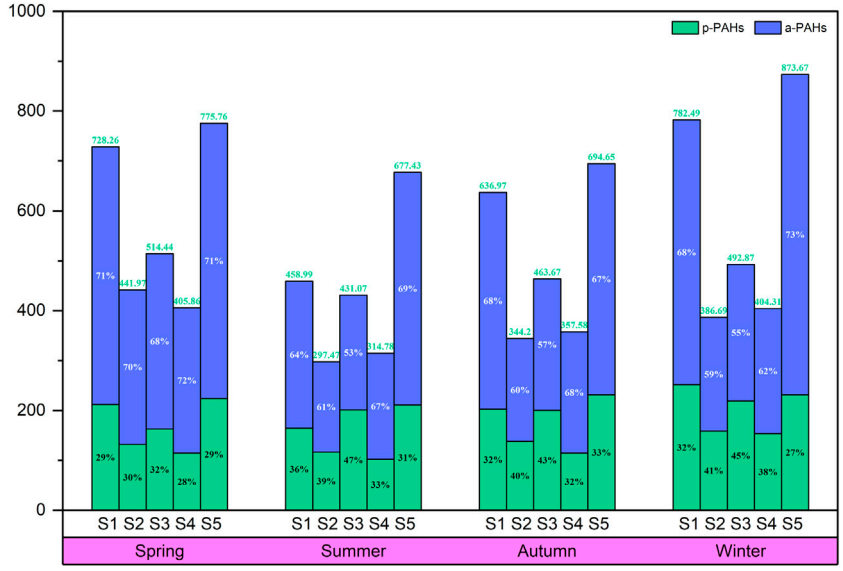

FIGURE 2
Distribution of p-PAHs and a-PAH in karst soils for different seasons.

S5 and the lowest value of 69.14 ± 13.37 ng/g in the S2, with an average value of 88.04 ± 18.56 ng/g, accounting for 25.38%. The 3-ring a-PAHs had the highest value of 367.59 ± 125.05 ng/g in the S5 and the lowest value of 139.75 ± 41.28 ng/g in the S2, with an average value of 230.22 ± 76.08 ng/g, accounting for 66.37%. The 4–5-ring a-PAHs had the highest value of 41.84 ± 13.84 ng/g in the S5 and the lowest value of 19.06 ± 8.88 ng/g in the S4, with an average value of 28.62 ± 10.28 ng/g, accounting for 8.25%.

Seen from the analysis of different sampling seasons (Figures 2, 3), the average concentrations of 2–3-ring p-PAHs were 47.27 ± 7.10 ng/g (spring), 46.97 ± 9.37 ng/g (summer), 54.38 ± 6.99 ng/g (autumn) and 58.36 ± 8.60 ng/g (winter); the average concentrations of 4-ring p-PAHs were 59.18 ± 13.04 ng/g (spring), 50.89 ± 22.75 ng/g (summer), 54.68 ± 11.22 ng/g (autumn) and 59.33 ± 11.90 ng/g (winter); the average concentrations of 5–6-ring p-PAHs were 62.86 ± 12.33 ng/g (spring), 61.32 ± 17.36 ng/g (summer), 68.51 ± 10.86 ng/g (autumn) and 85.40 ± 12.65 ng/g (winter). The average concentrations of 2-ring a-PAHs in spring, summer, autumn, and winter were 116.70 ± 20.66 ng/g, 57.47 ± 16.23 ng/g, 95.39 ± 19.93 ng/g, and 82.63 ± 17.42 ng/g, respectively; the average concentrations of 3-ring a-PAHs in spring, summer, autumn, and winter were 250.15 ± 79.98 ng/g, 193.58 ± 66.12 ng/g, 194.24 ± 74.46 ng/g, and 282.89 ± 83.74 ng/g, respectively. The average concentrations of 4~5-ring a-PAHs were 37.10 ± 10.12 ng/g in spring, 25.72 ± 8.96 ng/g in summer, 32.25 ± 9.80 ng/g in autumn, and 19.39 ± 12.22 ng/g in winter, respectively. As seen from the analysis of a-PAHs homologs of the same type, the concentration of alkylated-naphthalene and alkylated-anthracene homologs were significantly higher than that of other a-PAHs homologs, while alkylated-BaP homologs had the smallest concentration and proportion (Figure 4). The 4–5-ring p-PAHs was a relatively high proportion, and there was a small difference between p-PAHs with different ring numbers, with a maximum value of 50.44% in winter. The a-PAHs with different ring numbers varied significantly, and the 3-ring a-PAHs were significantly higher proportion than 2-ring and 4–5-ring, and the largest proportion was 70.03% in winter.

Polycyclic aromatic compounds risk assessment

The soil PAHs pollution standard (Maliszewska-Kordybach 1996) was combined with the substance toxicity equivalent factor (Table 5) to evaluate the toxic concentration of p-PAHs and a-PAHs in the coal mining area and then conduct a risk assessment of the sample site in the coal area (Figure 5). The results showed that when only 16 kinds of p-PAHs were considered, except that the average concentration of the S5 (0.22 μg/g) and the average concentration of the S1 (0.21 μg/g) were slight pollutions, the samples of other sites were all non-pollution (Figure 5B). The concentration of a-PAHs in different sites and seasons was significantly higher than that of p-PAHs, and the pollution level was also significantly increased. The S5 was moderately contaminated in winter, and the S2 was

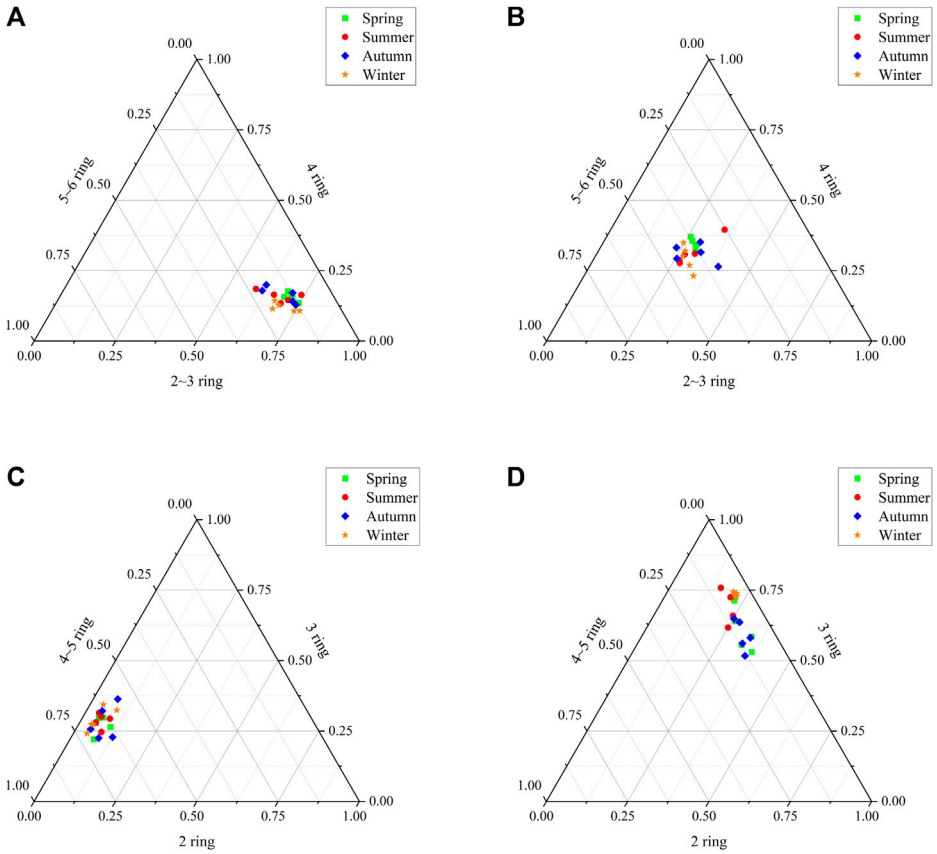

FIGURE 3
Triangle diagram of different kinds of PAHs for the seasonal distribution [Seasonal distribution of low and high ring of total PAHs **(A)**; Seasonal distribution of 2–3, 4 and 5–6 ring of p-PAHs **(B)**; Seasonal distribution of 2, 3 and 4–5 ring of p-PAHs **(C)**; Seasonal distribution of 2, 3 and 4–5 ring of a-PAHs **(D)**].

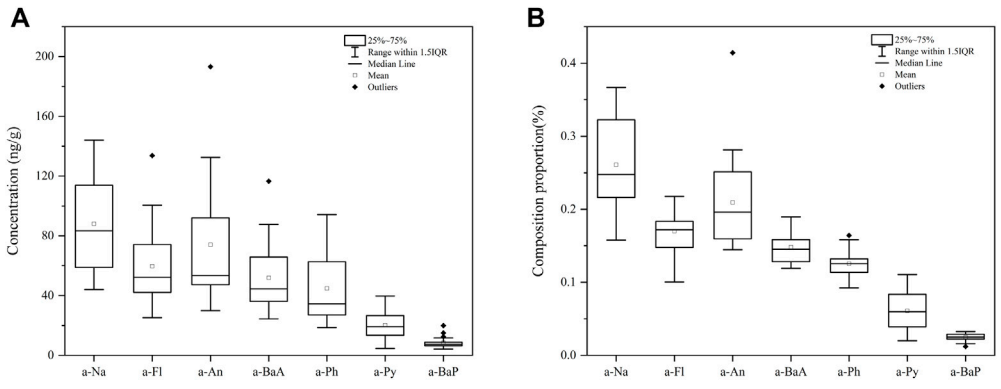

FIGURE 4
Box plot of a-PAHs homolog [concentration **(A)**; proportion **(B)**].

TABLE 5 Toxic equivalent factors (TEFs), and BaP equivalent concentration (BaP_{eq}).

PAHs	TEF	Sites (1–5) (ng/g)	TEQ_{BaP}	Percentage (%)
Nap	0.001	49.970	0.050	0.03
Acy	0.001	0.000	0.000	0.00
Ace	0.001	0.000	0.000	0.00
Flu	0.001	66.155	0.066	0.03
Phe	0.001	74.673	0.075	0.04
Ant	0.010	67.928	0.679	0.34
Fla	0.001	80.055	0.080	0.04
Pyr	0.001	79.575	0.080	0.04
BaA	0.100	60.190	6.019	3.02
Chr	0.010	60.268	0.603	0.30
BbF	0.100	96.443	9.644	4.84
BkF	0.100	42.583	4.258	2.14
BaP	1.000	62.348	62.348	31.27
DaA	1.000	37.815	37.815	18.96
InP	0.100	45.615	4.562	2.29
BgP	0.010	62.815	0.628	0.32
C_{1-3} Nap	0.001	440.203	0.440	0.22
C_{1-2} Flu	0.001	297.895	0.298	0.15
C_{1-3} Ant	0.010	343.781	3.438	1.72
C_{1-3} BaA	0.100	259.143	25.914	13.00
C_{1-3} Phe	0.001	223.978	0.224	0.11
C_1 Pyr	0.001	100.988	0.101	0.05
C_1 BaP	1.000	42.088	42.088	21.11
∑p-PAHs		886.430	126.906	63.64
∑a-PAHs		1708.073	72.503	36.36
∑PACs		2594.503	199.409	100.00

non-pollution in summer and autumn, and the rest of the sample sites were all weakly polluted (Figure 5C). As seen from the analysis of total PAH concentrations, PAHs of all soil samples were above the level of weak contamination. Except for the S1 in summer, S1 and S5 samples of other sites and seasons were moderately contaminated (Figure 5A).

The equivalent concentration factor of a-PAHs was calculated based on p-PAHs (Chen et al., 2016). The toxicity equivalent concentration results showed that (Table 5): the maximum concentration of p-PAHs was BbF (96.44 ng/g); the minima were Acy and Ace; the maximum concentration of a-PAHs was C_{1-3} Nap (440.20 ng/g); the minimum was C_1-BaP (42.09 ng/g). The evaluation results showed that BaP with a maximum toxic equivalent of 62.35 ng/g, C_1-BaP (42.09 ng/g), DaA (37.82 g/g) and C_{1-3} BaA (26.91 ng/g) were the most important 4 types of PAHs with high toxicity risk. The risk value of ∑p-PAHs accounted for 63.64%, and it was the most important toxic risky PAHs in the soil of the karst coal mining area. As seen from the analysis of monomers and homologs, BaP and C_1-BaP contributed 52.38% of the toxicity risk, which were the most important toxic risky substances. It was worth noting that both DaA and C_{1-3} BaA toxicity risk accounted for more than 10%, which were also the main types of PAHs that affect the regional ecological risk. In the cultivated soil S3 and S4, a certain content of BaP may cause the enrichment of plants, which were transmitted in the food chain and caused certain toxicity risks to the local residents.

Discussion

Coal mining and consumption were the main sources of PAHs in soil. The average concentration of p-PAHs in the soil of karst coal mining areas was177.29 ng/g. Shang et al. (2019) showed that the average concentration of p-PAHs in Chinese surface soil was 1217 ng/g, and the average content in Guizhou province was 117.8 ng/g. Compared with other chemical areas in China (Table 6), the pollution concentration of PAHs in the coal mining area of Guizhou province was at a low level. Compared with the PAHs pollution concentration in other regions of Guizhou province, the total concentration of PAHs in this study was at a moderate level, but was significantly lower than

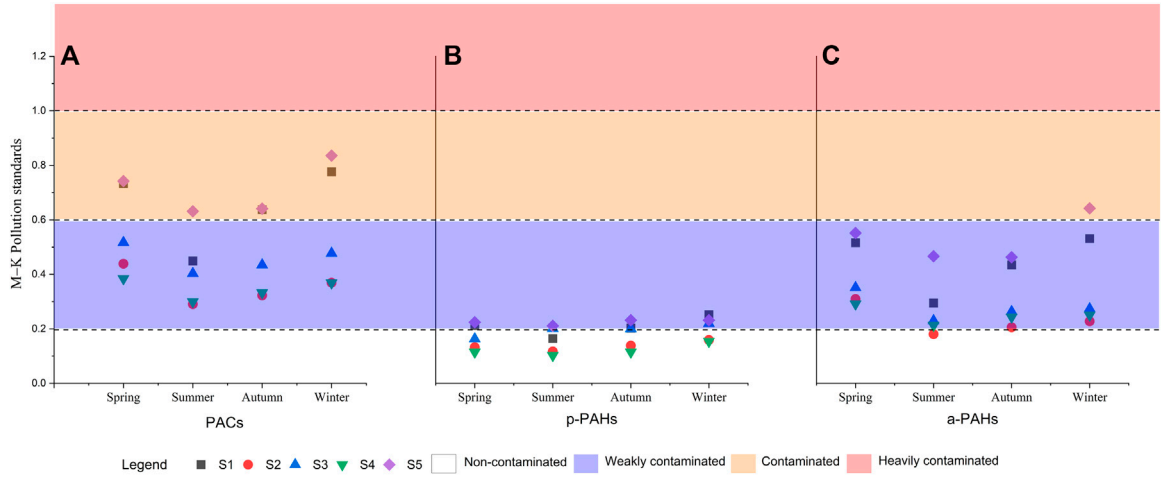

FIGURE 5
Sample soils contamination grade based on the Maliszewska-Kordybach criteria [Total PAHs **(A)**; p-PAHs **(B)**; a-PAHs **(C)**].

TABLE 6 Concentrations of PAHs in surface soils from different areas in China.

Study area	PAHs	Minimum	Maximum	Middle	Average	References	Samples time
Surface soil, China	16	ND	65500	381.9	1214	Shang et al. (2019)	1999–2018
Surface soil, China	16	9.90	5910	159	377	Zhao et al. (2015)	2015
Agricultural soil, China	16	ND	27580	ND	772	Sun et al. (2018)	2015
Agricultural top-soil,	16	277.79	3217.20	ND	1023	Liu et al. (2016)	2013
Urban soil, China	16	92	4733	ND	ND	Han et al. (2019)	2001–2017
Urban soil, China	16	30.1	23300	661	584	Ma et al. (2015)	2004–2013
Rural soil, China	16	3.7	6250	147	148	Ma et al. (2015)	2004–2013
Tangshan mining area, Hebei	16	115.30	1042.31	349.17	486.37	Jia et al. (2017).	ND
Yangtze River Delta Chemical Industry Park	19	16.3	4694	ND	688	Jia et al. (2021)	2019
Heshan coal district, Guangxi GGuangxi,China	16	79.56	4256.96	ND	1280.12	Huang et al. (2016)	2013
Coal mine district of Lu ling, Anhui	28	350	6210	ND	1690	Liu, (2014)	2010
Ningdong Chemical Industry District, Ningxia	16	ND	123120	ND	10190	Yang et al. (2020)	ND
Niangziguan karst catchment, Shanxi ,Niangziguan	16	47.13	705.3	194.4	259.96	Li et al. (2019)	ND
Suburb of Guiyang, Guizhou	16	61	511	339	281.8	Hu et al. (2006)	ND
Urban area of Guiyang, Guizhou	16	247	1560	692	663	Hu et al. (2006)	ND
Zunyi, Guizhou	16	0.8	251	ND	36.48	Zhang et al. (2009)	2008
Top-soil of Guiyang, Guizhou	16	10.02	1708.86	99.98	139.14	Zhang et al. (2021)	ND
Bijie, Guizhou	16	196	11592	780	1500	Chen et al. (2016)	2014–2015
Power plants in Bijie, Guizhou	16	200	12200	5350	4866	Zhang et al. (2021)	ND
Qiannan, Guizhou	16	3.7	259.6	ND	56.8	Lin et al. (2015)	2010
Coal mine district of Hezhang county, Guizhou	16	136.67	224.66	196.04	177.29	This study	2021
Coal mine district of Hezhang county, Guizhou	21	249.21	530.72	279.48	346.87	This study	2021

Note: ND means no data available in reference.

the regional pollution concentration of PAHs in Guizhou province coal power plants (4866 ng/g on average). The concentration in the karst area soil was at a moderate level, which may be because coal was the main energy consumption patterns in the southwest karst area. Most of the coal consumption was at a low grade in northwest Guizhou

province, and the emission of PAHs from coal was significantly higher than that from high grade anthracite. Geng et al. (2014) believed that the overall emission coefficient of Guizhou province anthracite was 129.47 mg/kg, which was significantly higher than that of anthracite in other parts of China. Therefore, the accumulation of PAHs in the soil of Guizhou province coal mining areas may be derived from coal combustion and the emission of lithogenic PAHs during coal mining. In addition, the southwest karst area with high altitude, humid air, relatively closed terrain, and short illumination time hindered the diffusion of PAHs in the atmosphere, thereby increasing the concentration of PAHs in the soil matrix. The author's previous research showed that the karst soil with calcium-enriched characteristics might reduce the adsorption of PAHs. The main reason was that, in a complex karst environment, the soil inorganic ions repeatedly dissolve and precipitate, and occupied the high-energy sites for soil adsorption of PAHs, and filled soil pores. As a result, the PAHs entering the soil in karst areas may further migrate into groundwater or other environmental substrates, thus increasing the risk of environmental toxicity (An et al., 2021; An et al., 2022).

Soil organic matter, organic carbon, pH, particle composition, and soil microstructure are all factors to affect the occurrence state of PAHs. Many studies have shown that SOM was the key component for the sorption of organic pollutants by providing highly active combination sites, which was the key component for the adsorption and desorption of PAHs. It was believed that the PAHs desorption fractions and fast desorption rate constants of soils decreased with SOM increase (Li et al., 2007). Luo et al. (2012) illustrated that the fast-migrating components of PAHs in soil were directly related to organic carbon and the distribution of mesopores and micropores in soil. Ukalska-Jaruga et al. (2019) pointed out that different types of soil organic matter significantly affected the availability and durability of PAHs, and soil organic matter components of FA and HA were unstable components of organic matter, which had a significant positive correlation with the potential utilization of PAHs. HM was a stable organic matter with high hydrophobicity and poor degradability, which was the main factor affecting the durability of PAHs in soil. The sample site of S5 was rich in woodland and less affected by human activities.

The soil organic carbon content of S5 was significantly higher than other 4 sample sites. The total concentration of PAHs, the concentration of p-PAHs and a-PAHs of S5 was significantly higher than other 4 sample sites, which showed that PAHs concentration in the soil of the karst rocky desertification area was mainly controlled by soil organic carbon. High-ring (4-ring and 5–6-ring) p-PAHs and a-PAHs were more enriched for the sample sites of S5 and S3 with higher organic carbon content, indicating that high ring PAHs were more likely to bond with colloids such as soil organic matter and had greater migration difficulty in soil, which were consistent with previous findings

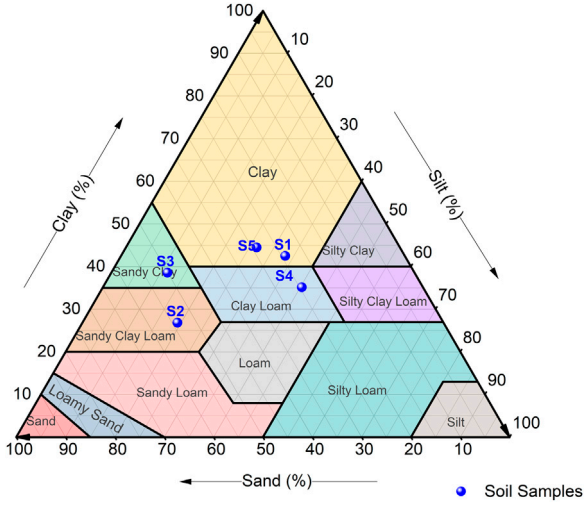

FIGURE 6
Soil texture classes of sample sites.

(Łyszczarz et al., 2021). At the same time, soil type was also an important factor to affect the environmental migration of PAHs. In this study, the soils of the S1 and S5 belonged to the clay soil type (Figure 6), which had a large sorption capacity for PAHs. The concentration of total PAHs in the study area had a good positively correlated with the soil clay content (Figure 7) (R^2 = 0.88). This was consistent with the findings of Luo et al. (2008) found that PAHs were mainly enriched in soil clay components. Pearson correlation analysis indicated that the total concentration of PAHs in soil was not only correlated with soil organic carbon and clay, but also had a significant positive correlation with the total calcium content of soil (Figure 7). Some studies pointed out that the higher the content of water-soluble calcium ions was in the soil, the greater the desorption components of PAHs were (An et al., 2022). The complex environmental conditions of karst may change the existing form of calcium ions in the soil, thus affecting the occurrence state of PAHs. Soil calcium can be divided into five forms: water-soluble calcium, exchangeable calcium, acid-soluble calcium, organically bound calcium and residual calcium. Soil calcium may also be an important driver of karst rocky desertification (Tang et al., 2019). The author believed that high calcium ions in karst soil might affect the occurrence and environmental migration of PAHs from two aspects: on the one hand, calcium ions affected the adsorption and desorption environmental conditions of PAHs, such as the cation exchange capacity; on the other hand, calcium ions was chemically changed in the complex karst environment, by forming inorganic precipitation or mineral polymer to affect the specific surface area of soil and its organic matter, reduce the high energy site of adsorption of PAHs, and the adsorption pores

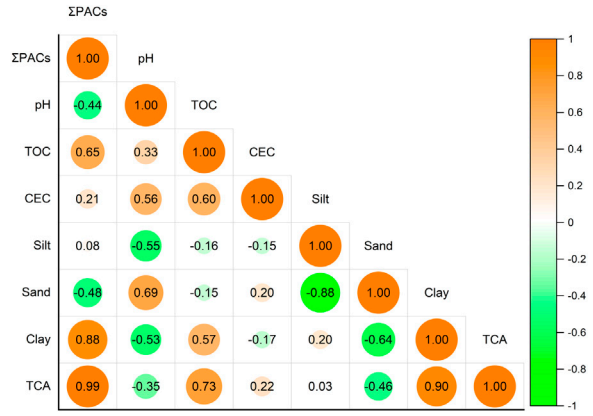

FIGURE 7
Correlation analysis of ΣPAHs concentration and soil properties.

(An et al., 2021). The role of various forms of calcium in the environmental transport of PAHs has not been systematically reported. Therefore, the effects of different calcium forms on PAHs carry great significance for karst soil management and remediation, and more in-depth studies are needed.

The natural environmental conditions in the karst rocky desertification area were complex, and the alternation of dry and wet, freeze-thaw cycles, rainfall leaching, and temperature fluctuations may change the occurrence state of PAHs in the regional soil and affect their migration. Seasonal alternation, temperature, rainfall, and large fluctuations in coal combustion can significantly affect the pollution concentration of PAHs in karst soils. Studies found that soil samples of PAHs concentration were higher in winter and spring than in summer and autumn, mainly due to the excessive coal combustion and the higher concentration of PAHs in the air in winter. In the karst mountain area, the temperature was relatively low in spring, and the amount of coal combustion was also high. In addition, there was continuous light rain before sampling in spring, making a large number of solid particles adsorb PAHs in the air and settle on the soil surface. Meijer et al. (2003) believed that the main factors affecting the distribution of PAHs between soil and atmosphere were soil characteristics, PAHs type and concentration, and air temperature. The concentration of PAHs in the soil was lower in summer, mainly because the amount of coal combustion was reduced and the temperature was high enough in summer, which made PAHs with higher volatility tend to re-volatilize in the atmosphere. At the same time, after the leaching of heavy rain, the vertical migration of PAHs concentration in soil was strengthened, which affected the PAHs concentration in the surface soil. It was worth noting that a-PAHs have greater concentration reduction than p-PAHs during rainfall (the average soil concentration of p-PAHs reduced by 5.98% in summer than spring, and the average concentration of a-PAHs reduced by 31.48% in summer than spring). In particular, the low-ring a-PAHs had the most obvious reduction, which showed that the a-PAHs were greater environmental migration characteristics, so the environmental risk impact was more obvious, which may be closely related to the properties of the a-PAHs. Studies had shown that the physicochemical properties of a-PAHs (such as solubility, partition coefficient, etc.) were significantly different from those of p-PAHs (Kang et al., 2016). The solubility of 9-methylanthracene was 0.39 mg/L, which was significantly higher than the 0.044 mg/L of anthracene, (Kwon and Kwon, 2012), which related to the position and symmetrical structure of the alkylated substituent (Pinal 2004). Rainfall can significantly alter soil water content, affecting SOM's ability to adsorb PAHs. Schneckenburger and Thiele. (2020) pointed out that SOM matrix rigidity varied with prehydration status; the water content of SOM could change the soil matrix rigidity, which affected the adsorption and desorption of PAHs, altering the environmental migration of PAHs and their homologs. The complex karst environmental conditions such as the dry-wet cycle and freeze-thaw cycle also affect the migration behavior of PAHs in soil. Dry-wet cycles and freeze-thaw effects can alter the soil structure and affect the form of mineral ions in the soil, thereby changing the occurrence state of PAHs. Studies have shown that multiple freeze-thaw cycles of karst soils would reduce the soil's ability to desorb PAHs, making more PAHs turn into isolated states (An et al., 2021).

Risk assessments of PAHs in soil tend to focus on the 16 kinds of p-PAHs. However, a-PAHs were more environmentally toxic (Zhang et al., 2020; Huang et al., 2021), which may be related to the structure (Bay region) of a-PAHs (Baird et al., 2007). According to the air quality standards published in Canada, the BaP equivalent toxicity of dimethyl substituted BaA was 100 times that of parent BaA (Atmospheric quality standards and criteria, 2021). Without considering the concentration of a-PAHs, the S1 and S5 belonged to slightly polluted soil, while the concentration of a-PAHs in the five sampling sites was above the threshold of 200 ng/g of slight soil pollution (Maliszewska-Kordybach 1996). In general, the coal mining area soils and forest soils in the karst mining areas of southwest China were moderately polluted, while the cultivated soils were slightly polluted. Although the total concentration of PAHs was not equal to the bioavailability concentration of PAHs, the environmental risks of PAHs still should be paid more concern from local governments and residents. Therefore, to assess the risk of PAHs in soil, more consideration should be given to PAH substitutions such as the alkylated and nitro functional group to truly and accurately calculate the environmental risk of PAHs.

Conclusion

The concentration of p-PAHs and a-PAHs in surface soils of karst coal mining areas in Guizhou province, China displayed significantly different spatial and temporal distribution characteristics. The a-PAHs in the soil of the coal mining area had significantly higher pollution concentration than p-PAHs. The average concentration of p-PAHs and a-PAHs were 177.29 ± 37.36 ng/g and 346.87 ± 104.91 ng/g, respectively. The pollutant concentrations of PAHs exhibited a seasonal tendency with winter > spring > autumn > summer. The two types of PAHs in the study area were both affected by environmental events such as seasonal rainfall, and the a-PAHs were more greatly affected by rainfall than the p-PAHs, which closely related to the soil properties of the sampling site and the properties of a-PAHs. The soils of coal mining area and forest soils were moderately polluted, while cultivated soil and abandoned soil were slightly polluted. The toxicity results showed that p-BaP, C_1-BaP, DaA and $C_{1\text{-}3}$ BaA were the most important four types of toxic PAHs. Pearson correlation analysis illustrated that soil calcium content in the karst area was also an important factor affecting the distribution of regional PAHs. The environmental migration and fate of PAHs under different forms of calcium in karst soils require to be more deeply and systematically study in future. The research is helpful for guiding significance for the control and restoration of soil PAH in the karst area of southwest China with fragile ecology and complex environment.

Data availability statement

The original contributions presented in the study are included in the article/Supplementary Materials, further inquiries can be directed to the corresponding author.

Author contributions

XA: Conceptualization, Methodology, Validation, Resources, Data Curation, and Writing-Original draft preparation. WL: Supervision, Investigation, Writing-reviewing and Editing. JL: Investigation, Data Curation, and Software. XD: Visualization, Software, and Formal analysis. MA: Writing-reviewing, Editing, and Data curation.

Funding

This work was supported the National Natural Science Foundation of China (No. 41761091); The First-class Discipline Group of Geography of Guizhou Province (No. [2019]125); Guizhou Education Department Youth Science and Technology Talents Growth Project, China (KY[2022] 001); Fundamental Scientific Research Funds of Guiyang University, China (GYU-KY-[2022]); The Joint Foundation of Guizhou Province (LH[2017]7348); The Doctor Foundation of Guizhou Normal University (GZNUD [2017]10).

Acknowledgments

We thank the editor and three anonymous reviewers for their valuable comments on the manuscript. The authors thank the support of Open Project Fund of school of Mountain Research of Guizhou Education University.

Conflict of interest

The authors declare that the research was conducted in the absence of any commercial or financial relationships that could be construed as a potential conflict of interest.

Publisher's note

References

An, X. J., Li, W., Di, X. Y., and Xiao, B. H. (2021). Effects of supergene geochemical processes on desorption and bioavailability of polycyclic aromatic hydrocarbons in soil of karst area. *Environ. Pollut. Bioavailab.* 33 (1), 402–414. doi:10.1080/26395940.2021.1990799

An, X. J., Li, W., Lan, J. C., and Di, X. Y. (2022). Study on the desorption behavior and bioavailability of polycyclic aromatic hydrocarbons in different rocky desertification soils. *Pol. J. Environ. Stud.* 31 (5), 1–15. doi:10.15244/pjoes/149999

Andersson, J. T., and Achten, C. (2015). Time to say goodbye to the 16 EPA PAHs? Toward an up-to-date use of PACs for environmental purposes. *Polycycl. Aromat. Compd.* 35 (2-4), 330–354. doi:10.1080/10406638.2014.991042

Atmospheric quality standards and criteria (2021). *Gouvernement du Québec*. Quebec: Canada.

Baird, S. J., Bailey, E. A., and Vorhees, D. J. (2007). Evaluating human risk from exposure to alkylated PAHs in an aquatic system. *Hum. Ecol. Risk Assess. An Int. J.* 13 (2), 322–338. doi:10.1080/10807030701226277

Chen, F., Wang, C. C., Zhang, L. J., Wei, X. H., and Wang, Q. (2016). Characteristics, sources apportionment and risk assessment of polycyclic aromatic hydrocarbons in agricultural soils from zinc smelting area, Guizhou Province. *Acta Sci. Circumstantiae* 37 (04), 1515–1523. (In Chinese). doi:10.13671/j.hjkxxb.2016.0325

Geng, C. M., Chen, J. H., Yang, X. H., Ren, L. H., Yin, B. H., Liu, X. Y., et al. (2014). Emission factors of polycyclic aromatic hydrocarbons from domestic coal combustion in China. *J. Environ. Sci.* 26 (1), 160–166. doi:10.1016/S1001-0742(13)60393-9

Golzadeh, N., Barst, B. D., Baker, J. M., Auger, J. C., and McKinney, M. A. (2021). Alkylated polycyclic aromatic hydrocarbons are the largest contributor to polycyclic aromatic compound concentrations in traditional foods of the Bigstone Cree Nation in Alberta, Canada. *Environ. Pollut.* 275, 116625. doi:10.1016/j.envpol.2021.116625

Han, J., Liang, Y. S., Zhao, B., Wang, Y., Xing, F. T., and Qin, L. B. (2019). Polycyclic aromatic hydrocarbon (PAHs) geographical distribution in China and their source, risk assessment analysis. *Environ. Pollut.* 251, 312–327. doi:10.1016/j.envpol.2019.05.022

Hellou, J., Mackay, D., and Banoub, J. (1999). Levels, persistence and bioavailability of organic contaminants present in marine harbor sediments impacted by raw sewage. *Chemosphere* 38 (2), 457–473. doi:10.1016/S0045-6535(98)00184-2

Hu, J., Zhang, G., and Lui, C. Q. (2006). Pilot study of polycyclic aromatic hydrocarbons in surface soils of Guiyang city, People's Republic of China. *Bull. Environ. Contam. Toxicol.* 76 (1), 80–89. doi:10.1007/s00128-005-0892-8

Huang, H. F., Xing, X. L., Zhang, Z. Z., Qi, S. H., Yang, D., Yuen, D. A., et al. (2016). Polycyclic aromatic hydrocarbons (PAHs) in multimedia environment of heshan coal district, guangxi: Distribution, source diagnosis and health risk assessment. *Environ. Geochem. Health* 38 (5), 1169–1181. doi:10.1007/s10653-015-9781-1

Huang, Q., Zhu, Y. X., Wu, F., and Zhang, Y. (2021). Parent and alkylated polycyclic aromatic hydrocarbons in surface sediments of mangrove wetlands across Taiwan Strait, China: Characteristics, sources and ecological risk assessment. *Chemosphere* 265, 129168. doi:10.1016/j.chemosphere.2020.129168

Jia, H. B., Zhang, L. X., Li, Y., Zhang, X. N., Wang, X. M., Feng, S. D., et al. (2017). Concentration characteristics and sources apportionment of PAHs from the coal mining area soil. *J. Hebei Agric. Univ.* 40 (02), 24–31. (In Chinese). doi:10.13320/j.cnki.jauh.2017.0029

Jia, T. Q., Guo, W., Xing, Y., Lei, R. R., Wu, X. L., Sun, S. R., et al. (2021). Spatial distributions and sources of PAHs in soil in chemical industry parks in the Yangtze River Delta, China. *Environ. Pollut.* 283, 117121. doi:10.1016/j.envpol.2021.117121

Kang, H. J., Lee, S. Y., and Kwon, J. H. (2016). Physico-chemical properties and toxicity of alkylated polycyclic aromatic hydrocarbons. *J. Hazard. Mat.* 312, 200–207. doi:10.1016/j.jhazmat.2016.03.051

Kang, H. J., Lee, S. Y., and Kwon, J. H. (2016). Physico-chemical properties and toxicity of alkylated polycyclic aromatic hydrocarbons. *J. Hazard. Mat.* 312, 200–207. doi:10.1016/j.jhazmat.2016.03.051

Kwon, H. C., and Kwon, J. H. (2012). Measuring aqueous solubility in the presence of small cosolvent volume fractions by passive dosing. *Environ. Sci. Technol.* 46 (22), 12550–12556. doi:10.1021/es3035363

Lan, J. C., Sun, Y. C., Xiao, S. Z., and Yuan, D. X. (2016). Polycyclic aromatic hydrocarbon contamination in a highly vulnerable underground river system in Chongqing, Southwest China. *J. Geochem. Explor.* 168, 65–71. doi:10.1016/j.gexplo.2016.05.013

Lan, J. C., Sun, Y. C., and Yuan, D. X. (2018). Transport of polycyclic aromatic hydrocarbons in a highly vulnerable karst underground river system of southwest China. *Environ. Sci. Pollut. Res.* 25 (34), 34519–34530. doi:10.1007/s11356-018-3005-z

Larson, E. B., and Mylroie, J. E. (2018). Diffuse versus conduit flow in coastal karst aquifers: The consequences of island area and perimeter relationships. *Geosciences* 8 (7), 268. doi:10.3390/geosciences8070268

Li, C. C., Zhang, X., Gao, X. B., Qi, S. H., and Wang, Y. X. (2019). The potential environmental impact of PAHs on soil and water resources in air deposited coal refuse sites in Niangziguan Karst Catchment, Northern China. *Int. J. Environ. Res. Public Health* 16 (8), 1368. doi:10.3390/ijerph16081368

Li, J. G., Sun, H. W., and Zhang, Y. (2007). Desorption of pyrene from freshly-amended and aged soils and its relationship to bioaccumulation in earthworms. *Soil Sediment Contam. An Int. J.* 16 (1), 79–87. doi:10.1080/15320380601079665

Liang, M., Liang, Y. C., Liang, H. D., Rao, Z., and Cheng, H. F. (2018). Polycyclic aromatic hydrocarbons in soil of the backfilled region in the Wuda coal fire area, Inner Mongolia, China. *Ecotoxicol. Environ. Saf.* 165, 434–439. doi:10.1016/j.ecoenv.2018.08.065

Lin, Y., Fang, Z. Q., Wang, Z. K., and Luo, Y. C. (2015). Pollution characteristics of polycyclic aromatic hydrocarbon in topsoil of Guizhou Qiannan District. *Guizhou Agric. Sci.* 43 (1), 159–161. (In Chinese).

Lin, Y. X., Deng, W., Li, S. Y., Li, J. F., Wang, G. G., Zhang, D. H., et al. (2017). Congener profiles, distribution, sources and ecological risk of parent and alkyl-PAHs in surface sediments of Southern Yellow Sea, China. *Sci. Total Environ.* 580, 1309–1317. doi:10.1016/j.scitotenv.2016.12.094

Liu, J. J. (2014). *Geochemical cycling of hydrocarbon compounds in soil of typical coal mine district*. Hefei: University of Science and Technology of China.

Liu, J. L., Zhang, S. Y., Jia, J. L., Lou, M. J., Li, X., Zhao, S. W., et al. (2022). Distribution and source apportionment of polycyclic aromatic hydrocarbons in soils at different distances and depths around three power plants in bijie, Guizhou province. *Polycycl. Aromat. Compd.*, 1–12. doi:10.1080/10406638.2022.2039232

Liu, M. X., Yang, Y. Y., Yun, X. Y., Zhang, M. M., and Wang, J. (2016). Occurrence, sources, and cancer risk of polycyclic aromatic hydrocarbons and polychlorinated biphenyls in agricultural soils from the Three Gorges Dam region, China. *J. Soil Water Conserv.* 71 (4), 327–334. doi:10.2489/jswc.71.4.327

Luo, L., Lin, S., Huang, H. L., and Zhang, S. Z. (2012). Relationships between aging of PAHs and soil properties. *Environ. Pollut.* 170, 177–182. doi:10.1016/j.envpol.2012.07.003

Luo, L., Zhang, S. Z., and Ma, Y. B. (2008). Evaluation of impacts of soil fractions on phenanthrene sorption. *Chemosphere* 72 (6), 891–896. doi:10.1016/j.chemosphere.2008.03.051

Łyszczarz, S., Lasota, J., Szuszkiewicz, M. M., and Błońska, E. (2021). Soil texture as a key driver of polycyclic aromatic hydrocarbons (PAHs) distribution in forest topsoils. *Sci. Rep.* 11 (1), 14708–14711. doi:10.1038/s41598-021-94299-x

Ma, W. L., Liu, L. Y., Tian, C. G., Qi, H., Jia, H. L., Song, W. W., et al. (2015). Polycyclic aromatic hydrocarbons in Chinese surface soil: Occurrence and distribution. *Environ. Sci. Pollut. Res.* 22 (6), 4190–4200. doi:10.1007/s11356-014-3648-3

Maliszewska-Kordybach, B. (1996). Polycyclic aromatic hydrocarbons in agricultural soils in Poland: Preliminary proposals for criteria to evaluate the level of soil contamination. *Appl. Geochem.* 11 (1-2), 121–127. doi:10.1016/0883-2927(95)00076-3

Meijer, S. N., Shoeib, M., Jantunen, L. M. M., Jones, K. C., and Harner, T. (2003). Air– soil exchange of organochlorine pesticides in agricultural soils. 1. Field measurements using a novel *in situ* sampling device. *Environ. Sci. Technol.* 37 (7), 1292–1299. doi:10.1021/es020540r

Pinal, R. (2004). Effect of molecular symmetry on melting temperature and solubility. *Org. Biomol. Chem.* 2 (18), 2692–2699. doi:10.1039/B407105K

Qian, Y. H., Wang, T., Hong, X. P., Luo, Z. G., and Liang, H. D. (2022). Quantitative method of alkyl polycyclic aromatic hydrocarbons in surface soils of coal mines. *J. Chin. Mass Spectrom. Soc.* 43 (02), 168–177. (In Chinese). doi:10.7538/zpxb.2021.0065

Qian, Z., Mao, Y., Xiong, S., Peng, B., Liu, W., Liu, H. F., et al. (2020). Historical residues of organochlorine pesticides (OCPs) and polycyclic aromatic hydrocarbons (PAHs) in a flood sediment profile from the Longwang Cave in Yichang, China. *Ecotoxicol. Environ. Saf.* 196, 110542. doi:10.1016/j.ecoenv.2020.110542

Schneckenburger, T., and Thiele-Bruhn, S. (2020). Sorption of PAHs and PAH derivatives in peat soil is affected by prehydration status: The role of SOM and sorbate properties. *J. Soils Sediments* 20 (10), 3644–3655. doi:10.1007/s11368-020-02695-z

Shang, Q. B., Duan, Y. H., Xu, L. S., Duan, H. R., He, J. L., Cheng, R., et al. (2019). Spatial distribution and genesis of polycyclic aromatic hydrocarbons (PAHs) in the

surface soil in China. *J. Ecol. Rural Environ.* 35 (09), 917–924. doi:10.19741/j.issn.1673-4831.2018.0866

Sun, J. T., Pan, L. L., Tsang, D. C. W., Zhan, Y., Zhu, L. Z., and Li, X. D. (2018). Organic contamination and remediation in the agricultural soils of China: A critical review. *Sci. Total Environ.* 615, 724–740. doi:10.1016/j.scitotenv.2017.09.271

Tang, J., Tang, X. X., Qin, Y. M., He, Q. S., Yi, Y., and Ji, Z. L. (2019). Karst rocky desertification progress: Soil calcium as a possible driving force. *Sci. Total Environ.* 649, 1250–1259. doi:10.1016/j.scitotenv.2018.08.242

Ukalska-Jaruga, A., Smreczak, B., and Klimkowicz-Pawlas, A. (2019). Soil organic matter composition as a factor affecting the accumulation of polycyclic aromatic hydrocarbons. *J. Soils Sediments* 19 (4), 1890–1900. doi:10.1007/s11368-018-2214-x

Wei, C., Bandowe, B. A. M., Han, Y. M., Cao, J. J., Zhan, C. L., and Wilcke, W. (2015). Polycyclic aromatic hydrocarbons (PAHs) and their derivatives (alkyl-PAHs, oxygenated-PAHs, nitrated-PAHs and azaarenes) in urban road dusts from Xi'an, Central China. *Chemosphere* 134, 512–520. doi:10.1016/j.chemosphere.2014.11.052

Xu, S. S., Liu, W. X., and Tao, S. (2006). Emission of polycyclic aromatic hydrocarbons in China. *Environ. Sci. Technol.* 40 (3), 702–708. doi:10.1021/es0517062

Yan, Y. J., Dai, Q. H., Jin, L., and Wang, X. D. (2019). Geometric morphology and soil properties of shallow karst fissures in an area of karst rocky desertification in SW China. *Catena* 174, 48–58. doi:10.1016/j.catena.2018.10.042

Yang, F., Luo, H. X., Zhong, Y. X., Wang, Y. Q., and Bai, Y. R. (2020). Spatial distribution characteristics, source apportionment, and risk assessment of topsoil PAHs in the core area of the ningdong energy and chemical industry base. *Environ. Sci.* 42 (05), 2490–2501. (In Chinese). doi:10.13227/j.hjkx.202009096

Ye, X. C., Yang, P. H., and Zhang, Q. (2015). Hydrogeochemical processes and vulnerability of a typical karst underground river system, southwest China. *Geochem. J.* 49 (3), 259–269. doi:10.2343/geochemj.2.0354

Zhang, G. L., Lan, T. T., Yang, G. Q., Li, J. M., and Zhang, K. K. (2021). Contamination, spatial distribution, and source contribution of persistent organic pollutants in the soil of Guiyang city, China: A case study. *Environ. Geochem. Health*, 1–14. doi:10.1007/s10653-021-01089-5

Zhang, M. S., Teng, M. D., Li, Q. H., Lin, Y., and Ye, F. (2009). Distribution characteristics of polycyclic aromatic hydrocarbons in top soils in zunyi, Guizhou province. *J. Jiangxi Normal Univ. Nat. Sci. Ed.* 33 (6), 716–720. DO1:(In Chinese). doi:10.16357/lj.cnki.issn1000-5862.2009.06.019

Zhang, Y., Shen, Z. X., Sun, J., Zhang, L. M., Zhang, B., Zhang, T., et al. (2020). Parent, alkylated, oxygenated and nitro polycyclic aromatic hydrocarbons from raw coal chunks and clean coal combustion: Emission factors, source profiles, and health risks. *Sci. Total Environ.* 721, 137696. doi:10.1016/j.scitotenv.2020.137696

Zhang, Y., Shen, Z. X., Sun, J., Zhang, L. M., Zhang, B., Zou, H. J., et al. (2021). Parent, alkylated, oxygenated and nitrated polycyclic aromatic hydrocarbons in PM2. 5 emitted from residential biomass burning and coal combustion: A novel database of 14 heating scenarios. *Environ. Pollut.* 268, 115881. doi:10.1016/j.envpol.2020.115881

Zhang, Y. X., Tao, S., Cao, J., and Coveney, R. M. (2007). Emission of polycyclic aromatic hydrocarbons in China by county. *Environ. Sci. Technol.* 41 (3), 683–687. doi:10.1021/es061545h

Zhao, X., Qiu, H. R., Zhao, Y. L., Shen, J. M., Chen, Z. L., and Chen, J. X. (2015). Distribution of polycyclic aromatic hydrocarbons in surface water from the upper reach of the Yellow River, Northwestern China. *Environ. Sci. Pollut. Res.* 22 (9), 6950–6956. doi:10.1007/s11356-014-3846-z

Zhu, Y. X., Liang, B., Xia, W. W., Gao, M., Zheng, H. J., Chen, J., et al. (2022). Assessing potential risks of aquatic polycyclic aromatic compounds via multiple approaches: A case study in jialing and yangtze rivers in downtown chongqing, China. *Environ. Pollut.* 294, 118620. doi:10.1016/j.envpol.2021.118620

frontiers | Frontiers in Environmental Science

TYPE Original Research
PUBLISHED 09 September 2022
DOI 10.3389/fenvs.2022.974237

OPEN ACCESS

EDITED BY
Jun Zhou,
University of Massachusetts Lowell,
United States

REVIEWED BY
Maurizio Barbieri,
Sapienza University of Rome, Italy
Ting Wang,
University of Massachusetts Lowell,
United States

*CORRESPONDENCE
Mark Baskaran,
Baskaran@wayne.edu

SPECIALTY SECTION
This article was submitted to Toxicology, Pollution and the Environment,
a section of the journal
Frontiers in Environmental Science

RECEIVED 21 June 2022
ACCEPTED 29 July 2022
PUBLISHED 09 September 2022

CITATION
Denny M, Baskaran M, Burdick S, Tummala C and Dittrich T (2022), Investigation of pollutant metals in road dust in a post-industrial city: Case study from Detroit, Michigan.
Front. Environ. Sci. 10:974237.
doi: 10.3389/fenvs.2022.974237

Investigation of pollutant metals in road dust in a post-industrial city: Case study from Detroit, Michigan

Max Denny[1], Mark Baskaran[1]*, Scott Burdick[1], Chandra Tummala[2] and Timothy Dittrich[2]

[1]Department of Environmental Science and Geology, Wayne State University, Detroit, MI, United States, [2]Department of Civil and Environmental Engineering, Wayne State University, Detroit, MI, United States

Inhalation and/or ingestion of toxic heavy metals enriched in road dust have toxic effects on humans. From inhalation and ingestion of dust, release of readily bioavailable elements sorbed on to dust, could lead to health issues such as lung or skin cancer, kidney dysfunction, hypertension, dermal lesions, peripheral neuropathy, and vascular disease. On 49 road dust and soil samples collected in the Metro Detroit area, we analyzed a suite of trace metals in <63 μm and size-separated fractions to quantify the extent of metal enrichment and contamination status. We evaluated Enrichment Factor (EF), Pollution Index (PI), Geoaccumulation Index (GI), and Pollution Load Index (PLI). The average Chromium (Cr) concentration of 198 ppm is the highest reported for any global city in literature while in ~80% samples, Barium (Ba), Cr, Lead (Pb), and Zinc (Zn) concentrations exceeded the USEPA limit. The EF for Barium (Ba) was found to be ≥9 in all samples, and for the rest of other elements was >1.5. The PI values for Cr, Ba, Zinc (Zn), Lead (Pb), and Selenium (Se) indicate elevated levels and for Ba, Cr, and Zn up to a moderate level. PLI values in >50% of road dusts were ≥3, indicating many sites are 'heavily polluted'. The PLI value in Detroit road dust is higher than those reported for some other global cities including Shanghai. Observed strong correlations between Cr-Zn and Cadmium (Cd)-Silver (Ag) likely indicate a common metal source. Cluster analysis of data for Cd, Arsenic (As), Pb, and Zn appears to be distinct between different proximally related clusters, while Nickel (Ni) and Ba are potentially more distinct between property type clusters. In general, metal concentrations of industrial samples are more commonly distinct with over half of metals (≥6 of 11) differing from residential and/or soil samples. Three generalized "groups" were identified from the combination of hierarchical cluster and PCA analyses followed by varimax rotation: Group 1 characterized by Cr, Cd, Ni, Ag, Zn, and Copper (Cu); Group 2 characterized by Pb, As, Mercury (Hg), and minor Ba; and Group 3 characterized by Se. This is the first study to report all four metrics of metal pollution along with rigorous statistical analysis.

KEYWORDS

heavy metals, road dust, enrichment factor, geoaccumulation index, pollution load index, Hierarchical analysis, PCA analysis

1 Introduction

Detroit, a sprawling post-industrial city interwoven with a network of roads and highways, has numerous possible sources of organic and inorganic pollutants. Heavy metals (defined as metals with densities >5 g cm^{-3} and include Pb, Cr, Cd, As, Hg, Ni, Zn, and Cu) are of particular concern. Detroit became a world-class industrial powerhouse during the early 1920s due to a booming auto industry, and grew to become the fourth-largest city in the United States. This growth was accompanied with large scale industrial pollution. One possible source of metal pollution that has garnered much attention in recent years is fugitive road dust. Fugitive dust is generally defined as "natural or human-associated dusts (particulate only) that become airborne due to the forces of wind, human activity, or both" (USEPA, 1975). Road dusts are defined in this study as solid particulate materials, <63 μm in size, that are deposited on road surfaces. These dusts are a complex mélange of natural and anthropogenic materials that are in a constant cycle of transport, deposition, and resuspension. Sources of heavy metals to road dust include traffic emission (e.g., vehicle exhaust aerosols, tire-wear particles, brake lining wear particles, weathered street surface particles), and industrial emission which includes chemical plants, metallurgical industry, coal combustion, oil refineries, petrochemical plants, and mining (Wei and Yang, 2010).

Heavy metals from urban road dusts and surface soils can reach the human body via ingestion, direct inhalation, and dermal contact. Exposure to heavy metals may cause various negative health outcomes at differing scales. For example, lead contamination is of particular concern with a recent global report estimating over 674,000 deaths attributable to lead exposure in 2010 (Lim et al., 2012). Excessive exposure to heavy metals can damage the nervous, skeletal, circulatory, enzymatic, endocrine, and immune systems (Li et al., 2013). The chronic effects of Cd-enriched soil dust through inhalation consist of lung cancer, chronic obstructive lung disease, and impaired pulmonary function (Nordberg et al., 2007).

Unlike many organic pollutants, heavy metals do not degrade over time but only change species and move between different reservoirs. There are two distinct sources contributing to the heavy metals in the environment: 1) from the natural weathering of the parent rocks and minerals, commonly referred as "background level" and 2) metals derived from human impacts (anthropogenic origin) which includes mining, smelting, and other industrial processes (De Miguel et al., 1997, 1999; Thorpe and Harrison, 2008; Charlesworth et al., 2011; Loganathan et al., 2013; Sappa et al., 2020). Because most of the heavy metals have higher distribution coefficients, K_d (ratio of concentrations in solid to that in the solution phase), with increasing concentrations in decreasing particle-sized solid particulate matter, the variations of metal concentration are a function of particle-size and concentrations of total organic matter (e.g., Ravichandran et al., 1995). Thus, it is helpful to normalize the metal concentration in dust samples to the average concentration of the same metal in the upper crust (Wedepohl, 1995) or to the background concentrations in the study area (i.e., pre-anthropogenic level, Murray et al., 2004).

Sources of heavy metals are grouped into point and non-point sources of pollution. In most of the road dust studies, the sources are diffused, arising from multiple sources. Point sources of heavy metal pollution such as mining, foundries, smelters, and other metal-based industrial operations, while still dangerous, are logistically less complicated to understand and remediate than non-point sources (Tchounwou et al., 2012). Prohibition of tetraethyl lead in gasoline and cessation of lead-based paint usage are examples of large-scale regulatory actions taken in the United States that have reduced two major non-point sources of lead pollution in the environment (Mielke and Reagan, 1998; Mielke et al., 2011). According to Mielke et al. (2011), the Pb contamination in Detroit was ranked 4th highest in the contiguous United States in terms of estimated Pb additives released during 1950–1982. While several measures have greatly reduced the introduction of lead into the environment, the impact of past usage still remains since the lead is stored in soil, sediment, and dusts (Wong et al., 2006; Mielke et al., 2011; Loganathan et al., 2013; Souto-Oliveira et al., 2019).

Road dust are potent media for transportation and distribution of heavy metals in urban environments (Mielke and Reagan, 1998; Denier van der Gon et al., 2013). Numerous authors around the globe have reported substantial enrichment of metals in urbanized areas with road dusts having the highest enrichment, greatest mobility of solid particulate media, and having impacts on storm water (De Miguel et al., 1997; Tong, 1998; Manta et al., 2002; Banerjee, 2003; Fakayode and Olu-Owolabi, 2003; Ferreira-Baptista and De Miguel, 2005; Wei and Yang, 2010; Apeagyei et al., 2011; Laidlaw et al., 2012; Sorenson, 2013). In this work, a suite of road dust samples from residential, commercial, and industrial sites in Detroit were collected, dried and sieved to different size fractions. From the measurements of a suite of trace metals, the present study is designed to address the following research questions:

i) How do the concentrations of As, Ba, Cd, Cr, Cu, Pb, Hg, Ni, Se, Ag, and Zn metals vary in road dust in Detroit, MI and how do these values compare with values reported for other cities in US as well as in other cities in the world? Are there any difference in the enrichment factors in bulk and size fractions for these metals?

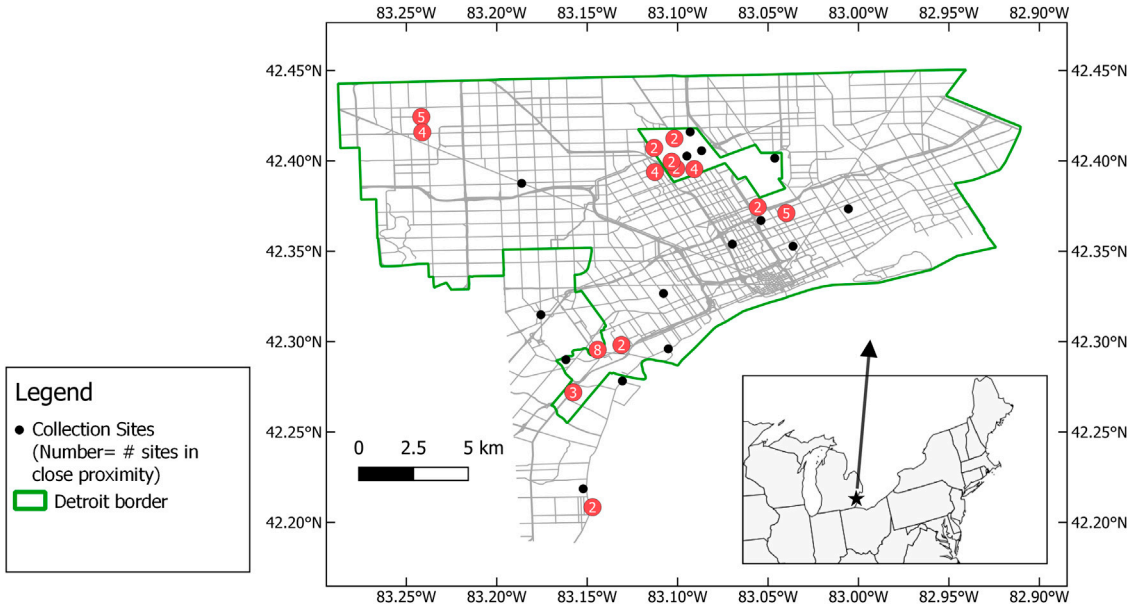

FIGURE 1
Road dust sampling sites.

ii) How does the pollution index, geoaccumulation index, and pollution load index vary among the samples? How do these values compare with the values reported in other cities in US and other cites globally?
iii) Are the concentrations of trace metals more distinct between proximally related or property type related clusters? and
iv) Using hierarchical cluster analysis and principal component analysis, can we identify potential contamination profiles (i.e., chemical "signatures" of contamination)?

This study provides detailed analysis of heavy metal data from a suite of sampling sites and provides insights on the contamination level and contamination profiles/patterns of road dusts. This is the first study that combines the use of four pollution metrics (enrichment factor, geoaccumulation factor, pollution index, and pollution load index), in conjunction with metal analysis in size-fractionated road dust, and utility of, descriptive statistics (correlation analysis and hypothesis testing), and multivariate statistics (PCA and cluster analysis) to provide a comprehensive analysis of heavy metal contamination of road dust in Detroit.

2 Materials and methods

2.1 Field sampling

Road dust samples were collected on 8th August 2019 and 13th September 2019 in Detroit and surrounding areas (42.2°–42.45°N, 83.0°–83.3°W). A total of 51 samples (47 dust and 4 soil) were collected with 34 samples from the first trip (coded as A, B, and C) and 17 from the second trip (coded as D and E, Figure 1, Supplementary Table S1). The sample collection sites were chosen to represent variations in current and historical land use, as estimated by property tax zoning and traffic density. Additional sites were selected based on likely major sources of aerosol particles such as trash incinerators, fuel refineries, coal fired power plants, and other industrial activities. Remaining sites were selected to provide additional spatial coverage in the region, localized sources of dust generation/transport (i.e., demolition sites and open fields), and areas that showed obvious dust collection.

Soil samples were also collected in open field areas. Four soil samples were collected approximately ~10 m off of dust collection site and collected upper ~10 cm of the soil. Road samples were collected using precleaned brooms and dustpans and transferred into 1-gallon LDPE plastic bags. Soil samples were collected using a shovel and stored in similar bags. Roughly 1–3 kg of dust/soil was collected for each sample, which was then labelled and double bagged. All tools were cleaned of any residual dust using distilled water, paper towel, and canned compressed air duster (1,1-difluoroethane) between successive samples. Due to rain days before the second sampling trip, many samples collected were found to be damp.

All samples were sieved with 2 mm and 63 μm sieves with only the portion <63 μm being kept for analysis (<63 μm fraction referred to as "bulk"). This size is chosen as it is the size boundary between silt and sand, with silt being more mobile with higher surface area per unit mass than sand. For example, when a

surface area of 54 μm-size spherical grain undergoing weathering to several 16 μm-size spherical grains, the size of the grain decreases by a factor of 3.4 while the total surface area of the smaller grains becomes 11.4 times larger. Since sorption of anthropogenic and/or bioavailable heavy metal contaminants is surface-area dependent, a subset of 10 samples were chosen for further size-separation using 45 μm and 32 μm sieves to produce three size fractions (45–63 μm, 32–45 μm, and <32 μm).

2.2 Trace metal preparation and analysis

Trace metals were analyzed at the Activation Laboratories Ltd. using their "Ultratrace 6-Near Total Digestion-ICP and ICP-MS" package. Mercury concentrations were measured using "1G-Aqua Regia—Hg Cold Vapour FIMS" package [ALL (Activation Laboratories Ltd.,) 2020a,b]. Activations Laboratories is a SCC GLP (Standards Council of Canada, Good Laboratory Practice) compliant facility with 45 techniques certified by ISO/IEC 17025:2017 (International Organization for Standardization/International Electrotechnical Commission) certification and is FDA (Food and Drug Administration) registered and inspected. Trace metals were analyzed for all bulk and size fractionated samples from 2019 (bulk = 51; size fractionated = 30). The Ultratrace 6 method was used to determine the concentrations of 61 major and trace elements (ALL, 2020a, ALL, 2020b). Briefly, ~0.25 g of the bulk (<63 um) road dust/soil sample was digested first by concentrated hydrofluoric acid and then a mixture of perchloric and nitric acid. Digestion was conducted in a microprocessor-controlled hotbox until incipient dryness was attained, at which time aqua regia was introduced to bring sample back into solution. Solution was then analyzed by ICP-OES for determination of major, minor and some of the trace elements (Al, Ca, Fe, K, Mg, Mn, Na, P, S, and Sc). Each batch also contained 14% quality control samples for digestion and 13% quality control for instrumental analysis which consists of 5 method reagent blanks, 10 in-house controls, 10 sample duplicates, and 8 certified reference materials. Remaining elements were determined by ICP-MS following dilution of sample solution. Quality control samples include one blank per 40 samples, one in-house control per 20 samples, digested standards per 80 samples, and one duplicate per 15 samples with the instrument being recalibrated every 80 samples.

A 0.5 g aliquot was taken from each sample and digested in aqua regia at 90°C to minimize Hg volatilization. In this solution, the Hg is considered stable as it has been oxidized to Hg^{2+}. Stannous chloride is added to the solution to reduce the Hg^{2+} to elemental Hg which is preferable for its determination *via* the 253.7 nm absorption peak. Through the sample and reductant solution, argon is bubbled to transfer Hg atoms into the absorption cell which is then analyzed in a Perkin Elmer FIMS 100 cold vapor Hg analyzer.

Quality control measurements agreed within 20%, on average, for all elements studied with certified reference values for 14 individual reference standards (Supplementary Table S2). Additionally, all six sample and duplicate measurements agreed within an average of 20% for all elements.

2.3 Multivariate statistical analysis

Identification of possible relationships between concentrations of heavy metals and geochemical relationships in road dusts are complex due to many different factors influencing distribution of heavy metals, which hinder elucidation of geochemical and/or their origin relationships. Both descriptive and multivariate statistical analyses are commonly utilized to reveal underlying relationships between heavy metals and their geochemistry and/or their origin (Lee et al., 2006; Yongming et al., 2006; Zheng et al., 2008; Lu et al., 2010; Zhang et al., 2016). The methods used in this study are Pearson's correlation, k-means clustering, principal component analysis (PCA), and hierarchical cluster analysis (CA). These are commonly used in environmental studies to identify potential relationships between samples and metals, potential contamination profiles, and relative strength of the relationships. Statistical analyses were performed using Matlab 2021 with the Statistics and Machine Learning Toolbox (Matlab, 2021), on As, Ba, Cd, Cr, Cu, Pb, Hg, Ni, Se, Ag, and Zn. Pearson's correlation analysis was applied to form a correlation matrix to obtain correlation coefficient and p values between heavy metals. We consider the correlation coefficient to be significantly different from zero when $p < 0.05$. Geospatial clustering (k-means clustering) was performed on latitude and longitude data in MATLAB to identify 6 geographic clusters of samples. This clustering was performed due to high sampling density in several areas and in attempts to investigate relationships within and between areas of high sampling density. The data was analyzed on samples with metal concentrations >3σ which were then removed to prevent bias in PCA. Due to large ranges and variations in metal concentrations, the concentration data were normalized by Z-scores using the standard deviation before PCA and CA analysis. The Euclidean distance metric was calculated using standardized metal concentration and plotted following Ward's method. Ward's method utilizes the incremental summation of squares when forming clusters (Matlab, 2021). PCA was performed using a singular value decomposition algorithm of standardized metal data to produce principal components that are representative of the data. The loadings of these components describe the variance in a dataset with the first principal component accounting for the most variance and each successive component accounting for lesser amounts of variance. This description of variance by the components may be interpreted as a result of some underlying influence from some

TABLE 1 Summary of concentration (ppm), enrichment factor (EF)*, pollution index (PI)*, and geoaccumulation. Index (GI)* of Heavy Metals (n = 49).

Metal	Mean concentration (ppm)	Mean EF[b]	Mean PI	Mean GI
As	8.0 ± 2.3 (3.1–14.2)	3.9 ± 1.1 (0.9–7.2)	1.51 ± 0.43 (0.58–2.68)	−0.05 ± 0.41 (−1.36–0.84)
Ba	346 ± 53 (267–501)	13.6 ± 2.7 (9.0–23.1)	5.2 ± 0.8 (4.0–7.6)	1.8 ± 0.2 (1.4–2.3)
Cd	1.09 ± 0.6 (0.3–2.9)	3.0 ± 1.9 (0.6–8.7)	1.1 ± 0.6 (0.3–2.9)	−0.7 ± 0.8 (−2.3–1.0)
Cr	198 ± 132 (38.0–716)	26.9 ± 21.5 (3.4–106)	9.4 ± 6.3 (1.8–34.1)	2.4 ± 0.9 (0.3–4.5)
Cu	91.6 ± 39.9 (29.9–221)	10.5 ± 5.8 (2.4–27.6)	3.8 ± 1.7 (1.2–9.2)	1.2 ± 0.7 (−0.3–2.6)
Pb	134 ± 78.8 (25.3–359)	11.3 ± 6.1 (1.6–28.2)	4.5 ± 2.6 (0.8–12.0)	1.3 ± 0.8 (−0.8–3.0)
Hg	0.09 ± 0.07 (0.03–0.5)	0.2 ± 0.1 (0.05–1.1)	0.09 ± 0.07 (0.03–0.5)	−4.3 ± 0.8 (−5.8–1.5)
Ni	39.1 ± 14.8 (17.2–75.2)	4.7 ± 2.4 (1.4–10.4)	1.7 ± 0.7 (0.8–3.3)	0.1 ± 0.5 (−1.0–1.1)
Se	1.4 ± 0.4 (0.7–3.1)	5.1 ± 1.6 (1.4–9.9)	1.9 ± 0.5 (0.9–4.1)	0.3 ± 0.4 (−0.7–1.5)
Ag	0.43 ± 0.39 (0.07–2.54)	0.4 ± 0.4 (0.04–2.9)	0.2 ± 0.1 (0.03–1.0)	−3.6 ± 1.0 (−5.8–0.6)
Zn	556 ± 460 (74–2,950)	20.1 ± 17.3 (1.4–88.3)	7.2 ± 6.0 (1.0–38.3)	2.0 ± 0.9 (−0.6–4.7)

[a]Calculation of these parameters require background metal concentration and taken from. Murray et al., 2004; Metal concentrations are given Supplementary Table S3.
[b]Al is used as a normalizing element and the average upper crustal concentration is taken from Wedepohl, 1995.

initial source. Interpretation of PC load is often difficult, therefore rotation such as Varimax rotation are applied which enhance the variances of loads, following removal of components with eigenvalues <1 (Harrison et al., 1996; Mostert et al., 2010).

3 Results

3.1 Heavy metal concentrations

The concentration of eleven trace metals (As, Ba, Cd, Cr, Cu, Pb, Hg, Ni, Se, Ag, and Zn) are summarized in Table 1 and raw data is given in Supplementary Table S3. In all samples, the Al variations is the lowest by factor 3 (factor = maximum concentration/minimum concentration) and such variations is attributed to variations in granulometric parameters (Supplementary Table S3 and Supplementary Table S4). Relatively large variations are found for Mn, Zn, Hg, Ag, Cr, Pb and Cd by factors of 27, 23, 21, 20, 19, 14 and 10, respectively (Supplementary Table S3). Relatively lower variations are found by factors for Ba (1.8), Se (4.4), Ni (4.3), As (4.6), and with Cu and Fe (7.4 and 7.8). The average concentrations of heavy metals in 49 road dust samples decreased in the order Zn (556 ± 460 ppm) >Ba (346 ± 53 ppm) > Cr (198 ± 132 ppm) > Pb (134 ± 78.8 ppm) > Cu (91.6 ± 39.9 ppm) > Ni (39.1 ± 14.8 ppm) > As (8.0 ± 2.3 ppm) > Se (1.4 ± 0.4 ppm) > Cd (1.09 ± 0.6 ppm) > Ag (0.43 ± 0.39 ppm) > Hg (0.09 ± 0.07 ppm). This is similar to findings in an earlier study on road dust samples in which select metal concentrations was reported in the decreasing order: Pb > Cr, Ni > As > Cd (Howard et al., 2019), except for Cr. The differences in metal concentrations are likely due to the greater number of road dust samples collected in this study (this study n = 49 vs. previous n = 23) and larger study area. The elevated metal concentrations compared to the background levels, which vary due to variations in mineralogy, are related to anthropogenic activities. A large variations in the concentrations of these metals from road dusts have been widely reported, with data distributions being reported as normal, lognormal, nonparametric, or highly variable (Charlesworth et al., 2003, Charlesworth et al., 2011; Wei and Yang, 2010; Apeagyei et al., 2011; Loganathan et al., 2013; Hanfi et al., 2020). In a subset of samples analyzed, the concentrations exceed the general soil screening level (SSL) of the EPA based on target hazard quotient (THQ) = 0.1 tables, with the THQ being target value for the hazard quotient defined as a unitless ratio of exposure concentration to reference concentration where a value greater than unity indicates an individual will likely experience adverse health effects (US EPA, 1998; USEPA, 2020). Arsenic is the only element that exceeds the EPA's SSL level in all 49 samples, with a relative bioavailability factor of 0.6 (US-EPA, 1996; US EPA, 2007).

The heavy metals that most commonly reported in road dust is Pb followed closely by Cu, Cr, Zn, and Cd. The average Pb concentration of road dust in this study (134 ± 78.8 ppm) was less than the average values reported in 11 of the 14 studies (range: 31.8–2,583 ppm) conducted globally (Supplementary Table S5; Hopke and Natusch, 1980; Fergusson and Ryan, 1984; Stone and Marsalek, 1996; De Miguel et al., 1997; Tong, 1998; Ferreira-Baptista and De Miguel, 2005; Yongming et al., 2006; Shi et al., 2008; Zhang and Wang, 2009; Lu et al., 2010; Apeagyei et al., 2011; Quiñonez-Plaza et al., 2017; Howard et al., 2019). Studies reporting much higher levels of Pb are >20 years old data which represent studies in road dusts that may have been derived from the use of leaded gasoline. The average concentration of Cu reported in this study is less than the average concentration reported in 8 of the 12 studies compiled. The mean concentration of Zn in road dusts reported here was greater than the reported average concentration in 8 of the 11 studies compiled. Average Cd concentration in road dusts reported in this study is less than 6 of the 8 compiled studies.

Note that the average concentration of Cr reported in this study is higher than the reported average concentration of any of the 14 studies listed. The ranking of Cr contamination in Detroit road dusts in comparison to other urban areas is not definitive, mainly due to the relatively smaller sample size of data set (n = 45) and lack of speciated Cr data needed for risk assessment. The remaining heavy metals of interest for this study are less commonly reported and their discussion is given later. Bulk metal concentrations in road dusts and urban soils are reported in numerous studies and are compared to results in this study in Supplementary Table S5 and Supplementary Table S6 (Spittler and Feder, 1979; Carey et al., 1980; Czarnowska, 1980; Gibson and Farmer, 1986; Lux, 1986; Pfeiffer, 1988; Angelone et al., 1995; Paterson et al., 1996; Wong et al., 1996; De Miguel et al., 1998; Wilcke et al., 1998; Cal-Prieto et al., 2001; Murray et al., 2004; Mielke et al., 2011; Howard et al., 2019).

3.2 Metal pollution indicators

The pollution indicators calculated from the metal concentrations are useful in estimating the relative levels of pollution and anthropogenic impacts. The most commonly used four indices are: 1) enrichment factor (EF); 2) pollution index (PI); 3) Geoaccumulation index (GI); and 4) pollution load index (PLI). Calculation of these indices require local geochemical background metal concentrations and we have used the mean concentrations in subsurface silty clay from easternmost geologic units of Southeast Michigan (Murray et al., 2004).

3.2.1 Pollution index

Pollution index (PI) is useful for basic estimation of a sample's relative degree of pollution of a single metal and calculated as follows:

$$PI_i = (C_i)_s / (C_i)_{bkg} \quad (1)$$

where $(C_i)_s$ *and* $(C_i)_{bkg}$ are concentrations of metal *i* in sample (s) and background (bkg) (e.g., Chen et al., 2015). Commonly, PI values are used in the quantification of other pollution indicators such as Tomlinson's pollution load index (PLI) (discussed later), the Nemerow integrated pollution index (NIPI), and the integrated pollution index (IPI) (Tomlinson et al., 1980; Nemerow, 1991; Chen et al., 2005). The pollution level is categorized as follows (Chen et al., 2005): PI ≤ 1 is Low, 1 < PI ≤ 3 is Mid-Level, and PI > 3 is High. This study did not adopt a classification system based on PI as it is less commonly utilized for pollution classification index than Geoaccumulation index (Müller, 1969; Wei and Yang, 2010; Loganathan et al., 2013; Chen et al., 2015; Hanfi et al., 2020).

A summary of mean PI values for all bulk samples is reported in Table 1 with PI values of individual samples presented in Supplementary Table S7. Chromium and Zn have the highest PI values, with 38 and 34, respectively. The average values of PI for Cr and Zn are 9.4 ± 6.3 and 7.2 ± 6.0, respectively (Table 1). The lowest range and mean values are found for Hg (range: 0.03–0.5; mean: 0.09 ± 0.07) and Ag (0.03–1.0; 0.20 ± 0.10). The mean PI values of 9 of 11 trace metals are >1, suggesting some elevated metal pollution relative to local background soil. The mean PI values of trace metals in samples decreases in the order Cr > Zn > Ba > Pb > Cu > Se > Ni > As > Cd > Ag > Hg. Note that Ba, Cr, Zn, and Cu have minimum PI ≥ 1, suggesting persistent elevation of these trace metals in Detroit road dusts. Likewise, the minimum PI of Pb and Se are >0.84. For two soil samples, (A05S and A03S) the PI < 1.0 for all metals.

3.2.2 Enrichment factor

Enrichment factor (EF) is a measure of the fraction of the total amount derived from anthropogenic activities. This can be calculated by normalizing metal concentrations to an element that varies minimally in concentration and does not vary due to anthropogenic or natural processes. We choose aluminum as the reference element in this study because it's concentration remains unaffected by the soil redox processes and biogeochemical cycling (Buat-Menard and Chesselet, 1979; Ravichandran et al., 1995). Furthermore, its concentration does not vary greatly between upper continental crust (UCC Al = 8.04% by weight) and bulk continental crust (BCC Al = 8.41%) (Taylor and McLennan, 1995) while the other commonly used element, Ti, differs from the UCC (Ti = 0.3 wt%) to BCC (Ti = 0.54 wt%) and thus Al is used as a normalization index element. The EF is calculated using the Eq. 2:

$$EF_i = \left(C_i / C_{ref}\right)_s / \left(C_i / C_{ref}\right)_{bkg} \quad (2)$$

where EF_i is enrichment factor for metal '*i*', C_i and C_{ref} are concentrations (ppm) of metal *i*, and reference element and subscripts *s* and *bkg* denote sample and background sample, respectively (Buat-Menard and Chesselet, 1979; Lawson and Winchester, 1979; Sutherland, 2000). If the pre-anthropogenic metal concentration and metal/Al ratios at a given site differ from those of the average upper crust values, then, the site-specific pre-anthropogenic values need to be determined. In such a case, when calculated EF levels are >1.5 (in principle, >1.0), the samples are considered to be enriched. The metal enrichment level categories, based on EF, are as follows (Sutherland (2000)): EF < 2: depleted to minimally enriched; EF 2–5: moderate enrichment; EF 5–20: significant enrichment and EF 20–40: very highly enriched, and EF > 40: extremely enriched. Note that the samples with low EF (i.e., near 1) does not necessarily mean that the metal lacks any anthropogenic influence, but that the metal is not specifically enriched relative to the chosen background values.

The average enrichment factors in all samples suggest high enrichment, EFs as high as 106 for Cr, 88 for Zn, 28 for Cu and Pb, and 23 for Ba (Table 1, Supplementary Table S8). These are

some of the highest values reported in global literature. Chromium occurs in two valence states, trivalent (Cr III) and hexavalent (Cr VI), of which Chromium VI is the most toxic. While Cr (III) is an essential element in humans, Cr (VI) targets the respiratory tract organ for toxicity, for acute (short-term) and chronic (long-term) inhalation exposures. Exposure to Cr (VI) via ingestion and inhalation of superfine soil dust that are enriched in Cr (VI) could result in shortness of breath, coughing, and wheezing as well bronchitis, decreased pulmonary function, pneumonia, and other respiratory effects (US. EPA United States Environmental Protection Agency, 1998; USEPA, 1998; Wilbur et al., 2012). For Ag and Hg, the average EF values are less than 1.0, indicating depletion and is likely due to the used background values which may not reflect the actual pre-anthropogenic concentrations. The average EFs decrease in the order: Cr > Zn > Ba > Pb > Cu > Se > Ni > As > Cd > Ag > Hg. The mean EF of Cr and Zn being >20 classify these metals as "very highly enriched" while Ba, Cu, Pb, and Se mean EF values of >5 as "significantly enriched". The average EFs of soil samples are consistently lower than the averages from road dusts suggesting a greater degree of anthropogenic influence on road dusts.

3.2.3 Geoaccumulation index

Geoaccumulation index (GI) takes in to account the natural fluctuations in background concentrations. GI is calculated as follows:

$$GI = log_2\left[(C_i)_s \Big/ \left(1.5(C_i)_{bkg}\right)\right] \quad (3)$$

where $(C_i)_s$ and $(C_i)_{bkg}$ *are* concentrations of metal *i* in sample (ppm) and background concentration, respectively. The background (BKG) concentration is multiplied by 1.5 to account for natural BKG variations. Categorization of pollution levels in GI index are as follows: practically unpolluted (PUP): GI ≤ 0; PUP to moderately polluted (MP): 0 < GI ≤ 1; MPP: 1 < GI ≤ 2; moderately to heavily polluted: 2 < GI ≤ 3; heavily polluted: 3 < GI ≤ 4; heavily to extremely polluted: 4 < GI ≤ 5; and extremely polluted: GI > 5; (Müller, 1969). A summary of mean GI values for all bulk samples (Table 1) and individual samples (Supplementary Table S9) indicate GI values of heavy metals decreases in the following order: Cr > Zn > Ba > Pb > Cu > Se > Ni > As > Cd > Ag > Hg. The heavily polluted metals are Zn (average: 2.0 and highest: 4.7), Cr (2.4, 4.5), and Pb falls in the moderately polluted category (average: 1.3, 3.0) (Table 1) along with Pb, Cu, and Ba.

3.2.4 Pollution Load Index

Pollution load index (PLI) is used as a metric to assess the overall pollutant loading in sediment, soil, and road dust (Tomlinson et al., 1980; Chen et al., 2015; Gloaguen et al., 2021). Since this indicator considers the level of metal contamination from several metals, it is a better index of the overall pollution status of a sampling site. PLI is calculated as follows:

$$PLI = (PI_1 * PI_2 * PI_3 * \ldots * PI_n)^{1/n} \quad (4)$$

where PI_1, PI_2, and PI_3 are the PI of heavy metals 1, 2, and 3 respectively, and n is number of trace metals (Tomlinson et al., 1980). The PI values of Hg and Ag are <1.0 and hence were not included in the PLI calculation. Based on PLI, road dust samples can be categorized as follows: unpolluted: PLI ≤1; slightly polluted: 1 < PLI ≤2; moderately polluted: 2 < PLI ≤3; and heavily polluted: PLI ≥3 (Chen et al., 2015; Liu et al., 2016).

A summary of PLI and sample type are reported in Supplementary Table S10 with PLI and location type of individual bulk samples in Supplementary Table S11. The four location types initially identified for this study are residential, industrial, commercial, and soil which were designated based on property tax zoning. The average PLI of sample types decreases in the order: industrial > residential > commercial > and soil. In total, 92% of all samples had a PLI >2 including 100% of commercial and industrial samples.

3.3 Heavy metal concentration and pollution indicators in size-fractionated road dusts

The variation in mean heavy metal concentration within bulk (<63 μm) and size-fractionated samples are reported in Supplementary Table S12 and individual size fractionated samples in Supplementary Table S4. The average concentrations of heavy metals in the bulk and size-fractionated samples decreased in the order Zn > Ba > Cr > Pb > Cu > Ni > As > Se > Cd > Ag > Hg which is similar to the bulk samples. Metal concentration generally increases with decreasing grain-size for As, Cu, Pb, Hg, Ni, Ag, and Zn, although the variations between fractions are all within ±1σ. Cd and Se do not show clear change with grain-size, while Ba and Cr show a general increase with increasing grain-size, although variations remain within ±1σ.

The variations in mean pollution indicators for bulk (<63 μm) and size-fractionated samples are reported in Table 2, with individual size-fractionated samples in Supplementary Tables S13–S16. The mean PLI generally increases with decreasing grain size, with PLI of the <32 μm fraction is similar to that of the bulk (within ± 1σ). The average EF of all metals generally increases with decreasing grain size although the differences between fractions are not significant within ±1σ. The mean GI values for As, Cu, Hg, Ni, Se, and Ag generally increase with decreasing grain size while for other elements generally either there is a decreasing

TABLE 2 Comparison of Pollution Load Index (PLI), geoaccumulation index (GI), and enrichment factor (EF) in bulk and size fractions.

Sample ID	Mean bulk (range)	Mean < 32 μm (range)	Mean 32–45 μm (range)	Mean 45–63 μm (range)
PLI	3.0 ± 0.6 (1.5–3.8)	2.9 ± 0.7 (1.7–3.8)	2.8 ± 0.6 (1.6–3.6)	2.6 ± 0.5 (1.5–3.4)
EF As	4.6 ± 1.3 (2.8–6.9)	5.1 ± 1.2 (3.9–7.1)	4.6 ± 1.2 (2.8–6.4)	3.9 ± 0.9 (2.5–5.7)
EF Ba	13 ± 1.4 (11–16)	13 ± 1.8 (10–16)	12 ± 1.9 (9.7–16)	12 ± 1.7 (9.8–16)
EF Cd	2.8 ± 1.0 (1.4–5.3)	2.7 ± 0.7 (1.2–3.4)	2.5 ± 0.6 (1.1–3.2)	2.1 ± 0.6 (1.0–3.0)
EF Cr	24 ± 12 (11–49)	25 ± 17 (11–63)	24 ± 15 (9.4–52)	23 ± 11 (8.5–47)
EF Cu	9.1 ± 4.3 (3.8–17)	10 ± 4.6 (5.2–20)	9.1 ± 4.6 (3.9–19)	7.7 ± 3.6 (3.1–15)
EF Pb	12 ± 5.9 (4.3–20)	14 ± 6.4 (5.3–25)	13 ± 6.8 (4.7–24)	11 ± 5.5 (3.3–20)
EF Hg	0.2 ± 0.1 (0.1–0.3)	0.2 ± 0.1 (0.1–0.4)	0.2 ± 0.1 (0.1–0.4)	0.1 ± 0.1 (0.1–0.3)
EF Ni	4.2 ± 1.4 (2.3–7.4)	5.2 ± 2.0 (3.2–9.2)	4.3 ± 1.2 (2.5–6.7)	3.6 ± 0.9 (2.1–5.4)
EF Se	5.3 ± 0.9 (3.8–6.7)	4.7 ± 2.1 (0.9–7.4)	4.2 ± 2.2 (0.8–7.6)	3.7 ± 2.0 (0.4–7.3)
EF Ag	0.4 ± 0.2 (0.1–1.0)	0.4 ± 0.2 (0.2–0.9)	0.4 ± 0.2 (0.2–0.7)	0.2 ± 0.1 (0.1–0.5)
EF Zn	17 ± 4.9 (7.1–23)	20 ± 6.2 (8.9–27)	17 ± 4.8 (8.0–23)	14 ± 3.6 (6.0–18)
GI As	0.15 ± 0.40 (−0.58–0.84)	0.24 ± 0.39 (−0.34–0.96)	0.16 ± 0.40 (−0.34–0.93)	0.03 ± 0.36 (−0.56–0.63)
GI Ba	1.7 ± 0.2 (1.4–2.3)	1.6 ± 0.3 (1.1–2.2)	1.6 ± 0.2 (1.3–2.2)	1.7 ± 0.2 (1.5–2.2)
GI Cd	−0.60 ± 0.46 (−1.6–0.09)	−0.72 ± 0.49 (−1.9 to −0.21)	−0.71 ± 0.55 (−1.9 to −0.10)	−0.92 ± 0.45 (−1.9 to −0.21)
GI Cr	2.4 ± 0.7 (1.4–3.7)	2.3 ± 0.7 (1.3–3.8)	2.4 ± 0.8 (1.2–3.8)	2.5 ± 0.7 (1.2–3.5)
GI Cu	1.0 ± 0.6 (−0.17–2.0)	1.1 ± 0.6 (0.24–2.3)	1.0 ± 0.6 (−0.07–2.3)	0.89 ± 0.59 (−0.23–1.8)
GI Pb	1.4 ± 0.9 (0.02–2.6)	1.5 ± 0.9 (0.21–2.9)	1.5 ± 0.9 (0.20–2.8)	1.3 ± 0.9 (−0.12–2.5)
GI Hg	−4.3 ± 0.5 (−5.2 to −3.5)	−4.2 ± 0.7 (−5.1 to −3.3)	−4.4 ± 0.8 (−5.5 to −3.3)	−4.8 ± 0.8 (−5.8 to −3.5)
GI Ni	−0.005 ± 0.456 (−0.91–0.69)	0.20 ± 0.52 (−0.59–1.1)	0.05 ± 0.45 (−0.70–0.60)	−0.08 ± 0.39 (−0.81–0.44)
GI Se	0.39 ± 0.29 (−0.17–1.0)	−0.07 ± 1.00 (−2.5–0.76)	−0.24 ± 1.23 (−2.5–1.1)	−0.41 ± 1.37 (−3.5–1.1)
GI Ag	−3.5 ± 0.8 (−4.9 to −1.6)	−3.4 ± 0.6 (−4.5 to −2.4)	−3.5 ± 0.5 (−4.6 to −2.7)	−4.1 ± 0.6 (−5.3 to −3.2)
GI Zn	2.0 ± 0.5 (0.74–2.4)	2.1 ± 0.4 (1.0–2.5)	2.1 ± 0.4 (0.97–2.4)	1.8 ± 0.4 (0.73–2.3)

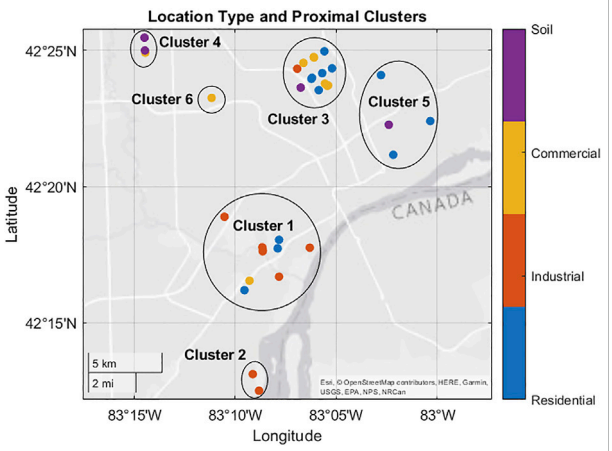

FIGURE 2
Clusters identified by k-means clustering and classified by location type (Identified by tax zoning code).

trend or lack of clear change with grain size. Overall, there appear to be no statistically significant variations in heavy metal content or contamination level between the different size fractions.

3.4 Statistical analyses

Statistical analyses provide additional information allowing a more complete understanding of underlying patterns in heavy metal contamination. The relationships between concentrations of As, Ba, Cd, Cr, Cu, Pb, Hg, Ni, Se, Ag, and Zn and sample locations were investigated using descriptive statistics, k-means geographic clustering, hierarchical clustering, and principal component analysis followed by varimax rotation. Preceding statistical analysis, preliminary analysis revealed four samples (A07, A08, E04, and E09) are statistical outliers with concentration values >3σ of mean metal concentration. The large variations in geochemical data often result in outliers and non-normal distributions which will bias many statistical methods unless outliers are removed (Reimann et al., 2002) and therefore, they were eliminated from multivariate analysis. The remaining samples were then normalized by z-scores prior to analysis.

3.4.1 Geographic and location type categorization

The K-means clustering was performed on location datum (latitude and longitude) to identify geographic clusters of

TABLE 3 Pearson's correlation matrix.

	Hg	Cd	Cr	Ni	Ag	Se	Zn	As	Ba	Cu	Pb
Hg	1	0.03	0.16	0.50	0.52	0.21	0.93	<0.01	<0.01	0.31	<0.01
Cd	0.33	1	<0.01	<0.01	<0.01	0.08	<0.01	0.18	0.67	<0.01	<0.01
Cr	−0.22	0.49	1	<0.01	<0.01	0.08	<0.01	0.09	*0.04*	<0.01	0.26
Ni	0.10	0.50	0.65	1	<0.01	0.22	<0.01	0.98	0.10	<0.01	0.48
Ag	0.10	0.70	0.55	0.43	1	0.13	<0.01	0.23	0.24	<0.01	0.03
Se	0.19	0.26	0.26	0.19	0.23	1	0.01	0.06	0.47	0.12	0.05
Zn	0.01	0.54	0.76	0.56	0.47	0.40	1	0.51	0.05	<0.01	0.85
As	0.53	0.21	−0.26	0.004	0.18	0.29	−0.10	1	<0.01	0.54	<0.01
Ba	0.51	0.07	−0.31	−0.25	0.18	−0.11	−0.29	0.44	1	0.88	<0.01
Cu	0.15	0.59	0.48	0.69	0.48	0.23	0.57	0.09	−0.02	1	0.18
Pb	0.64	0.42	−0.17	0.11	0.32	0.30	0.03	0.65	0.50	0.20	1

[a]Below diagonal are correlation coefficients and above diagonal are p values; Bold = Correlation coefficient >0.40; Italic = p value < 0.05.

TABLE 4 Student's Two Sample *t*-Test Results for k-Means Clusters.

Tested[a]	Hg	Cd	Cr	Ni	Ag	Se	Zn	As	Ba	Cu	Pb
1 to 2		X						X		X	
1 to 3			X	X			X	X			X
1 to 4		X	X	X	X	X	X		X	X	X
1 to 5	X		X		X		X	X	X		X
2 to 3							X			X	
2 to 4		X					X	X			
2 to 5										X	
3 to 4		X		X	X	X	X	X		X	X
3 to 5	X		X								
4 to 5	X	X		X	X	X		X			X

[a]X = Significant as α = 0.05; Test assumed unequal variance; n for clusters 1-5 are 14, 2, 15, 7, and 6 respectively.

samples (circled clusters Figure 2). This analysis classifies points by their distance to k centroids (k = 6 chosen; Euclidean distance used as metric). Six cluster centers are determined that minimize the average distance between samples to a common center, resulting in sample clusters near each other. Cluster 6 contained only one point (E02) located nearly equidistant from cluster 3 and cluster 5, and thus it is ignored. Clustered samples are interpreted as proximally related, and the relationships within and between these groupings is compared to groups identified by location type (dots Figure 2).

3.4.2 Correlation analysis

A Pearson's correlation matrix was constructed using normalized metal data with the correlation coefficients (r coefficients) and p values reported in Table 3. All metals are moderately correlated ($r \geq 0.4$) with $p \leq 0.05$ with Cd and Zn each being correlated to six other metals.

3.4.3 Student's *t*-test

To assess whether proximity or location type produces more distinctive groupings, the average values of metal data categorized by proximal cluster and location type were compared by Student's two-sample t-test. The T-tests were performed assuming unequal variance with a significance threshold of α = 0.05. For this study, a comparison (e.g., one location type to another or one proximal group to another) is deemed distinct if the null hypothesis that the groups have the same mean may be rejected. This is done as a preliminary step in identifying methods of categorization that may be most useful for further study. The results for proximal clusters are reported in Table 4 and for location type in Supplementary Table S17. Zinc and As in Table 4 are the elements most commonly distinct between clusters with each being distinct in 6 of 10 cluster comparisons. Ba, Se, and Hg are least commonly distinct between proximal clusters with Hg and Se being distinct in 3 of 10 comparisons and Ba being distinct in 2 of 10.

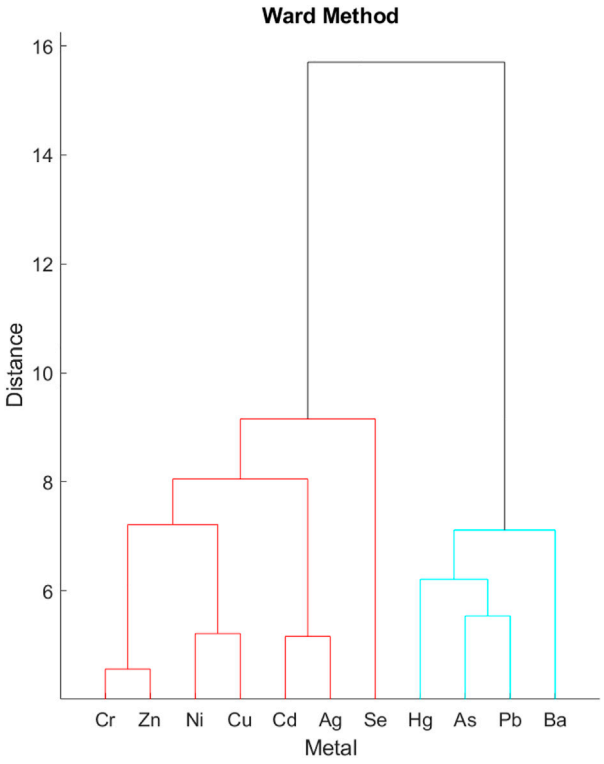

FIGURE 3
Dendrogram of trace metals. Colored groups indicate cluster separation at 70% maximum linkage distance (~11).

Additionally, the Hg in Cluster 5 is distinct from all other clusters besides cluster 2. The most geochemically distinct clusters are 1 and 4 with 9 of 11 elements being distinct. Overall, Cluster 4 is the most distinct from other clusters although is not as distinct from Cluster 2 with only 3 metals being distinct. Cluster 2 is the least geochemically distinct.

Location-type clusters (Supplementary Table S17) show fewer distinct patterns than the proximal clusters. The metals that are most distinct between location types are Ni and Ba which were distinct in 5 of 6 and 4 of 6 comparisons, respectively. As and Cd are notably not distinct in any of the location type comparisons. Strong distinctions exist between industrial locations and soil (7 of 11 elements) and residential locations (6 of 11 elements). In addition, residential and soil samples are the least geochemically distinct with only 2 of 11 elements having statistically significant differences in concentration. Commercial locations were only distinct from other location types in 3 of 11 metals in each comparison, although not the same elements for each.

3.4.4 Hierarchical cluster analysis

To better understand the relationships between trace metals, hierarchical cluster analysis was performed. We applied Ward's method, which produces clusters by minimizing variance (or maximizing R^2) within each successive cluster. Two main clusters are observed, with Cluster 1 containing Cd, Ag, Cr, Zn Ni, and Cu and Cluster 2 containing Pb, As, Hg, and Ba (Figure 3).

TABLE 5 Varimax rotated components.

Element	Component 1	Component 2	Component 3
Hg	0.030	**0.461**	−0.064
Cd	**0.425**	0.150	−0.080
Cr	**0.405**	−0.206	0.150
Ni	**0.402**	−0.050	0.072
Ag	**0.438**	0.077	−0.184
Se	−0.063	0.309	**0.757**
Zn	0.340	**−0.050**	0.314
As	−0.062	0.503	0.091
Ba	0.038	0.324	**−0.497**
Cu	**0.415**	0.036	−0.015
Pb	0.065	**0.506**	−0.024

Bold: |Load| ≥0.4

3.4.5 Principal component analysis

Principal component analysis (PCA) was conducted on the normalized metal concentration data. Initial loadings and the variance explained by each component are reported in Supplementary Table S18. The first 3 principal components (PC) explain >70% of the variance in the data, with each individual PC explaining ≥9%. Varimax rotation was applied to aid in interpretation of PCs. The results of varimax rotation are reported in Table 5.

4 Discussion

The quantitative metrics, i.e., Pollution Index, Enrichment Factor, Pollutant Load Index and Geoaccumulation Index, to determine anthropogenic metals pollution critically depend on the pre-anthropogenic concentrations. Most studies have focused on a subset of these metrices in quantifying road dust metal pollution, but we have calculated all four metrics used to assess metal pollution in road dust, soil, and sediment matrices. It is anticipated that the EF, PI, and GI are expected to exhibit same order of decreasing values, based on their calculations given above. The PI values of Hg and Ag are <1.0 for all samples suggesting that there is no Hg contamination above background levels in Detroit road dusts or soils, although, it should be noted that the background value of Hg in subsurface silty clay reported in Murray et al. (2004) is relatively high with an average concentration of 0.98 ppm. Therefore, it is possible that PI

values for Hg doesn't represent actual pollution level. Overall, there is a persistent elevation of measured trace metals in Detroit road dusts.

4.1 Enrichment factor

It is widely known that the sorbed (or bioavailable and anthropogenic) concentration of metals are higher in finer grain-size fraction, due to increased surface per unit mass of soil compared to larger grain size fraction. A comparison of EFs for <32 μm, 32–45 μm and 45–63 μm (Table 3) indicates the enrichment factors generally follow the sequence: 32 μm > 32–45 μm > 45–63 μm. However, the differences in the EF between different size fractions in a sample is <10% which is much smaller than the range of values for all samples (Table 2). It was shown that on < 10 μm road dust samples from California, the range of EF reported values for Cr, Ni, Cu, Zn, and Pb are: 137–605, 1.2–87.6, 4.9–98.9, 6.0–735, and 5.0–18.9, respectively, with such high EF values attributed to very fine particle analyzed (McKenzie et al., 2008). Note that the surface area per unit mass in a 10 μm grain size is about 15 times higher than that of a 39 μm size. Earlier study of sediments from Clinton River in the southeast Michigan watershed located north of the study area reported maximum EF values of 8.7 (Cd), 7.3 (Pb), 3.4 (Zn), 2.6 (Cu), 1.6 (Ni), and <1 (As) using background concentrations of the local glacial lobe (van Hees et al., 2010). Another study in Baoji, China reported average EF values in road dust of 3.51 (Cu), 9.03 (Pb), 6.20 (Zn), and 1.20 (Ni) using background values in Chinese soil and Fe as a reference element (Lu et al., 2009). A study from Dhanbad and Bokaro regions of India reported EF in road dust ranging from 0.58–0.94 (Cu), 1.76–3.29 (Zn), 0.41–0.8 (Ni), 0.51–1.22 (Cr), and 9.1–36.6 (Pb) using average crustal composition and Sr as a reference element (Singh, 2011). Residential and industrial areas in Singapore reported median EF in street dusts of 5.4–7.2 (Cr), 2.3–7.2 (Ni), 30–46 (Cu), 19–25 (Pb), and 34–38 (Zn) using upper crustal average values and Al as a reference element (Yuen et al., 2012). Overall, this study reports relatively higher enrichment factors for several metals.

4.2 Geoaccumulation index

The calculated GI values for <32 μm fraction is slightly higher than that for bulk (<63 μm) fraction for As, Cu, Pb, Ni, and Zn (Table 2) and the values in <32 μm fraction is higher than that in 45–63 μm fraction (Table 3). The only metals observed with minimum GI values of >1.0 are Ba, Cr, Pb, and Zn, indicating moderate pollution in all Detroit road dusts. Two samples are classified as heavily polluted with GI of 4.7 (A08) and 4.5 for Cr (B07). These values can be compared to the values reported from other global cities: average GI of 0.18 (Cr), 1.48 (Cu), 1.81 (Pb), 1.48 (Zn), 0.34 (Ni), and 2.64 (Cd) in road dusts of several cities in China (Wei and Yang, 2010); In Dhanbad and Bokaro regions (India) Singh. (2011) reported GI values ranging from 1–3 (Pb) and <0 for all other metals (i.e., Cu, Zn, Ni, and Cr) (Singh, 2011). In New York, GI values of 0.45 (Cr), 3.39 (Cu), 6.05 (Pb), 3.59 (Zn), -4.41 (Ni), and 5.74 (Cd) in road dusts were reported in mid-1980s (Fergusson and Ryan, 1984). In Sault Ste Marie, Canada average GI values of road dusts were reported to be 0.01 (Cr), 1.36 (Cu), 1.21(Pb), 0.60 (Zn), −0.61 (Ni), and 2.5(Cd) (Stone and Marsalek, 1996). Road dusts of Luanda, Angola, Ferreira-Baptista and De Miguel (2005 reported GI values of −1.82 (Cr), 0.31 (Cu), 3.01 (Pb), 1.08 (Zn), −2.01 (Ni), and 2.87 (Cd) in road dusts (Ferreira-Baptista and De Miguel, 2005). In summary, some of GI values for Detroit is higher than those in many of these cities.

4.3 Pollution load index

The average Pollution Load index (PLI) in road dusts in this study are classified as "heavily polluted" according to the classification of Liu et al. (2016), with the majority of road dust samples classified as "highly polluted" (51% of dust samples; n = 45), suggesting ubiquitous high metal contamination in road dusts. No samples had PLI ≤1 suggesting that all road dusts and urban soils in Detroit are at minimum classified as "slightly polluted" (Liu et al., 2016). Direct comparison of PLI values from different regions of the world is difficult due to differences in geochemical background, land use, industrial history, population, number of vehicles driven per unit population, etc., between cities as well as differences in the metals used for PLI calculation. Earlier studies of road dusts reported average PLI values of 2.0–2.6 (averages of different areas in Shanghai, China), 1.5–6.5 (Loudi, China), 14.6 (residential area, Singapore) 20.6 (industrial area, Singapore), and 1.51 (Wuhan, China) (Yang et al., 2010; Yuen et al., 2012; Zhang et al., 2012; Wang et al., 2019). Previous studies also reported PLI values in urban soils of 2.38 (Kaifeng City, China), 1.1 (range = 0.2–13.4; various soils in China), 3.64 (Subaé River, Brazil), and 2.3–9.2 (Detroit, United States) (Chen et al., 2015; Liu et al., 2016; Howard et al., 2019; Gloaguen et al., 2021). Further risk and/or hazard-based research into Detroit road dusts is required to assess potential negative public health outcomes and/or negative ecological effects.

4.4 Student's T-test

We performed T-tests to determine whether mean metal concentrations are more statistically distinct in clusters defined by geographic clustering or by land use zoning. A higher degree of distinction between the proximity clusters supports the hypothesis that variations in those elements is influenced by proximity to common sources. Additionally, we

looked for individual elements or sets of elements that are distinct between clusters, which may support the possibility of local sources in or nearby a cluster. For example, if the Hg concentration in a cluster is distinctly elevated in a proximal cluster compared to other proximal clusters, it would support the hypothesis of a source of Hg contamination nearby that cluster. Conversely, under the assumption that tax zoning serves as a proxy for types of land use (e.g., industry, commercial business, or residence), greater distinction of elements between location types would support a hypothesis that variations are influenced by how that area is used. We interpret the results in Table 4 and Supplementary Table S17 with these assumptions.

Overall, we find mean metal concentrations at clusters defined by proximity are more often distinct at a significant level than those defined by land use type. In Table 4 the distinct means of Zn and As in 6 of 10 comparisons potentially suggests variations in these metals are partially controlled by proximal sources. In contrast, the relative similarity in averages of Ba, Se, and Hg (distinct in 2-3 of 10 comparisons) suggests that these metals may have a source not specific to one location. Notably, Hg in proximal cluster 5 is distinct from all other clusters except cluster 2, which has a small sample size ($n = 2$). This suggests a possible local source of Hg proximal to cluster 5. Note that cluster 4 also contains two soil samples which have low concentrations, thus some of the distinctions with this cluster may be somewhat biased if proximity is the only criteria for categorization.

The relatively fewer distinct patterns between location types in Supplementary Table S17 than proximal clusters potentially suggests that proximally related sources may control geochemical distinctions in contamination than location type. Although, the difference in number of groups compared in two datasets and relative number of samples in the datasets may bias direct comparisons between the datasets. The distinction of Ni and Ba in 4-5 of 6 comparisons suggests that differences in their contamination may be related to use characteristics such as traffic density or industrial activity. Control of Ba contamination by use characteristics is supported further from a lack of distinction between proximal clusters (i.e., only distinct in 2 of 10 comparisons). Absence of distinction between groups for As and Cd suggests these metals may not be controlled by use characteristics. In conjunction with observations in Table 4 where As and Cd are distinct in 6 of 10 and 5 of 10 clusters, respectively, variations of these metals may be controlled by location and/or local sources. The distinction of 6-7 of 11 elements between both residential and soil suggests industrial locations may be geochemically distinctive from soil or residential samples. Conversely, the distinction of 2 of 11 elements between residential and soil suggests they are relatively similar.

4.5 Hierarchical cluster analysis

The strong clustering of Hg, Pb, As, and Ba in Cluster 1 suggests a common source between these metals, with strong connection between As and Pb. A strong clustering of Cd, Ag, Cr, Zn, Ni, and Cu in Cluster 2 possibly indicate a common source for these metals with a relatively strong connection between Cr and Zn. The linkage between Cd and Ag at a higher level in Cluster 1 indicates a weaker association with the possible common source or a mixing of contributions from multiple sources. The high-level linkage of Se with the Cluster 1 indicates a weak association of Se with other elements in the cluster.

4.6 Principal component analysis

Following varimax rotation, the first principal component is dominated by Cd, Cr, Ni, Ag, and Cu, each with loadings ≥0.4, along with a lesser loading of Zn (Table 5). These metals were linked in cluster analysis further suggesting a common source (more details given in section 4.7). PC 2 is dominated by Pb, As, and Hg with a lesser loading from Ba. These metals were also linked in Cluster 1, which supports the suggestion of a common source. Finally, PC 3 is dominated almost solely by Se and a strong negative loading of Ba, with a minor loading of Zn. The negative loading of Ba may be interpreted as a negative correlation of Ba with the overall direction of this load.

4.7 Statistical analysis summary and interpretations

The application of multiple statistical methods allows for a more complete understanding of heavy metal distribution and possible sources. Previous studies have applied different methods of pollution source characterization and apportionment such as analysis of specific sources (brake pads, tire wear, exhaust, etc.), different pollution sources (smelters, coal fired power plants, e-waste recycling, etc.), and specific grain type analysis (slag glass, road paint, etc.) (Adachi and Tainosho, 2004; Thorpe and Harrison, 2008; Sepúlveda et al., 2010; Charlesworth et al., 2011; Zhang et al., 2011; Loganathan et al., 2013). Adachi and Tainosho (2004) characterized tire embedded particles based on composition and morphology resulting in the following groups: brake dust (Cu and Ba), yellow paint (Cr and Pb), “mixed” (Cr, Cu, Zn, Ba, and Pb), and tires (Zn). Another study using a combination of EF and multivariate statistics identified sources as Commercial/Domestic (Ag and Hg), Industrial/traffic (Cr, Cu, Pb, and Zn), and Soil (As) (Yongming et al., 2006). In an extensive literature review, Thorpe and Harrison (2008) summarized concentrations of different non-exhaust particle sources including brake wear, tires, road surface abrasion, and

re-suspension of road dusts and concluded that there are no suitable elemental tracers that specifically discriminate non-exhaust particle contributions, other than the use of Cu:Sb ratios for brake dust. The study reported that Ba was commonly reported in road dusts and attributed part of its abundance to $BaSO_4$ fillers used in brake linings. Barium-containing compounds are also extensively used as dispersants in various vehicular fluids (Thorpe and Harrison, 2008; Charlesworth et al., 2011).

Three contamination profiles identified in this study are classified based on the rough chemical classifications of the constituent elements, and represent the three general patterns that describe overall metal contamination in Detroit road dusts/soils. Group 1 is labelled "transition metal rich" and coincides with the profile identified in PC 1 and cluster 1 which contains Cr, Cd, Ni, Ag, Zn and Cu. Group 2 is labelled "post-transition and metalloid rich" and coincides with PC 2 and cluster 2 which contains Pb, As, Hg, and minor Ba. Group 3 is labelled "non-metal rich" and coincides with PC 3 and is partially indicated by the high-level linkage of Se in cluster analysis. Previous studies have identified several of the metals studied here as "natural" or geogenic elements (As, Cr), although the EF values of road dusts in this study indicate these metals are not enriched via natural processes (Manta et al., 2002; van Hees et al., 2010). Results from the hypothesis testing of location types and clusters both suggest certain metals such as Cr are distinctively elevated in industrial areas and proximal cluster 1 which is itself a heavily industrialized area. Several elements elevated in industrial areas (e.g., Cr, Zn, and Ni) coincide with those in the transition metal rich group suggesting that this group may represent the signature of contamination from industrial sources. Although, the results of location type hypothesis testing suggest that it is Ni and Ba that show greater distinction between location types which somewhat contradict this connection. Overall, the relationship between the transition metal rich group to industrial activity requires further investigation to test the validity of such association.

5 Conclusion

This study represents a multifaceted approach on the characterization of road dusts in the Detroit area with datasets consisting of trace metal data analyzed using pollution indicators, and univariate and multivariate statistical analysis. From the collection and analysis of a suite of bulk (<63 μm) and a sub-set of size-fractionated road dust and soil samples for a suite of heavy metals (Pb, Cr, Cd, As, Ag, Hg, Se, Ba, Ni, Zn, and Cu), from a post-industrial city in southeast Michigan, the following conclusions are drawn:

i) We report the highest concentration of Cr in Detroit compared to any other major global city, with average concentration of 198 ppm (range: 38–716), and mean pollutant metrics of: EF 27 (3–106), PI 9.4 (1.8–34), and GI 2.4 (0.3–4.5). While this study didn't address the speciation of Cr, inhalation and ingestion of finer soil-laden Cr (VI) could cause major health problems;
ii) The mean enrichment factor for As, Cd, Cu, Ni and Pb are 3.9, 3.0, 10.5, 4.7, and 11.3, respectively; the corresponding PI values are 1.5, 1.1, 3.8, 1.7, and 4.5 respectively, showing highly polluted nature of road dust;
iii) Zinc and Ba have the highest enrichment factors after Cr, with values of 20 and 14, respectively and the corresponding PI values of 7.2 and 5.2, respectively, suggesting all road dusts and soils in Detroit are significantly enriched in Zn and Ba due to anthropogenic influences;
iv) The mean Pb concentration of 134 ppm is about 10 times higher than the crustal average concentration and thus lead pollution is prevalent;
v) The Geoaccumulation Index values of all road dusts are higher for Ba, Cr, Cu, Pb, and Zn, indicating high pollution. The Pollution Load Index values of road dusts and soils in Detroit indicate pollution levels of As, Ba, Cr, Cu, Pb, Ni, Se, and Zn are high suggesting all samples are at least slightly polluted with >50% of road dust values of ≥3 classifying them as "heavily polluted". Average PLI is higher than reported in some other global cities such as Shanghai, although direct comparison is difficult due to a variety of factors;
vi) There are significant linear correlations between trace metals, with the stronger correlations being between the pairs Cr-Zn ($r = 0.76$, $p < 0.01$) and Cd-Ag ($r = 0.70$, $p < 0.01$) potentially suggesting a common source for these metal pairs;
vii) Concentrations of Cd, As, Pb, and Zn in road dust are potentially more distinct between different proximally related clusters, while Ni and Ba are between property type clusters. In general, metal concentrations of industrial samples are more commonly distinct for about half of metals (≥6 of 11) differing from residential and/or soil samples;
viii) Three generalized contamination profiles or "groups" were identified by the combination of hierarchical cluster and PCA analyses followed by varimax rotation. These groups are:
    - Group 1 ("transition metal rich"): characterized by Cr, Cd, Ni, Ag, Zn, and Cu;
    - Group 2 ("post-transition and metalloid rich"): characterized by Pb, As, Hg, and minor Ba; and
    - Group 3 ("non-metal rich"): characterized by Se.

This study lays a foundation for tracking toxic trace metal clusters in road dust in Detroit and future study should focus on areas where children are likely to get higher levels of toxic metals exposure, which include children's playground, preschool and other highly used public places. Given the potential distinction of

Cd, As, Pb, and Zn being influenced by proximal sources, the areas with greatest contamination may warrant investigation into potential point sources in the study area. Additionally, the elevated concentration of Hg in proximal cluster 5 requires further investigation into possible nearby Hg sources.

Data availability statement

The original contributions presented in the study are included in the article/Supplementary Material, further inquiries can be directed to the corresponding author.

Author contributions

The idea of this research was conceived by MB and MD. The field sampling was conducted jointly by MD, MB, CT and TD. All the laboratory work was conducted by MD as part of his master's thesis. Statistical analyses on the data were performed by SB and MD. All authors have contributed by reviewing multiple versions of the manuscript.

Conflict of interest

The authors declare that the research was conducted in the absence of any commercial or financial relationships that could be construed as a potential conflict of interest.

Publisher's note

All claims expressed in this article are solely those of the authors and do not necessarily represent those of their affiliated organizations, or those of the publisher, the editors and the reviewers. Any product that may be evaluated in this article, or claim that may be made by its manufacturer, is not guaranteed or endorsed by the publisher.

Supplementary material

The Supplementary Material for this article can be found online at: https://www.frontiersin.org/articles/10.3389/fenvs.2022.974237/full#supplementary-material

References

Activation Laboratories Ltd (2020a). 1G - aqua regia - Hg cold Vapour FIMS. Actlabs.comAvailable at: https://actlabs.com/geochemistry/exploration-geochemistry/mercury/.

Activation Laboratories Ltd (2020b). Ultratrace 6 - near total digestion - ICP and ICP-ms. Actlabs.comAvailable at: https://actlabs.com/geochemistry/exploration-geochemistry/4-acid-near-total-digestion/.

Adachi, K., and Tainosho, Y. (2004). Characterization of heavy metal particles embedded in tire dust. *Environ. Int.* 30, 1009–1017. doi:10.1016/j.envint.2004.04.004

Angelone, M., Corrado, T., and Dowgiallo, G. (1995). Lead and cadmium distribution in urban soil and plants in the city of Rome: a preliminary study." in Proceedings of the Third International Conference on the Biogeochemistry ofTrace Elements, 23–24. France: INRA Institut National de la Recherche Agronomique, Versailles France.

Apeagyei, E., Bank, M. S., and Spengler, J. D. (2011). Distribution of heavy metals in road dust along an urban-rural gradient in Massachusetts. *Atmos. Environ. X.* 45, 2310–2323. doi:10.1016/j.atmosenv.2010.11.015

Banerjee, A. D. K. (2003). Heavy metal levels and solid phase speciation in street dusts of Delhi, India. *Environ. Pollut.* 123, 95–105. doi:10.1016/S0269-7491(02)00337-8

Buat-Menard, P., and Chesselet, R. (1979). Variable influence of the atmospheric flux on the trace metal chemistry of oceanic suspended matter. *Earth Planet. Sci. Lett.* 42, 399–411. doi:10.1016/0012-821X(79)90049-9

Cal-Prieto, M. J., Carlosena, A., Andrade, J. M., Martínez, M. L., Muniategui, S., López-Mahía, P., et al. (2001). Antimony as a tracer of the anthropogenic influence on soils and estuarine sediments. *Water. Air. Soil Pollut.* 129, 333–348. doi:10.1023/A:1010360518054

Carey, A. E., Gowen, J. A., Forehand, T. J., Tai, H., and Wiersma, G. B. (1980). Heavy metal concentrations in soils of five United States cities, 1972 urban soils monitoring program. *Pestic. Monit. J.* 13, 150.

Charlesworth, S., de Miguel, E., and Ordóñez, A. (2011). A review of the distribution of particulate trace elements in urban terrestrial environments and its application to considerations of risk. *Environ. Geochem. Health* 33, 103–123. doi:10.1007/s10653-010-9325-7

Charlesworth, S., Everett, M., McCarthy, R., Ordóñez, A., and de Miguel, E. (2003). A comparative study of heavy metal concentration and distribution in deposited street dusts in a large and a small urban area: Birmingham and coventry, west midlands, UK. *Environ. Int.* 29, 563–573. doi:10.1016/S0160-4120(03)00015-1

Chen, H., Teng, Y., Lu, S., Wang, Y., and Wang, J. (2015). Contamination features and health risk of soil heavy metals in China. *Sci. Total Environ.* 512–513, 143–153. doi:10.1016/j.scitotenv.2015.01.025

Chen, T. Bin, Zheng, Y. M., Lei, M., Huang, Z. C., Wu, H. T., Chen, H., et al. (2005). Assessment of heavy metal pollution in surface soils of urban parks in Beijing, China. *Chemosphere* 60, 542–551. doi:10.1016/j.chemosphere.2004.12.072

Czarnowska, K. (1980). Akumulacja metali ciężkich w glebach, roślinach i niektórych zwierzętach na terenie Warszawy. *Rocz. Glebozn.* 31, 77.

De Miguel, E., Jiménez De Grado, M., Llamas, J. F., Martín-Dorado, A., and Mazadiego, L. F. (1998). The overlooked contribution of compost application to the trace element load in the urban soil of Madrid (Spain). *Sci. Total Environ.* 215, 113–122. doi:10.1016/S0048-9697(98)00112-0

De Miguel, E., Llamas, J. F., Chacón, E., Berg, T., Larssen, S., Røyset, O., et al. (1997). Origin and patterns of distribution of trace elements in street dust: Unleaded petrol and urban lead. *Atmos. Environ. X.* 31, 2733–2740. doi:10.1016/S1352-2310(97)00101-5

Denier van der Gon, H. A. C., Gerlofs-Nijland, M. E., Gehrig, R., Gustafsson, M., Janssen, N., Harrison, R. M., et al. (2013). The PolicyRelevance of WearEmissions fromRoad transport, nowand in the future-an InternationalWorkshop report and consensus statement. *J. Air Waste Manag. Assoc.* 63, 136–149. doi:10.1080/10962247.2012.741055

Fakayode, S. O., and Olu-Owolabi, B. I. (2003). Heavy metal contamination of roadside topsoil in Osogbo, Nigeria: Its relationship to traffic density and proximity to highways. *Environ. Geol.* 44, 150–157. doi:10.1007/s00254-002-0739-0

Fergusson, J., and Ryan, D. (1984). The elemental composition of street dust from large and small urban areas related to city type, source and particle size. *Sci. Total Environ.* 34, 101–116. doi:10.1016/0048-9697(84)90044-5

Ferreira-Baptista, L., and De Miguel, E. (2005). Geochemistry and risk assessment of street dust in Luanda, Angola: A tropical urban environment. *Atmos. Environ. X.* 39, 4501–4512. doi:10.1016/j.atmosenv.2005.03.026

Gibson, M. J., and Farmer, J. G. (1986). Multi-step sequential chemical extraction of heavy metals from urban soils. *Environ. Pollut. Ser. B Chem. Phys.* 11, 117–135. doi:10.1016/0143-148X(86)90039-X

Gloaguen, T. V., Motta, P. N. S. D., and Couto, C. F. (2021). A grain-size correction for metal pollution indexes in river sediments. *Int. J. Sediment Res.* 36, 362–372. doi:10.1016/j.ijsrc.2020.10.005

Hanfi, M. Y., Mostafa, M. Y. A., and Zhukovsky, M. V. (2020). Heavy metal contamination in urban surface sediments: Sources, distribution, contamination control, and remediation. *Environ. Monit. Assess.* 192, 32. doi:10.1007/s10661-019-7947-5

Harrison, R. M., Smith, D. I. T., and Luhana, L. (1996). Source apportionment of atmospheric polycyclic aromatic hydrocarbons collected from an urban location in Birmingham, U.K. *Environ. Sci. Technol.* 30, 825–832. doi:10.1021/es950252d

Hopke, P. K., and Natusch, D. F. S. (1980). Multielemental characterization of urban roadway dust. *Environ. Sci. Technol.* 14, 164–172. doi:10.1021/es60162a006

Howard, J., Weyhrauch, J., Loriaux, G., Schultz, B., and Baskaran, M. (2019). Contributions of artifactual materials to the toxicity of anthropogenic soils and street dusts in a highly urbanized terrain. *Environ. Pollut.* 255, 113350. doi:10.1016/j.envpol.2019.113350

Laidlaw, M. A. S., Zahran, S., Mielke, H. W., Taylor, M. P., and Filippelli, G. M. (2012). Re-suspension of lead contaminated urban soil as a dominant source of atmospheric lead in Birmingham, Chicago, Detroit and Pittsburgh, USA. *Atmos. Environ. X.* 49, 302–310. doi:10.1016/j.atmosenv.2011.11.030

Lawson, D. R., and Winchester, J. W. (1979). A standard crustal aerosol as a reference for elemental enrichment factors. *Atmos. Environ. X.* 13, 925–930. doi:10.1016/0004-6981(79)90003-9

Lee, C. S. L., Li, X., Shi, W., Cheung, S. C. N., and Thornton, I. (2006). Metal contamination in urban, suburban, and country park soils of Hong Kong: A study based on gis and multivariate statistics. *Sci. Total Environ.* 356, 45–61. doi:10.1016/j.scitotenv.2005.03.024

Li, H., Qian, X., Hu, W., Wang, Y., and Gao, H. (2013). Chemical speciation and human health risk of trace metals in urban street dusts from a metropolitan city, Nanjing, SE China. *Sci. Total Environ.* 456–457, 212–221. doi:10.1016/j.scitotenv.2013.03.094

Lim, S. S., Vos, T., Flaxman, A. D., Danaei, G., Shibuya, K., Adair-Rohani, H., et al. (2012). A comparative risk assessment of burden of disease and injury attributable to 67 risk factors and risk factor clusters in 21 regions, 1990-2010: A systematic analysis for the global burden of disease study 2010. *Lancet* 380, 2224–2260. doi:10.1016/S0140-6736(12)61766-8

Liu, D., Ma, J., Sun, Y., and Li, Y. (2016). Spatial distribution of soil magnetic susceptibility and correlation with heavy metal pollution in Kaifeng City, China. *Catena* 139, 53–60. doi:10.1016/j.catena.2015.11.004

Loganathan, P., Vigneswaran, S., and Kandasamy, J. (2013). Road-deposited sediment pollutants: A critical review of their characteristics, source apportionment, and management. *Crit. Rev. Environ. Sci. Technol.* 43, 1315–1348. doi:10.1080/10643389.2011.644222

Lu, X., Wang, L., Lei, K., Huang, J., and Zhai, Y. (2009). Contamination assessment of copper, lead, zinc, manganese and nickel in street dust of Baoji, NW China. *J. Hazard. Mat.* 161, 1058–1062. doi:10.1016/j.jhazmat.2008.04.052

Lu, X., Wang, L., Li, L. Y., Lei, K., Huang, L., and Kang, D. (2010). Multivariate statistical analysis of heavy metals in street dust of Baoji, NW China. *J. Hazard. Mat.* 173, 744–749. doi:10.1016/j.jhazmat.2009.09.001

Lux, W. (1986). *Schwermetallgehalte und-isoplethen in Böden, subhydrischen Ablagerungen und Pflanzen im Südosten Hamburgs: Beurteilung eines Immissionsgebietes*. Hamburg: Verein zur Förderung d. Bodenkunde.

Manta, D. S., Angelone, M., Bellanca, A., Neri, R., and Sprovieri, M. (2002). Heavy metals in urban soils: a case study from the city of palermo (sicily), Italy. *Sci. Total Environ.* 300, 229–243. doi:10.1016/S0048-9697(02)00273-5

Matlab (2021). Statistics and machine learning Toolbox user's guide, 9954. Available at: https://se.mathworks.com/help/stats/index.html.

McKenzie, E. R., Wong, C. M., Green, P. G., Kayhanian, M., and Young, T. M. (2008). Size dependent elemental composition of road-associated particles. *Sci. Total Environ.* 398, 145–153. doi:10.1016/j.scitotenv.2008.02.052

Mielke, H. W., Laidlaw, M. A. S., and Gonzales, C. R. (2011). Estimation of leaded (Pb) gasoline's continuing material and health impacts on 90 US urbanized areas. *Environ. Int.* 37, 248–257. doi:10.1016/j.envint.2010.08.006

Mielke, H. W., and Reagan, P. L. (1998). Soil is an important pathway of human lead exposure. *Environ. Health Perspect.* 106, 217–229. doi:10.2307/3433922

Mostert, M. M. R., Ayoko, G. A., and Kokot, S. (2010). Application of chemometrics to analysis of soil pollutants. *TrAC Trends Anal. Chem.* 29, 430–445. doi:10.1016/j.trac.2010.02.009

Müller, G. (1969). Index of geoaccumulation in sediments of the rhine river. *Geol. J.*

Murray, K. S., Rogers, D. T., and Kaufman, M. M. (2004). Heavy metals in an urban watershed in southeastern Michigan. *J. Environ. Qual.* 33, 163–172. doi:10.2134/jeq2004.1630

Nemerow N. L. (Editor) (1991). *Stream, lake, estuary, and ocean pollution*. 2nd edition (United States: New York, NY (United States): Van Nostrand Reinhold Publishing Co). Available at: https://www.osti.gov/biblio/7030475.

Nordberg, G. F., Fowler, B. A., Nordberg, M., and Friberg, L. (2007). *Handbook on the Toxicology of metals*. Elsevier. doi:10.1016/B978-0-12-369413-3.X5052-6

Paterson, E., Sanka, M., and Clark, L. (1996). "Urban soils as pollutant sinks - a case study from Aberdeen, Scotland," in *Applied geochemistry* (Elsevier), 129–131. doi:10.1016/0883-2927(95)00081-X

Pfeiffer, E.-M., (1988). *Trace elements and heavy metals in soils and plants of the Southeast Asian metropolis Metro Manila and of some rice cultivation provinces in Luzon, Philippines*. Verein zur Förderung der Bodenkunde in Hamburg.

Quiñonez-Plaza, A., Wakida, F. T., Temores-Peña, J., Rodriguez-Mendivil, D. D., Garcia-Flores, E., Pastrana-Corral, M. A., et al. (2017). Total petroleum hydrocarbons and heavy metals in road-deposited sediments in Tijuana, Mexico. *J. Soils Sediments* 17, 2873–2886. doi:10.1007/s11368-017-1778-1

Ravichandran, M., Baskaran, M., Santschi, P. H., and Bianchi, T. S. (1995). History of trace metal pollution in sabine-neches estuary, beaumont Texas. *Environ. Sci. Technol.* 29, 1495–1503. doi:10.1021/es00006a010

Reimann, C., Filzmoser, P., and Garrett, R. G. (2002). Factor analysis applied to regional geochemical data: Problems and possibilities. *Appl. Geochem.* 17, 185–206. doi:10.1016/s0883-2927(01)00066-x

Sepúlveda, A., Schluep, M., Renaud, F. G., Streicher, M., Kuehr, R., Hagelüken, C., et al. (2010). A review of the environmental fate and effects of hazardous substances released from electrical and electronic equipments during recycling: examples from China and India. *Environ. Impact Assess. Rev.* 30, 28–41. doi:10.1016/j.eiar.2009.04.001

Shi, G., Chen, Z., Xu, S., Zhang, J., Wang, L., Bi, C., et al. (2008). Potentially toxic metal contamination of urban soils and roadside dust in Shanghai, China. *Environ. Pollut.* 156, 251–260. doi:10.1016/j.envpol.2008.02.027

Singh, A. K. (2011). Elemental chemistry and geochemical partitioning of heavy metals in road dust from Dhanbad and Bokaro regions, India. *Environ. Earth Sci.* 62, 1447–1459. doi:10.1007/s12665-010-0630-3

Sorenson, J. R. (2013). *Potential reductions of street solids and phosphorus in urban watersheds from street cleaning*. Cambridge, MassachusettsReston: U.S. Geological Survey, 2009–2011. doi:10.3133/sir20125292

Souto-Oliveira, C. E., Babinski, M., Araújo, D. F., Weiss, D. J., and Ruiz, I. R. (2019). Multi-isotope approach of Pb, Cu and Zn in urban aerosols and anthropogenic sources improves tracing of the atmospheric pollutant sources in megacities. *Atmos. Environ. X.* 198, 427–437. doi:10.1016/j.atmosenv.2018.11.007

Spittler, T. M., and Feder, W. A. (1979). A study of soil contamination and plant lead uptake in Boston urban gardens. *Commun. Soil Sci. Plant Anal.* 10, 1195–1210. doi:10.1080/00103627909366973

Stone, M., and Marsalek, J. (1996). Trace metal composition and speciation in street sediment: Sault Ste. Marie, Canada. *Water Air Soil Pollut.* 87, 149–169. doi:10.1007/BF00696834

Sutherland, R. A. (2000). Bed sediment-associated trace metals in an urban stream, Oahu, Hawaii. *Environ. Geol.* 39, 611–627. doi:10.1007/s002540050473

Taylor, S. R., and McLennan, S. M. (1995). The geochemical evolution of the continental crust. *Rev. Geophys.* 33, 241–265. doi:10.1029/95rg00262

Tchounwou, P. B., Yedjou, C. G., Patlolla, A. K., and Sutton, D. J. (2012). Molecular, clinical and environmental toxicicology volume 3: Environmental Toxicology. *Exp. Suppl.* 101, 133–164. doi:10.1007/978-3-7643-8340-4_6

Thorpe, A., and Harrison, R. M. (2008). Sources and properties of non-exhaust particulate matter from road traffic: A review. *Sci. Total Environ.* 400, 270–282. doi:10.1016/j.scitotenv.2008.06.007

Tomlinson, D. L., Wilson, J. G., Harris, C. R., and Jeffrey, D. W. (1980). Problems in the assessment of heavy-metal levels in estuaries and the formation of a pollution index. *Helgol. Meeresunters.* 33, 566–575. doi:10.1007/BF02414780

Tong, S. T. Y. (1998). Indoor and outdoor household dust contamination in Cincinnati, Ohio, USA. *Environ. Geochem. Health* 20, 123–133. doi:10.1023/A:1006561832381

US EPA (1998). *Ecological risk assessment guidance for superfund: Process for designing and conducting risk assessments*.

US EPA (2007). Guidance for evaluating the oral bioavailability of metals in soils for use in human health risk assessment. Available at: https://semspub.epa.gov/work/03/2218794.pdf.

US-EPA (1996). *Soil screening guidance : User 's guide*. Environ. Prot. Agency. Available at: https://rais.ornl.gov/documents/SSG_nonrad_user.pdf.

USEPA (1975). *Fugitive emissions and fugitive dust emissions*. U.S. Environmental Protection Agency, Office of Air and Water Management, Office of Air Quality Planning and Standards, Control Programs Development Division.

USEPA (1998). *IRIS toxicological review of Chromium VI (1998 final)*. Washington, USEPA 1998: U.S. Environmental Protection Agency.

USEPA (2020). Regional screening level (RSL) summary table 2020 november corrected (TR=1E-06, THQ=1.0). 11. Available at: https://semspub.epa.gov/src/document/HQ/400431.

US. EPA United States Environmental Protection Agency (1998). Toxicological review of trivalent Chromium." in *Toxicol. Rev. Trivalent Chromium (CAS No. 16065-83-1) - support summ. Inf. Integr. Risk inf. Syst*. Available at: https://iris.epa.gov/static/pdfs/0028tr.pdf.

van Hees, E. H. P., Chopin, E. I. B., Sebastian, T. M., Washington, G. D., Germer, L. A. M., Domanski, P., et al. (2010). Distribution, sources, and behavior of trace elements in the Clinton River Watershed, Michigan. *J. Gt. Lakes. Res.* 36, 606–617. doi:10.1016/j.jglr.2010.08.007

Wang, G., Chen, J., Zhang, W., Chen, Y., Ren, F., Fang, A., et al. (2019). Relationship between magnetic properties and heavy metal contamination of street dust samples from Shanghai, China. *Environ. Sci. Pollut. Res.* 26, 8958–8970. doi:10.1007/s11356-019-04338-4

Wedepohl, H. K. (1995). The composition of the continental crust. *Geochim. Cosmochim. Acta* 59, 1217–1232. doi:10.1016/0016-7037(95)00038-2

Wei, B., and Yang, L. (2010). A review of heavy metal contaminations in urban soils, urban road dusts and agricultural soils from China. *Microchem. J.* 94, 99–107. doi:10.1016/j.microc.2009.09.014

Wilbur, S., Abadin, H., Fay, M., Yu, D., Tencza, B., Ingerman, L., et al. (2012). *Toxicological profile for Chromium*. Atlanta (GA): Agency for Toxic Substances and Disease Registry US.

Wilcke, W., Müller, S., Kanchanakool, N., and Zech, W. (1998). Urban soil contamination in Bangkok: heavy metal and aluminium partitioning in topsoils. *Geoderma* 86, 211–228. doi:10.1016/S0016-7061(98)00045-7

Wong, C. S. C., Li, X., and Thornton, I. (2006). Urban environmental geochemistry of trace metals. *Environ. Pollut.* 142, 1–16. doi:10.1016/j.envpol.2005.09.004

Wong, M. H., Wong, J. W. C., and Chen, T. B. (1996). "Trace metal contamination of the Hong Kong soil environment: a review," in *Contaminants and the soil environment in the australasia-pacific region* Kluwer Academic Publ, 501.

Yang, T., Liu, Q., Li, H., Zeng, Q., and Chan, L. (2010). Anthropogenic magnetic particles and heavy metals in the road dust: magnetic identification and its implications. *Atmos. Environ. X.* 44, 1175–1185. doi:10.1016/j.atmosenv.2009.12.028

Yongming, H., Peixuan, D., Junji, C., and Posmentier, E. S. (2006). Multivariate analysis of heavy metal contamination in urban dusts of Xi'an, Central China. *Sci. Total Environ.* 355, 176–186. doi:10.1016/j.scitotenv.2005.02.026

Yuen, J. Q., Olin, P. H., Lim, H. S., Benner, S. G., Sutherland, R. A., and Ziegler, A. D. (2012). Accumulation of potentially toxic elements in road deposited sediments in residential and light industrial neighborhoods of Singapore. *J. Environ. Manage.* 101, 151–163. doi:10.1016/j.jenvman.2011.11.017

Zhang, C., Qiao, Q., Appel, E., and Huang, B. (2012). Discriminating sources of anthropogenic heavy metals in urban street dusts using magnetic and chemical methods. *J. Geochem. Explor.* 119–120, 60–75. doi:10.1016/j.gexplo.2012.06.014

Zhang, C., Qiao, Q., Piper, J. D. A., and Huang, B. (2011). Assessment of heavy metal pollution from a Fe-smelting plant in urban river sediments using environmental magnetic and geochemical methods. *Environ. Pollut.* 159, 3057–3070. doi:10.1016/j.envpol.2011.04.006

Zhang, J., Wang, Y., Liu, J., Liu, Q., and Zhou, Q. (2016). Multivariate and geostatistical analyses of the sources and spatial distribution of heavy metals in agricultural soil in Gongzhuling, Northeast China. *J. Soils Sediments* 16, 634–644. doi:10.1007/s11368-015-1225-0

Zhang, M., and Wang, H. (2009). Concentrations and chemical forms of potentially toxic metals in road-deposited sediments from different zones of Hangzhou, China. *J. Environ. Sci.* 21, 625–631. doi:10.1016/S1001-0742(08)62317-7

Zheng, Y. M., Chen, T. Bin, and He, J. Z. (2008). Multivariate geostatistical analysis of heavy metals in topsoils from Beijing, China. *J. Soils Sediments* 8, 51–58. doi:10.1065/jss2007.08.245

frontiers | Frontiers in Environmental Science

TYPE Original Research
PUBLISHED 15 September 2022
DOI 10.3389/fenvs.2022.979922

OPEN ACCESS

EDITED BY
Buyun Du,
Jiangsu Open University, China

REVIEWED BY
Wenjie Ren,
Institute of Soil Science (CAS), China
Xingang Zhou,
Northeast Agricultural University, China

*CORRESPONDENCE
Pan Wu,
pwu@gzu.edu.cn

SPECIALTY SECTION
This article was submitted to Toxicology, Pollution and the Environment, a section of the journal Frontiers in Environmental Science

RECEIVED 28 June 2022
ACCEPTED 18 August 2022
PUBLISHED 15 September 2022

CITATION
Sun C, Wu P, Wang G and Kong X (2022), Heavy metal pollution decreases the stability of microbial co-occurrence networks in the rhizosphere of native plants.
Front. Environ. Sci. 10:979922.
doi: 10.3389/fenvs.2022.979922

Heavy metal pollution decreases the stability of microbial co-occurrence networks in the rhizosphere of native plants

Caili Sun[1,2,3], Pan Wu[1,2]*, Guanghao Wang[1,2] and Xingjie Kong[1,2]

[1]College of Resource and Environmental Engineering, Guizhou University, Guiyang, China, [2]Key Laboratory of Karst Georesources and Environment, Ministry of Education, Guizhou University, Guiyang, China, [3]College of Eco-Environmental Engineering, Guizhou Minzu University, Guiyang, China

Soil microorganisms play an important role in maintaining soil quality and function, although the response of soil microbial biodiversity to heavy metals has been extensively investigated, the microbe-microbe associations under the influence of both native plant species and extremely high heavy metal contamination are not well documented. We examined the diversity and composition of microbial communities and the physicochemical properties in the rhizosphere of three native plant species, *Carex breviculmis*, *Buddleja davidii*, and *Artemisia annua* growing on and around a Pb-Zn waste heap with a nearly 100-year history of natural recovery. Both plant species and heavy metals influence soil microbial diversity and composition. *C. breviculmis* and *A. annua* showed a prominent advantage in increasing rhizosphere microbial diversity and richness as well as network complexity compared with plant *Buddleja davidii* at severely contaminated soil, which was mainly related to the accumulation of soil nutrients such as soil organic carbon (SOC), total nitrogen ammonium nitrogen and nitrate nitrogen rather than a reduction in heavy metal concentrations. Moreover, the heavy metal concentration and soil nutrient levels significantly affected the microbial groups affiliated with Proteobacteria, Chloroflexi, Ascomycota, and Basidiomycota, in which those affiliated with Chloroflexi and Ascomycota were positively associated with heavy metals. Soil microbial network on the Pb-Zn waste heap exhibited higher average degree and a higher proportion of positive links than those around the waste heap, and thus soil microbial structure became more complexity and unstable with increasing heavy metal pollution.

KEYWORDS

trace element, Pb-Zn waste heap, biodiversity, co-occurrence patterns, plant-soil interaction

Introduction

Over the past several decades, prosperous mining activities have promoted the development of the Chinese economy. However, they have generated vast amounts of solid waste, which results in the degradation of the surrounding ecosystem (Becerra-Castro et al., 2012; Li et al., 2021). Li (2006) and Liu *et al.* (2020) reported that mining activities alone have generated approximately 3.2 Mha of wasteland and that this value is increasing by 46,700 ha/year in China. Waste materials contain large amounts of heavy metals and metalloids that often reach toxic levels and are susceptible to dispersing into the adjacent ecosystem *via* wind dispersion and water erosion (Luo et al., 2019), imposing a threat to life, including humans, plants, and microorganisms (Epelde et al., 2014). Some heavy metals and metalloids, such as Pb, Cd, Cr, and As, are nonessential for living organisms. However, because of their reactivity with thiols or other groups, these heavy metals can interfere with physiological processes even at low concentrations by disturbing enzymatic reactions, triggering cell membrane damage, and modifying deoxyribose nucleic acid (DNA) structure (Dubey et al., 2018; DalCorso et al., 2019). In China, soil heavy metal contamination resulting from mining activities has become a severe environmental problem, especially in areas rich in nonferrous metal resources (Li Q. et al., 2020).

Heavy metals impact ecosystems through a variety of effects on plants, soils, and microbial communities (Azarbad et al., 2013; Barra Caracciolo and Terenzi, 2021). Metalliferous soils, such as waste heaps, are often sandy and dry, with low organic matter and nutrient availability, as well as elevated heavy metal contents (Borymski et al., 2018). This leads to strong selective pressure driving the evolution and adaptation of plants and microorganisms (Epelde et al., 2014). In this context, some metal-tolerant plants have been the focus of previous studies (Becerra-Castro et al., 2012; Elbehiry et al., 2020) because of their biological mechanisms that resist and tolerate heavy metals. Pseudo-metallophyte populations of *Carex breviculmis* (Lei and Duan, 2008; Xu et al., 2020), *Buddleja davidii* (Margui et al., 2006), and *Artemisia annua* (Petriccione et al., 2013; Inelova et al., 2021) are metal-tolerant plant species that have exhibited good abilities in colonizing Pb, Zn, and Cd contaminated soils. Soil microorganisms play an important role in maintaining soil quality and function by decomposing organic matter, participating in nutrient cycling, and reducing heavy metal toxicity (Banning et al., 2011). Heavy metal/metalloids alter various metabolic processes of microorganisms, including blocking essential functional groups, displacing other metal ions, and inactivating biological molecules (Chen et al., 2020). The effect of heavy metal contamination on soil microbial communities is usually adverse, resulting in the reduction of microbial biomass and activity, the disturbance of specific taxa, and shifts in the composition of the microbiome (Azarbad et al., 2013; Epelde et al., 2014). Although previous studies have revealed that soil microbial structure, composition, and diversity, can change under heavy metal contamination, it is unclear how microbe-microbe associations change with increasing heavy metal pollution, especially when considering the complex interactions between heavy metal/metalloid-contaminated soils and plants (Borymski et al., 2018; Chun et al., 2021). Therefore, identifying inter-taxa correlations is crucial for comprehensively understanding microbial community structures and predicting the response of soil ecosystems to future degenerative and pollution processes (Cheng et al., 2020).

In addition to the phytoextraction and phytostabilization of soil heavy metals, metal-tolerant plants strongly affect soil microbial biomass and activity through the rhizosphere effect, which is thought to arise from the deposition of various organic compounds, including amino acids, carbohydrates, and flavonoids, from plants into soils (Haichar et al., 2008; Montiel-Rozas et al., 2016). The nutrient-rich microenvironment provided by rhizosphere deposition allows certain microbial communities to thrive, as different plant species produce different exudates with specific compositions (Haichar et al., 2008; Borymski et al., 2018). Ali et al. (2013) reported that the metabolic activities of rhizosphere microorganisms are 10–100 times higher than those in bulk soil because of the exudates secreted by plants. Metal-tolerant plants select specialized metal-tolerant microorganisms to inhabit their rhizosphere, with a preference for plant growth-promoting bacteria that enhance the phytoremediation of heavy metal-contaminated soils (Hamidpour et al., 2019; Li Z. et al., 2020). Therefore, the interactions between metal-tolerant plants and accompanying microorganisms, as well as the surrounding environment, play key roles in maintaining nutrient cycling and element turnover (Epelde et al., 2010). On this basis, it is important to study the biodiversity of rhizosphere microbial communities linked with plant-soil-microbe interactions to better understand soil functions impacted by both heavy metal pollution and plant species to improve phytoremediation of mine sites in the future.

Northwestern Guizhou, China, is an area rich in nonferrous metal resources, especially lead zinc ore. This region has an approximately 300-year-old history of zinc mining and smelting using indigenous methods, and large volumes of Pb-Zn waste (more than 20 million tons by 2000) have been left and piled onto the surrounding farmland with almost no safety treatment (Yang et al., 2016). In this study, we examined a Pb-Zn waste heap with a nearly 100-year history, which has been naturally colonized by some native wild plant species (*C. breviculmis*, *B. davidii*, and *A. annua*) with limited human disturbance. We hypothesized that plant species will significantly affect rhizosphere microbial richness, diversity and interaction, and that soil microbe-microbe association will be different on and around the Pb-Zn waste heap. To test this hypothesis, we collected the rhizosphere of the aforementioned plant species both on and

around the Pb-Zn waste heap. Heavy metals/metalloids and soil properties were quantified, and microbial diversity was measured using high-throughput sequencing to: 1) assess the response of soil properties to plant species and sampling sites, including soil nutrients and heavy metal contents, as well as the diversity and composition of microbial communities; 2) explore the major environmental factors contributing to soil microbial community variations; and 3) profile the microbial association in the rhizosphere soil of three metal-tolerant plants on and around the Pb-Zn waste heap. The results of this study will provide crucial insights into the restoration of heavy metal-contaminated soils.

Methods and materials

Study site

An abandoned Pb-Zn waste heap located in the northwest of the Guizhou Province, China (26°54′N, 104°54′W) was used as the study site. The local climate is subtropical humid, with a mean annual precipitation of 800–1000 mm and an average temperature of 10 °C. Rainfall is irregularly distributed throughout the year, with 55% occurring from June to August. This area is famous for its long history of Zn smelting using indigenous methods, which generated large amounts of waste slag (more than 20 million tons by 2000) and formed numerous Pb-Zn waste heaps (Yang et al., 2016). Waste slag from Zn smelting is a mixture of ore smelting slag and small amounts of unburned cinders and contains high levels of toxic heavy metals, including Cu, Pb, Zn, and Cd (Luo et al., 2019).

Sample collection

At the time of this study, the selected Pb-Zn waste heap is nearly 100 years old, during which period it has been restored naturally, almost without human interference. *C. breviculmis*, *B. davidii*, and *A. annua* are common native wild plant species on and around the Pb-Zn waste heap. *C. breviculmis* is the dominant perennial herb. *A. annua* is a late-successional plant in the herbaceous stage, and *B. davidii* is a pioneer plant in the shrub stage.

Four replicate rhizosphere samples of *C. breviculmis*, *B. davidii*, and *A. annua* were collected on and around the abandoned Pb-Zn waste heap. Relatively isolated plants were selected to reduce the impact of nearby plants and consistent environmental conditions were ensured to reduce the impact of environmental heterogeneity, when collecting the rhizosphere of each plant. The rhizosphere soil samples were collected by shaking off the loosely attached bulk soil adhered to the root systems. In addition, unvegetated soil was collected from the Pb-Zn waste heap as a control (CK). Each sample was divided into two subsamples after all roots, stones, and litter were removed. One subsample was immediately stored at -80 °C for microbiological analysis, and a second subsample was air-dried for physicochemical analysis. Sampling sites on and around the Pb-Zn waste heap were defined as S1 and S2, respectively, and the rhizosphere samples of *C. breviculmis*, *B. davidii*, and *A. annua* were defined as CB, BD, and AA, respectively.

Physicochemical analyses

Soil organic carbon (SOC), total nitrogen (TN), total phosphorus (TP), available phosphorus (AP) ammonium nitrogen (AN), nitrate nitrogen (NN), soil pH, and heavy metals were quantified using standard methods and detailed descriptions are provided in the Supplementary Materials.

DNA extraction, sequencing, and data processing

DNA was extracted from 0.5 g of each soil sample using a FastDNA Spin Kit (MP Biomedicals, Cleveland, United States) following the manufacturer's specifications. DNA extracts were diluted ten-fold and assessed for quality and quantity using a spectrophotometer (NanoDrop ND-1000, NanoDrop Technologies, Wilmington, United States). The integrity of the DNA extracts was confirmed by 1% agarose gel electrophoresis. The bacterial 16S rRNA and fungal 18S rRNA genes were amplified using the primer pairs 338F/806R (Deng et al., 2018) and ITS1F/ITS2R (Bellemain et al., 2010), respectively. The primers were tagged with unique barcodes for each sample. A PCR was performed in a 30 μL solution containing 2 μL of sterile ultrapure water, 15 μL of Phusion Master Mix (2X), 3 μL of 6 μM primer, and 10 μL of template DNA (5–10 ng). A PCR was conducted at 98°C for 60 s, followed by 30 cycles of 98°C for 10 s, 50°C for 30 s, 72°C for 30 s, and 72°C for 5 min. The amplicons were purified and high-quality libraries were generated using the TruSeq® DNA PCR-Free Sample Preparation Kit (Illumina, United States) following the manufacturer's recommendations. All samples were pooled in equimolar amounts and sequenced on an Illumina HiSeq PE300 platform.

Bacterial and fungal sequences were analyzed using the UPARSE pipeline (Edgar 2013). Briefly, paired-end reads were merged into single sequences, after which the chimeras were removed using the UCHIME algorithm (Caporaso et al., 2010). Sequences with 97% similarity were clustered into operational taxonomic units (OTUs). Low-abundance OTUs

were eliminated from the OTU table if they did not present at least two counts across all samples in the experiment. Bacteria were identified using the Silva reference database (http://www.arb-silva.de) with the RDP classifier (Wang et al., 2007) and fungi were identified using the Unite database (https://unite.ut.ee/) with the BLAST tool in QIIME (Abarenkov et al., 2010).

Statistical analysis

Soil properties, microbial diversity, and abundance at each sampling site were evaluated among the three plant species, using a one-way analysis of variance, followed by an LSD post hoc test at $p < 0.05$. Soil properties, microbial diversity, and abundances between the two sampling sites were compared using a *t*-test ($p < 0.05$). The Shannon and Richness indices were used to represent plant diversity, and Chao1 and Shannon indices were used to indicate the richness and diversity of the soil microbial communities. A two-way ANOVA was conducted to determine the individual and interacting effects of plant species and sampling sites on each soil property, bacterial and fungal composition and α-diversity. Principal Co-ordinates Analysis (PCoA) and an ANOSIM test based on the Bray–Curtis distances of the sequencing data was used to assess differences in the structures of the microbial communities. Mantel tests based on Bray-Curtis distance similarities calculated at the OTU (operational taxonomic unit) level were used to identify the plant and soil factors correlated with microbial community composition. A hierarchical partitioning was used to estimate the importance of individual and group of environmental variables (edaphic variables and heavy metals) in predicting soil microbial communities. Statistical tests and graphic plotting were performed using the packages vegan, reshape2, sem, packfor, picante, and ggplot2 in R v.4.0.3 (R Development Core Team, 2019).

Networks were constructed for the microbial communities for bare soils and rhizosphere soils of three metal-tolerant plants at S1 and S2. All pairwise Sparse Correlations for Compositional (SparCC) data among microbial nodes using the Fastspar algorithm with 1000 bootstraps and 1000 permutations were calculated to control the false discovery rate. A robust correlation coefficient of $|r| > 0.9$ and $p < 0.01$ were retained to construct networks. The networks were visualized using Gephi (version 0.9.2; https://gephi.org/). The nodes in the networks represent OTUs, in which the node size is proportional to the number of connections (degrees), and the node color represents microbial taxonomy. The edges between each pair of nodes (i.e., links) correspond to positive or negative correlations between the nodes.

Results

Soil characteristics and heavy metal contents

In general, plant species significantly affected the soil nutrient contents, especially SOC, TN, and pH, while heavy metals significantly differed between the two sampling sites (Table 1). The rhizosphere of AA exhibited the highest contents of SOC (11.669 and 15.656 g kg^{-1}) and TN (4.367 and 4.534 g kg^{-1}) compared with the other two plant species at both S1 and S2 and that in the non-vegetated soil (CK) at S1. The pH of the CB rhizosphere was the highest at S1 and S2, and was significantly higher than that of CK at S1. Overall, the heavy metal content and pH values in the rhizosphere of all three plant species had higher values at S1 than at S2.

Abundance and diversity of soil bacteria and fungi

A total of 1,558,675 high-quality sequences of bacteria and 1,840,010 high-quality sequences of fungi were obtained. The richness (Richness index) and diversity (Shannon index) of the soil bacterial communities in the rhizosphere of plant BD were significantly lower than in plants CB and AA but were not significantly different from that of the CK at S1; similarly, the richness (Richness index) and diversity (Shannon index) of the soil fungal communities in the rhizosphere of plant BD were significantly lower than in AA but were not significantly different from that of the plant CB and CK at S1. The diversity of the bacterial community was significantly higher in the rhizosphere of plants CB and BD than in AA, and the richness of the fungal community was significantly higher in the rhizosphere of plant CB than in plant BD at S2. Moreover, the richness and diversity of the bacterial and fungal communities in the rhizosphere of plant BD were significantly lower at S1 than at S2 (Table 2).

Overall patterns of soil bacterial and fungal communities

A total of eight soil bacterial phyla (relative abundances >1%) were obtained, decreasing in relative abundance as follows: Actinobacteria (25.7%), Proteobacteria (21.2%), Chloroflexi (19.4%), Acidobacteria (15.6%), Gemmatimonadota (3.6%), Myxococcota (2.5%), Planctomycetota (2.1%), and Firmicutes (1.9%) (Figure 1 and Supplementary Table S1). Plant species had a significant effect on Proteobacteria and Chloroflexi, of which Proteobacteria showed a significantly higher relative abundance in the rhizosphere of AA than in CB at both S1 and S2, while Chloroflexi exhibited the opposite trend. Between sampling sites, the relative abundance of Proteobacteria in the rhizosphere of

TABLE 1 Physico-chemical parameters and heavy metal content in sampled soils.

Sampling sites	Plant species	SOC (g kg^{-1})	TN (g kg^{-1})	TP (g kg^{-1})	AP (mg kg^{-1})	An (mg kg^{-1})	NN (mg kg^{-1})	pH	Moisture	Cu (mg kg^{-1})	Zn (mg kg^{-1})	As (mg kg^{-1})	Cd (mg kg^{-1})	Pb (mg kg^{-1})
S1	CK	8.2 ± 0.4bc	1.0 ± 0.1b	0.1 ± 0.0a	7.1 ± 0.9a	3.6 ± 0.6a	11.2 ± 1.4b	5.8 ± 0.1c	0.3 ± 0.0a	411.7 ± 46.8a	47,879.5 ± 8747.3a	1407.8 ± 148.4a	40.6 ± 9.0ab	6315.9 ± 1246.5a
	CB	6.3 ± 0.511c	1.0 ± 0.2b	0.4 ± 0.1a	8.0 ± 0.8a	3.6 ± 0.3a*	12.1 ± 1.1b	6.5 ± 0.1a*	0.3 ± 0.0a	343.4 ± 34.3a*	44,561.9 ± 5149.7a*	1155.9 ± 206.5a*	56.8 ± 11.4a*	4212.8 ± 472.6a*
	BD	9.3 ± 0.6bc*	1.9 ± 0.5b	0.2 ± 0.1a	8.2 ± 1.3a	3.8 ± 0.3a	10.5 ± 0.8b	6.2 ± 0.1ab	0.3 ± 0.0a	366.2 ± 19.0a*	48,827.2 ± 3614.7a*	1729.4 ± 75.8a*	30.1 ± 4.8ab*	4398.3 ± 697.7a*
	AA	11.7 ± 1.0a	4.4 ± 0.6a	0.3 ± 0.1a	9.3 ± 1.6a	4.5 ± 0.5a	22.4 ± 2.4a	6.0 ± 0.1bc*	0.4 ± 0.1a	408.9 ± 54.7a*	35,966.8 ± 5848.9b*	1408.0 ± 250.5a*	21.4 ± 3.3b*	6714.7 ± 1070.6a*
S2	CB	8.8 ± 1.0B	2.4 ± 0.2B	1.6 ± 1.2A	5.4 ± 0.47A	6.3 ± 0.3A	18.1 ± 2.5A	5.8 ± 0.3A	0.4 ± 0.0A	203.1 ± 15.1A	22,295.0 ± 4118.2A	624.9 ± 81.5A	28.8 ± 3.6A	2897.6 ± 605.8A
	BD	15.9 ± 1.9A	2.8 ± 0.2B	0.6 ± 0.1A	6.1 ± 1.1A	6.3 ± 0.9A	17.0 ± 2.7A	5.7 ± 0.2 A B	0.3 ± 0.1A	222.4 ± 23.6A	1609.5 ± 334.8B	51.0 ± 16.5B	3.3 ± 0.7B	128.6 ± 68.0B
	AA	15.7 ± 0.8A	4.5 ± 0.6A	0.7 ± 0.1A	8.4 ± 1.7A	7.0 ± 0.7A	14.5 ± 1.5A	5.1 ± 0.1B	0.5 ± 0.0A	167.4 ± 8.9A	3344.7 ± 303.143B	58.2 ± 16.3B	6.0 ± 0.9B	340.3 ± 110.3B
Two-way ANOVA														
Plant species		<0.001	<0.001	0.192	0.222	0.276	0.070	<0.001	0.025	0.772	0.008	0.450	<0.001	0.080
Sampling site		<0.001	0.035	0.009	0.081	<0.001	0.344	<0.001	0.047	<0.001	<0.001	<0.001	<0.001	<0.001
Sampling site×Plant species		0.175	0.410	0.046	0.767	0.992	0.002	0.366	0.567	0.188	0.017	0.002	0.457	0.002

CB, BD, and AA respectively represented *C. breviculmis*, *B. davidii*, and *A. annua*. S1, sample site on the zinc smelter waste heap; S2, sample site around the zinc smelter waste heap. Mean values (mean ± se, n = 4) followed by different lowercase letters presented significant differences of sampled soils collected on the zinc smelter waste heap (S1), by different capital letters represent significant differences of sampled soils collected near the zinc smelter waste heap (S2). SOC, soil organic carbon; TN, total nitrogen; TP, total phosphorus; AP, available phosphorus; AN, ammonium nitrogen; NN, nitrate nitrogen * indicates significant differences between S1 and S2. $p < 0.05$ is considered as a statistical difference (LSD, test). The significant p values ($p < 0.05$) from two-way ANOVA, are in bold.

10.3389/fenvs.2022.979922

TABLE 2 Soil bacterial and fungal diversities for bare soils and rhizosphere soils of three metal-tolerant plants at S1 and S2.

Sampling Sites	Plant Species	Bacterial Community			Fungal Community		
		Richness	Shannon	Chao1	Richness	Shannon	Chao1
S1	CK	1141.8 ± 133.0ab	8.3 ± 0.3ab	1351.6 ± 118.0a	225.3 ± 39.0ab	4.5 ± 0.6a	246.2 ± 41.3ab
	CB	1311.3 ± 77.9a	8.7 ± 0.1a	1477.7 ± 99.4a	258.5 ± 35.7ab	4.4 ± 0.6a	282.5 ± 42.5ab
	BD	970.3 ± 115.7b	7.8 ± 0.4b	1201.2 ± 106.1a	188.8 ± 37.8b	3.6 ± 0.6a	205.2 ± 45.6b
	AA	1299.3 ± 41.3a	8.6 ± 0.1a	1483.7 ± 37.7a	308.3 ± 23.2a	4.5 ± 0.1a	339.9 ± 35.2a
S2	CB	1430.3 ± 14.3A	8.8 ± 0.1A	1645.3 ± 8.2A	425.5 ± 11.1A*	5.5 ± 0.4A	449.5 ± 13.4A*
	BD	1389.3 ± 58.5A*	8.9 ± 0.1A*	1550.6 ± 54.1A*	355.3 ± 18.3B*	5.6 ± 0.2A*	370.0 ± 23.3B*
	AA	1147.3 ± 35.0A*	8.1 ± 0.3B	1334.3 ± 27.1B*	375.5 ± 27.7 A B	4.9 ± 0.4A	431.3 ± 21.3 A B
Two-way ANOVA							
Plant species		0.074	0.042	0.253	0.357	0.594	0.140
Sampling site		0.027	0.117	0.035	<0.001	0.003	<0.001
Sampling site×Plant species		<0.001	0.003	0.001	0.013	0.201	0.041

CB, BD, and AA respectively represented *C. breviculmis*, *B. davidii*, and *A. annua*. S1, sample site on the zinc smelter waste heap; S2, sample site around the zinc smelter waste heap. Mean values (mean ± se, n = 4) followed by different lowercase letters presented significant differences of sampled soils collected on the zinc smelter waste heap (S1), by different capital letters represent significant differences of sampled soils collected near the zinc smelter waste heap (S2). * followed after letters indicates significant differences between S1 and S2. $p < 0.05$ is considered as a statistical difference (LSD, test). The significant p values ($p < 0.05$) from two-way ANOVA, are in bold.

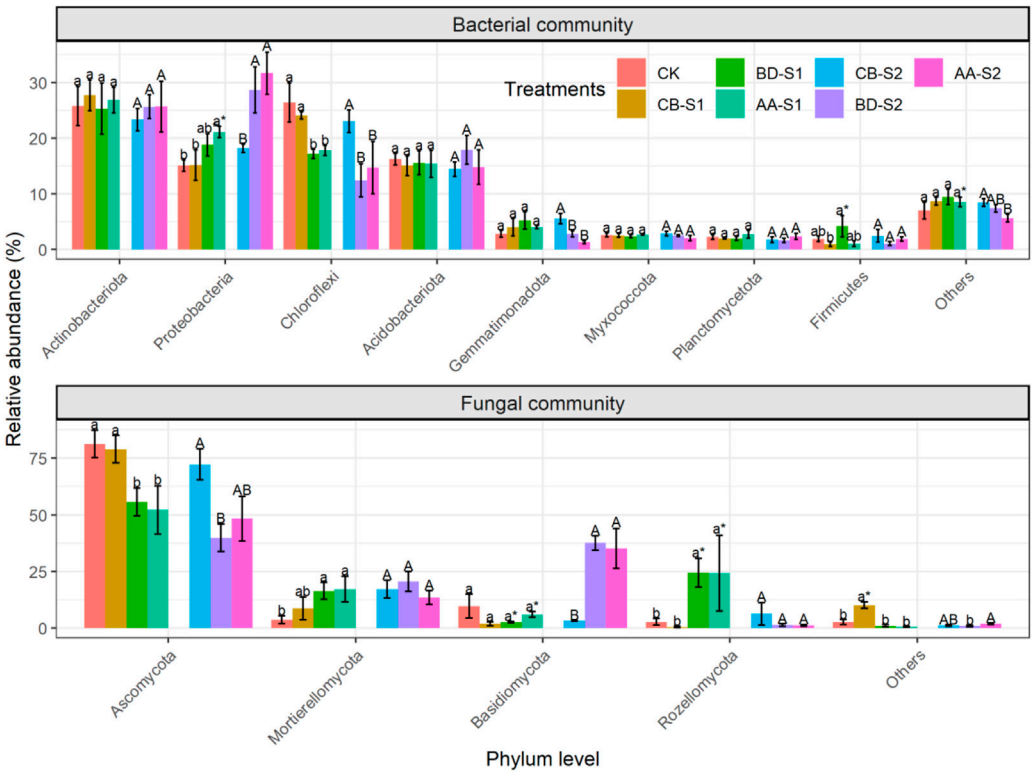

FIGURE 1
Soil microbial composition at the phylum level for bare soils and rhizosphere soils of three metal-tolerant plants at S1 and S2. CB, BD and AA respectively represented *C. breviculmis*, *B. davidii*, and *A. annua*. S1, sample site on the zinc smelter waste heap; S2, sample site around the zinc smelter waste heap. Mean values (mean ± se, n = 4) followed by different lowercase letters presented significant differences of sampled soils collected on the zinc smelter waste heap (S1), by different capital letters represent significant differences of sampled soils collected near the zinc works (S2). * followed after letters indicates significant differences between S1 and S2. $p < 0.05$ is considered as a statistical difference (LSD test).

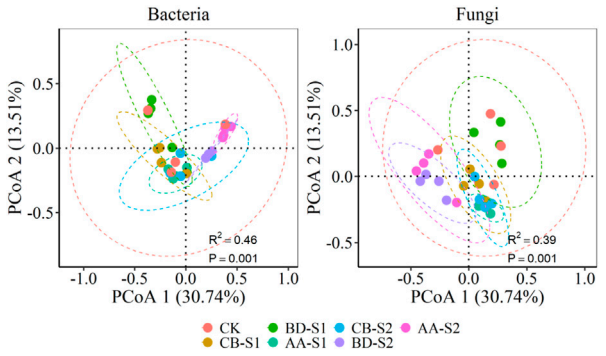

FIGURE 2
The NMDS ordinations of bacterial and fungal communities (OTU level) for bare soils and rhizosphere soils of three metal-tolerant plants at S1 and S2. Individual data points with different colors represent individual soil samples. Analysis of similarity (ANOSIM) test showing the difference of bacterial and fungal community structure among bare soils and rhizosphere soils of three metal-tolerant plants at S1 and S2. CB, BD and AA respectively represented *C. breviculmis*, *B. davidii*, and *A. annua*. S1, sample site on the zinc smelter waste heap; S2, sample site around the zinc smelter waste heap.

AA was significantly lower at S1 than at S2. Regarding the fungal community, four fungal phyla with a relative abundance >1% were obtained, including Ascomycota (61.2%), Mortierellomycota (13.8%), Basidiomycota (13.7%), and Rozellomycota (8.6%). The relative abundance of Ascomycota was significantly higher and that of Rozellomycota was significantly lower in the rhizosphere of CB than in the rhizospheres of BD and AA at both S1 and S2. For the rhizospheres of BD and AA, the relative abundances of Basidiomycota and Rozellomycota were significantly lower and higher, respectively, at S1 than at S2.

PCoA accompanied with ANOSIM test showed results that rhizosphere bacterial and fungal community composition was significantly different among plant species as well as between sampling sites (Figure 2). Furthermore, pairwise ANOSIM test showed that both bacterial and fungal community from S1 were different from those of S2. Rhizosphere bacterial and fungal community of plants CB and BD were not significantly different but they were significantly distinct from those of plant AA at S1. Moreover, rhizosphere bacterial community of plant BD and rhizosphere fungal community of plants CB and BD were significantly different from those of CK. At sampling site of S2, rhizosphere bacterial and fungal community of plant CB were significantly different from those of plants BD and AA, which showed no significant difference (Supplementary Table S2). Additionally, some soil microbial functional profiles also differed significantly between S1 and S2 (Supplementary Figure S1). For example, the proportion of bacterial functional profiles related to glycine, serine, and threonine metabolism and the fungal functional profiles related to endophyte-plant pathogens were remarkably higher at S1 than at S2. Conversely, samples from S2 had significantly higher fungal functional profiles related to endophyte-soil saprotrophs, animal pathogen-clavicipitaceous endophyte-fungal parasites, wood saprotrophs and plant saprotroph-wood saprotrophs, as compared with those from S1.

Co-occurrence networks for rhizosphere microbial community of three metal-tolerant plants

Co-occurrence networks of soil microbial community for bare soils and rhizosphere soils of three metal-tolerant plants at S1 and S2 were constructed (Figure 3), and topological properties were calculated to describe the complex pattern of network and to compare the real network with an identically sized Erdös-Réyni random network (Table 3). Overall, the structure properties of the real networks were greater than the Erdös-Réyni random networks, indicating that the former are more clustered than the latter. Soil microbial network of CK was the largest (more edges) and most complex (higher average degree) compared with rhizosphere microbial networks of three plants at S1. Furthermore, rhizosphere microbial networks of plant CB and AA were larger and more complex than that of plant BD at S1, but rhizosphere microbial networks showed no obvious different among plant species at S2. Compared with site S2, rhizosphere microbial networks at S1 were larger and more complex, and the ratio of positive to negative edges of the microbial network was higher. Moreover, there were fewer nodes affiliated with Ascomycota but more nodes affiliated with Chlofoflexi, Planctomycetota and Myxococcota at S1 compared with S2 (Supplementary Table S3). Ascomycota, Actinobacteriota, Chloroflexi, Actinobacteriota and Rozellomycota were the keystone taxa in networks for bare soils and rhizosphere soils of three metal-tolerant plants at S1 and S2 (Supplementary Table S4).

Relating soil microbial communities to environmental factors

The Mantel test results for the correlation between community composition and environmental variables revealed that both the bacterial and fungal communities were significantly correlated with heavy metals (Cu, Zn, As, Cd and Pb). In addition, the bacterial community had significant correlations with SOC, TN, AN, pH, and moisture, while the fungal community only had significant correlations with SOC and AN. Additionally, there was a significant positive correlation within indices of soil nutrients, which were negatively correlated and heavy metals

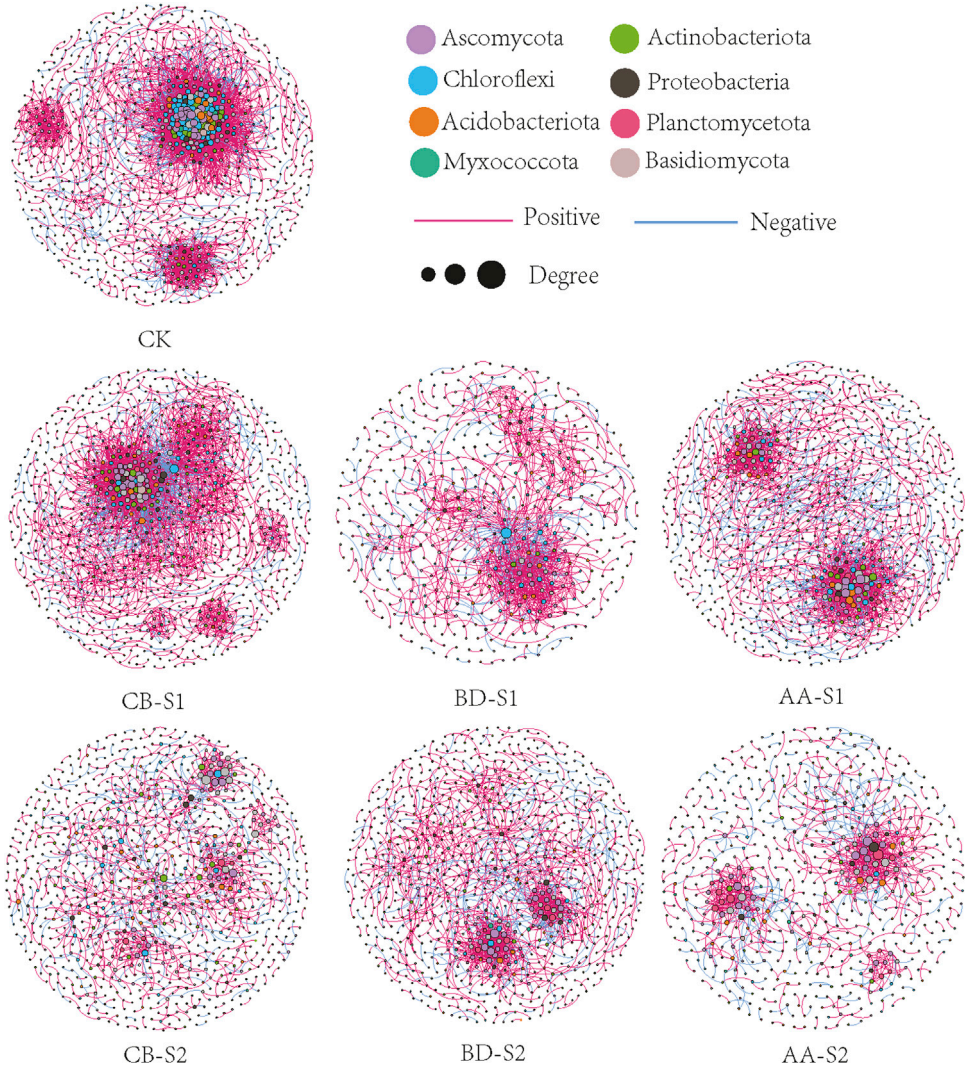

FIGURE 3
Co-occurrence networks of soil microbial community for bare soils and rhizosphere soils of three metal-tolerant plants at S1 and S2. The nodes are colored by the phylum level, and size of each node is proportional to its degree. The line between each pair of nodes represent positive (red) and negative (blue) correlation with $p < 0.01$ and $|r| > 0.9$. CB, BD and AA respectively represented *C. breviculmis*, *B. davidii*, and *A. annua*. S1, sample site on the zinc smelter waste heap; S2, sample site around the zinc smelter waste heap.

(Supplementary Figure S2). In general, the edaphic variables showed a higher relative importance in predicting both bacterial and fungal communities compared with heavy metals, and edaphic variables of SOC, AN, NN and pH together with heavy metals of Zn, As and Pb were important predictors of bacterial and fungal communities compared with the other environmental variables (Figure 4). The correlation heatmaps showed that all heavy metals and pH were negatively correlated with Proteobacteria and Basidiomycota, and positively correlated with Ascomycota and Chloroflexi. Conversely, SOC, TN, and AN were significantly positively correlated with Proteobacteria and Basidiomycota and negatively correlated with Ascomycota (Figure 5).

Discussion

Native plant species influence on soil nutrients

In this study, the heavy metal contamination levels at S1 and S2 exceeded the allowable limits set by Chinese standards for agricultural soils (Ministry of Ecological Environment of the People's Republic of China, 2018), in which the concentrations of multiple heavy metals at S1 were at least two times higher than those at S2. Thus, S1 was defined as "severely contaminated soil," while S2 was defined as "moderately contaminated soil." Our results show that AA had a better ability to increase the SOC and TN contents in

the rhizosphere, but most heavy metal contents were not significantly affected by plant species at S1. The differences in rhizosphere SOC and TN contents among the three studied plant species could be attributed to differences in the quantity and quality of root exudates and the organic litter inputs of each plant species (Bardgett et al., 2014). However, although there was no obvious difference in the heavy metal contents among the three plant species, this does not indicate that the plants had no effect on the total metal concentrations. This is mainly because the background heavy metal content value in the Pb-Zn waste heap is extremely high, and any changes in heavy metal content caused by plant colonization would be comparatively insignificant, rendering them statistically undetectable. Moreover, the phytoremediation of heavy metals generally involves one or more mechanisms such as phytoaccumulation, phytostabilization, phytodegradation, phytovolatilization, and hydraulic control, depending on the plant species (Muthusaravanan et al., 2018). Thus, phytoremediation is more relevant to the bioavailability of heavy metals (Fu et al., 2019) than their absolute abundance. However, in this study, only the heavy metal contents of the soil samples were measured. Therefore, the response of the heavy metal speciation distributions to plant species must be further studied to confirm these findings. Nevertheless, we found that the contents of Zn and Cd in the rhizosphere of AA was significantly lower than CK at S1, which is consistent with the findings of Inelova et al. (2021) and Petriccione et al. (2013), who found that *A. annua* has a large accumulation capacity for heavy metals, especially Cd and Zn. Note that the difference among the heavy metal content among the three plant species at S2 was mainly attributable to differences in sampling location rather than the effect of plant species because *C. breviculmis* was growing closer to S1 than the other plants.

Native plant species altered rhizosphere microbial composition and diversity

Certain plant species have the ability to take up or immobilize heavy metal contaminants in soils while enriching rhizosphere nutrients by transporting various organic compounds (such as amino acids, organic acids, and phenolic compounds) from plants into the soil (Borymski et al., 2018; Muthusaravanan et al., 2018). Plant characteristics and rhizosphere effects greatly contribute to changes in the rhizosphere microbial community (Borymski et al., 2018; Barra Caracciolo and Terenzi, 2021). Our results showed that, at S1, the richness and diversity of the bacterial communities of BD were lower than those of CB and AA but were not significantly different from those of the CK, and the fungal community showed a similar trend. The difference in soil microbial community among plant species was mainly the result of an accumulation of soil nutrients rather than a reduction in heavy metal concentrations, which was supported by our findings that the edaphic variables showed a higher relative importance in predicting both bacterial and fungal communities compared with the heavy metal variables, especially the SOC, AN, NN and pH (Figure 4). The different effects of plant species on the rhizosphere microbial community were also verified by the NMDS results, which showed that the rhizosphere bacterial and fungal community were significantly different

TABLE 3 Topological properties of empirical networks and Erdös–Rényi random networks for bare soils and rhizosphere soils of three metal-tolerant plants at S1 and S2.

	Network Properties	S1				S2		
		CK	CB	BD	AA	CB	BD	AA
Real networks	Total edges	7443	3196	1188	2026	1201	1523	1029
	Positive edges	7120	2722	978	1670	917	1242	804
	Negative edges	323	474	210	356	284	281	225
	positive/negative edges	22.04	5.74	4.66	4.69	3.23	4.42	3.57
	Total nodes	963	981	546	895	954	905	634
	Average degree	15.46	6.52	4.35	4.53	2.52	3.37	3.25
	Average path length	4.33	4.57	5.16	11.72	7.96	12.21	4.91
	Degree centrality	0.13	0.07	0.14	0.06	0.02	0.04	0.05
	Betweenness centrality	0.04	0.06	0.24	0.25	0.04	0.23	0.03
	Clustering coefficient	0.35	0.24	0.26	0.2	0.13	0.22	0.19
	Modularity	0.29	0.52	0.60	0.67	0.87	0.78	0.76
Erdös–Rényi random networks	Average path length	2.79	3.88	4.42	4.64	7.15	7.82	5.49
	Clustering coefficient	0.02	0.01	0.01	0.01	0.00	0.00	0.01
	modularity	0.18	0.30	0.40	0.38	0.59	0.63	0.49

CB, BD, and AA respectively represented *C. breviculmis*, *B. davidii*, and *A. annua*. S1, sample site on the zinc smelter waste heap; S2, sample site around the zinc smelter waste heap.

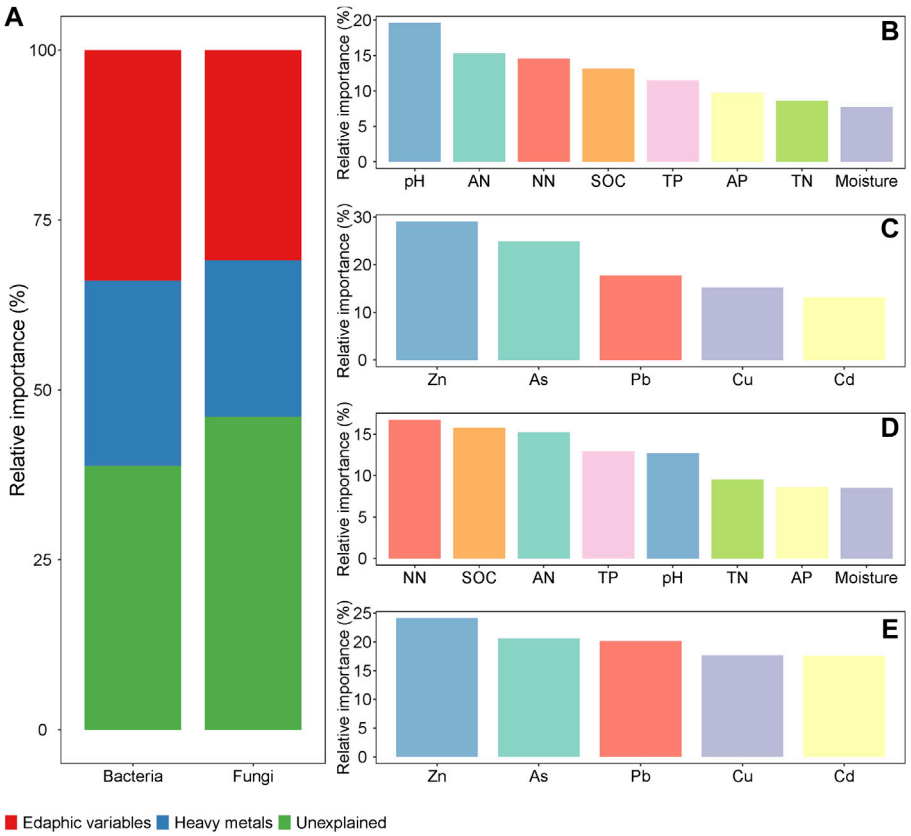

FIGURE 4
The relative importance of individual and group of environmental variables in predicting soil microbial communities. **(A)** group of edaphic variables and heavy metals variables in predicting soil microbial communities; **(B)** individual edaphic variables in predicting bacterial communities; **(C)** individual heavy metal variables in predicting bacterial communities; **(D)** individual edaphic variables in predicting fungal communities; **(E)** individual heavy metal variables in predicting fungal communities. SOC, soil organic carbon; TN, total nitrogen; TP, total phosphorus; AP, available phosphorus; AN, ammonium nitrogen; NN, nitrate nitrogen.

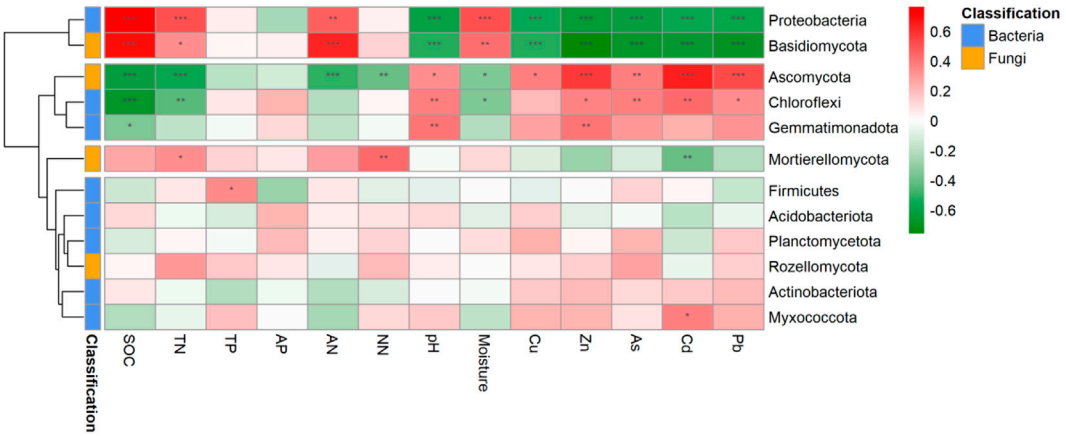

FIGURE 5
Correlation heat maps for the correlation between community composition and environmental variables at the phylum level. The left dendogram linkages represent clustering results of these microbial groups. SOC, soil organic carbon; TN, total nitrogen; TP, total phosphorus; AP, available phosphorus; AN, ammonium nitrogen; NN, nitrate nitrogen. *, <0.05; **, <0.01; ***, <0.001.

among species both at S1. Borymski et al. (2018) suggested that a nutrient-deficit microenvironment was not effective in attracting and stimulating microbial groups around their roots. Several other previous studies also demonstrated that the rhizosphere effect usually increases microbial diversity (Azarbad et al., 2013; Zhao et al., 2020). Notably, we found the soil bacterial and fungal α-diversity in CK was not significantly different from that in the rhizosphere of the three plant species at S1. This discrepancy may be because the S1 sampling site is on an artificial Pb-Zn waste heap that has undergone natural restoration for nearly a hundred years, and *C. breviculmis* and *A. annua* are dominant pioneer species with a large degree of coverage, which may cause its rhizosphere effect to influence the soils uncovered by plants. Moreover, as heavy metal contamination has persisted for nearly a hundred years, the soil microbes have adapted to heavy metal contamination and increased their diversity and richness (Bourceret et al., 2016).

The rhizosphere bacterial composition also responded to plant species, in which Proteobacteria showed a significantly higher relative abundance in the rhizosphere of AA, as compared with CB at both sites, while Chloroflexi showed the opposite trend. As Proteobacteria are usually considered copiotrophic r-strategists and prefer to utilize fresh photosynthates (Bastida et al., 2016), the observed increase in its relative abundance resulted from the higher amount of photosynthates in the rhizosphere of AA than that in CB. Chloroflexi are slow-growing oligotrophic bacteria that are particularly resistant to heavy metals (Rastogi et al., 2011). Herein, the significantly higher relative abundance of Chloroflexi in the rhizosphere of CB was related to its high content of heavy metals, especially Zn and Cd. Regarding fungal composition, the dominant phylum of Ascomycota was significantly higher and Rozellomycota had a significantly lower relative abundance in the rhizosphere of CB than in that of BD and AA at both S1 and S2. The dominance of Ascomycota in the rhizosphere of all three plant species reveals its strong tolerance and profound impact on certain ecological and biogeochemical conditions under severe heavy metal contamination (Lin et al., 2020). Both Ascomycota and Rozellomycota are heavy metal-tolerant fungi (Iram et al., 2009; Lin et al., 2019), and improvements in soil quality usually weaken the dominance of Ascomycota (Yuan et al., 2020). Meanwhile, Rozellomycota has been found to be positively affected by soil organic matter (Lin et al., 2019). In this study, nutrients, such as SOC and TN, were relatively higher for BD and AA (Table 1), which contributed to the differences in the Ascomycota and Rozellomycota abundances in the rhizosphere of each plant species.

Soil microbial structure becomes more unstable with increasing heavy metal pollution

Microbes do not thrive in isolation but instead interact and adapt to survive in harsh environments (Faust and Raes, 2012; Chun et al., 2021). Soil microbial networks unravel the associations among network members and reflect the response of the microbial community to environmental changes (Banerjee et al., 2019). Co-occurrence networks of soil microbial community for bare soils and rhizosphere soils of three metal-tolerant plants at S1 and S2 showed that rhizosphere microbial networks of plant CB and AA were larger and more complex than that of plant BD at S1, but rhizosphere microbial networks showed no obvious different among plant species at S2. This indicate that interactions or niche-sharing in rhizosphere microbial community of plant CB and AA are maximal relative to plant BD at the severely contaminated soil, however, influence of plant species on microbial interactions are reduced at the moderately contaminated soil. Soil microbial communities with a large proportion of positively connected members are unstable because members may respond in tandem with environmental changes (Deng et al., 2012). In this sense, soil microbial networks at S1 had a higher numbers of edges and higher ratio of positive to negative edges relative to S2 indicate that soil microbial communities at S1 are less stable with multi-metal contamination increasing. A possible explanation for these findings is that the association in microbial communities were strengthened under harsh environmental conditions, such as heat, drought, and heavy metal pollution (Zaefarian et al., 2021). In this study, the extremely high content of multiple heavy metals at S1 affected the microbial community, forcing some metal-tolerant bacteria to survive *via* stronger positive cooperation and trophic interaction, in which such cooperation may cause the formation of a microbial biofilm (Li Q. et al., 2020; Chun et al., 2021). However, this assumption must be corroborated by further studies. In addition, soil temperature at S1 are higher than S2 because it is located on a lead-zinc waste heap, and the warm environment has been demonstrated to activate dormant microbial members and strengthen the interactions among microbial communities (Chen et al., 2012). One potential limitation of co-occurrence network analysis is that species associations based on correlation analysis can yield spurious results and cannot be automatically interpreted as interactions, consequently, it may not be possible to comprehensively depict the microbial interactions under real-world conditions (Jiao et al., 2021). Even so, the information about negative/positive correlations between taxa is still essential for estimating potential species interrelationships within complex environments, and they are frequently used to investigate microbial interconnection patterns (Banerjee et al., 2018; Jin et al., 2022).

Both heavy metal pollution and soil nutrients lead to changes in microbial groups

Microbes interact with plants to adapt to and alter soil environments (Chun et al., 2021). In this study, the rhizosphere microbial community was influenced by heavy metals (Pb, Zn and As), soil nutrients (SOC, TN, NN and AN), moisture, and pH (Supplementary Figure S2 and Figure 4). Moreover, the

relationship between heavy metals, pH, and the microbial community was opposite to the relationship between soil physical properties and the microbial community (Figure 5). Similar results have been reported in previous studies (Haichar et al., 2008; Li C. et al., 2020; Lopez-Marcos et al., 2020), and the opposing effects of heavy metals and soil nutrients on soil microbial communities may be one of the driving forces for maintaining soil microbial community stability. Metal-contaminated environments exert strong selective pressure on microbial compositions by affecting microbial metabolism, including the production of oxidative stress or the destruction of microbial proteins and DNA (Mejias Carpio et al., 2017). This results in the evolution of several metal-tolerant microbial groups with better metal resistance mechanisms, such as extracellular and intracellular sequestration, exclusion by permeability barriers, and enzymatic detoxification (Epelde et al., 2014). Bacterial groups affiliated with Chloroflexi and fungal groups affiliated with Ascomycota were positively associated with almost all the heavy metals involved in this study, indicating that they are tolerant to heavy metal pollution and play leading roles in the bioremediation of heavy metals. Additionally, soil nutrients (especially SOC, TN, NN and AN), moisture, and pH play important roles in shaping soil microbial communities (Figure 3). Although microorganisms participate in the decomposition of soil organic matter and the generation of available nitrogen and phosphorus, microbial metabolisms are affected by soil moisture and pH, which alter extracellular enzyme activity and the absorption rate of soluble substrates (Schimel and Schaeffer, 2012; Calicioglu et al., 2018).

Conclusion

Both plant species and heavy metals influence soil microbial diversity and composition. The influence of native plant species on the microbial structure and diversity of soils contaminated with different degrees of heavy metal pollution was mainly the result of an accumulation of soil nutrients rather than a reduction in heavy metal concentrations. Herein, AA and CB showed relatively higher rhizosphere microbial diversity, richness and network complexity than BD at the severely contaminated soil (S1), which was mainly because of a significant accumulation of soil nutrients, including SOC, TN, AN and NN. Moreover, the heavy metal concentration and soil nutrient levels significantly affected the microbial groups affiliated with Proteobacteria, Basidiomycota, Ascomycota, and Chloroflexi. In particular, the microbial groups affiliated with Chloroflexi and Ascomycota were tolerant to heavy metals and may play an important role in the bioremediation of heavy metals, as they were positively associated with almost all the heavy metals involved in this study. Effect of plant species on rhizosphere microbial networks was more obvious under higher heavy metal pollution. Furthermore, microbial networks at S1 exhibited higher average degree and a higher proportion of positive links than those at S2, indicating that soil microbial structure became more complexity and unstable with increasing heavy metal pollution.

Data availability statement

The original contributions presented in the study are included in the article/Supplementary Material, further inquiries can be directed to the corresponding author.

Author contributions

CS, GW and XK initiated and designed the research, collected the materials, and performed the experiments. CS and PW obtained funding for this study. CS analyzed the data and wrote the manuscript. All authors read and approved the manuscript.

Funding

This work was financially supported by the China Postdoctoral Science Foundation (2020M683373), Guizhou Provincial Science and Technology Projects [(2020)1Y192], National Natural Sciences Foundation of China (41967058), United Foundation of the Guizhou Province Government and the Natural Science Foundation of China (No. U1612442), High-Level Talent Training Program in Guizhou [(2016)5664].

Conflict of interest

The authors declare that the research was conducted in the absence of any commercial or financial relationships that could be construed as a potential conflict of interest.

Publisher's note

Supplementary material

The Supplementary Material for this article can be found online at: https://www.frontiersin.org/articles/10.3389/fenvs.2022.979922/full#supplementary-material

References

Abarenkov, K., Henrik Nilsson, R., Larsson, K. H., Alexander, I. J., Eberhardt, U., Erland, S., et al. (2010). The UNITE database for molecular identification of fungi - recent updates and future perspectives. *New Phytol.* 186, 281–285. doi:10.1111/j.1469-8137.2009.03160.x

Ali, H., Khan, E., and Sajad, M. A. (2013). Phytoremediation of heavy metals-Concepts and applications. *Chemosphere* 91, 869–881. doi:10.1016/j.chemosphere.2013.01.075

Azarbad, H., Niklińska, M., van Gestel, C. A. M., van Straalen, N. M., Röling, W. F. M., and Laskowski, R. (2013). Microbial community structure and functioning along metal pollution gradients. *Environ. Toxicol. Chem.* 32, 1992–2002. doi:10.1002/etc.2269

Banerjee, S., Schlaeppi, K., and van der Heijden, M. G. A. (2018). Keystone taxa as drivers of microbiome structure and functioning. *Nat. Rev. Microbiol.* 16 (9), 567–576. doi:10.1038/s41579-018-0024-1

Banerjee, S., Walder, F., Büchi, L., Meyer, M., Held, A. Y., Gattinger, A., et al. (2019). Agricultural intensification reduces microbial network complexity and the abundance of keystone taxa in roots. *Isme J.* 13, 1722–1736. doi:10.1038/s41396-019-0383-2

Banning, N. C., Gleeson, D. B., Grigg, A. H., Grant, C. D., Andersen, G. L., Brodie, E. L., et al. (2011). Soil microbial community successional patterns during forest ecosystem restoration. *Appl. Environ. Microbiol.* 77, 6158–6164. doi:10.1128/AEM.00764-11

Bardgett, R. D., Mommer, L., and De Vries, F. T. (2014). Going underground: Root traits as drivers of ecosystem processes. *Trends Ecol. Evol.* 29, 692–699. doi:10.1016/j.tree.2014.10.006

Barra Caracciolo, A., and Terenzi, V. (2021). Rhizosphere microbial communities and heavy metals. *Microorganisms* 9, 1462. doi:10.3390/microorganisms9071462

Bastida, F., Torres, I. F., Moreno, J. L., Baldrian, P., Ondoño, S., Ruiz-Navarro, A., et al. (2016). The active microbial diversity drives ecosystem multifunctionality and is physiologically related to carbon availability in Mediterranean semi-arid soils. *Mol. Ecol.* 25, 4660–4673. doi:10.1111/mec.13783

Becerra-Castro, C., Monterroso, C., Prieto-Fernández, A., Rodríguez-Lamas, L., Loureiro-Viñas, M., Acea, M. J., et al. (2012). Pseudometallophytes colonising Pb/Zn mine tailings: A description of the plant-microorganism-rhizosphere soil system and isolation of metal-tolerant bacteria. *J. Hazard. Mater.* 217-218, 350–359. doi:10.1016/j.jhazmat.2012.03.039

Bellemain, E., Carlsen, T., Brochmann, C., Coissac, E., Taberlet, P., and Kauserud, H. (2010). ITS as an environmental DNA barcode for fungi: An *in silico* approach reveals potential PCR biases. *BMC Microbiol.* 10, 189. doi:10.1186/1471-2180-10-189

Borymski, S., Cycoń, M., Beckmann, M., Mur, L. A. J., and Piotrowska-Seget, Z. (2018). Plant species and heavy metals affect biodiversity of microbial communities associated with metal-tolerant plants in metalliferous soils. *Front. Microbiol.* 9, 1425. doi:10.3389/fmicb.2018.01425

Bourceret, A., Cébron, A., Tisserant, E., Poupin, P., Bauda, P., Beguiristain, T., et al. (2016). The bacterial and fungal diversity of an aged PAH- and heavy metal-contaminated soil is affected by plant cover and edaphic parameters. *Microb. Ecol.* 71, 711–724. doi:10.1007/s00248-015-0682-8

Calicioglu, O., Shreve, M. J., Richard, T. L., and Brennan, R. A. (2018). Effect of pH and temperature on microbial community structure and carboxylic acid yield during the acidogenic digestion of duckweed. *Biotechnol. Biofuels.* 11, 275. doi:10.1186/s13068-018-1278-6

Caporaso, J. G., Kuczynski, J., Stombaugh, J., Bittinger, K., Bushman, F. D., Costello, E. K., et al. (2010). QIIME allows analysis of high-throughput community sequencing data. *Nat. Methods* 7, 335–336. doi:10.1038/nmeth.f.303

Chen, B., Landry, M. R., Huang, B., and Liu, H. (2012). Does warming enhance the effect of microzooplankton grazing on marine phytoplankton in the ocean? *Limnol. Oceanogr.* 57, 519–526. doi:10.4319/lo.2012.57.2.0519

Chen, X., Zhao, Y., Zhao, X., Wu, J., Zhu, L., Zhang, X., et al. (2020). Selective pressures of heavy metals on microbial community determine microbial functional roles during composting: Sensitive, resistant and actor. *J. Hazard. Mater.* 398, 122858. doi:10.1016/j.jhazmat.2020.122858

Cheng, C., Li, Y., Long, M., Gao, M., Zhang, Y., Lin, J., et al. (2020). Moss biocrusts buffer the negative effects of karst rocky desertification on soil properties and soil microbial richness. *Plant Soil* 475, 153–168. doi:10.1007/s11104-020-0460210.1007/s11104-020-04602-4

Chun, S. J., Kim, Y. J., Cui, Y., and Nam, K. H. (2021). Ecological network analysis reveals distinctive microbial modules associated with heavy metal contamination of abandoned mine soils in Korea. *Environ. Pollut.* 289, 117851. doi:10.1016/j.envpol.2021.117851

DalCorso, G., Fasani, E., Manara, A., Visioli, G., and Furini, A. (2019). Heavy metal pollutions: State of the art and innovation in phytoremediation. *Ijms* 20 (14), 3412. doi:10.3390/ijms20143412

Deng, J., Yin, Y., Zhu, W. X., and Zhou, Y. (2018). Variations in soil bacterial community diversity and structures among different revegetation types in the Baishilazi nature reserve. *Front. Microbiol.* 9, 2874. doi:10.3389/fmicb.2018.02874

Deng, Y., Jiang, Y. H., Yang, Y., He, Z., Luo, F., and Zhou, J. (2012). Molecular ecological network analyses. *BMC Bioinforma.* 13, 113. doi:10.1186/1471-2105-13-113

Dubey, S., Shri, M., Gupta, A., Rani, V., and Chakrabarty, D. (2018). Toxicity and detoxification of heavy metals during plant growth and metabolism. *Environ. Chem. Lett.* 16, 1169–1192. doi:10.1007/s10311-018-0741-8

Edgar, R. C. (2013). Uparse: Highly accurate OTU sequences from microbial amplicon reads. *Nat. Methods* 10, 996–998. doi:10.1038/nmeth.2604

Elbehiry, F., Elbasiouny, H., Ali, R., and Brevik, E. C. (2020). Enhanced immobilization and phytoremediation of heavy metals in landfill contaminated soils. *Water Air Soil Pollut.* 231, 204. doi:10.1007/s11270-020-04493-2

Epelde, L., Becerril, J. M., Barrutia, O., González-Oreja, J. A., and Garbisu, C. (2010). Interactions between plant and rhizosphere microbial communities in a metalliferous soil. *Environ. Pollut.* 158, 1576–1583. doi:10.1016/j.envpol.2009.12.013

Epelde, L., Lanzén, A., Blanco, F., Urich, T., and Garbisu, C. (2014). Adaptation of soil microbial community structure and function to chronic metal contamination at an abandoned Pb-Zn mine. *FEMS Microbiol. Ecol.* 91, 1–11. doi:10.1093/femsec/fiu007

Faust, K., and Raes, J. (2012). Microbial interactions: From networks to models. *Nat. Rev. Microbiol.* 10, 538–550. doi:10.1038/nrmicro2832

Fu, S., Wei, C., Xiao, Y., Li, L., and Wu, D. (2019). Heavy metals uptake and transport by native wild plants: Implications for phytoremediation and restoration. *Environ. Earth. Sci.* 78, 103. doi:10.1007/s12665-019-8103-9

Haichar, F., Marol, C., Berge, O., Rangel-Castro, J. I., Prosser, J. I., Balesdent, J., et al. (2008). Plant host habitat and root exudates shape soil bacterial community structure. *ISME J.* 2, 1221–1230. doi:10.1038/ismej.2008.80

Hamidpour, M., Nemati, H., Abbaszadeh Dahaji, P., and Roosta, H. R. (2019). Effects of plant growth-promoting bacteria on EDTA-assisted phytostabilization of heavy metals in a contaminated calcareous soil. *Environ. Geochem Health.* 42 (8), 2535–2545. doi:10.1007/s10653-019-00422-3

Inelova, Z., Nurzhanova, A., Yerubayeva, G., Aitzhan, M., Djansugurova, L., and Bekmanov, B. (2021). Heavy metal contents in plants of phytocenoses of the point of besqaynar, kyzylkairat and taukaraturyk. *Pak. J. Bot.* 53, 511–516. doi:10.30848/PJB2021-2(3310.30848/pjb2021-2(33)

Iram, S., Ahmad, I., Javed, B., Yaqoob, S., Akhtar, K., Kazmi, M. R., et al. (2009). Fungal tolerance to heavy metals. *Pak J. Bot.* 41, 2583–2594.

Jiao, S., Peng, Z., Qi, J., Gao, J., and Wei, G. (2021). Linking bacterial-fungal relationships to microbial diversity and soil nutrient cycling. *mSystems* 6 (2), e01052–20. doi:10.1128/mSystems.01052-20

Jin, X., Wang, Z., Wu, F., Li, X., and Zhou, X. (2022). Litter mixing alters microbial decomposer community to accelerate tomato root litter decomposition. *Microbiol. Spectr.* 10 (3), e0018622. doi:10.1128/spectrum.00186-22

Lei, D., and Duan, C. (2008). Restoration potential of pioneer plants growing on lead-zinc mine tailings in Lanping, southwest China. *J. Environ. Sci.* 20, 1202–1209. doi:10.1016/S1001-0742(08)62210-X

Li, C., Quan, Q., Gan, Y., Dong, J., Fang, J., Wang, L., et al. (2020a). Effects of heavy metals on microbial communities in sediments and establishment of bioindicators based on microbial taxa and function for environmental monitoring and management. *Sci. Total Environ.* 749, 141555. doi:10.1016/j.scitotenv.2020.141555

Li, M. S. (2006). Ecological restoration of mineland with particular reference to the metalliferous mine wasteland in China: A review of research and practice. *Sci. Total Environ.* 357, 38–53. doi:10.1016/j.scitotenv.2005.05.003

Li, Q., You, P., Hu, Q., Leng, B., Wang, J., Chen, J., et al. (2020b). Effects of co-contamination of heavy metals and total petroleum hydrocarbons on soil bacterial community and function network reconstitution. *Ecotoxicol. Environ. Saf.* 204, 111083. doi:10.1016/j.ecoenv.2020.111083

Li, S., Wu, J., Huo, Y., Zhao, X., and Xue, L. (2021). Profiling multiple heavy metal contamination and bacterial communities surrounding an iron tailing pond in Northwest China. *Sci. Total Environ.* 752, 141827. doi:10.1016/j.scitotenv.2020.141827

Li, Z., Song, C., Yi, Y., and Kuipers, O. P. (2020c). Characterization of plant growth-promoting rhizobacteria from perennial ryegrass and genome mining of novel antimicrobial gene clusters. *Bmc. Genomics* 21 (1), 157. doi:10.1186/s12864-020-6563-7

Lin, Y., Ye, Y., Hu, Y., and Shi, H. (2019). The variation in microbial community structure under different heavy metal contamination levels in paddy soils. *Ecotoxicol. Environ. Saf.* 180, 557–564. doi:10.1016/j.ecoenv.2019.05.057

Lin, Y., Xiao, W., Ye, Y., Wu, C., Hu, Y., and Shi, H. (2020). Adaptation of soil fungi to heavy metal contamination in paddy fields-a case study in eastern China. *Environ. Sci. Pollut. Res.* 27, 27819–27830. doi:10.1007/s11356-020-09049-9

Liu, K., Zhang, H., Liu, Y., Li, Y., and Yu, F. (2020). Investigation of plant species and their heavy metal accumulation in manganese mine tailings in Pingle Mn mine, China. *Environ. Sci. Pollut. Res.* 27, 19933–19945. doi:10.1007/s11356-020-08514-9

López-Marcos, D., Turrión, M., and Martínez-Ruiz, C. (2020). Linking soil variability with plant community composition along a mine-slope topographic gradient: Implications for restoration. *Ambio* 49, 337–349. doi:10.1007/s13280-019-01193-y

Luo, Y., Wu, Y., Qiu, J., Wang, H., and Yang, L. (2019). Suitability of four woody plant species for the phytostabilization of a zinc smelting slag site after 5 years of assisted revegetation. *J. Soils Sediments* 19, 702–715. doi:10.1007/s11368-018-2082-4

Marguí, E., Iglesias, M., Queralt, I., and Hidalgo, M. (2006). Lead isotope ratio measurements by ICP-QMS to identify metal accumulation in vegetation specimens growing in mining environments. *Sci. Total Environ.* 367, 988–998. doi:10.1016/j.scitotenv.2006.03.036

Mejias Carpio, I., Ansari, A., and Rodrigues, D. (2017). Relationship of biodiversity with heavy metal tolerance and sorption capacity: A meta-analysis approach. *Environ. Sci. Technol.* 52 (1), 184–194. doi:10.1021/acs.est.7b04131

Ministry of Ecological Environment of the People's Republick of China (2018). *Soil environment quality-risk control standard for soil contamination of agriculture land (GB 15618-2018)*. Beijing, China: Environment of the People's Republick of China.

Montiel-Rozas, M. M., Madejón, E., and Madejón, P. (2016). Effect of heavy metals and organic matter on root exudates (low molecular weight organic acids) of herbaceous species: An assessment in sand and soil conditions under different levels of contamination. *Environ. Pollut.* 216, 273–281. doi:10.1016/j.envpol.2016.05.080

Muthusaravanan, S., Sivarajasekar, N., Vivek, J. S., Paramasivan, T., Naushad, M., Prakashmaran, J., et al. (2018). Phytoremediation of heavy metals: Mechanisms, methods and enhancements. *Environ. Chem. Lett.* 16, 1339–1359. doi:10.1007/s10311-018-0762-3

Petriccione, M., Di Patre, D., Ferrante, P., Papa, S., Bartoli, G., Fioretto, A., et al. (2013). Effects of Pseudomonas fluorescens seed bioinoculation on heavy metal accumulation for mirabilis jalapa phytoextraction in smelter-contaminated soil. *Water Air Soil Pollut.* 224, 1645. doi:10.1007/s11270-013-1645-7

R Development Core Team (2019). *R: A language and environment for statistical computing*. Vienna, Austria: R Foundation for Statistical Computing. AvaliableAt: http:/www.R-project.org.

Rastogi, G., Barua, S., Sani, R. K., and Peyton, B. M. (2011). Investigation of microbial populations in the extremely metal-contaminated coeur d'Alene river sediments. *Microb. Ecol.* 62, 1–13. doi:10.1007/s00248-011-9810-2

Schimel, J., and Schaeffer, S. (2012). Microbial control over carbon cycling in soil. *Front. Microbio.* 3, 348. doi:10.3389/fmicb.2012.00348

Wang, Q., Garrity, G. M., Tiedje, J. M., and Cole, J. R. (2007). Naïve bayesian classifier for rapid assignment of rRNA sequences into the new bacterial taxonomy. *Appl. Environ. Microbiol.* 73, 5261–5267. doi:10.1128/AEM.00062-07

Xu, J., Zheng, L., Xu, L., and Wang, X. (2020). Uptake and allocation of selected metals by dominant vegetation in Poyang Lake wetland: From rhizosphere to plant tissues. *Catena* 189, 104477. doi:10.1016/j.catena.2020.104477

Yang, S., Cao, J., Li, F., Peng, X., Peng, Q., Yang, Z., et al. (2016). Field evaluation of the effectiveness of three industrial by-products as organic amendments for phytostabilization of a Pb/Zn mine tailings. *Environ. Sci. Process. Impacts* 18, 95–103. doi:10.1039/c5em00471c

Yuan, J., Wen, T., Zhang, H., Zhao, M., Penton, C. R., Thomashow, L. S., et al. (2020). Predicting disease occurrence with high accuracy based on soil macroecological patterns of Fusarium wilt. *ISME J.* 14, 2936–2950. doi:10.1038/s41396-020-0720-5

Zaefarian, F., Rezvani, M., Rejali, F., Ardakani, M. R., and Noormohammadi, G. (2021). Effect of heavy metals and arbuscular mycorrhizal fungal on growth and nutrients (N, P, K, Zn, Cu and Fe) accumulation of alfalfa (medicago sativa L.). *American-Eurasian J. Agric. Environ Sci.* 11 (3), 346–352. doi:10.1007/s11356-020-08538-1

Zhao, X., Sun, Y., Huang, J., Wang, H., and Tang, D. (2020). Effects of soil heavy metal pollution on microbial activities and community diversity in different land use types in mining areas. *Environ. Sci. Pollut. Res.* 27 (16), 20215–20226. doi:10.1007/s11356-020-08538-1

frontiers | Frontiers in Environmental Science

TYPE Original Research
PUBLISHED 05 October 2022
DOI 10.3389/fenvs.2022.1039470

OPEN ACCESS

EDITED BY
Jun Zhou,
University of Massachusetts Lowell,
United States

REVIEWED BY
Chuncai Zhou,
Hefei University of Technology, China
Yuanfang Huang,
China Agricultural University, China
Huichun YE,
Aerospace Information Research Institute, Chinese Academy of Sciences (CAS), China

*CORRESPONDENCE
Shiwen Zhang,
mamin1190@126.com

SPECIALTY SECTION
This article was submitted to Toxicology, Pollution and the Environment,
a section of the journal
Frontiers in Environmental Science

RECEIVED 08 September 2022
ACCEPTED 16 September 2022
PUBLISHED 05 October 2022

CITATION
Feng Z, Zhang S, Yang B, Zhou T and Rui T (2022), Iron-copper interaction in soil spectra and its effect on the estimation of copper content.
Front. Environ. Sci. 10:1039470.
doi: 10.3389/fenvs.2022.1039470

Iron-copper interaction in soil spectra and its effect on the estimation of copper content

Zhijun Feng[1], Shiwen Zhang[2]*, Bin Yang[1], Tao Zhou[1] and Tingting Rui[1]

[1]School of Spatial Informatics and Geomatics Engineering, Anhui University of Science and Technology, Huainan, China, [2]School of Earth and Environment, Anhui University of Science and Technology, Huainan, China

It is important to clarify the iron-copper interaction pattern to effectively extract the characteristic bands and improve the inversion accuracy of copper content in soil. In this study, based on experimental samples, spectral feature analysis and analysis of variance (ANOVA) were used to deeply uncover the iron-copper interaction pattern. And used natural samples to build a random forest model to analyze the effect of interaction patterns on inversion accuracy. The results of the study showed that the effect of iron content in soil on spectral reflectance varied with copper content in soil, and similarly, the effect of copper content in soil on spectral reflectance varied with iron content in soil. The effect of iron, copper and their interaction on the spectral reflectance of soil varied with the wavelength. In the wavelength from 400 to 2,500 nm, the effect of iron on the spectral features was more than copper, and in the characteristic wavelength of iron (600–700 nm), even more than 5 times that of copper, the effect of iron on the spectral reflectance played a major role, and the iron content in soil must be considered in the inversion of copper content in soil. The Pearson correlation coefficient method was used as the selected characteristic wavelength, the selected wavelength was used as the independent variable, and the copper content in the soil was the dependent variable. Inversion model was built by the random forest algorithm, and the determination coefficient was 0.73. Under the condition of considering the interaction, the coefficient of determination was 0.87. It was shown that the characteristic wavelength was selected by considering the iron-copper interaction, which can better characterize the response signal of copper in soil. This paper provided a new idea for the accurate inversion of copper content in soil, which can provide technical support for the rapid detection of copper content in soil.

KEYWORDS

soil, spectral analysis, iron-copper interaction, characteristic band selection, estimation of copper content

1 Introduction

Soil is an important resource for human survival and agricultural production (Maitra et al., 2021) Along with the rapid development of industrialization, heavy metal elements continue to accumulate in the soil through sewage discharge, atmospheric fallout and other means, resulting in soil heavy metal pollution (Yang et al., 2021; Zhang et al., 2021), which even have a serious impact on the growth of crops and easily enter the human body through the food chain, posing a great threat to human health (Qin et al., 2021). Therefore, extensive testing of heavy metal content in soil is of great significance to safeguard agricultural production, protect human health and ecosystem security (Lin et al., 2022).

In recent years, hyperspectral remote sensing technology with its advantages of dynamics and high efficiency has been widely used in many fields such as agriculture, geology and food detection (Lu et al., 2020; Ren et al., 2022), and there have been many studies in heavy metal contamination of soils. Li et al. (2021) used single spectral transformation index and multi-spectral transformation index to invert the arsenic (As) content in soil by different spectral transformation methods and achieved good inversion results; Guo et al. (2021) used principal components analysis (PCA) to reduce the dimensionality of hyperspectral data, and Partial Least Square Regression, Support Vector Machines, Artificial Neural Network and Random Forest (RF) models were used to estimate the Cadmium content in soil, and it was found that PCA-RF outperformed other counterparts. Although the above-mentioned studies have successfully used hyperspectral to heavy metal content in soil estimate, most of the improvement of estimate accuracy was through spectral transformation and model improvement, the spectral features of some heavy elements were easily masked by organic matter, carbonate, hygroscopic moisture, iron and manganese oxides, etc. Higher accuracy is often not achieved by direct estimation (He et al., 2019). Some scholars had also conducted corresponding studies for this kind of problems. Zhang et al. (2020a) proposed a method for estimate based on the characteristic spectra of iron oxide, this method reduced data redundancy and improved the estimation accuracy of lead (Pb) content in soil. Jiang et al. (2018) explored the response regulation of soil cadmium (Cd) and spectral characteristics through the preparation of class standardized samples, found that estimation accuracy can be significantly improved based on class standardized samples, which can provide *a priori* knowledge for estimation of heavy metal in soil content in a model of multi-element confounding pollution; Zhang et al. (2020b) introduced water-salt interactions into the water-salt theory model, the accuracy of spectral reflectance estimation is significantly improved.

In summary, scholars have studied the influence of a single heavy metal on spectral characteristics, however, there were few reports on the interaction of different heavy metals on soil spectral characteristics and their effect on estimation accuracy, there was a symbiotic and aggregation relationship between iron and copper elements in the soil (Chen et al., 2022), and the correlations between soil Fe and soil Cu components were significant (Gong et al., 2010), the 3d orbitals of soil Fe was half-filled, it had a higher energy level response, and the 3d orbitals of both soil Fe and soil Cu are unfilled and have a similar energy level response to spectral reflectance (Cheng et al., 2018), therefore, which can hide the spectral information of copper, leading to low accuracy in direct estimate of copper content in soil (Lin et al., 2021), Therefore, it was significant to clarify the interaction of iron and copper and their on the spectral reflectance of soil for the extraction of effective spectral features of copper in soil. In this paper, spectral feature analysis and analysis of variance (ANOVA) were used to deeply reveal the interaction of iron and copper based on experimental samples, and used natural samples to analyze the effect of interaction to estimate of copper content in soil, which can provide technical support for the direct estimation of copper content in soil.

2 Materials and methods

2.1 Collection of soil samples

Soil collection included laboratory preparation of standardized samples and natural soil sampling of the mine site. Soil within the surface layer (0–15 cm) was collected at the same location in the mine area for about 15 kg, mixed and brought back in a special sealed bag for laboratory preparation of standardized samples. Natural soil samples were collected by the five-point sampling method, the collected soil samples were brought back in special sealed bags. First, the soil sample was dried naturally, then the impurities were removed, and finally the soil sample was ground and sieved through 100 mesh sieve. Each of the treated natural soil samples from the mine site was divided into 2 parts, of which one of them was used to monitor heavy metal content, soil iron content was determined by the atomic absorption spectrophotometer (JC-17002) and soil copper content was determined by flame atomic absorption spectrophotometry, another one was used for laboratory testing of its soil composition content and one was used for soil spectral reflectance collection.

2.2 Preparation of standardized samples

The soil samples collected for the preparation of standardized samples were passed through a 10 mesh sieve, removing grass roots, stones and other debris, pass through 100 mesh nylon sieve after natural dried and ground, the treated soil was mixed well to

ensure consistent background values of the soil samples. Added a small amount of distilled water to moisten the soil sample, soil organic matter was removed by adding 30% H_2O_2 solution to eliminate the effect of soil organic matter on the spectral reflectance of the soil, the soil organic matter was continuously monitored during the removal process to ensure full removal. The removed soil sample was dried and placed in a container, and added sodium citrate and sodium bicarbonate solution, heated up to 80°C in a water bath, then added sodium disulfite to remove iron in soil, and this operation was repeated continuously, and iron content in soil was monitored continuously during the repetition until all iron content in soil was removed.

The iron content in soil gradient was set to 0, 2, 3.5, 5, 6.5, and 10% according to the types of soil in China and the Chinese soil database provided by the Institute of Soil Research, Chinese Academy of Sciences, and the iron content in natural soil samples. Reference to the actual situation in the study area and the soil environmental quality soil pollution risk control standards for agricultural land issued by the Ministry of Ecology and Environment, the copper content in soil gradient was set as 50 mg/kg, 70 mg/kg, 80 mg/kg, 90 mg/kg, 100 mg/kg, and 120 mg/kg; to facilitate the calculation of two-factor ANOVA, the iron content in soil was divided into three groups of 0%–3%, 3%–6% and 6%–10%, and the copper content in soil was divided into three groups of 50–80 mg/kg, 80–100 mg/kg and 100–120 mg/kg, and a total of 9 was set of experimental data with the same number of samples in each group, and the spectral reflectance of all experimental samples was obtained.

2.3 Soil sample spectral data acquisition and data processing

2.3.1 Spectral data acquisition

Indoor soil spectral data were acquired using a FieldSpec 4 spectrometer from ASD, United States, which was equipped with color RS3 software. The instrument has a wavelength range of 350–2,500 nm, covering the full range from visible to near infrared. Considered the susceptibility to external light in the acquisition of spectra, indoor spectra were acquired in a dark room without light, used a 12 V, 50 W tungsten bulb to provide a stable light source and a 25° bare fiber optic lens for spectral data acquisition. For indoor soil spectral data acquisition, the spectrometer needed to be preheated for half an hour. For soil spectral data acquisition, the soil sample needed to be laid flat in a Petri dish with a black flannel under the Petri dish. The distance of the light source from the Petri dish was 60 cm, and the angle with the horizontal direction was 45°. The fiber optic lens was positioned 7 cm directly above the Petri dish. To reduce the interference of external factors, a whiteboard correction was conducted after acquiring the spectra of 5 soil samples. Twenty spectral curves were obtained for each soil sample, and the average value was taken as the spectral data of the soil sample after excluding the abnormal (noisy) curves.

2.3.2 Spectral data pre-processing

Spectral data acquisition process will be affected by many factors, in addition to external environmental factors (such as atmospheric humidity, temperature and components, etc.) and the soil sample itself (such as soil color, mechanical composition, microaggregates, soil formation conditions, surface roughness, humidity, etc.), also influenced by the difference in response of the spectrometer itself to different wavelengths, these make the correlation between the original spectral reflectance and the measured object is low and does not meet the demand of spectral prediction. Therefore, the first order differential (FDR) pre-processing transform is performed on the soil spectral data (Luo, et al., 2022) Eq. 1.

$$R'(\lambda \mathrm{i}) = \frac{[R(\lambda i + 1) - R(\lambda i - 1)]}{2\Delta\lambda} \quad (1)$$

In the formula, λ represented the position of wavelength in the i nm, and $R(\lambda_{i+1})$ and $R(\lambda_{i-1})$ represented the original spectral reflectance at the wavelength position of λ_{i+1} and λ_{i-1}, $R'(\lambda_i)$ represented the first order differential spectral reflectance at the wavelength position of λ_i, $2\Delta\lambda$ is the interval from the wavelength $\lambda_{i-1}$to λ_{i+1}.

2.4.1 Pearson's correlation coefficient

Pearson's correlation coefficient (PCC) can better find the sensitivity of soil heavy metals to spectral reflectance (Shu, et al., 2021) The characteristic spectral bands were extracted by correlation analysis for estimating content of heavy metal in soil. The spectral reflectance was subjected to Pearson correlation analysis with the heavy metal content, and the characteristic bands were selected according to their significance levels.

2.4.2 Iron-copper interaction

According to the statistical definition of the interaction, the Iron-Copper interaction can be explained by the fact that the spectral reflectance of soil changes depending on the copper content in soil when the iron content in soil is the same, and similarly, the spectral reflectance of soil changes depending on the iron content in soil when the copper content in soil is the same.

2.5 Calculation of F-action values

ANOVA is a statistical method to analyze the effect of explanatory variables on the explained variables (Hong and Hyundoo, 2021). ANOVA can be divided into one-factor ANOVA and two (multi) factor ANOVA according to the categories, and the two-factor ANOVA that only considers

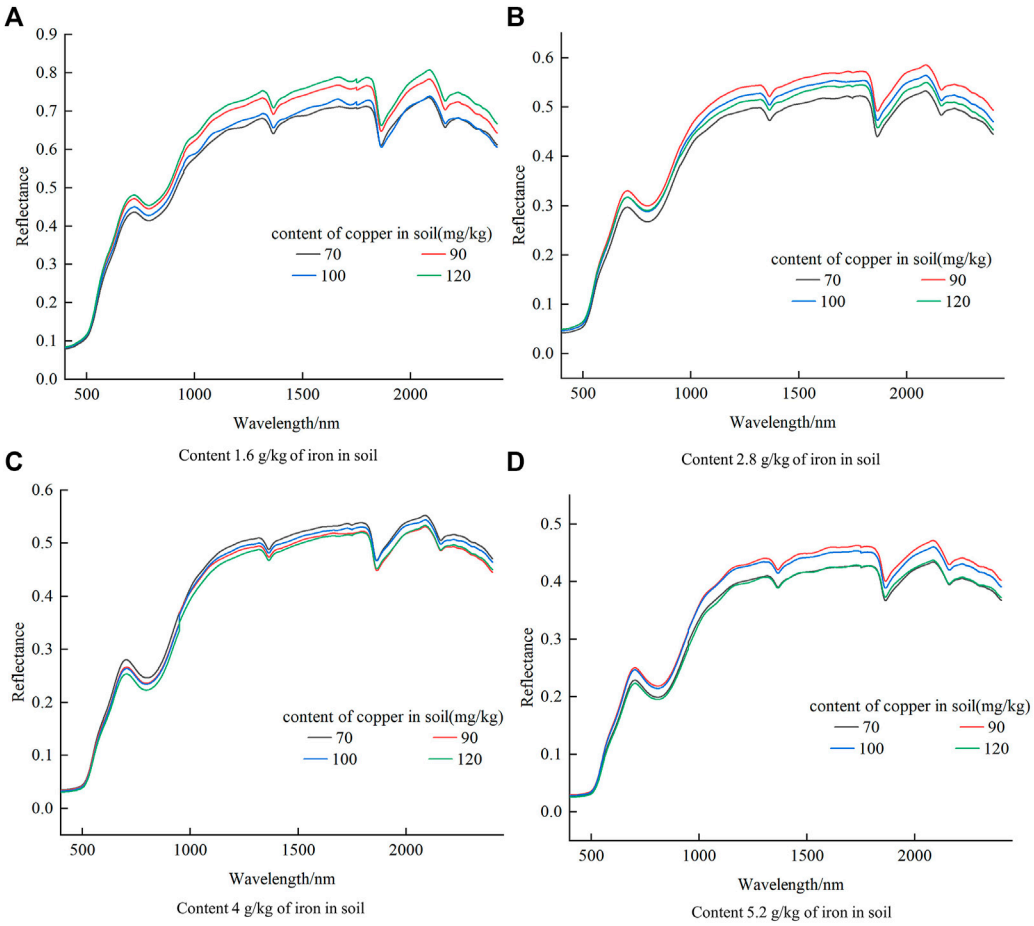

FIGURE 1
Variation curves of soil spectral characteristics with copper content for four identical iron content cases.

the main effect without considering the interaction effect is the non-repetitive two-factor ANOVA, the repeated two-factor ANOVA that considers both main effects and interaction effects is a repeated two-factor ANOVA; and the interaction effect that considers both the effect of the explanatory variables on the explanatory variables alone and the effect of the combination of the explanatory variables on the explanatory variables, which is the Iron-Copper interaction in this paper. The *F*-test in ANOVA is a numerical representation which is used to test the significance of the degree of influence of the explanatory variables on the explained variables, and its significance is concretely expressed by the *F*-value, a larger *F*-value indicates a more significant effect of the explanatory variable on the explained variable. Therefore, the repeated two-factor ANOVA was used quantitatively analysis the effects of iron, copper and their interactions on soil spectral reflectance, that was, the effect of iron, copper and interaction on the spectral reflectance was expressed numerically using the *F*-value.

2.6 Model building and accuracy validation

Random forest (RF) is a classifier that uses multiple trees to train and predict samples, and is one of the most widely used algorithms in Bagging integrated learning (Agrawal and Petersen, 2021). Random forest constructs a large number of decision trees and then averages them. The calibration of the decision tree starts with a single node containing all the training samples, then the heterogeneity measure in the resultant node is minimized using predictive features and a threshold that splits the node into two nodes until all the end nodes are isomorphic. Since the partitioning of each node variable in the decision tree is chosen randomly, there is almost no correlation between each decision tree, which can better avoid overfitting (Tan et al., 2019). The implementation process of the RF algorithm was done in Matlab R2018b, and the accuracy of the algorithm was evaluated using the coefficient of determination (R^2) and root mean square error (RMSE), the closer R^2 is to 1, the more stable the algorithm is, the smaller RMSE is, and the higher the algorithm accuracy is.

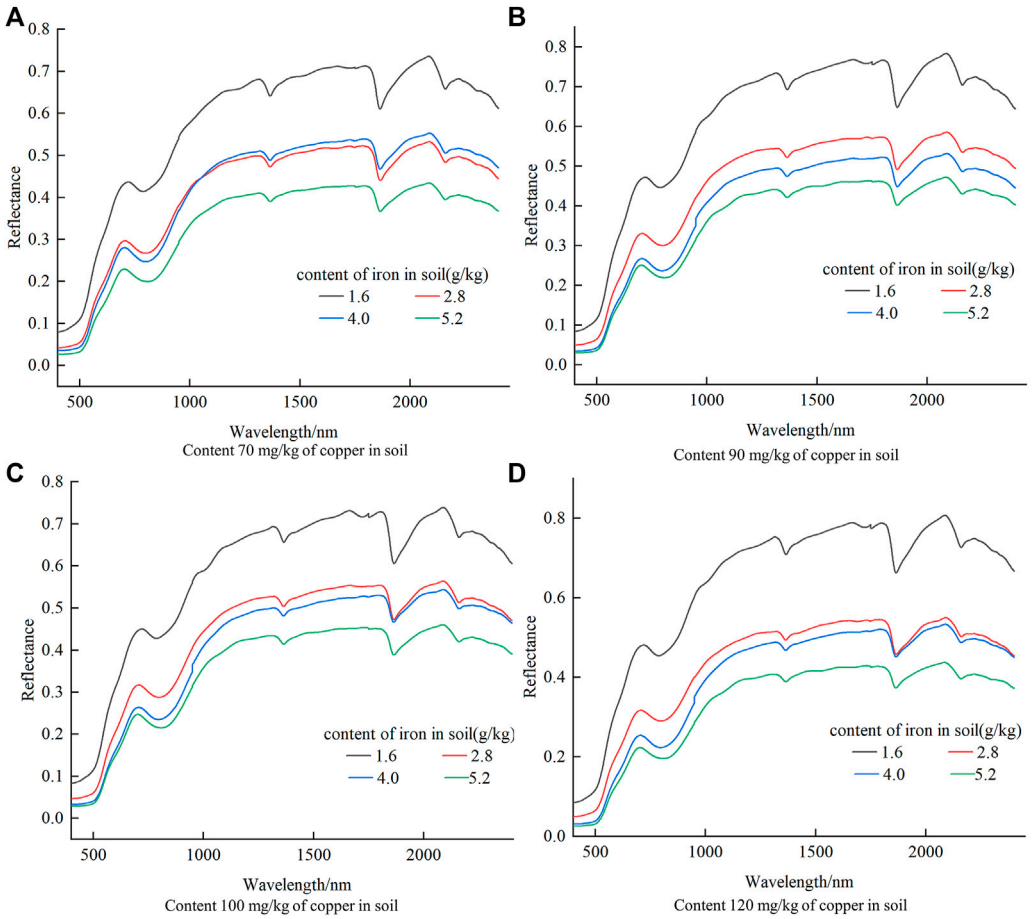

FIGURE 2
Variation curves of soil spectral characteristics with iron content for four identical copper content cases.

3 Results and analysis

3.1 Effects of iron, copper and their interactions on the spectral reflectance of soil

3.1.1 Spectral reflectance at different iron and copper contents in soil

Based on the data of iron content and copper content in soil the experimental samples, the samples with the same iron content but different copper content in soil were screened and the corresponding spectral reflectance graphs were plotted (Figure 1), so as to analyze the relationship between different copper content and spectral reflectance at the same iron content.

In general, the spectral reflectance and iron content in soil were negatively correlated, that was, as the iron content in soil increases, the spectral reflectance decreases (Peng et al., 2013). As shown in Figure 1, the maximum reflectance gradually decreased with increasing of iron content in soil, which was consistent with the negative correlation between spectral reflectance and soil content in soil, which indicated that change of copper content in soil had a smaller effect on the spectral characteristics than change of iron content in soil. The pattern of the effect of the change of iron content in soil on the spectral reflectance was different for different iron contents in soil. When the content was 1.6 g/kg of iron in soil, the spectral reflectance was the smallest when the copper content was the smallest; the spectral reflectance rate was the largest when the copper content was the largest. When the content was 4 g/kg of iron in soil, the spectral reflectance was the smallest when the copper content was the largest and the spectral reflectance was the smallest when the copper content was the largest. The above analysis showed that the relationship between spectral reflectance and copper content in soil varies depending on the iron content.

To analyze the relationship between different iron contents and spectral reflectance at the same copper content, the spectral

reflectance curves with different iron contents at the same copper content were plotted (Figure 2).

As can be seen from Figure 2, the spectral reflectance was all maximum when the iron content was the smallest and minimum when the iron content was the largest, which satisfied the negative correlation between the spectral reflectance and iron content in soil, and the spectral reflectance basically decreased strictly with the increase of iron content in the case of different copper content in soil, which indicated that the change of copper content in soil had less effect on the spectral reflectance, which was consistent with the study that the absorption coefficient of hydrated iron ions in water on spectral reflectance was stronger than that of hydrated copper ions in water on spectral reflectance (Deng et al., 2016; Liang et al., 2016), and the conclusion of these two literatures also proves that the greater effect of iron in soil on spectral characteristics than copper is not due to the influence of content (magnitude). The pattern of the effect of changing iron content in soil on the spectral reflectance was different when the copper content was different, and the maximum spectral reflectance was different when the copper content was different, with the maximum spectral reflectance at content 120 mg/kg of copper in soil and the minimum spectral reflectance at content 100 mg/kg of copper in soil. The above analysis showed that the relationship between spectral reflectance and iron content in soil varies depending on the copper content.

It is also shown in Figure 2 that the spectral reflectance decreased with increasing iron content in 400–1,000 nm when the copper content in soil was 70 mg/kg, while the spectral reflectance was lower in 1,000–2,450 nm at content 2.8 g/kg of iron in soil than at content 4 g/kg of iron in soil, when the copper content in soil was 90 mg/kg, 100 mg/kg and 120 mg/kg, respectively. The spectral reflectance decreased strictly with the increase of iron content, which indicated that the variability of the relationship between spectral reflectance and iron content in soil at different wavelengths also differs depending on the copper content. Therefore, the inversion accuracy of iron content in soil using the characteristic band of iron may be affected under the condition that copper in soil was not considered.

3.1.2 Characteristics of two-dimensional correlation spectra at different iron contents and copper contents in soil

One-dimensional spectra can only analyze the general pattern of soil spectral reflectance changing with soil iron content and copper content in soil, and cannot accurately analyze the changes of fine features in the spectra, while two-dimensional correlation spectra can extend the soil spectral signal to the second dimension, and improve the spectral resolution by analyzing the differences in vibrational behaviors of molecules of different component groups, separating overlapping peaks, and probing the interactions between different functional groups (Yang et al., 2019), making weak peaks and overlapping peaks in the one-dimensional spectra are more obvious. The two-dimensional correlation spectroscopy technique was used to resolve the changes in the fine features of the spectra using the iron content and copper content in soil as external perturbation conditions, respectively, and finding the characteristic information of the correlation spectra under micro perturbation. The results are shown in Figure 3.

The two-dimensional correlation spectroscopy theory shown that its two-dimensional correlation spectrogram is symmetric about the diagonal, where the peaks located on the main diagonal are called autocorrelation peaks, which are the autocorrelation of group vibrations in response to external perturbations and represent the autocorrelation intensity of reflectance intensity changes in a specific band (Hou and Wu, 2022). These peaks, which are generated due to spectral autocorrelation and are usually positive, represent the sensitivity to external perturbation factors (iron content and copper content in soil), with a redder color indicating a higher sensitivity and a bluer color indicating a lower sensitivity. Cross peaks, which can be positive or negative, are also present in the two-dimensional correlation spectrogram, usually symmetric about the main diagonal, representing possible inter- or intra-molecular interactions between the two functional groups, and these interactions are usually closely related to the variation of the external disturbance factors (iron content and copper content in soil) (Liu et al., 2020).

From Figure 3, four more obvious autocorrelation peaks and one cross peak appeared in both figures in the two-dimensional correlation spectra, and the locations of the autocorrelation peaks and cross peaks were basically the same. The autocorrelation peaks correspond to the gene vibration peaks at 600–700 nm, 1,300–1,400 nm, 1,650–1850 nm, and 2,100–2,200 nm, which were consistent with the absorption peaks of the original spectra. From the intensity of the autocorrelation peaks, the highest intensity of the autocorrelation peaks in both plots was found near 2,200 nm, indicating that there was a strong autocorrelation near 2,200 nm, and it was most sensitive to the microturbulence of iron content and copper content in soil. The microturbulence of both iron content and copper content had a consistent effect on the intensity of changes in the soil spectral signal when the iron content and copper content were changed.

3.2 F-action values of iron, copper and their interactions on spectral reflectance

The *F*-test in ANOVA is a numerical representation which is used to test the significance of the degree of influence of the explanatory variables on the explained variables, so the *F*-action can quantitatively calculate the effect of iron content and copper

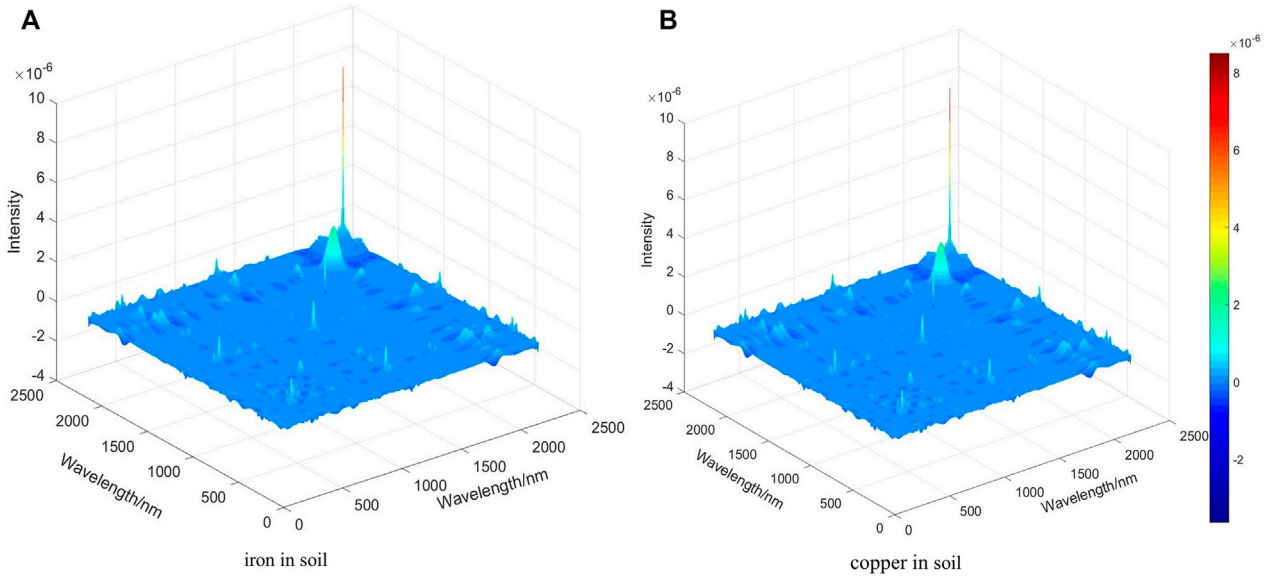

FIGURE 3
3D correlation synchronous and asynchronous spectrograms.

content in soil on the spectral reflectance. The *F* values are shown in Figure 4.

Figure 4 represented the contribution of iron, copper and their interaction on the soil spectral reflectance by *F*-value. The maximum value of the effect of iron on the soil spectral reflectance in the band 600–700 nm was 171.44 and the minimum value was 23.20, indicating that the effect of iron on the soil spectral characteristics in the band 600–700 nm was the largest and the minimum effect was more than 20 times the value of the effect of copper and interaction, and the value of the effect of copper on the soil spectral reflectance was similar to that of the interaction, but greater than that of the interaction. Therefore, in the 600–700 nm band, iron played a major role in the spectral characteristics of soil, which was consistent with the fact that the 600–700 nm band was the characteristic band of iron. Therefore, when estimated the iron content in soil with this characteristic band, it was not necessary to consider the effect of copper content in soil and its interaction, and when estimated the copper content in soil, the effect of iron content in soil on spectral characteristics of copper must be considered. In the bands 1,300–1,400 nm, 1,650–1850 nm and 2,100–2,200 nm, the values of iron and copper on spectral reflectance of soil were similar, and the effect of iron on soil spectral reflectance had less influence on the estimation of copper content in soil; in the bands 1,340–1,370 nm and 2,100–2,130 nm, the values of the effect of copper on spectral reflectance of soil. Therefore, the effect of interaction on the estimation of copper content in soil should be considered when estimation of copper content in soil was performed.

The overall analysis shown that in the 600–700 nm band, the effect of iron on spectral reflectance of soil was the largest, which was more than 20 times the effect of copper on spectral characteristics of soil, indicating that this band is the characteristic band of iron, which was consistent with the study of Wang et al. (2021), therefore, the band in this range should be excluded in the estimation of copper content in soil; The effect of soil iron on the estimation of copper content in soil can be disregarded in the bands with small values of soil iron, but the effect of interaction on the inversion of copper content in soil should be considered when the effect of interaction on the spectral reflectance and the effect of soil copper are similar, so the bands in which the effect of interaction on the spectral reflectance was greater than the effect of copper should be excluded. In summary, when estimation of copper content in soil, characteristic bands of copper should be selected according to the principle that copper had a greater effect on the spectral reflectance and iron and interaction had a relatively smaller effect on the spectral reflectance, so as to extract a more effective characteristic band for copper content in soil estimation.

3.3 Feature band selection

The selection of the characteristic bands is the key to the accuracy of the estimation of the prediction model (Chen et al., 2022), and in this paper, Pearson's correlation coefficient (PCC) was first used to select the spectral characteristic bands ($p < 0.01$), and the bands with highly

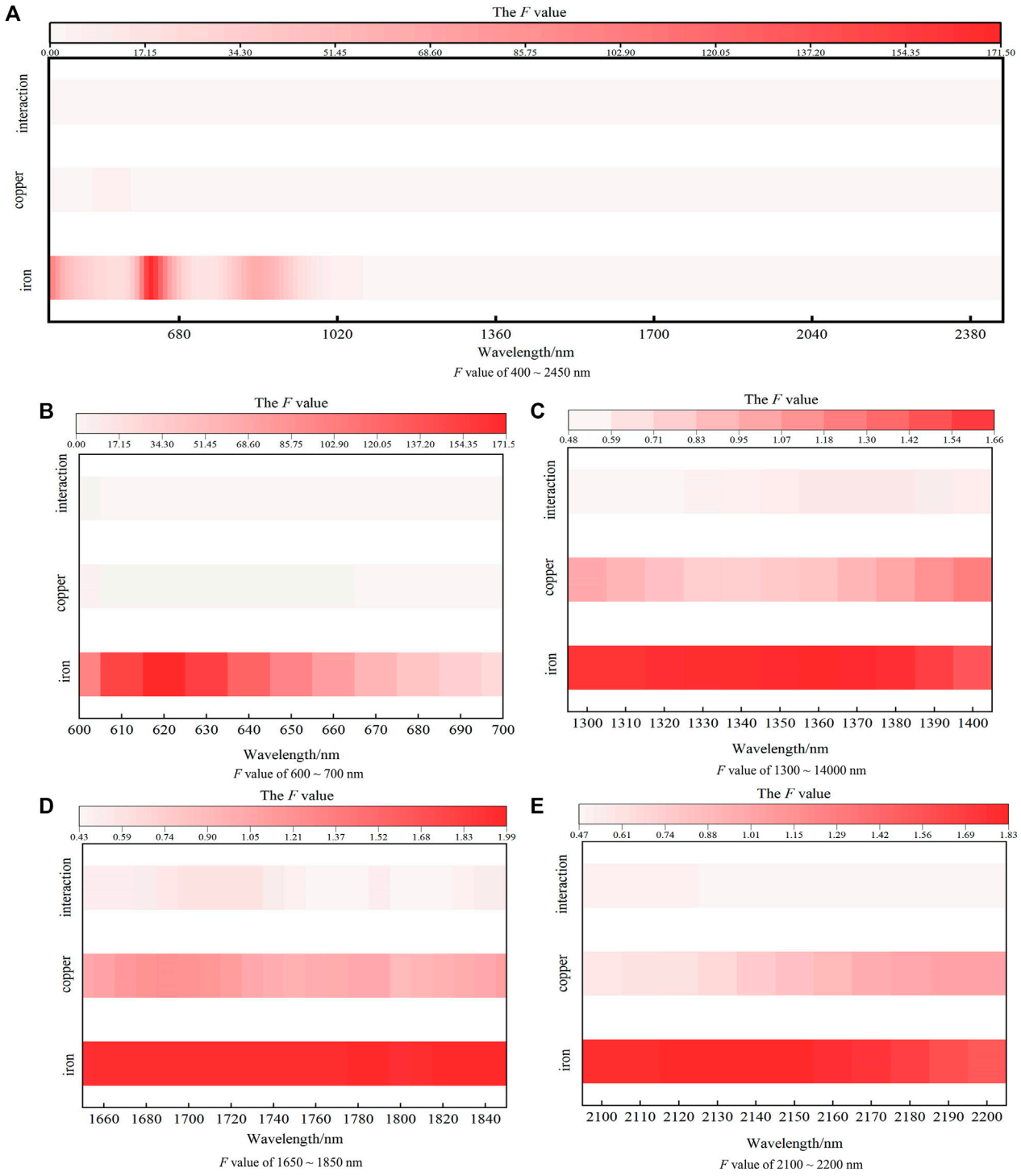

FIGURE 4
F-values in the full band and in the peak band of gene vibrations corresponding to the automatic peak.

significant correlation between copper content in soil and spectral reflectance of soil were selected for the estimation of copper content in soil, The results are shown in Figure 5.

As can be seen from Figure 5, the characteristic bands of copper content in soil screened by using PCC algorithm were distributed in the vicinity of 600 nm, 800–1,200 nm, 1,600 nm,

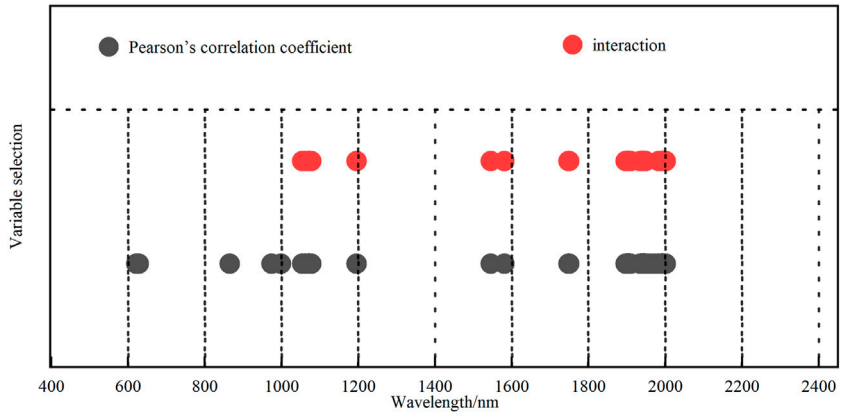

FIGURE 5
Characteristic variable of selection.

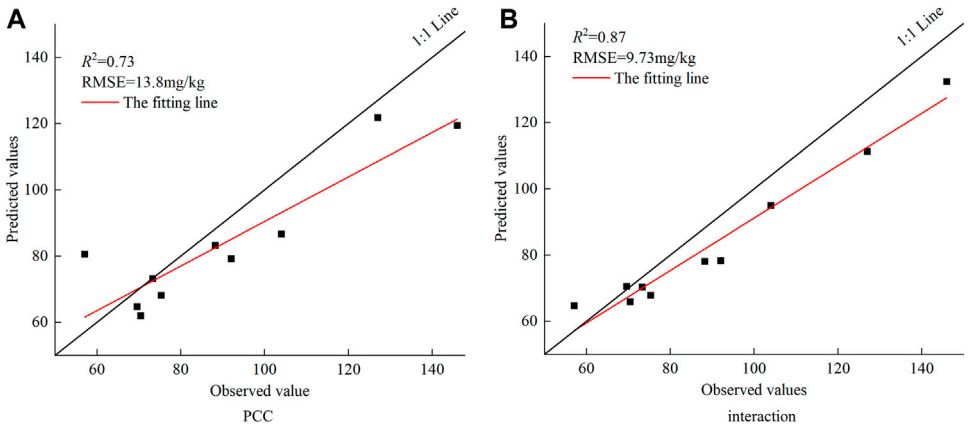

FIGURE 6
Scatter plots between observed values and predicted values of the content of copper in soil.

1800 nm and 1900–2000 nm, and the characteristic bands were widely distributed, among which the vicinity of 600 nm and 800 nm were the characteristic bands of soil iron. From the quantitative calculation results in Figure 4, it can be obtained that the Within the characteristic band, the influence of soil iron on the spectral characteristics was more than 5 times than the influence of soil copper on the spectral characteristics, which had a greater impact on the direct estimation of copper content in soil and should be excluded, while within 1900–2000 nm, in the bands 1950 nm, 1956 nm, 1963 nm, 1974 nm, and 1982 nm, the influence of iron-copper interaction on the spectral reflectance was greater than that of copper on the spectral reflectance, so them should be excluded.

3.4 Modeling accuracy improvement analysis

In this paper, the PCC algorithm and the feature bands selected by the interaction were used as input variables to estimate the copper content in soil with the RF model, and by comparing the effects of the feature bands selected by PCC and the interaction on the accuracy of the model, and then verified the necessity of considering the interaction on the accuracy improvement of copper content in soil. The results are shown in Figure 6.

Figure 6 showed that the R^2 of the model was 0.73 and the RMSE was 13.8 mg/kg when using only the feature bands selected by the PCC algorithm for soil Cu content estimation,

and the R^2 of the model was 0.87 and the RMSE was 9.73 mg/kg when considering the interaction. The accuracy of the validation set was significantly improved, and the coefficient of determination R^2 increased by 19% and the RMSE decreased by 32%, indicating that considering the interaction can effectively improve the accuracy of the inversion of copper content in soil when estimation of copper content in soil.

4 Discussion

Soil spectral characteristics are a comprehensive reflection of soil physicochemical properties, and different soil components have different responses to different bands, which is the basis for achieving quantitative estimation of soil physicochemical properties. However, the characteristic bands are not in one-to-one correspondence with soil constituents, and some bands may be characteristic bands of multiple elements, and substances with high response to spectral characteristics can mask the spectral characteristics of substances with low response, resulting in the characteristic bands of low-response substances not being easily extracted. Iron and copper in soil are companions, and they have similar effects on the spectral characteristics through the response of 3d unfilled orbital energy levels (Cheng et al., 2018). The iron content in soil is determined to affect the inversion of copper content in soil based on spectral characteristic analysis and ANOVA, which was similar to the results of Shen et al. (2019). From the definition of interaction in statistics, the interaction can be explained by the fact that the soil spectrum is altered by the difference in copper content when the iron content in the soil is constant, and similarly, the soil spectrum is altered by the difference in iron content when the copper content is the same, which indicated that the interaction is real. The extent of iron on the spectrum in some bands is more than 7 times greater than that of copper, for example, in the 620 nm band, the extent of iron on the spectrum is more than 100 times greater than that of copper, so the presence of these bands will affect the estimation accuracy of copper when estimation of copper content in soil; in the band 1930–2000 nm, the effect of interaction on the spectrum is greater than that of copper on the spectrum.

Accurate estimation of soil composition is essential for soil testing, and hyperspectral can achieve rapid detection of soil composition, but there are many hyperspectral bands, and selection of effective spectral bands is the key to ensure the estimation accuracy. Usually, the selection of characteristic bands is performed by correlation analysis, but there are many material components in soil, and only by correlation analysis, it can cause duplication of information among hyperspectral bands, and for some substances that have a greater influence on spectral reflectance, such as water and organic matter (Ge, 2021; Sun et al., 2022), the inversion accuracy is higher because they are less influenced by other substances when estimation with characteristic bands, but for spectral substances with relatively small influence on the reflectance, such as copper, etc., some of the characteristic bands selected by using only Pearson correlation coefficients will overlap with those of substances such as iron, and the influence of iron on the spectral reflectance is greater than that of copper, resulting in lower accuracy in the direct estimation of copper content. In this study, the original feature band selection method and interaction were combined to select the feature band with the greatest influence of copper and the least influence of iron for the estimation, and the accuracy of the estimation of copper content was better improved.

This study focuses on the effect of iron content in soil on the estimation of copper content in soil. Although it has been established that iron content is a major factor affecting copper content estimation, more research is needed to determine the relationship between copper content and spectral reflectance, and how it is affected by other intrinsic soil properties such as soil type, soil color, and soil organic matter, for further potential applications under field conditions. Nevertheless, it is feasible to achieve high accuracy estimation of copper content as long as the bands that are sensitive to copper content but less influential to the collection of other factors can be identified. With this, subsequent studies on the influence of other influencing factors on copper content in soil provide technical and theoretical support for the direct estimation of copper content.

5 Conclusion

In this paper, based on the interaction law derived from experimental samples, the random forest algorithm was used to verify with natural samples, and the following conclusions were drawn.

(1) The one-dimensional spectral feature analysis concludes that the spectral reflectance and iron content in soil satisfy a negative correlation, and the effect law of iron content in soil change on soil spectral reflectance was different when copper content in soil was different; similarly, the relationship between copper content in soil and spectral reflectance of soil can be different with iron content in soil, the effect of iron content in soil on soil spectral reflectance played a major role; the effect law of iron and copper content in soil on soil spectral reflectance can change with the ratio of iron and copper; The two-dimensional correlation analysis yielded that the effects of iron and copper on the soil spectral characteristics were similar, and both formed four autocorrelation peaks and

one cross peak, and the positions of the four autocorrelation peaks and one cross peak were similar; therefore, the mutual effect between iron and copper needed to be considered when estimation of copper content in soil.

(2) Quantitative analysis of the four autocorrelation peaks by ANOVA can be concluded that the action value of iron content in soil on spectral reflectance of soil within the four autocorrelation peaks was the largest, and the *F* action value of iron content in soil on spectral reflectance of soil in the 600–700 nm band was even 5 times higher than those of copper content in soil, and the values of copper content in soil and interaction on soil spectral reflectance were similar.

(3) The R^2 of PCC-RF model was 0.73, and the R^2 of the model built under the condition of considering iron and the Iron-Copper interaction was 0.87. The results shown that the accuracy of the model for the spectral estimation of copper content in soil can be effectively improved when considering the interaction, and the R^2 of its model reaches the standard of a good model, which can be used for the quantitative estimation of copper content in soil.

Data availability statement

The original contributions presented in the study are included in the article/Supplementary Material, further inquiries can be directed to the corresponding author.

Author contributions

ZF: Designed the study and writing original draft. SZ: Supervision, discussion, writing-reviewing and editing. BY, TZ, and TR: Grammar modification and polishing.

Funding

This research was supported by the Natural Resources Science and Technology Project of Anhui Province (2020-K-8).

Conflict of interest

The authors declare that the research was conducted in the absence of any commercial or financial relationships that could be construed as a potential conflict of interest.

Publisher's note

All claims expressed in this article are solely those of the authors and do not necessarily represent those of their affiliated organizations, or those of the publisher, the editors and the reviewers. Any product that may be evaluated in this article, or claim that may be made by its manufacturer, is not guaranteed or endorsed by the publisher.

References

Agrawal, A., and Petersen, M. R. (2021). Detecting arsenic contamination using satellite imagery and machine learning. *Toxics* 9 (12), 333. doi:10.3390/toxics9120333

Chen, D. S., Zhang, F., Tan, M. L., Chan, N. W., Shi, J. C., Liu, C. J., et al. (2022). Improved Na+ estimation from hyperspectral data of saline vegetation by machine learning. *Comput. Electron. Agric.* 196, 106862. doi:10.1016/j.compag.2022.106862

Chen, F. J. (2020). *Studies on Cu and Zn Content of Agricultural land Soil based on the hyper-spectrum estimation model.* Chengdou: Chengdu University of Technology.

Cheng, h., Wan, Y., Chen, Y. Y., Wan, Q. J., Shi, T. Z., Shen, R. L., et al. (2018). Study on the characteristics and mechanism of visible and near infrared reflectance spectra of soil heavy metals. *Spectrosc. Spectr. Analysis* 38 (3), 771–778. doi:10.3964/j.issn.1000-0593(2018)03-0771-08

Deng, R. R., Liang, Y. H., Gao, Y. K., Qin, Y., and Liu, X. L. (2016). Measuring absorption coefficient spectrum (400—900 nm) of hydrated and complex ferric ion in water. *Natl. Remote Sens. Bull.* 20 (01), 35–44. doi:10.11834/jrs.20164278

Ge, X. Y., Ding, J., Jin, X., Wang, J., Chen, X., Li, X., et al. (2021). Estimating agricultural soil moisture content through UAV-based hyperspectral images in the arid region. *Remote Sens. (Basel).* 13 (8), 1562. doi:10.3390/rs13081562

Gong, S. Q., Wang, X., Shen, R. P., Liu, Z. B., and Li, Y. M. (2010). Study on heavy metal element content in the coastal saline soil by hyperspectral remote sensing. *Remote Sens. Technol. Appl.* 25 (02), 169–177. doi:10.11873/j.issn.1004-0323.2010.2.169

Guo, F., Xu, Z., Ma, H. H., Liu, X. J., Yang, Z., and Tang, S. Q. (2021). A comparative study of the hyperspectral inversion models based on the PCA or retrieving the Cd content in the soil. *Spectrosc. Spectr. Analysis* 41 (05), 1625–1630. doi:10.3964/j.issn.1000-0593(2021)05-1625-06

He, J. L., Han, C. S., Wei, R., Zhou, Z. Y., and Dong, Q. L. (2019). Research on indirect hyperspectral estimating model of heavy metal Cd based on partial least squares regression. *Remote Sens. Nat. Resour.* 31 (04), 96–103. doi:10.6046/gtzyyg.2019.04.13

Hong, G., and Hyundoo, J. (2021). F-value time-frequency analysis: Between-within variance analysis. *Front. Neurosci.* 15, 729449. doi:10.3389/fnins.2021.729449

Hou, L., and Wu, Y. P. (2022). Applications of Two-dimensional correlationinfrared spectroscopy in the characterization of polymers. *Acta Polym. Sin.* 53 (05), 522–538. doi:10.11777/j.issn1000-3304.2021.21362

Jiang, X. L., Zou, B., Tu, Y. L., Feng, H. H., and Chen, X. (2018). Quantitative Estimation of Cd concentrations of type standard soil samples using hyperspectral data. *Spectrosc. Spectr. Analysis* 38 (10), 3254–3260. doi:10.3964/j.issn.1000-0593(2018)10-3254-07

Li, Z. Y., Deng, F., He, J. L., and Wei, W. (2021). Hyperspectral estimation model of heavy metal arsenic in soil. *Spectrosc. Spectr. Analysis* 41 (09), 2872–2878. doi:10.3964/j.issn.1000-0593(2021)09-2872-07

Liang, Y. H., Deng, R. R., Gao, Y. K., Qin, Y., and Liu, X. L. (2016). Measuring absorption coefficient spectrum (400—900 nm) of copper ions in water. *Natl. Remote Sens. Bull.* 20 (01), 27–34. doi:10.11834/jrs.20165132

Lin, H., Wang, Z. W., Liu, C. J., and Dong, Y. B. (2022). Technologies for removing heavy metal from contaminated soils on farmland: A review. *Chemosphere* 305, 135457. doi:10.1016/j.chemosphere.2022.135457

Lin, N., Liu, H. L., Meng, X. F., Liu, H. Q., and Yang, J. J. (2021). Hyperspectral estimation of heavy metal contents in black soil region. *Trans. Chin. Soc. Agric. Mach.* 52 (03), 218–225. doi:10.6041/j.issn.1000-1298.2021.03.024

Liu, Y. C., Li, Y. Y., Peng, Y. K., Yan, S., Wang, Q., and Han, D. H. (2020). Application of Two-Dimensional correlation spectra in the identification of adulterated rice. *Spectrosc. Spectr. Analysis* 40 (05), 237–242. doi:10.3964/j.issn.1000-0593(2020)05-1559-06

Lu, B., Dao, P. D., Liu, J. G., He, Y. H., and Shang, J. L. (2020). Recent advances of hyperspectral imaging technology and applications in agriculture. *Remote Sens. (Basel).* 12 (16), 2659. doi:10.3390/rs12162659

Luo, L. L., Chang, Q. R., Gao, Y. F., Jiang, D. Y., and Li, F. L. (2022). Combining different transformations of ground hyperspectral data with unmanned aerial vehicle (UAV) images for anthocyanin estimation in tree peony leaves. *Remote Sens. (Basel).* 14 (9), 2271. doi:10.3390/rs14092271

Maitra, S., Brestic, M., Bhadra, P., Shankar, T., Praharaj, S., Palai, J. B., et al. (2021). Bioinoculants-natural biological resources for sustainable plant production. *Microorganisms* 10 (1), 51. doi:10.3390/microorganisms10010051

Peng, J., Li, X., Zhou, Q., Shi, Z., Ji, W. J., and Wang, J. Q. (2013). Influence of iron oxide on the spectral characteristics of organic matter. *Natl. Remote Sens. Bull.* 17 (06), 1396–1412. doi:10.11834/jrs.20132273

Qin, G. W., Niu, Z. D., Yu, J. D., Li, Z. H., Ma, J. Y., and Xiang, P. (2021). Soil heavy metal pollution and food safety in China: Effects, sources and removing technology. *Chemosphere* 267, 129205. doi:10.1016/j.chemosphere.2020.129205

Ren, Z. L., Zhai, Q. P., and Sun, L. (2022). A novel method for hyperspectral mineral mapping based on clustering-matching and nonnegative matrix factorization. *Remote Sens. (Basel).* 14 (4), 1042. doi:10.3390/rs14041042

Shen, Q., Xia, K., Zhang, S. W., Kong, C. C., Hu, Q. Q., and Yang, S. W. (2019). Hyperspectral indirect inversion of heavy-metal copper in reclaimed soil of iron ore area. *Spectrochimica Acta Part A Mol. Biomol. Spectrosc.* 222, 117191. doi:10.1016/j.saa.2019.117191

Shu, M. Y., Zuo, J. Y., Shen, M. Y., Yin, P. F., Wang, M., Yang, X. H., et al. (2021). Improving the estimation accuracy of SPAD values for maize leaves by removing UAV hyperspectral image backgrounds. Int. J. *Remote Sens.* 42 (15), 5864–5883.

Sun, M. Y., Li, Q., Jiang, X. Z., Ye, T. T., Li, X. J., and Niu, B. B. (2022). Estimation of soil salt content and organic matter on arable land in the yellow river delta by combining UAV hyperspectral and landsat-8 multispectral imagery. *Sensors* 22 (11), 3990. doi:10.3390/s22113990

Tan, K., Ma, W. B., Wu, F. Y., and Du, Q. (2019). Random forest–based estimation of heavy metal concentration in agricultural soils with hyperspectral sensor data. *Environ. Monit. Assess.* 191 (7), 446. doi:10.1007/s10661-019-7510-4

Wang, J. H., Zuo, L., Li, Z. Z., Mu, H. Y., Zhou, P., Yang, J. J., et al. (2021). A detection method of trace metal elements in black soil based on hyperspectral technology: Geological implications. *J. Geomechanics* 27 (03), 418–429. doi:10.12090/j.issn.1006-6616.2021.27.03.038

Yang, H. R., Wang, F. E., Yu, J., Huang, K., Zhang, H. C., and Fu, Z. H. (2021). An improved weighted index for the assessment of heavy metal pollution in soils in Zhejiang, China. *Environ. Res.* 192, 110246. doi:10.1016/j.envres.2020.110246

Yang, W. M., Liu, G., Ou, Q. H., An, R., Li, J. M., Fu, Z. Q., et al. (2019). Study on natural aging legume seeds by infrared spectroscopy combined with curve fitting. *Chin. J. Anal. Chem.* 47 (12), 2004–2016. doi:10.19756/j.issn.0253-3820.181610

Zhang, Q., Zhang, F. F., and Huang, C. M. (2021). Heavy metal distribution in particle size fractions of floodplain soils from Dongchuan, Yunnan Province, Southwest China. *Environ. Monit. Assess.* 193 (2), 54. doi:10.1007/s10661-020-08836-8

Zhang, X., Wang, Y. B., Sun, W. C., Huang, C. P., and Zhang, M. (2020a). Inversion of Pb content in soil based on iron oxide characteristic spectrum and improved genetic algorithm. *Trans. Chin. Soc. Agric. Eng.* 36 (16), 103–109. doi:10.11975/j.issn.1002-6819.2020.16.013

Zhang, Z. T., Du, R. L., Yang, S., Yang, N., Wei, G. F., Yao, Z. H., et al. (2020b). Effects of water-salt interaction on soil spectral characteristics in Hetao Irrigation Areas of Inner Mongolia, China. *Trans. Chin. Soc. Agric. Eng.* 36 (18), 153–164. doi:10.11975/j.issn.1002-6819.2020.18.019

frontiers | Frontiers in Environmental Science

TYPE Original Research
PUBLISHED 10 October 2022
DOI 10.3389/fenvs.2022.1008900

OPEN ACCESS

EDITED BY
Chunhao Gu,
University of Delaware, United States

REVIEWED BY
Sadia Bibi,
University of Agriculture, Faisalabad, Pakistan
Wenjie Ren,
Institute of Soil Science (CAS), China

*CORRESPONDENCE
Abdulsamie Hanano,
ashanano@aec.org.sy

SPECIALTY SECTION
This article was submitted to Toxicology, Pollution and the Environment,
a section of the journal
Frontiers in Environmental Science

RECEIVED 01 August 2022
ACCEPTED 26 September 2022
PUBLISHED 10 October 2022

CITATION
Mahfouz S, Mansour G and Hanano A (2022), Compositional, genetic and functional characterization of soil culturable microbial communities in polychlorinated dibenzo-p-dioxins/furans contaminated soil.
Front. Environ. Sci. 10:1008900.
doi: 10.3389/fenvs.2022.1008900

Compositional, genetic and functional characterization of soil culturable microbial communities in polychlorinated dibenzo-*p*-dioxins/furans contaminated soil

Sabrin Mahfouz[1], Gaytha Mansour[1] and Abdulsamie Hanano[2]*

[1]Department of Plant Biology, Faculty of Sciences, University of Damascus, Damascus, Syria, [2]Department of Molecular Biology and Biotechnology, Atomic Energy Commission of Syria (AECS), Damascus, Syria

Dioxins (PCDD/Fs) are one of the most toxic environmental pollutants known to date. Due to their structural stability and extreme hydrophobicity dioxins persist in the ecosystems and can be bioaccumulated to critical levels in both human and animal food chains. Soils are the most important reservoirs of dioxins, thus soil microbes are highly exposed to dioxins, impacting their diversity, genetics and functional characteristics. To experimentally evaluate these effects, the diversity and functionality of soil microbes were assessed in seven local sites potentially exposed to PCDD/Fs.

Concentration of dioxins in soils samples was firstly determined and the soils cultivable microbes were identified and molecularly characterized as a function of their *in vitro* ability to degrade the TCDD. Our results revealed that the diversity of microbial communities largely varied among the sites and was likely inversely proportional to their level of contamination with PCDD/Fs. Furthermore, the genetics profiling of dioxin-degrading bacteria revealed that the Cytochrome P450 *CYPBM3*-positive species largely belong to the genus *Bacillus* and were randomly distributed among the soils samples, while the angular dioxygenase (*AD*)-positive species were mainly found in highly polluted soils with a major presence of the genus *Pseudomonas*. Finally, the functionality of dioxin-biodegrading genes (*AD* or *CYPBM3*), was confirmed by the ability of bacteria to consume 2,3,7,8-TCDD, and this was synchronized with an induced level of both pathways. Our results suggest that different dioxin-metabolizing pathways exist under the same environmental conditions and work differentially for an effective removal of PCDD/Fs.

Abbreviations: AD, angular dioxygenase; CYP450BM3, cytochrome P450 from *B. megaterium*; Koa, octanol: air partition coefficients; KOC, organic carbon–water partition; Kow, Octanol/Water partition coefficients; PCBs, polychlorinated biphenyls; PCDDs, polychlorinated dibenzodioxins; PCDFs, polychlorinated dibenzofurans; POPs, Persistent Organic Pollutants; TCDD, Tetrachlorodibenzo-p-dioxin; TEF, toxic equivalency factor; TEQ, toxic equivalent.

KEYWORDS

dioxins impact soil microbial communities soil microbial community, polychlorinated dibenzo-p-dioxins/furans (PCDD/Fs), angular dioxygenase (AD), biodiversity, cytochrome P450 (CYPBM3), biodegradation

Introduction

Polychlorinated dibenzo-p-dioxins (PCDDs) and polychlorinated dibenzofurans (PCDFs), collectively termed "dioxins" are highly potent class of persistent organic pollutants (POPs) that are covered by the Stockholm Convention (Stockholm, 2001). According to chlorination degree (P = 1–8), dioxins comprise 75 PCDD congeners and 135 PCDF congeners with different toxicities. Specifically, PCDD/F congeners possessing chlorine atoms in 2′, 3′, 7′ and 8′ positions of the aromatic rings are the most toxic. Typically, the toxicity of PCDD/Fs is defined as Toxicological Equivalence or TEQ units. The sum of TEQ for a given environmental sample is depending on the Toxic Equivalency Factors (TEFs). The TEF values indicate the level of toxicity compared to 2′,3′,7′,8′-tetrachlorinated dibenzo-p-dioxin (2′,3′,7′,8′-TCDD), the most toxic congener of dioxins, that has been given a reference TEF value of 1 (World Health Organization, 2016).

Naturally, dioxins can be released into the environment through volcanic eruptions and forest fires (Hay, 1981). Such scenarios are becoming more frequent with the actual increases of forest fires (Salamanca et al., 2016; Oliveira et al., 2020). Dioxins can also enter the environment through domestic and municipal incinerations (Tuppurainen et al., 2003), by various manufacturing processes including the synthesis of chlorinated aromatic products, such as herbicides, pesticide and paper processing. Electronic waste (e-waste) is also an important and active source of PCDD/Fs (Jin et al., 2020). Once emitted into the environment, dioxins contaminate specific environmental compartments, bioaccumulate, and therefore, transmit through the food chain due to their structural stability and high lipid-solubility (Geyer et al., 1993). Their adverse effects on human health are now well established, e.g., immunotoxicity (Marshall and Kerkvliet, 2010), wasting syndrome (Huuskonen et al., 1994), dysfunction of immune and reproductive systems (Carney et al., 2006), carcinogenicity (Toth et al., 1979), and teratogenicity (Baker et al., 1995).

Due to their high affinity to soil organic matter, PCDD/Fs have a high value of organic carbon–water partition coefficient (KOC). This confers a low mobility together with a low water solubility to such compounds, thus enabling them to accumulate in soil, affecting plants as well as soil microorganisms (Chrostowski and Foster, 1996; Hanano et al., 2014b; Hanano et al., 2015a; Hanano et al., 2018a; Hanano et al., 2018b). Once accumulated in the soil, PCDD/Fs affect "soil health" (Gul et al., 2021). Soil microbiota plays determinant roles in the maintenance of soil health and in the detoxification of detrimental chemicals, including PCDD/Fs (Cerniglia et al., 1979). Soil microbes respond to dioxin exposure by a set of biological modulations that impact their diversity and functionality. In this context, multiple parameters, e.g., density, diversity and enzymatic activities, are now used as indicators for monitoring and assessing the exposure levels of soil microbial communities to stressors (Yao et al., 2018; Mahfouz et al., 2020). Consequently, diverse bacterial and fungal species were identified and characterized as potential biodegraders of dioxins (Magan et al., 2010; Stella et al., 2017; Hanano et al., 2019a).

So far, diverse bacterial enzymatic pathways have been characterized with respect to the biodegradation of dioxins such as the angular dioxygenases (Sato et al., 1997; Armengaud et al., 1998; Habe et al., 2001), certain microbial peroxidases and anaerobic dehalogenases (Bumpus et al., 1985; Bunge et al., 2003). Furthermore, it was shown that specific enzymes of bacterial P450s, initially identified as homologs of xenobiotic-mammalian metabolizing P450s, exhibited similar activities towards dioxins (Narhi and Fulco, 1987; Boddupalli et al., 1992). The first bacterial P450 was characterized in *Bacillus megaterium* ATCC 14581 by the group of Fulco et al. (Matson et al., 1977), conducting a detailed characterization of three distinguished isoforms of P450 from *B. megaterium*, referred as to $P450_{BM-1}$, $P450_{BM-2}$ and $P450_{BM-3}$ (Kim and Fulco, 1983; Schwalb et al., 1985). Beyond their original activities as fatty acids oxygenases, both native or engineered $P450_{BM-1}$ and $P450_{BM-3}$ have shown remarkable activities to oxidize an emergent range of exogenous substrates including certain drugs such as phenacetin and methoxyresorufin (Kim et al., 2010), certain chlorinated insecticides (Seralathan et al., 2014; Meena et al., 2016) and even more certain dioxins notably 2,3,7-trichloro-dibenzo-*p*-dioxin (Sulistyaningdyah et al., 2004).

The main objective of this work is firstly to demonstrate whether the diversity, genetics and functional signatures of soil microbial community are specifically affected by the contamination of soil with dioxins. Secondly, if these signatures vary according to the concentration of dioxins in soil. Our work presents a new set of data on the composition, genetics and functional properties of microbial communities in soil samples contaminated with PCDD/Fs. Soil microbial communities were subjected to a detailed characterization in terms of density and diversity linked with contamination level of soils with PCDD/Fs. Moreover, large-scale analyses were performed for genes transcripts of specific dioxin-degradation pathways in Gram-positive and Gram-negative bacterial species. Our report suggests that the most characterized bacterial pathways responsible for degradation of dioxins, angular dioxygenase (AD) and cytochrome P450 BM3 (CYPBM3), are

found in both Gram-negative and Gram-positive bacteria. Effectively, this new statement raises questions on a possible functional connection between these two distinct dioxin-degradation pathways when both are found in such bacteria.

Materials and methods

Information about the sites and soil sampling

Supplementary Table S1 presents a set of informative data about the sampling sites (A1, A2, A3, A4, B, C, and D) that have been targeted in this study. The sites A1 to A3 are located at 10 km (6.2 mi) Southwest of Damascus, the Syrian capital, corresponding to waste incineration stations. The site A4 corresponds to an olive grove located next to waste incineration sites (A1, A2, and A3). The site B is an open site of industrial and domestic wastewater collection located in Deir al-Asafir, 12 km Southeast of Damascus. The site C is nearby Homs's refinery, located in Western Syria, 162 km North of Damascus. The site D corresponds to an open waste incineration site in Al Suwayda city located in southwestern of Damascus. Two soil samples were collected form the site A4 and three soil samples were respectively collected form the sites A1, A2, A3, B, C, and D. The samples (S1-S20) (about 500 g each) were taken from the surface of soil (0–5 cm depth), put in sterile bags and promptly stored at + 4°C until further use.

Nitrogen content analysis in soil samples

The soil samples were air-dried, sieved using a 1 mm-sieve to eliminate rough materials. Total organic nitrogen, NO_3 and NH_4 were determined as described before (Kjeldahl, 1883). Briefly, the Kjeldahl method consists of three successive steps: 1) the soil sample is digested by sulfuric acid in the presence of a catalyst that helps in converting the amine nitrogen to ammonium ions (NH_4^+); 2) the NH_4^+ ions are then converted into ammonia gas that is heated, distilled and trapped into a solution where it is dissolved again; 2) finally the amount of the ammonia that has been trapped is determined by titration with a standard solution.

Bacteria isolation and culture conditions

One Gram of each soil sample was added into 5 ml of one X PBS (Phosphate buffer Saline, pH 7.2) and vigorously shaken for 5 min. The suspensions were diluted by the same buffer, then 100 µL of dilutions from 10^{-3} to 10^{-6} were cultured on Luria–Bertani (LB) agar plates. The plates were incubated at 28 ± 2°C until the appearance of distinct colonies (Hanano et al., 2014c). Single colonies were transferred onto fresh LB plates and kept at 4°C for further analysis. The density of cultured bacteria was estimated by measuring colony forming unit (CFU) per Gram dry weight soil and expressed as CFU g^{-1} DW. Finally, all bacterial isolates were stored at—80°C in LB with 20% glycerol.

Extraction of total PCDD/Fs from soil samples

Before proceeding, soil samples were dried at room temperature, ground and sieved. PCDD/Fs extraction was performed as described previously (Hanano et al., 2014c). Briefly, 5 g of soil were mixed with 20 ml of hexane containing 20% acetone and the mix was horizontally shaken at 200 rpm for 1 h at room temperature. The organic phase was separated by a brief centrifugation at 4,000 rpm for 5 min, then carefully recovered and promptly mixed with 8 ml of sulfuric acid (~0.9 mM) and briefly shaken for 2 min in the same conditions. Subsequently, the upper organic phase, corresponding to hexane extract, was carefully transferred into a clean 40-ml vial. The cleaned up of fractions was performed with a column composed of 0.5 g anhydrous Na_2SO_4 on top and 1.0 g of florisil at the bottom. This column was first activated with 3 ml of dichloromethane/hexane/methanol (50:45:5). PCDD/Fs were then eluted with 5 ml of the same solvents mix. The extract volume was reduced to 1 ml under nitrogen flow. One hundred microlitres of Dimethyl sulfoxide (DMSO) was added to the extract and the mix was dried to remove all trace of solvents. 500 µL of DMSO was added and the final volume of the extracts was adjusted to 1 ml by deionized H_2O. Dilution of 1:10 with 50% DMSO in deionized water was used for analysis of dioxin by enzyme-linked immunosorbent assay (ELISA). To evaluate the quality of extraction protocol, a TCDD-free soil sample was spiked with 100 ng L^{-1} of 2,3,7,8-TCDD and the same extraction protocol was applied.

Detection and measuring of PCDD/Fs by enzyme-linked immunosorbent assay

An Abraxis TCDD-ELISA kit was used to determine the PCDD/Fs concentration in the extracts according to the manufacturer's instructions (Abraxis LLC, United States). The absorbance was measured at 450 nm by a microplate reader (Multiskan EX, Thermo/Labsystems, United States).

PCR amplification of 16S rRNA

The extraction of bacterial genomic DNA was done using a Genomic DNA extraction kit (Qiagen-Germany) according to the manufacturer's manual. The isolated gDNA was eluted in 50 µL of distilled water and the concentration was adjusted to

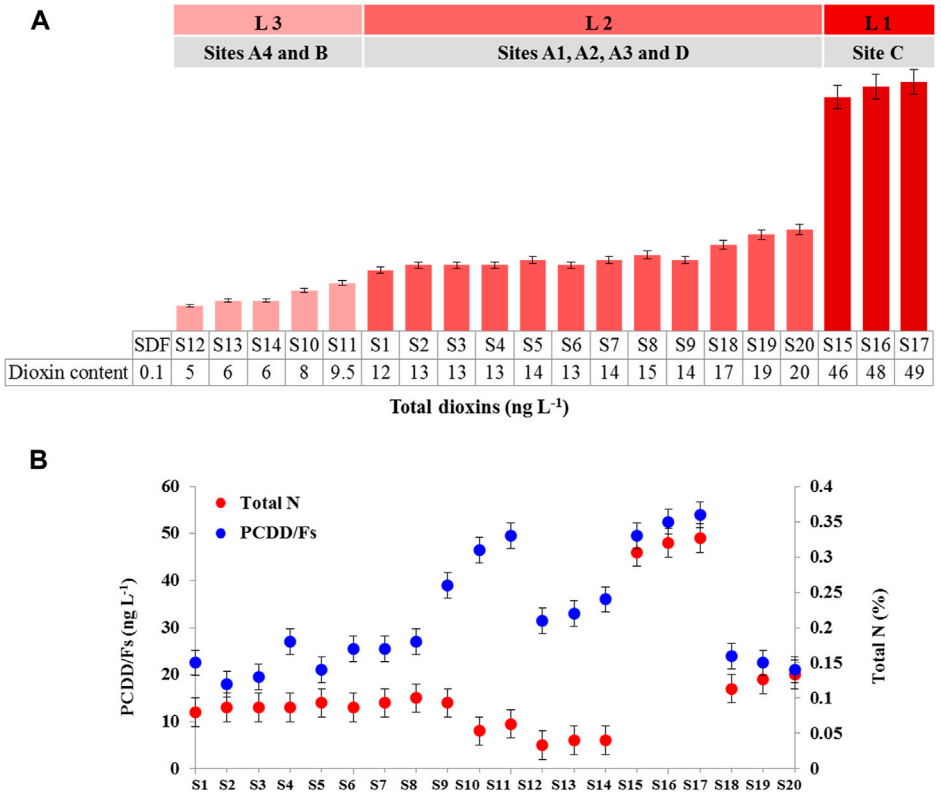

FIGURE 1
Level of PCDD/Fs in soil samples. **(A)** PCDD/Fs were extracted from soil samples and the total PCCD/Fs in each sample was determined by a PCDD/Fs-specific ELISA kit. Dioxins levels in soil samples were categorized into three levels; level L 1 (~50 ng L^{-1}), the level L2 (from 12 to 20 ng L^{-1}), and level L3 (from 5 to ~10 ng L^{-1}). **(B)** The relation between the total nitrogen content in soil samples and their levels of contamination with PCDD/Fs. All measurement were done in triplicate. Values are means ± S.D (n = 9).

200 ng μL^{-1} and kept at −20°C. A 1450 bp-fragment of 16S rRNA gene was amplified by PCR using the primers 27F and 1492R (Supplementary Table S2, Supplementary Material S1) (Marcial Gomes et al., 2008). The PCR was performed as described before by (Hanano et al., 2014c). The 25 µL final volume reaction was composed of 3 mM $MgSO_4$, 200 µM each of the four dNTPs, 10 µM of each primers, 2.5 U *Taq* DNA polymerase and 200 ng of gDNA. PCR conditions were 94°C for 4 min, 35 cycles at 94°C for 30 s, 56°C for 30 s, 72°C for 1 min, followed by a final extension step at 72°C for 10 min.

Molecular identification of bacteria by 16S rRNA sequencing

The PCR products of 16S rRNA were sequenced using an ABI 310 Genetic Analyzer (Applied Biosystems). 16S rRNA PCR products were sequenced in both direction forward and reverse. The quality of sequencing was confirmed by sequencing a 16s rRNA amplicon of reference strain of *B. megaterium* (Hanano et al., 2019b). The reads of 16S rRNA sequence were analysed using the BLAST search program from GenBank-NCBI database (https://www.ncbi.nlm.nih.gov/). Bacterial genus and species were identified with a score of similarity of (≥99%). The 16S rRNA sequences reported in this study were submitted to the GenBank-NCBI (GenBank ID: from MW475085 to MW475154).

Analysis of dioxin-degrading genes transcripts

Transcripts of dioxin-degrading genes were quantified by reverse-transcription quantitative PCR (RT-qPCR) according to (Hanano et al., 2015b). RNAs were extracted from cultured bacteria as previously described (Hanano et al., 2019b). The extracted RNA was diluted to 50 ng μL^{-1} using RNase-free water and conserved at −80°C. One µg total RNA were used for first-strand cDNA synthesis (Hanano et al., 2014c). Real-time PCR was carried out in 96-well plates using an AriaMx Real-time PCR System (Agilent technologies, United States). Where, 25 µL-reaction mixtures were composed of 0.5 µM of each primers (Supplementary Table S2), 12.5 µL of SYBR Green PCR mix

TABLE 1 CFU and Gram stain results of cultivable bacterial isolates.

Site	Soil sample	Microbial density CFU g^{-1}dw	Total bacteria isolates	Gram+/−
A1	S1	60 × 106	5	1/4
	S2	29 × 105	6	5/1
	S3	34 × 105	6	5/1
A2	S4	28 × 105	8	3/5
	S5	58 × 105	10	5/5
A3	S6	23 × 106	5	4/1
	S7	159 × 107	3	0/3
	S8	23 × 107	7	2/5
A4	S9	64 × 107	8	3/5
	S10	84 × 106	9	7/2
	S11	77 × 106	5	1/4
B	S12	24.5 × 107	4	0/4
	S13	10 × 107	3	1/2
	S14	15 × 106	4	2/2
C	S15	35 × 106	4	0/4
	S16	135 × 107	2	0/2
	S17	212 × 107	2	0/2
D	S18	75 × 104	7	6/1
	S19	92 × 105	6	3/3
	S20	56 × 105	3	2/1
Total			**107 (total of isolates)**	**50/57 (ratio of +gram/-gram staining)**

(Bio-Rad, United States) and 100 ng cDNA. Fragments of 168, 144, and 433 bp from the coding sequence of bacterial angular dioxygenase (*ADα-subunit*), *CYPBM1* and 16S rRNA, were respectively amplified using gene-specific primers as described before (Hanano et al., 2019b). The relative quantification (RQ = $2^{(-\Delta\Delta CT)}$) of target genes was determined by the AriaMx qPCR system.

Essay of 2,3,7,8-TCDD biodegradation

Bacterial isolates that harbor dioxin-degradation genes were assessed for their ability to metabolize 2,3,7,8-TCDD in a laboratory-scale experiment**.** A pure colony of the bacterial isolate was pre-cultured in LB medium and incubated overnight at 28 ± 2°C. Five hundred microlitres (500 µL) of bacterial culture having an OD_{600} = 1 was taken, centrifuged and washed with 1 ml of mineral salt medium (MSM) to eliminate all traces of LB medium. Mineral salt medium was composed as reported before (Hanano et al., 2014c). Isolates were cultured into 10 ml of MSM supplemented with 100 ng L^{-1} (0.1 ppb) of 2,3,7,8-TCDD (final concentration), as a sole carbon source. The cultures were incubated for 6 weeks at 28 ± 2°C. A negative control, the same culture without 2,3,7,8-TCDD was performed. Bacterial growth was measured and expressed as CFU mL^{-1}.

Statistics and biodiversity indices

Data were expressed as means ± standard deviation (SD). The comparisons between control and treatments were statistically confirmed by one-way analysis of variance (ANOVA) SPSS Statistics software. Differences between control and treatments were significant as $p < 0.05$ or very significant as $p < 0.01$. Microbial diversity for each soil samples was assessed using two diversity indexes; Shannon's diversity index (H) and Simpson's diversity index (D). Shannon's diversity index (H), an informative statistic index, which means that all species present in a sample are randomly sampled. Shannon's Index (H) is calculated by the following equal: $H' = -\sum_{i=1}^{S} p_i \ln p_i$, where p is the proportion (n/N) of individuals of one given species found (n) divided by the total number of individuals found (N), ln is the natural log, $\sum$ is the sum of the calculations, and s is the number of species. Simpson's diversity index (D) is calculated by the following equal:

$D = 1/\sum^{S}{}_{i=1}\, p_i^2$, where p is the proportion (n/N) of individuals of one specific species found (n) divided by the total number of individuals found (N), $\sum$ is still the sum of the calculations, and s is the number of species. Bacterial species richness was evaluated by Margalef's index D_{Mg} and calculated by the following equal: $D_{Mg} = (S\text{-}1)/(\ln N)$, where S is the number of species recorded, N is the total number of individuals in the sample and ln is the natural log. D_{Mg}, H' and D indices were calculated using an online calculator for species richness and biodiversity at http://www.alyoung.com/labs/biodiversity_calculator.html.

Results

Evaluation of the PCDD/Fs pollution level in soil samples

The analysis of PCDD/Fs content in the soils samples (S1-S20) showed that they vary significantly in respect to the concentrations of PCDD/Fs, compared to a reference soil sample (SDF; dioxin-free soil) (Hanano et al., 2014c). As shown in Figure 1A, the concentration of dioxins in soil samples ranged from 5 to ~50 ng L^{-1}. Accordingly, the concentration of PCDD/Fs was categorized into three levels. The highest one, Level I (LI) corresponds to a concentration of 50 ng L^{-1} of PCDD/Fs, and comprises soils samples S15, S16 and S17, collected from the site C. The Level 2 (L2) categorizes the soils samples that contained 12 and 20 ng L^{-1} of PCDD/Fs, including S1 to S9, S18, S19 and S20 collected from the sites A1, A2, A3 and D. Whilst, the lowest level, Level 3 (L3), represents concentrations ranged from 5 to ~10 ng L^{-1} of PCDD/Fs, comprising soil samples S12, S13, S14, S10 and S11 collected from the sites B and A4, respectively. These data indicate that the soils samples of the site C, situated nearby Homs refinery showed the highest level of dioxin contamination. Soils samples of the sites A1, A2, A3, and D, located around the waste incineration stations, were moderately contaminated with dioxins. While, the lowest contaminated soil samples belonged to the site A4, corresponding to the olive grove located close to a waste incineration sites as well as to the site B, corresponding to an open site of industrial and domestic wastewater collection.

PCDD/Fs level of soils in connection with their content of organic nitrogen

Total N_2 in soils samples of the sites A1, A2, and A3, presented in Supplementary Table S3, ranged between 0.12% and 0.18%, which was relatively similar to the total N at site D (from 0.14% to 0.16%). Whereas, the highest values of the total N were detected in the soil samples of site C with a range of 0.33%–0.36%. Also, high levels of total N were found in the samples of site A4 that ranged between 0.26% and 0.33%. Furthermore, the NH_4/NO_3 ratio considerably varied among soil samples, the highest NH_4/NO_3 ratios (8.4–9.6) were found in soil samples from the site A4, while the lowest ones (1.9–2.7) were in soil samples from the sites A1, A2, and A3. However, the NH_4/NO_3 ratio was similar (5.5–7.9) for the sites B and D and lower in the site C (3.5–5.1). Next, the total N content of soil samples was evaluated as a function of their level of contamination with dioxins, and as Figure 1B shows, there is no correlation between the total N content in soil samples and their level of contamination with dioxins. In exception of that, the highest polluted soil samples with PCDD/Fs (S15, S16 and S17 from site C) showed a significant correlation ($p < 0.01$) with the content of total nitrogen. Altogether, these data indicate that soils from the site C, situated nearby Homs refinery, showed the highest level of contamination with dioxins and this was significantly correlated with a high level of total nitrogen.

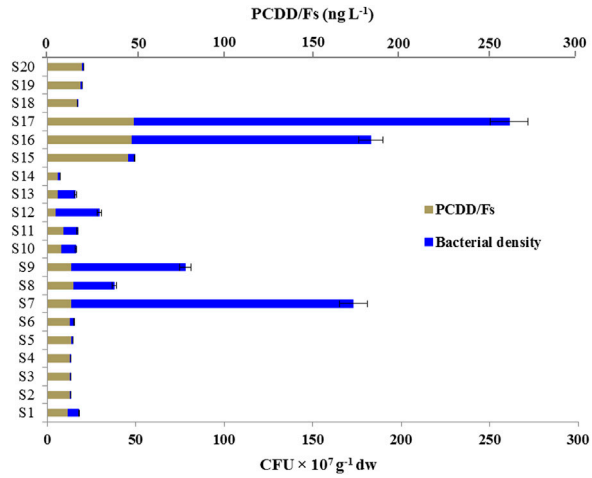

FIGURE 2
Density of microbial communities in soil samples with respect to PCDD/Fs concentrations. The densities of soil microbial communities are expressed as CFU × 10^7 per g of dry soil (dw). Level of PCCD/Fs in soil samples was determined as described before. CFUs were determined in triplicate. Values are means ± S.D (n = 3).

Density of culturable microbial communities in soils samples

The bacterial population densities, evaluated for each soil samples and expressed as CFU g^{-1} of dry weight, differed considerably among soil samples. As Table 1 shows, the highest bacterial densities were found in soil samples S7, S17, S16, S9, S12, S8 and S13 (from sites C, A3, A4 and B) corresponding to 159 × 10^7, 212 × 10^7, 135 × 10^7, 64 × 10^7, 24.5 × 10^7, 23 × 10^7 and 10 × 10^7 CFU g^{-1}dw, respectively. Whilst,

TABLE 2 Relative abundance of bacterial genera in each soil sample.

Site	A1			A2			A3			A4			B			C			D		
Soil sample	S1	S2	S3	S4	S5	S6	S7	S8	S9	S10	S11	S12	S13	S14	S15	S16	S17	S18	S19	S20	
Bacterial isolates																					**Total (%)**
Bacillus sp.	1	3	4	3	4	2		2	3	5	1			2				6	2	2	37.38
Pseudomonas sp.	3	1		5	2					1	3	2					1	1	3	1	21.49
Acinetobacter sp.					1		2	5	5					2							14.01
Enterobacter sp.							1						1		1	2					4.67
Klebsiella sp.	1											2	1								3.73
Massilia sp.			1		1					1											2.80
Staphylococcus sp.		2																			1.86
Arthrobacter sp.										2											1.86
Cronobacter sp.															2						1.86
Solibacillus sp.					1																0.93
Lysinibacillus sp.			1																		0.93
Brevibacillus sp.						1															0.93
Brevundimonas sp.						1															0.93
Oxalicibacterium sp.					1																0.93
Microbacterium sp.						1															0.93
Macrococcus sp.																			1		0.93
Chryseobacterium sp.											1										0.93
Pantoea sp.															1						0.93
Citrobacter sp.																	1				0.93
Cellulosimicrobium sp.													1								0.93
Total 107 (ratio of +gram /-gram staining)	5	6	6	8	10	5	3	7	8	9	5	4	3	4	4	2	2	7	6	3	**100**

the bacterial densities in soil samples S10, S11, S1, S15, S6 and S14 were ranged between 15×10^6 and 84×10^6 CFU g^{-1} dw. However, the samples of sites A1, A2 and D (S2, S3, S4, S5, S18, S19, and S20), with densities ranging between 92×10^5 and 75×10^4 CFU g^{-1}dw, were less populated compared to other sites. In respect to their level of contamination with PCDD/Fs, two of the highest bacterial densities were found in the highest contaminated soil samples (S16 and S17) (Figure 2). This was supported a relatively strong positive Pearson correlation (r = 0.7759), which means that high bacterial densities scores go with high PCDD/Fs level scores (and *vice versa*). These data indicate that the highest densities of bacterial populations were found in soil samples from sites A3, A4, B and C and the lowest were found in soil samples from the site D.

Compositional characteristics of culturable bacterial communities

We noted that *Bacillus* genus was the most abundant in soil samples with 37.3% of total bacterial genera identified, followed by the genera *Pseudomonas* and *Acinetobacter* that represent 21.4% and 14%, respectively (Table 2). The genera *Enterobacter* and *Klebsiella* constitutes about 4.6% to 3.7% of the whole bacterial community. Beyond the top five, the bacterial genera e.g., *Massilia*, *Staphylococcus*, *Arthrobacter* and *Cronobacter* were also identified and constitutes 8.83% of the total bacterial community. Bacteria genera with less than 1% contribution to the bacterial community include *Solibacillus*, *Lysinibacillus*, *Brevibacillus*, *Brevundimonas*, *Oxalicibacterium*, *Microbacterium*, *Macrococcus*, *Chryseobacterium*, *Pantoea*, *Citrobacter* and *Cellulosimicrobium*.

Supplementary Table S4 shows that the bacterial community of site A1 (S1, S2 and S3) was predominantly composed of *Bacillus* genus with *B. subtilis* and *B. cereus* being the most abundant. Also, the genus *Pseudomonas* was interestingly represented by *P. stutzeri* and *P. putida*. While *Bacillus* and *Pseudomonas* genera also dominated at site A2 (S4, S5, and S6), different species of the genera were recovered at the site. These include *B. mycoides*, *B. circulans*, *B. mobilis*, *P. bauzanensis* and *P. saudiphocaensis*. The composition of bacterial community in the site A3 (S7, S8 and S9) was remarkably typified by the presence of *Acinetobacter* genus, where *A. calcoaceticus*, *A. tjernbergiae*, *A. radioresistence* and *A. pittii* were the major species of the bacterial

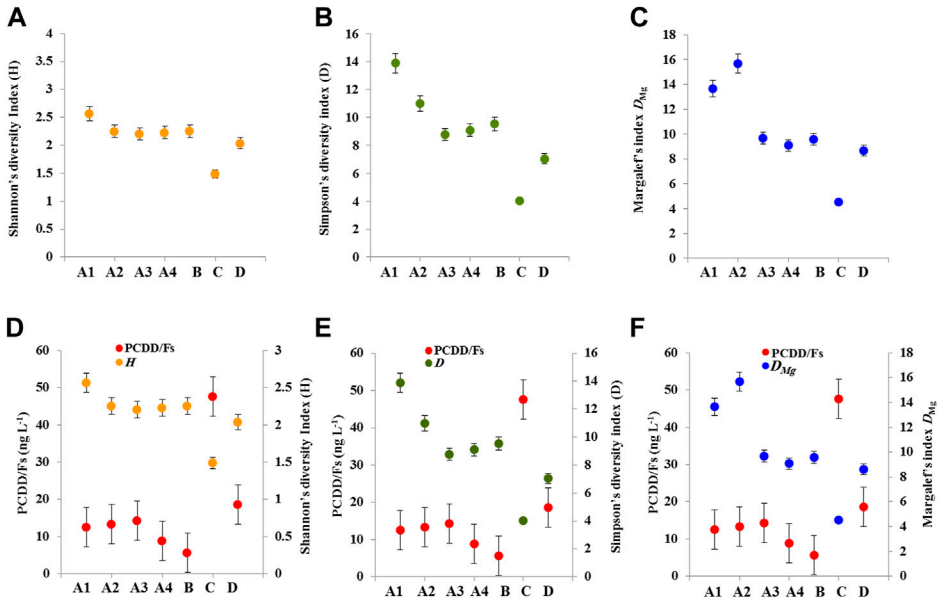

FIGURE 3
Diversity indices of microbial communities as a function of contamination level with PCDD/Fs in different sites. **(A–C)** Diversity and bacterial species richness were evaluated by The Shannon's diversity Index (H), The Simpson's diversity index (D) and Margalef's index D_{Mg}. **(D–F)** The relations between diversity and richness species, H, D and D_{Mg}, and the concentration of PCDD/Fs in different sites. Values are means ± S.D (n = 3). Diversity indices were significantly lower in soil samples that are contaminated with the highest concentration of PCDD/Fs ($p < 0.01$).

community in this site. Although the structure of bacterial community at the site A4 (S10 and S11) was comparatively similar to those of sites A1 and A2, the bacterial species, *Arthrobacter crystallopoietes*, was exclusively detected at the site. Bacterial community in the site B (S12, S13 and S14) was proportionally composed of *Bacillus*, *Pseudomonas*, *Acinetobacter* and *Klebsiella* genera with a particular appearance of *K. aerogenes* and *K. pneumonia*. The structure of bacterial community of the site C (S15, S16, and S17) was limited in term of species number, these species were mainly belonging to *Enterobacter* and *Cronobacter*. Finally, the composition of bacterial community of the site D (S18, S19, and S20) was predominantly consisting of *Bacillus* and *Pseudomonas* genera, and the species *Bacillus licheniformis* and *Pseudomonas stutzeri* were the most abundant in this site. The bacterial strains identified by sequencing of 16S rRNA with a high score of certainty (72 strains) were submitted in the NCBI GeneBank databases under the accession numbers from MW475085 to MW475154 (please refer to Supplementary Table S4).

Informative relationship between soil microbial diversity and dioxin level

Microbial diversity for each site was determined using two diversity indices, the Shannon's diversity Index (H) and the Simpson's diversity index (D), however, the microbial species richness was determined by Margalef's index D_{Mg} (please refer to Supplementary Tables S5–S11). Figure 3A shows the variation in H index according to sites, while this index ranged between 2.5 and 2.2 for the sites A1, A2, A3, A4, and B, it showed its lowest value (1.49) in the site C, and was ~2.0 in the site D. In a similar tendency, the index D held a record (~13.8) in the site A1, then lowered in the sites A2, A3, A4 and B, and was about 4.0 in the site C (Figure 3B). In parallel, the Margalef's index D_{Mg}, expressing the species richness of microbial communities varied according the sites and showed high values (4.59 and 4.78) in the sites A1 and A2, intermediated values in the sites A3, A4 and B, and a low value (1.92) in the site C (Figure 3C). In connection with the level of PCDD/Fs detected in the sites, it is worth noting that the values of H, D and D_{Mg} indices were significantly lower in soil samples that are contaminated with the highest concentration of PCDD/Fs ($p < 0.01$). While, the highest values of H, D and D_{Mg} (2.5, 13.8, 4.78) were found in the sites with low levels of PCDD/Fs (A1 and A2), the lowest values of H, D and D_{Mg} (1.49, 4.0, 1.92) were found in the heavily contaminated sites with PCDD/Fs, C and D (Figures 3D–F). Together, our data show that the indices of biodiversity and species richness of microbial communities largely varied according to the sites and are inversely proportioned to their level of contamination with PCDD/Fs.

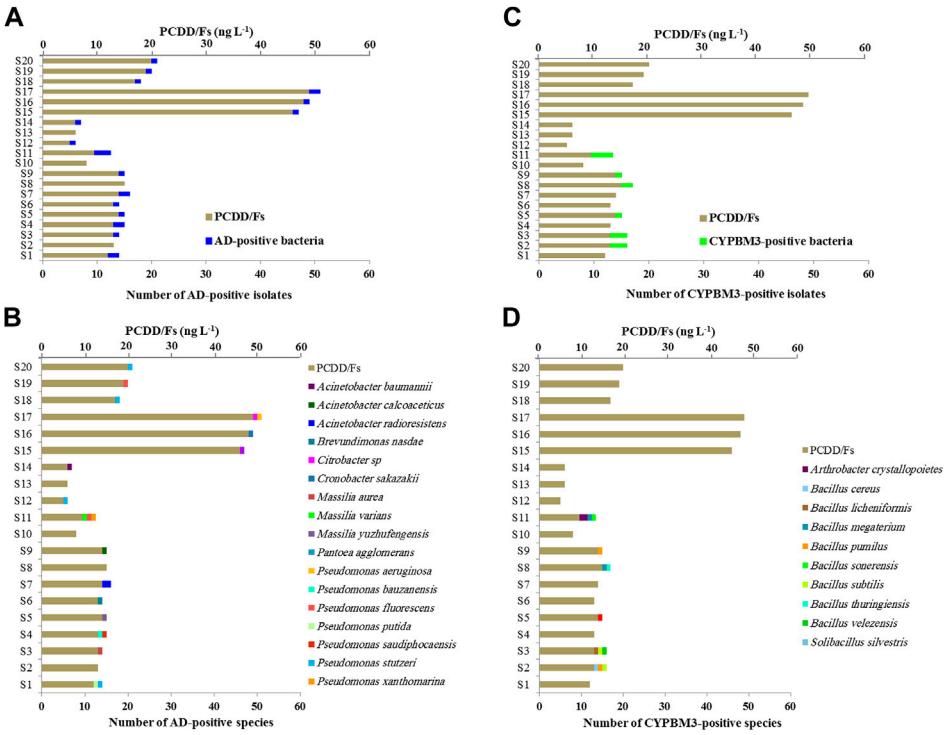

FIGURE 4
Genetic screening for dioxin-degrading genes in bacterial communities. Screening for dioxin-metabolizing genes in bacterial isolates was done using gene-specific primers against the bacterial angular dioxygenase (*AD*) and cytochrome P450 *CYPBM3*. **(A,C)** The number in AD-positive or CYPBM3-positive bacterial isolates in connection with the concentration of PCDD/Fs in soil samples are presented respectively. **(B,D)** Distribution of bacterial species among the soil samples. The number of isolates from each species found in the soil samples are presented.

Genetic profiling for potential PCDD/Fs-degrading bacteria

The bacterial communities of soil samples were genetically screened for the presence of angular dioxygenases (*AD*) and the cytochrome P450 BM3 (*CYPBM3*) genes, the most characterized bacterial pathways responsible for degradation of dioxins. We identified 22 Gram-negative isolates possessing an *AD*-encoding gene and 14 Gram-positive isolates with a *CYPBM3*-encoding gene. Figure 4A shows that although there is random distribution of *AD*-positive species among soils samples, about 31% of them were found in the highest PCDD/Fs-polluted soils (S15-S20). A moderate positive Pearson correlation (r = 0.6427) was found, which means there is a tendency for high AD-positive species number scores go with high PCDD/Fs level scores (and *vice versa*). The identities of *AD*-positive species were determined for each soil samples, and as Figure 4C shows, the *AD*-positive bacterial species that found in the highest PCDD/Fs-contaminated soils (S15-S20) belonged mainly to the genus *Pseudomonas* (57.14%), and to the genera *Citrobacter*, *Cronobacte* and *Pantoea* with 14.25% for each. A different scenario was observed for the *CYPBM3*-positive species, while the highest abundance of these species was detected in the soil samples collected from the sites A1, A2, A3 and A4, showing an intermediate level of contamination with PCDD/Fs. These species were absent in the highest contaminated soils samples (S15-S20) (Figure 4B). The most abundant *CYPBM3*-positive species belonged to the genus *Bacillus* (85.71%), while one species belong to *Arthrobacter* and another to *Solibacillus* (Figure 4D). Our data indicate that most of bacterial species that harbor the *AD* encoding gene were found in the highest polluted soils with a major presence of the genus *Pseudomonas*.

Functional identification of 2,3,7,8-TCDD-degrading bacteria

Laboratory-scale experiments were conducted to evaluate the ability of 36 bacterial isolates, harbouring the dioxin-degrading genes, to degrade 2,3.7.8-TCDD using the pollutant as the sole carbon source. Results showed that only six bacterial strains grew on the 2,3,7,8-TCDD, with different abilities. Figure 5A shows the growth curves of these stains expressed as CFU mL^{-1}. Of them, the strain A4-2 d of *Bacillus megaterium* grew more

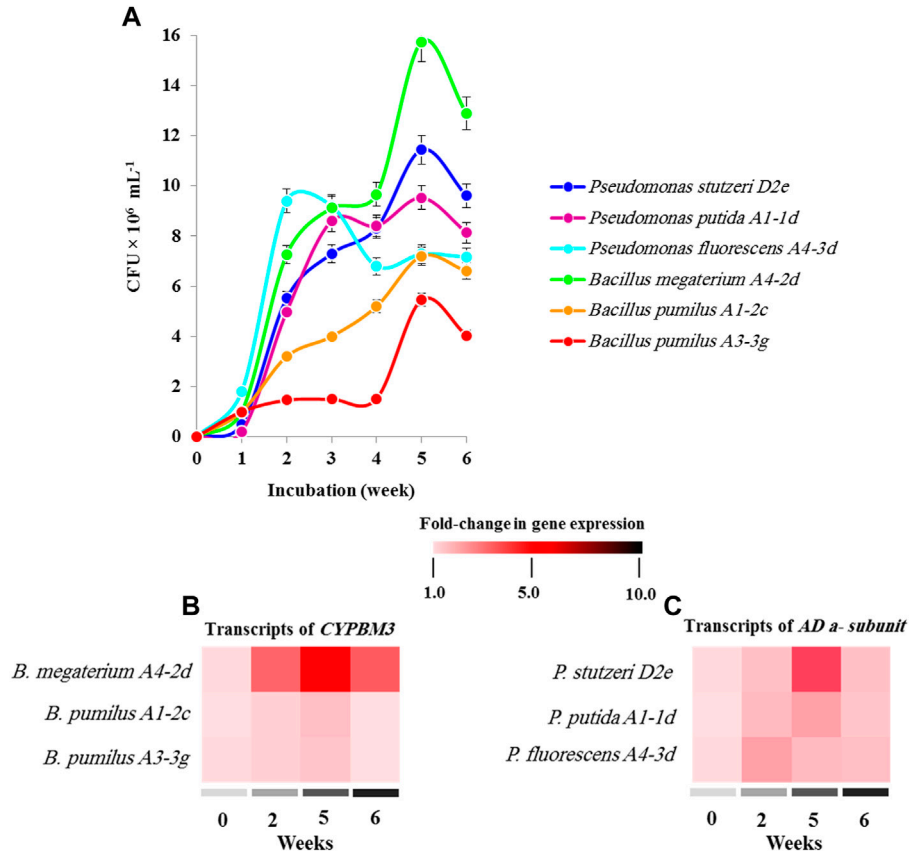

FIGURE 5
Functional identification of 2,3,7,8-TCDD-degrading bacteria. **(A)** The functionality of dioxin-biodegrading genes (*AD* and *CYPBM3*) was assayed by evaluating bacterial growth on 2,3,7,8-TCDD, as sole carbon source in a laboratory-scale experiment. The growth of each strain was expressed as CFU × 10^6 ml^{-1} per week for a period of 6 weeks. **(B,C)** The transcripts levels of *CYPBM3* and *AD α-subunit* genes in different strains growing in the presence of 2,3,7,8-TCDD at 2, 5 and 6 weeks. The colour scale (white-red-black) indicates relative changes of transcript abundance of 1, 5 and 10 fold, respectively. All measurement were performed in triplicates. Values are means ± S.D (n = 9).

actively in comparison with others strains and reached about of 15.7 × 10^6 CFU ml^{-1} after 5 weeks. *Bacillus pumilus* (A1-2c and A4-2d) showed a weak growth curve with a maximum CFU mL^{-1} of 7.2 × 10^6 and 5.4 × 10^6, respectively. On the other hand, the strain *Pseudomonas stutzeri* D2e effectively grew in the presence of 2,3,7,8-TCDD plateauing to 11.44 × 10^6 CFU ml^{-1} at week 5, which is relatively higher than the growth of *Pseudomonas putida* A1-1d, while *Pseudomonas fluorescens* A4-3d, reached 9.52 × 10^6 and 7.28 × 10^6 CFU ml^{-1} at the same time point.

Furthermore, the transcripts of bacterial angular dioxygenase (*AD a-subunit*) and the cytochrome *CYPBM3* was quantified using RT-qPCR following the growth of the studied strains in the presence of 2,3,7,8-TCDD. As shown in Figure 5B, the level of *CYPBM3* gene transcripts in the strain *B. megaterium* A4-2d was significantly ($p < 0.01$) increased and reached about 5-fold at week 5 compared with first week of inoculation. While, the transcripts level of *CYPBM3* gene did not changed significantly in both strain of *B. pumilus* (A1-2c and A4-2d). On the other hand, a significant abundance ($p < 0.05$) (~3-fold) for the *AD α-subunit* gene transcripts was measured in *P. stutzeri* D2e growing on 2,3,7,8-TCDD at week 5. Whereas a tight change in *AD α-subunit* gene expression (1.65-fold) was detected in *P. putida* A1-1d and *P. fluorescens* A4-3d at week 5 and week 2, respectively (Figure 5C). Our data suggest that both *AD*- and *CYPBM3*-mediating pathways for degradation of dioxin were identified in the microbial communities isolated from soil samples polluted with dioxins.

Discussion

Dioxins are extremely potent environmental toxins with proven toxicological effects in humans, animals, plants and microorganisms (Wu et al., 2002; Kong et al., 2018; Hanano et al., 2019a; Hanano et al., 2019b; González and Domingo, 2021; Hanano et al., 2021; Li et al., 2021; Sun et al., 2021).

Nowadays, it is well known that the main pathway by which mammalians are exposed to dioxins is occurring *via* the consuming of dioxin-contaminated food, thus it is worth to avoid, as downstream as possible, these contaminants to go into the food chain. Following this logic, the investigation of interaction between dioxins and soil microbes should be prioritized because soils, together with sediments, are considered the major reservoirs of such contaminants in most ecosystems. In this context, the contaminated soils with dioxin have been considered as rich sources for the isolation of microorganisms with potential abilities in metabolizing such compounds (Hiraishi, 2003; Jacques et al., 2009; Hanano et al., 2014c; Hanano et al., 2019b; Nguyenag et al., 2021). Therefore, the current study highlights the interrelationship between the contamination level of soils with dioxin and the composition, genetic and functional characteristics of soil microbial communities, and follows up our previous works for identifying bacterial strains as potential dioxins degraders (Hanano et al., 2014c; Hanano et al., 2019b; Almnehlawi et al., 2021; Nguyenag et al., 2021).

Compared to our pervious study, selectively conducted on environmental sites of coastal and middle regions in Syria with potential contamination sources of PCDD/Fs, the current study particularly targets sites that historically were dedicated as waste incineration stations around the capital, Damascus. Our results indicated that the soils samples of the sites located around the waste incineration stations, were moderately contaminated with dioxins while the soil samples collected from a site nearby Homs refinery showed the highest level of contamination with dioxins (Hanano et al., 2014c). Although the total N content of soil samples did not correlate with their level of contamination with dioxins, it is well worth noting that the highest polluted soil samples with PCDD/Fs had also the highest content of total nitrogen. This statement could be possibly supported by the high affinity of dioxin towards soil organic materials (Huyen et al., 2015; Li et al., 2021; Yuan et al., 2021).

Next, the soil microbial communities of the selected sites were characterized in terms of population densities, diversity and species richness. Our results showed that although the density of microbial communities varied largely between soil samples, the highest densities of cultivable bacteria were found in the highest contaminated soil samples which comes in line with previous reports (Hanano et al., 2014c). Regarding the composition of microbial communities, it was observed that the five most abundant genera in soil samples were *Bacillus*, *Pseudomonas, Acinetobacter, Enterobacter* and *Klebsiella*. The presence of such genera was reported in soils contaminated with dioxins, thus suggesting the implication of certain *Bacillus* species (*B. megaterium* and *B. pumilus*), *Pseudomonas* sp. and *Klebsiella* sp. in the transformation of PCCD/Fs in the environment (Choi et al., 2003; Hong et al., 2004; Hanano et al., 2019b). In this context, it was suggested that the contaminants can induce an immediate increase in the tolerance of soil microbial community due to their initial toxicity followed by a more gradual enhancement (Van Der Meer, 1994). Expectedly, our data show also that the indices of biodiversity and species richness of microbial communities largely varied according to the sites and inversely proportioned to their level of contamination with PCDD/Fs. These results can be supported by the event that any stressor will lead to a preliminary decrease in biodiversity of soil microbes (Van Bruggen and Semenov, 2000).

Microbial biodegradation of dioxins is now well established for various microorganisms. In bacteria, several mechanisms involved in the biodegradation of dioxins have been described in detail, including but not limited to oxidative degradation by the angular dioxygenases (AD) of aerobic bacteria (Habe et al., 2001) and the cytochrome P450 (CYPBM3) (Sulistyaningdyah et al., 2004) or reductive dechlorination by anaerobic bacteria (Bunge et al., 2003). As we showed, plenty of bacterial strains that harbor the *AD* encoding gene were found in the highest polluted soils. While, the *B. megaterium* CYPBM3 was randomly distribution among soils. The genetic screening of microbial communities for *AD α-subunit* and *CYPBM3* encoding gene revealed that the *AD*-positive bacteria found in the highest PCDD/Fs-contaminated soils belonged mainly to the genera *Pseudomonas*, *Citrobacter*, *Cronobacte* and *Pantoea*. While, the *CYPBM3*-positive species were abundant in the soil samples having an intermediate level of contamination with PCDD/Fs. A similar scenario was also found on a previous study, where the abundance of bacteria possessing the *AD α-subunit* encoding gene was more abundant in the highly polluted soils (Hanano et al., 2014c). In this regard, it was reported that the functional profiling of dioxin-degrading pathways in soils microbes could possibly be affected by the chlorination degree of PCDD/Fs substituents. Apparently, the angular dioxygenases (AD) attack the position 1,10a in dibenzo-*p*-dioxin and the position 4,4a in dibenzofuran without preference for the level of chloride substituent (Habe et al., 2001; Desta et al., 2021). Therefore, three types of angular dioxygensases have been characterized; a carbazole 1,9a dioxygenase (CARDO) from *Pseudomonas* sp. strain CA10 (Habe et al., 2001); a dibenzofuran 4,4a dioxygenase (DFDO) from *Terrabacter* sp. strain DBF63 (Kasuga et al., 2001); and a dibenzo-*p*-dioxygenase 1,10a from *Sphingomonas* sp. strain RW1 (Wittich et al., 1992; Armengaud et al., 1998; Armengaud and Timmis, 1998). In a different fashion, a particular link between the CYPBM3 activities and the number of chloride substituent of PCDDs has been documented. While, the highest activity of CYPBM3 was found with substrates with one or two chloride substituents (Sulistyaningdyah et al., 2004), other isoforms of CYPBM3 actively metabolized tetrachlorinated substituents (Hanano et al., 2019b).

The functional abilities of *AD* and *CYPBM3*-positive strains were assayed by evaluating the bacterial growth in the presence of

2,3,7,8-TCDD. Of particular interest, the strain *B. megaterium* A4-2 d grew more actively in comparison with others strains and reached the highest values of CFU mL^{-1} at week 5 after inoculation and this was likely correlated to a remarkable induction of *CYPBM3* gene expression. While two other stains of *B. pumilus* (A1-2c and A4-2d) showed a weak growth. In line with this, other strains of *B. megaterium* were identified as potential metabolizers of environmental pollutants such as dioxins, petroleum hydrocarbons, agrochemicals and polystyrene (Quensen and Matsumura, 1983; Thavasi et al., 2011; Bardot et al., 2015; Achiles Do Prado et al., 2021; Meng et al., 2021). Interestingly, these catalytic activities are likely synchronized to specific biological adaptations assisting microorganisms to uptake such hydrophobic contaminants in an efficient manner. e.g., enhancing biosurfactant production, modulating of surface hydrophobicity and composition of the cell membrane in *B. megaterium* (Thavasi et al., 2008; Bouassida et al., 2018; Hanano et al., 2019b; Singh et al., 2021) or in other microorganisms (Hanano et al., 2014a; Hanano et al., 2015b; Plaza et al., 2016; Hanano et al., 2017; Paraszkiewicz et al., 2018). Intriguingly, the PCDDs-biotransforming activity of *CYPBM3* has been experimentally demonstrated for the native or recombinant $P450_{BM-3}$ protein, where the purified enzymes can hydroxylate 2,3-dichloro-, 2,3,7-trichloro-dibenzo-*p*-dioxin and 2,3,7,8-tetrachloro-dibenzo-*p*-dioxin into less toxic intermediates (Sulistyaningdyah et al., 2004; Hanano et al., 2019b). On the other hand, our result also showed that certain strains of *P. stutzeri*, *P.putida* and *P. fluorescens* effectively grew on 2,3,7,8-TCDD with a significant increase of the *AD α-subunit* gene transcripts in the *P. stutzeri* D2e. Indeed, several earlier studies reported that such species, and others from the genus *Pseudomonas* were remarkable degraders of carbazole and dioxins (Shintani et al., 2003; Larentis et al., 2011).

In conclusion, the current study presents a set of biological indicators on the density, diversity, species richness and functional genetics of microbial communities in contaminated soils with dioxins. This was with the objective of identifying new bacteria species with remarkable metabolizing activities against dioxins. This led to identify two bacterial strains with remarkable abilities to metabolize 2,3,7,8-TCDD in laboratory-scale experiment, *B. megaterium* A4-2d and *P. stutzeri* D2e with distinct catalytic pathways for the biotransformation of TCDD, the angular dioxygenase (*AD α-subunit*) and cytochrome P450 (*CYPBM3*). Based on the different composition of PCDD/Fs and subsequently of their toxicities, the microbial biodegradation of dioxins seems to be a complicated process, requiring different metabolizing pathways that work cooperatively for an effective removal of PCDD/Fs from contaminated soil. As future work, it will be important to focus on certain Gram-positive isolates, mainly those from *Bacillus megaterium*, with more detailed molecular and biochemical characterization of their angular dioxygenases (AD), which are typically found in Gram-negative bacteria. Moreover, it would be interesting to determine the functional aspect of these distinct dioxin-degradation pathways (AD and CYPBM3) when both are found in such bacteria.

Data availability statement

The datasets presented in this study can be found in online repositories. The names of the repository/repositories and accession numbers can be found below: www.ncbi.nlm.nih.gov/nuccore/, from MW475085 to MW475154.

Author contributions

SM and GM collected related materials. SM performed all experimental work. AH conceptualized and wrote the manuscript. All authors read and approved the final manuscript.

Acknowledgments

We would like to thank Prof. I. OTHMAN, Director General of the AECS and to the Head of Molecular Biology and Biotechnology Department for their crucial support. Also, we thank the International Network on Microbial Ecotoxicology (EcotoxicoMic) (https://ecotoxicomic.org/) for its crucial support throughout our research activities.

Conflict of interest

The authors declare that the research was conducted in the absence of any commercial or financial relationships that could be construed as a potential conflict of interest.

Publisher's note

Supplementary material

The Supplementary Material for this article can be found online at: https://www.frontiersin.org/articles/10.3389/fenvs.2022.1008900/full#supplementary-material

References

Achiles Do Prado, C. C., Pereira, R. M., Durrant, L. R., Scorza Júnior, R. P., Raquel, M., and Bonfá, L. (2021). Fipronil biodegradation and metabolization by *Bacillus megaterium* strain E1. *J. Chem. Technol. Biotechnol.* 17, 474–481.

Almnehlawi, H., Dean, R. K., Capozzi, S., Rodenburg, L. A., Zylstra, G. J., and Fennell, D. E. (2021). *Agromyces* and *Arthrobacter* isolates from surficial sediments of the Passaic River degrade dibenzofuran, dibenzo-p-dioxin and 2-monochlorodibenzo-p-dioxin. *Bioremediation J.* 25, 204–224. doi:10.1080/10889868.2021.1892027

Armengaud, J., Happe, B., and Timmis, K. N. (1998). Genetic analysis of dioxin dioxygenase of *Sphingomonas* sp. Strain RW1: Catabolic genes dispersed on the genome. *J. Bacteriol.* 180, 3954–3966. doi:10.1128/jb.180.15.3954-3966.1998

Armengaud, J., and Timmis, K. N. (1998). The reductase RedA2 of the multi-component dioxin dioxygenase system of Sphingomonas sp. RW1 is related to class-I cytochrome P450-type reductases. *Eur. J. Biochem.* 253, 437–444. doi:10.1046/j.1432-1327.1998.2530437.x

Baker, T. K., Kwiatkowski, A. P., Madhukar, B. V., and Klaunig, J. E. (1995). Inhibition of gap junctional intercellular communication by 2, 3, 7, 8-tetrachlorodibenzo-p-dioxin (TCDD) in rat hepatocytes. *Carcinogenesis* 16, 2321–2326. doi:10.1093/carcin/16.10.2321

Bardot, C., Besse-Hoggan, P., Carles, L., Le Gall, M., Clary, G., Chafey, P., et al. (2015). How the edaphic Bacillus megaterium strain Mes11 adapts its metabolism to the herbicide mesotrione pressure. *Environ. Pollut.* 199, 198–208. doi:10.1016/j.envpol.2015.01.029

Boddupalli, S. S., Hasemann, C. A., Ravichandran, K. G., Lu, J. Y., Goldsmith, E. J., Deisenhofer, J., et al. (1992). Crystallization and preliminary x-ray diffraction analysis of P450terp and the hemoprotein domain of P450BM-3, enzymes belonging to two distinct classes of the cytochrome P450 superfamily. *Proc. Natl. Acad. Sci. U. S. A.* 89, 5567–5571. doi:10.1073/pnas.89.12.5567

Bouassida, M., Ghazala, I., Ellouze-Chaabouni, S., and Ghribi, D. (2018). Improved biosurfactant production by Bacillus subtilis SPB1 mutant obtained by random Mutagenesis and its Application in enhanced oil Recovery in a Sand System. *J. Microbiol. Biotechnol.* 28, 95–104. doi:10.4014/jmb.1701.01033

Bumpus, J. A., Tien, M., Wright, D., and Aust, S. D. (1985). Oxidation of persistent environmental pollutants by a white rot fungus. *Science* 228, 1434–1436. doi:10.1126/science.3925550

Bunge, M., Adrian, L., Kraus, A., Opel, M., Lorenz, W. G., Andreesen, J. R., et al. (2003). Reductive dehalogenation of chlorinated dioxins by an anaerobic bacterium. *Nature* 421, 357–360. doi:10.1038/nature01237

Carney, S. A., Prasch, A. L., Heideman, W., and Peterson, R. E. (2006). Understanding dioxin developmental toxicity using the zebrafish model. *Birth Defect. Res. A* 76, 7–18. doi:10.1002/bdra.20216

Cerniglia, C. E., Morgan, J. C., and Gibson, D. T. (1979). Bacterial and fungal oxidation of dibenzofuran. *Biochem. J.* 180, 175–185. doi:10.1042/bj1800175

Choi, S. D., Hong, H. B., and Chang, Y. S. (2003). Adsorption of halogenated aromatic pollutants by a protein released from *Bacillus pumilus*. *Water Res.* 37, 4004–4010. doi:10.1016/s0043-1354(03)00308-7

Chrostowski, C. P., and Foster, A. S. (1996). A methodology for assessing congener-specific partitioning and plant uptake of dioxins and dioxin-like compounds. *Chemosphere* 32, 2285–2304. doi:10.1016/0045-6535(96)00118-x

Desta, M., Zhang, L., Wang, W., Xu, P., and Tang, H. (2021). Molecular mechanisms and biochemical analysis of fluorene degradation by the Pseudomonas sp. SMT-1 strain. *3 Biotech.* 11, 416. doi:10.1007/s13205-021-02946-x

Geyer, H. J., Scheunert, I., Rapp, K., Gebefügi, I., Steinberg, C., and Kettrup, A. (1993). The relevance of fat content in toxicity of lipophilic chemicals to terrestrial animals with special reference to dieldrin and 2, 3, 7, 8-tetrachlorodibenzo-p-dioxin (TCDD). *Ecotoxicol. Environ. Saf.* 26, 45–60. doi:10.1006/eesa.1993.1040

González, N., and Domingo, J. L. (2021). Polychlorinated dibenzo-p-dioxins and dibenzofurans (PCDD/Fs) in food and human dietary intake: An update of the scientific literature. *Food Chem. Toxicol.* 157, 112585. doi:10.1016/j.fct.2021.112585

Gul, N., Khan, B., Khan, H., Muhammad, S., Ahmad, I., and Gul, N. (2021). Levels of polychlorinated dibenzo-p-dioxins and dibenzofurans (PCDD/Fs) in municipal waste dumping site, incinerator and brick kiln residues: Evaluation for potential risk assessment. *Arab. J. Geosci.* 14, 741. doi:10.1007/s12517-021-07108-0

Habe, H., Chung, J. S., Lee, J. H., Kasuga, K., Yoshida, T., Nojiri, H., et al. (2001). Degradation of chlorinated dibenzofurans and dibenzo-p-dioxins by two types of bacteria having angular dioxygenases with different features. *Appl. Environ. Microbiol.* 67, 3610–3617. doi:10.1128/aem.67.8.3610-3617.2001

Hanano, A., Al-Arfi, M., Shaban, M., Daher, A., and Shamma, M. (2014a). Removal of petroleum-crude oil from aqueous solution by *Saccharomyces cerevisiae* SHSY strain necessitates at least an inducible CYP450ALK homolog gene. *J. Basic Microbiol.* 54, 358–368. doi:10.1002/jobm.201200525

Hanano, A., Almousally, I., and Shaban, M. (2019a). Exposure of Aspergillus flavus NRRL 3357 to the environmental toxin, 2, 3, 7, 8-tetrachlorinated dibenzo-p-dioxin, results in a Hyper Aflatoxicogenic phenotype: A possible role for caleosin/peroxygenase (AfPXG). *Front. Microbiol.* 10, 2338. doi:10.3389/fmicb.2019.02338

Hanano, A., Almousally, I., Shaban, M., Moursel, N., Shahadeh, A., and Alhajji, E. (2015a). Differential tissue accumulation of 2, 3, 7, 8-Tetrachlorinated dibenzo-p-dioxin in *Arabidopsis thaliana* affects plant chronology, lipid metabolism and seed yield. *BMC Plant Biol.* 15, 193. doi:10.1186/s12870-015-0583-5

Hanano, A., Almousally, I., Shaban, M., and Murphy, D. J. (2018a). Arabidopsis plants exposed to dioxin result in a WRINKLED seed phenotype due to 20S proteasomal degradation of WRI1. *J. Exp. Bot.* 69, 1781–1794. doi:10.1093/jxb/ery027

Hanano, A., Almousally, I., and Shaban, M. (2014b). Phytotoxicity effects and biological responses of *Arabidopsis thaliana* to 2, 3, 7, 8-tetrachlorinated dibenzo-p-dioxin exposure. *Chemosphere* 104, 76–84. doi:10.1016/j.chemosphere.2013.10.060

Hanano, A., Ammouneh, H., Almousally, I., Alorr, A., Shaban, M., Alnaser, A. A., et al. (2014c). Traceability of polychlorinated dibenzo-dioxins/furans pollutants in soil and their ecotoxicological effects on genetics, functions and composition of bacterial community. *Chemosphere* 108, 326–333. doi:10.1016/j.chemosphere.2014.01.061

Hanano, A., Shaban, M., Almousally, I., and Al-Ktaifani, M. (2015b). *Saccharomyces cerevisiae* SHSY detoxifies petroleum n-alkanes by an induced CYP52A58 and an enhanced order in cell surface hydrophobicity. *Chemosphere* 135, 418–426. doi:10.1016/j.chemosphere.2014.11.011

Hanano, A., Shaban, M., and Almousally, I. (2017). Biochemical, molecular, and transcriptional highlights of the Biosynthesis of an effective biosurfactant produced by Bacillus safensis PHA3, a petroleum-Dwelling bacteria. *Front. Microbiol.* 8, 77. doi:10.3389/fmicb.2017.00077

Hanano, A., Shaban, M., Almousally, I., and Murphy, D. J. (2018b). Identification of a dioxin-responsive oxylipin signature in roots of date palm: Involvement of a 9-hydroperoxide fatty acid reductase, caleosin/peroxygenase PdPXG2. *Sci. Rep.* 8, 13181. doi:10.1038/s41598-018-31342-4

Hanano, A., Shaban, M., Almutlk, D., and Almousally, I. (2019b). The cytochrome P450BM-1 of Bacillus megaterium A14K is induced by 2, 3, 7, 8-Tetrachlorinated dibenzo-p-dioxin: Biophysical, molecular and biochemical determinants. *Chemosphere* 216, 258–270. doi:10.1016/j.chemosphere.2018.10.103

Hanano, A., Shaban, M., and Murphy, D. J. (2021). Functional involvement of caleosin/peroxygenase PdPXG4 in the accumulation of date palm leaf lipid droplets after exposure to dioxins. *Environ. Pollut.* 281, 116966. doi:10.1016/j.envpol.2021.116966

Hay, A. (1981). Chlorinated dioxins and the environment. *Nature* 289, 351–352. doi:10.1038/289351a0

Hiraishi, A. (2003). Biodiversity of dioxin-degrading microorganisms and potential utilization in bioremediation. *Microbes Environ.* 18, 105–125. doi:10.1264/jsme2.18.105

Hong, H. B., Nam, I. H., Murugesan, K., Kim, Y. M., and Chang, Y. S. (2004). Biodegradation of dibenzo-p-dioxin, dibenzofuran, and chlorodibenzo-p-dioxins by *Pseudomonas veronii* PH-03. *Biodegradation* 15, 303–313. doi:10.1023/b:biod.0000042185.04905.0d

Huuskonen, H., Unkila, M., Pohjanvirta, R., and Tuomisto, J. (1994). Developmental toxicity of 2, 3, 7, 8-tetrachlorodibenzo-p-dioxin (TCDD) in the most TCDD-resistant and -susceptible rat strains. *Toxicol. Appl. Pharmacol.* 124, 174–180. doi:10.1006/taap.1994.1021

Huyen, D. T., Igarashi, T., and Shiraiwa, T. (2015). Vertical distribution of dioxins in soil of Bien Hoa airbase, Vietnam. *SpringerPlus* 4, 300. doi:10.1186/s40064-015-1064-x

Jacques, R. J., Okeke, B. C., Bento, F. M., Peralba, M. C., and Camargo, F. A. (2009). Improved enrichment and isolation of polycyclic aromatic hydrocarbons (PAH)-degrading microorganisms in soil using anthracene as a model PAH. *Curr. Microbiol.* 58, 628–634. doi:10.1007/s00284-009-9381-3

Jin, R., Bu, D., Liu, G., Zheng, M., Lammel, G., Fu, J., et al. (2020). New classes of organic pollutants in the remote continental environment—Chlorinated and brominated polycyclic aromatic hydrocarbons on the Tibetan plateau. *Environ. Int.* 137, 105574. doi:10.1016/j.envint.2020.105574

Kasuga, K., Habe, H., Chung, J. S., Yoshida, T., Nojiri, H., Yamane, H., et al. (2001). Isolation and characterization of the genes encoding a novel oxygenase component of angular dioxygenase from the gram-positive dibenzofuran-degrader *Terrabacter* sp. strain DBF63. *Biochem. Biophysical Res. Commun.* 283, 195–204. doi:10.1006/bbrc.2001.4763

Kim, B. H., and Fulco, A. J. (1983). Induction by barbiturates of a cytochrome P-450-dependent fatty acid monooxygenase in Bacillus megaterium: Relationship between barbiturate structure and inducer activity. *Biochem. Biophysical Res. Commun.* 116, 843–850. doi:10.1016/s0006-291x(83)80219-8

Kim, D. H., Kim, K. H., Kim, D., Jung, H. C., Pan, J. G., Chi, Y. T., et al. (2010). Oxidation of human cytochrome P450 1A2 substrates by Bacillus megaterium cytochrome P450 BM3. *J. Mol. Catal. B Enzym.* 63, 179–187. doi:10.1016/j.molcatb.2010.01.017

Kjeldahl, J. A. (1883). A new method for the estimation of nitrogen in organic compounds. *Anal. Biochem.* 22, 366–382.

Kong, F. X., Sun, G. D., and Liu, Z. P. (2018). Degradation of polycyclic aromatic hydrocarbons in soil mesocosms by microbial/plant bioaugmentation: Performance and mechanism. *Chemosphere* 198, 83–91. doi:10.1016/j.chemosphere.2018.01.097

Larentis, A. L., Sampaio, H. C. C., Carneiro, C. C., Martins, O. B., and Alves, T. L. M. (2011). Evaluation of growth, carbazole biodegradation and anthranilic acid production by *Pseudomonas stutzeri*. *Braz. J. Chem. Eng.* 28, 37–44. doi:10.1590/s0104-66322011000100005

Li, M., He, W., and Li, Y. (2021). Enhanced plant-microbe remediation of PCBs in soil using enzyme modification technique combined with molecular docking and molecular dynamics. *Biochem. J.* 478, 1921–1941. doi:10.1042/bcj20210104

Magan, N., Fragoeiro, S., and Bastos, C. (2010). Environmental factors and bioremediation of xenobiotics using white rot fungi. *Mycobiology* 38, 238–248. doi:10.4489/myco.2010.38.4.238

Mahfouz, S., Mansour, G., Murphy, J. D., and Hanano, A. (2020). Dioxin impacts on lipid metabolism of soil microbes: Towards effective detection and bioassessment strategies. *Bioresour. Bioprocess.* 7, 59. doi:10.1186/s40643-020-00347-1

Marcial Gomes, N. C., Borges, L. R., Paranhos, R., Pinto, F. N., Mendonca-Hagler, L. C., and Smalla, K. (2008). Exploring the diversity of bacterial communities in sediments of urban mangrove forests. *FEMS Microbiol. Ecol.* 66, 96–109. doi:10.1111/j.1574-6941.2008.00519.x

Marshall, N. B., and Kerkvliet, N. I. (2010). Dioxin and immune regulation: Emerging role of aryl hydrocarbon receptor in the generation of regulatory T cells. *Ann. N. Y. Acad. Sci.* 1183, 25–37. doi:10.1111/j.1749-6632.2009.05125.x

Matson, R. S., Hare, R. S., and Fulco, A. J. (1977). Characteristics of a cytochrome P-450-dependent fatty acid omega-2 hydroxylase from bacillus megaterium. *Biochimica Biophysica Acta - Lipids Lipid Metabolism* 487, 487–494. doi:10.1016/0005-2760(77)90218-1

Meena, S. S., Sharma, R. S., Gupta, P., Karmakar, S., and Aggarwal, K. K. (2016). Isolation and identification of Bacillus megaterium YB3 from an effluent contaminated site efficiently degrades pyrene. *J. Basic Microbiol.* 56, 369–378. doi:10.1002/jobm.201500533

Meng, T. K., Mohd Kassim, A. S. B., Bin a Razak, A. H., and Binti Mohd Fauzi, N. A. (2021). *Bacillus megaterium*: A potential and an efficient BioDegrader of polystyrene. *Braz. Arch. Biol. Technol.* 64, e21190321. doi:10.1590/1678-4324-2021190321

Narhi, L. O., and Fulco, A. J. (1987). Identification and characterization of two functional domains in cytochrome P-450BM-3, a catalytically self-sufficient monooxygenase induced by barbiturates in Bacillus megaterium. *J. Biol. Chem.* 262, 6683–6690. doi:10.1016/s0021-9258(18)48296-8

Nguyenag, B. T., Hsieh, J. L., Lo, S. C., Wang, S. Y., Hung, C. H., Huang, E., et al. (2021). Biodegradation of dioxins by Burkholderia cenocepacia strain 869T2: Role of 2-haloacid dehalogenase. *J. Hazard. Mater.* 401, 123347. doi:10.1016/j.jhazmat.2020.123347

Oliveira, M., Costa, S., Vaz, J., Fernandes, A., Slezakova, K., Delerue-Matos, C., et al. (2020). Firefighters exposure to fire emissions: Impact on levels of biomarkers of exposure to polycyclic aromatic hydrocarbons and genotoxic/oxidative-effects. *J. Hazard. Mater.* 383, 121179. doi:10.1016/j.jhazmat.2019.121179

Paraszkiewicz, K., Bernat, P., Kusmierska, A., Chojniak, J., and Plaza, G. (2018). Structural identification of lipopeptide biosurfactants produced by Bacillus subtilis strains grown on the media obtained from renewable natural resources. *J. Environ. Manag.* 209, 65–70. doi:10.1016/j.jenvman.2017.12.033

Plaza, G. A., Chojniak, J., Mendrek, B., Trzebicka, B., Kvitek, L., Panacek, A., et al. (2016). Synthesis of silver nanoparticles by Bacillus subtilis T-1 growing on agro-industrial wastes and producing biosurfactant. *IET Nanobiotechnol.* 10, 62–68. doi:10.1049/iet-nbt.2015.0016

Quensen, J. F., and Matsumura, F. (1983). Oxidative degradation of 2, 3, 7, 8-tetrachlorodibenzo-P-dioxin by microorganisms. *Environ. Toxicol. Chem.* 2, 261–226. doi:10.1897/1552-8618(1983)2[261:odotbm]2.0.co;2

Salamanca, M., Chandia, C., and Hernandez, A. (2016). Impact of forest fires on the concentrations of polychlorinated dibenzo-p-dioxin and dibenzofurans in coastal waters of central Chile. *Sci. Total Environ.* 573, 1397–1405. doi:10.1016/j.scitotenv.2016.07.113

Sato, S. I., Nam, J. W., Kasuga, K., Nojiri, H., Yamane, H., and Omori, T. (1997). Identification and characterization of genes encoding carbazole 1, 9a-dioxygenase in Pseudomonas sp. strain CA10. *J. Bacteriol.* 179, 4850–4858. doi:10.1128/jb.179.15.4850-4858.1997

Schwalb, H., Narhi, L. O., and Fulco, A. J. (1985). Purification and characterization of pentobarbital-induced cytochrome P-450BM-1 from Bacillus megaterium ATCC 14581. *Biochimica Biophysica Acta - General Subj.* 838, 302–311. doi:10.1016/0304-4165(85)90227-2

Seralathan, M. V., Sivanesan, S., Bafana, A., Kashyap, S. M., Patrizio, A., Krishnamurthi, K., et al. (2014). Cytochrome P450 BM3 of Bacillus megaterium - a possible endosulfan biotransforming gene. *J. Environ. Sci.* 26, 2307–2314. doi:10.1016/j.jes.2014.09.016

Shintani, M., Nojiri, H., Yoshida, T., Habe, H., and Omori, T. (2003). Carbazole/dioxin-degrading car gene cluster is located on the chromosome of Pseudomonas stutzeri strain OM1 in a form different from the simple transposition of Tn4676. *Biotechnol. Lett.* 25, 1255–1261. doi:10.1023/a:1025079027730

Singh, V., Waris, Z., Banat, I. M., Saha, S., and Padmanabhan, P. (2021). Assessment of Rheological Behaviour of water-in-oil Emulsions mediated by glycolipid biosurfactant produced by *Bacillus megaterium* SPSW1001. *Appl. Biochem. Biotechnol.* 194, 1310–1326. doi:10.1007/s12010-021-03717-3

Stella, T., Covino, S., Cvancarova, M., Filipova, A., Petruccioli, M., D'annibale, A., et al. (2017). Bioremediation of long-term PCB-contaminated soil by white-rot fungi. *J. Hazard. Mater.* 324, 701–710. doi:10.1016/j.jhazmat.2016.11.044

Stockholm, C. (2001). *Stockholm convention on persistent organic pollutants (POPs)*. Geneva: Secretariat of the Stockholm Convention. http://chm.pops.int.

Sulistyaningdyah, W. T., Ogawa, J., Li, Q. S., Shinkyo, R., Sakaki, T., Inouye, K., et al. (2004). Metabolism of polychlorinated dibenzo-p-dioxins by cytochrome P450 BM-3 and its mutant. *Biotechnol. Lett.* 26, 1857–1860. doi:10.1007/s10529-004-5317-y

Sun, S., Cao, R., Jin, J., Zhang, Y., Gao, Y., Lu, X., et al. (2021). Accumulation characteristics and estimated dietary intakes of polychlorinated dibenzo-p-dioxins, polychlorinated dibenzofurans and polychlorinated biphenyls in plant-origin foodstuffs from Chinese markets. *Sci. Total Environ.* 775, 145830. doi:10.1016/j.scitotenv.2021.145830

Thavasi, R., Jayalakshmi, S., Balasubramanian, T., and Banat, I. M. (2008). Production and characterization of a glycolipid biosurfactant from Bacillus megaterium using economically cheaper sources. *World J. Microbiol. Biotechnol.* 24, 917–925. doi:10.1007/s11274-007-9609-y

Thavasi, R., Jayalakshmi, S., and Banat, I. M. (2011). Effect of biosurfactant and fertilizer on biodegradation of crude oil by marine isolates of Bacillus megaterium, Corynebacterium kutscheri and *Pseudomonas aeruginosa*. *Bioresour. Technol.* 102, 772–778. doi:10.1016/j.biortech.2010.08.099

Toth, K., Somfai-Relle, S., Sugar, J., and Bence, J. (1979). Carcinogenicity testing of herbicide 2, 4, 5-trichlorophenoxyethanol containing dioxin and of pure dioxin in Swiss mice. *Nature* 278, 548–549. doi:10.1038/278548a0

Tuppurainen, K., Asikainen, A., Ruokojarvi, P., and Ruuskanen, J. (2003). Perspectives on the formation of polychlorinated dibenzo-p-dioxins and dibenzofurans during municipal solid waste (MSW) incineration and other combustion processes. *Acc. Chem. Res.* 36, 652–658. doi:10.1021/ar020104+

Van Bruggen, A. H. C., and Semenov, A. M. (2000). In search of biological indicators for soil health and disease suppression. *Appl. Soil Ecol.* 15, 13–24. doi:10.1016/s0929-1393(00)00068-8

Van Der Meer, J. R. (1994). Genetic adaptation of bacteria to chlorinated aromatic compounds. *FEMS Microbiol. Rev.* 15, 239–249. doi:10.1016/0168-6445(94)90115-5

Wittich, R. M., Wilkes, H., Sinnwell, V., Francke, W., and Fortnagel, P. (1992). Metabolism of dibenzo-p-dioxin by Sphingomonas sp. strain RW1. *Appl. Environ. Microbiol.* 58, 1005–1010. doi:10.1128/aem.58.3.1005-1010.1992

World Health Organization (2016). *Executive Summary on the Assessment of the health risk of dioxins*. WHO Consultation. May 25-29 1998 www.who.int/pcs/docs/dioxin-exec-sum-final.

Wu, Q., Ohsako, S., Baba, T., Miyamoto, K., and Tohyama, C. (2002). Effects of 2, 3, 7, 8-tetrachlorodibenzo-p-dioxin (TCDD) on preimplantation mouse embryos. *Toxicology* 174, 119–129. doi:10.1016/s0300-483x(02)00047-1

Yao, H., Lu, S., Zhang, X., Pei, J., and Lu, Y. T. (2018). Pollution status and risks of dioxin-like polychlorinated biphenyls in the soil of the yellow river. *Huan jing ke xue* 39, 123–129. doi:10.13227/j.hjkx.201704100

Yuan, Q., Sallach, J. B., Rhodes, G., Bach, A., Crawford, R., Li, H., et al. (2021). Natural organic matter does not diminish the mammalian bioavailability of 2, 3, 7, 8-tetrachlorodibenzo-p-dioxin. *Chemosphere* 264, 128420. doi:10.1016/j.chemosphere.2020.128420

frontiers | Frontiers in Environmental Science

TYPE Original Research
PUBLISHED 17 October 2022
DOI 10.3389/fenvs.2022.1045093

OPEN ACCESS

EDITED BY
Hongbiao Cui,
Anhui University of Science and Technology, China

REVIEWED BY
Tangfu Xiao,
Guangzhou University, China
Yanshan Cui,
University of Chinese Academy of Sciences, China
Hailong Liu,
Yangzhou University, China

*CORRESPONDENCE
Shangyi Gu,
sygu@gzu.edu.cn

SPECIALTY SECTION
This article was submitted to Toxicology, Pollution and the Environment, a section of the journal Frontiers in Environmental Science

RECEIVED 15 September 2022
ACCEPTED 03 October 2022
PUBLISHED 17 October 2022

CITATION
Guo Z, Gu S, Li Q, Zhang T, Xie X and Zhao F (2022), Carbonate mineral controls the transport of Cd from tailings to surrounding soils: An example from Cd-rich Niujiaotang Zn mine in Guizhou Province, Southwest China. *Front. Environ. Sci.* 10:1045093. doi: 10.3389/fenvs.2022.1045093

Carbonate mineral controls the transport of Cd from tailings to surrounding soils: An example from Cd-rich Niujiaotang Zn mine in Guizhou Province, Southwest China

Zidong Guo[1], Shangyi Gu[1,2]*, Qingguang Li[1,2], Tianyi Zhang[1], Xiaofeng Xie[1] and Fengqi Zhao[1]

[1]College of Resources and Environmental Engineering, Guizhou University, Guiyang, Guizhou, China, [2]Key Laboratory of Karst Geological Resources and Environment, Ministry of Education, Guizhou University, Guiyang, Guizhou, China

Heavy metal pollution derived from the oxidation of sulfides in Pb-Zn mine tailings has been a common public concern. Although the oxidative dissolution of sphalerite will release cadmium into the soil environment, it is still unclear whether other minerals contain a large amount of cadmium and how much these minerals contribute to the surrounding environmental media. In this paper, XRD, particle size analyzer, SEM-EDS and improved BCR sequential extraction method were used to analyze cadmium rich zinc mine tailing and adjacent farmland soil in Duyun, Guizhou Province. The results show that the average contents of Pb, Zn, and Cd in tailing are 214 ± 71 mg/kg, 2668 ± 773 mg/kg, and 37.5 ± 9.97 mg/kg respectively. While in the surrounding soil, they were 519 ± 280 mg/kg, 3,779 ± 2614 mg/kg, and 30.8 ± 14.4 mg/kg respectively. The mineralogical composition of tailing is mainly dolomite and less pyrite. Cadmium in tailing is mainly in weak acid extractable state, indicating that cadmium mainly exists in dolomite of tailing. Pyrite in tailing generates acid through oxidation, which accelerates the dissolution of dolomite, thus releasing Cd from minerals and migrating to surrounding farmland, resulting in soil cadmium pollution. This study reveals an important process that has been neglected. Carbonate minerals play an important role in the migration of cadmium in the tailing of the Mississippi Valley-type (MVT) lead-zinc mine and the soils affected by the tailing.

KEYWORDS

cadmium, dolomite, environmental risk, MVT Zn-Pb mine, niujiaotang, tailings

1 Introduction

Cadmium is a highly toxic and mobile element in the environment (Clemens and Ma, 2016). It can substitute zinc or calcium in living organisms because of its similar ionic radius and chemical behavior to zinc and calcium. It can also accumulate in several human organs (Wang et al., 2019a; Mamatchi et al., 2022) and cause kidney dysfunction and osteoporosis (Aoshima, 2016). Human exposure to cadmium is predominated by the food chain (Inaba et al., 2005; Luo et al., 2022). In recent years, Cd concentrations in rice grains exceeding the Chinese food limit have been reported in southern China (Chen et al., 2018; Wang et al., 2019a). The natural sources of cadmium include weathering of rocks, forest fires, and volcanic eruptions (Richardson et al., 2001), while anthropogenic sources consist of non-ferrous metal production, steel production, fossil fuel combustion, cement production, and waste incineration (Pacyna and Pacyna, 2001). The production of nonferrous metals from mines contributes the most cadmium to the environment (Nriagu, 1990). During mining and milling, Cd-bearing minerals at certain depths underground are exposed to the surface environment, causing sulfide oxidation and dissolution, which accelerates Cd release to the environment (Xu et al., 2019). Tailing produced by mineral processing have attracted much attention due to their large volume, high cadmium content and potential pollution risks to the surrounding environment (Sasmaz et al., 2019; Kan et al., 2020).

Cadmium is commonly recovered from Zn deposits because the independent Cd deposit is rarely formed in nature. Mississippi Valley type (MVT) lead-zinc deposit is one of the most important Zn ones. The deposit is named after the Mississippi Valley basin in the central United States in which it is produced. The MVT Zn deposits provide about 25% of the world's Zn resources (Hedenquist et al., 2005) and are regarded as the most Cd-rich ones among the various Zn deposits (Schwartz, 2000; Frenzel et al., 2016; Zhu et al., 2020). MVT deposit is hosted by carbonate rocks and characterized by weak alteration and simple mineralogical assemblage with sphalerite (ZnS), galena (PbS), and pyrite being ore minerals and calcite and/or dolomite being major gangue minerals. Due to its geochemical affinity for Zn, Cd is mainly hosted by sphalerite in primary ores or smithsonite in oxidized ores. Limited by mineral processing technology, tailing often contain a large number of sulfide minerals, of which the content of heavy metals (Cd, Zn, and Pb) is high (Tao et al., 2019; Wei et al., 2021). These heavy metals in tailing pose a potential threat to human health when spreading into the surrounding environment and causing crops to exceed the national standard (Boussen et al., 2013; Wang et al., 2019a; Kan et al., 2020; Sun, et al., 2022). Therefore, the Zn tailing produced during the beneficiation of Zn ores have become one of the main sources of Cd in the environment.

The impact of the tailing heavy metals on the environment is closely linked to their speciation. In previous studies, it has been recognized that the total content of heavy metals in environmental media (e.g., soil, sediment, and tailing) usually does not reflect their hazard to the surrounding environment. A five step sequential extraction procedure based on single chemical reagent extraction (Tessier et al., 1979; Rosado et al., 2016; Lohmann et al., 2022) and the three-step protocol developed by Bureau Community of Reference (BCR) (Alan and Kara, 2019; Khoeurn et al., 2019; Qureshi et al., 2020) have been well-established to study the operationally-defined speciation of heavy metals in tailing and other materials, which have greatly improved our understanding of the impact of heavy metals. However, the variety of the mineral composition of tailing frequently leads to a lack of selectivity in extracting reagents, which makes the schemes been criticized (Förstner, 1993; Hsu et al., 2015; Uchimiya et al., 2020). As a result, the heavy metal chemical speciation of tailing should be more effectively assessed by combining the mineral composition through a sequential extraction procedure (Smieja-Król et al., 2022; Yaciuk et al., 2022).

Traditionally, Cd in Zn mine tailing is regarded to be hosted by sphalerite and its release is closely linked to sphalerite oxidation dissolution (O'Day et al., 1998; Mazeina and Bessonov, 1999; Rodríguez et al., 2009; Long et al., 2022). Nevertheless, high Cd contents in the mineralized carbonate rocks reported by some studies (Quezada-Hinojosa et al., 2009; Jacquat et al., 2011; Ye et al., 2011) raise the possibility that carbonate minerals could be a major host phase of Cd in MVT Zn tailing. In this paper, Niujiaotang Zn mine in Guizhou, Southwestern China, with an unusually high Cd content (4,081 mg/kg on average) (Ye et al., 2011), were selected as the study area. The particle size, mineralogy, pH, and content of Cd were analyzed to decipher Cd speciation in the tailing. Paddy soil samples impacted by the tailing were also collected to assess Cd environmental risk. It is suggested that carbonate mineral dolomite, not sphalerite, is the predominant Cd host mineral in Niujiaotang Cd-rich Zn tailing. This provides a new insight into the environmental impact of cadmium on MVT zinc deposit, because it is rich in cadmium and widely distributed around the world.

2 Materials and methods

2.1 Site description and sample collection

Niujiaotang Zn deposit in Guizhou Province of southwest China is the highest Cd grade deposit ever discovered (Ye et al., 2011). The deposit is located about 20 km east of Duyun City, Guizhou Province, and the elevation of the study area is in the range of 800–1251 m. The study area has a humid subtropical

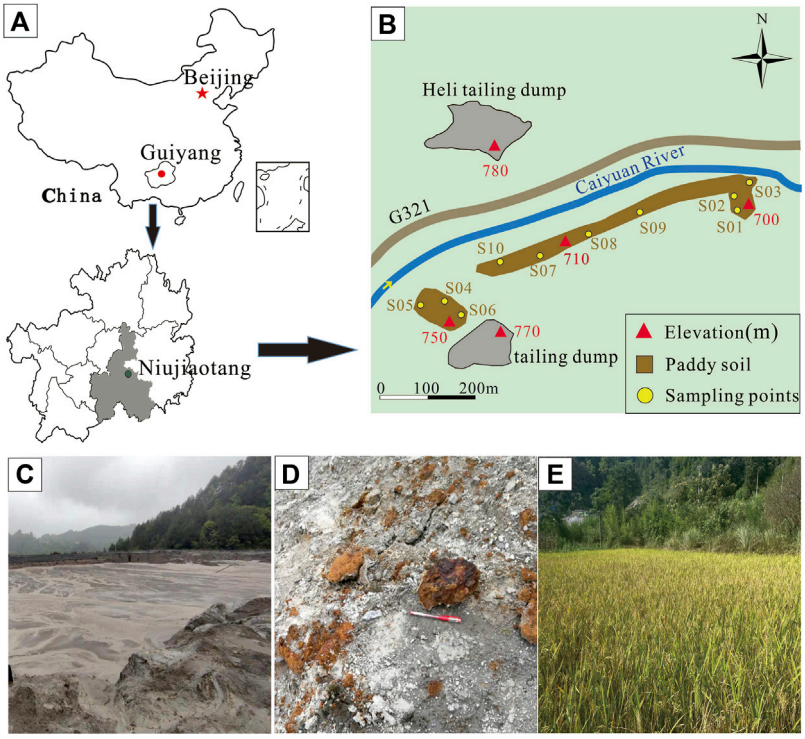

FIGURE 1
Niujiaotang Zn-rich mine **(A)**, tailing and soil sample locations **(B)**, tailing dump **(C)**, iron (oxyhydr) oxides in tailing **(D)**, and paddy soil **(E)**.

monsoon climate with an average annual temperature of 16.1°C, and an average annual rainfall of 1,431 mm. The karst landforms are well developed in the study area. The Niujiaotang Zn deposit is an MVT Zn deposit hosted within lower Cambrian Qingxudong Formation dolostone. The grade of the ore is ranged from 5.9% to 24.5% (average 19.8%) Zn and 3,000–9,800 mg/kgCd (average 4081 mg/kg) with the sulfide ore being the major mining target (Ye et al., 2011). The main ore minerals are sphalerite, pyrite, and minor galena, while gangue mineralogy is characterized by dolomite, subordinate calcite, and minor quartz (Ye et al., 2011). The Niujiaotang Zn deposit has the proven zinc reserves of $350*10^3$t and cadmium reserves of 5299t (Ye et al., 2011). Zinc concentrate ore was obtained through flotation and the flotation waste was discharged to the tailing dumps.

Tailing samples and agricultural soil samples were collected from Heli tailing dump and the surrounding paddy soil besides Fanjia River, respectively (Figure 1). Heli tailing dump was constructed in 2,000 and closed in 2021 covering an area of about 3.2 hm^2 and accumulating about 350,000 m^3 of tailing. We selected nine samples of tailing (0–20 cm) in Heli tailing dump with a depth of 0–20 cm using the random point distribution method corresponding to the possible ore variation and 10 samples of paddy soil (0–20 cm) along Fanjia River, each about 1 kg. All tailing and soil samples were collected with a plastic shovel and stored in polyethylene bags and transported to the laboratory.

2.2 Analysis of physical and chemical parameters

The collected samples were air-dried at room temperature. Then, the sample was ground and sieved to below 200 mesh. Sample particle size fraction of the soils and tailings were measured by a Laser particle size analyzer (Bettersize 3,000 Plus) and the pH was determined with a solid: water ratio of 1:2.5 (w/v) with a Mettler Toledo FE28 potentiometer. Mineralogy of soil and tailing was determined with a diffractometer PANalytical X'Pert PRO with CuKα (λ = 1.5406 Å) and Ni filter. Scans settings were from $5^\circ < 2\theta < 90^\circ$ (0.02° step size). Microstructural morphology and element mapping of tailing particles were measured by scanning electron microscope coupled with energy dispersive spectroscopy (SEM-EDS) HITACHI SU8010 using an accelerating voltage of 20 kV. The SEM-EDS analyses were conducted at the State Key Laboratory of Public Big Data, Guizhou University, China.

2.3 Total concentration of Cd, Zn, and Pb

The total concentrations of Cd, Zn, and Pb were measured by inductively coupled plasma mass spectrometry (ICP- MS XII, Thermo Fisher, United States) in the Key Laboratory of Karst Geological Resources and Environment, Ministry of Education, Guizhou University, China. The aliquot (50 mg) of tailing or soil samples were dissolved with a concentrated HNO_3- HF (1:4) mixture in a Teflon bomb maintained in an oven at 185°C for 72 h. The obtained solutions were dried on a hot plate to evaporate HF and then were re-dissolved in a final 3 ml 2 N HNO_3 stock solution. Finally, the obtained solution was diluted 4,000 times with ~2% HNO_3. During analysis, Rh (10 μg/kg) was added as an internal spike to calibrate instrument drift. USGS standards W-2a and BHVO-2 were used for data quality control. The detailed ICP-MS analytical procedure follows the protocol of Liang et al. (2000). The analytical error for Cd, Zn, and Pb is less than 10%.

2.4 Modified bureau community of reference sequential extraction procedure

The tailing samples were selected for modified three-step sequential extractions (Rauret et al., 1999). Accordingly, 0.2 g of dry tailing was extracted in a 50 ml centrifuge tube with reagents. The first fraction (F1) was extracted with 20 ml 0.11 mol/L acetic acid at 50°Ceshaking for 16 h. The tube was centrifuged for 10 min at 4500r/min and the supernatant was collected in another tube. This step was repeated once with a shaking time of 12 h. The residue in the tube was extracted with 10 ml of de-ionized water and centrifuged again. The second fraction (F2) was obtained by 20 ml 0.5 mol/L NH_2OHHCl extracting the residue from the first fraction. The subsequent centrifugation and deionized water extraction are the same as the first fraction. The third fraction (F3) was obtained by adding 5 ml 8.8 mol/L H_2O_2 at 85°C for 1 h and 1 mol/L ammonium acetate at 25°C for 16 h. The subsequent centrifugation and deionized water extraction are the same as the first fraction. The residual fraction (F4) was estimated as the difference between Cd concentration in the tailing samples and the sum of the above three fractions.

All the supernatants in each fraction were filtered with a 0.45 μm membrane filter and diluted by 2% HNO_3. The Cd concentration in the tailing extracts obtained during each sequential extraction step was determined by ICP-MS (ICP-MS XII, Thermo Fisher, United States). The tailing extracts and blanks were analyzed in duplicates. The recovery of the sample is 107% through certified reference material for the chemical composition of the soil (GBW07980).

3 Results and discussion

3.1 Mineralogy and size distribution of the tailings and soils

The results of mineral phases identified by XRD in tailing and soil samples of the Niujiaotang Cd-rich Zn mine are presented in Table 1. The representative XRD patterns are presented in Figure 2. It is noticeable that dolomite [$CaMg(CO_3)_2$] is present in all tailing samples as an abundant phase. Pyrite is presented in minor quantities as revealed by the intensity of its peak and no independent Pb and Zn minerals are detected. Soil samples present more abundant quartz and kaolinite and slightly less dolomite compared to the tailing samples. SEM element mapping results confirm the dominance of dolomite and pyrite in the tailing samples (Figure 3). The consistent element mapping distribution of S, Fe, Zn, and Pb and dominance of S and Fe implies that pyrite is the mainly sulfide phase and independent Cd, Zn, and Pb minerals [e.g., greenockite (CdS), sphalerite (ZnS) and galena (PbS)] are not detected by SEM analyses. Particle size distribution of the tailings and paddy soils showed that both the tailings and soils were composed of primarily silt and clay (71% and 79%, respectively) with median particle size (D50) being 32.94 μm and 21.76 μm, respectively.

3.2 pH of the tailings and soils

All tailing and soil samples present slightly alkaline with an average pH of 7.64 and 7.55, respectively (Table 2). The result that dolomite is dominant in tailing and soil samples is consistent with the karst background of the study area.

3.3 Total concentration of Cd, Pb, and Zn

The total contents of heavy metal elements Cd, Pb, and Zn in tailings and farmland soils are shown in Table 2. The maximum value of 55.1 mg/kg of Cd occurring in the Heli tailing dump and the minimum value of 10.6 mg/kg occurring in farmland soils. The Cd content in the Niujiaotang Pb-Zn tailing is comparable to the level of the Jalta tailing (55 mg/kg) in Northern Tunisia, a typical MVT Zn-Pb mining area (Boussen et al., 2013). The content of Cd in the paddy soil samples near Fanjia River (10.6–53.4 mg/kg, average 30.8 mg/kg) exceeded the risk screening value (0.8 mg/kg) and the risk control value (4.0 mg/kg) of the Chinese Soil Environmental (GB15618-2018). The maximum Cd level in the soil sample S04 (53.04 mg/kg) has reached more than 13 times of the risk control value of Cd, reflecting that the paddy soil has suffered from serious Cd contamination. The average values of Pb and Zn in the paddy soil samples were

TABLE 1 Mineralogical composition (%) of the tailing and paddy soil samples based upon XRD patterns.

Sample type	Sample no.	Dolomite	Quartz	Kaolinite	Pyrite	Montmorillonite	Illite
Tailings	T01	93.4	4.5	0	2.1	0	0
	T02	94.3	4.0	0	1.7	0	0
	T03	92.7	3.0	0	4.3	0	0
	T04	85.6	11.1	0	3.3	0	0
	T05	83.0	6.8	3.4	3.6	3.2	0
	T06	74.6	15.5	3.3	3.4	3.2	0
	T07	83.0	9.7	2.5	2.2	2.6	0
	T08	92.9	5.0	0	2.1	0	0
	T09	90.7	4.5	1.1	3.7	0	0
Paddy soil soils	S01	60.1	27.7	4.1	3.1	5.0	0
	S02	57.7	32.4	3.9	2.4	0	3.6
	S03	59.5	34.7	0	0	5.8	0
	S04	21.9	62.5	6.3	2.6	6.7	0
	S05	26.8	60.2	7.0	0	6.0	0
	S06	36.3	56.7	4.5	2.5	0	0
	S07	21.5	67.7	5.5	0	0	5.3
	S08	19.7	61.1	5.7	2.6	5.6	5.3
	S09	16.0	71.8	5.7	0	0	6.5
	S10	25.2	65.4	4.4	0	5.0	0

214 and 2,667 mg/kg, respectively, which exceeded the risk screening values specified in the standard (240 mg/kg for Pb and 300 mg/kg for Zn) and were 6.7 and 28.2 times of the background values of soil in Guizhou Province (32.08 mg/kg and 94.57 mg/kg for Pb and Zn, respectively). It suggests that there is a greater risk of heavy metal Cd, Pb, and Zn contamination in the soil environment affected by the Niujiaotang Pb-Zn tailing dump. It is noteworthy that the contents of heavy metals (Cd, Zn, and Pb) in some paddy soils (S04-S06) were much higher than those from tailings. There are nine tailing dumps along the Fanjia River and four dumps are located in the upstream of the paddy soil sampling sites. Reported maximum average content of Cd, Zn, and Pb in the tailings is 174.85 mg/kg, 10,200 μg/g, and 900 μg/g respectively (Zhang et al., 2018). Therefore, we proposed other tailings with high heavy metal input to these paddy soils.

In the Zn-Cd elemental cross-plot (Figure 4A), eight tailing samples except tailing T09 showed a significant positive correlation with the paddy soils S01, S02, and S03 (n = 11, α < 0.001), while T09 was significantly positively correlated with S04, S05, S06, S07, S08, S09, and S10 (n = 8, α < 0.001). Correlation coefficient of dolomite content and Cd content in soil and sediment form Fanjiahe River r = 0.741 (Figure 4B). The tailing samples and soil samples present a better linear correlation for Zn and Pb (r = 0.877) than Zn and Cd (r = 0.659) (Figures 4C,D), which is odd with the affinity of Zn and Cd.

3.4 Cd geochemical speciation in the tailings

The Cd contents and their percentages of acid extractable/exchangeable fraction (F1), easily reducible fraction (F2), the oxidizable fraction (F3), and the residual fraction (F4) were obtained by the improved BCR sequential extraction procedure, as shown in Table 3; Figure 5. The Cd contents of various fractions varied among tailing samples with the average contents of Cd in the F1, F2, F3, and F4 19.56 mg/kg, 11.07 mg/kg, 2.53 mg/kg, and 3.94 mg/kg, accounting for 52.72%, 29.84%, 6.82%, and 10.62% of the total Cd content, respectively. The average Cd content of F2 much greater than that of F3 is unexpected given the sulfide ore being the main mining and processing object in the Niujiaotang Zn mine, which indicates that a great portion of pyrite and/or sphalerite have been weathered and oxidized in the tailings as evidenced from Figure 1D. It is noteworthy that sample WK09 has the highest percentage Cd in F1, reaching 93% of the total Cd level. This reflects that cadmium mainly exists in carbonate minerals.

3.5 Cd host phases in the tailings

The first step (F1) in the BCR procedure consists of exchangeable fraction and fraction bound to carbonates. The exchangeable fraction is commonly attributed to the metal that is loosely held by the clay minerals. As discussed in Section 3.1, kaolinite is the dominant clay

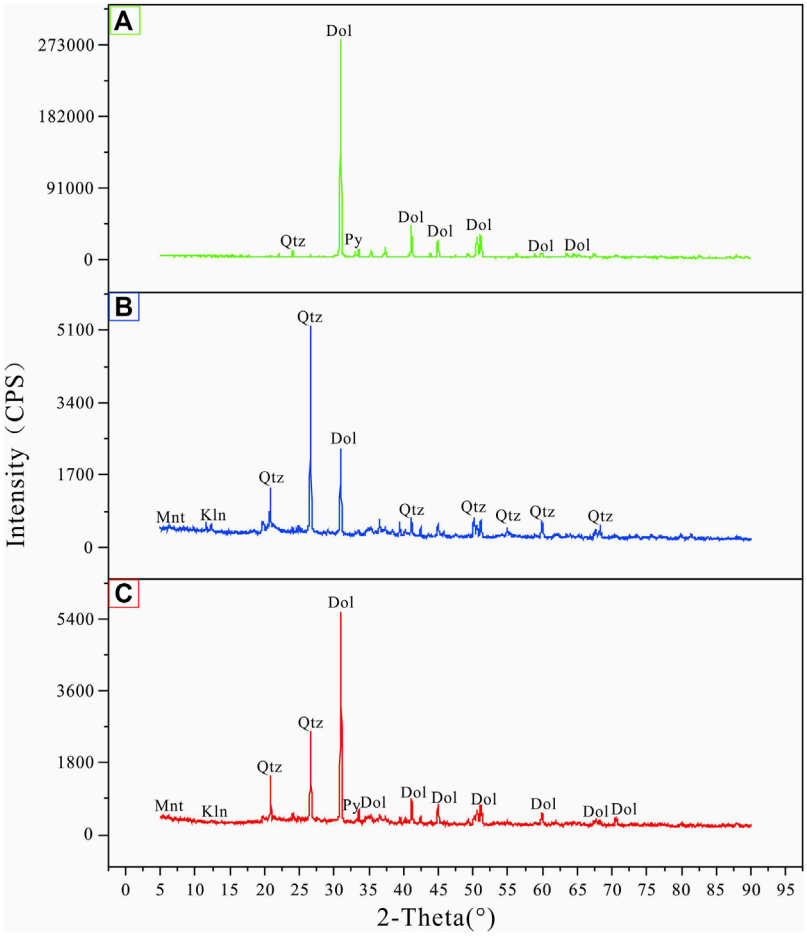

FIGURE 2
Representative XRD patterns of the tailing and soil samples. **(A)** T02 tailing, **(B)** S03 paddy soil, **(C)** S05 paddy soil. Dol: dolomite, Qtz: quartz, Mnt: Montmorillonite, Kln: Kaolinite, Py: pyrite.

mineral in the tailing samples. The reported Cd adsorption capacity of kaolinite is ranged from 3.0 mg/g to 14.11 mg/g dependent upon kaolinite purity and adsorption conditions (Ulmanu et al., 2003; Bhattacharyya and Gupta, 2008; Sari and Tuzen, 2014). Given the low cation exchange capacity of kaolinite and its low content in the tailing samples (Table 2; Figure 3), kaolinite is not regarded as the candidate phase to host Cd in the first step of the BCR procedure. Thus, the candidate phase in F1 fraction is a most likely carbonate mineral, namely, dolomite.

Cadmium has a similar ion radio to Ca, therefore, Cd can substitute Ca in the dolomite crystal lattice to form (Cd, Ca) $Mg(CO_3)_2$ (Goldsmith, 1972). Cadmium incorporated into dolomite is also through otavite ($CdCO_3$) surface precipitate (Callagon et al., 2017; La Plante et al., 2018). As a result, dolomite is widely used to remove Cd in the environmental media (Mohammadi et al., 2015; Liu et al., 2021; Zhang and Liu, 2022). In Section 3.1, we suggested that dolomite is the predominant mineral in the tailing samples by XRD and SEM-EDS. Improved BCR sequential procedure demonstrates that Cd bound to carbonate is the main fraction of total Cd in the tailing samples. Dolomite in the tailing samples is derived from hydrothermal dolomite in ores and host rocks. Ye et al. (2011) reported that the average Cd content in the hydrothermal dolomite (n = 7) and host rock dolomite (n = 10) is 190 mg/kg and 30 mg/kg, respectively. The average Cd content in bulk samples (35 mg/kg) and F1 fraction (23 mg/kg) of the tailings indicate that dolomite in the host rock is the prevailing Cd host phase. Low average Zn grade (16.9%) of the ores and disseminated and brecciated texture of the ores (Ye et al., 2011) provide the evidence that dolomite from the wall rock predominated over hydrothermal dolomite.

The improved BCR sequential extraction result demonstrates that the easily reducible fraction and oxidizable fraction account for most of the rest of cadmium except for one bound to dolomite. As introduced in Section 3.4, these two fractions are ascribed to sulfide-bound cadmium

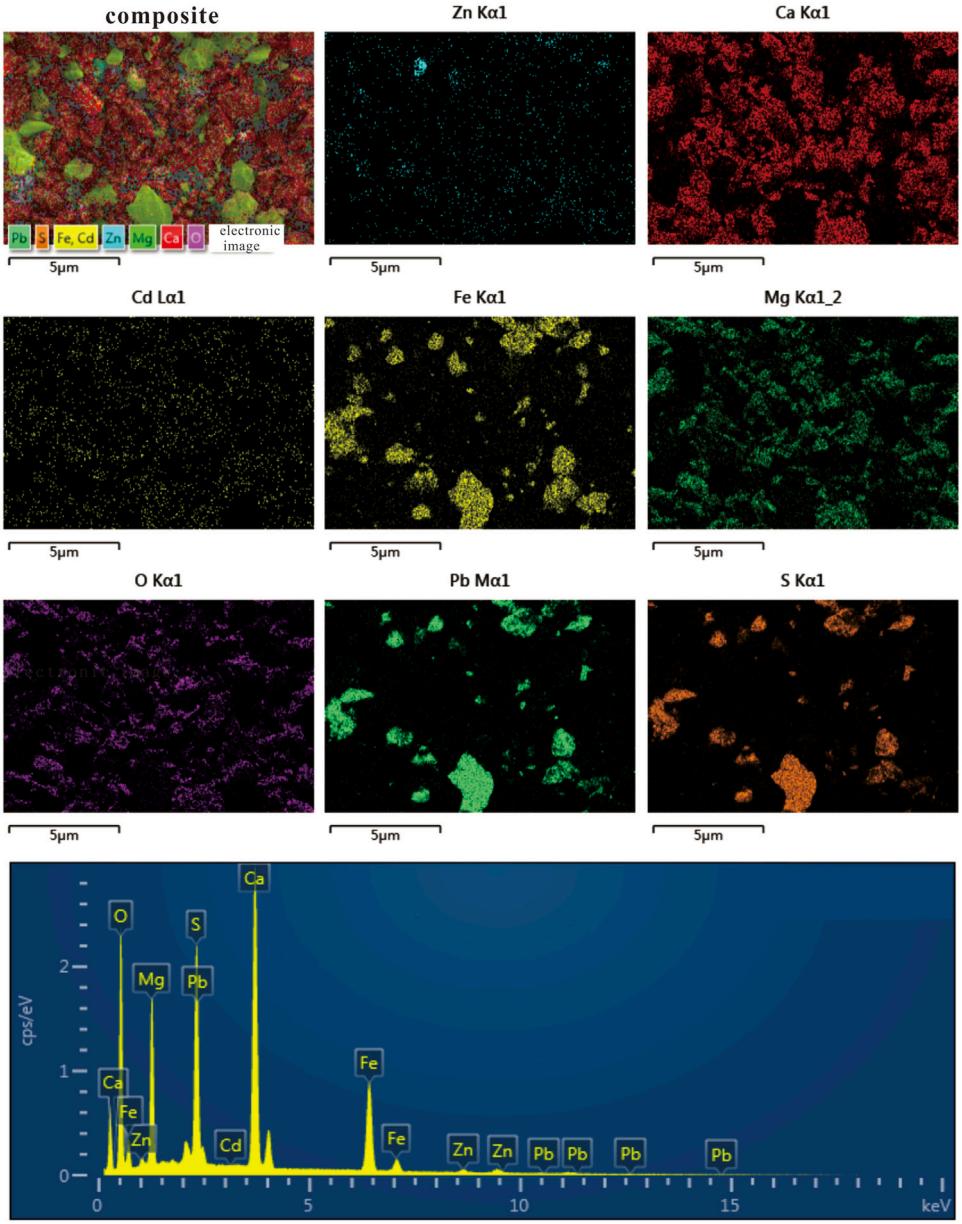

FIGURE 3
Representative SEM patterns of tailing sample from Niujiaotang Zn mine.

in un-weathered tailings. While XRD and SEM-EDX analyses suggested that pyrite is the major sulfide mineral and no sphalerite and galena were detected, we propose that pyrite is the major Cd host phase of sulfide minerals in the fresh tailings. This argument is also evidenced by the consistent elemental mapping of Cd, Fe, and S from SEM-EDX analyses of the tailing samples. When pyrite was precipitated from Cd-bearing aqueous solution, Cd was incorporated into pyrite by interaction with the surface of the pyrite (Parkman et al., 1999; Borah and Senapati, 2006). Ye et al. (2011) reported that pyrite in the ore of the Niujiaotang has a Cd content of 183 mg/kg to 2500 mg/kg with an average of 1,345 mg/kg (n = 4). Therefore, pyrite is the important Cd-host phase following dolomite in the primary tailing of the Niujiaotang mine.

When the pyrite was exposed to ambient air and water, it was oxidized by microbial-mediated reactions (Singer and Stumm, 1970):

TABLE 2 pH, contents (mg/kg) of Zn, Cd, and Pb in the tailings and paddy soils.

Sample type	Sample no.	pH	Zn	Cd	Pb
Tailings	T01	8.11	2,250	34.5	146
	T02	7.75	1,680	24.7	130
	T03	7.92	3,290	55.1	247
	T04	7.75	2,440	36.3	192
	T05	7.75	2,560	40.3	311
	T06	7.92	2,700	40.2	273
	T07	7.89	3,350	51.2	306
	T08	7.49	1,600	25.1	109
	T09	7.93	4,140	30.1	217
Paddy soils	S01	7.63	1,958	31.9	184
	S02	7.69	2,490	35.7	365
	S03	7.49	2,160	30.4	307
	S04	7.22	8,660	53.4	1,090
	S05	7.18	7,710	48.0	961
	S06	7.27	6,490	45.5	620
	S07	7.91	1,450	10.6	309
	S08	8.16	3,450	26.0	553
	S09	7.87	1810	12.9	412
	S10	7.85	1,610	14.0	394

$$2FeS_2 + 7O_2(aq) + 2H_2O = 2Fe^{2+} + 4SO_4^{2-} + 4H^+ \quad (1)$$

$$4Fe^{2+} + O_2(aq) + 4H^+ = 4Fe^{3+} + 2H_2O \quad (2)$$

$$Fe^{3+} + 3H_2O = Fe(OH)_3 + 3H^+ \quad (3)$$

$$FeS_2 + 14Fe^{3+} + 8H_2O = 15Fe^{2+} + 2SO_4^{2-} + 16H^+ \quad (4)$$

In the neutral or alkaline pH environment of the dolomite-dominated tailings, the ferrous ions (Fe^{2+}) produced by the oxidation of pyrite (Eq. 1) were further oxidized by dissolved oxygen to form Fe^{3+} (Eq. 2), which was hydrolyzed to form iron (oxyhydr) oxides (Eq. 3; Figure 1D). Thus, iron (oxyhydr) oxides formation prevents ferric iron (Fe^{3+}) from further oxidizing pyrite (Eq. 4). Since the primary ore mined at the Niujiaotang Zn mine is mainly sphalerite and pyrite, the iron (oxyhydr) oxides in the tailing dump are likely formed by the oxidation of pyrite within it. Meanwhile, the oxidative weathering process of pyrite released the Cd in it, which is consistent with the study of Ettler (2016) and others. Iron (oxyhydr)oxides of the tailings in Niujiaotang are amorphous material, rather than goethite (α-FeOOH), lepidocrocite (γ-FeOOH) and/or hematite (α-Fe_2O_3), as evidenced by the absence of the diffraction peaks of the goethite, lepidocrocite and hematite shown in the XRD patterns of the tailing samples. We hypothesize that iron (oxyhydr) oxide in the Niujiaotang tailings is ferrihydrite. Ferrihydrite has a high specific surface area and a significant number of reactive hydroxyl on the surface which interacts with cadmium in aqueous solution to form mono-nuclear or bi-nuclear complexes (Shi et al., 2020; Li et al., 2021). Therefore, the F2 fraction in the BCR procedure is Cd hosted by ferrihydrite which was formed by pyrite oxidation and scavenged Cd from pyrite oxidation. Khoeurn et al. (2019) reached a similar conclusion by leaching experiments for tailings.

The residual fraction of the BCR procedure is Cd incorporated into the silicate crystal lattice and/or cannot be extracted by the reactants in three steps and accounts for a small percentage in the tailing samples. For its low bioavailability, we do not discuss it further.

3.6 Environmental risk of the Cd polluted paddy soil affected by Zn tailings

The mean values of Cd, Pb, and Zn in paddy soils were 30.8 mg/kg, 519 mg/kg, and 3,778 mg/kg, respectively, which were much higher than the background values of soil heavy metals in Guizhou Province (Cd, Pb, and Zn were 1.75 mg/kg, 32.08 mg/kg, and 94.57 mg/kg, respectively) (Zhu et al., 2014). Thus, it indicates that exogenous heavy metals were added to the paddy soils, most likely due to the migration of heavy metals from the Zn tailings to the Caiyuan River which is the most important irrigation water source for the paddy soils. Based on the migration mechanism of tailing and the chemical mechanism of dolomite dissolution, we establish the physical process of tailing migration to soil and the conceptual model of Cd environmental risk (Figure 6).

The XRD results found that high content of dolomite was present in both the tailings and the paddy soil (Figure 2). Mineralogy of the paddy soil in the background area not affected by Zn tailings is characterized by the dominance of quartz and illite and the absence of dolomite (Liu et al., 2022b). Combined with the similar size distribution of tailing and paddy soil, we speculate that the physical migration of Zn mine tailing is the major path of heavy metal Cd, Zn, and Pb enrichment in agricultural soils around the Caiyuan River. Grain size distribution, dolomite dominance, and its close relation to Cd content in the paddy soil and sediment samples (Figure 4), no dissolved Cd was detected in the Caiyuan River and Cd isotope composition (Liu et al., 2022b) of the paddy soils and sediments together point to dolomite is the predominant Cd host phase in the paddy soils. Thus, most Cd transport to the paddy soil from the tailing is physically through wind and surface runoff. In addition, significant correlations between Mg and Zn contents of sediments and paddy soils (Xia et al., 2020) also provide evidence that Zn, like Cd, is hosted predominantly by dolomite and was physically migrated to the surrounding soil and sediment.

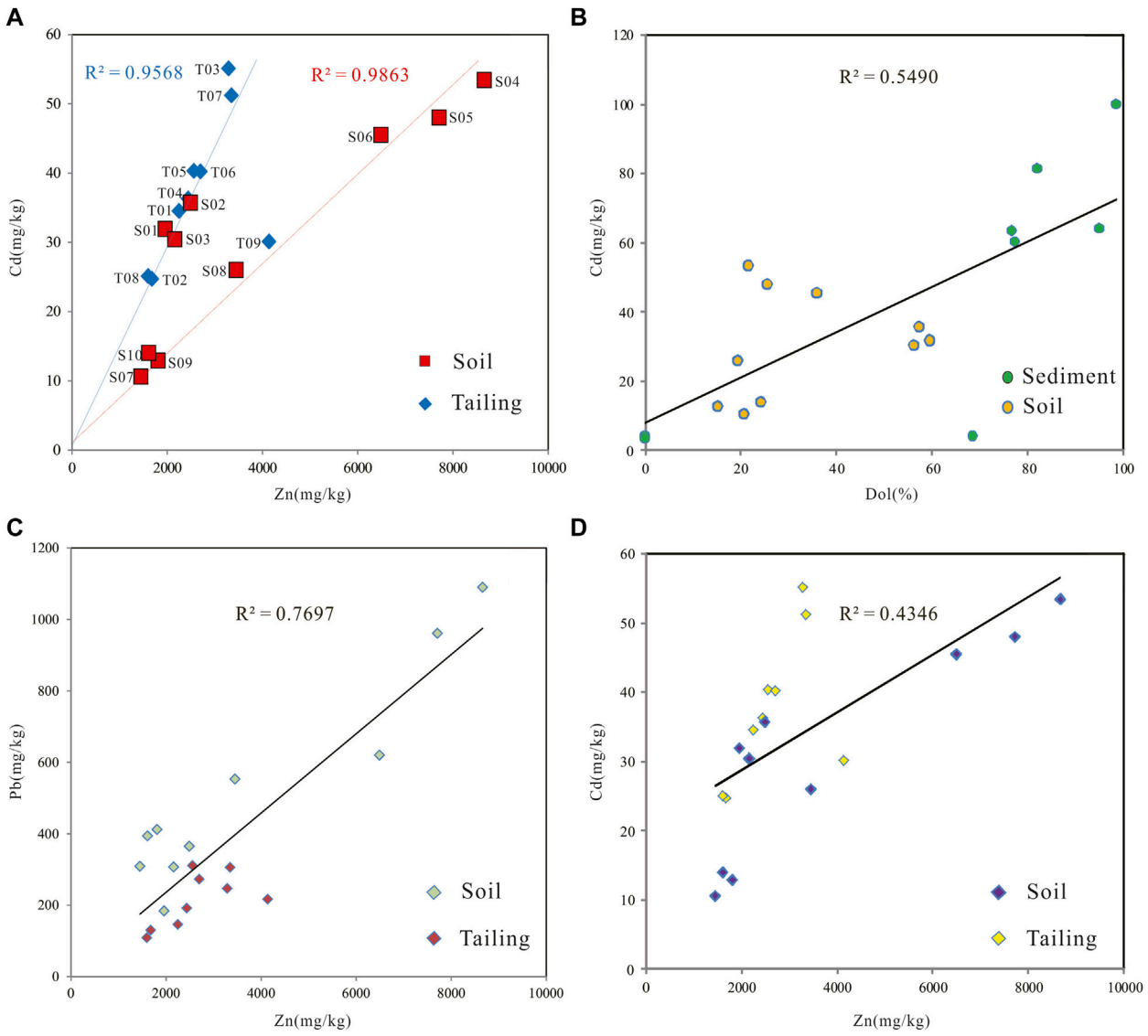

FIGURE 4
Cross-plot of Zn and Cd from tailing and soil samples (showing two different linear trends) **(A)** and correlation diagram between dolomite content and Cd content in soils and sediments from Fanjia River **(B)** (sediment samples from Liu et al. (2022a) **(C)** Cross-plot of Zn and Pb from tailing and soil samples **(D)** Linear correlation diagram between Zn and Cd contents from tailing and soil samples (showing total correlation).

Dolomite-dominated Cd enrichment in the paddy soils has two contrary effects on its environmental risk. On the one hand, elevated pH and dolomite's high affinity for Cd immobilize Cd of the paddy soil through adsorption (Wang et al., 2001; Liu et al., 2022a). As a result, liming (e.g., addition of carbonate minerals) of acid paddy soil has become the economic and effective measure to decrease Cd accumulation in rice grain. On the other hand, the addition of Cd-rich dolomite from tailings to the paddy soil greatly increases environment risk given Cd levels in the paddy soil samples are 3.2–13.4 times than that of the risk control value (4.0 mg/kg) of the Chinese Soil Environmental (GB15618-2018).

It is widely agreed that Cd bioavailability in soils is highly pH dependent (Ma and Uren, 1998; Rajaie et al., 2006; Kubier et al., 2019; Feng et al., 2021). The decrease of soil pH enhances Cd entering rice grain and poses a potential environmental risk. Local decrease of soil pH could be caused by pyrite oxidation from tailings as indicated in Eqs 1–4 and evidenced from sample S05 in Figure 2. The agricultural soil

TABLE 3 Tailing Cd concentration (mg/kg) in various fractions by modified BCR procedure.

Sample no.	F1	F2	F3	F4
T01	23.65	6.62	1.34	2.89
T02	18.59	3.72	1.38	1.01
T03	27.05	20.62	3.58	3.85
T04	14.41	14.0	3.13	4.76
T05	12.61	17.41	3.43	6.85
T06	16.46	15.85	3.83	4.06
T07	18.67	17.83	5.28	9.42
T08	20.28	3.10	0.44	1.28
T09	27.90	0.45	0.38	1.37

acidification resulting from long-term nitrogen fertilizer addition is another possible reason for soil pH decrease (Li et al., 2019). Moreover, soil pH decrease is also caused by high CO_2 levels after the flooding of the paddy soil (Kirk, 2004). Therefore, Cd solubility and bioavailability in paddy soil would increase about four folds with one unit pH decrease (Smolders and Mertens, 2012; Wang et al., 2019b). A large-scale survey demonstrates that 16 fold increase in Cd transfer ratio when soil pH decrease from 8.0 to 7.0 (Zhu et al., 2016). In the presence of dolomite, pH decrease from alkaline to neutral and an increase of sulfate generated by pyrite oxidation together facilitate dolomite dissolution (Pokrovsky and Schott, 2001). As a result, Cd released from the dolomite to the paddy soil solution. To evaluate Cd levels in rice grain compared to the

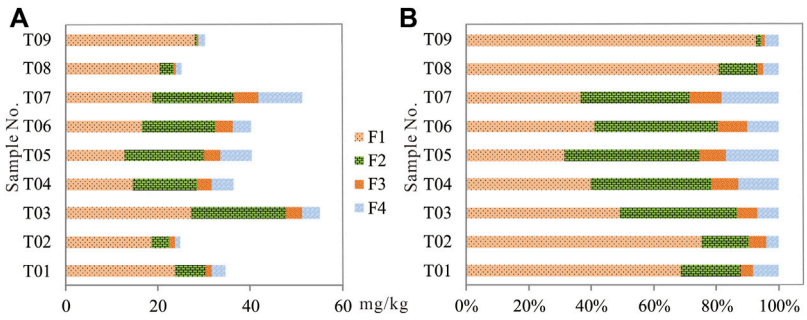

FIGURE 5
Tailing Cd concentration **(A)** and percentage **(B)** distribution in various fractions by modified BCR procedure.

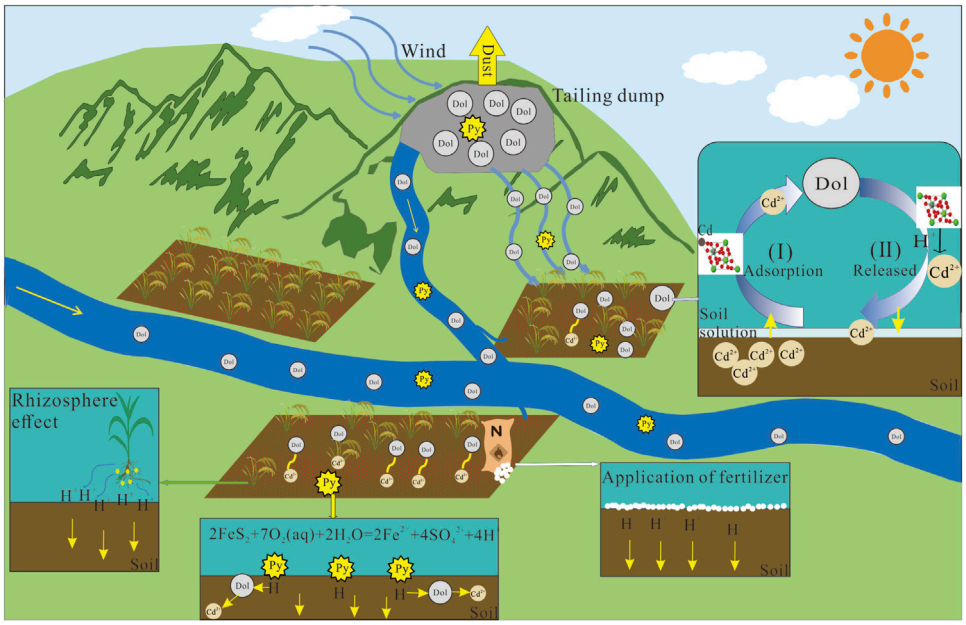

FIGURE 6
Conceptual model of soil environmental risk from Cd-rich dolomite derived from Zn mine tailing.

national standard (0.2 mg/kg), we use the models developed by Zhu et al. (2016) to predict Cd contents in rice grain based upon total Cd contents and pH values of the paddy soils. Predicted average Cd contents of the rice grain is 0.98 ± 1.06 mg/kg, which points to the high Cd environmental risk posed by rice consumption. Accordingly, considering the high Cd levels in the paddy soil, the environmental risk of Cd from paddy soil to rice grain is of great concern.

As mentioned before, MVT zinc deposits are highly Cd enriched compared to other types of zinc deposits (Schwartz, 2000). Gangue mineral in MVT zinc deposit is dominated by calcite and/or dolomite. As the similar ion radius of Ca and Cd, Cd also is incorporated into calcite and/or dolomite by substituting Ca. However, although previous works paid great focus on Cd distribution in sphalerite, some studies conducted Cd speciation and found high Cd contents in carbonate minerals of the tailing samples (Carroll et al., 1998; O'Day et al., 1998; Boussen et al., 2013). Cd contents in oolitic carbonates in the Jura Mountains of Switzerland provide another line of evidence of Cd chiefly hosted by carbonate minerals associated with hydrothermal Zn mineralization (Quezada-Hinojosa et al., 2009; Jacquat et al., 2011). Given the dominance of calcite and/or dolomite in the tailings from MVT zinc mines, environmental risk derived from high Cd carbonate minerals in the tailings of MVT zinc deposits should be carefully assessed in future works.

4 Conclusion

We conducted a systematic work on the mineralogy of the Niujiaotang Cd-rich Zn tailings by XRD, SEM-EDS, grain size distribution, and BCR geochemical speciation of Cd. The results suggested that dolomite is the predominant Cd host phase in the Zn mine tailing. Cadmium was transported to the surrounding paddy soils from the tailing by runoff and aeolian processes. The paddy soils affected by Zn mine tailing had Cd contents greatly exceeding China's national control standard and their high Cd contents also originated from Cd-rich dolomite accumulation derived from the tailing. The integrated evaluation demonstrates that the paddy soils affected by the tailing have a great environmental risk for the populations by rice consumption despite the slightly alkaline pH values. This study sheds new light on Cd speciation of tailings in MVT Zn deposits and its environmental and ecological risk for the tailing affecting soils .

Data availability statement

The original contributions presented in the study are included in the article/supplementary material, further inquiries can be directed to the corresponding author.

Author contributions

Conceptualization, SG, QL, and ZG; methodology, SG, QL, ZG, TZ, FZ, and XX; chemical analysis, ZG, TZ, FZ, and XX; investigation, SG, ZG, TZ, FZ, and XX; writing—original draft preparation, ZG, TZ, and XX; writing—review and editing, ZG, SG, and QL; supervision, SG; project administration, SG; funding acquisition, SG All authors have read and agreed to the published version of the manuscript.

Funding

This research was funded by the National Key R and D Program of China (No. 2018YFC1802601).

Acknowledgments

We would like to thank Jiangxun Huang at Guizhou University for his help in the laboratory experiment.

Conflict of interest

The authors declare that the research was conducted in the absence of any commercial or financial relationships that could be construed as a potential conflict of interest.

Publisher's note

References

Alan, M., and Kara, D. (2019). Comparison of a new sequential extraction method and the BCR sequential extraction method for mobility assessment of elements around boron mines in Turkey. *Talanta* 194, 189–198. doi:10.1016/j.talanta.2018.10.030

Aoshima, K. (2016). Itai-itai disease: Renal tubular osteomalacia induced by environmental exposure to cadmium—Historical review and perspectives. *Soil Sci. Plant Nutr.* 64 (4), 319–326. doi:10.1080/00380768.2016.1159116

Bhattacharyya, K. G., and Gupta, S. S. (2008). Adsorption of a few heavy metals on natural and modified kaolinite and montmorillonite: A review. *Adv. Colloid Interface Sci.* 140 (2), 114–131. doi:10.1016/j.cis.2007.12.008

Borah, D., and Senapati, K. (2006). Adsorption of Cd (II) from aqueous solution onto pyrite. *Fuel* 85 (12-13), 1929–1934. doi:10.1016/j.fuel.2006.01.012

Boussen, S., Soubrand, M., Bril, H., Ouerfelli, K., and Abdeljaouad, S. (2013). Transfer of lead, zinc and cadmium from mine tailings to wheat (*Triticum aestivum*) in carbonated Mediterranean (Northern Tunisia) soils. *Geoderma* 192, 227–236. doi:10.1016/j.geoderma.2012.08.029

Callagon, E. B. R., Lee, S. S., Eng, P. J., Laanait, N., Sturchio, N. C., Nagy, K. L., et al. (2017). Heteroepitaxial growth of cadmium carbonate at dolomite and calcite surfaces: Mechanisms and rates. *Geochim. Cosmochim. Acta* 205, 360–380. doi:10.1016/j.gca.2016.12.007

Carroll, S. A., O'day, P. A., and Piechowski, M. (1998). Rock-Water interactions controlling zinc, cadmium, and lead concentrations in surface waters and sediments, US Tri-state Mining District. 2. Geochemical interpretation. *Environ. Sci. Technol.* 32 (7), 956–965. doi:10.1021/es970452k

Chen, H. P., Yang, X. P., Wang, P., Wang, Z. X., Li, M., and Zhao, F. J. (2018). Dietary cadmium intake from rice and vegetables and potential health risk: A case study in xiangtan, southern China. *Sci. Total Environ.* 639, 271–277. doi:10.1016/j.scitotenv.2018.05.050

Clemens, S., and Ma, J. F. (2016). Toxic heavy metal and metalloid accumulation in crop plants and foods. *Annu. Rev. Plant Biol.* 67 (1), 489–512. doi:10.1146/annurev-arplant-043015-112301

Ettler, V. (2016). Soil contamination near non-ferrous metal smelters: A review. *Appl. Geochem.* 64, 56–74. doi:10.1016/j.apgeochem.2015.09.020

Feng, J., Shen, R. F., and Shao, J. F. (2021). Transport of cadmium from soil to grain in cereal crops: A review. *Pedosphere* 31 (1), 3–10. doi:10.1016/S1002-0160(20)60015-7

Förstner, U. (1993). Metal speciation-general concepts and applications. *Int. J. Environ. Anal. Chem.* 51, 5–23. doi:10.1080/03067319308027608

Frenzel, M., Hirsch, T., and Gutzmer, J. (2016). Gallium, germanium, indium, and other trace and minor elements in sphalerite as a function of deposit type—a meta-analysis. *Ore Geol. Rev.* 76, 52–78. doi:10.1016/j.oregeorev.2015.12.017

Goldsmith, J. R. (1972). Cadmium dolomite and the system CdCO3-MgCO3. *J. Geol.* 80, 617–626. doi:10.1086/627785

Hsu, L. C., Liu, Y. T., and Tzou, Y. M. (2015). Comparison of the spectroscopic speciation and chemical fractionation of chromium in contaminated paddy soils. *J. Hazard. Mat.* 296, 230–238. doi:10.1016/j.jhazmat.2015.03.044

Inaba, T., Kobayashi, E., Suwazono, Y., Uetani, M., Oishi, M., Nakagawa, H., et al. (2005). Estimation of cumulative cadmium intake causing Itai-itai disease. *Toxicol. Lett.* 159 (2), 192–201. doi:10.1016/j.toxlet.2005.05.011

Jacquat, O., Rambeau, C., Voegelin, A., Efimenko, N., Villard, A., Föllmi, K. B., et al. (2011). Origin of high Zn contents in jurassic limestone of the Jura mountain range and the burgundy: Evidence from Zn speciation and distribution. *Swiss J. Geosci.* 104 (3), 409–424. doi:10.1007/s00015-011-0086-9

Kan, X., Dong, Y., Feng, L., Zhou, M., and Hou, H. (2020). Contamination and health risk assessment of heavy metals in China's lead-zinc mine tailings: A meta-analysis. *Chemosphere* 267, 128909. doi:10.1016/j.chemosphere.2020.128909

Khoeurn, K., Sakaguchi, A., Tomiyama, S., and Igarashi, T. (2019). Long-term acid generation and heavy metal leaching from the tailings of Shimokawa mine, Hokkaido, Japan: Column study under natural condition. *J. Geochem. Explor.* 201, 1–12. doi:10.1016/j.gexplo.2019.03.003

Kirk, G. (2004). "Reduction and oxidation," in *The biogeochemistry of submerged soils* (Chichester: John Wiley and Sons), 93–131.

Kubier, A., Wilkin, R. T., and Pichler, T. (2019). Cadmium in soils and groundwater: A review. *Appl. Geochem.* 108, 104388. doi:10.1016/j.apgeochem.2019.104388

La Plante, E. C., Lee, S. S., Eng, P. J., Stubbs, J. E., Fenter, P., Sturchio, N. C., et al. (2018). Dissolution kinetics of epitaxial cadmium carbonate overgrowths on dolomite. *ACS Earth Space Chem.* 3 (2), 212–220. doi:10.1021/acsearthspacechem.8b00115

Hedenquist, J. W., Thompson, J. F. H., Goldfarb, R. J., and Richards, J. P. (2005). "Sediment-hosted lead-zinc deposit: A global perspective," in *Economic Geology One Hundredth Anniversary Volume* . Editors D. L. Leach (Littleton, Colorado: Society of Economic Geologists, inc.), 561–607. doi:10.5382/AV100.18

Li, Q., Li, S., Xiao, Y., Zhao, B., Wang, C., Li, B., et al. (2019). Soil acidification and its influencing factors in the purple hilly area of southwest China from 1981 to 2012. *Catena* 175, 278–285. doi:10.1016/j.catena.2018.12.025

Li, P., Luo, S., Zhang, L., Wang, Q., Huang, X., Zhang, Y., et al. (2021). Study on preparation and performance of iron tailings-based porous ceramsite filter materials for water treatment. *Sep. Purif. Technol.* 276, 119380. doi:10.1016/j.seppur.2021.119380

Liang, Q., jing, H., and Gregoire, D. C. (2000). Determination of trace elements in granites by inductively coupled plasma mass spectrometry. *Talanta* 51 (3), 507–513. doi:10.1016/S0039-9140(99)00318-5

Liu, B., He, Z., Liu, R., Montenegro, A. C., Ellis, M., Li, Q., et al. (2021). Comparative effectiveness of activated dolomite phosphate rock and biochar for immobilizing cadmium and lead in soils. *Chemosphere* 266, 129202. doi:10.1016/j.chemosphere.2020.129202

Liu, H., Zhang, T., Zhu, Q., Huang, D., and Zeng, X. (2022a). Effect of humic and calcareous substance amendments on the availability of cadmium in paddy soil and its accumulation in rice. *Ecotoxicol. Environ. Saf.* 231, 113186. doi:10.1016/j.ecoenv.2022.113186

Liu, Y. H., Xia, Y. F., Wang, Z. R., Gao, T., Zhu, J. M., Qi, M., et al. (2022b). Lithologic controls on the mobility of Cd in mining-impacted watersheds revealed by stable Cd isotopes. *Water Res.* 220, 118619. doi:10.1016/j.watres.2022.118619

Lohmann, M. S., Ramezany, S., Kästner, F., Raab, T., Heinrich, M., and Grimm, M. (2022). Using modified Tessier sequential extraction to specify potentially toxic metals at a former sewage farm. *J. Environ. Manag.* 304, 114229. doi:10.1016/j.jenvman.2021.114229

Long, Z., Zhu, H., Bing, H., Tian, X., Wang, X., Ma, Z., et al. (2022). Predicting soil cadmium uptake by plants in a tailings reservoir during 48-year vegetation restoration. *Sci. Total Environ.* 818, 151802. doi:10.1016/j.scitotenv.2021.151802

Luo, J., Xing, W. Q., Ippolito, J. A., Zhao, L. L., Han, K., Wang, Y. L., et al. (2022). Bioaccessibility, source and human health risk of Pb, Cd, Cu and Zn in windowsill dusts from an area affected by long-term Pb smelting. *Sci. Total Environ.* 842, 156707. doi:10.1016/j.scitotenv.2022.156707

Ma, Y. B., and Uren, N. C. (1998). Transformations of heavy metals added to soil — Application of a new sequential extraction procedure. *Geoderma* 84 (1-3), 157–168. doi:10.1016/S0016-7061(97)00126-2

Mamatchi, M., Rajaram, R., Ganeshkumar, A., Kpemissi, M., Pakoussi, T., Agbere, S., et al. (2022). Assessment of renal and hepatic dysfunction by co-exposure to toxic metals (Cd, Pb) and fluoride in people living nearby an industrial zone. *J. Trace. Elem. Med. Bio.* 69, 126890. doi:10.1016/j.jtemb.2021.126890

Mazeina, L. P., and Bessonov, D. U. (1999). Zinc and Cadmium behaviour in tailings. Geochemistry of the Earth's Surface: Proceedings of the 5th international symposium. Reykjavik, 16-20 August 1999. Rotterdam, Netherlands: CRC Press, 207.

Mohammadi, M., Ghaemi, A., Torab-Mostaedi, M., Asadollahzadeh, M., and Hemmati, A. (2015). Adsorption of cadmium (II) and nickel (II) on dolomite powder. *Desalination Water Treat.* 53 (1), 149–157. doi:10.1080/19443994.2013.836990

Nriagu, J. O. (1990). Global metal pollution: Poisoning the biosphere? *Environ. Sci. Policy Sustain. Dev.* 32 (7), 7–33. doi:10.1080/00139157.1990.9929037

O'Day, P. A., Carroll, S. A., and Waychunas, G. A. (1998). Rock-water interactions controlling zinc, cadmium, and lead concentrations in surface waters and sediments, US Tri-State mining district. 1. Molecular identification using X-ray absorption spectroscopy. *Environ. Sci. Technol.* 32 (7), 943–955. doi:10.1021/es970453c

Pacyna, J. M., and Pacyna, E. G. (2001). An assessment of global and regional emissions of trace metals to the atmosphere from anthropogenic sources worldwide. *Environ. Rev.* 9 (4), 269–298. doi:10.1139/a01-012

Parkman, R. H., Charnock, J. M., Bryan, N. D., Livens, F. R., and Vaughan, D. J. (1999). Reactions of copper and cadmium ions in aqueous solution with goethite, lepidocrocite, mackinawite, and pyrite. *Am. Mineral.* 84 (3), 407–419. doi:10.2138/am-1999-0326

Pokrovsky, O. S., and Schott, J. (2001). Kinetics and mechanisms of dolomite dissolution in neutral to alkaline solutions revisited. *Am. J. Sci.* 301 (7), 597–626. doi:10.2475/ajs.301.7.597

Quezada-Hinojosa, R. P., Matera, V., Adatte, T., Rambeau, C., and Föllmi, K. B. (2009). Cadmium distribution in soils covering Jurassic oolitic limestone with high Cd contents in the Swiss Jura. *Geoderma* 150 (3-4), 287–301. doi:10.1016/j.geoderma.2009.02.013

Qureshi, A. A., Kazi, T. G., Baig, J. A., Arain, M. B., and Afridi, A. H. (2020). Exposure of heavy metals in coal gangue soil, in and outside the mining area using BCR conventional and vortex assisted and single step extraction methods. Impact on orchard grass. *Chemosphere* 255, 126960. doi:10.1016/j.Chemosphere.2020.126960

Rajaie, M., Karimian, N., Maftoun, M., Yasrebi, J., and Assad, M. T. (2006). Chemical forms of cadmium in two calcareous soil textural classes as affected by application of cadmium-enriched compost and incubation time. *Geoderma* 136 (3-4), 533–541. doi:10.1016/j.geoderma.2006.04.007

Rauret, G., López-Sánchez, J. F., Sahuquillo, A., Rubio, R., Davidson, C., Ure, A., et al. (1999). Improvement of the BCR three step sequential extraction procedure prior to the certification of new sediment and soil reference materials. *J. Environ. Monit.* 1 (1), 57–61. doi:10.1039/a807854h

Richardson, M. G., Garrett, R., Mitchell, I. A., Mah-Paulson, M., and Hackbarth, T. (2001). "Critical review on natural global and regional emissions of six trace metals to the atmosphere," in *International lead zinc research organisation, the international copper association, and the nickel producers environmental research association*, 52.

Rodríguez, L., Ruiz, E., Alonso-Azcárate, J., and Rincón, J. (2009). Heavy metal distribution and chemical speciation in tailings and soils around a Pb-Zn mine in Spain. *J. Environ. Manage.* 90 (2), 1106–1116. doi:10.1016/j.jenvman.2008.04.007

Rosado, D., Usero, J., and Morillo, J. (2016). Ability of 3 extraction methods (BCR, Tessier and protease K) to estimate bioavailable metals in sediments from Huelva estuary (Southwestern Spain). *Mar. Pollut. Bull.* 102 (1), 65–71. doi:10.1016/j.marpolbul.2015.11.057

Sari, A., and Tuzen, M. (2014). Cd (II) adsorption from aqueous solution by raw and modified kaolinite. *Appl. Clay Sci.* 88, 63–72. doi:10.1016/j.clay.2013.12.021

Sasmaz, M., Öbek, E., and Sasmaz, A. (2019). Bioaccumulation of cadmium and thallium in Pb-Zn tailing waste water by Lemna minor and Lemna gibba. *Appl. Geochem.* 100, 287–292. doi:10.1016/j.apgeochem.2018.12.011

Schwartz, M. O. (2000). Cadmium in zinc deposits: Economic geology of a polluting element. *Int. Geol. Rev.* 42 (5), 445–469. doi:10.1080/00206810009465091

Shi, M. Q., Min, X. B., Ke, Y., Lin, Z., Yang, Z. H., Wang, S., et al. (2020). Recent progress in understanding the mechanism of heavy metals retention by iron (oxyhydr) oxides. *Sci. Total Environ.* 752, 141930. doi:10.1016/j.scitotenv.2020.141930

Singer, P. C., and Stumm, W. (1970). Acidic mine drainage: The rate-determining step. *Science* 167 (3921), 1121–1123. doi:10.1126/science.167.3921.1121

Smieja-Król, B., Pawlyta, M., and Gałka, M. (2022). Ultrafine multi-metal (Zn, Cd, Pb) sulfide aggregates formation in periodically water-logged organic soil. *Sci. Total Environ.* 820, 153308. doi:10.1016/j.scitotenv.2022.153308

Smolders, E., and Mertens, J. (2012). "Chapter 10. Cadmium," in *Heavy metals in soils: Trace metals and metalloids in soils and their bioavailability*. Editor B. J. Alloway (Dordrecht: Springer Science + Business Media), 283–311.

Sun, R. G., Gao, Y., and Yang, Y. (2022). Leaching of heavy metals from lead-zinc mine tailings and the subsequent migration and transformation characteristics in paddy soil. *Chemosphere* 291, 132792. doi:10.1016/j.chemosphere.2021.132792

Tao, M., Zhang, X., Wang, S., Cao, W., and Jiang, Y. (2019). Life cycle assessment on lead-zinc ore mining and beneficiation in China. *J. Clean. Prod.* 237, 117833. doi:10.1016/j.jclepro.2019.117833

Tessier, A., Campbell, P. G. C., and Bisson, M. (1979). Sequential extraction procedure for the speciation of particulate trace metals. *Anal. Chem.* 51 (7), 844–851. doi:10.1021/ac50043a017

Uchimiya, M., Bannon, D., Nakanishi, H., McBride, M. B., Williams, M. A., and Yoshihara, T. (2020). Chemical speciation, plant uptake, and toxicity of heavy metals in agricultural soils. *J. Agric. Food Chem.* 68 (46), 12856–12869. doi:10.1021/acs.jafc.0c00183

Ulmanu, M., Marañón, E., Fernández, Y., Castrillón, L., Anger, I., and Dumitriu, D. (2003). Removal of copper and cadmium ions from diluted aqueous solutions by low cost and waste material adsorbents. *Water Air Soil Pollut.* 142 (1), 357–373. doi:10.1023/a:1022084721990

Wang, H., Zhou, W., and Lin, B. (2001). Effect of calcium carbonate on adsorptin and esorption of cadmium in soils. *Acta Ecol. Sinica* 21 (6), 932–937. doi:10.3321/j.issn:1000-0933.2001.06.012

Wang, J., Wang, P. M., Gu, Y., Kopittke, P. M., Zhao, F. J., and Wang, P. (2019a). Iron-manganese (oxyhydro)oxides, rather than oxidation of sulfides, determine mobilization of Cd during soil drainage in paddy soil systems. *Environ. Sci. Technol.* 53 (5), 2500–2508. doi:10.1021/acs.est.8b06863

Wang, P., Sun, Z., Hu, Y., and Cheng, H. (2019b). Leaching of heavy metals from abandoned mine tailings brought by precipitation and the associated environmental impact. *Sci. Total Environ.* 695, 133893. doi:10.1016/j.scitotenv.2019.133893

Wei, Q., Dong, L., Qin, W., Jiao, F., Qi, Z., Feng, C., et al. (2021). Efficient flotation recovery of lead and zinc from refractory lead-zinc ores under low alkaline conditions. *Geochemistry* 81 (4), 125769. doi:10.1016/j.chemer.2021.125769

Xia, Y., Gao, T., Liu, Y., Wang, Z., Liu, C., Wu, Q., et al. (2020). Zinc isotope revealing zinc's sources and transport processes in karst region. *Sci. Total Environ.* 724, 138191. doi:10.1016/j.scitotenv.2020.138191

Xu, D., Zhan, C., Liu, H., and Lin, H. (2019). A critical review on environmental implications, recycling strategies, and ecological remediation for mine tailings. *Environ. Sci. Pollut. Res.* 26 (35), 35657–35669. doi:10.1007/s11356-019-06555-3

Yaciuk, P. A., Colombo, F., Lecomte, K. F., Micco, G. D., and Bohé, A. E. (2022). Cadmium sources, mobility, and natural attenuation in contrasting environments (carbonate-rich and carbonate-poor) in the Capillitas polymetallic mineral deposit, NW Argentina. *Appl. Geochem.* 136, 105152. doi:10.1016/j.apgeochem.2021.105152

Ye, L., Cook, N. J., Liu, T., Ciobanu, C. L., Gao, W., and Yang, Y. (2011). The Niujiaotang Cd-rich zinc deposit, Duyun, Guizhou province, southwest China: Ore Genesis and mechanisms of cadmium concentration. *Min. Depos.* 47 (6), 683–700. doi:10.1007/s00126-011-0386-z

Zhang, D., and Liu, Z. (2022). Immobilization of chromium and cadmium in contaminated soil using layered double hydroxides prepared from dolomite. *Appl. Clay Sci.* 228, 106654. doi:10.1016/j.clay.2022.106654

Zhang, J., Wei, H., Yang, R., Gao, J., and Ou, Y. (2018). Study on distribution characteristics of heavy metals in tailings from NiujiaotangLead-zinc mine area, Duyun city, Guizhou province. *Nonferrous Met. Eng.* 8 (1), 122–127. (in Chinese). doi:10.3969/j.issn.2095-1744.2018.01.024

Zhu, H. L., Liu, H. Y., Long, J. H., and Yan, Z. Y. (2014). Contamination characteristics analysis of heavy metals in soils of typical contaminated areas in Guizhou Province. *Erath Environ.* 42, 505–511. doi:10.14050/j.cnki.1672-9250.2014.04.017

Zhu, H. H., Chen, C., Xu, C., Zhu, Q. H., and Huang, D. Y. (2016). Effects of soil acidification and liming on the phytoavailability of cadmium in paddy soils of central subtropical China. *Environ. Pollut.* 219, 99–106. doi:10.1016/j.envpol.2016.10.043

Zhu, C. W., Wen, H. J., Luo, C., Du, S. J., et al. (2020). Gallium (Ga), germanium (Ge), thallium (Tl) and cadmium (Cd) resources in China. *Chin. Sci. Bull.* 65, 3688–3699. doi:10.1360/TB-2020-0267

frontiers | Frontiers in Environmental Science

TYPE Original Research
PUBLISHED 17 October 2022
DOI 10.3389/fenvs.2022.1032005

OPEN ACCESS

EDITED BY
Jun Zhou,
University of Massachusetts Lowell,
United States

REVIEWED BY
Omowunmi H. Fred-Ahmadu,
Covenant University, Nigeria
Rakesh Kumar,
Nalanda University, India
Akan Williams,
Covenant University, Nigeria

*CORRESPONDENCE
Lucas Kurzweg,
lucas.kurzweg@htw-dresden.de
Kathrin Harre,
kathrin.harre@htw-dresden.de

SPECIALTY SECTION
This article was submitted to Toxicology, Pollution and the Environment,
a section of the journal
Frontiers in Environmental Science

RECEIVED 30 August 2022
ACCEPTED 30 September 2022
PUBLISHED 17 October 2022

CITATION
Kurzweg L, Schirrmeister S, Hauffe M, Adomat Y, Socher M and Harre K (2022), Application of electrostatic separation and differential scanning calorimetry for microplastic analysis in river sediments. *Front. Environ. Sci.* 10:1032005. doi: 10.3389/fenvs.2022.1032005

Application of electrostatic separation and differential scanning calorimetry for microplastic analysis in river sediments

Lucas Kurzweg[1]*, Sven Schirrmeister[1], Maurice Hauffe[1], Yasmin Adomat[2], Martin Socher[1] and Kathrin Harre[1]*

[1]Faculty of Agriculture, Environment and Chemistry, University of Applied Sciences Dresden, Dresden, Germany, [2]Faculty of Civil Engineering, University of Applied Sciences Dresden, Dresden, Germany

A method with the potential for comprehensive microplastic monitoring in river sediments is presented in this study. We introduce a novel combination of electrostatic separation, density separation, and differential scanning calorimetry (DSC). Currently, microplastic analysis in sediments is limited in terms of sample masses, processing time, and analytical robustness. This work evaluated a method to process large sample masses efficiently and still obtain robust results. Four particulate matrices, including commercial sands and river sediments, were spiked with PCL, LD-PE, and PET microplastic particles (63–200 µm). Samples with a mass of 100 g and 1,000 g (sand only) contained 75 mg of each microplastic. After electrostatic separation, the mass of sand samples was reduced by 98%. Sediment samples showed a mass reduction of 70–78%. After density separation, the total mass reduction of sediment samples was above 99%. The increased concentration of total organic carbon seems to have the highest impact on mass reduction by electrostatic separation. Nevertheless, the recovery of microplastic was independent of the particulate matrix and was polymer-specific. In 100 g samples, the average recovery rates for PCL, LD-PE, and PET were 74 ± 9%, 93 ± 9%, and 120 ± 18%, respectively. The recoveries of microplastic from 1,000 g samples were 50 ± 8%, 114 ± 9%, and 82 ± 11%, respectively. In scale up experiments, high recoveries of all microplastics were observed with a decrease in standard deviation. Moreover, the biodegradable polymer PCL could be used as an internal standard to provide quality assurance of the process. This method can overcome the current limitations of routine microplastic analysis in particulate matrices. We conclude that this method can be applied for comprehensive microplastic monitoring in highly polluted sediments. More studies on electrostatic separation and polymer-specific recovery rates in complex matrices are proposed.

KEYWORDS

microplastic, monitoring, sediment, electrostatic separation, DSC, recovery, differential scanning calorimetry

Introduction

Polymer particles with diameters between 1 and 1,000 µm are called microplastic (Hartmann et al., 2019). Microplastic release into the environment is diverse and includes tire wear, pellet loss, surface runoff, and littering followed by degradation of larger plastic debris (Schernewski et al., 2020; Kallenbach et al., 2022; Periyasamy and Tehrani-Bagha, 2022). The main sources of microplastic are land-based (Andrady, 2011). Estimations show that microplastic input can be 73 g/(capita a) in soils and 1.8 g/(capita a) in freshwater systems in Switzerland (Kawecki and Nowack, 2019). Once microplastic particles are emitted into the environment, they enter aquatic and geological cycles (Kane and Clare, 2019; De-la-Torre et al., 2021; Weber et al., 2021) and distribute within water–sediment systems (Akdogan and Guven, 2019). Particulate matrices, such as sediments, can retain microplastic particles and act as sinks for them (Nizzetto et al., 2016; Besseling et al., 2017; Horton and Dixon, 2018). Hence, microplastic is of great interest in the environmental sciences as an emerging contaminant (Morin-Crini et al., 2022). The environmental impact of microplastics in sediments has been investigated for potential eco-toxicological effects (Bellasi et al., 2020), including starvation, oxidative stress, and potential release of adsorbed pollutants (Wright et al., 2013; Anbumani and Kakkar, 2018; Rodrigues et al., 2019; Bellasi et al., 2020).

The assessment of sinks, risks, and remediation measures requires a comprehensive microplastic monitoring strategy. Monitoring of river sediments is of particular importance due to the allocated benthic organisms and their role in the food web and energy and contaminant transfer processes (Väinölä et al., 2008; Bellasi et al., 2020). However, several challenges have to be addressed for reliable microplastic analysis in sediments. A major challenge is that the variety of methodologies for microplastic sampling, processing, and analysis can hamper the harmonization and standardization (Hanvey et al., 2017; Shim et al., 2017; Mai et al., 2018; Adomat and Grischek, 2021). Generally, microplastic analysis in sediments consists of the extraction of microplastic particles from the matrix and subsequent identification and quantification. During the extraction, a matrix such as sediment particles is removed to isolate microplastic for analysis. Hence, a mass reduction of the sample occurs.

Determination of microplastic in river sediments requires large sample masses to ensure representative results of low microplastic contents. Density separation is the most common extraction method (Dioses-Salinas et al., 2020); however, this method might not be suitable when it comes to larger sample masses due to increased processing time and equipment effort (Enders et al., 2020a; Dioses-Salinas et al., 2020). Electrostatic separation of microplastic and sediment is a promising method to reduce the total mass of sediment samples before density separation (Stock et al., 2019). This technology is particularly applied for metal–polymer waste separation and mineral refinement (Manouchehri, 2000; Köhnlechner and Sander, 2009; Das et al., 2010; Gehringer, 2021). A different chargeability of metals, minerals, and polymers are exploited to separate these components (Köhnlechner, 1999; Mirkowska et al., 2016). Particularly, electrostatic separation has gained attention for microplastic sediment separation (Felsing et al., 2018; Enders et al., 2020b). Besides cost- and time-efficiency, the benefits are high sample throughput and the reduction of large samples (Enders et al., 2020b). A lack of toxic or corrosive chemicals, the preservation of the particle surface during the process, and the potential for process automation underline the potential of this method. However, electrostatic separation is limited to a minimum particle size of 100 µm (Hoffmann, 2020). Additionally, matrix properties such as total organic carbon (TOC) and the mineral composition of sediments can hamper the separation efficiency (Enders et al., 2020b). Subsequent density separation can be applied to overcome this limitation to conduct reliable microplastic analysis.

Analytical methods for microplastic determination are divided into particle counting methods (i.e., Fourier-transformation infrared or Raman microscopy) and mass determining methods (i.e., pyrolysis or thermal desorption gas chromatography-mass spectrometry (pyro/ted-GC-MS; Shim et al., 2017). Both methods are complementary, but their application should be designed to match individual research goals. Regarding microplastic monitoring in sediments, mass determining methods might be sufficient (Braun, 2020). These methods provide fast data acquisition for polymer types and their quantity in environmental samples. Moreover, the risk of contamination is lower for these methods because of the reduced atmospheric exposition compared to particle counting methods. Mass determining methods are thermo-analytical techniques, such as pyro/ted-GC-MS and differential scanning calorimetry (DSC), and chemical methods including nuclear magnetic resonance (NMR) spectroscopy (Shim et al., 2017). GC-MS techniques are sensitive to organic residues in an environmental sample. Hence, sample purification with acids, bases, hydrogen peroxide, or enzymes is necessary (Kittner et al., 2022). DSC might be a promising approach for microplastic determination in environmental samples because organic residues would not influence the analysis. Polymer identification and quantification by DSC or DSC-coupled thermogravimetry also have been investigated (Majewsky et al., 2016; Rodríguez Chialanza et al., 2018; Bitter and Lackner, 2020). A recent study shows the potential of DSC for microplastic analysis in sediments (Harzdorf et al., 2022). To achieve reliable results, however, mass reduction and low microplastic losses are necessary. If these requirements are fulfilled, DSC might provide an alternative to determine semi-crystalline polymers in a range of 0.05–1.5 mg per measurement in sediment samples (Harzdorf et al., 2022).

The objective of this work was to evaluate the application of electrostatic separation and DSC for a fast and robust microplastic analysis in sediments. A combination of electrostatic separation and density separation, followed by DSC, was investigated. Electrostatic separation can enable the enrichment of large sediment samples without the use of chemicals, as required for example for the Munich Plastic Sediment Separator (Imhof et al., 2012). Additionally, the exploitation of physical properties of polymers, such as melting and crystallization, can increase analytical robustness. In comparison to pyro/ted-GC-MS methods, extensive sample purification is obsolete for DSC (Kittner et al., 2022). Moreover, an approach to establishing an internal standard was investigated. Such internal standards can ensure the quality and reliability of results (Enders et al., 2020b). The biopolymer polycaprolactone (PCL) will be applied. Its biodegradability reduces the risk of blank values in environmental samples. Furthermore, melting and crystallization signals do not interfere with the signals of common polymers (Harzdorf et al., 2022). Hence, PCL as an internal standard could provide for the recovery of microplastic particles. The scope of this study is the extraction and analysis of spiked microplastic particles from four different particulate matrices. We will discuss 1) the effects of matrix properties on the mass reduction of particulate matrices by electrostatic separation, 2) the dependence of microplastic recovery on the matrix and polymer type by DSC, and 3) the potential application of PCL as an internal standard.

Materials and methods

Particulate matrices

Four different particulate matrices (sand 1, sand 2, sediment 1, and sediment 2) were tested. Sand 1 (Cemex AG, Dresden, Germany) and sand 2 (Saxonia Baustoffe, Dresden, Germany) were commercial sands. Sediment 1 and sediment 2 were collected at the Elbe River (GPS: 51.047371, 13.816418) and the Weisseritz River (GPS: 51.062151, 13.687450), respectively. The river sediment samples were collected with a metal shovel approximately 0.5 m from the shore at a water depth of 0.2–0.4 m. All matrices were dried at 60°C until a constant mass was reached. The air supply of the utilized dry box (Heratherm OHM400, Thermo Fisher Scientific, Schwert, Germany) was equipped with a particle filter. After drying, particles with diameters >2 mm were removed from all matrices by sieving. Finally, the sieved matrices were further characterized by sieve analysis, TOC, and x-ray diffraction measurements.

Sieve analysis

For the determination of particle size distribution, 200 g of each matrix was analyzed. The sieve analysis was conducted with a vibratory sieve shaker (AS 200, Retsch, Haan Germany) using sieves with mesh sizes from 63 µm to 2000 µm according to DIN 4220 (version 2008–11). The parameters for sieve analyses were a shaking amplitude of 1 mm and a duration of 5 min under dry conditions. After sieving, the software EasySieve 2.6 (Retsch, Haan, Germany) was used to determine the average particle size (d_{50}-values) and fraction ratios.

Total organic carbon

Two grams of each matrix were milled to a powder with the vibratory micro mill (Pulverisette 0, Fritsch, Idar-Oberstein, Germany) equipped with a steel mortar and grinding ball (d = 50 mm). An amplitude of 1 mm for 2 min was applied to mill the matrices. TOC measurements were conducted with 200 mg of each powdered matrix (n = 3). Particulate matrices were pretreated with 200 µl 10% HCl to remove inorganic carbon before analysis. The TOC content of the matrices was determined with a multi C/N-system 1,300 (analytic Jena, Jena, Germany) at 1,200°C by combustion.

X-ray diffraction measurements

The powders as prepared for TOC measurements were used for diffraction measurements in reflection mode. A powder diffractometer XRD3003 TT from GE Inspection Technologies (Boston, MA, United States) equipped with the energy dispersive Si-drift detector Meteor 0D was used. The measurements were conducted with Cu-Kα radiation with 2θ between 10 and 80° and an increment of 0.02° with 8 seconds per increment. For a quantitative phase analysis, the programs Profex Version 4.1.0 and BGMN Version 4.2.22 and the database ICDD PDF-2 Release 2021 were applied.

Microplastic particles

Microplastic particles of low-density polyethylene (LD-PE, MKCP2615, Sigma-Aldrich, Darmstadt, Germany), recycled polyethylene terephthalate (PET, KRUPET-A IV, Kruschitz GmbH, Völkermarkt Austria), and polycaprolactone (PCL, abifor1639, Abifor AG, Zurich, Switzerland) were used. The PCL was already available as a powder. Microplastic particles of LD-PE and PET were ground using a cryo-mill (Pulverisette 0, Fritsch, Idar-Oberstein, Germany) and liquid nitrogen (Harzdorf et al., 2022). After grinding, the particles were dried at 40°C until a constant mass was reached. To obtain the targeted size range of 63–200 µm microplastic particles were sieved (see *Sieve analysis* Section Sieve analysis).

TABLE 1 Optimized parameter settings for electrostatic separation experiments.

Parameter	Setting
Mass flow	0.3 kg/h
Drum rotation	115.5 rpm
High voltage	15 kV

Sample preparation

A sample of 100 g of each matrix was spiked with 75 mg of each microplastic type. Five replicas of each matrix were prepared and used for electrostatic separation experiments. Additionally, scale-up experiments were conducted with 1,000 g samples of sand 1 and 75 mg of each microplastic type ($n = 3$). All samples were homogenized by stirring with a metal spoon and subsequently covered with aluminum foil.

Electrostatic separation

A corona drum separator (KWS XS, Hamos, Prenzberg, Germany) was used for electrostatic separation experiments (Supplementary Material SM1). The device was selected based on previous studies (Felsing et al., 2018; Enders et al., 2020b). However, in comparison to these studies 1) the sample entry funnel was not modified (output opening: 12 cm), and 2) particle shields made of PVC were used as delivered from the manufacturer. Modifications include 3) additional weights underneath the vibrating conveyor for better control of the vibration intensity, and 4) the device had two position flaps and only the non-conductor fraction was used as a polymer-rich sample fraction. More information about the device is given in the Supplementary Material SM1.

Tests of different settings for high voltage, drum rotation, and vibration intensity were carried out to determine optimal instrument settings. Here, the mass reduction of sand 1 and recovery of LD-PE particles were used as validation criteria. The optimized instrument settings were then used for further separation experiments (Table 1).

The electrostatic separation of the prepared samples was conducted according to the following protocol: the relative humidity in the laboratory was set between 35% and 40%. Then, the device was booted and the instrument setting was entered as shown in Table 1. Next, the sample was added to the entry funnel and all residues were transferred from the storage vessel into the funnel with a brush. When the entire sample was transported from the conveyer, the vibration intensity was increased to 90% to flush the conveyer. The remaining material on the conveyer was carefully blown onto the rotating drum using pressurized air. After this procedure, all parameters were set to default and the device was turned off. The sample, which was collected on the drum scraper, was transferred into the box for the polymer-rich sample fraction. Only one separation cycle was carried out to reduce the loss of microplastic particles. Subsequently, the polymer-rich sample fraction was transferred with a brush into a storage vessel and covered with aluminum foil.

Density separation

Only the polymer-rich samples from the electrostatic separation of river sediments and the samples from scale-up experiments were further enriched by density separation. For this separation, a 500-ml separation funnel and potassium iodide solution (50 wt%., density: 1.5 g/cm³, potassium iodide 99.0–100.5% Ph. Eur., VWR, Darmstadt, Germany) were used. The protocol of Enders et al. (2020) was followed to process the samples (Enders et al., 2020a). Potassium iodide solution (100 ml) was used for all samples and an extended sedimentation time of 18 h was applied. After sedimentation, the settled fraction was drained through the valve, and the remaining polymer-rich fraction was drained through the opening of the separation funnel. The sample fraction was filtrated with a paper filter. Cleaning of the funnel and the filtrated sample was conducted according to the protocol (Enders et al., 2020a). Subsequently, the samples were freeze-dried on the paper filter. Then the enriched sample was transferred into a glass vessel using a brush.

Differential scanning calorimetry

For DSC measurements (DSC 214 Polyma, Netzsch, Selb, Germany), 5–20 mg of an enriched sample was transferred in aluminum crucibles (Concavus 40 µm, Netzsch, Selb, Germany). The crucibles were sealed with a lid and subsequently pierced. Eight sub-samples ($n = 8$) were measured from every enriched sample. The following temperature program was used: three cycles (heating, cooling, heating) were applied between –50 and 300°C with a heating rate of 20 K/min. Additionally, there was an isothermal phase of 3 minutes between each cycle. The peak temperatures of melting and crystallization, as well as enthalpies during the cooling and the second heating phase, were determined for PCL, LD-PE, and PET using the program Proteus (version 8.0.2, Netzsch, Selb, Germany). The integration limits for the determination of melting and crystallization enthalpies (dh_m and dh_c) of the polymers are included in the Supplementary Materials (Supplementary Figure S2). A linear baseline was applied for the determination of enthalpies. Subsequently, the

TABLE 2 Data reported by Harzdorf et al. (2022) for the multivariate calibration curve to quantify PCL, LD-PE, and PET by DSC measurements.

Polymer	Melting term (a_1)	Crystallization term (a_2)	Intercept
PCL	−0.0074	−0.02428	0.01247
LD-PE	0.02560	−0.00932	0.00182
PET	0.01807	−0.01653	0.04127

polymer mass per measurement was quantified according to the calibration data reported by Harzdorf et al. (2022) (Table 2). Equation 1 was used to calculate the polymer mass per DSC measurement:

$$m_{polymer,DSC} = a_1 * dh_m + a_2 * dh_c + intercept, \quad (1)$$

where a_1 and a_2 are empirical coefficients for the melting and crystallization enthalpies (Table 2).

Determination of recovery rates

The determined polymer mass per DSC measurement $m_{polymer,DSC}$ was projected to the total polymer-rich fraction (Equation 2). Consequently, the recovery rate of the polymer was calculated as the ratio of projected mass in the polymer-rich fraction $m_{polymer,\ enriched}$ and the known mass from the sample preparation $m_{polymer,0}$ (Equation 3). Subsequently, an average recovery rate of each polymer was calculated for each particulate matrix:

$$m_{polymer,enriched} = \frac{m_{polymer,DSC}}{m_{DSC}} * m_{enriched}, \quad (2)$$

$$recovery\ rate = \frac{m_{polymer,enriched}}{m_{polymer,0}}, \quad (3)$$

where m_{DSC} and $m_{enriched}$ are the mass of the sample used for DSC measurement and the mass of the polymer-rich fraction, respectively.

Quality assurance

All personal protective equipment was made of cotton. Sample preparation and the transfer were carried out with metal or glass tools and natural hairbrushes, which were pre-cleaned with plastic-free cellulose tissues and ethanol. All samples were stored in glass vessels sealed with aluminum foil. Contamination with airborne microplastic was decreased by reducing the exposure time to the atmosphere to a minimum. Further, the applied dry box was equipped with an H14 particle filter (retention 99.995%). The KWS XS was also applied in a laminar-flow box with an H14 particle filter.

Results

Matrix characterization

Four particulate matrices were characterized regarding their particle size distribution, TOC, and quartz concentration. The particle size distribution of sand 1 had the highest d_{50} value whereas sand 2 had the lowest (Table 3). Similar average particle size was found for the sediment samples. In these samples, the d_{50} differed only by 80 µm. Moreover, the TOC concentrations for both sand samples are equal within their standard deviations (SDs). Compared to the sand samples, the sediment samples had a higher TOC. The highest TOC was found in sediment 2 and was ~5 mg/kg above the TOC of sediment 1.

The powdered matrices were examined by XRD to determine their mineral composition (Table 3). The results show, that sand 1, sand 2, and sediment 1 contained almost equal amounts of quartz (mean: 85%). Sediment 2 had a lower quartz concentration than the other matrices. Additionally, a higher kaolinite concentration of 3.5% was found in sediment 2. Feldspar minerals, such as plagioclase and orthoclase, were identified in all matrices. Quantification of the individual feldspar minerals was not carried out.

Mass reduction

Electrostatic separation has reduced the initial mass of all matrices by at least 69% after one separation step (Figure 1). Nevertheless, clear differences between sand samples and sediment samples were found. Sand samples had higher mass reductions of 98.90 ± 0.21% (sand 1, mean ± standard deviation) and 99.1 ± 0.4% (sand 2) than sediment samples. In sediment 1 and sediment 2, the mass reduction was 69.7 ± 0.1% and 78 ± 6%, respectively. The additional density separation led to a total mass reduction above 99% for the sediment samples.

During the electrostatic separation process, a loss of sample mass was observed. For all matrices, the fine dust particles settled on the interior part of the KWS-XL and were not separated correctly. Fine particles accumulated on the metal scrapper. These particles were transferred into the sample fraction after the separation process was completed. The particles attached to the rest of the interior of the separator were discarded and

TABLE 3 Particle size distribution and TOC concentration of the four investigated matrices.

Matrix	Particle size range (d_{10} to d_{90}) [µm]	Average particle size (d_{50}) [µm]	TOC [mg/kg]
Sand 1	257–1701	640 ± 40	1.75 ± 0.14
Sand 2	110–604	346 ± 10	1.83 ± 0.17
Sediment 1	218–1,274	450 ± 10	3.53 ± 0.10
Sediment 2	142–1,653	530 ± 10	8.19 ± 0.13

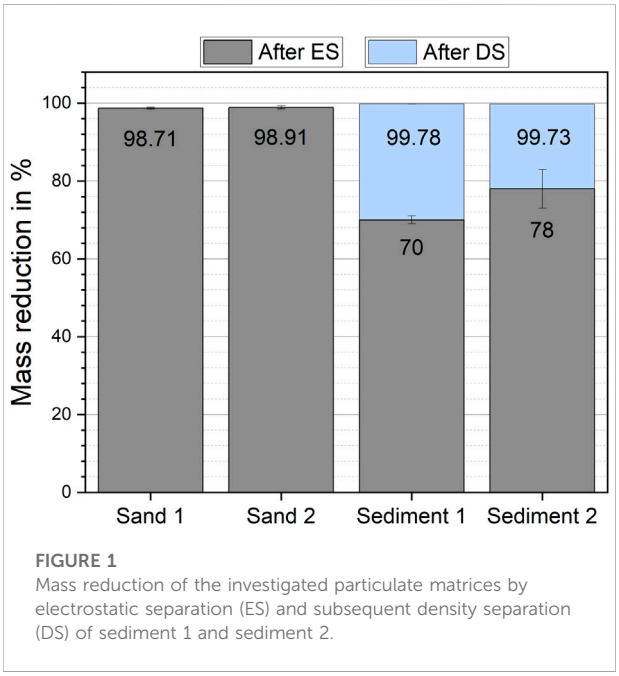

FIGURE 1
Mass reduction of the investigated particulate matrices by electrostatic separation (ES) and subsequent density separation (DS) of sediment 1 and sediment 2.

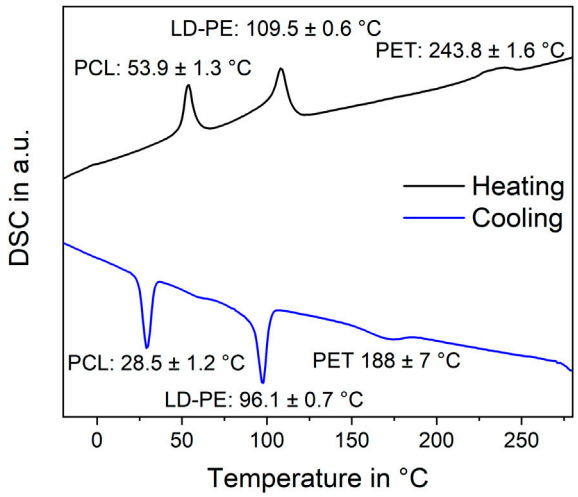

FIGURE 2
Thermogram of DSC measurements to determine peak temperatures and enthalpies of PCL, LD-PE, and PET. The three polymers were measured simultaneously.

counted as sample loss. This loss was 0.46 ± 0.23% (sand 1, mean ± SD), 0.31 ± 0.07% (sand 2), 0.47 ± 0.17% (sediment 1), and 0.97 ± 0.05% (sediment 2) of the initial sample mass. It was also observed, that the matrix particles whirled up when entering the electric field of the corona electrode. This interaction increased dust formation during the separation. Further, we found that control of the relative humidity in the separation chamber was an important factor to obtain reproducible results. A difference of 5% in relative humidity could lead to a difference in mass reduction for the same particulate matrix. Here a higher relative humidity in the separation chamber led to a higher mass reduction.

Polymer identification and recovery rates

DSC measurements were conducted for identification and quantification of the microplastic particles in the polymer-rich sample fraction after separation. The parallel identification of the spiked microplastic types PCL, LD-PE, and PET by the peak temperatures was successful (Figure 2). The SD of the peak temperatures was below 1.6 K for all peaks except for the crystallization peak temperature of PET. Here the SD was 7 K. Moreover, no superposition of the peaks was found. Hence, the calibration curves reported by Harzdorf et al. (2022) were applied to determine the polymer mass in all enriched sample fractions. The recovery rates of PCL, LD-PE, and PET from the four investigated matrices are shown in Figure 3.

In general, the recovery rates of the individual microplastic types showed no distinct variation in the particulate matrices. However, in terms of SD, in some cases, there were significant differences in the recovery rates of the same microplastic type in different matrices. The recoveries for PCL and LD-PE differed significantly between sediment 1 and sediment 2. In sediment 2, the average recovery rates were 14–19% higher than in sediment 1. There were also differences between sand 2 and sediment 1 for LD-PE and between sand 1 and sediment 2 for PET. No significantly different recoveries were found for the other matrices.

Polymer-specific recovery rates were observed for the different microplastic types. PCL has shown an average

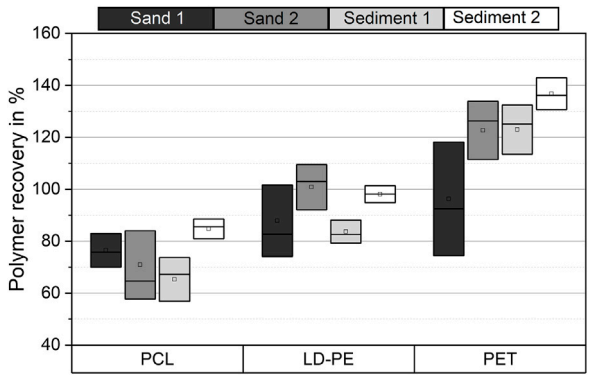

FIGURE 3
Boxplot of recovery rates of PCL, LD-PE, and PET microplastic particles from different particulate matrices (n = 5). Recovery rates were determined by DSC measurements. The SD of the data is shown as the width of the boxes.

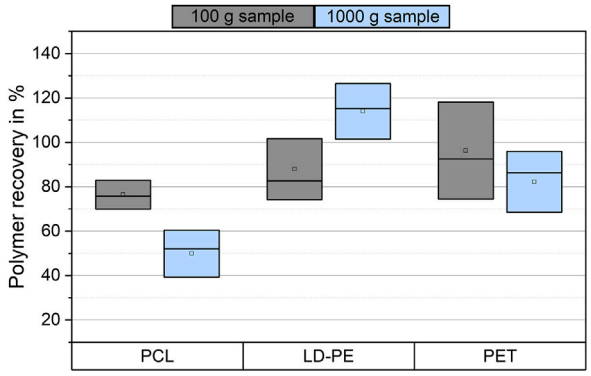

FIGURE 4
Boxplot of the average polymer recovery of PCL, LD-PE, and PET from 100 g (n = 5) and 1,000 g samples (n = 3) from sand 1. The SD of the data is shown as the width of the boxes.

recovery of 74 ± 9% (mean ± SD) over all matrices (n = 4). An average recovery of 93 ± 9% and 120 ± 18% was found for LD-PE and PET, respectively. Hence, LD-PE showed a higher recovery than PCL and lower recovery rates than PET. The recovery of 120% for PET indicates an overestimation of this polymer in our analysis and will be discussed later. Within the SD, comparable recovery rates were found for all microplastic types from sand 1 only.

Scale-up experiments

The mass reduction and microplastic recovery were investigated for 1,000 g samples of sand 1. After electrostatic separation, the mass reduction was 99.241 ± 0.028%. An average sample loss of 4.1 g was observed during electrostatic separation, but a large deviation between the samples was found in the range of 0.8–8.2 g per sample. A total mass reduction of 99.98 ± 0.01% was reached after density separation. The recovery rates of all polymers were in a moderate range (Figure 4). This means the recovery rates of PCL, LD-PE and PET were 50 ± 11% (mean ± SD), 114 ± 13%, and 82 ± 14%, respectively. Compared to the 100 g samples of sand 1, the mean values of the microplastic recovery were decreased for PCL and PET and increased for LD-PE. The results for LD-PE showed an overestimation by 14%.

Discussion

Effect of matrix properties on mass reduction by electrostatic separation

In this study, the microplastic analysis was realized by electrostatic separation followed by density separation to reach a sufficient mass reduction. Subsequently, microplastics were examined by DSC. Matrix properties such as particle size, TOC, and mineral composition might have an impact on mass reduction (Enders et al., 2020b). This was investigated by processing four different particulate matrices and comparing their mass reduction and microplastic recovery (Figure 1). Two sand samples and two sediment samples were tested.

Both sand samples were commercial sands with different average particle sizes. According to DIN 4220, sand 1 was classified as coarse sand and sand 2 as medium sand. In commercial sands, low TOC concentrations were found because these matrices were not exposed to the environment. Hence, no organic matter, such as algae, bacteria, or plant residues, increased the TOC concentration in the sand samples. On the other hand, both sediment samples were classified as medium sand but had different TOC concentrations. The different TOC in sediment samples could be attributed to different flow velocities and catchment areas of the rivers. In the case of sediment 2, the increased concentrations of TOC and particles <63 µm could be attributed to better sedimentation conditions of the Weisseritz River.

When applying electrostatic separation to particulate matrices, particle size is an important factor. The manufacturer of the applied KWS recommends a particle size >100 µm to process minerals, such as sand and sediments (Hoffmann, 2020). However, electrostatic separation achieved a high mass reduction for sand samples independent of the particle size distribution. The mass reduction of both sediment samples was significantly different even though the average particle size was similar in sediment 1 and sediment 2. Moreover, sieve analysis revealed similar concentrations of particles <63 µm despite the distinct average particle size in all sediments (Supplementary Materials SM3). The concentration of particles <63 µm was in the range of 0.5–3.3%. In comparison,

TABLE 4 Quartz concentration in the investigated matrices as determined by XRD analysis.

Matrix	Quartz concentration [%]
Sand 1	86
Sand 2	84
Sediment 1	85
Sediment 2	55

silty sands contain 10–52% of particles <63 µm (DIN 4220). Thus, the low concentration of fine particles and the average particle size did not influence the mass reduction by electrostatic separation. However, a decrease in mass reduction was reported for soil samples with higher concentrations of fine particles (Enders et al., 2020b). The removal of particles <100 µm from particulate samples led to an increase in mass reduction from an initial 1% to 15% in that study (Enders et al., 2020b). Our study shows that the investigation of particulate matrices with defined ratios of particles in different size classes is necessary to evaluate and quantify the influence of particle size on electrostatic separation.

We observed a significantly different mass reduction between sand and sediment samples (Figure 1). The mass reduction of both sediment samples was about 20–30% lower than for the sand samples. Both sediment samples showed increased TOC concentrations. Thus, TOC could have influenced the mass reduction process by electrostatic separation. Elevated TOC concentrations could originate from organic material, such as plants, leaves, and roots, as these particles have different electrostatic properties than quartz particles. On the other hand, a biofilm of organic matter originating from algae or bacteria would have increased the TOC and altered the electrostatic properties of sediment particles (Flemming and Wingender, 2010; Fang et al., 2017). Biofilms may have reduced the net conductivity of the particles and thus favor the assignment of these particles to the polymer-rich fraction. Our results showed a lower mass reduction of sediments with increased TOC (3.53 ± 0.10 to 8.19 ± 0.13 mg/kg). The variation between the mass reduction of sediment 1 and sediment 2, however, did not correlate with the TOC. Sediment 1 had a lower TOC concentration, but still a lower mass reduction than sediment 2. Hence, the total mass reduction of a particulate matrix could be dependent on both TOC and the particle size distribution. The quantification of this effect was beyond the scope of this work and requires further research.

Enders et al. (2020) discussed the role of different mineral compositions in particulate matrices to influence the efficiency of electrostatic separation (Enders et al., 2020b). According to their study, the mass reduction of sand samples was disturbed in presence of small calcite particles (<50 µm) (Enders et al., 2020b). In our study, varieties in the mineral composition of our matrices were determined (Table 4). However, XRD measurements did not identify calcite in the matrices. We found quartz to be the main mineral in all matrices. Different concentrations of feldspar were detected, as well as an increased kaolinite concentration in sediment 2. Peretti et al. (2012) reported that feldspar and quartz minerals could be separated electrostatically, with different recoveries (Peretti et al., 2012). These experiments were carried out in a free-fall separation chamber instead of a KWS. The separation of different minerals required a triboelectric charge, which occurs only to a limited extent during the separation with a KWS (Oberrauner, 2012; Peretti et al., 2012; Mirkowska et al., 2016; Gehringer, 2021). Moreover, clay particles consist typically of kaolinite and show diameters <2 µm. Such small particles cannot be removed from the metal drum by the drum scraper. Adhered clay particles on the metal drum could form an insulating layer, which would have led to a decrease in separation efficiency. Nevertheless, from our results, no correlation between mass reduction and mineral composition could be derived. Sediment 2 had a different mineral composition than the other matrices, but the obtained mass reduction showed no abnormalities despite an increased SD. Hence, the variance of mass reduction was more likely to originate from the distinct particle size distribution and TOC content in the particulate matrices.

The observed differences between the mass reduction of sand and sediment samples were contrary to the results of Felsing et al. (2018). In their study, equal mass reductions for particulate matrices were found independent of particle size and TOC after three separation steps (Felsing et al., 2018). Still, the experimental set-up between this study and the studies of Felsing et al. (2018) and Enders et al. (2020) was different in terms of high voltage, the definition of the polymer-rich sample fraction, and the number of separation steps (Felsing et al., 2018; Enders et al., 2020b). Further, the humidity of air can influence electrostatic separation (Manouchehri, 2000). Therefore, separation was carried out at a relative humidity of 35–40%. Other studies did not report the air humidity during electrostatic separation, which hampers comparisons. Nevertheless, electrostatic separation removed >70% of the initial sample mass of different particulate matrices. Subsequent density separation has been inevitable for the identification of microplastics. An efficient electrostatic separation, however, can significantly reduce the required volume of separation medium for density separation. Scale-up experiments have shown that equal mass reduction was reached independently from the sample mass. This again shows the potential of electrostatic separation. In combination with density separation, this process was efficient to extract microplastics from large particulate samples. Furthermore, lipophilic separation could be further used as an alternative to density separation to increase the greenness of microplastic analysis (Mani et al., 2019; Lechthaler et al., 2020).

Recovery rates

DSC measurements successfully identified spiked microplastic particles after their extraction from particulate matrices (Figure 2). PCL, LD-PE, and PET particles were identified simultaneously in the same DSC measurement. Moreover, the simultaneous presence of these polymers did not influence their melting and crystallization signals. Hence, the calibration curves reported by Harzdorf et al. (2022) were applied to determine the recovery rates of microplastic.

In a few cases, the matrix could have influenced the recovery of the same microplastic type. This accounted most dominantly for sediment samples. These samples were enriched by additional density separation. A loss of microplastic could have occurred in sediment 1, which was the sample with the lowest mass reduction after electrostatic separation. The sample mass after electrostatic separation was ~30 g. Possibly, shaking the separation funnel was not sufficient to separate microplastic and sediment particles in such large samples. This could explain the lower recoveries for sediment 1. Thus, an increase in the recovery of microplastic from such samples could be achieved by applying a spiral conveyor for mixing (Enders et al., 2020a). For the same reason, the different recovery rates of LD-PE from sand 2 and sediment 1 could have occurred. Therefore, matrix properties could have a higher impact on the enrichment of particulate matrices than on the microplastic determination by DSC.

We found that the recovery of microplastics seems to be polymer-specific (Figure 3, Figure 4). Significant differences in the recovery rate were found in 100 g samples and scale-up experiments. It was most striking that the average recovery of PET was >100% in 100 g samples. Sample heterogeneity by granular convection and contamination from environmental samples and sample handling could not lead to such overestimation. Samples for DSC measurements were randomly taken from the polymer-rich fraction. Moreover, measures for quality assurance have reduced the risk of contamination. Accordingly, polymer-specific properties of PET itself were the most likely explanation. PET has a more sterically demanding chemical structure than LD-PE and PCL. For this reason, the ratio of crystalline and amorphous phases of PET depends on its thermal processing (Demirel et al., 2011). Additionally, this change of crystallinity and hence the change of the phase transition enthalpies could have been influenced by the presence of quartz dust and organic matter during melting and crystallization. An increase of phase transition enthalpy compared to the calibration data would then result in the observed overestimation of PET.

Harzdorf et al. (2022) proposed an influence of hetero-nucleation with fine sediment particles. The high SD of the PET melting peak temperature could indicate that phase transition processes were influenced (Figure 2). However, this hypothesis requires experimental evidence, which is still to be done. Nevertheless, in scale-up experiments, no overestimation of PET occurred. There could have been a higher loss of PET due to the additional density separation in the scale-up experiments. Furthermore, additional density separation reduced the quartz dust fraction and thus decreased the chance of hetero-nucleation. Therefore, the hypothesis of hetero-nucleation favoring a change of crystallinity was supported. To what extent hetero-nucleation influences the reliability of the results should be evaluated further.

The recovery rates of LD-PE were ~100% in both experimental setups. Yet, the scale-up experiments showed an overestimation of 14%, which cannot be explained by the SD of the data. A calculation of the uncertainty of the whole process was conducted (Supplementary Materials SM4) and estimated at ±50% for a sample mass of 1 kg. The uncertainty of DSC measurement particularly contributed to the total uncertainty. Inter-laboratory tests have shown a relative standard uncertainty of 7–13% for DSC measurements (Wampfler et al., 2022). Including these data, an overestimation of 14% could be explained by the uncertainty of DSC measurements and the calibration data.

Moreover, PCL was tested as a potential internal standard for quality assurance. We showed that the recovery of PCL was below those of LD-PE and PET. However, the recovery rates could be dependent on the polymer type. Hence, the application of PCL internal standards to represent the recovery of all polymers was limited. Nevertheless, PCL as an internal standard is still promising because of its low recovery rates (Figure 3). It could be used as a benchmark for the minimum recovery in measurements of environmental samples.

The scale-up experiments had similar recovery rates as for 100 g samples, except for PET samples (Figure 4). Hence, electrostatic separation of microplastic and particulate matrices was possible for samples with masses up to 1 kg. A further increase in sample mass could be possible. The implementation of density separation increased the mass reduction to a sample size that could be analyzed by DSC measurements. This would be possible with an even lower volume of separation solution than 100 ml (Enders et al., 2020a). However, the recovery rates of PET and PCL were significantly lower than for LD-PE. Possibly, the recovery of PET and PCL was reduced due to the smaller density difference to the applied potassium iodide solution. Potassium iodide was applied because of its reduced hazardous properties compared to zinc chloride or sodium polytungstate. The application of separation solutions with a density >1.7 g/cm^3 may increase the recovery of PET and PCL. Furthermore, lipophilic separation can overcome the limitations of density separation as mentioned before.

Recovery rates were determined for a microplastic content of 75 mg/kg (ppm) in the scale-up experiments. This content was much higher than in other environmental samples (Klein et al., 2015; Adomat and Grischek, 2021). However, theoretical LOQs for semi-crystalline polymers of 2.3 mg microplastic in 1 kg

sediment were calculated for this method (Supplementary Materials SM5), assuming an average mass reduction of 99.7% and recovery of 86% (Way et al., 2022).

Conclusion

The present study facilitates a proof of concept for the application of electrostatic separation and DSC for microplastic analysis in particulate matrices. We conclude that electrostatic separation allows a fast treatment of representative samples for microplastic analysis in sediments. DSC facilitates robust microplastic determination for particulate matrices with high microplastic contaminations. Such samples could come from harbor basins, city beaches, or river sections with low flow rates. Hence, comprehensive microplastic monitoring could be realized with this method. However, there is a certain risk of microplastic loss during enrichment and uncertainty of microplastic determination by DSC. Further adjustments to the method can help to overcome these limitations and should focus on the following aspects:

- The impact of air humidity on electrostatic separation of microplastic and sediment.
- A quantification of matrix-related effects by TOC and fine particles.
- Application of green and sustainable alternatives to density separation.
- Polymer-specific behaviors during the DSC measurements in complex matrices.
- Investigation of the recoveries for more microplastic types, including PCL.

Data availability statement

The original contributions presented in the study are included in the article/Supplementary Material, further inquiries can be directed to the corresponding author.

Author contributions

LK, SS, KH, and MS designed the study, LK, MH, and YA conducted lab and field work, LK and SS analyzed the data, LK wrote the manuscript with contributions from and final approval of all authors.

Funding

This study was supported by the European Social Fund (ESF) and by the Federal State of Saxony (Project VEMIWA—Vorkommen und Verhalten von Mikroplastik in sächsischen Gewässern; Grant No. 100382142). Open Access publication was supported by the Deutsche Forschungsgemeinschaft DFG (Grant No. GO 3639/1-1) and the Forschungsinnovationsfonds (FINF) of the University of Applied Sciences Dresden.

Acknowledgments

The authors want to thank Dr. Udo Steiner from the University of Applied Sciences for XRD measurements and the support in data analysis and interpretation. Moreover, the author thank the two editors for the proofreading.

Conflict of interest

The authors declare that the research was conducted in the absence of any commercial or financial relationships that could be construed as a potential conflict of interest.

Publisher's note

Supplementary material

The Supplementary Material for this article can be found online at: https://www.frontiersin.org/articles/10.3389/fenvs.2022.1032005/full#supplementary-material

References

Adomat, Y., and Grischek, T. (2021). Sampling and processing methods of microplastics in river sediments - a review. *Sci. Total Environ.* 758, 143691. doi:10.1016/j.scitotenv.2020.143691

Akdogan, Z., and Guven, B. (2019). Microplastics in the environment: A critical review of current understanding and identification of future research needs. *Environ. Pollut.* 254, 113011. doi:10.1016/j.envpol.2019.113011

Anbumani, S., and Kakkar, P. (2018). Ecotoxicological effects of microplastics on biota: A review. *Environ. Sci. Pollut. Res.* 25, 14373–14396. doi:10.1007/s11356-018-1999-x

Andrady, A. L. (2011). Microplastics in the marine environment. *Mar. Pollut. Bull.* 62, 1596–1605. doi:10.1016/j.marpolbul.2011.05.030

Bellasi, A., Binda, G., Pozzi, A., Galafassi, S., Volta, P., and Bettinetti, R. (2020). Microplastic contamination in freshwater environments: A review, focusing on interactions with sediments and benthic organisms. *Environments* 7, 30. doi:10.3390/environments7040030

Besseling, E., Quik, J. T. K., Sun, M., and Koelmans, A. A. (2017). Fate of nano- and microplastic in freshwater systems: A modeling study. *Environ. Pollut.* 220, 540–548. doi:10.1016/j.envpol.2016.10.001

Bitter, H., and Lackner, S. (2020). First quantification of semi-crystalline microplastics in industrial wastewaters. *Chemosphere* 258, 127388. doi:10.1016/j.chemosphere.2020.127388

Braun, U. (2020). *Statuspapier mikroplastikanalytik*. Berlin: BMBF Forschungsschwerpunkt.

Das, S., Kohnlechner, R., Aman, F., and Dascalescu, L. (2010). Corona separation of fly ash. *IEEE Trans. Ind. Appl.* 46, 2157–2164. doi:10.1109/TIA.2010.2071170

De-la-Torre, G. E., Dioses-Salinas, D. C., Pizarro-Ortega, C. I., and Santillán, L. (2021). New plastic formations in the Anthropocene. *Sci. Total Environ.* 754, 142216. doi:10.1016/j.scitotenv.2020.142216

Demirel, B., Yaras, A., and Elçiçek, H. (2011). Crystallization behavior of PET materials. *BAÜ fen. Bil. Enst. Derg. Cilt* 13, 26–35.

Dioses-Salinas, D. C., Pizarro-Ortega, C. I., and De-la-Torre, G. E. (2020). A methodological approach of the current literature on microplastic contamination in terrestrial environments: Current knowledge and baseline considerations. *Sci. Total Environ.* 730, 139164. doi:10.1016/j.scitotenv.2020.139164

Enders, K., Lenz, R., Ivar do Sul, J. A., Tagg, A. S., and Labrenz, M. (2020a). When every particle matters: A QuEChERS approach to extract microplastics from environmental samples. *MethodsX* 7, 100784. doi:10.1016/j.mex.2020.100784

Enders, K., Tagg, A. S., and Labrenz, M. (2020b). Evaluation of electrostatic separation of microplastics from mineral-rich environmental samples. *Front. Environ. Sci.* 8, 346. doi:10.3389/fenvs.2020.00112

Fang, H., Chen, Y., Huang, L., and He, G. (2017). Biofilm growth on cohesive sediment deposits: Laboratory experiment and model validation. *Hydrobiologia* 799, 261–274. doi:10.1007/s10750-017-3224-1

Felsing, S., Kochleus, C., Buchinger, S., Brennholt, N., Stock, F., and Reifferscheid, G. (2018). A new approach in separating microplastics from environmental samples based on their electrostatic behavior. *Environ. Pollut.* 234, 20–28. doi:10.1016/j.envpol.2017.11.013

Flemming, H.-C., and Wingender, J. (2010). The biofilm matrix. *Nat. Rev. Microbiol.* 8, 623–633. doi:10.1038/nrmicro2415

Gehringer, S. (2021). Leoben: Montanuniversität, Lehrstuhl für Aufbereitung und Veredlung. Berlin: Zu Fragen einer kontrollierten Aufladung von Mineraloberflächen für eine erfolgreiche Trennung im elektrostatischen Feld. Dissertation.

Hanvey, J. S., Lewis, P. J., Lavers, J. L., Crosbie, N. D., Pozo, K., and Clarke, B. O. (2017). A review of analytical techniques for quantifying microplastics in sediments. *Anal. Methods* 9, 1369–1383. doi:10.1039/C6AY02707E

Hartmann, N. B., Hüffer, T., Thompson, R. C., Hassellöv, M., Verschoor, A., Daugaard, A. E., et al. (2019). Are we speaking the same language? Recommendations for a definition and categorization framework for plastic debris. *Environ. Sci. Technol.* 53, 1039–1047. doi:10.1021/acs.est.8b05297

Harzdorf, J., Zeumer, R., Schirrmeister, S., Adomat, Y., Kurzweg, L., Faist, S., et al. (2022). Mikroplastik in sächsischen Gewässern. *Schriftenreihe des LfULG*, 1–147.

Hoffmann, K. (2020). *Bedienungsanleitung (manual) - elektrostatischer korona-abscheider typ KWS-XS*. Prenzberg: Hamos GmbH.

Horton, A. A., and Dixon, S. J. (2018). Microplastics: An introduction to environmental transport processes. *WIREs Water* 5, 419. doi:10.1002/wat2.1268

Imhof, H. K., Schmid, J., Niessner, R., Ivleva, N. P., and Laforsch, C. (2012). A novel, highly efficient method for the separation and quantification of plastic particles in sediments of aquatic environments. *Limnol. Oceanogr. Methods* 10, 524–537. doi:10.4319/lom.2012.10.524

Kallenbach, E. M. F., Rødland, E. S., Buenaventura, N. T., and Hurley, R. (2022). "Microplastics in terrestrial and freshwater environments," in *Microplastic in the environment: Pattern and process*. Editor M. S. Bank (Cham: Springer International Publishing), 87–130. doi:10.1007/978-3-030-78627-4_4

Kane, I. A., and Clare, M. A. (2019). Dispersion, accumulation, and the ultimate fate of microplastics in deep-marine environments: A review and future directions. *Front. Earth Sci.* 7, 2241. doi:10.3389/feart.2019.00080

Kawecki, D., and Nowack, B. (2019). Polymer-specific modeling of the environmental emissions of seven commodity plastics as macro- and microplastics. *Environ. Sci. Technol.* 53, 9664–9676. doi:10.1021/acs.est.9b02900

Kittner, M., Kerndorff, A., Ricking, M., Bednarz, M., Obermaier, N., Lukas, M., et al. (2022). Microplastics in the danube river basin: A first comprehensive screening with a harmonized analytical approach. *ACS Est. Water* 2, 1174–1181. doi:10.1021/acsestwater.1c00439

Klein, S., Worch, E., and Knepper, T. P. (2015). Occurrence and spatial distribution of microplastics in river shore sediments of the rhine-main area in Germany. *Environ. Sci. Technol.* 49, 6070–6076. doi:10.1021/acs.est.5b00492

Köhnlechner, R., and Sander, S. (2009). Praktischer einsatz elektrostatischer separatoren in der Sekundärrohstoffindustrie. *Berg. Huettenmaenn Monatsh* 154, 136–139. doi:10.1007/s00501-009-0453-2

Köhnlechner, R. (1999). Triboelectric charging and electrostatic separation of diverse, non-conductive mixed waste, especially plastic, CA2397506A1.

Lechthaler, S., Hildebrandt, L., Stauch, G., and Schüttrumpf, H. (2020). Canola oil extraction in conjunction with a plastic free separation unit optimises microplastics monitoring in water and sediment. *Anal. methods Adv. methods Appl.* 12, 5128–5139. doi:10.1039/D0AY01574A

Mai, L., Bao, L.-J., Shi, L., Wong, C. S., and Zeng, E. Y. (2018). A review of methods for measuring microplastics in aquatic environments. *Environ. Sci. Pollut. Res. Int.* 25, 11319–11332. doi:10.1007/s11356-018-1692-0

Majewsky, M., Bitter, H., Eiche, E., and Horn, H. (2016). Determination of microplastic polyethylene (PE) and polypropylene (PP) in environmental samples using thermal analysis (TGA-DSC). *Sci. total Environ.* 568, 507–511. doi:10.1016/j.scitotenv.2016.06.017

Mani, T., Frehland, S., Kalberer, A., and Burkhardt-Holm, P. (2019). Using castor oil to separate microplastics from four different environmental matrices. *Anal. Methods* 11, 1788–1794. doi:10.1039/C8AY02559B

Manouchehri, H.-R. (2000). Triboelectric charge characteristics and electrical separation of industrial minerals. Beijing: Ulea: University of Technology, Department of Chemical and Metallurgical Engineering. Dissertation.

Mirkowska, M., Kratzer, M., Teichert, C., and Flachberger, H. (2016). Principal factors of contact charging of minerals for a successful triboelectrostatic separation process – A review. *Berg. Huettenmaenn Monatsh* 161, 359–382. doi:10.1007/s00501-016-0515-1

Morin-Crini, N., Lichtfouse, E., Liu, G., Balaram, V., Ribeiro, A. R. L., Lu, Z., et al. (2022). Worldwide cases of water pollution by emerging contaminants: A review. *Environ. Chem. Lett.* 18, 779. doi:10.1007/s10311-022-01447-4

Nizzetto, L., Bussi, G., Futter, M. N., Butterfield, D., and Whitehead, P. G. (2016). A theoretical assessment of microplastic transport in river catchments and their retention by soils and river sediments. *Environ. Sci. Process. Impacts* 18, 1050–1059. doi:10.1039/C6EM00206D

Oberrauner, A. (2012). Leoben: Montanuniversität, Lehrstuhl für Aufbereitung und Veredlung. China: Nutzung der Elektroscheidung zur trockenen Aufbereitung von fein- und feinstdispersen Körnerschwärmen. Dissertation.

Peretti, R., Serci, A., and Zucca, A. (2012). Electrostatic K-feldspar/Na-feldspar and feldspar/quartz separation: Influence of feldspar composition. *Mineral Process. Extr. Metallurgy Rev.* 33, 220–231. doi:10.1080/08827508.2011.563156

Periyasamy, A. P., and Tehrani-Bagha, A. (2022). A review on microplastic emission from textile materials and its reduction techniques. *Polym. Degrad. Stab.* 199, 109901. doi:10.1016/j.polymdegradstab.2022.109901

Rodrigues, J. P., Duarte, A. C., Santos-Echeandía, J., and Rocha-Santos, T. (2019). Significance of interactions between microplastics and POPs in the marine environment: A critical overview. *TrAC Trends Anal. Chem.* 111, 252–260. doi:10.1016/j.trac.2018.11.038

Rodríguez Chialanza, M., Sierra, I., Pérez Parada, A., and Fornaro, L. (2018). Identification and quantitation of semi-crystalline microplastics using image analysis and differential scanning calorimetry. *Environ. Sci. Pollut. Res. Int.* 25, 16767–16775. doi:10.1007/s11356-018-1846-0

Schernewski, G., Radtke, H., Hauk, R., Baresel, C., Olshammar, M., Osinski, R., et al. (2020). Transport and behavior of microplastics emissions from urban sources in the baltic sea. *Front. Environ. Sci.* 8, 1105. doi:10.3389/fenvs.2020.579361

Shim, W. J., Hong, S. H., and Eo, S. E. (2017). Identification methods in microplastic analysis: A review. *Anal. Methods* 9, 1384–1391. doi:10.1039/C6AY02558G

Stock, F., Kochleus, C., Bänsch-Baltruschat, B., Brennholt, N., and Reifferscheid, G. (2019). Sampling techniques and preparation methods for microplastic analyses in the aquatic environment – a review. *TrAC Trends Anal. Chem.* 113, 84–92. doi:10.1016/j.trac.2019.01.014

Väinölä, R., Witt, J. D. S., Grabowski, M., Bradbury, J. H., Jazdzewski, K., and Sket, B. (2008). Global diversity of amphipods (Amphipoda; Crustacea) in freshwater. *Hydrobiologia* 595, 241–255. doi:10.1007/s10750-007-9020-6

Wampfler, B., Affolter, S., Ritter, A., and Schmid, M. (2022). *Measurement uncertainty in analysis of plastics: Evaluation by interlaboratory test results*. Cincinnati, Ohio: Hanser Publications.

Way, C., Hudson, M. D., Williams, I. D., and Langley, G. J. (2022). Evidence of underestimation in microplastic research: A meta-analysis of recovery rate studies. *Sci. Total Environ.* 805, 150227. doi:10.1016/j.scitotenv.2021.150227

Weber, C. J., Opp, C., Prume, J. A., Koch, M., Andersen, T. J., and Chifflard, P. (2021). Deposition and in-situ translocation of microplastics in floodplain soils. *Sci. Total Environ.* 819, 152039. doi:10.1016/j.scitotenv.2021.152039

Wright, S. L., Rowe, D., Thompson, R. C., and Galloway, T. S. (2013). Microplastic ingestion decreases energy reserves in marine worms. *Curr. Biol. CB* 23, R1031–R1033. doi:10.1016/j.cub.2013.10.068

frontiers | Frontiers in Environmental Science

TYPE Original Research
PUBLISHED 01 November 2022
DOI 10.3389/fenvs.2022.1028699

OPEN ACCESS

EDITED BY
Hongbiao Cui,
Anhui University of Science and Technology, China

REVIEWED BY
Lei Xu,
Nanyang Normal University, China
Ruibo Sun,
Anhui Agricultural University, China

*CORRESPONDENCE
Xiujiang Zhang,
13903844472@139.com

†These authors have contributed equally to this work and share the first authorship

SPECIALTY SECTION
This article was submitted to Toxicology, Pollution and the Environment,
a section of the journal
Frontiers in Environmental Science

RECEIVED 26 August 2022
ACCEPTED 18 October 2022
PUBLISHED 01 November 2022

CITATION
Hu H, Li L, Gao F, Diao W, Ma H, Feng F, Quan S, Xiang L and Zhang X (2022), Screening, identification, and degradation characteristics of 3-methylindole degrading bacteria. *Front. Environ. Sci.* 10:1028699. doi: 10.3389/fenvs.2022.1028699

Screening, identification, and degradation characteristics of 3-methylindole degrading bacteria

Hong Hu[1†], Lei Li[1†], Feng Gao[2†], Wentao Diao[1], Huan Ma[1], Fei Feng[1], Shujing Quan[1], Lingyun Xiang[1] and Xiujiang Zhang[1*]

[1]Henan Engineering Research Center of Industrial Enzymes, Institute of Biology Co., Ltd., Henan Academy of Sciences, Zhengzhou, China, [2]Anyang Academy of Agricultural Sciences, Anyang, China

3-Methylindole is a major component of organic pollutants in livestock compost, which can contribute to the deterioration of the environment in livestock farms and their surrounding areas. This study demonstrates that using microorganisms to degrade 3-methylindole is an effective method for energy conservation and environmental protection. The microbe capable of efficiently degrading 3-methylindole was isolated and screened from fecal samples. The isolated bacteria were identified as *Acinetobacter oleivorans* after morphological characterization and 16S rRNA sequencing. This project demonstrated that 3-methylindole was completely degraded under optimal conditions (initial concentration of 3MI: 100 mg/L, 30°C, pH8.0, and shaking at 160 rpm for 48 h). N_2-Acetyl-L-ornithine, Phenylacetaldehyde, Phenylacetic acid, Indole-3-carboxylic acid, and Indole-3-carboxaldehyde were the primary metabolites of this degradation process. This study provides a theoretical foundation for other microbe-mediated environmental remediation approaches as well as a basis for future work to apply bacteria that degrade 3-methylindole for the purification of polluted environments. It has a promising application in the control of malodorous gas pollution in the large-scale livestock and poultry breeding industries.

KEYWORDS

biodegradation, 3-methylindole, degradation characteristics, screen, *Acinetobacter olivaceus*

1 Introduction

Animal husbandry efforts have advanced rapidly in scale and complexity in China over recent years owing to the progressive improvement of national standards of living. Because of the increasing demand for meat, milk, and eggs among the Chinese population, the number of livestock and poultry herds that are kept in China has steadily increased, which has led to the production of a significant amount of malodorous fecal waste. China produced 3.884 billion tons of livestock and poultry manure and sewage in 2015 alone, including 636, 565, and 2,633 million tons of fresh manure, urine, and sewage, respectively

(Qian et al., 2018; Zou et al., 2020). However, our understanding of the generation, identification, prevention, and abatement/treatment of unpleasant odors is incomplete. Therefore, the treatment of livestock and poultry manure odor gas pollution has become increasingly important and urgent (Cheng et al., 2018).

3-Methylindole (3MI) is a common and well-known N-heterocyclic aromatic compound with a fecal odor that can be found in a variety of environmental matrices. 3MI is found naturally in animal faeces, coal tar, beetroot, and camphor wood, and it is used as a precursor in the production of many food additives and chemicals used in industrial and agricultural settings. Animal manure and wastewater treatment plant samples have been the focus of the majority of studies on the detection and quantification of skatole. However, skatoles can enter various environments *via* waste stream discharge, gas emissions, manure fertilizer application, wildlife excretion, and alga decomposition. Skatoles can also be produced by indigenous microorganisms (Ma et al., 2021).

As a harmful odorous compound released by poultry and livestock, 3MI has a strong fecal odor with an odor threshold of less than 0.003 mg/m^3, making it detectable at extremely low concentrations (Liu et al., 2018). In addition to having an unpleasant odor, 3MI has been associated with the development of pulmonary edema and emphysema in sheep and cattle. It can also increase the risk of developing a tumor in the respiratory tract and contribute to the development of neuroendocrine and immunological diseases in humans. It can further attract flies, mosquitoes, and beetles, thereby contributing to the spread of diseases transmitted by insects (Yang et al., 2019; Zhang et al., 2022). Consequently, it is urgently necessary to conduct a thorough investigation of 3MI environmental pollution.

To date, effective physical adsorption and chemical oxidation methods have been developed for the elimination of 3MI contamination. However, physical adsorption approaches are expensive, energy-intensive, and susceptible to poor environmental conditions. In addition to these limitations, chemical oxidation techniques can also contribute to secondary pollution (Luo, 2015). Biodegradation is a viable and eco-friendly method of removing skatole (Qu, 2020). Biodegradation has emerged as an attractive alternative method for removing 3MI and other environmental contaminants that do not entail the same range of drawbacks. Several 3MI-degrading microbes have since been identified (Ma et al., 2021; Wu et al., 2021), including *Clostridium maleominatum* A-3 under anaerobic conditions (Kohda et al., 1997), methanogenic bacteria in the context of sulfur reduction (Gu et al., 2002), and *Pseudomonas putida* lpc24 under conditions of oxygen restriction. Moreover, aerobic bacterial species such as *Lactobacillus brevis* (Meng et al., 2013), *Rhodopseudomonas palustris* wku-kdns3 (Sharma et al., 2015), *Acinetobacter toweneri* NTA1-2A, *Acinetobacter gullouiae* tat1-6 (Tesso et al., 2019), *Burkholderia* sp. IDO3, *Rhodococcus* sp. dmu1 and *Rhodococcus pyridinvorans* rp3 (Wu et al., 2021) can degrade this compound. However, these microbes generally exhibit only limited 3MI degradation activity, which is impaired in the presence of high 3MI concentrations. These microorganisms may grow under strict conditions that prevent their use in production settings because they are unable to break down this compound effectively. Future efforts to screen for bacteria that degrade 3MI are thus obviously necessary.

A bacterial strain with 3MI-degrading activity was isolated from pig manure compost soil in this study through screening efforts. Its capacity to break down manure as well as its growth performance and degradation activity under various culture conditions (inoculum amount, temperature, pH, and initial manure concentration) were then evaluated. In addition, metabolites produced by this strain were identified using ultra-high performance liquid chromatography-mass spectrometry (UHPLCQ-TOF MS). The purpose of this study was to develop effective strain resources for fecal odor degradation and to create a foundation suitable for using this strain to purify odor-polluted environments.

2 Materials and methods

2.1 Test materials

2.1.1 Microbial strain origins

The microbial strains screened in this study were isolated from samples of pig feces, fattening pig feces, sow feces, and pig plant manure collected in Luoshan County, Xinyang, Henan Province, China.

2.1.2 Culture medium

Inorganic salt medium (g/L): $(NH_4)_2SO_4$ 1.0, KH_2PO_4 0.2, K_2HPO_4 0.8, $MgCl_2{\cdot}7H_2O$ 1.1, $FeCl_2{\cdot}4H_2O$ 0.016, NaCl 0.5, pH7.0 ± 0.2. LB medium was prepared as follows (g/L): NaCl 10.0, peptone 10.0, yeast powder 5.0, pH 7.0, and Agar 15.0 was utilized to produce solidified medium. PBS was prepared as follows (g/L): $Na_2HPO_4{\cdot}12H_2O$ 10.8, $NaH_2PO_4{\cdot}2H_2O$ 2.3, pH 7.0.

2.1.3 Reagents and equipment

In this study, the analyses were performed using pure 3MI standards, pure methanol, anhydrous ethanol, glacial acetic acid, and NaCl. Equipment and approaches used for this study included high-performance liquid chromatography (HPLC), liquid chromatography-mass spectrometry (LC-MS), a UV spectrophotometer, PCR, scanning electron microscopy, an AB Triple TOF 6600 Mass Spectrometer (AB SCIEX)/Q Exactive HF Mass Spectrometer (Thermo), an Agilent 1290 Infinity LC Ultra High-Pressure Liquid Chromatography (Agilent)/Thermo Ultra High-Pressure Liquid Chromatography (Thermo) system, a low-temperature high-speed centrifuge (Eppendorf 5430R), an ACQUITY UPLC BEH Amide column (1.7 μm, 2.1 mm × 100 mm), acetonitrile (Merck,1499230-935),

ammonium acetate (Sigma,70221), methanol (Fisher, A456-4), and ammonia (Fisher, A470-500).

2.1.4 Bacterial suspension

Initial screening efforts resulted in the isolation of a single bacterial strain, which was chosen and grown for 24 h at 30°C with constant shaking in 150 ml of sterile liquid LB medium (160 rpm). The culture medium was then centrifuged for 10 min at 6,000 rpm at 4°C, the pellet was washed 2-3 times with PBS (pH 6.8), and the centrifugation process was repeated. Then PBS was used to suspend the cells.

3 Methods

3.1 3MI standard preparation

A 5 g/L 3MI standard solution was produced by dissolving 0.5 g of 3MI standard in 100 ml of anhydrous ethanol. This mixture was then sterilized with an organic filter membrane of 0.2 μm and stored at 4°C for subsequent use.

3.2 Isolation and screening of 3MI-degrading bacteria

In total, 1.0 g of pig manure compost soil was added to a sterile enriched liquid medium and cultured for 24 h at 30°C with constant shaking at 180 rpm. This medium was then used to inoculate (5%) a flask of inorganic salt medium supplemented with 100 mg/L 3MI, followed by 24 h of incubation at 30°C with 180 rpm. This subculturing procedure was repeated four times under identical conditions. Following this, 1 ml of the enriched solution was diluted 10-fold to 10^{-5} 10^{-6}, and 10^{-7} dilution levels, and 100 μl of each of these diluted samples was then spread on an enrichment solid medium. After incubation, the color, morphology, and size of the colonies were evaluated, and single colonies were selected to ensure that they possessed consistent morphological characteristics. Beef extract peptone solid (LB) medium was then used to perform further purification to yield colonies with a single morphological profile. An inclined culture medium was inoculated with the isolated bacterial strains that could grow when 3MI was the only carbon source available, and they were stored at 4°C.

3.3 Identification of 3MI-degrading bacteria

Identification of isolated 3MI-degrading bacteria was carried out using morphological, physiological, and biochemical methods, as in previous studies (Tesso et al., 2019; Whitman et al., 2012).

3.4 16S rRNA sequencing

The bacterial 16S rRNA gene sequence was amplified with the following universal primers: forward 27F:5′-AGAGTTTGATCATGGCTCAG-3′,reverse1492R:5′-ACGGTTACCTTACCTTGTTACGACTT-3′. All amplifications were carried out in 50 μl reactions containing 2 μl of gDNA, 2 μl of suitable primers (10 μmol/L), 25 μl of 2Taq PCR Mix, and 19 μl of purified water. The settings for the thermocycler were as follows: 98°C for 2 min; 98°C for 10 s, 55°C for 15 s, and 72°C for 90 s across 38 cycles; 72°C for 5 min.

Amplicons were sequenced by a commercial company, and the obtained sequences were compared with those in the NCBI GenBank. The isolated strains were identified by constructing a phylogenetic tree using the neighbor-joining method and the MEGA 6 software.

3.5 HPLC measurement of 3MI concentrations

For the HPLC-based detection of sample 3MI concentrations, 10 mg of 3MI was suspended at 1 mg/ml in anhydrous ethanol and diluted to standard concentrations of 50, 100, 200, 300, and 500 μg/ml. These standards were passed through a 0.2 μm organic filter membrane, and their peak area values were determined using HPLC, with three measurements per concentration level. The sample concentrations and peak area values were used to establish a linear regression. Chromatographic separation was carried out utilizing an Agilent 5 TC-C18 (250 mm × 4.6 mm, 5 μm) column at 30°C with a UV detection wavelength of 260 nm and a mobile phase of 1% acetic acid: water (1:1). The flow rate was maintained at 1.0 ml/min, while the injection volume was 20 μl.

3.6 Analyses of bacterial growth

The isolated AO-06 experimental strain of highly efficient 3MI-degrading bacteria was selected as the primary focus of this study. These bacteria were used to inoculate inorganic salt medium (10% inoculum), which was then cultured at 30°C in the presence of 100 mg/L 3MI as a carbon source while being continuously shaken at 140 rpm. Bacteria were cultured in triplicate for 72 h, and their growth was evaluated every 12 h. As a blank solution, an inorganic salt medium containing 3MI was used, and the absorbance at 600 nm (OD_{600}) in each sample was measured using a UV spectrophotometer, with samples

being thoroughly mixed with a whirlpool oscillator before measurement.

3.7 Analysis of 3MI degradation activity

To evaluate the ability of isolated bacteria to degrade 3MI, these cells were cultured for 72 h at 30°C and 140 rpm in liquid inorganic salt medium (10% inoculum) containing 500 mg/L 3MI. No bacteria were added to a control sample that served as a blank. The 3MI concentrations in these culture flasks were measured every 12 h in triplicate.

3.8 Analysis of the growth and degradation activity of strain AO-06

The ability of strain AO-06 to grow and degrade 3MI when 3MI (100 mg/L) was the only carbon source available was tested using a 10% inoculation, with cells being cultured at a natural pH at 30°C (180 rpm). Samples were collected every 12 h in triplicate, and OD_{600} values were measured as described above to monitor bacterial growth. The liquid phase samples were then subjected to 3MI extraction by combining them with an equal volume of methanol, centrifuging them at 5,000 rpm for 10 min, passing 1 ml of solution through a 0.22 μm organic filter membrane, and storing it at 4°C for testing. Samples with excessive concentrations were diluted before HPLC analysis.

3.9 The impact of environmental conditions on the 3MI-degrading activity of strain AO-06

The effect of various environmental conditions on the degradation of 3MI was studied. The following were the basic culture conditions: Medium with a natural pH containing 100 mg/L 3MI; temperature: 30°C; shaking speed: 180 rpm; inoculum concentration: 5%. Periodically, samples were collected to evaluate 3MI concentrations and bacterial growth, as described above. Rates of 3MI degradation were the primary metric of interest, and they were computed as follows:

3MI degradation rate (%) = (3MI content in uninoculated medium—3MI content in inoculated medium)/3MI content in uninoculated medium ×100%

The effects of different starting concentrations of 3MI (100, 150, 200, 250, 300 mg/L), pH levels (4.0, 5.0, 6.0, 8.0, 9.0), temperatures (20, 25, 30, 37, 42°C), and shaking speeds (0, 60, 120, 180, 240 rpm) on 3MI degradation were evaluated, with samples collected every 12 h in triplicate. The 3MI concentration was fixed at 100 mg/L for all assays unless otherwise indicated.

3.10 Metabolite detection

The preliminary analysis of metabolites produced by strain AO-06 when it degrades 3MI over a 48 h period was performed using a UHPLCQ-TOF MS approach. The experimental procedure is as follows:

1) based on the above analyses of growth and 3MI degradation characteristics, a sample collection time point of 48 h was selected, as bacteria were at a stable level with relatively vigorous growth and the highest observed 3MI degradation activity, allowing for more robust analyses of metabolite production. Three replicate samples were established in both the control and culture groups.
2) The samples were thawed at 4°C, combined with an equal amount of chilled methanol/acetonitrile/aqueous solution (2:2:1, v/v), mixed by vortexing, subjected to low-temperature ultrasonication for 30 min, allowed to stand for 10 min at −20°C, and centrifuged at 14,000 xg for 20 min at 4°C. The supernatants were then vacuum-dried, redissolved in a 100 μl acetonitrile aqueous solution (acetonitrile: water, 1:1, v/v), vortexed, centrifuged for 15 min at 14,000xg at 4°C, and the supernatants were utilized for subsequent procedures.
3) All samples were separated using an Agilent 1290 Infinity LC ULTRA high-performance liquid chromatography (UHPLC) HILIC column. The column was maintained at 25°C with a flow rate of 0.5 ml/min, an injection volume of 2 μl, and a mobile phase of water containing 25 mM ammonium acetate and 25 mM ammonia (A) and acetonitrile (B). Linear gradient elution was conducted as follows: 0–0.5 min, 95% B; 0.5–7 min, 95%–65% B; 7–8 min, 65%–40% B; 8–9 min, 40% B; 9–9.1 min, 40%–95% B; 9.1–12 min, 95% B. During this analytical procedure, samples were placed in an automatic sampler at 4°C. Random sequences were utilized for continuous sample analysis to control for the influence of instrument detection signal fluctuations. Quality control (QC) samples were added at random to the sample queue to monitor system stability and result reliability.
4) An AB Triple TOF 6600 mass spectrometer was used to collect a sample of first- and second-order spectrograms. Samples were separated using an Agilent 1290 Infinity LC UHPLC system, as described above, before being analyzed with the Triple TOF 6600 mass spectrometer (AB SCIEX). Positive and negative electrospray ionization (ESI) ion modes were used for detection, with the following ESI source parameters: Atomizing gas auxiliary heating 1 (Gas1): 60, auxiliary heating 2 (Gas2): 60, Air curtain gas (CUR): 30P SI, ion source temperature: 600°C, spray voltage (ISVF) ±5500 V (positive and negative modes); Primary mass charge ratio detection range: 60–1000 Da, secondary ion mass charge ratio detection range: 25–1000 Da, primary mass spectrometry scanning cumulative time: 0.20 s/spectra, secondary mass spectrometry scanning cumulative time: 0.05 s/spectra.

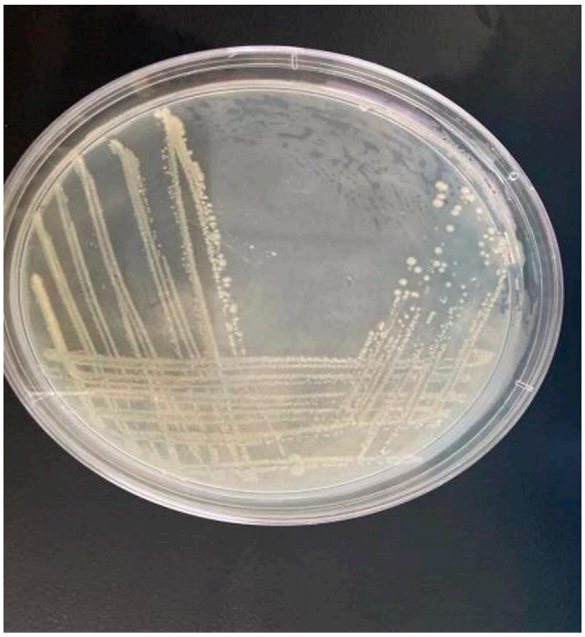

FIGURE 1
The morphology of strain AO-06 on LB medium.

Secondary mass spectrometry data were collected in data-dependent acquisition mode (IDA) using peak intensity value screening mode. The cluster removal voltage (DP) was ±60 V (positive and negative modes), and the collision energy was 35 ± 15eV. The IDA settings used a dynamic exclusion isotope ion range of 4 Da and 10.

4 Results and discussion

4.1 Screening identifies bacteria capable of degrading 3-methylindole

Three bacterial strains capable of growth when 3MI was the only available carbon source were isolated through repeated dilution and screening assays, indicating that these bacteria could degrade 3MI. Analyses of the 3MI degradation activity of these strains using HPLC revealed that one strain, tentatively designated AO-06, displayed a more robust activity than the other two. As a result, strain AO-06 was selected for additional experimental characterization. Functional microorganisms play an important role in the biological deodorization of livestock and poultry faces, so the key to Biological deodorization is used to identify strains that have a high deodorization efficiency (Hort et al., 2009). Chinese researchers have been working on microbial screening for deodorants for a very long time, but due to the limitations of screening techniques, microbial specificity, and other factors, the deodorant microorganisms being screened have issues with poor adaptability, single effects, and low efficiency. The deodorizing strain was therefore very important because it was chosen among those with strong adaptability and high efficiency.

TABLE 1 The microbiological characteristics of strain AO-06 capable of growing in the presence of 3MI as the only available carbon source.

Characteristics	Test results
Oxidase	–
Catalase	+
Amylohydrolysis	–
Gelatin hydrolysate	–
The utilization of n-hexadecane	+
D-biodisaccharide	+
D-glucose	+
D-mannitose	+
Sodium citrate	+
Malonate	+
Coumarone	+
L-lactic acid	+
Succinate	+
L-histidine	+

4.2 Morphological, physiological, biochemical, and molecular characterization of strain AO-06

Following plate streaking separation, strain AO-06 was discovered to have round bacterial colonies with a smooth, white, protruding surface that appeared moist and shiny, with clearly defined edges (Figure 1). Bacteria were rod-shaped, Gram-negative, and non-sporulating upon microscopic examination. According to the "Manual of Systematic Identification of Common Bacteria," starch hydrolysis, gelatin hydrolysis, and glucose/mannose utilization assays were performed, with the results of such biochemical and physiological characterization summarized in Table 1.

A 16S rRNA sequencing approach produced a 1434 bp gene product, which was compared to known sequences in the NCBI GenBank database before constructing a phylogenetic tree using the neighbor-joining method. This strain exhibited 99.9% sequence homology and 99.9% sequence similarity with *Acinetobacter oleivorans* (Figure 2). As a result, *A. oleivorans* was tentatively identified. There are many microorganisms in the environment, and these indigenous microorganisms play an important role in environmental purification. Because of the high variability of microorganisms, a large number of microorganisms suitable for survival in this environment can be left to be selected through natural domestication

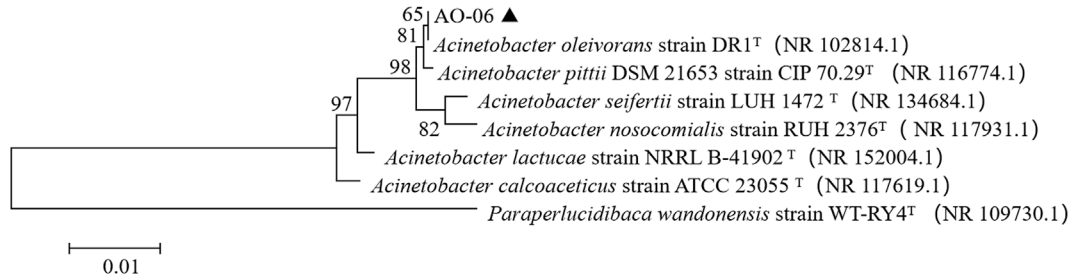

FIGURE 2
A 16S rRNA phylogenetic tree containing strain AO-06.

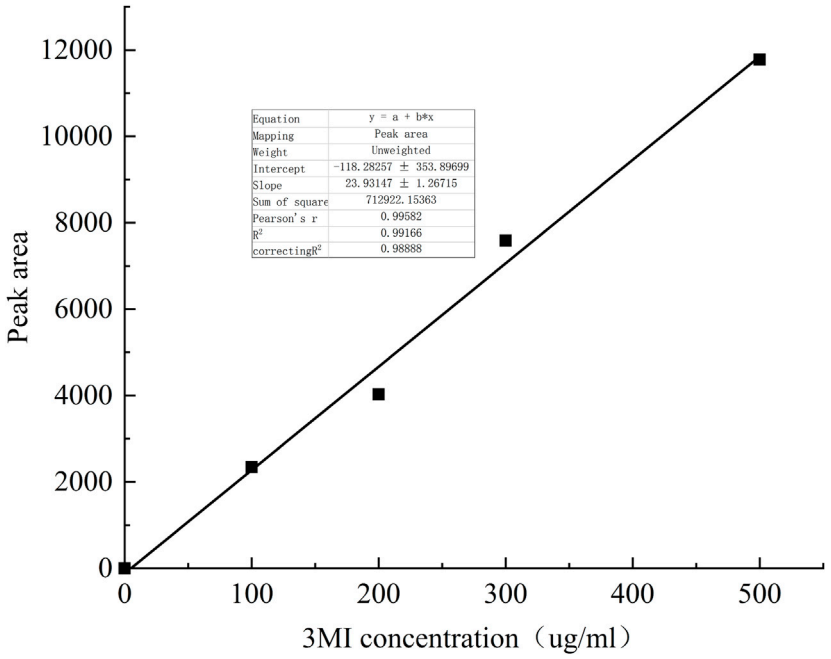

FIGURE 3
3MI liquid chromatography.

(Verschuere et al., 2001). The samples collected in this experiment were composted pig manure and activated sludge from pig farms. The reason for this is that pig manure in the composting process contains a large number of microorganisms and is rich in species.

4.3 Characterization of the growth of strain AO-06

To facilitate the accurate quantification of 3MI concentrations in culture samples, 50, 100, 200, 300, and 500 μg/ml 3MI standards were prepared and detected *via* HPLC. Then, a standard curve was constructed by plotting concentrations against peak area values (Figure 3). The retention time of 3MI in liquid chromatograms at 270 nm was 5.092 min (Figure 4). The linear regression equation for the 3MI standard curve was y = 23.931x–118.28 (R^2 = 0.9917).

According to OD600 measurements, AO-06 exhibited a logarithmic growth phase during which 3MI concentrations gradually decreased. After 48 h, maximum growth and complete 3MI degradation were evident. Thereafter, the growth rate decreased gradually (Figure 5).

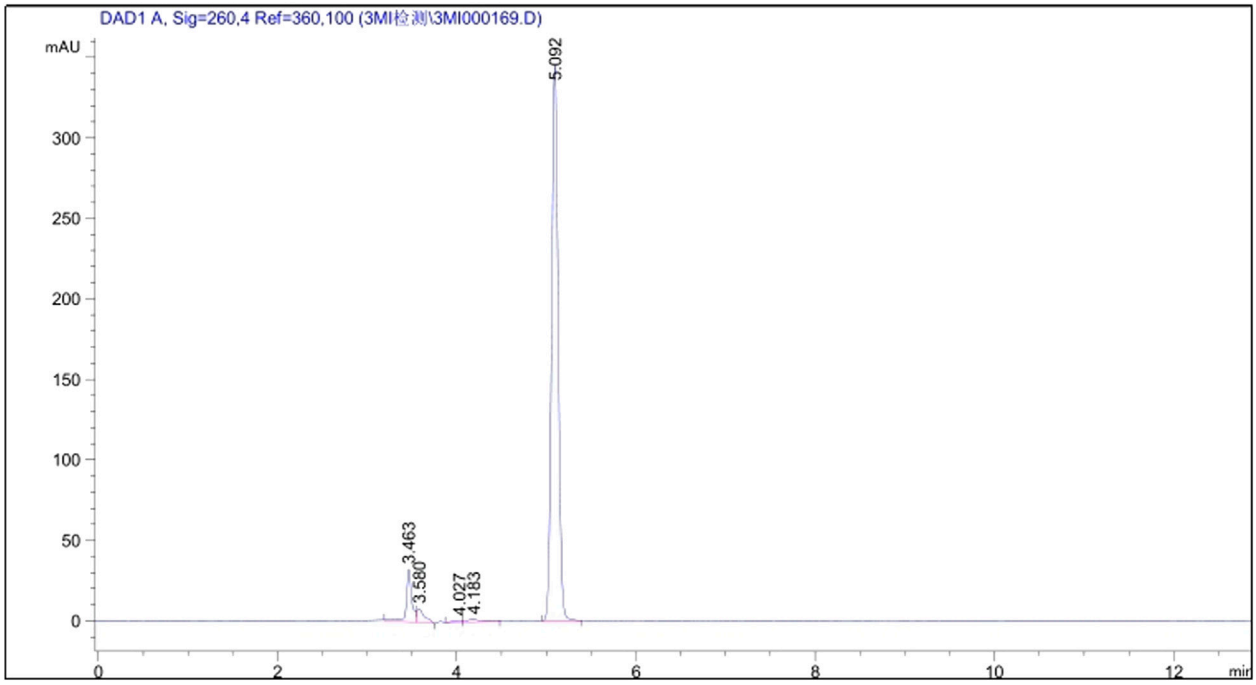

FIGURE 4
Standard curve of 3MI detected by liquid chromatography.

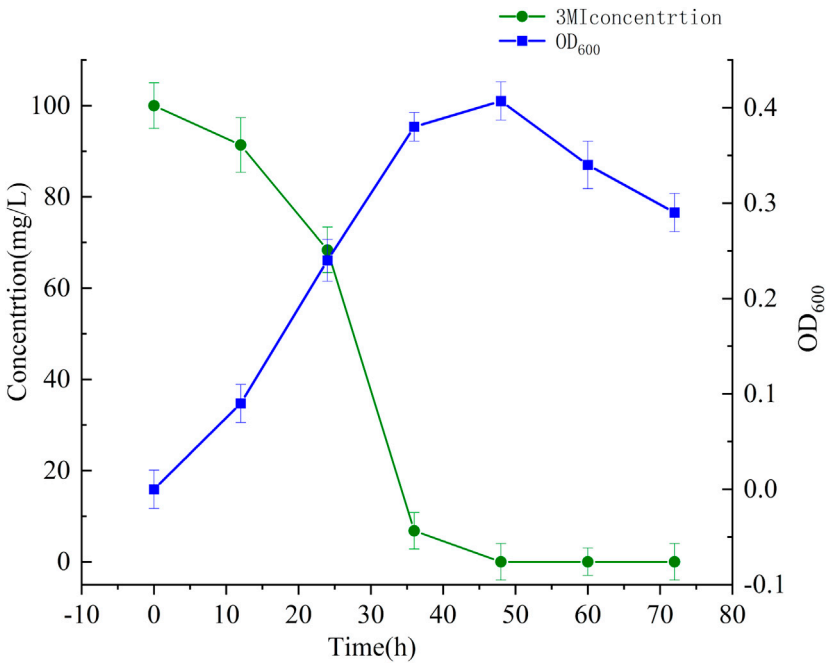

FIGURE 5
Growth and 3MI degradation activity for *Acinetobacter oleivorans* AO-06.

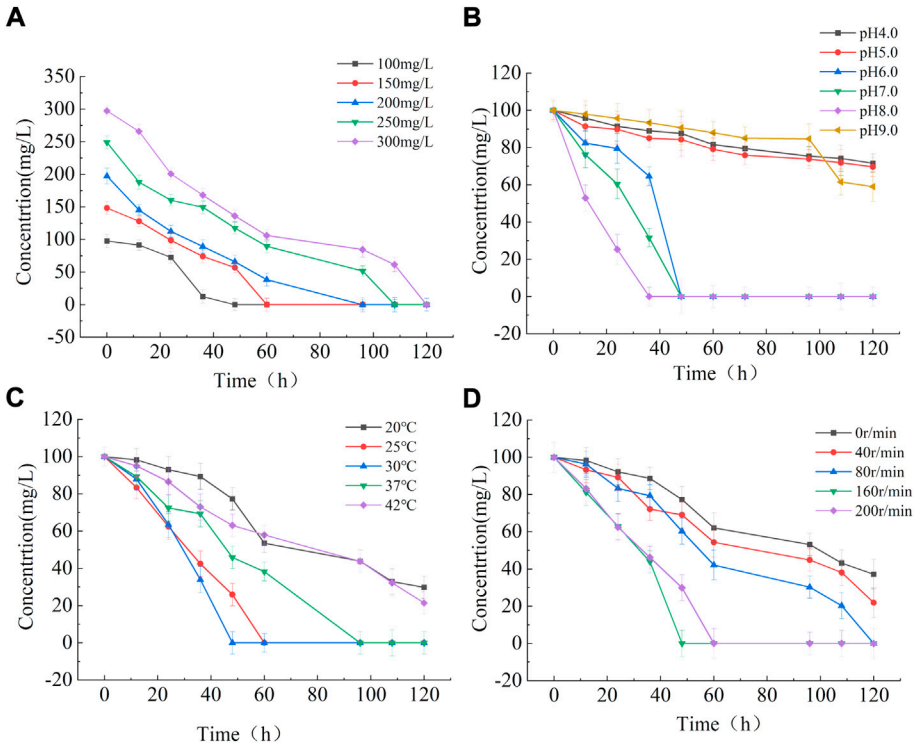

FIGURE 6
The impact of starting 3MI concentrations **(A)**, pH **(B)**, temperature **(C)**, and shaking speed **(D)** on 3MI degradation.

4.4 The impact of culture conditions on the growth and 3Midegrading activity of strain AO-06

4.4.1 The effects of 3MI concentration on bacterial growth and 3MI degradation

In this study, a variety of starting 3MI concentrations (0, 50, 100, 150, 200, 250, and 300 mg/L) were used to evaluate the effect of these concentrations on 3MI degradation activity. Complete 3MI degradation was observed after 48 h at a starting 3MI concentration of 100 mg/L (Figure 6A), whereas higher 3MI concentrations required a longer period. This may be the result of a delay in degradation timing caused by continuous bacterial adaptation to environmental toxicity during the growth process.

4.4.2 The impact of pH on bacterial growth and 3MI degradation

A range of pH values (4.0, 5.0, 6.0, 8.0, and 9.0) was then used to investigate the relationship between this variable and 3MI degrading activity changes in pH can affect nutrient availability, membrane charge and stability, membrane permeability, the ability of cells to absorb specific compounds, and the efficacy of certain intracellular reactions (Zhang et al., 2022). At a pH of 8.0, *A. oleivorans* AO-06 displayed optimal 3MI degrading activity, achieving 100% degradation in 36 h (Figure 6B). This activity was significantly inhibited by excessively acidic or alkaline conditions, with degradation rates of <50% even after 120 h.

4.4.3 The impact of temperature on bacterial growth and 3MI degradation

Temperature effects on 3MI degradation were studied at five different temperatures: 20°C, 25°C, 30°C, 37°C, and 42°C. At 30°C, *Acinetobacter Oleivorans* AO-06 had the highest degradation efficiency for 3MI (Figure 6C), and the degradation rate reached 100% within 48 h. The temperature range that allowed *Acinetobacter Oleivorans* AO-06 to achieve a 100% degradation rate in 48 h was 25–37°C (Figure 6C). The temperature had an effect on the degradation efficiency of *Acinetobacter Oleivorans* AO-06, indicating that 30°C was the optimal growth temperature for strain AO-06.

4.4.4 The impact of shaking speed on 3MI degradation

Five different shaking speeds (0, 40, 80, 160, and 200 rpm) were investigated to see if they had an effect on 3MI degradation. Complete 3MI degradation was observed at speeds ranging from

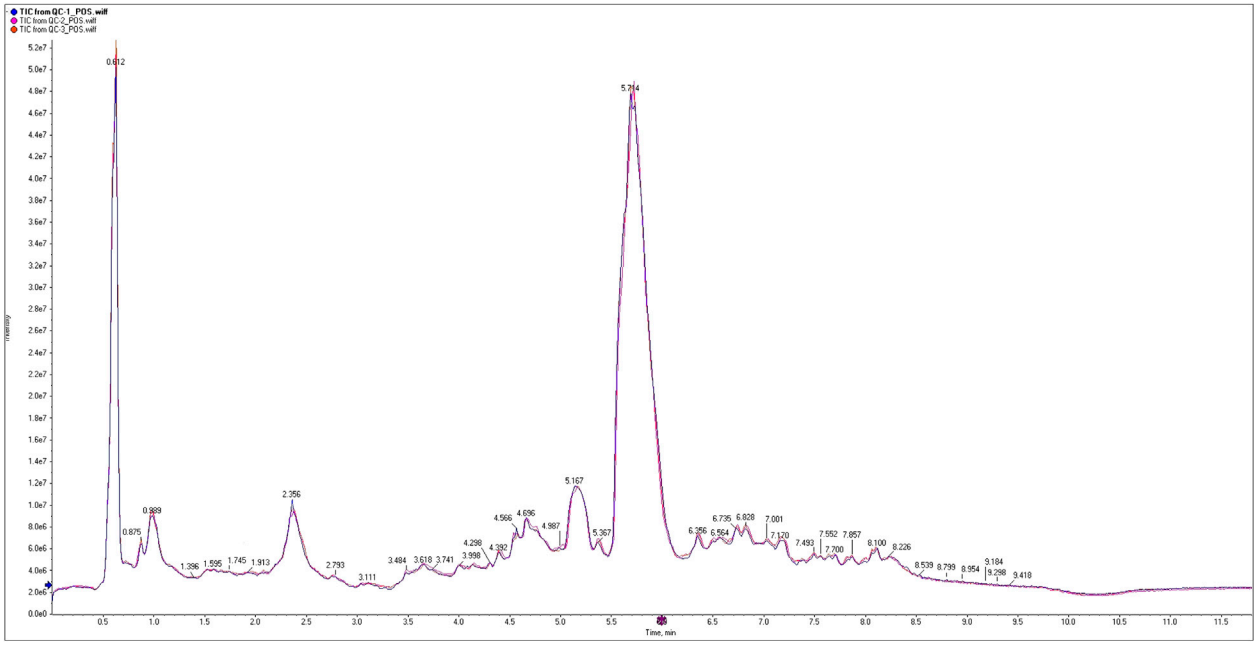

FIGURE 7
Total ion chromatogram for 3MI degradation products produced by strain AO-06.

80 to 200 rpm (Figure 6D), with a speed of 160 rpm exhibiting 100% degradation after 48 h. The rate of shaking affects the dissolved oxygen content of the media, which can indirectly influence bacterial growth. As a result, faster-shaking results in higher oxygen levels in the culture medium. However, once a certain speed is reached, no further increase in dissolved oxygen levels can be achieved.

The optimal culture conditions for strain AO-06 to most efficiently degrade 3MI (starting concentration: 100 mg/L) were pH 8.0 at 30°C with 160 rpm shaking. These conditions allow for 100% degradation efficiency. Therefore, this strain may be well-suited for the biodegradation of 3MI-contaminated environments in the field. Future studies will focus on elucidating the toxicity and metabolic characteristics of strain AO-06 to provide a theoretical basis for the future industrial-scale removal of 3MI from the environment, particularly in pig farm waste.

4.5 Metabolite detection

Analyses of metabolomics provide a method for quantifying all metabolites present in specific biological samples. Potentially harmful metabolites produced by strain AO-06 during 3MI degradation under optimized conditions were then assessed after 48 h and compared to a blank control sample using UHPLC-MS (Figure 7).

TABLE 2 Numbers of metabolites detected in positive and negative ion modes.

Detection mode	The number of metabolites identified
Positive ion mode (Pos)	388
Anion mode (Neg)	217

This analysis found 605 metabolites in total, with 388 and 217 detected in positive and negative ion modes, respectively (Table 2). These metabolites were identified using an in-house database (Shanghai Applied Protein Technology), with structures identified by matching the retention time, molecular weight (molecular mass error <10 ppm), secondary fragmentation spectrum, collision energy, and other information for these metabolites. In total, 6 putative metabolites associated with 3MI metabolism were identified, including 3-methyloxindole,1H-Indole-2,3-dione, Phenylacetaldehyde, Phenylacetic acid, 1H-indole-3-carboxaldehyde, and indole-3-carboxylic acid (Figure 8).

The absence of systematic studies evaluating the 3MI metabolism pathway has resulted in the identification of only putative metabolites based on the observations of individual studies. Fukuoka (Fukuoka et al., 2015) also detected 1H-Indole-3-carboxaldehyde and Indole-3-carboxylic acid when identifying the metabolites of 3MI, whereas 3-methyloxindole

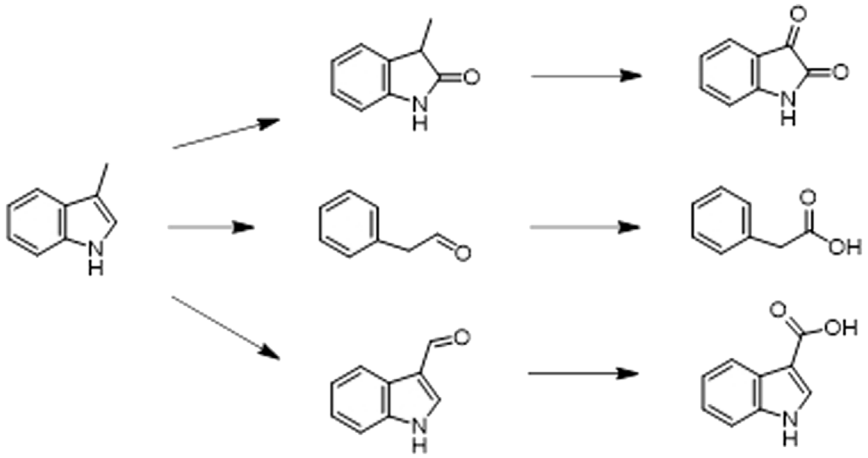

FIGURE 8
Chemical structural formulae of possible 3-methylindole metabolites.

TABLE 3 Summary of known 3MI-degrading bacteria.

Name of bacterial species	Degradation characteristics	References
Pseudomonas putida LPC24	2.0 mmol/L 3MI was degraded within 30 days in aerobic condition	Li et al. (2010)
Lactobacillus brevis 1.12	Maximum degradation rate was 65% within 120 h (The 3MI of initial concentration is 1.0 mg/L)	Meng et al. (2013)
Rhodopseudomonas palustris WKU-KDNS3	The degradation rate was higher than 90% Within 21 days (The 3MI of initial concentration is 13.12 mg/L)	Sharma et al. (2015)
Acinetobacter toweneri NTA1•2A	The initial concentration of 3MI was less than 200 mg/L, and the degradation rate was higher than 85% within 6 days	Tesso et al. (2019)
Rhodococcus sp. DMU1 and *Rhodococcus sp.* DMU2	The 50 mg/L of 3MI can be degraded in 24 h, at pH 4.0–9.0, 30–35°C	Ma et al. (2020)
Burkholderia sp. IDO3	The degradation performance of skatogen was best at pH 4.0–9.0, 30–35°C, but 3MI was not degraded completely	Ma et al. (2020)
Acinetobacter oleivorans AO-06	It can be degraded for 3MI below 300 mg/L completely within 120 h	this text

has frequently been reported in the literature as a metabolite produced from 3MI by methanogens enriched from wetland soil (Gu and Berry, 1992). There have also been reports of indole-3-carboxylic acid, which was identified as a byproduct of 3MI degradation mediated by *Pseudomonas aeruginosa*, along with indoline-3-ol (Yin and Gu, 2006). The presence of 1H-indole-2,3-dione (indigo red) was also detected in this experiment, possibly as a result of further oxidation of 3-methyl hydroxyindole. Indigo red has been identified as a common indole metabolite, and may therefore be the subsequent byproduct of indole metabolism following the degradation of 3MI to indole.

Previous studies on 3MI-degrading bacteria have been carried out, and some strains with degradation ability, such as *Pseudomonas putida* LPC24, *Lactobacillus brevis* 1.12 (Meng et al., 2013), *Rhodopseudo-monas palustris* WKU-KDNS3 (Sharma et al., 2015), *Acinetobacter toweneri* NTA1-2A (Tesso et al., 2019), *Rhodococcus sp.* DMU1 and DMU2, and *Burkholderia sp.* IDO3, have been reported. *Acinetobacter* species are widespread in natural environments and have been implicated as important oil degradation mediators (Fukuoka et al., 2015) (Table 3). In the present study, *A. oleivorans* AO-06 was isolated and it could degrade 3MI below 300 mg/L completely within a short time. This study provides a theoretical foundation for other microbe-mediated environmental remediation approaches as well as a basis for future work to apply bacteria that degrade 3-methylindole for the purification of polluted environments. It has a promising application in the control of malodorous gas pollution in the large-scale livestock and poultry breeding industries.

5 Conclusion

In conclusion, the present screening efforts identified *Acinetobacter oleivorans* strain AO-06 as capable of degrading 3MI with a high degree of efficiency. The 3MI degradation of this strain was independent of the initial 3MI concentration but was affected by pH, temperature, and shaking speed; optimal culture conditions were established (initial 3MI concentration: 100 mg/L, pH: 8.0, shaking speed: 160 rpm, 30°C for 48 h). An LC-MS approach was used to identify putative 3MI metabolites produced by strain AO-06, yielding N_2-acetyl-L-Ornithine, Phenylacetaldehyde, Phenylacetic acid, Indole-3-carboxylic acid, and indole-3-carboxaldehyde. However, more investigation is needed to determine the mechanisms by which strain AO-06 metabolizes 3MI.

Data availability statement

The original contributions presented in the study are included in the article/Supplementary Material, further inquiries can be directed to the corresponding author.

Author contributions

The authors have contributed to this article as follows: Conceptualization, HH and XZ; methodology, HH and XZ; formal analysis, SQ; writing-original draft, FG and FF; investigation, WD, HM, and LX writing-review and editing, XZ, LL, and HH; funding acquisition, LL and HH. All authors have read and agreed to the published version of the article.

Funding

This research was funded by the Project of Outstanding Talents Training Program of Henan Academy of Sciences (Grant Number 210405004), Central Plains Science and technology innovation leader Project (Grant Number 214200510011), and Outstanding Talents Training Program of Henan Academy of Sciences (Grant Number 210405002).

Conflict of interest

Authors HH, LL, WD, HM, FF, SQ, and XZ were employed by the company Institute of Biology Co., Ltd.

The remaining author declares that the research was conducted in the absence of any commercial or financial relationships that could be construed as a potential conflict of interest.

Publisher's note

All claims expressed in this article are solely those of the authors and do not necessarily represent those of their affiliated organizations, or those of the publisher, the editors and the reviewers. Any product that may be evaluated in this article, or claim that may be made by its manufacturer, is not guaranteed or endorsed by the publisher.

References

Cheng, S., Li, Z., Uddin, S. M. N., Mang, H. P., Zhang, L., Zhang, J., et al. (2018). Toilet revolution in China. *J. Environ. Manage.* 216, 347–356. doi:10.1016/j.jenvman.2017.09.043()

Fukuoka, K., Ozeki, Y., and Kanaly, R. A. (2015). Aerobic biotransformation of 3-methylindole to ring cleavage products by Cupriavidus sp. strain KK10. *Biodegradation* 26, 359–373. doi:10.1007/s10532-015-9739-0

Gu, J. D., and Berry, D. F. (1992). Metabolism of 3-methylindole by a methanogenic consortium. *Appl. Environ. Microbiol.* 58, 2667–2669. doi:10.1128/aem.58.8.2667-2669.1992

Gu, J. D., Fan, Y. Z., and Shi, H. C. (2002). Relationship between structures of substituted indolic compounds and their degradation by marine anaerobic microorganisms. *Mar. Pollut. Bull.* 45, 379–384. doi:10.1016/S0025-326X(02)00091-7

Hort, C., Gracy, S., Platel, V., and Moynault, L. (2009). Evaluation of sewage sludge and yard waste compost as a biofilter media for the removal of ammonia and volatile organic sulfur compounds (VOSCs). *Chemical Engineering Journal* 152 , 1, 44–53.

Kohda, C., Ando, T., and Nakai, Y. (1997). Isolation and characterization of anaerobic indole- and skatole-degrading bacteria from composting animal wastes. *J. Gen. Appl. Microbiol.* 43, 249–255. doi:10.2323/jgam.43.249

Li, P., Wang, Y. H., Jiang, Z., and Tong, L. (2010). Bioaugmentation of cellulose degradation in swine wastewater treatment with a composite microbial consortium. *Fresenius Environ. Bull.* 19, 3107–3112. doi:10.1007/978-90-481-9558-9-10

Liu, D. Z., Wei, Y. F., Liu, X. Y., Zhou, Y., Jiang, L., Yin, J. Y., et al. (2018). Indoleacetate decarboxylase is a glycyl radical enzyme catalysing the formation of malodorant skatole. *Nat. Commun.* 9, 4224. doi:10.1038/s41467-018-06627-x

Luo, H. E. (2015). *Study on the screening and biodegradation characteristics of indole-degrading bacteria*. dissertation/master's thesis (China (Guodong): Guangdong University of Technology).

Ma, Q., Meng, N., Li, Y. J., and Wang, J. W. (2021). Occurrence, impacts, and microbial transformation of 3-methylindole (skatole): A critical review. *J. Hazard. Mat.* 416, 126181. doi:10.1016/j.jhazmat.2021.126181

Ma, Q., Qu, H., Meng, N., Li, S. Z., Wang, J. W., Liu, S. W., et al. (2020). Biodegradation of skatole by Burkholderia sp. Ido3 and its successful bioaugmentation in activated sludge systems. *Environ. Res.* 182, 109123. doi:10.1016/j.envres.2020.109123

Meng, X., He, Z. F., Li, H. J., and Zhao, X. (2013). Removal of 3-methylindole by lactic acid bacteria *in vitro*. *Exp. Ther. Med.* 6, 983–988. doi:10.3892/etm.2013.1251

Qian, Y., Song, K., Hu, T., and Ying, T. (2018). Environmental status of livestock and poultry sectors in China under current transformation stage. *Sci. Total Environ.* 622–623, 702–709. doi:10.1016/j.scitotenv.2017.12.045

Sharma, N., Doerner, K. C., Alok, P. C., and Choudhary, M. (2015). Skatole remediation potential of Rhodopseudomonas palustris WKU-KDNS3 isolated from an animal waste lagoon. *Lett. Appl. Microbiol.* 60, 298–306. doi:10.1111/lam.12379

Tesso, T. A., Zheng, A., Cai, H., and Liu, G. (2019). Isolation and characterization of two Acinetobacter species able to degrade 3-methylindole. *PLoS One* 14, 0211275. doi:10.1371/journal.pone.0211275

Verschuere, L., Rombaut, G., Sorgeloos, P., and Verstraete, W. (2000). Probiotic bacteria as biological control agents in aquaculture. *Microbiology and molecular biology reviews* 64 , 4, 655, 671.

Whitman, W. B., Goodfellow, M., Kämpfer, P., Busse, H. J., Trujillo, M. E., and Suzuki, K. I. (2012). Bergey's manual of systematic bacteriology: volume 5: the Actinobacteria. Springer Science and Business Media.

Wu, Y. H., Zhang, S. C., Tian, Q., Ma, G. Z., Guo, R. J., Li, S. D., et al. (2021). Isolation and identification of a high-efficiency bacterial strain Rp3 to degrade skatole: An odor chemical in compost. *J. Agric. Resour. Environ.* 38, 576–584.

Yang, B. Y., Lin, Y. X., Dai, C. X., Yan, Y. Q., Piao, S. Y., Liu, X. Y., et al. (2018). Degradation characteristics of indole by Alcaligenes sp. YBY. *Environ. Sci. Technol.* 41, 1–6.

Yang, G., Zhang, P., Liu, H., Zhu, X., and Dong, W. (2019). Spatial variations in intestinal skatole production and microbial composition in broilers. *Anim. Sci. J.* 90, 412–422. doi:10.1111/asj.13164

Yin, B., and Gu, J. D. (2006). Aerobic degradation of 3-methylindole by *Pseudomonas aeruginosa* gs isolated from mangrove sediment. *Hum. Ecol. Risk Assess. Int. J.* 12, 248–258. doi:10.1080/10807030500531539

Zhang, Z. Y., Zhou, L. Z., Yue, D. D., Guo, W. Y., Pan, M. S., Qi, L., et al. (2022). Isolation, identification and degradation characteristics of skato-degrading bacteria YKSW-6. *Bull. Microbiol.* 49, 2486–2499. doi:10.13344/j.microbiol.china.211012

Zou, S., Wang, B., Chen, L., Pang, X., Hu, W., and Chen, F. (2020). Technical points and prospect of treating livestock and poultry manure with black horsefly larvae. *Guangdong feed.* 7, 39–42.

frontiers | Frontiers in Environmental Science

TYPE Original Research
PUBLISHED 09 November 2022
DOI 10.3389/fenvs.2022.1054554

OPEN ACCESS

EDITED BY
Jun Zhou,
University of Massachusetts Lowell,
United States

REVIEWED BY
Sadia Bibi,
University of Agriculture, Faisalabad,
Pakistan
M. Belal Hossain,
Noakhali Science and Technology
University, Bangladesh

*CORRESPONDENCE
Sarah Louise Robin,
sarah.robin@unc.nc

SPECIALTY SECTION
This article was submitted to
Biogeochemical Dynamics,
a section of the journal
Frontiers in Environmental Science

RECEIVED 04 October 2022
ACCEPTED 20 October 2022
PUBLISHED 09 November 2022

CITATION
Robin SL, Marchand C, Mathian M,
Baudin F and Alfaro AC (2022),
Distribution and bioaccumulation of
trace metals in urban semi-arid
mangrove ecosystems.
Front. Environ. Sci. 10:1054554.
doi: 10.3389/fenvs.2022.1054554

Distribution and bioaccumulation of trace metals in urban semi-arid mangrove ecosystems

Sarah Louise Robin[1]*, Cyril Marchand[1], Maximilien Mathian[1], François Baudin[2] and Andrea C. Alfaro[3]

[1]Institut de Sciences Exactes et Appliquées (ISEA EA7484), Université de la Nouvelle-Calédonie, Nouméa, New Caledonia, [2]Institut des Sciences de la Terre de Paris, UMR 7193, Sorbonne Université, CNRS, Paris, France, [3]Aquaculture Biotechnology Research Group, School of Science, Faculty of Health and Environmental Sciences, Auckland University of Technology, Auckland, New Zealand

Mangrove ecosystems are known to act as filters for contaminants between land and sea. In New Caledonia, urbanization has increased along the coastline during the last decades. However, the impact of urbanization on contaminant cycling in mangrove forests has remained unexplored. In this study, we investigated trace metals (TM) dynamics in an urban mangrove soil and their transfer to mangrove tissues for the two dominant mangrove species in New Caledonia: *Avicennia marina* and *Rhizophora stylosa*. The results suggest that decades of urban rainwater runoff from an upper neighborhood induced large variations of mangrove soil physico-chemical properties compared to a control mangrove site sharing the same geological watershed. The urban mangrove site had a neutral pH and low salinity in the upper soil, while the control mangrove site presented acidic pH and a salinity ranging from 24 to 62 g L^{-1}. Most TM were significantly less concentrated in the urban mangrove soil varying from 1.3 ± 0.3 µg g^{-1} at the urban site and 1.9 ± 0.5 µg g^{-1} at the control site for Cd, to 30 ± 8 mg g^{-1} and 49 ± 11 mg g^{-1} for Fe at the urban and control site, respectively. However, higher root bioconcentration factors were measured for As, Cd, Co, Cr, Fe, Mn, Ni, and Pb in the urban mangrove soil (1.7 ± 0.9, 0.14 ± 0.06, 0.23 ± 0.13, 0.042 ± 0.026, 0.088 ± 0.057, 0.47 ± 0.39, 0.21 ± 0.12, and 0.25 ± 0.09, respectively) compared to the control mangrove soil (0.11 ± 0.03, 0.041 ± 0.016, 0.045 ± 0.021, 0.010 ± 0.004, 0.013 ± 0.007, 0.094 ± 0.030, 0.022 ± 0.011, and 0.12 ± 0.03, respectively). The bioavailability of TM in the urban mangrove soil may be favored by suboxic conditions associated to less Cl-TM complexes and pyrite-TM complexes in the soil. Only Cu, Pb, Ti, and Zn, usually associated with urbanization, were more concentrated in the urban mangrove soil with mean concentrations of 27 ± 4, 17 ± 2, 4,571 ± 492, and 62 ± 12 µg g^{-1} at the urban site, respectively, and 21 ± 4, 10 ± 3, 2,834 ± 541, and 57 ± 12 µg g^{-1} at the control site, respectively. No significant difference in translocation factors

Abbreviations: BCF, Bioconcentration factor; DCB, Dithionite citrate bicarbonate; ERL, Effect range low; ERM, Effect range median; NOAA, National oceanic and atmospheric administration; OM, Organic matter; TF, Translocation factor; TM, Trace metals; SEM, Scanning electron microscopy; XRD, X-ray diffraction.

was measured between the two sites, evidencing a regulation of TM translocation to the upper tissues by mangrove trees.

KEYWORDS

mangrove forests, trace metals, urbanization, bioaccumulation, anthropogenic pressure, *Avicennia marina*, Rhizophora *stylosa*

1 Introduction

Mangrove forests are tidal ecosystems developing in intertropical areas (Thomas et al., 2017). These ecosystems provide many ecosystem services, such as the function of buffers for sediments and contaminants between diverse watersheds and the adjacent aquatic ecosystems (e.g., lagoon, estuaries, sea) (Lee et al., 2014). Mangrove forests cover littoral areas of more than 100 countries. Out of the 20 countries with the most mangrove surface areas, 17 are referred to as developing countries, according to the International Monetary Fund (International Monetary Fund, 2022), and a third of their population lives on the coast (Center for International Earth Science Information Network, 2012). There is inevitably competition for space between mangrove ecosystems and economic and urban development.

Accordingly, mangrove forests are endangered ecosystems despite awareness of their benefits. Economic and urban development have resulted in high mangrove deforestation rates with about 35% of the mangrove surface area that was lost between the 80s and the 90s (Valiela et al., 2001; Alongi, 2002). In addition to direct mangrove forests destruction, urbanization can also impact mangrove forests through the input of anthropogenic effluents, and specifically rainwater runoff enriched with trace metals (TM). These effluents can contaminate and stress mangrove ecosystems, but also change hydrological and geochemical conditions, creating a disequilibrium in coastal areas (Cavalcante et al., 2009; Lewis et al., 2011; Kristensen et al., 2017; Alemu et al., 2021).

TM are one of the many types of pollutants in mangrove forests and mainly originate from anthropogenic activities. TM are naturally occurring elements in the Earth crust (<1,000 mg kg^{-1}) and are therefore present in the environment (Turekian and Wedepohl, 1961; Thornton, 2012). Anthropogenic activities such as industrial, mine, agricultural, and housing development activities increase their concentrations in the environment (Bayen, 2012). TM are of great concern because even though most of them are micronutrients, which can be used by a range of organisms, they can have significant negative impacts beyond specific thresholds (e.g., toxicity). For instance, TM can inhibit developmental processes and decrease photosynthetic activity of plants (Bayen, 2012). In contrast to organic pollutants, TM cannot be biologically or chemically degraded and can therefore be transported over long distances or accumulate in the environment (Prasad et al., 2006), adsorbed on organic complexes and reactive mineral surfaces, or trapped within mineral structures (Brown and Parks, 2001).

Mangrove ecosystems act as reservoirs for TM due to their high sedimentation rate, high organic matter (OM) content, and high biogeochemical reactivity (Harbison, 1986). TM dynamics in mangrove soil are generally well documented and depend on many factors, with the main ones being bonding phases and physico-chemical parameters (Duan et al., 2020; Huang S et al., 2020; Jayachandran et al., 2018). For example, the modification of redox conditions can limit or favour the precipitation of pyrite (FeS_2), which can trap TM, supporting TM immobility in the mangrove soil (Noël et al., 2015; Chakraborty et al., 2016). Also, the amount of OM in the soil and the quality of the OM can influence TM accumulation and bioavailability in mangrove soils. TM can form complexes with the OM, and the capacity of formation is dependent on the nature of the OM with a preference of TM for mature OM with high lignin content (Marchand et al., 2005; Kristensen et al., 2008; Thakur et al., 2016, 2014; Ge and Li, 2018; Duan et al., 2020). TM can also be exported to mangrove trees or outside the mangrove forest in the dissolved phase with litterfall or tidal flushing and tidal pumping (Silva et al., 1998; Ferreira et al., 2007; Holloway et al., 2018, 2016). In urban contexts, previous studies have measured moderate to highly TM contaminated mangrove soils due to urban inputs (Marx and McGowan, 2010; Singh et al., 2010; Bastakoti et al., 2019).

Mangrove plants are considered resistant to metallic stress, partly due to the production of antioxidants limiting reactive oxygen species (MacFarlane, 2002). However, some direct effects of TM on mangrove trees were reported, including growth inhibition, increased peroxidase activity, and death of vegetal species (MacFarlane and Burchett, 2002, 2001; Cheng et al., 2014; Naidoo et al., 2014). The transfer of TM from mangrove soils to mangrove trees depend on the bioavailability of the TM in the soil as plants can only assimilate TM in the soluble form (Tremel-Schaub and Feix, 2005). Soil factors such as redox potential, pH, and cationic exchange capacity drive TM bioavailability in mangrove soils, and therefore transfer to mangrove trees (Batty, 2000; Bourgeois et al., 2020; Fritioff et al., 2005; Huang X et al., 2020; Marchand et al., 2016; Robin et al., 2021). TM transfer to mangrove plants differs greatly between TM, tissues, and species since it depends on metabolic requirements (He et al., 2014; Marchand et al., 2016; Rezaei et al., 2021; Robin et al., 2021). Mangrove species have developed mechanisms to prevent metallic stress. Some species, such as *Avicennia* spp., have pneumatophores (aerial roots exhibiting negative geotropism), which allow for gas

exchange between the atmosphere and the rhizosphere, notably O_2 (Purnobasuki et al., 2017). The O_2 can oxidize labile Fe(II) available in the rhizosphere to form an iron (III) plaque at the root surface (Taylor and Crowder, 1983). Studies have shown that this iron plaque can trap TM and therefore prevent their transfer to the plant tissues (Pi et al., 2011; Yamaguchi et al., 2014; Robin et al., 2021). Other species, such as *Rhizophora* spp., rely on the thickness of their roots and lignification processes to limit TM absorption within their tissues (Cheng et al., 2014, 2012).

In New Caledonia, mangrove ecosystems account for about 80% of the West coast of the main island and 15% of its East coast (Marchand et al., 2007). While the human population density is low (17 inhabitants per km^2) (Insee, 2020), and the island is relatively pristine, anthropogenic activities still threaten these ecosystems to various degrees. Due to the lateritic nature of one-third of the soil on the island (e.g., rich in oxides and TM) (Tardy and Roquin, 1992), most studies were interested in the impact of mining activities, that increase erosional processes, and lateritic sediments inputs on mangrove forests (Marchand et al., 2016, 2012; Bourgeois et al., 2020; Robin et al., 2021). Few studies have also considered the impact of aquaculture and its discharge (Marchand et al., 2011). However, the impact of urbanization on TM inputs and distribution in mangrove forests remains unexplored and is of critical importance. The understanding of the impact of urbanization in a pristine island is necessary to manage future urban development and limit the threat of TM contamination. In addition, the Caledonian population rely on mangrove forests and their resources for personal and economic use. Studies worldwide have already shown the potential threat of urbanization as a source of TM contamination in mangrove forests (Ray et al., 2006; He et al., 2014; Celis-Hernandez et al., 2020).

Our main objectives were to assess TM dynamics in mangrove soils receiving urban rainwater runoff for more than 50 years, as well as their bioaccumulation in tissues of two main mangrove species, *Avicennia marina* and *Rhizophora stylosa*. To this end, we collected soil, porewater, roots, and leaves in an urban and a control mangrove forest. The control site had the same geological watershed as the urban site, but was not exposed to urban runoff. Our hypotheses are 1) that trace metals are in higher concentrations at the urban site due to a greater input of these contaminants within the mangrove forest with the urban rainwater runoff, 2) that their physico-chemical conditions also differ because of a more waterlogged soil at the urban site, and 3) that their bioaccumulation in mangrove tissues at the urban mangrove site will differ from natural mangrove forests such as the control mangrove site due to those differences in physico-chemical conditions. To evaluate these hypotheses, sequential extractions were performed on soil samples and bioconcentration factors (BCF) were determined for the roots and the leaves of the two mangrove species.

2 Material and methods

2.1 Study sites

New Caledonia is a French archipelago located between 20°S and 23°S in the South Pacific. Mangrove forests cover more than 35,000 ha of the archipelago (Marchand et al., 2007). The climate of the western coast of the main island is semi-arid with semi-diurnal tidal cycles (Douillet et al., 2001). In New Caledonia, mangrove species develop in monospecific stands along gradients depending on soil geochemical parameters, such as salinity and topography (Marchand et al., 2011; Deborde et al., 2015). More than 20 mangrove species are found in New Caledonia, but two are dominant. *Rhizophora* spp. represent 50% of mangrove area and grow along the sealine in soils with porewater salinity ranging from 5 to 40 g L^{-1}. *Avicennia marina* represents more than 15% of the mangrove area and grows in areas of higher elevation with porewater salinity between 35 and 70 g L^{-1} (Marchand et al., 2016, 2007).

The archipelago is composed of 33 towns and is characterized by a very low human population density. 57% of the population lives in the four main cities, all located in the southwest coast of the main island (Insee, 2020). This population aggregation generates substantial urban activities. Dumbéa, the second most populated city, has increased its population by 33% in the past 10 years, leading to an outbreak of anthropogenic activities and urban development (Insee, 2020), while the littoral area of this city is almost completely covered by mangrove forests.

Two mangrove sites containing both dominant mangrove species were chosen as study sites on the littoral of Dumbéa to investigate the impact of urbanization (Figure 1). Both sites have the same geological watershed, characterized by a Cretaceous sedimentary formation (sandstone and limestone) that often host volcano-clastic fragments (Service de la Géologie de Nouvelle-Calédonie, 2016), and are only 2 km apart. The first mangrove site is the undisturbed "control" mangrove site located in the Apogoti Bay (22°12′08″S, 166°26′20″E). The site is adjacent to a recent housing lot, still under construction, without any direct anthropogenic inputs. The wastewater discharges and rainwater effluents are not released in this control mangrove site. The second mangrove site is the "urban" mangrove site (22°12′39″S, 166°27′19″E) and is characterized by an input of rainwater runoff streaming from the upper allotments for more than 50 years. The upper allotments have few petrol stations and are mainly residential with a population of about 10,000 inhabitants. This urban freshwater is therefore potentially charged in contaminants. At the urban site, the *R. stylosa* trees are about 8–10 m tall, which is much higher than those at the control site and other typical mangrove stands in New Caledonia, which are usually about 2 m tall. Also, in contrast to the control site, the species zonation at the urban site is unusual, with *R. stylosa* trees developing further away from the sealine where *A. marina* trees

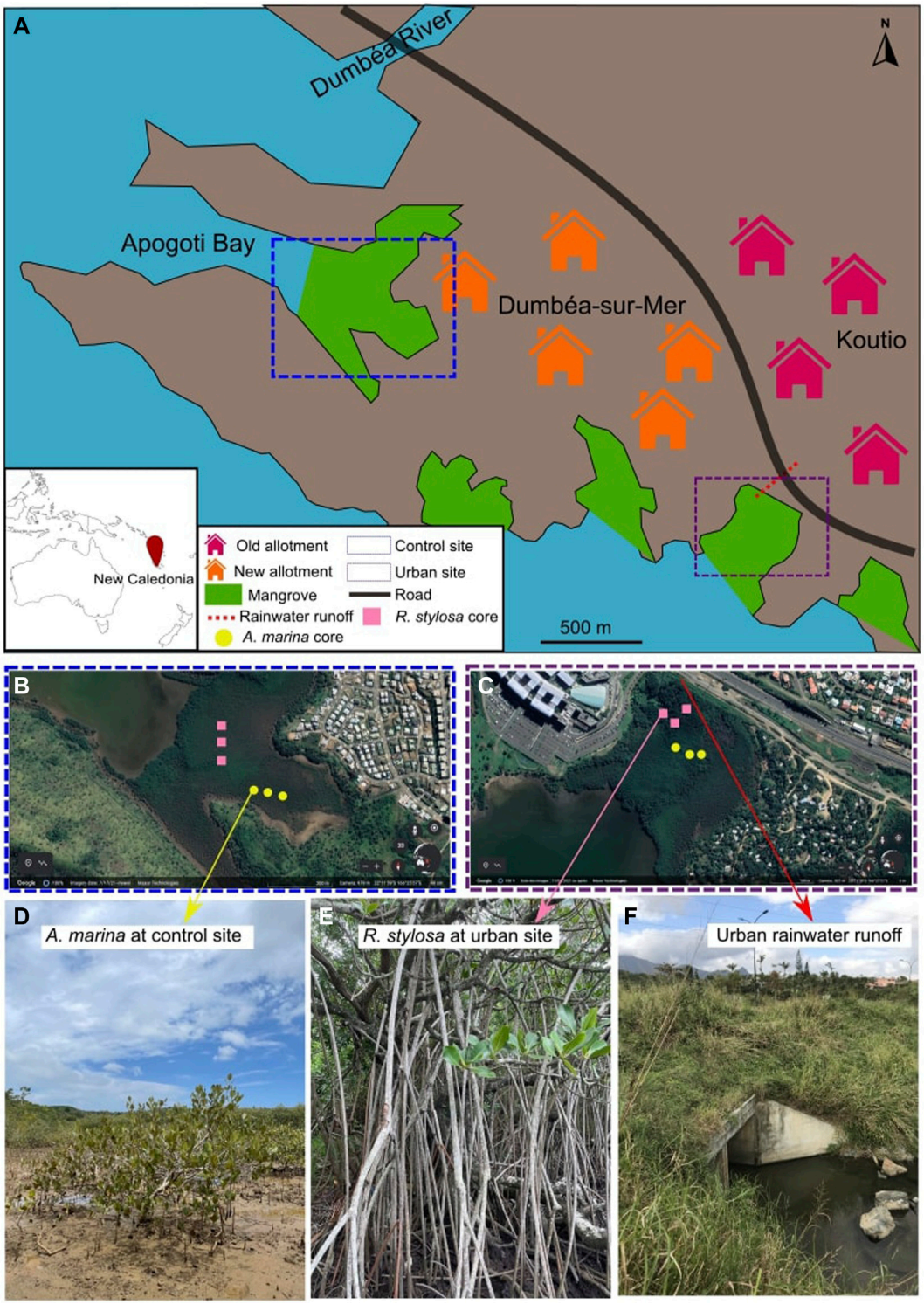

FIGURE 1
Map of the two studied mangrove sites **(A)** with triplicate soil cores taken under *A. marina* and *R. stylosa* at the control site **(B)** and urban site **(C)**, and pictures of *A. marina* at the control site **(D)**, *R. stylosa* at the urban site **(E)**, and the entrance of the urban rainwater in the urban site **(F)**.

usually develops and where the runoff enters the mangrove ecosystem.

2.2 Sampling and processing

2.2.1 Sampling

Samples were collected in May 2021, at the end of the rainy season, characterized by a La Niña phenomena. In both sites and at each mangrove stand (*A. marina* and *R. stylosa*), triplicate soil cores (40 cm long) were collected with an Eijkelkamp gouge auger about 30 m apart from one another. The 40 cm depth allowed for differential analysis with an above and below portion of the root system. Soil cores were cut along the depth with a wooden knife into six sections (0–5 cm, 5–10 cm, 10–15 cm, 15–20 cm, 20–30 cm, and 30–40 cm). The pH and redox potential were immediately measured using a pH meter (pH3110—WTW). A glass electrode (SENTIX–Xylem Analytics) was inserted in the middle of the soil section to measure the pH, calibrated with standards prior to measurements, while a combined Pt and Ag/AgCl electrode (SENTIX–Xylem Analytics) was inserted in the soil to measure the redox, calibrated with standards prior to measurements. Eh values correspond to the redox values obtained on site +202 mV to adjust to a H electrode. The soil sections were placed into tightly closed plastic bags. To extract porewater from soil samples, rhizon samplers (Rhizon SMS—10 cm, diameter 2.5 mm–Rhizosphere) were inserted into the soil sections. Each rhizon was connected to a 20 ml syringe. The plastic bags with the soil and the attached syringes were immediately placed into a cooler (~4°C) until processed at the laboratory, less than 6 h after collection. Within the same area where the soil cores were collected, coarse roots of *R. stylosa* were extracted with a stainless-steel saw. For *A. marina*, pneumatophores were gently teared from the main roots. Leaf samples were also collected from both tree species. One leaf sample corresponds to 20 leaves collected from five different trees. All biotic samples were immediately placed into plastic bags and kept in a cooler (~4°C) until processed at the laboratory, less than 6 h after sampling.

2.2.2 Processing

Upon arrival at the laboratory, salinity was measured in the porewater samples using a refractometer (ATC). Porewater samples were filtered at 0.45 µm and two drops of H_2SO_4 were added before storage at 4°C. The soil samples were tightly closed and kept in the freezer at −20°C. The biotic samples (roots and leaves) were thoroughly washed with MilliQ water and dried in a heat chamber at 40°C until reaching constant mass.

Frozen soil samples were lyophilized 72 h (FreeZone—LABCONCO) before sieving at 2 mm. Half of each sample was grounded with a ball mill (FRITSCH) and the other half kept ungrounded for scanning electron microscopy (SEM). Biotic samples for TM analysis were grounded using a cutting mill (POLYMIX–px-mfc90d) after drying. Dried samples were kept at room temperature, in the dark, and away from humidity.

2.2.3 Iron plaque extraction

In order to extract the iron plaque from the root surface, a treatment with a solution of dithionite-citrate-bicarbonate (DCB) established by Taylor and Crowder (1983) and modified by Lin et al. (2018) was used. Briefly, pneumatophores were immersed in 40 ml of the DCB solution (13% w/v $Na_3C_6H_5O_7 \bullet 2H_2O$, 16% w/v $NaHCO_3$, and 37% w/v $Na_2S_2O_4$ in MilliQ water) for 3 h at room temperature. Samples were then rinsed with MilliQ water to obtain 50 ml of final volume. The extract was filtered at 0.45 µm and kept at 4°C. Treated samples were dried in a heat chamber at 40°C until reaching constant mass.

2.3 Analyses

2.3.1 Total elements extraction in soil samples

Total elements were extracted from soil samples by multiwave digestion. Samples between 5 and 20 cm, where the root system is mainly located, were used for BCF calculations. Briefly, 100 mg of sample was weighed in the vessel. 5 ml of 70% HNO_3, 1 ml of 32% HCl, and 1 ml of 70% HF were added. Digestion was performed on an Ethos Easy–Milestone apparatus starting with a 25 min heating step from room temperature to 220°C followed by a 15 min plateau and a 20 min cooldown step. The extract was transferred to a Teflon tube and heated at 180°C on a heating plate to get rid of HF. After complete evaporation, 1 ml of HCl was added for dissolution of resistant particles. The extract was then transferred to a polypropylene tube, the volume was adjusted to 10 ml with MilliQ water and placed at 4°C until analysis. For quality control, certified material (MESS-3 Marine sediments) was also extracted and analyzed (Supplementary Table S1).

2.3.2 Trace metals extraction in biota

Trace metals were extracted from biotic samples by multiwave digestion. Briefly, 500 mg of sample was weighed in the vessel. 5 ml of 70% HNO_3 and 1 ml of 30% H_2O_2 were added. The digestion program started with a 10 min heating step from room temperature to 160°C, then 15 min step to 210°C, followed by a 10 min plateau and a 20 min cooldown step. The extract was transferred to a polypropylene tube, the volume was adjusted to 15 ml with MilliQ water and placed at 4°C until analysis. For quality control, certified material (IPE sample ID 949) was also extracted and analyzed (Supplementary Table S2).

2.3.3 Soil sequential extractions

The Community Bureau of Reference sequential extractions were used for elemental analysis in soil samples (Rauret et al., 1999). Briefly, 500 mg of sample were weighed in a centrifuge tube. For the exchangeable fraction, 20 ml of 0.11 M acetic acid (pH 5) was added, and the sample was placed on a horizontal shaker for 16 h. The sample was centrifuged at 3,000 rpm for 20 min, and the supernatant was filtered at 0.45 µm and transferred to another tube. Water was added to the sample for washing, and after 20 min centrifugation at 3,000 rpm the water was discarded. For the reducible fraction, 20 ml of 0.5 M hydroxylamine hydrochloride (pH 2) was added to the sample. After 16 h of shaking, the extract was filtered and transferred to a tube. After the washing step, 5 ml of 8.8 M H_2O_2 was added to the sample to extract the oxidizable fraction. The sample sat for 1 h partially opened, and then placed in a diethylene glycol bath fully opened at 85°C. After 1 h, 5 ml of 8.8 M H_2O_2 were added and heated until completely dried. A total of 25 ml of 1 M ammonium acetate was then added to the sample, which was shaken for 16 h. After transfer of the supernatant to a tube and washing, the sample was dried at 80°C in a heat chamber. A dried residue of 400 mg was weighed in a vessel for total microwave digestion of the residual fraction (see 2.3.1).

2.3.4 Elemental analyses

Elemental concentrations in soil extracts, biotic extracts (leaves, roots of *R. stylosa*, and pneumatophores of *A. marina*), DCB solutions, and porewater were obtained *via* ICP-OES (Varian 730-ES) at the chemistry laboratory LAMA of the French Research Institute for Sustainable Development in New Caledonia. Concentrations were obtained using a calibration curve previously prepared with the right matrices from a stock solution of elements at 100 mg L^{-1}. Certified reference materials were used to calculate a z-score for each element when available (Supplementary Table S1 and Supplementary Table S2). The |z-scores| range from 0.30 to 3.00 for the soil samples and 0.17 and 2.33 for the biotic samples.

2.3.5 Mineralogical analyses

The mineralogical composition of each soil sample was determined by X-Ray Diffraction (XRD), using a PANalytical - AERIS XRD Diffractometer equipped with a Co source at the ISEA laboratory. XRD patterns were recorded between 5 and 80 °2θ, with steps of 0.01, an acquisition time of 480 ms $step^{-1}$, and using a generator power of 600 W. Diffractograms were treated and analyzed with the High Score software. XRD peaks were identified based on the Crystallography Open Database (COD_may22_2019).

2.3.6 Scanning electron microscopy

The petrography of bulk soil samples was performed by SEM using a JEOL JSM-IT 300 LV apparatus coupled with an energy dispersive spectroscopy Oxford CAM 80 device. The measurements were performed at a working distance of 10 mm and an energy of 15 kV.

2.4 Data analyses

2.4.1 Bioconcentration factors and translocation factors

The root and leaf BCF were calculated by dividing the concentration of TM in the tissue by the total mean concentration of TM in the soil between 5 and 20 cm, which corresponds to the depth sections where roots and pneumatophores were collected. The translocation factor (TF) was calculated by dividing the concentration of TM in leaves by the TM concentration in the roots of the same sample.

2.4.2 Iron plaque concentration calculation

The iron plaque was calculated following this equation:

$$Iron\ plaque\ (mg\,kg^{-1}) = \frac{m_{Fe\ in\ DCB}\ (mg)*0.1591}{m_{dried\ pneumatophore}\ (kg)}$$

where 0.1591 is the correction due to the fact that the iron plaque has the formula FeOOH but only Fe is measured in the DCB solution.

2.4.3 Statistical analyses

Statistical analyses were performed using R studio software (version 1.2.5001). For comparison between species or study sites the Mann-Whitney test was performed. All other statistical analyses with more than two variables were tested with a Kruskal–Wallis test followed by a Wilcoxon test. All tests were performed with a 95% confidence interval and n ≥ 3. kendall correlation analyses were performed to obtain correlation matrices.

3 Results

3.1 Physico-chemical parameters

Soil porewater salinity was significantly ($p < 0.001$) lower at the urban site compared to the control site. Soil porewater salinity at the urban site ranged between 0 g L^{-1} and 39 g L^{-1}. At the control site, salinity ranged between 25 and 62 g L^{-1}. Along the soil core of the control site, salinity under *A. marina* (mean = 48 g L^{-1}) was significantly ($p < 0.05$) higher than under *R. stylosa* (mean = 39 g L^{-1}). For both sites and both species, salinity was significantly ($p < 0.05$) lower close to the surface (Figure 2A).

The urban site was significantly ($p < 0.001$) less acidic with a mean pH value of 6.9, compared with the control site, which had a mean pH value of 6.3. At the control site, the pH along the soil

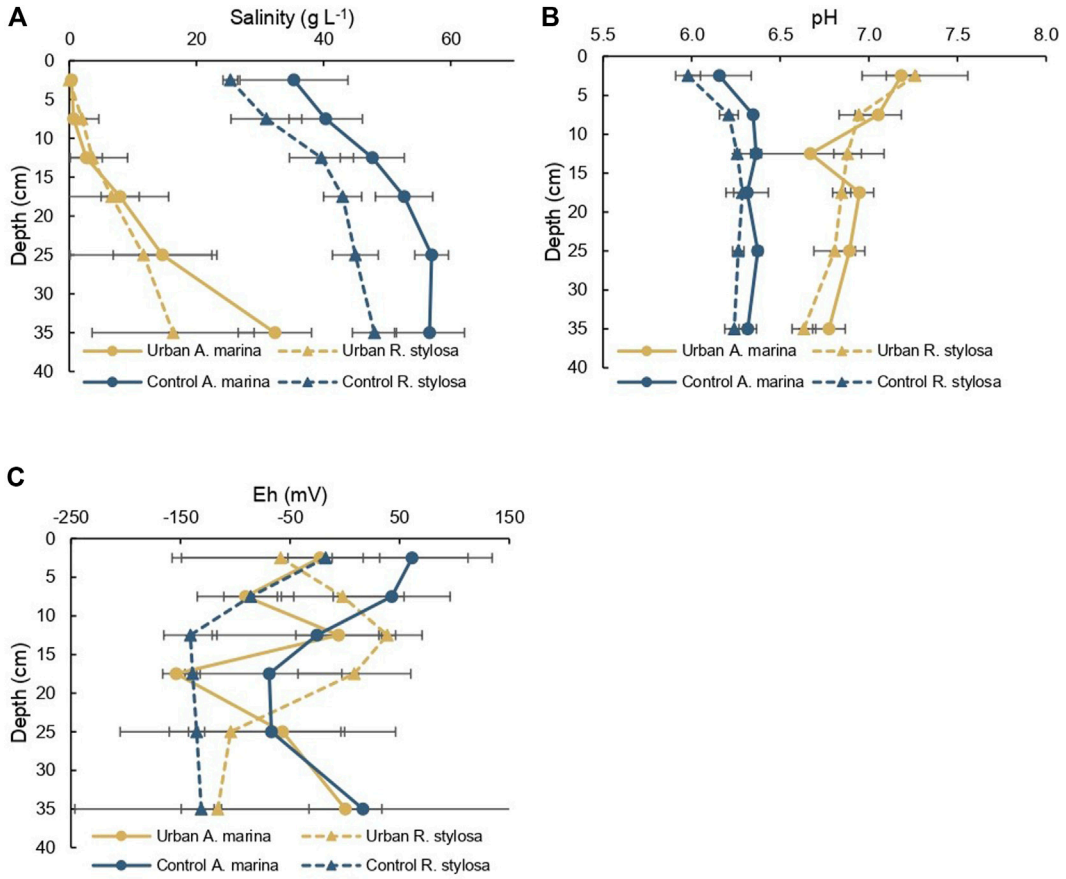

FIGURE 2
Mean values for **(A)** salinity in g L^{-1}, **(B)** pH, and **(C)** Eh in mV along the soil cores of the urban and control sites under both mangrove species (*A. marina* and *R. stylosa*) with error bars corresponding to standard deviation of triplicates.

core was significantly ($p < 0.01$) more acidic beneath *R. stylosa*. At the urban site, the pH was significantly ($p < 0.05$) more basic at the surface than in depth (Figure 2B).

Eh values varied between −214 and 134 mV, and variability among triplicates was high. The Eh of the soil at the control site under *R. stylosa* (mean = −108 mV) was significantly more negative than the soil of the control site under *A. marina* (mean = −7 mV, $p < 0.01$), and the urban site under *R. stylosa* (mean = −39 mV, $p < 0.05$) (Figure 2C).

3.2 Mineralogy

Both sites develop downstream the same geological watershed characterized by a rock basement made of sandstones and limestones rich in quartz (SiO_2). Quartz is the main species present in both mangrove soils. Several minerals from the mangrove soils seem to be also inherited from this substrate in both sites such as illite ($KAl_2Si_4O_{12}$), laumontite ($Ca[AlSi_2O_6]_2$), lizardite ($Mg_3Si_2O_5(OH)_4$) and plagioclase ($Na/Ca[AlSi_3O_8]$), likely albite (Figure 3). Pyrite (FeS_2) was detected at both sites, from the surface to the bottom of the sample soil core at the control site, and only observed at 10 cm and below at the urban site. At the urban site, chlorite ($((Fe,Mg,Al)_6(Si,Al)_4O_{10}(OH)_8$) was observed above 20 cm (Figure 3A). At the control site only, hematite (Fe_2O_3) was also determined (Figure 3B).

3.3 Total elemental concentrations in soil

Most elements in the soil had concentrations significantly higher at the control site compared to the urban site (Table 1). Only, Cu, Pb, Ti beneath both mangrove species, and Mn and Zn beneath *R. stylosa*, were found in significantly higher concentrations in the urban mangrove soil compared with the control site. Under both mangrove species, Fe was the

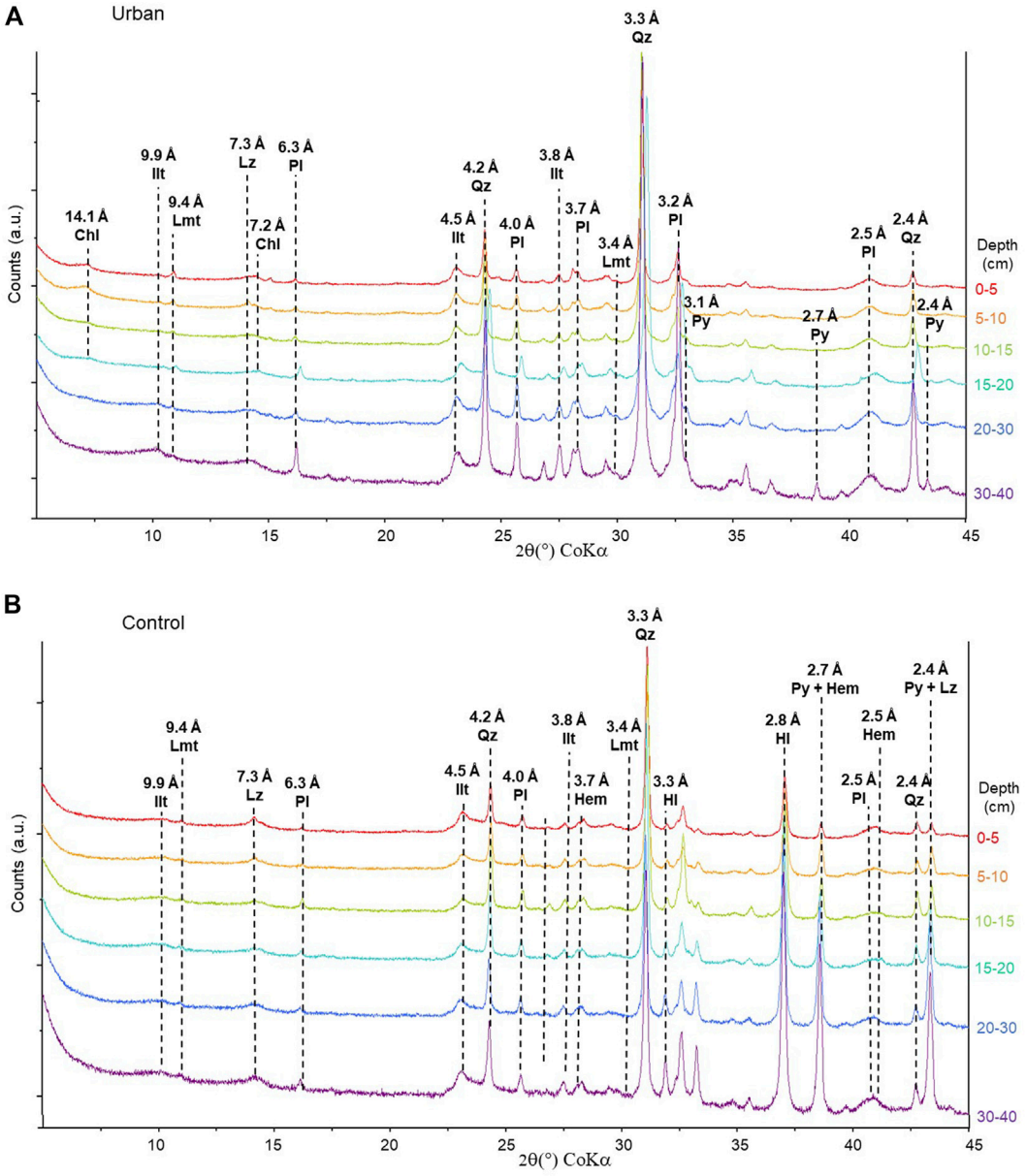

FIGURE 3
XRD diffractograms of the **(A)** urban site and **(B)** control site along soil core with depth and characteristic peaks labelled in d-spacing (Å). Chl–Chlorite, Hl–Halite, Hem–Hematite, Ilt–Illite, Lmt–Laumontite, Lz–Lizardite, Pl–Plagioclase, Py–Pyrite, Qz–Quartz.

most concentrated measured element in the soil, with mean values of 30 g kg^{-1} at the urban site and 49 g kg^{-1} at the control site. The most concentrated TM after Fe at the urban site were Ti and Mn (4.6 and 0.1 g kg^{-1}, respectively), and Ti and Cr at the control site (2.8 and 0.8 g kg^{-1}, respectively). The least concentrated TM at both sites were As and Cd, with mean values of 1.5 and 1.3 mg kg^{-1} at the urban site, and 9.4 and 1.9 mg kg^{-1} at the control site, respectively.

3.4 Elemental soil fractions distribution

At the control site, all TM, except for As, were predominantly measured in the refractory fraction of the soil, representing 41% for Mg and 96% for Al (Figure 4A). At the urban site, Cd and Mg were primarily determined in the exchangeable fraction of the soil with 34% and 46%, respectively; As in the reducible fraction (86%), and Al and Cr in the oxidizable fraction of the soil with 58% and 50%, respectively (Figure 4B). In the exchangeable

TABLE 1 Mean ± SD elemental total concentrations in soil (mg kg^{-1}) from both sites and under both mangrove species with significant differences displayed and Effect Range Low (ERL) and Effect Range Median (ERM) of TM in marine sediments from NOAA.

Site	Urban		Control			
Species	*A. marina*	*R. stylosa*	*A. marina*	*R. stylosa*	ERL	ERM
As***	1.7 ± 1.1	1.4 ± 0.6	8.8 ± 3.4	10 ± 5	8.2	70
Cd***	1.4 ± 0.4	1.1 ± 0.3	1.9 ± 0.3	2.0 ± 0.7	1.2	9.6
Co***	8.9 ± 3.1	8.2 ± 1.4	36 ± 6	37 ± 1		
Cr***	121 ± 60	108 ± 37	797 ± 23	775 ± 115	81	370
Cu***	28 ± 4	25 ± 4	22 ± 3	20 ± 5	34	270
Fe***	32,795 ± 9,640	27,596 ± 5,895	47,611 ± 7,362	50,280 ± 16,463		
K*	10,100 ± 1,032	7,697 ± 189	12,320 ± 634	8,819 ± 152		
Mg***	1,146 ± 513	1,782 ± 867	10,730 ± 927	11,437 ± 1,319		
Mn	125 ± 3	148 ± 27	127 ± 10	125 ± 20		
Na***	8,865 ± 983	10,748 ± 1,503	31,855 ± 1,085	38,872 ± 2,148		
Ni***	37 ± 5	39 ± 8	563 ± 59	498 ± 60	20.9	51.6
Pb***	18 ± 1	17 ± 2	13 ± 0	7.9 ± 0.3	46.7	218
Ti***	4,741 ± 486	4,403 ± 534	3,316 ± 101	2,353 ± 157		
Zn	61 ± 6	63 ± 18	68 ± 2	46 ± 2	150	410

*$p < 0.05$, ***$p < 0.001$ between sites.

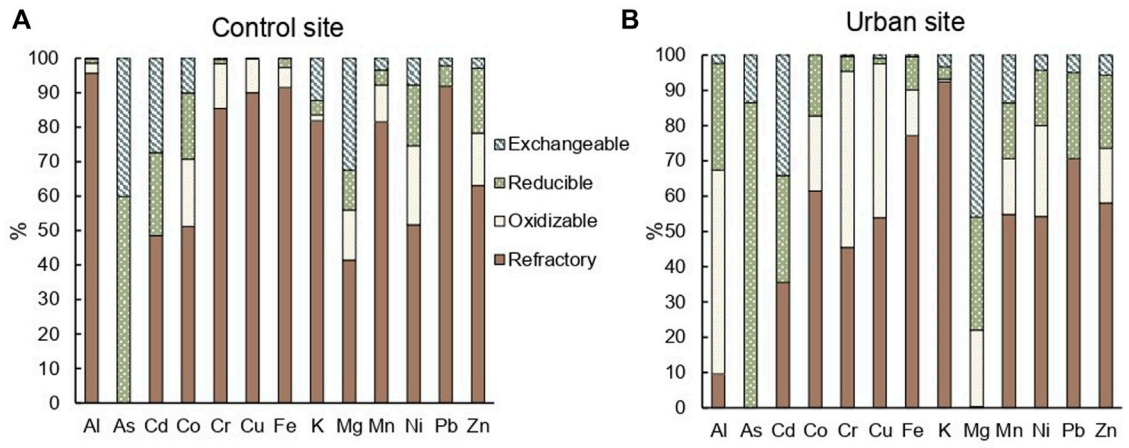

FIGURE 4
Mean percentage composition of elements in each fraction (exchangeable, reducible, oxidizable, refractory) obtained by sequential extractions of the entire soil cores in triplicates at the **(A)** control site and **(B)** urban site.

fraction of the soil, Al, Cu, Fe, and Mn were significantly ($p < 0.05$) more concentrated at the urban site. The same elements and Pb were significantly ($p < 0.01$) more concentrated in the reducible fraction at the urban site. Cu was significantly ($p < 0.001$) more concentrated in the oxidizable fraction at the urban site (Supplementary Table S3). All elements except for As and K were significantly ($p < 0.05$) less concentrated in the refractory fraction of the urban site compared to the control site (Supplementary Table S3).

3.5 Trace metals in biota

Fe was the most concentrated TM in the roots of both species and at both sites with mean concentrations reaching up to 5.1 g kg^{-1} followed by Al with mean values up to 4.1 g kg^{-1}. The least concentrated TM in the roots was Cd with mean values up to 0.2 mg kg^{-1}. Al, Cd, Mn, and Ti were significantly more concentrated in the roots collected at the urban site compared to those collected at the control site (Table 2). At the urban site,

TABLE 2 Mean ± SD TM concentrations in roots and leaves in mg kg^{-1} at both sites for both mangrove species.

Roots

Site	Species	Al*	As	Cd*	Co	Cr	Cu	Fe	Mn*	Ni	Pb	Ti*	Zn
Urban	*A. marina*	1,933 ± 1,514	3.1 ± 1.5	0.2 ± 0.1	2.8 ± 1.4	3.3 ± 1.6	6.1 ± 3.0	2,355 ± 1,668	23 ± 3	7.4 ± 1.9	4.1 ± 1.7	45 ± 30	22 ± 13
	R. stylosa	4,079 ± 2,215	1.9 ± 0.5	0.2 ± 0.1	1.3 ± 0.7	27 ± 36	3.8 ± 1.3	2,943 ± 2,035	115 ± 62	8.7 ± 8.4	4.5 ± 1.5	72 ± 23	12 ± 3
Control	*A. marina*	824 ± 181	2.4 ± 2.2	0.1 ± 0.04	2.2 ± 0.4	11 ± 1	7.0 ± 0.7	5,143 ± 7,414	11 ± 2	14 ± 5	1.5 ± 0.1	37 ± 9	16 ± 9
	R. stylosa	312 ± 153	0.9 ± 0.3	0.03 ± 0.03	1.0 ± 0.6	5.3 ± 2.3	2.9 ± 1.9	403 ± 222	27 ± 25	8.5 ± 5.2	0.6 ± 0.6	12 ± 6	2.4 ± 0.9

Leaves

Site	Species	Al	As	Cd	Co	Cr	Cu	Fe	Mn	Ni**	Pb	Ti	Zn
Urban	*A. marina*	6.2 ± 1.2	1.0 ± 0.4	0.08 ± 0.04	0.2 ± 0.03	0.4 ± 0.1	8.6 ± 0.7	42 ± 2	66 ± 7	1.4 ± 0.1	0	1.6 ± 0.5	14 ± 1
	R. stylosa	29 ± 10	0.5 ± 0.1	0.03 ± 0.02	0.2 ± 0.1	0.3 ± 0.1	4.6 ± 0.6	67 ± 16	321 ± 130	2.1 ± 1.1	0.2 ± 0.2	2.0 ± 0.5	6.5 ± 1.4
Control	*A. marina*	13 ± 1	3.3 ± 1.5	0.04 ± 0.01	0.2 ± 0.02	0.05 ± 0.01	14 ± 6	122 ± 24	33 ± 9	4.3 ± 0.3	0.2 ± 0.3	2.6 ± 0.7	18 ± 3
	R. stylosa	31 ± 44	0.5 ± 0.1	0	0.09 ± 0.05	0.5 ± 0.3	2.6 ± 0.7	45 ± 51	99 ± 9	3.7 ± 0.6	0.6 ± 0.2	1.6 ± 2.0	3.5 ± 2.1

*$p < 0.05$, **$p < 0.01$ between sites.

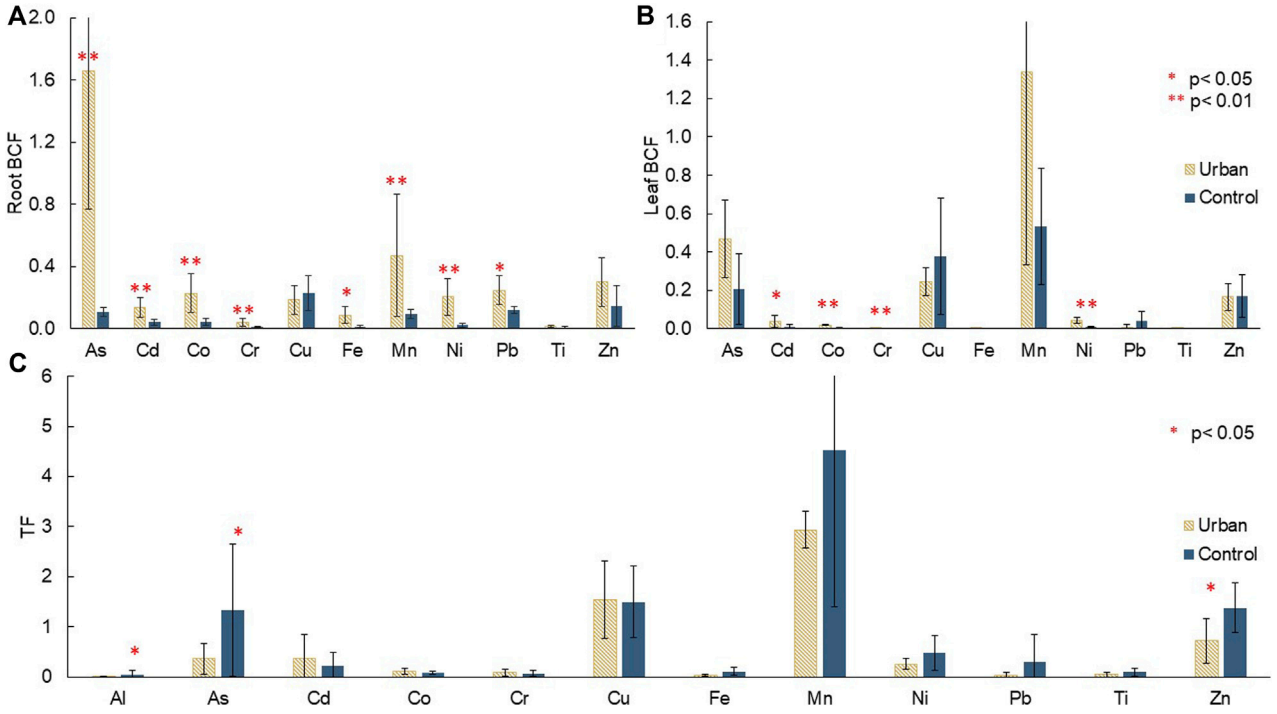

FIGURE 5
Mean **(A)** root bioconcentration factors (root BCF), **(B)** leaf bioconcentration factors (leaf BCF), and **(C)** translocation factors (TF) with error bars corresponding to standard deviation of triplicates for both species (*A. marina* and *R. stylosa*) at the urban and control sites, with significant differences displayed.

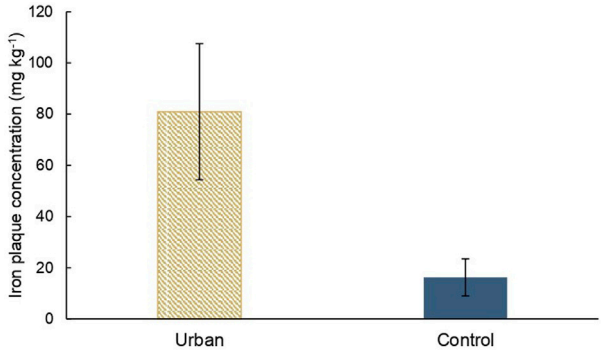

FIGURE 6
Mean iron plaque concentrations on *A. marina* pneumatophores' surfaces (mg kg^{-1}) at both sites with error bars.

Cd, Mn, Ni, and Pb concentrations in the roots were positively correlated to their concentrations in the exchangeable fraction of the soil with r = 0.73, 0.58, 0.47, and 0.47, respectively.

No significant difference was observed between sites for TM concentrations in the leaves, except for Ni, which had higher concentrations at the control site compared with the urban site. Mn and Fe were the most concentrated TM in the leaves with mean concentrations up to 321 and 122 mg kg^{-1}, respectively. Cd, Co, and Pb were the least concentrated in the leaves. At both sites, Mn was more concentrated in the leaves than in the roots. At the control site, Zn was more concentrated in the leaves than in the roots of both species, and As and Cu only for *A. marina* (Table 2).

3.6 Bioconcentration factors and translocation factors

Mean root BCF ranged between 0.008 and 1.7. All TM, except Cu, Ti, and Zn, had significantly higher root BCF at the urban site. This site displayed the highest root BCF for As and Mn with 1.7 and 0.5, respectively. At the control site, Cu and Zn were the most proportionally transferred to the roots with root BCF of 0.23 and 0.14, respectively. Cr and Ti had the lowest root BCF with 0.042 and 0.013 at the urban site, and 0.010 and 0.008 at the control site, respectively (Figure 5A).

Some elements (Cd, Co, Cr, Ni) showed higher leaf BCF at the urban site. The most transferred TM from soil to leaves was Mn with leaf BCF of 1.34 at the urban site and 0.53 at the control site. The least transferred TM were Cr, Fe, and Ti with leaf BCF of 0.003, 0.002, and under detection limit at the urban site, and 0.0005, 0.002, and 0.001 at the control site, respectively (Figure 5B).

A greater proportion of As, Al, and Zn was significantly transferred from roots to leaves at the control site compared to the urban site (Figure 5C). Mn was once again the most transferred with TF values of 2.9 and 4.5 at the urban and control sites, respectively, and Al the least with 0.008 at the urban site and 0.51 at the control site.

3.7 Iron plaque

The iron plaque concentration at the surface of the pneumatophores of *A. marina* at the urban site is significantly higher than at the control site with means value of 81 mg kg^{-1} and 16 mg kg^{-1}, respectively (Figure 6).

4 Discussion

4.1 Soil characteristics of the mangrove forests

Mangrove species zonation at the control site is typical of semi-arid mangrove forests, with *Rhizophora* spp. trees developing on the seaside of the mangrove ecosystem, and *A. marina* developing on the landside at higher elevation. Being less frequently inundated, the soil in *A. marina* stand at the control site is more subjected to evaporation, explaining why porewater salinity was higher (Deborde et al., 2015). These differences in soil porewater salinity between mangrove species were not observed at the urban site. The inputs of urban rainwater runoff during decades, with a salinity of almost zero, disrupt the typical mangrove forests zonation. In fact, at the urban site, *Rhizophora* spp. trees develop also in the landside of the urban mangrove forest where the urban rainwater runoff enters the site. In addition, mangrove trees at the urban site, especially *R. stylosa* trees, are visually much taller than in most mangrove forests in New Caledonia, including the control site. The lower soil porewater salinity can explain this observation as mangrove trees spend less energy to adapt to highly saline conditions and have therefore more energy to spend to growth (Clough, 1984). At both sites, porewater salinity increased with depth, which may result from dilution with rain in the upper layer and salts percolation down the cores (Marchand et al., 2004; Bourgeois et al., 2020).

Beneath *R. stylosa* at the control site, Eh values were low (<100 mv), dissolved Fe concentrations were close to zero (Supplementary Figure S1), and pyrite was observed all along the core, even in the top soil, suggesting that sulphate-reduction was the dominant decay process as early as the first upper centimetres. Conversely at the urban mangrove site, Eh values were less negative, dissolved Fe concentrations reached up to 4,164 µg L^{-1} (Supplementary Figure S1), and pyrite was observed only at depth. Consequently, under *R. stylosa*, conditions were less anoxic at the urban mangrove site and other decay processes, like iron respiration, may dominate in the upper soil.

Despite suboxic conditions in the upper soil, pH values were less acidic than at the control site, and almost basic for some layers. Usually, in mangrove ecosystems, OM decomposition, along with pyrite oxidation, which can both be enhanced in suboxic conditions, induces a soil acidification (Marchand et al., 2004; Kristensen et al., 2017, 2008; Noël et al., 2014). However, in this specific urban mangrove ecosystem, the main pH driver is the amount of rainwater from the urban runoff, as the rainwater collected had a pH higher than 7.

Regarding *A. marina*, it is known that oxic to suboxic conditions usually prevail in the upper soil due to its root system, capable of diffusing O_2 in its rhizosphere (Purnobasuki and Suzuki, 2005; Kristensen et al., 2017). At the control site, Eh values under *A. marina* varied between 61 and -69 mV, and large concentrations of dissolved Fe were measured (3,000–13,000 μg L^{-1}) (Supplementary Figure S1), confirming suboxic conditions. Surprisingly, at the urban site, despite similar redox values, dissolved Fe concentrations were low (114–760 μg L^{-1}) (Supplementary Figure S1). This result may either indicate different OM decay processes or export of dissolved elements from the mangrove soil. However, the absence of pyrite in the upper layer indicates that sulphate-reducing process is limited.

The disturbed mangrove forest zonation, the very low porewater salinity, and the high pH values measured at the urban site are clear indicators of the impact of the urban rainwater runoff on the mangrove forest. TM dynamics in the environment being dependant on these parameters, the partitioning and bioaccumulation of TM in soil and mangrove tissues must be evaluated in the urban and control mangrove sites.

4.2 Trace metals concentrations in mangrove soils

The two mangrove sites studied have a Cretaceous sedimentary watershed, dominated by sandstone and limestone (Service de la Géologie de Nouvelle-Calédonie, 2016), and are therefore less subjected to high concentrations of TM compared to mangrove forests located downstream lateritic soils (Noël et al., 2014). In both the urban and the control mangrove sites, lower soil concentrations of Co, Cr, Fe, Mn, and Ni (characteristic of New Caledonia's lateritic soils) were measured compared to mangrove forests developing downstream mining activities in New Caledonia (Bourgeois et al., 2020; Robin et al., 2021). For instance, Cr and Ni concentrations measured in a mangrove site downstream a lateritic watershed were 17 times and 89 times greater than the mean concentrations at the urban site (Supplementary Table S3) (Robin et al., 2021). However, the studied mangrove sites were still characterized by higher concentrations of Cd, Cr, Fe, and Ni than many mangrove soils in the world such as in Australia, in New Zealand, in Mexico, in China, or in the Sundarbans (Supplementary Table S3) (Chaudhuri et al., 2014; Chowdhury et al., 2015; Bastakoti et al., 2019; Deng et al., 2019; Celis-Hernandez et al., 2020). Cr and Ni soil concentrations at the control site were much higher than the effect range median (ERM), which corresponds to the level of contamination of marine sediments, where biological toxicity effects are generally observed according to the National Oceanic and Atmospheric Administration (NOAA) (Table 1) (Buchman, 1999).

Regarding some TM (As, Cu, Pb, Zn) often associated to urbanization and of major public health concern according to the World Health Organization (Vracko et al., 2007), their concentrations were lower than the effect range low (ERL) (Table 1), a value below which biological toxicity effects are scarcely observed (Buchman, 1999). For instance, As, Cu, Pb, and Zn soil concentrations were up to 10 times lower than in the other mangrove forests of the world such as in China (He et al., 2014; Deng et al., 2019), in Tanzania (Kruitwagen et al., 2008), in Mexico (Celis-Hernandez et al., 2020), or in India (Ray et al., 2006), where extensive urbanization and industrial activities occur (Supplementary Table S3).

The high TM background of New Caledonia must therefore affect both sites, even though they have a sedimentary rocks-dominated watershed (Fernandez et al., 2006; Beliaeff et al., 2011; Maurizot et al., 2020), but the concentrations are well under those measured in mangrove forests directly affected by upstream lateritic soils. In addition, TM associated to urbanization and industrial activities do not reach hazardous concentrations, and are lower than in other urbanized world mangrove forests (Ray et al., 2006; Kruitwagen et al., 2008; He et al., 2014; Cao et al., 2018), implying that a large part of New Caledonia has not reached an alarming state for urban mangrove forest TM contamination.

The two studied sites share the same geological watershed, but the urban site has been influenced by an urban rainwater runoff for decades. It has been observed and mathematically modelled that urbanization leads to an increase in watershed erosion during the construction process, but can then inhibit sediment transport from the upper watershed to the coastal area (Randhir, 2003; O'Driscoll et al., 2010). Therefore, soil erosion and TM transport into the urban mangrove stands from the volcano-sedimentary watershed may be limited, explaining lower concentrations of the majority of TM in the urban mangrove soils. Conversely, at the control site, the presence of hematite, which is generally absent of the New Caledonia volcano-sedimentary watershed (Maurizot et al., 2020), indicates possible inputs from an adjacent watershed composed of lateritic soils (Service de la Géologie de Nouvelle-Calédonie, 2016; Robin et al., 2021). Even though the currents do not directly flow from the lateritic watershed to the control mangrove site (Douillet, 2001), the intense rainfall events that occurred during the rainy season impacted by a La Niña

phenomena, or punctual cataclysmic events such as cyclones, may have induced larger inputs of minerals from the adjacent watershed in this control mangrove soil. For the elements significantly more concentrated at the urban site (Cu, Pb, Ti, Zn), they are typical of urban anthropogenic activities. In the environmental monitoring of the construction of the Dumbéa-sur-Mer allotment, the urban mangrove site showed higher Cu and Zn concentrations than all other monitored mangrove sites in Dumbéa (Ruiz et al., 2020). Cu, Pb, Ti, and Zn are used in many urban items in buildings and transportation. For instance, particles from car brakes increase the amount of Cu in environments close to highways, which is the case for our urban mangrove site (Davis et al., 2001). Cu, Pb, Ti, and Zn are also used in building sidings (e.g., bricks, painted walls), roofs, and tire wear (Davis et al., 2001; Neal et al., 2011; Panagos et al., 2018). These TM can therefore be in higher concentrations in the urban mangrove soils due to greater inputs from the rainwater runoff.

As detailed in the previous section, mangrove soil at the urban site is characterized by suboxic conditions in the upper layer, and anoxic ones at depth. These suboxic conditions in the upper layer result in high TM concentrations in the dissolved phase. In fact, Cr and Fe were significantly more concentrated in the porewater of the urban site beneath *R. stylosa* stand (Supplementary Figure S1). Noël *et al.* (2014) suggested that tidal fluctuations may be a major cause for continuous Fe reduction-oxidation cycles in mangrove soils, which could significantly affect the Fe mass balance with the exports of dissolved Fe in stands closest to the sea. Deborde *et al.* (2015) suggested that the loss of some elements towards the seaside may be related to sulphur oxidation and to more intense tidal flushing of dissolved elements. In the present study, redox conditions induced the presence of high concentrations of dissolved TM, which can be easily exported towards adjacent ecosystems or being subject to plant uptake. These observations could explain in part why concentrations of most TM are lower in the urban mangrove soils compared to the control site.

4.3 Trace metals transfer to mangrove roots

In the mangrove sites studied, root concentrations of Co, Cr, Cu, Fe, Ni, Pb, and Zn were lower than in roots collected downstream highly eroded lateritic soil in New Caledonia (Marchand et al., 2016; Bourgeois et al., 2020; Robin et al., 2021). In fact, Fe and Ni mean root concentrations were 8 and 150 times greater in mangrove plants collected downstream a Ni mine (Bourgeois et al., 2020). However, root concentrations of As, Cr, Fe, and Ni were between 8 and 30 times greater in the present study than in the poorly urbanized mangrove forest of the Sundarbans (Chowdhury et al., 2015), which can be attributed to the high TM background of New Caledonia. Nonetheless, Cu, Pb, and Ti, which are usually associated to urbanization, were 20–40 times more concentrated in the roots of mangrove trees collected in the Sydney harbour, where there is an extensive boat traffic that can cause greater discharge of those TM in the environment (Chaudhuri et al., 2014).

In the urban mangrove site, despite lower TM concentrations in the soil, concentrations of some TM in the roots were higher than at the control site, suggesting different TM uptake mechanisms by the mangrove trees between sites, and/or distinct TM bioavailability in the soil. Al, Cd, Mn, and Ti were between 2 and 5 times more concentrated in the roots collected at the urban site. In addition, root BCF were significantly higher at the urban site, up to 20 times for some TM, with values similar or higher to what is observed in mangrove stands developing downstream highly eroded lateritic soils in New Caledonia (Marchand et al., 2016; Bourgeois et al., 2020).

TM in the exchangeable fraction of the soil are supposedly more bioavailable for plant uptake (Marchand et al., 2016; Bourgeois et al., 2020). Here, in the exchangeable fraction, Al, Cu, Fe, and Mn were significantly more concentrated at the urban site compared to the control site (Supplementary Table S4) explaining higher root BCF at the urban site. In addition, there was a positive correlation between concentrations in the roots and concentrations in the exchangeable fractions of the soil for Cd, Mn, Ni, and Pb in the urban site. This relationship was not observed at the control site possibly because of sulphate-reducing processes and the presence of salt. As soon as TM enters the dissolved phase, they can be trapped immediately either by pyrite (Noël et al., 2017) or salt (Cheng et al., 2014). XRD analysis showed that pyrite was present all along the core at the control site, but only at depth in the urban mangrove site, which has suboxic conditions in top soils. In addition, Ni associated to framboidal pyrite has been observed on SEM at the surface of the control site (Supplementary Figure S2), but not at the urban site. Consequently, mangrove roots at the urban site have more access to TM such as Ni and Cd that are not trapped within pyrite crystals. In addition, soil porewater salinity was significantly lower at the urban site due to the input of urban rainwater. It has been reported that soil salinity affects TM uptake by mangrove roots as Cl-TM complexes can form, which makes it more difficult to absorb by the plant (Cheng et al., 2014). Li et al. (2018) observed high negative correlations between the concentrations of Cd in the roots of a mangrove species and its content of Na and Cl. The urban mangrove soil may form less Cl-TM complexes, favouring TM uptake by mangrove roots. TM bioavailability in the soil seems therefore to be the main factor influencing the transfer to mangrove roots, as previously suggested (Ray et al., 2006; Chaudhuri et al., 2014; Thanh-Nho et al., 2019). A combined analysis with leaf BCF and TF helps identify the role and the biological mechanisms of mangrove trees facing TM bioavailability.

4.4 Trace metals transfer to mangrove leaves

There was no difference in TM concentrations in leaves between the urban and the control mangrove sites, except for Ni, which was more concentrated in the leaves at the control site. Concentrations in leaves of Cr, Pb, and Zn, TM with potentially an urban origin, were at least 5 times lower than what is reported in the literature for a large urban area in Futian, China (He et al., 2014). Regarding TM that mainly originate from lateritic soils in New Caledonia, Co, Fe, and Ni, their concentrations in the leaves of the urban mangrove site were 10 to 50 times lower than in leaves collected downstream an open-cast Ni mine in New Caledonia (Marchand et al., 2016). Therefore, the studied mangrove sites do not seem affected in terms of TM accumulation in the leaves compared to other stressed mangrove forests.

With lower TM total concentrations in the soil, and similar concentrations in the leaves, the urban mangrove trees have higher leaf BCF for Cd, Co, Cr, and Ni. The leaf BCF of Co and Ni were actually greater at the urban site compared to the values obtained in a mangrove forest developing nearby a large urban area in China (He et al., 2014) and compared to a mangrove forest downstream a big city in Vietnam (Thanh-Nho et al., 2019). Ni leaf BCF were also higher than downstream a Ni mine in New Caledonia (Bourgeois et al., 2020). The results suggest that transfer of elements in the leaves, other than macronutrients, are rather negatively correlated to soil concentrations, either because TM are not bioavailable in the soil for plant uptake, or because of biological mechanisms, immobilizing TM in the root system. For example, chelation of TM cations with the roots cell walls can inhibit TM transfer to the vascular bundle, and thus to other organs (MacFarlane et al., 2007). Arbuscular mycorrhizal fungi in symbiosis with mangrove trees in the root system (D'Souza, 2016) can also help prevent TM transfer to the higher organs (Garg and Chandel, 2011; Hassan et al., 2013). For *A. marina*, the formation of an iron plaque at the surface of the roots and pneumatophore can help retain extensive amounts of some TM (Pi et al., 2011; Robin et al., 2021). The results show that there is significantly more iron plaque formation at the surface of the pneumatophores at the urban site. This mechanism limits the uptake of TM in the roots of the urban mangrove trees, and therefore protects the higher tissues from metallic stress.

The measured TF for most TM were similar to those measured in other mangrove forests around the globe, such as in China (Huang X et al., 2020; Zhou et al., 2011), in Hong Kong (Eric, 2003), and in Iran (Rezaei et al., 2021). However, TF were lower in our studied mangrove sites by up to two order of magnitudes, compared to the TF values obtained in the Sundarbans (Ray et al., 2021). The concentrations of Al, Cd, Co, Fe, Pb, and Zn measured in the leaves by Ray et al. (2021) were similar or higher than the concentrations measured in this study, while TM concentrations in the roots were much lower than those measured herein. This result indicates transfer regulation of TM from roots to leaves. Ray et al. (2021) suggested that exceeding nutrients or toxic elements can be excluded from the plant organism *via* litterfall, but the lower TF measured in our study sites suggests that this is not the primary strategy adopted by the mangrove trees in the urban context studied. With similar concentrations in the roots at the urban site, and comparable concentrations in the leaves, TF of most TM were similar at the urban and control sites implying that, even in an urban context, mangrove trees limit the transfer of potentially toxic TM to the higher organs where vital processes occur such as photosynthesis.

Our results show that the urban rainwater runoff increases the bioavailability of TM in the urban mangrove soil compared to the control site by modifying TM bearing phases and soil physico-chemical parameters. Consequently, urbanization, *via* the inputs of urban effluents in the mangrove forest, is a factor able to affect roots uptake. However, its influence on TM transfer from roots to shoots seems to be limited. TM soil concentrations and bearing phases influence primarily the root BCF, while mangrove species biology and physiology regulate TF and accumulation in the leaves.

5 Conclusion

This study provides new insights on the influence of urban rainwater runoff on mangrove forests. The comparison between an urban mangrove forest and a control mangrove forest sharing the same geological watershed demonstrates that the almost continuous runoff of urban rainwater modified the natural physico-chemical properties of the mangrove soil and disrupt TM dynamics. The basic freshwater urban runoff controlled mangrove soil porewater salinity and pH, and induced suboxic conditions influencing TM distribution. Most total TM soil concentrations were lower in the mangrove soil influenced by urbanization due potentially to, on the one hand, watershed urbanization that reduced TM inputs, and on the other hand, to more TM bioavailability resulting from the suboxic conditions. Only Cu, Pb, Ti, and Zn presented higher concentrations in the urban mangrove soils; these TM are known to derive from urban activities and inputs can be attributed to the urban rainwater runoff. The urban rainwater runoff limits salt-TM complexes or pyrite-TM trapping in soil, which can lead to the lower TM bioavailability. The higher bioavailability resulted in higher root bioconcentration factors for both mangrove species, *A. marina* and *R. stylosa*. However, TM concentrations in leaves are similar between the two studied mangrove forests and translocation factors do not differ between sites suggesting a regulation of the transfer of TM to the leaves by

the mangrove trees. In order to improve the understanding of the effects of the urban runoff on the mangrove ecosystem, further analysis should be performed on the nature of the OM in the soil and on TM exports to adjacent coastal waters. A monitoring of various parameters of the urban rainwater runoff should also be done periodically over a year to assess the nature of the inputs in the urban mangrove site.

Data availability statement

The original contributions presented in the study are included in the article/Supplementary material, further inquiries can be directed to the corresponding author.

Author contributions

SR: Conceptualization, Methodology, Investigation, Resources, Writing—Original draft, Writing—Review and editing, Visualization CM: Conceptualization, Methodology, Resources, Writing—Review and editing, Supervision, Funding acquisition MM: Term, Investigation, Writing—Review and editing FB: Investigation, Writing—Review and editing AA: Writing—Review and editing.

Funding

This work was supported by Banque de la Nouvelle-Calédonie, Cegelec, SECAL, and Fibrelec *via* the University of New Caledonia Foundation.

Acknowledgments

The authors acknowledge Kapeliele Gututauava for technical help on site. Aurélie Monin and Olivia Barthélémy are acknowledged for the technical assistance during SEM observations. The authors thank Leocadie Jamet and Monika Lemestre for ICP-OES measurements.

Conflict of interest

The authors declare that the research was conducted in the absence of any commercial or financial relationships that could be construed as a potential conflict of interest.

Publisher's note

All claims expressed in this article are solely those of the authors and do not necessarily represent those of their affiliated organizations, or those of the publisher, the editors and the reviewers. Any product that may be evaluated in this article, or claim that may be made by its manufacturer, is not guaranteed or endorsed by the publisher.

Supplementary material

The Supplementary Material for this article can be found online at: https://www.frontiersin.org/articles/10.3389/fenvs.2022.1054554/full#supplementary-material

References

Alemu, J. B., Richards, D. R., Gaw, L. Y.-F., Masoudi, M., Nathan, Y., and Friess, D. A. (2021). Identifying spatial patterns and interactions among multiple ecosystem services in an urban mangrove landscape. *Ecol. Indic.* 121, 107042. doi:10.1016/j.ecolind.2020.107042

Alongi, D. M. (2002). Present state and future of the world's mangrove forests. *Envir. Conserv.* 29, 331–349. doi:10.1017/S0376892902000231

Bastakoti, U., Bourgeois, C., Marchand, C., and Alfaro, A. C. (2019). Urban-rural gradients in the distribution of trace metals in sediments within temperate mangroves (New Zealand). *Mar. Pollut. Bull.* 149, 110614. doi:10.1016/j.marpolbul.2019.110614

Batty, L. (2000). The effect of pH and plaque on the uptake of Cu and Mn in phragmites australis(cav.) trin ex. Steudel. *Ann. Bot.* 86, 647–653. doi:10.1006/anbo.2000.1191

Bayen, S. (2012). Occurrence, bioavailability and toxic effects of trace metals and organic contaminants in mangrove ecosystems: A review. *Environ. Int.* 48, 84–101. doi:10.1016/j.envint.2012.07.008

Beliaeff, B., Bouvet, G., Fernandez, J.-M., David, C., and Laugier, T. (2011). *Guide pour le suivi de la qualité du milieu marin en Nouvelle-Calédonie, programme ZONECO et programme CNRT Le Nickel.* Nouméa: CNRT Nickel et son environnement.

Bourgeois, C., Alfaro, A. C., Bisson, E., Alcius, S., and Marchand, C. (2020). Trace metal dynamics in soils and plants along intertidal gradients in semi-arid mangroves (New Caledonia). *Mar. Pollut. Bull.* 156, 111274. doi:10.1016/j.marpolbul.2020.111274

Brown, G. E., and Parks, G. A. (2001). Sorption of trace elements on mineral surfaces: Modern perspectives from spectroscopic studies, and comments on sorption in the marine environment. *Int. Geol. Rev.* 43, 963–1073. doi:10.1080/00206810109465060

Buchman, M. F. (1999). *NOAA screening quick reference tables (No. 99–1), HAZMAT report*. Seattle, WA: National Oceanic and Atmospheric Administration.

Cao, C., Wang, L., Li, H., Wei, B., and Yang, L. (2018). Temporal variation and ecological risk assessment of metals in soil nearby a Pb–Zn mine in Southern China. *Int. J. Environ. Res. Public Health* 15, 940. doi:10.3390/ijerph15050940

Cavalcante, R. M., Sousa, F. W., Nascimento, R. F., Silveira, E. R., and Freire, G. S. S. (2009). The impact of urbanization on tropical mangroves (Fortaleza, Brazil): Evidence from PAH distribution in sediments. *J. Environ. Manag.* 91, 328–335. doi:10.1016/j.jenvman.2009.08.020

Celis-Hernandez, O., Giron-Garcia, M. P., Ontiveros-Cuadras, J. F., Canales-Delgadillo, J. C., Pérez-Ceballos, R. Y., Ward, R. D., et al. (2020). Environmental risk of trace elements in mangrove ecosystems: An assessment of natural vs oil and urban inputs. *Sci. Total Environ.* 730, 138643. doi:10.1016/j.scitotenv.2020.138643

Center for International Earth Science Information Network (2012). Population, landscape, and climate estimates. (PLACE), v3 (1990, 2000, 2010) [WWW Document]. NASA Socioeconomic Data and Applications Center. Available at: https://sedac.ciesin.columbia.edu/data/set/nagdc-population-landscape-climate-estimates-v3 (accessed 18 4, 22).

Chakraborty, P., Chakraborty, S., Vudamala, K., Sarkar, A., and Nath, B. N. (2016). Partitioning of metals in different binding phases of tropical estuarine sediments: Importance of metal chemistry. *Environ. Sci. Pollut. Res.* 23, 3450–3462. doi:10.1007/s11356-015-5475-6

Chaudhuri, P., Nath, B., and Birch, G. (2014). Accumulation of trace metals in grey mangrove *Avicennia marina* fine nutritive roots: The role of rhizosphere processes. *Mar. Pollut. Bull.* 79, 284–292. doi:10.1016/j.marpolbul.2013.11.024

Cheng, H., Chen, D.-T., Tam, N. F.-Y., Chen, G.-Z., Li, S.-Y., and Ye, Z.-H. (2012). Interactions among Fe2+, S2−, and Zn2+ tolerance, root anatomy, and radial oxygen loss in mangrove plants. *J. Exp. Bot.* 63, 2619–2630. doi:10.1093/jxb/err440

Cheng, H., Jiang, Z.-Y., Liu, Y., Ye, Z.-H., Wu, M.-L., Sun, C.-C., et al. (2014). Metal (Pb, Zn and Cu) uptake and tolerance by mangroves in relation to root anatomy and lignification/suberization. *Tree Physiol.* 34, 646–656. doi:10.1093/treephys/tpu042

Chowdhury, R., Favas, P. J. C., Pratas, J., Jonathan, M. P., Ganesh, P. S., and Sarkar, S. K. (2015). Accumulation of trace metals by mangrove plants in Indian sundarban wetland: Prospects for phytoremediation. *Int. J. Phytoremediation* 17, 885–894. doi:10.1080/15226514.2014.981244

Clough, B. (1984). Growth and salt balance of the mangroves *Avicennia marina* (Forsk.) Vierh. and Rhizophora stylosa Griff. in relation to salinity. *Funct. Plant Biol.* 11, 419. doi:10.1071/PP9840419

Davis, A. P., Shokouhian, M., and Ni, S. (2001). Loading estimates of lead, copper, cadmium, and zinc in urban runoff from specific sources. *Chemosphere* 44, 997–1009. doi:10.1016/S0045-6535(00)00561-0

Deborde, J., Marchand, C., Molnar, N., Patrona, L., and Meziane, T. (2015). Concentrations and fractionation of carbon, iron, sulfur, nitrogen and phosphorus in mangrove sediments along an intertidal gradient (semi-arid climate, New Caledonia). *J. Mar. Sci. Eng.* 3, 52–72. doi:10.3390/jmse3010052

Deng, J., Guo, P., Zhang, X., Shen, X., Su, H., Zhang, Y., et al. (2019). An evaluation on the bioavailability of heavy metals in the sediments from a restored mangrove forest in the Jinjiang Estuary, Fujian, China. *Ecotoxicol. Environ. Saf.* 180, 501–508. doi:10.1016/j.ecoenv.2019.05.044

Douillet, P. (2001). *Atlas hydrodynamique du lagon sud-ouest de Nouvelle-Calédonie*. Nouméa: Institut national de la recherche et du développement (IRD).

Douillet, P., Ouillon, S., and Cordier, E. (2001). A numerical model for fine suspended sediment transport in the southwest lagoon of New Caledonia. *Coral Reefs* 20, 361–372. doi:10.1007/s00338-001-0193-6

D'Souza, J. (2016). "Arbuscular mycorrhizal diversity from mangroves: A review," in *Recent advances on mycorrhizal fungi, fungal biology*. Editor M. C. Pagano (Cham: Springer International Publishing), 109–116. doi:10.1007/978-3-319-24355-9_10

Duan, D., Lan, W., Chen, F., Lei, P., Zhang, H., Ma, J., et al. (2020). Neutral monosaccharides and their relationship to metal contamination in mangrove sediments. *Chemosphere* 251, 126368. doi:10.1016/j.chemosphere.2020.126368

Eric, T. P. K. (2003). Heavy metals contents in sediments, mangroves and bivalves from Ting Kok, Hong Kong. *China Environ. Sci.* 23, 480–484.

Fernandez, J.-M., Ouillon, S., Chevillon, C., Douillet, P., Fichez, R., and Gendre, R. L. (2006). A combined modelling and geochemical study of the fate of terrigenous inputs from mixed natural and mining sources in a coral reef lagoon (New Caledonia). *Mar. Pollut. Bull.* 52, 320–331. doi:10.1016/j.marpolbul.2005.09.010

Ferreira, T. O., Otero, X. L., Vidal-Torrado, P., and Macías, F. (2007). Effects of bioturbation by root and crab activity on iron and sulfur biogeochemistry in mangrove substrate. *Geoderma* 142, 36–46. doi:10.1016/j.geoderma.2007.07.010

Fritioff, Å., Kautsky, L., and Greger, M. (2005). Influence of temperature and salinity on heavy metal uptake by submersed plants. *Environ. Pollut.* 133, 265–274. doi:10.1016/j.envpol.2004.05.036

Garg, N., and Chandel, S. (2011). "Arbuscular mycorrhizal networks: Process and functions," in *Sustainable agriculture volume 2*. Editors E. Lichtfouse, M. Hamelin, M. Navarrete, and P. Debaeke (Dordrecht: Springer Netherlands), 907–930. doi:10.1007/978-94-007-0394-0_40

Ge, Y., and Li, Z. (2018). Application of lignin and its derivatives in adsorption of heavy metal ions in water: A review. *ACS Sustain. Chem. Eng.* 6, 7181–7192. doi:10.1021/acssuschemeng.8b01345

Harbison, P. (1986). Mangrove muds—a sink and a source for trace metals. *Mar. Pollut. Bull.* 17, 246–250. doi:10.1016/0025-326X(86)90057-3

Hassan, S. E., Hijri, M., and St-Arnaud, M. (2013). Effect of arbuscular mycorrhizal fungi on trace metal uptake by sunflower plants grown on cadmium contaminated soil. *New Biotechnol.* 30, 780–787. doi:10.1016/j.nbt.2013.07.002

He, B., Li, R., Chai, M., and Qiu, G. (2014). Threat of heavy metal contamination in eight mangrove plants from the Futian mangrove forest, China. *Environ. Geochem. Health* 36, 467–476. doi:10.1007/s10653-013-9574-3

Holloway, C. J., Santos, I. R., and Rose, A. L. (2018). Porewater inputs drive Fe redox cycling in the water column of a temperate mangrove wetland. *Estuar. Coast. Shelf Sci.* 207, 259–268. doi:10.1016/j.ecss.2018.04.016

Holloway, C. J., Santos, I. R., Tait, D. R., Sanders, C. J., Rose, A. L., Schnetger, B., et al. (2016). Manganese and iron release from mangrove porewaters: A significant component of oceanic budgets? *Mar. Chem.* 184, 43–52. doi:10.1016/j.marchem.2016.05.013

Huang, S., Jiang, R., Song, Q., Zhang, Y., Huang, Q., Su, B., et al. (2020). Study of mercury transport and transformation in mangrove forests using stable mercury isotopes. *Sci. Total Environ.* 704, 135928. doi:10.1016/j.scitotenv.2019.135928

Huang, X., Wang, X., Li, X., Yan, Z., and Sun, Y. (2020). Occurrence and transfer of heavy metals in sediments and plants of *Aegiceras corniculatum* community in the Qinzhou Bay, southwestern China. *Acta Oceanol. Sin.* 39, 79–88. doi:10.1007/s13131-020-1555-7

Insee (2020). *Population légale de la Nouvelle-Calédonie en 2019*. Institut de la statistique et des études économiques.

International Monetary Fund (2022). *Financial development index database*.

Jayachandran, S., Chakraborty, P., Ramteke, D., Chennuri, K., and Chakraborty, S. (2018). Effect of pH on transport and transformation of Cu-sediment complexes in mangrove systems. *Mar. Pollut. Bull.* 133, 920–929. doi:10.1016/j.marpolbul.2018.03.054

Kristensen, E., Bouillon, S., Dittmar, T., and Marchand, C. (2008). Organic carbon dynamics in mangrove ecosystems: A review. *Aquat. Bot.* 89, 201–219. doi:10.1016/j.aquabot.2007.12.005

Kristensen, E., Connolly, R. M., Otero, X. L., Marchand, C., Ferreira, T. O., and Rivera-Monroy, V. H. (2017). "Biogeochemical cycles: Global approaches and perspectives," in *Mangrove ecosystems: A global biogeographic perspective*. Editors V. H. Rivera-Monroy, S. Y. Lee, E. Kristensen, and R. R. Twilley (Cham: Springer International Publishing), 163–209. doi:10.1007/978-3-319-62206-4_6

Kruitwagen, G., Pratap, H. B., Covaci, A., and Wendelaar Bonga, S. E. (2008). Status of pollution in mangrove ecosystems along the coast of Tanzania. *Mar. Pollut. Bull.* 56, 1022–1031. doi:10.1016/j.marpolbul.2008.02.018

Lee, S. Y., Primavera, J. H., Dahdouh-Guebas, F., McKee, K., Bosire, J. O., Cannicci, S., et al. (2014). Ecological role and services of tropical mangrove ecosystems: A reassessment: Reassessment of mangrove ecosystem services. *Glob. Ecol. Biogeogr.* 23, 726–743. doi:10.1111/geb.12155

Lewis, M., Pryor, R., and Wilking, L. (2011). Fate and effects of anthropogenic chemicals in mangrove ecosystems: A review. *Environ. Pollut.* 159, 2328–2346. doi:10.1016/j.envpol.2011.04.027

Li, J., Yu, J., Yan, C., Du, D., Liu, J., and Lu, H. (2018). Distribution correlations of cadmium to calcium, phosphorus, sodium and chloridion in mangrove *Aegiceras corniculatum* root tissues. *Mar. Pollut. Bull.* 126, 179–183. doi:10.1016/j.marpolbul.2017.10.074

Lin, Y., Fan, J., Yu, J., Jiang, S., Yan, C., and Liu, J. (2018). Root activities and arsenic translocation of *Avicennia marina* (Forsk.) Vierh seedlings influenced by sulfur and iron amendments. *Mar. Pollut. Bull.* 135, 1174–1182. doi:10.1016/j.marpolbul.2018.08.040

MacFarlane, G. R., and Burchett, M. D. (2001). Photosynthetic pigments and peroxidase activity as indicators of heavy metal stress in the grey mangrove, *Avicennia marina* (Forsk.) Vierh. *Mar. Pollut. Bull.* 42, 233–240. doi:10.1016/s0025-326x(00)00147-8

MacFarlane, G. R., and Burchett, M. D. (2002). Toxicity, growth and accumulation relationships of copper, lead and zinc in the grey mangrove *Avicennia marina* (Forsk.) Vierh. *Mar. Environ. Res.* 54, 65–84. doi:10.1016/S0141-1136(02)00095-8

MacFarlane, G. R., Koller, C. E., and Blomberg, S. P. (2007). Accumulation and partitioning of heavy metals in mangroves: A synthesis of field-based studies. *Chemosphere* 69, 1454–1464. doi:10.1016/j.chemosphere.2007.04.059

MacFarlane, G. R. (2002). Leaf biochemical parameters in *Avicennia marina* (Forsk.) Vierh as potential biomarkers of heavy metal stress in estuarine ecosystems. *Mar. Pollut. Bull.* 44, 244–256. doi:10.1016/S0025-326X(01)00255-7

Marchand, C., Baltzer, F., Lallier-Vergès, E., and Albéric, P. (2004). Pore-water chemistry in mangrove sediments: Relationship with species composition and developmental stages (French guiana). *Mar. Geol.* 208, 361–381. doi:10.1016/j.margeo.2004.04.015

Marchand, C., Disnar, J. R., Lallier-Vergès, E., and Lottier, N. (2005). Early diagenesis of carbohydrates and lignin in mangrove sediments subject to variable

redox conditions (French Guiana). *Geochimica Cosmochimica Acta* 69, 131–142. doi:10.1016/j.gca.2004.06.016

Marchand, C., Fernandez, J.-M., Moreton, B., Landi, L., Lallier-Vergès, E., and Baltzer, F. (2012). The partitioning of transitional metals (Fe, Mn, Ni, Cr) in mangrove sediments downstream of a ferralitized ultramafic watershed (New Caledonia). *Chem. Geol.* 300 (301), 70–80. doi:10.1016/j.chemgeo.2012.01.018

Marchand, C., Fernandez, J.-M., and Moreton, B. (2016). Trace metal geochemistry in mangrove sediments and their transfer to mangrove plants (New Caledonia). *Sci. Total Environ.* 562, 216–227. doi:10.1016/j.scitotenv.2016.03.206

Marchand, C., Lallier-Vergès, E., and Allenbach, M. (2011). Redox conditions and heavy metals distribution in mangrove forests receiving effluents from shrimp farms (Teremba Bay, New Caledonia). *J. Soils Sediments* 11, 529–541. doi:10.1007/s11368-010-0330-3

Marchand, C., Virly, S., Buisson, D., and Duke, N. (2007). *Typologies et biodiversité des mangroves de Nouvelle-Calédonie 213*.

Marx, S. K., and McGowan, H. A. (2010). "Long-distance transport of urban and industrial metals and their incorporation into the environment: Sources, transport pathways and historical trends," in *Urban airborne particulate matter, environmental science and engineering*. Editors F. Zereini and C. L. S. Wiseman (Berlin, Heidelberg: Springer Berlin Heidelberg), 103–124. doi:10.1007/978-3-642-12278-1_6

Maurizot, P., Robineau, B., Vendé-Leclerc, M., and Cluzel, D. (2020). Chapter 1 Introduction to New Caledonia: Geology, geodynamic evolution and mineral resources. *Memoirs* 51, 1–12. doi:10.1144/M51-2019-33

Naidoo, G., Hiralal, T., and Naidoo, Y. (2014). Ecophysiological responses of the mangrove *Avicennia marina* to trace metal contamination. *Flora - Morphol. Distribution, Funct. Ecol. Plants* 209, 63–72. doi:10.1016/j.flora.2013.10.003

Neal, C., Jarvie, H., Rowland, P., Lawler, A., Sleep, D., and Scholefield, P. (2011). Titanium in UK rural, agricultural and urban/industrial rivers: Geogenic and anthropogenic colloidal/sub-colloidal sources and the significance of within-river retention. *Sci. Total Environ.* 409, 1843–1853. doi:10.1016/j.scitotenv.2010.12.021

Noël, V., Juillot, F., Morin, G., Marchand, C., Ona-Nguema, G., Viollier, E., et al. (2017). Oxidation of Ni-rich mangrove sediments after isolation from the sea (dumbea Bay, New Caledonia): Fe and Ni behavior and environmental implications. *ACS Earth Space Chem.* 1, 455–464. doi:10.1021/acsearthspacechem.7b00005

Noël, V., Marchand, C., Juillot, F., Ona-Nguema, G., Viollier, E., Marakovic, G., et al. (2014). EXAFS analysis of iron cycling in mangrove sediments downstream a lateritized ultramafic watershed (Vavouto Bay, New Caledonia). *Geochimica Cosmochimica Acta* 136, 211–228. doi:10.1016/j.gca.2014.03.019

Noël, V., Morin, G., Juillot, F., Marchand, C., Brest, J., Bargar, J. R., et al. (2015). Ni cycling in mangrove sediments from New Caledonia. *Geochimica Cosmochimica Acta* 169, 82–98. doi:10.1016/j.gca.2015.07.024

O'Driscoll, M., Clinton, S., Jefferson, A., Manda, A., and McMillan, S. (2010). Urbanization effects on watershed hydrology and in-stream processes in the southern United States. *Water* 2, 605–648. doi:10.3390/w2030605

Panagos, P., Ballabio, C., Lugato, E., Jones, A., Borrelli, P., Scarpa, S., et al. (2018). Potential sources of anthropogenic copper inputs to European agricultural soils. *Sustainability* 10, 2380. doi:10.3390/su10072380

Pi, N., Tam, N. F. Y., and Wong, M. H. (2011). Formation of iron plaque on mangrove roots receiving wastewater and its role in immobilization of wastewater-borne pollutants. *Mar. Pollut. Bull.* 63, 402–411. doi:10.1016/j.marpolbul.2011.05.036

Prasad, M. B. K., Ramanathan, A. L., Shrivastav, S. Kr., and AnshumaliSaxena, R. (2006). Metal fractionation studies in surfacial and core sediments in the Achankovil River basin in India. *Environ. Monit. Assess.* 121, 77–102. doi:10.1007/s10661-005-9108-2

Purnobasuki, H., Purnama, P. R., and Kobayashi, K. (2017). Morphology of four root types and anatomy of root-root junction in relation gas pathway of *Avicennia Marina* (Forsk) Vierh roots. *Vegetos- Inter. Jour. Plnt. Rese.* 30, 100. doi:10.5958/2229-4473.2017.00143.4

Purnobasuki, H., and Suzuki, M. (2005). Functional anatomy of air conducting network on the pneumatophores of a mangrove plant, *Avicennia marina* (Forsk.) Vierh. *Asian J. Plant Sci.* 4, 334–347. doi:10.3923/ajps.2005.334.347

Randhir, T. (2003). Watershed-scale effects of urbanization on sediment export: Assessment and policy. *Water Resour. Res.* 39. doi:10.1029/2002WR001913

Rauret, G., López-Sánchez, J. F., Sahuquillo, A., Rubio, R., Davidson, C., Ure, A., et al. (1999). Improvement of the BCR three step sequential extraction procedure prior to the certification of new sediment and soil reference materials. *J. Environ. Monit.* 1, 57–61. doi:10.1039/a807854h

Ray, A. K., Tripathy, S. C., Patra, S., and Sarma, V. V. (2006). Assessment of Godavari estuarine mangrove ecosystem through trace metal studies. *Environ. Int.* 32, 219–223. doi:10.1016/j.envint.2005.08.014

Ray, R., Mandal, S. K., González, A. G., Pokrovsky, O. S., and Jana, T. K. (2021). Storage and recycling of major and trace element in mangroves. *Sci. Total Environ.* 780, 146379. doi:10.1016/j.scitotenv.2021.146379

Rezaei, M., Kafaei, R., Mahmoodi, M., Sanati, A. M., Vakilabadi, D. R., Arfaeinia, H., et al. (2021). Heavy metals concentration in mangrove tissues and associated sediments and seawater from the north coast of Persian Gulf, Iran: Ecological and health risk assessment. *Environ. Nanotechnol. Monit. Manag.* 15, 100456. doi:10.1016/j.enmm.2021.100456

Robin, S. L., Marchand, C., Ham, B., Pattier, F., Laporte-Magoni, C., and Serres, A. (2021). Influences of species and watersheds inputs on trace metal accumulation in mangrove roots. *Sci. Total Environ.* 787, 147438. doi:10.1016/j.scitotenv.2021.147438

Ruiz, J.-L., Ravary, F., and Debar, L. (2020). *Suivi environnemental des milieux: ZAC PANDA et DSM-année 2019, suivie environnemental sur la ZAC PANDA et DSM*. Dumbéa: SECAL.

Service de la Géologie de Nouvelle-Calédonie (2016). Carte de la géologie de la Nouvelle-Calédonie. [WWW Document]. URL. Available at: https://dtsi-sgt.maps.arcgis.com/apps/webappviewer/index.html?id=da224a6ff1c24c029de4024d7ae8af26 (accessed 12 12, 21).

Silva, C. A. R., Lacerda, L. D., Ovalle, A. R., and Rezende, C. E. (1998). The dynamics of heavy metals through litterfall and decomposition in a red mangrove forest. *Mangroves Salt Marshes* 2, 149–157. doi:10.1023/a:1009923223882

Singh, G., Ranjan, R. K., Chauhan, R., and Ramanathan, A. L. (2010). "Dissolved metal distribution in Indian mangrove ecosystem: Case studies from East Coast of India," in *Management and sustainable development of coastal zone environments*. Editors A. L. Ramanathan, P. Bhattacharya, T. Dittmar, M. B. K. Prasad, and B. R. Neupane (Dordrecht: Springer Netherlands), 212–224. doi:10.1007/978-90-481-3068-9_14

Tardy, Y., and Roquin, C. (1992). "Geochemistry and evolution of lateritic landscapes," in *Weathering soils and paleosols* (Amsterdam: Elsevier), 407–443.

Taylor, G. J., and Crowder, A. A. (1983). Use of the DCB technique for extraction of hydrous Iron oxides from roots of wetland plants. *Am. J. Bot.* 70, 1254–1257. doi:10.1002/j.1537-2197.1983.tb12474.x

Thakur, S., Singh, L., Wahid, Z. A., Siddiqui, M. F., Atnaw, S. M., and Din, M. F. M. (2016). Plant-driven removal of heavy metals from soil: Uptake, translocation, tolerance mechanism, challenges, and future perspectives. *Environ. Monit. Assess.* 188, 206. doi:10.1007/s10661-016-5211-9

Thakur, V. K., Thakur, M. K., Raghavan, P., and Kessler, M. R. (2014). Progress in green polymer composites from lignin for multifunctional applications: A review. *ACS Sustain. Chem. Eng.* 2, 1072–1092. doi:10.1021/sc500087z

Thanh-Nho, N., Marchand, C., Strady, E., Huu-Phat, N., and Nhu-Trang, T.-T. (2019). Bioaccumulation of some trace elements in tropical mangrove plants and snails (Can Gio, Vietnam). *Environ. Pollut.* 248, 635–645. doi:10.1016/j.envpol.2019.02.041

Thomas, N., Lucas, R., Bunting, P., Hardy, A., Rosenqvist, A., and Simard, M. (2017). Distribution and drivers of global mangrove forest change, 1996–2010. *PLoS ONE* 12, e0179302. doi:10.1371/journal.pone.0179302

Thornton, I. (2012). "Geochemical aspects of the distribution and forms of heavy metals in soils," in *Effect of heavy metal pollution on plants: Metals in the environment, pollution monitoring series* (Springer Science & Business Media), 258.

Tremel-Schaub, A., and Feix, I. (2005). *Contamination des sols : Transferts des sols vers les plantes*. EDP Sciences.

Turekian, K. K., and Wedepohl, K. H. (1961). Distribution of the elements in some major units of the Earth's crust. *Geol. Soc. Am. Bull.* 72, 175. doi:10.1130/0016-7606(1961)72[175:DOTEIS]2.0.CO;2

Valiela, I., Bowen, J. L., and York, J. K. (2001). Mangrove forests: One of the world's threatened major tropical environments. *BioScience* 51, 807. doi:10.1641/0006-3568(2001)051[0807:mfootw]2.0.co;20807:MFOOTW]2.0.CO;2

Vracko, P., Tuomisto, J., Grad, J., and Kunseler, E. (2007). *Exposure of children to chemical hazards in food*. European Environment and Health Information System.

Yamaguchi, N., Ohkura, T., Takahashi, Y., Maejima, Y., and Arao, T. (2014). Arsenic distribution and speciation near rice roots influenced by Iron plaques and redox conditions of the soil matrix. *Environ. Sci. Technol.* 48, 1549–1556. doi:10.1021/es402739a

Zhou, Y., Peng, Y., Li, X., and Chen, G. (2011). Accumulation and partitioning of heavy metals in mangrove rhizosphere sediments. *Environ. Earth Sci.* 64, 799–807. doi:10.1007/s12665-011-0904-4

Frontiers in
Environmental Science

Explores the anthropogenic impact on our natural world

An innovative journal that advances knowledge of the natural world and its intersections with human society. It supports the formulation of policies that lead to a more inhabitable and sustainable world.

Discover the latest Research Topics

See more →

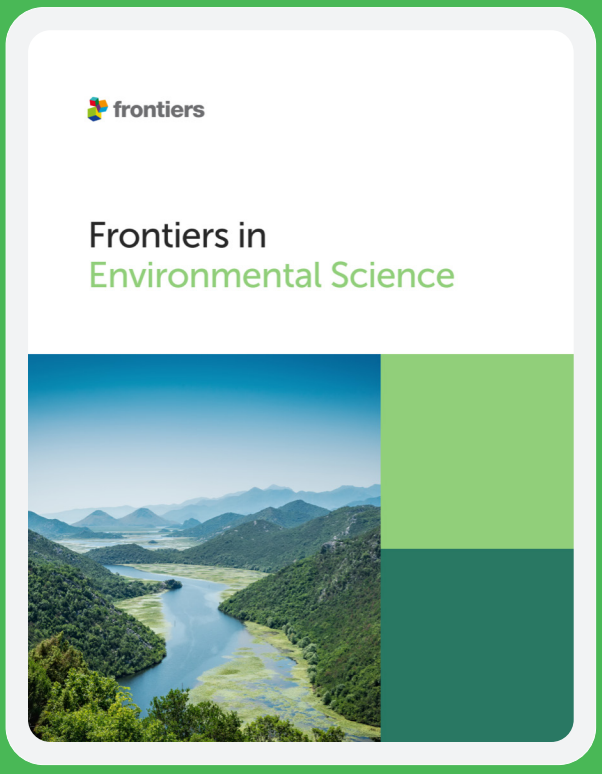

Frontiers

Avenue du Tribunal-Fédéral 34
1005 Lausanne, Switzerland
frontiersin.org

Contact us

+41 (0)21 510 17 00
frontiersin.org/about/contact